

Lecture Notes in Mechanical Engineering

Prita Pant
Sushil K. Mishra
Purna Chandra Mishra *Editors*

Advances in Mechanical Processing and Design

Select Proceedings of ICAMPD 2019

 Springer

Lecture Notes in Mechanical Engineering

Series Editors

Francisco Cavas-Martínez, Departamento de Estructuras, Universidad Politécnica de Cartagena, Cartagena, Murcia, Spain

Fakher Chaari, National School of Engineers, University of Sfax, Sfax, Tunisia

Francesco Gherardini, Dipartimento di Ingegneria, Università di Modena e Reggio Emilia, Modena, Italy

Mohamed Haddar, National School of Engineers of Sfax (ENIS), Sfax, Tunisia

Vitalii Ivanov, Department of Manufacturing Engineering Machine and Tools, Sumy State University, Sumy, Ukraine

Young W. Kwon, Department of Manufacturing Engineering and Aerospace Engineering, Graduate School of Engineering and Applied Science, Monterey, CA, USA

Justyna Trojanowska, Poznan University of Technology, Poznan, Poland

Lecture Notes in Mechanical Engineering (LNME) publishes the latest developments in Mechanical Engineering—quickly, informally and with high quality. Original research reported in proceedings and post-proceedings represents the core of LNME. Volumes published in LNME embrace all aspects, subfields and new challenges of mechanical engineering. Topics in the series include:

- Engineering Design
- Machinery and Machine Elements
- Mechanical Structures and Stress Analysis
- Automotive Engineering
- Engine Technology
- Aerospace Technology and Astronautics
- Nanotechnology and Microengineering
- Control, Robotics, Mechatronics
- MEMS
- Theoretical and Applied Mechanics
- Dynamical Systems, Control
- Fluid Mechanics
- Engineering Thermodynamics, Heat and Mass Transfer
- Manufacturing
- Precision Engineering, Instrumentation, Measurement
- Materials Engineering
- Tribology and Surface Technology

To submit a proposal or request further information, please contact the Springer Editor of your location:

China: Dr. Mengchu Huang at mengchu.huang@springer.com

India: Priya Vyas at priya.vyas@springer.com

Rest of Asia, Australia, New Zealand: Swati Meherishi at swati.meherishi@springer.com

All other countries: Dr. Leontina Di Cecco at Leontina.dicecco@springer.com

To submit a proposal for a monograph, please check our Springer Tracts in Mechanical Engineering at <http://www.springer.com/series/11693> or contact Leontina.dicecco@springer.com

Indexed by SCOPUS. All books published in the series are submitted for consideration in Web of Science.

More information about this series at <http://www.springer.com/series/11236>

Prita Pant · Sushil K. Mishra ·
Purna Chandra Mishra
Editors

Advances in Mechanical Processing and Design

Select Proceedings of ICAMPD 2019

 Springer

Editors

Prita Pant
Department of Metallurgical Engineering
and Materials Science
Indian Institute of Technology Bombay
Mumbai, Maharashtra, India

Sushil K. Mishra
Department of Mechanical Engineering
Indian Institute of Technology Bombay
Mumbai, Maharashtra, India

Purna Chandra Mishra
School of Mechanical Engineering
KIIT Deemed to be University
Bhubaneswar, Odisha, India

ISSN 2195-4356 ISSN 2195-4364 (electronic)
Lecture Notes in Mechanical Engineering
ISBN 978-981-15-7778-9 ISBN 978-981-15-7779-6 (eBook)
<https://doi.org/10.1007/978-981-15-7779-6>

© Springer Nature Singapore Pte Ltd. 2021

This work is subject to copyright. All rights are reserved by the Publisher, whether the whole or part of the material is concerned, specifically the rights of translation, reprinting, reuse of illustrations, recitation, broadcasting, reproduction on microfilms or in any other physical way, and transmission or information storage and retrieval, electronic adaptation, computer software, or by similar or dissimilar methodology now known or hereafter developed.

The use of general descriptive names, registered names, trademarks, service marks, etc. in this publication does not imply, even in the absence of a specific statement, that such names are exempt from the relevant protective laws and regulations and therefore free for general use.

The publisher, the authors and the editors are safe to assume that the advice and information in this book are believed to be true and accurate at the date of publication. Neither the publisher nor the authors or the editors give a warranty, expressed or implied, with respect to the material contained herein or for any errors or omissions that may have been made. The publisher remains neutral with regard to jurisdictional claims in published maps and institutional affiliations.

This Springer imprint is published by the registered company Springer Nature Singapore Pte Ltd. The registered company address is: 152 Beach Road, #21-01/04 Gateway East, Singapore 189721, Singapore

Preface

This International Conference on Advances in Mechanical Processing and Design-2019 (ICAMPD-2019) held in the School of Mechanical Engineering inside the beautiful campus of KIIT Deemed to be University, Bhubaneswar, Odisha, India, during 18–20 October 2019. With the pure flame of education, a visionary educationalist Dr. Achyuta Samanta established KIIT Deemed to be University, formerly Kalinga Institute of Industrial Technology, is a co-educational autonomous university located at Bhubaneswar in the eastern state of Odisha, India. It was established in 1992 as an Industrial Training Institution which was developed to KIIT Deemed to be University in 2004. It was one of the youngest institutions to be awarded the deemed university status in India and then the university status in 2004 and is recognized by Limca Book of Records. All the academic programmes are accredited by NAAC of UGC and NBA as per Washington Accord of AICTE, which are benchmarks of excellence. NAAC (government agency to evaluate universities) has awarded KIIT the highest grade of “A” with a CGPA of 3.36/4. KIIT Deemed to be University recently achieved the tag of Institution of Eminence (IoE) by the MHRD, Government of India. The School of Mechanical Engineering, established in the year 1997, produces graduates who can meet the rapidly changing needs of industry which demand new skills. Current consultancy and research and development areas of the school include residual stresses in fusion welded structure, surface finish optimization by high-pressure impingement cooling and CAD modelling. Material processing technology, cleaner manufacturing technology, renewable energy, automotive engineering and quality engineering and management are the other areas of interest. Research and development efforts of the school are supported by bodies like ARDB, BRNS, AICTE and DST, Government of India.

This book presents selected proceedings of the “International Conference on Advances in Mechanical Processing and Design-2019” (ICAMPD-2019) and highlights research hotspots in the next-generation mechanical system design, thermal and fluid system design, materials and smart manufacturing processes and industrial engineering. This field covers the topics which include modern-age smart materials, materials processing and applications, smart machinery and machine

design, system dynamics and simulation, biomimics, energy system, micro- and nanoscale transport, automotive engineering, advance material characterization and testing, green manufacturing, intelligent systems, human factors, production planning & control, etc. This book also provides the meaningful research content along with various applications to stimulate the intellectual excitement of the researchers. This proceedings book can be an imperative reference for researchers, professionals and industry personnel to take their research up to next echelon for proficient professional practice.

Efforts taken by peer reviewers contributed to improve the quality of manuscripts provided constructive critical comments, improvements and corrections to the authors are gratefully appreciated. We are very much grateful to the International/National Advisory Committee, session chairs, student volunteers and administrative assistants from institute management who selflessly contributed to the success of this conference. Also, we are thankful to all the authors who submitted papers, because of which the conference became a history of success. It was the quality of their presentations and their passion to communicate with the other participants that really made this conference a great success.

Last but not the least, we are thankful to Springer Nature for supporting us in every step of our journey towards success. Their cooperation was not only the strength but also an inspiration for the organizers.

Edited by:

Prof. Purna Chandra Mishra

Prof. Prita Pant

Prof. Sushil Kumar Mishra

Bhubaneswar, India

Prof. (Dr.) Purna Chandra Mishra
Conference Co-Chair-ICAMPD 2019
pcmishrafme@kiit.ac.in

Contents

Thermal and Fluid System Design

Comparative Study of Analytical and Simulation Method in Determination of Fuel Centerline and Clad Surface Temperature of Metallic Nuclear Fuel	3
Suman Saurav, M. Muthuganesh, P. K. Chaurasia, and S. Murugan	
CFD Analysis of Two-Phase Cavitating Flow in a Centrifugal Pump with an Inducer	17
Debarpan Paul, Himanshu Agarwal, and Babu Rao Ponangi	
Influence of Mass Flow Rate and Concentration of Al₂O₃ Nanofluid on Thermal Performance of a Double Pipe Heat Exchanger	33
Vikas Gulia and Anirban Sur	
Impact of Inlet Angle on Cooling of a Continuously Variable Transmission in a BAJA SAE Vehicle	47
Amitabh Das, Tarashekhar Padhy, and Kannan Chidambaram	
Coaxial Thermal Probe as a Heat Flux Sensor: An Analytical, Numerical, and Experimental Approach	57
Anil Kumar Rout, Nirranjan Sahoo, and Pankaj Kalita	
Thermo-economic and Environmental Analyses of Full Site Repowering Through Coal Gasification and Carbon Capture by Downstream MCFC Integration	67
Samiran Samanta and Sudip Ghosh	
Vortex Formation During Liquid Draining from a Cylindrical Tank with Conical Bottom—A Numerical Study	83
K. Sreenath, Mahadev Prabhu, R. Ajith Kumar, J. S. Jayakumar, and P. J. Joshy	

Evaluation of Noise and Air Pollution During Diwali in Berhampur City, India: An Inclusive Annoyance Study	95
A. K. Sahu, S. K. Nayak, J. K. Mohanty, P. K. Pradhan, and C. R. Mohanty	
Performance and Analysis of Phase Change Material by Using Hybrid Nanofluid (Zinc Cobalt Iron Oxide) on Thermal Energy Storage Device	107
Harish Kumar Sharma, Satish Kumar, and Mani Kant Paswan	
A Numerical Experiment on Thermo-fluidic Transport of Third-Grade Fluid Flow Through a Porous Microchannel Under the Influence of Combined Electromagnetohydrodynamic Effect	115
Motahar Reza, Amalendu Rana, and Raghunath Patra	
Experimental Investigation of Performance and Emissions of Single-Cylinder Diesel Engine Enriched by Hydroxy Gas for Various Compression Ratios	127
Manoj Dahake, Shrishant Patil, and Dileep Malkhede	
Biomethanation of Aloe Vera Waste for Energy Production	139
Diksha Srivastava, Deepak Sharma, and Nafisa Ali	
Heat Transfer and Pressure Drop Assessment of a Vortex Generator Supported Fin-And-Tube Heat Exchanger	149
Shailesh Kumar Sarangi, Nikhil Anand, Kushagra Srivastava, Pankaj Chamoli, Dipti Prasad Mishra, and Lakhbir Singh Brar	
Computational Modeling to Investigate the Heat Transfer Enhancement by Using Ethyl Glycol–Water–MWCNT Nanofluid Through Corrugated Pipe	161
Prakash Ghose and Rishitosh Ranjan	
Numerical Analysis of a Steady Turbulent Flow Over a Backward-Facing Step with Varying Step Angles Using OpenFOAM	171
R. S. Sarath and K. Arunkumar	
Investigation of Flow Structures Around a Circular Cylinder with Notch: A Flow Visualization Analysis	181
K. Arunkumar and R. S. Sarath	
Comparative Study on Gasoline and Methanol in a Twin Spark IC Engine	191
A. S. Divakar Shetty, Debjyoti Sahu, J. Arthur Davis, and Ravi Kumar	
Coal Water Slurry Flow in Pipelines Using Homogeneous Equilibrium Model	203
Anupama Routray, Aditya Abinash, M. K. Padhy, and Sudhansu S. Sahoo	

Two-Phase Flow Analysis in Elbow Bend Pipe Used in Oil Extraction Process: A Computational Approach	213
Aditya Abinash, Sudhansu S. Sahoo, and Raj Kumar Saini	
Aspects of Heat Transfer Augmentation Using Nanofluids as Coolant in Fusion Reactors: A Brief Review	227
Sayantan Mukherjee, Purna Chandra Mishra, Sayan Jana, Paritosh Chaudhuri, and Shanta Chakrabarty	
Investigation on Ranque–Hilsch Vortex Tube Using Different Turbulence Models	237
Satpreet Singh, K. P. Sinhamahapatra, and Nilotpala Bej	
Materials and Smart Manufacturing Processes	
Development of Bio-Material (Tiger Grass-Reinforced Gaur Gum Matrix Composite) for an Alternative Bio-Based Cutlery for Food Service Applications	247
Rahul Kurdekar, N. R. Banapurmath, S. A. Hallad, Arun Y. Patil, Ravi Guttal, Ashok S. Shettar, and Sachin Arakeri	
A Concise View Point on Effects of Agro and Industrial Waste as Reinforcement on Characteristic Properties of Aluminum Alloy-Based Metal Matrix Composites	261
Panda Sasank Shekhar, Senapati Ajit Kumar, and P. Srinivasa Rao	
A Study on Performance of Hydroxyapatite-Filled Polycarbonate and Polysulfone Composites Under Two-Body Abrasive Wear	271
Amit Kumar Mehar and Sreekanth Kotni	
Optimization of Laser Hardening Process Parameters for Cast Iron Using a Design of Experiment Method	293
Santoshkumar V. Wagh, Dhananjay V. Bhatt, Jyoti V. Menghani, and Sujit S. Pardeshi	
FMECA Analysis and Condition Monitoring of Kneader in Green Anode Plant of an Aluminium Smelter	305
J. K. Mohanty, I. Hota, P. Sarkar, A. K. Sahu, P. R. Dash, and P. K. Pradhan	
Effect of Hot Rolling on Physical and Mechanical Properties of Al 6061 Alloy-Based Metal Matrix Composite	319
Senapati Ajit Kumar, Panda Sasank Shekhar, and Mohanty Gopal Krushna	
Blast Mitigation Analysis of Clay Brick Masonry Wall	331
P. A. Shirbhate, Jagriti Mandal, and M. D. Goel	

Interdependence of Morphological, Mechanical and Fracture Behaviour of Toughened Bio-Based Polyamide 11	339
Saroj Kumar Samantaray, Shushil Kumar Gope, and Bhabani Kumar Satapathy	
Fabrication of Chitosan–Carboxymethyl Cellulose Silver Nanocomposite Films as Antimicrobial Materials	351
Mamata Das, Ganeswar Sahu, and Jasaswini Tripathy	
Multi-objective Optimization of EDM Process Parameters on Al-7075-Based Hybrid MMCs	361
Sudhansu Sekhar Singh, Ashutosh Satpathy, and Sasmita Kar	
Parametric Optimization of CNC Milling of Al-7075 Based MMCs	377
Ashutosh Satpathy, Sudhansu Sekhar Singh, and Sasmita Kar	
Tribo-Behaviour of Tin-Based Dry Bearing Material	389
Priya S. Gajjal	
Optimization of Process Parameters for Wired Electro-Discharge Machining of Titanium Based Hybrid Compo-Sites Using Response Surface Methodology	399
Soutrik Bose, Samiran Samanta, Vibhav, Prashant Bharti, and Titas Nandi	
Interaction of Ru-4'-(2-pyridyl)- 2,2':6',2''-Terpyridine with Diseased HER2 Protein	413
Satya Narayan Sahu, Tejaswini Sahoo, Biswajit Mishra, Subrat Kumar Pattanayak, and Rojalin Sahu	
Morphology and Mechanical Properties of Polyamide 12/polypropylene/multiwalled Carbon Nanotubes Nanocomposites	421
Sucharita Sethy and Bhabani K. Satapathy	
Effect of Cold Work on Microstructure and Corrosion Properties of 304L Stainless Steel	433
Asit Behera, Bikram Behera, D. K. Sahoo, Ashutosh Pattnaik, K. N. Barik, Priyabrata Mallick, Subrat Bhuyan, S. C. Mishra, and Ajit Behera	
Comparative Study of Mechanical Properties of Natural Fibers	441
Mukesh and S. S. Godara	
Parametric Appraisal of CNC Micro-drilling of Aerospace Material (PMMA) Using Taguchi-Based EDAS Method	449
Dilip Kumar Bagal, Sakti Kishore Panda, Abhishek Barua, Siddharth Jeet, Ajit Kumar Pattanaik, and Dulu Patnaik	
Multi-parametric Optimization of Wire-EDM of Inconel 718 Super Alloy Using Taguchi-Coupled WASPAS Method	459
Dilip Kumar Bagal, Santanu Kumar Mahapatra, Abhishek Barua, Siddharth Jeet, Ajit Kumar Pattanaik, and Dulu Patnaik	

Effect of Graphene Oxide and Temperature on Dielectric Relaxation Behavior of Poly(Vinyl Alcohol)-Based Nanocomposite	469
Ganeswar Sahu, Bibhu Prasad Sahoo, and Jasaswini Tripathy	
Effect of Sheet Temperature on Thickness Distribution of the Thermoformed Hemispherical Dome	479
Jeet P. Patil, Yogesh S. Gaikhe, Vilas Nandedkar, and Sushil Mishra	
A Review of Current Researches on Powder Mixed Electrical Discharge Machining (PMEDM) Technology	489
Pradipta Kumar Rout and Pankaj Charan Jena	
Understanding the Deformation Micro-mechanism in Ti-6Al-4V Alloy U-Notched Specimen	499
Hitarth Maharaja, Satyaprakash Mishra, Pawan Patel, Sushil K. Mishra, and Jyoti S. Jha	
Influence of Annealing Time on Local Texture Evolution in Forged Ti-6Al-4V Alloy	507
Satyaprakash Mishra, Hitarth Maharaja, Sushil K. Mishra, Jitesh Vasavada, and Jyoti S. Jha	
SUS304 Material Coating with Nickel Through Electroplating	515
D. Nurhadiyanto, Mujiyono, W. Abbas, Sutopo, and S. Haruyama	
Three-dimensional FE Model for Stress Analysis of Adhesively Bonded Single Lap Joints with Hard Steel Adherend	523
Ranjan K. Behera, S. K. Parida, and R. R. Das	
Numerical Simulation of Sand Casting Process: A Case Study on Globe Valve	533
Yash Mittal, Nikhil Parasar, Jambeswar Sahu, Umakant Mishra, and Chinmaya P. Mohanty	
Effect of Polarity on MRR and TWR in Electric Discharge Machining	543
Jambeswar Sahu, Sonam Shrivastava, Chinmaya Mohanty, Swagatika Mishra, and Tapan Kumar Mahanta	
Design of a Torque Controller with Application to a Single Degree of Freedom Haptic Device	551
Saurav Kumar Dutta, Jithin Krishnan Balathil, Paluchani Anirudh Reddy, and Annem Narayana Reddy	
Surface Gas Nitriding of Titanium (Ti-6Al-4V) Alloy	561
Shanta Chakrabarty, Smita R. Panda, Sonal, Jyoti S. Jha, and Sushil K. Mishra	

Mechanical Systems Design

- Navigation Method for Pioneer P3-DX Ground Wheeled Robot in V-REP Platform Using Type-2 Fuzzy Neural Network (T2FNN) Architecture** 571
Anish Pandey, Arnab Guha, Ambesh Kumar, Nilotpala Bej, and Dayal R. Parhi
- Design and Analysis of Weld Bead Cutting Tool Using FEA Technique with Experimental Verification of Cutting Force** 581
Santosh Kumar
- Design, Fabrication of Human-Powered Vehicle** 593
Pratik Kale and Pankaj Ardak
- Detection of Breathing Crack Using Vibration Signal Analysis** 599
Smaranika Nayak, Jatin Sadarang, Manisha Maurya, and Isham Panigrahi
- Wear Behavior of Orange Peel Reinforced Epoxy Composite** 607
P. Naik, S. Pradhan, S. K. Acharya, and P. Sahoo

Industrial Engineering

- Design and Implementation of a Safety Poka-Yoke for Workers Safety: A Case Study** 619
Nitin S. Solke and Anirban Sur
- Identifying the Features Influencing Sustainable Products: A Study on Green Cosmetics** 631
Akankshya Patnaik, Sushanta Tripathy, and Aishwarya Dash
- A Framework of Lean–Six Sigma: An Evolutionary Approach** 641
Biswajit Mohapatra, Aneesh Kuruvilla, Aishwarya Dash, and Sushanta Tripathy
- Study of Customer Relationship Management in Automobile Industry** 649
Lalit Kumar Pothal, Sushanta Tripathy, Kaustuv Kumar, and Aishwarya Dash
- Supplier Relationship Management Is a Key to Supply Chain Management** 661
Purab Mohapatra, Sushanta Tripathy, Aishwarya Dash, and Anshumaan Biswal
- Identification of Factors Influencing Mental Workload in Manual Sorting** 671
N. Sai Rama Krishna Harish, Madineni Vamshi, K. Bhanu Prakash, Putta Ezra, Francis J. Emmatty, and Vinay V. Panicker

About the Editors

Dr. Prita Pant received her MS and PhD degrees from the Materials Science and Engineering department at Cornell University (USA) in 2001 and 2004 respectively. After postdoctoral research at Cornell and Harvard Universities, she joined IIT Bombay as Assistant Professor in the Department of Metallurgical Engineering and Materials Science at IIT Bombay in 2006. She is currently Professor in the same department, and Associate Dean of Academic Programmes. Her research interests are in the general area of microstructure changes that occur during deformation, and their effect on the mechanical behaviour of materials. Her group carried out experiments on bulk and micro-scale deformation, along with optical and electron microscopy to investigate the evolution in microstructure. In addition, they work extensively on simulations such as dislocation dynamics (DD) and molecular dynamics (MD) to study the nucleation of defects such as dislocations, and their interactions with each other as well as with grain and twin boundaries. These interactions play a significant role in determining the strength and ductility of metals and alloys. She has guided 6 PhD students, and several Masters students at IIT Bombay. She teaches both undergraduate and postgraduate courses on mechanical behaviour, computational methods, and scientific communication.

Dr. Sushil K. Mishra is currently Associate Professor in the Department of Mechanical Engineering, IIT Bombay. Prior to this, he worked as Senior Manager in Aditya Birla Science and Technology Center, Mumbai and as senior researcher at General Motors Global R&D, Bangalore. He obtained his doctorate from IIT Bombay in 2008 and M. Tech. from IIT Madras in 2002. He has more than four years of postdoctoral research experience in corporate R&D. The focus of his research is multiscale physics based formability studies of metallic alloys. Currently he is heading Micro-Forming lab (www.microforming.in) in IIT Bombay, where more than 15 postgraduate students are working in the area of forming, microstructure, microtexture and materials modeling. He has published more than 40 peer reviewed international journal papers and holds 3 patents. Under his supervision 5 PhD and 13 Masters students have graduated, and currently 15 students are working under him in various sponsored projects. His major areas of

research are sheet metal forming, deformation behavior of metallic alloys, microstructure and mechanical characterization, and materials modelling.

Dr. Purna Chandra Mishra is currently working in the School of Mechanical Engineering, KIIT University, Bhubaneswar as a Professor and Dean (Research). He has held important positions like, Convener of Board of Studies (BoS), Associate Dean of School of Mechanical Engineering since 2014, Convener of AICTE-MHRD IIC since 2017 and Zonal Coordinator for AICTE-NDF Scheme since 2018. He received his B.E. degree in Mechanical Engineering from Berhampur University, Berhampur, India, in 2001, M.Tech. and Ph.D. in Mechanical Engineering from Jadavpur University, Kolkata, India, in 2006 and 2011, respectively. His current research interests include impingement heat transfer, thermal systems design and optimization, biofuels and renewable energy, nuclear fuels, nanofluidics, microfluidics, smart energy materials and composite materials. Dr. Mishra is a member of the Indian National Academy of Engineering; the National Academy of Science, India; the Institution of Engineers (India); and the Institution of Engineering and Technology (IET). He is a Life Member of the Indian Society for Technical Education (ISTE), ASME, SAE and Combustion Institute (India). Dr. Mishra has published more than 100 research articles in journals of international repute, supervised 10 PhD students, 22 Masters students and also holds 14 patents. His multi-disciplinary research interests are medical imaging and dental implants technology.

Thermal and Fluid System Design

Comparative Study of Analytical and Simulation Method in Determination of Fuel Centerline and Clad Surface Temperature of Metallic Nuclear Fuel



Suman Saurav, M. Muthuganesh, P. K. Chaurasia, and S. Murugan

Abstract To prevent nuclear fuel element failure during the reactor operating conditions, the knowledge on the radial and axial temperature distribution of the nuclear metallic fuel is essential as to hold the mechanical and thermal hydraulic threshold. Normally, fuels are operated at conditions where its centerline temperature remains well below the fuels hot spot temperature. In this paper, design safe limit of a nuclear fuel is calculated, and temperatures are set for safe operation of reactor. Here, 2D axisymmetric computation software COMSOL Multiphysics was used in determining the temperature distribution across the sodium-bonded metallic fuel (U–Pu–Zr ternary alloy) pin. In the computation, heat transfer module coupled with structural analysis which captures fuel deformation due to heat transfer was adopted. Thermal and structural analysis of fuel pin was carried out. The temperature distribution, stress profile and displacement in fuel pellet and clad were determined. It is seen that the fuel centerline temperature, deformation in fuel and clad were within safe limits.

Keywords Metallic fuel · Centerline temperature · Heat and structure analysis · COMSOL

1 Introduction

Nuclear reactor plants are essentially used to generate and supply electricity. It is clean and green energy compared to the thermal plant in terms of usage of fuel and waste production [1]. Nuclear energy is released as a result of nuclear reaction within the fuel. This energy as heat is transferred through cladding by conduction to the surface of fuel and finally convected to the flowing liquid coolant, which passes from the core to the external heat exchangers in which steam is generated to rotate

S. Saurav (✉) · S. Murugan
Homi Bhabha National Institute, Mumbai, India
e-mail: sumansaurav@igcar.gov.in

S. Saurav · M. Muthuganesh · P. K. Chaurasia · S. Murugan
Indira Gandhi Centre for Atomic Research, Kalpakkam-603102, Tamil Nadu, India

the turbine [2]. During operation of the reactor, the fuel has the tendency to face failure due to disintegration in the fuel structure, fuel clad interaction, etc. One of the most important factors includes thermal characteristics or behavior of the fuel pin. The fuel pellet swells as a result of nuclear reaction during reactor operation which may interact with the clad. Several studies in various nuclear plants have reported swelling in clad and outer surface of the pellet, and in few cases the fuel crack was also observed [3, 4]. Hence, it is important to determine the temperature distribution profile within the fuel pin. Therefore, research must be focused on the estimated result and in the design of the fuel pin such that failure of fuel pin is reduced by optimizing heat transfer and structural analysis [5].

Fast breeder reactors (FBRs) are going for metallic fuels as nuclear fuel due to lower doubling time [6, 7]. Different configurations of metallic fuel composition are being worked to evaluate their performance in FBR [8–10] of which a ternary sodium-bonded fuel pin of U 23%–Pu 6%–Zr alloy configuration is preferred. As part of the analysis of fuel pin to understand its performance in FBR operating conditions, computation using COMSOL Multiphysics software was carried out, and fuel centerline temperature, clad surface temperature, stress and displacement of the pellet and cladding were determined to arrive at the design safe limit for fuel pin.

2 Steady-State Analysis of Metallic Fuel Pin

FBR uses cylindrical fuel pin that contains ternary metallic fuel slug (U–Pu–Zr) in T91 (ferritic steel) cladding tube, and sodium is filled between the fuel slugs and clad as shown in Fig. 1. Zirconium (Zr) is used to provide strength to fuel pin in terms of increased melting point but due to nuclear reaction point of view, the zirconium and the plutonium composition is optimized. In this study, a lower limit of the 23% plutonium is chosen with 6% Zr in the ternary fuel, and enrichment is adjusted to obtain peak linear heat rate (LHR) of 450 W/cm [8]. Heat generated by nuclear fission is conducted through the fuel pin and convected by sodium coolant, which is flowing around the fuel pin. For analysis, governing parameters for fuel pin structure and material properties are summarized in Tables 1 and 2, respectively. The overall length of the fuel slug in the fuel pin is 320 mm.

For the analysis, overall fuel slug of 320 mm length was divided into 10 mm length portion each. LHR is cosine function of the length of the fuel slug [9], and the maximum value here is 450 W/cm. LHR for each portion of fuel slug varies as shown in Fig. 2.

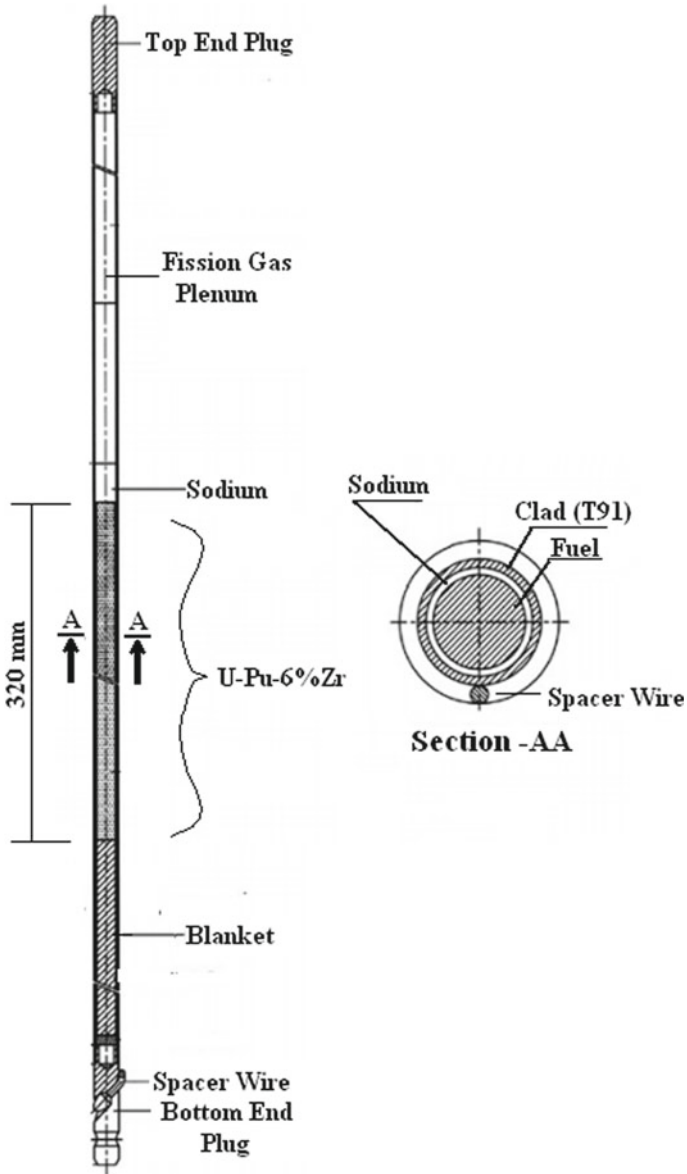


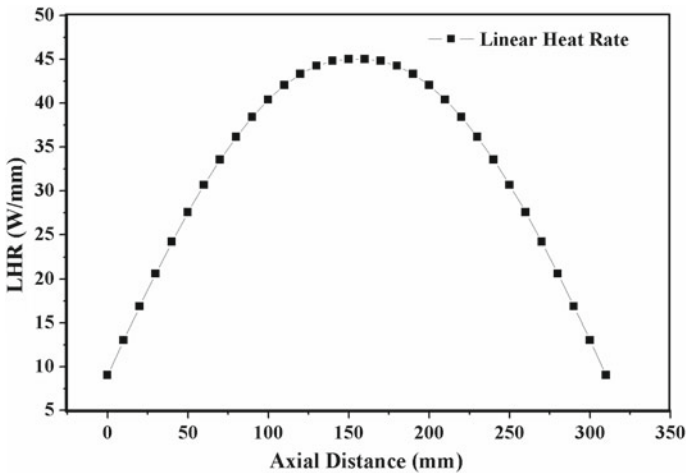
Fig. 1 Sodium-bonded metallic fuel pin

Table 1 Characters of the metallic fuel material used in the study

Pellet material: metallic fuel (uranium, plutonium, zirconium)	
Gap: liquid sodium	
Clad material: T91 (9Cr-1Mo)	
Coolant: liquid sodium	
Fuel slug length	320 mm
Fuel slug diameter	4.9 mm
Gap filled with sodium thickness	0.4 mm
Outer diameter of clad	6.6 mm
Inner diameter of clad	5.7 mm
Coolant channel inner diameter	16 mm

Table 2 Properties of fuel slug, clad, sodium-filled gap and sodium coolant

Property	Fuel slug	Clad [11]	Gap [11]	Coolant
Thermal conductivity (W/m K)	20.2 [12]	28.5	70.5	70.5
Specific heat capacity (J/kg K)	170 [13]	622	1270	1270
Density (kg m^{-3})	16,565.4 [13]	7760	876	876
Thermal expansion coefficient (1/K)	$19.9\text{e-}6$ [13]	$12.7\text{e-}6$	–	–
Liner heat generation rate (W/cm)	450	–	–	–
The inlet temperature of coolant (K)	– s	–	–	643
The mass flow rate of coolant (kg/s)	–	–	–	0.09

**Fig. 2.** Linear heat rate (LHR) along with the axial length of the fuel slug

2.1 Analytical Calculation

Steady-state heat transfer analysis was carried out to find out the fuel centerline temperature, fuel surface temperature, cladding inner and outer surface temperature. For analytical calculation of temperature distribution of fuel pin, a radial heat transfer model is used with the following basic assumptions

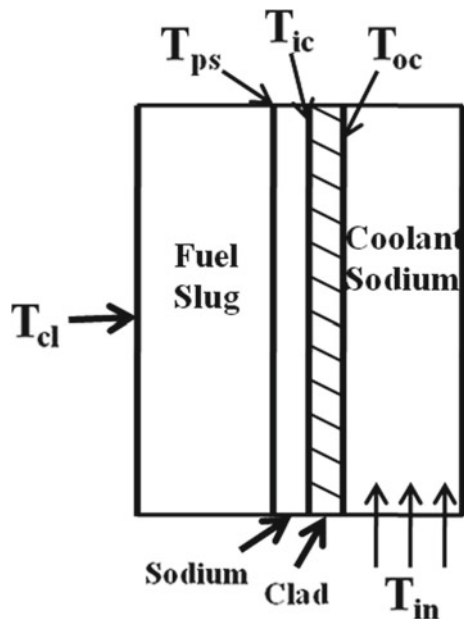
1. Length of the fuel pin is more than the diameter of the fuel pin, so that axial heat transfer can be neglected.
2. The heat transfer from the fuel pellet to coolant is considered as only conduction and convection; radiation heat transfer is not considered in this calculation as the effect is insignificant [9].
3. Thermal conductivity of the fuel slug and the clad tube each is considered constant.

Fuel slug, sodium-filled space, clad and coolant flow are taken separately to develop the temperature profile in each (as shown in Fig. 3) 10 mm length of fuel pellet.

T_{in} (coolant inlet temperature) and heat generation rate from the pellet (q') were taken as input values for the calculation of pellet outer surface temperature (T_{ps}), clad inner surface temperature (T_{ic}) and clad outer surface temperature (T_{oc}) from Eqs. (1)–(4).

Temperature of the clad outer surface (T_{oc}):

Fig. 3 Fuel pellet temperature profile



$$T_{oc} = \frac{q'}{2\pi} \left(\frac{1}{h_S(R_f + t_{gap} + t_{Clad})} \right) + \frac{q'}{\dot{m}C_p} + T_{in} \quad (1)$$

Temperature of the clad inner surface (T_{ic}):

$$T_{ic} = \frac{q'}{2\pi k_C} \ln \left(\frac{R_f + t_{gap} + t_{Clad}}{R_f + t_{gap}} \right) + T_{oc} \quad (2)$$

Fuel surface temperature (T_{ps}):

$$T_{ps} = \frac{q'}{2\pi k_{Na}} \ln \left(\frac{R_f + t_{gap}}{R_f} \right) + T_{ic} \quad (3)$$

Finally, the heat transfer equation of each 10 mm section of fuel, sodium gap, clad and coolant was combined together to determine the centerline temperature of the fuel pellet. The equation for the centerline temperature measurement is given Eq. (4).

$$T_{CL} = \frac{q'}{2\pi} \left(\frac{1}{2k_f} + \frac{1}{k_{Na}} \ln \left(\frac{R_f + t_{gap}}{R_f} \right) + \frac{1}{k_C} \ln \left(\frac{R_f + t_{gap} + t_{Clad}}{R_f + t_{gap}} \right) + \frac{1}{h_S(R_f + t_{gap} + t_{Clad})} \right) + \frac{q'}{\dot{m}C_p} + T_{in} \quad (4)$$

where $q' = \text{LHR}$, $\bar{k}_f =$ thermal conductivity of fuel slug, $k_{Na} =$ thermal conductivity of sodium, $R_f =$ radius of fuel slug, $t_{gap} =$ sodium-filled gap between fuel slug and clad tube, $t_{Clad} =$ thickness of clad tube, $h_S =$ heat transfer coefficient of sodium coolant, $\dot{m} =$ mass flow rate of sodium, $C_p =$ specific heat capacity of sodium, $T_{in} =$ coolant inlet temperature, $T_{CL} =$ centerline temperature.

For solving Eq. 4, values of the parameters are same as shown in Tables 1 and 2. The thermal conductivity of the ternary alloy fuel slug is calculated from the literature [12], and it is considered as average thermal conductivity.

2.2 Computation Simulation

The thermal analysis of the fuel slug was carried out using the COMSOL Multi-physics computer code. 2D axisymmetric model was created and taken for simulation studies as shown in Fig. 4. The total fuel slug of 320 mm was divided into 32 partitions, and each partition was assigned as a heat source according to the given LHR (Fig. 2), and all the design parameters considered are discussed (Tables 1 and 2).

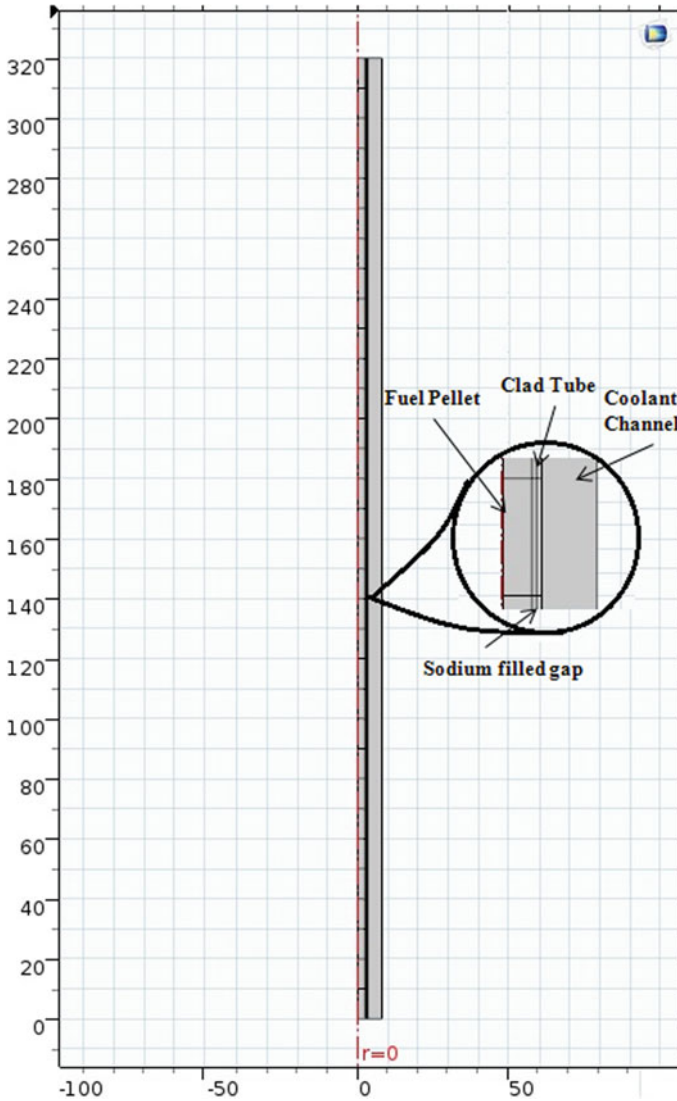


Fig. 4 2D axisymmetric model of fuel pin in simulation

The COMSOL software was used to solve steady-state coupled heat transfer and laminar flow in the simulation model. For the structure analysis of the fuel pellet, the thermal load is considered, and it was coupled with heat transfer analysis. Basic equations were used to solve the simulation model by software. After the designing of the simulation model, meshing of the model was done as a predefined fine mode of mesh size in COMSOL software. The predefined mesh (fine-mode mesh) provides more accurate results for mixed (triangular, quadrilateral, edge and vertex)

automatic meshes. The meshing minimum element quality and average element quality were 0.3593 and 0.8087, respectively. Each mesh element has three degree of freedom (DOF) at each node, one DOF to temperature and two DOF to structural analysis. Then finite element method (FEM) was used to solve the meshed model. The boundary conditions used to solve this model are as follows:

1. Fuel pellet and clad tube were considered as heat transfer in solid and in the sodium filled in the gap, and the coolant channel part was considered as a liquid (Fig. 4).
2. Sodium-filled gap is considered as the static heat transfer part while the coolant was considered as laminar flow and heat transfer in liquid.
3. Outer surface of the coolant flow channel was considered as the insulated surface.
4. Entry of the coolant (sodium) was taken as the laminar flow with a mass flow rate 0.09 kg s^{-1} inlet with temperature $370 \text{ }^\circ\text{C}$.
5. Heat generation rate (LHR) was taken at centerline of the fuel pin.
6. Upper part of the coolant flow channel was taken as outlet.
7. For the structure analysis, the lower end of the fuel pellet and clad tube was considered as a fixed and the rest kept free.

To determine the thermal stress, deformation in the fuel slug and clad tube, the temperature was considered as thermal load to overall geometry of the fuel pin.

3 Results and Discussion

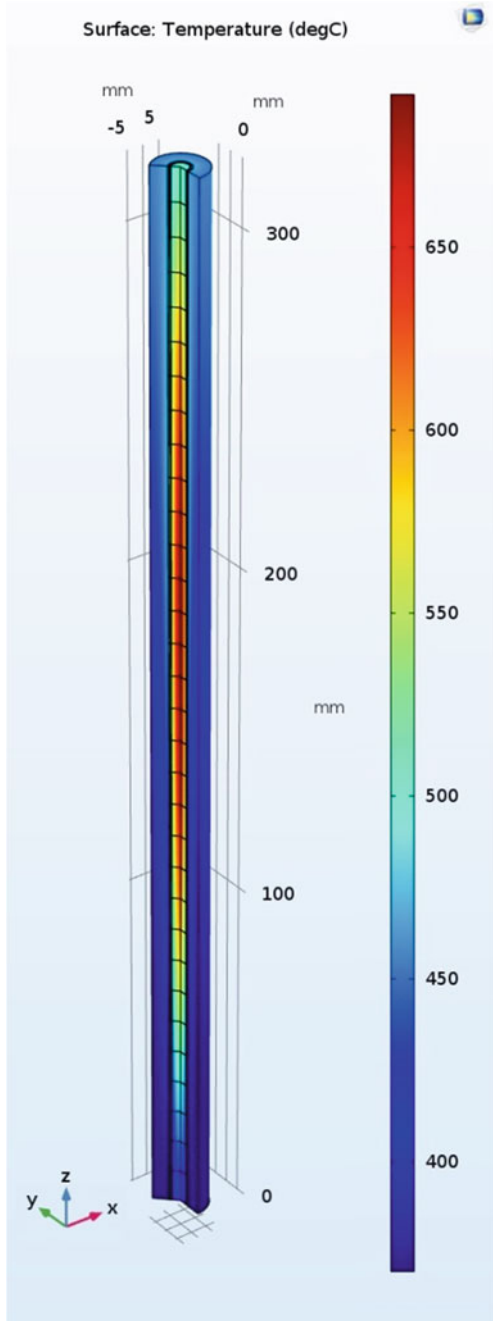
The objective of this work was to carry out the thermal and structural analysis of the metallic fuel element during the reactor operating condition using thermal analysis (Fig. 5).

3.1 *Temperature Distribution in Fuel Pin*

Heat transfer analysis is carried out to find the non-uniform temperature of the fuel pin as shown in Fig. 4. Results obtained from the analytical and simulation method, the clad surface temperature and the centerline temperature of fuel pin are shown in Fig. 6. According to the LHR (Fig. 2), the heat generation of the pellet varies corresponding to the axial length. Temperature distribution in the fuel pin is also found through the simulation. The temperature distribution result of fuel pin obtained through analytical and simulation techniques has been compared and shown in Fig. 6. In the middle of the fuel pin, the LHR is maximum but the centerline temperature of the pellet is not found maximum at the center of the pellet.

The maximum centerline temperature in the fuel was found to be $\sim 686 \text{ }^\circ\text{C}$ by both the method. In earlier studies, Rajkumar et al. [13] reported $889 \text{ }^\circ\text{C}$ as the centerline temperature as they considered hotspot condition. The maximum clad inner and outer

Fig. 5 Temperature distribution of the fuel pin



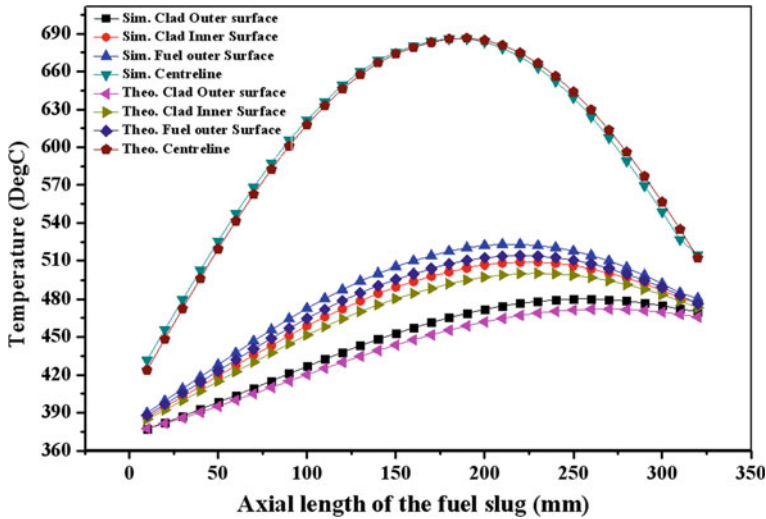


Fig. 6 Temperature distribution of the fuel pin graph by analytical method and simulation method

surface temperatures were found to be ~ 508 °C and 480 °C, respectively, while the clad safety limit temperature is 650 °C [14].

3.2 Coupled Structural Analysis

The thermal and structural analysis was coupled to determine the stress and displacement at different portions of the fuel pin. In the nuclear reactor, the lower end of the fuel pins is attached with the grid plate, and the upper end of the fuel pins is free to expand or move. Here, for the structural analysis lower end of the fuel pin was fixed constraint, and the upper end of the fuel pin was kept free. In the structural analysis, the von Mises stress was considered because this stress is used to determine if a given material will yield or fracture. It is mostly used for ductile materials, such as metals. The von Mises stress is used to predict yielding of materials under complex loading (like thermal loading) from the results of uniaxial tensile tests. The von Mises stress satisfies the property where two stress states with equal distortion energy have an equal von Mises stress. Figure 7 shows the maximum von Mises stress occurs in the fuel pellet and clad at the lower end of the fuel pin because it was fixed and not allowed to expand. Figure 8 shows the displacement of the fuel pellet and the clad from the original position. The minimum displacement occurs at the lower end of the fuel pin because this end was fixed. The maximum displacement occurs in the pin fuel at the position of maximum centerline temperature as shown in Fig. 9. In this analysis, it is found that there is no fuel clad interaction for considered fuel pin design.

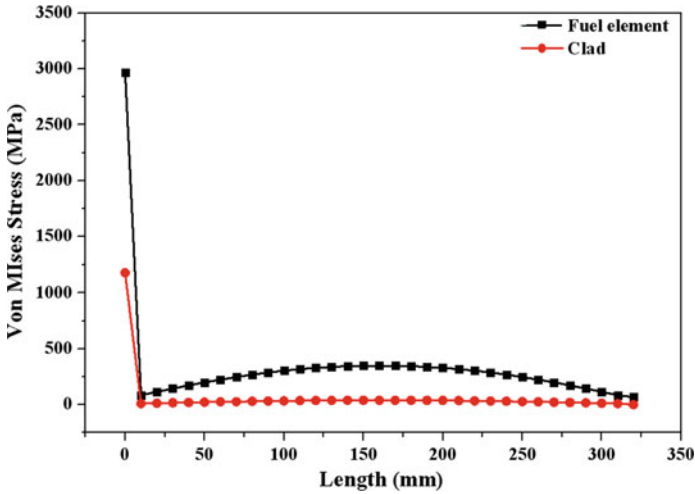


Fig. 7 Stress distribution of the fuel pin along with the axial length

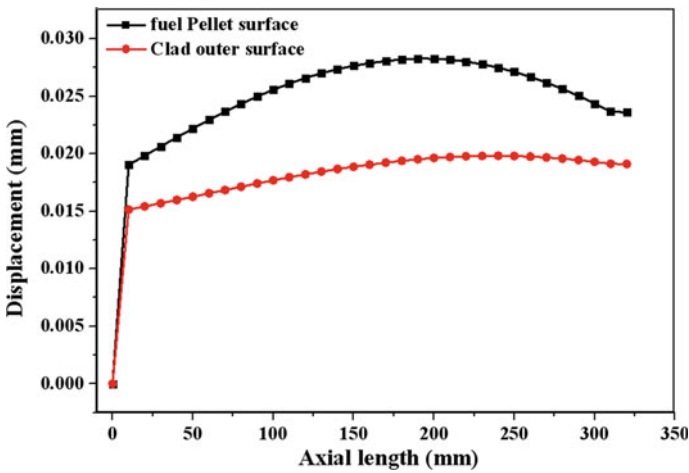
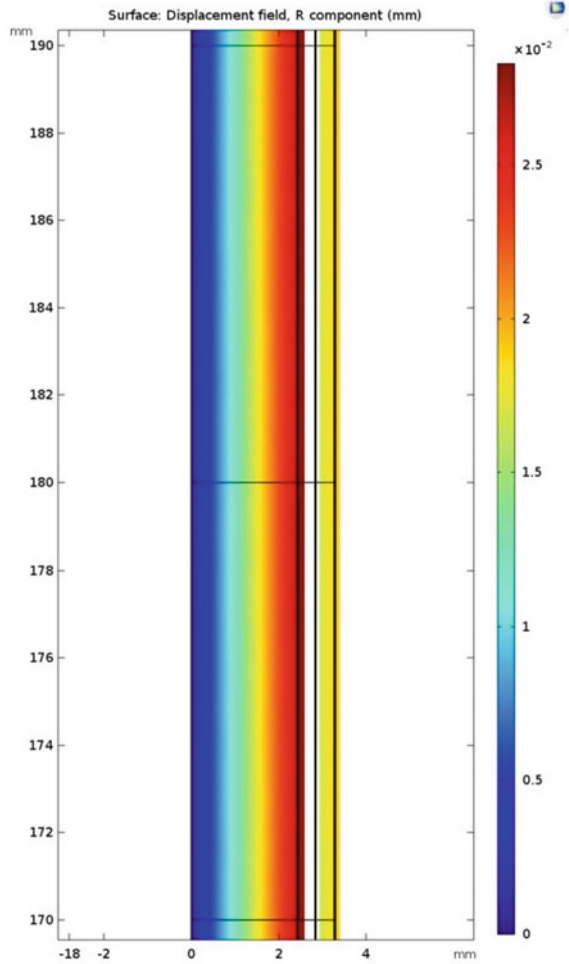


Fig. 8 Displacement of the fuel pellet and clad

4 Conclusions

In this work, coupled analysis was carried out to find the temperature distribution and the structural analysis of the sodium-bonded metallic fuel pin. It was found that the temperature distribution of fuel pin was similar to cosine function, but the maximum temperature was found above the center position of the fuel pin. The centerline temperature of the fuel slug, the clad inner and the outer temperature was under the safe limit for considered metallic fuel pin design. The temperature distribution result

Fig. 9 Displacements of a different section of the fuel pin at maximum centerline position of the fuel pin



of fuel pin obtained through analytical and simulation techniques was compared. The comparative results were obtained in the analysis. The maximum displacement of the fuel element and the clad occurs maximum at centerline temperature. No interaction between the fuel element and the clad for considered design fuel pin design was observed. The gap between the pellet and clad filled with the sodium provides uniform heat distribution to the pellet surface. From this study, it is found that due to thermal effect, the expansion of the pellet and the clad is within a safe working limits.

Acknowledgements Suman Saurav acknowledges the department of atomic energy (DAE) for fellowship.

References

1. <https://www.eia.gov/energyexplained/nuclear/nuclear-power-and-the-environment.php>. Accessed 4 June 2019
2. Pandey KM, Amrit S (2011) Structural analysis of nuclear fuel element with Ansys software. IACSIT-IJET 3:187–192
3. Tanju S (2015) A review of inherent safety characteristics of metal alloy sodium cooled fast reactor fuel against postulated accidents. Nucl Eng Technol 47:227–239
4. Marchal N, Campos C, Garnier C (2009) Finite element simulation of Pellet-Cladding Interaction (PCI) in nuclear fuel rods. Comput Mater Sci 45:821–826
5. Eskandari MR, Bavandi A, Mihandoost A (2012) Studies on nuclear fuel rod thermal performance. Energy Procedia 14:142–147
6. <https://publications.anl.gov/anlpubs/2010/05/67057.pdf>. Accessed 4 June 2019
7. Puthiyavinayagam P, Selvaraj P, Balasubramaniyan V, Raghupathy S, Velusamy K, Devan K, Nashine B K, Padma Kumar G, Suresh kumar KV, Varatharajan S, Mohanakrishnan P, Srinivasan G, Bhaduri Arun Kumar (2017) Development of fast breeder reactor technology in India. Prog Nucl Energy 101:19–42
8. Vishnu V, Ghosh AK (2011) Thermal analysis of metallic fuel for future FBRs. Energy Procedia 7:234–249
9. Devan K, Abhitab B, Riyas A, Sathiyasheela T, Mohanakrishnan P, Chetal SC (2011) Physics design of experiment metal fuelled fast reactor cores for full scale demonstration. Nucl Eng Des 241:3058–3067
10. <https://www.barc.gov.in/publications/eb/golden/nfc/nfc.pdf>. Accessed 10 July 2019
11. <https://www.metalspiping.com/t91-p91-steel.html>. Accessed 5 June 2019
12. <https://www.ne.anl.gov/eda/ANL-RE-95-2.pdf>. Accessed 5 June 2019
13. Kim YS, Cho TW, Sohn DS (2014) Thermal conductivities of actinides (U, Pu, Np, Cm, Am) and uranium-alloys (U-Zr, U-Pu-Zr and U-Pu-TRU-Zr). J Nucl Mater 445:272–280
14. Rajkumar T (2017) Design of sodium bounded metallic fuel pin (MFTP-Ty4) for test irradiation in FBTR. IGCAR Internal Report. FBTR/CES/31471/DN/20/R-A-2017

CFD Analysis of Two-Phase Cavitating Flow in a Centrifugal Pump with an Inducer



Debarpan Paul, Himanshu Agarwal, and Babu Rao Ponangi

Abstract This study addresses cavitation modelling of a single-stage centrifugal pump and aims at minimizing cavitation by introducing an inducer upstream of the impeller, which serves as a booster pump by increasing the pressure of the fluid before it enters the impeller. The generated meshed model is first validated against standard experimental data to ensure the credibility of the model and the results obtained from it. The results obtained show that the inducer is effective in reducing the amount of cavitation for a substantial number of operating conditions. It is seen that the inducer is effective in increasing the NPSH available of the pump by a maximum margin of 33%.

Keywords Cavitation · Inducer · Centrifugal pump · Multi-phase

Abbreviations

ρ	Mixture density
P_{in}	Inlet total pressure (Pa)
v_{eye}	Velocity magnitude at impeller eye (m/s)
M	Impeller moment (N m)
P_{s-eye}	Static pressure at impeller eye (Pa)
P_{op}	Operating pressure (Pa)
VOP	Volume fraction of the pump
η	Efficiency (%)
P_{out}	Outlet total pressure (Pa)
V_{out}	Outlet volume flow rate (m/s)
ω_k	Angular velocity (rad/s)
g	Gravitational acceleration (m ² /s)
NPSH	Net positive suction head (m)

D. Paul · H. Agarwal · B. R. Ponangi (✉)

Department of Mechanical Engineering, PES University, 100 feet ring road, 560085 Bangalore, India

e-mail: baburaoponangi@pes.edu

© Springer Nature Singapore Pte Ltd. 2021

P. Pant et al. (eds.), *Advances in Mechanical Processing and Design*, Lecture Notes in Mechanical Engineering, https://doi.org/10.1007/978-981-15-7779-6_2

VOP_{ind}	Volume fraction of the pump with inducer
H_t	Total head (m)
ρ_v	Vapour density

1 Introduction

Cavitation is a phenomenon where the liquid boils locally, giving rise to low-pressure bubbles, when they move to a region of higher pressure implodes on itself and creates intense shock waves. These shock waves near the metal surface lead to erosion and pitting of the components. The aftereffects cause material, structural damage, noise, vibration, load asymmetry and decrease the overall performance of the system. Therefore, protecting the system from cavitation becomes a major engineering challenge in designing of pump impellers, ship propellers and other components which operate in a fluid medium. Especially in centrifugal pumps, cavitation is one of the most important factors that need to be considered when the rotational speed of the pump increases or it is operated at low inlet pressure conditions.

For achieving the objective of reducing cavitation in a centrifugal pump, an appropriate inducer is used upstream of the pump impeller. An inducer is a bladed axial structure which serves as an additional booster system, as it increases the pressure of the fluid before it enters the impeller. This significantly reduces the chance for cavitation to take place in the impeller. Thus, inducer design becomes a critical aspect from point of view of cavitation.

The review paper by Binama et al. [1] provides a brief review of the effects of cavitation in a centrifugal pump and the variation of pump parameters under cavitating flow. The paper also highlights types of cavitation, cavitation parameters and mitigation techniques which are important factors to be considered while designing a pump to protect it against the ill effects of cavitation such as drop-in mass flow rate and efficiency [2].

Thus to reduce the effects of cavitation, without making any changes to the existing pump design or the operating conditions, a suitable inducer needs to be used. The studies by Li et al. [3] show that by employing an inducer upstream of a centrifugal pump could lead to a reduction of violent cavitation in areas near the impeller inlet where regions of low pressure are generally formed.

The studies by Kim et al. [4] highlight the importance of the inducer when pumps are needed to operate under cavitating conditions and the various nature of cavitation experienced by the pump impeller under different flow rates. The effect of critical NPSH and the increased level of vibration experienced in the pump under cavitating conditions are investigated by Hong et al. [5] and the use of inducer is suggested by the authors. The workflow methodology adopted is based on the proposed approach by Delgosha et al. [6].

For the inducer design and optimization process, the papers that relate the effects of cavitation to changes in the geometry of the inducer are studied. For deciding

the number of blades on the inducer, the works of Ning et al. [7] is referred which showed that for maximum cavitation reduction the blades of the inducer needs to be a multiple of the blades on the impeller. The peripheral blade angles are designed based on the observations of Mejri et al. [8] which showed that an optimal angle of 10° for the best-suited design.

Mejri et al. [9] have also conducted simulations relating cavitation and vibration characteristics of different hub configuration. The result shows that tapered hub has a relatively superior cavitation characteristic when compared to its other counterparts and is subsequently incorporated into the design.

2 Methodology

The proposed methodology for this project progresses along the following lines. First geometry of the pump model is modelled, and meshing operation is performed on it. The mesh quality of the model is reviewed and is subsequently prepared for simulation. For numerical analysis, the meshed model is simulated in ANSYS Fluent. Pressure based, steady-state solver used. The 3-D Reynolds averaged Navier–Stokes equation is used to solve for continuity and momentum in the domain. Turbulence in the system is modelled by the realizable k - \mathcal{E} model for faster convergence. SIMPLE scheme is applied for pressure–velocity coupling. First-order discretization is applied for momentum, volume fraction and turbulence kinetic energy, and higher-order terms are relaxed. Each scheme is run till convergence.

For checking the reliability and credibility of the meshed model, numerical simulation results are validated against standard experimental data available for centrifugal pumps. Once a satisfactory margin of error is reached, the numerical model is then set up for actual cavitation simulation.

Cavitation modelling within the flow field multiphase is switched on, and an additional vapour phase is introduced in the system. The saturation pressure is fixed at 3540 Pa. The Schnerr–Sauer model is used which is derived from the Rayleigh–Plesset equation is used for cavitation simulation and pressure staggering option (PRESTO) scheme is used for pressure interpolation.

The following equations are used to evaluate pump parameters

$$H_t = \frac{(P_{\text{out}} - P_{\text{in}})}{\rho g} \quad (1)$$

$$\eta = \frac{V_{\text{out}} \times (P_{\text{out}} - P_{\text{in}})}{\omega_k \times M} \times 100 \quad (2)$$

$$\text{NPSHa} = \frac{(P_{s-\text{eye}} + P_{\text{op}}) - P_v}{\rho g} + \frac{v_{\text{eye}}^2}{2g} \quad (3)$$

$$\text{Effectiveness} = \left(1 - \frac{\text{VOP}_{\text{ind}}}{\text{VOP}} \right) * 100 \quad (4)$$

2.1 Geometrical Parameters of the Pump

The CAD models used are of an industry standard pump. The pump assembly consists of the impeller, volute casing, an inlet duct and outlet duct. First the base model of the pump is assembled, following which an Inducer is added upstream of the impeller. The impeller used in this model is a six-bladed impeller. The inducer used for the model is a helical inducer with three-curved blades. The hub diameter is 48 mm while tip diameter is 38 mm. The inducer length and blade diameter are 269 mm and 170 mm, respectively. The blade pitch is 215 mm and is placed 120 degrees to each on the hub. All assembly operations are conducted in NX 11.0.

2.2 Computational Mesh

Post-assembly of both the pump geometries the models is imported to hyper-mesh for mesh generation. First, the geometry is checked and cleaned of any free edges or t -connections. Since a 3D mesh is to be generated, initially a 2D mesh is generated on all the surfaces, which is followed by the generation of volume tetra mesh. The pump components are organized into different domain volumes, namely suction, inducer, impeller, volute and outlet volume (supplementary information—Table 1).

For higher accuracy of the numerical model, the maximum mesh size is kept at 1 mm. Post-mesh creation the model is checked for various parameters like warpage, skewness, warpage, tet collapse, and the failed elements are remeshed with the required values. The final meshed model of the base pump has 10.955 million elements and 4.792 million nodes, and the pump model with inducer has 13.621 million elements and 4.192 million nodes (Figs. 1, 2, 3 and 4).

For reducing the computational time and the number of cells, the entire domain is converted into polyhedral in ANSYS Fluent. After conversion, the total number of cells in polyhedral mesh of the pump his 5.221 million with an orthogonal quality of 0.29 and the total number of cells in the polyhedral model with inducer is 7.184 million with an orthogonal quality of 0.12.

Fig. 1 3-D geometry of the inducer

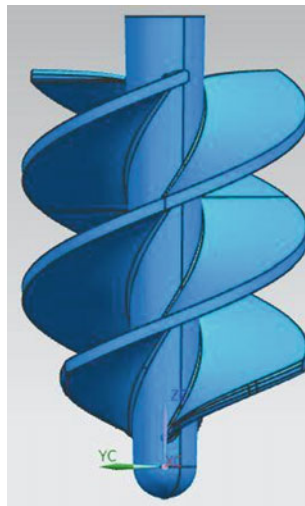


Fig. 2 Front view of the inducer

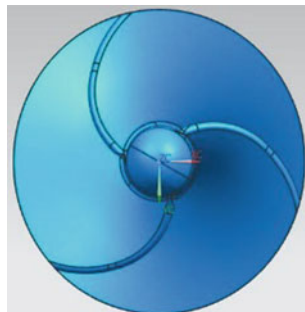


Fig. 3 Meshed model of pump

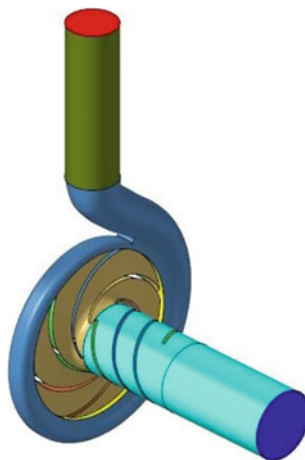
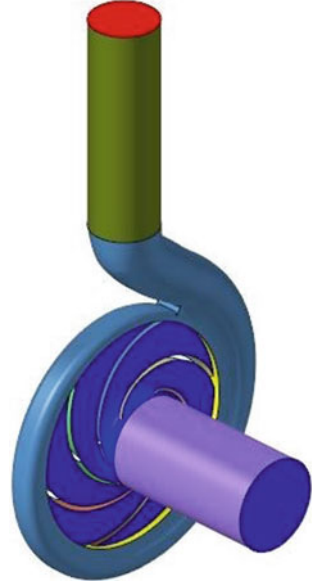


Fig. 4 Meshed model of pump with inducer



3 Results and Discussion

3.1 Validation

Before multiphase analysis is carried out the reliability, and the credibility of the numerical model must be established by, validating the results obtained from the numerical model against standard experimental data. Validation is an important step in the simulation process as it gives us an idea about the accuracy of the results obtained. The validation of the meshed model is carried out by comparing the numerical data obtained from the simulation against standard experimental data on centrifugal pump obtained from the industry. Validation is carried out for 1250 rpm at six different pressure conditions. The pump performance parameters are tabulated, and the final quality of the numerical model is discussed.

In order to validate our mesh, we have compared numerical data with given experimental data at six different operating conditions at 1250 rpm are considered referred from Table 2 (supplementary information).

The atmospheric operating conditions for all the cases are fixed at 101,325 Pa. Inlet pressure and outlet discharge from experimental data are set as operating conditions for the model.

From Fig. 5, it is seen that the numerically obtained head values are in very good co relation with the experimental ones with the maximum error being 1.2%. Figure 6 shows that the numerically obtained efficiency values are in very good agreement with the experimental ones with the maximum error being 1.5%. Figure 7,

Fig. 5 Validation of discharge versus head [10]

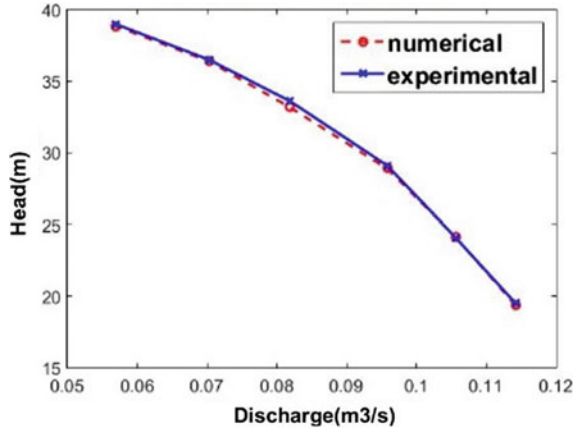


Fig. 6 Validation of discharge versus efficiency [10]

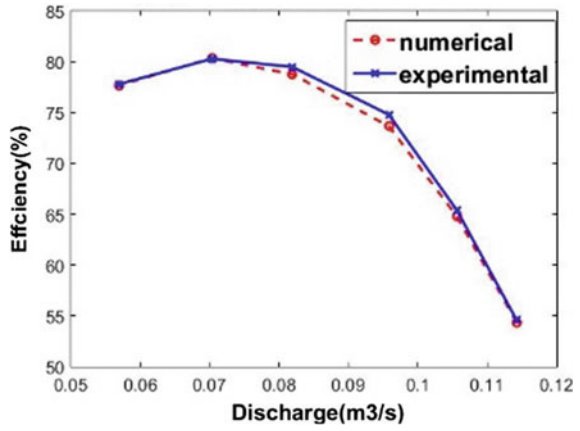
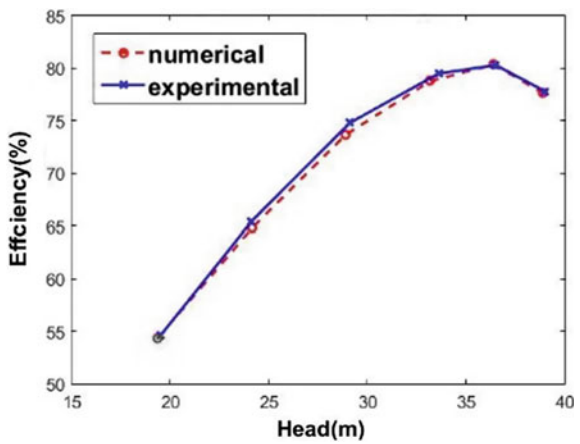


Fig. 7 Validation of head versus efficiency [10]



i.e. head vs Efficiency curves, also show minimum deviation between numerical and experimental values.

3.2 Multi-phase Analysis

In this phase of the project, multi-phase interaction is switched on. Liquid water, as well as vapour, is present simultaneously in the flow field. Multiphase analysis is an important component of the project as it provides us with information about the amount of vapour phase present in the system and gives us a graphical view of the region of cavitation in the pump.

The analysis is carried out first for the base model and then for the model with the inducer. The vapour phase plots, pressure plots as well as vapour phase volumes are obtained for comparison and checking the effectiveness of the inducer and pump parameters like head, efficiencies and discharge.

Another important parameter to judge cavitation performance is the available net positive suction head (NPSHa). The inducer greatly increases NPSHa of the system which is the prime requirement. Schnerr–Sauer cavitation model is invoked for the analysis with a saturation pressure of 3540 Pa

Seven different standard operating conditions were chosen to perform the simulation as inferred from Table 3 (supplementary information).

The discharge versus head graph, i.e. Figure 8 shows that the head of the pump tends to reduce with increase in discharge for both the models. The inducer has lower mass flow rate; hence, it is offset by a certain amount. The difference is observed to be minimal with increase in outlet pressure and also at the best efficiency point. We observe from Fig. 9 that the efficiency is slightly lower in the presence of the inducer.

Fig. 8 Two-phase discharge versus head

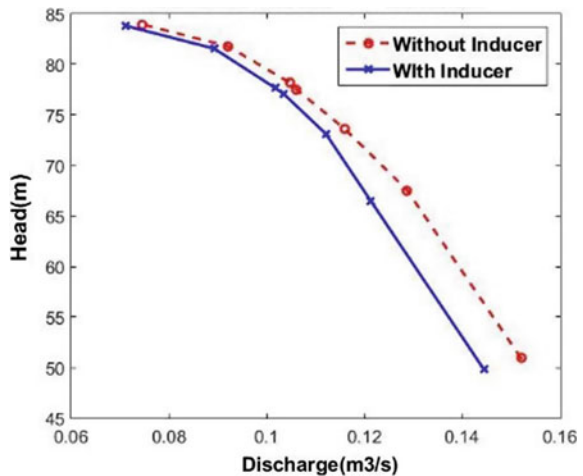
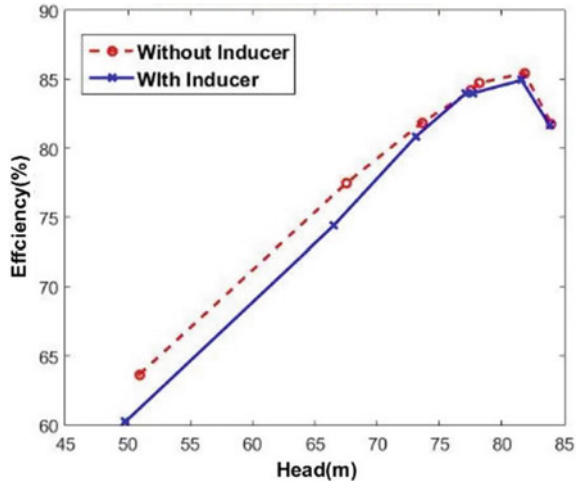


Fig. 9 Two-phase head versus efficiency



The difference minimizes for higher pressure cases and for the best efficiency cases. The efficiency drop is less than 2% which is acceptable.

The two plots above signify the variation of vapour phases with the total head. It can be seen from Fig. 10 that under off-design pressure conditions the inducer tends to increase the amount of cavitation in the system, whereas as we move towards the designed operating region of the pump the amount of cavitation reduces significantly. Figure 11 reiterates the points that the inducer is most effective for the designed operating conditions and loses its performance as we tend away from it.

Fig. 10 Head versus phase percentage

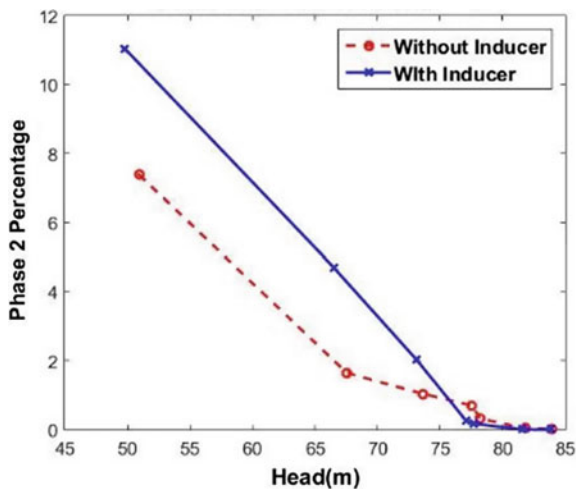
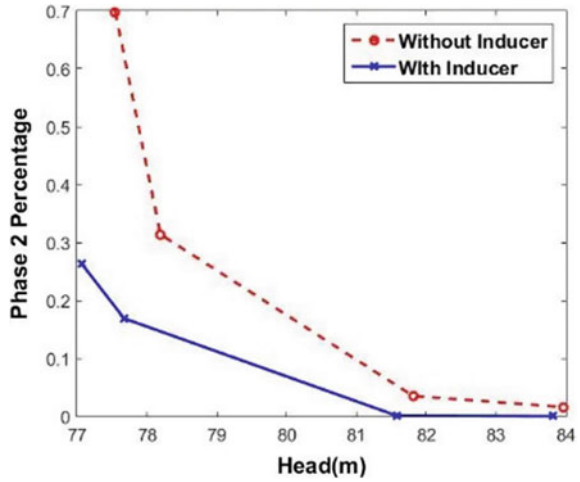


Fig. 11 Head versus phase percentage (higher head)



From Fig. 12, it is clearly observed that the effectiveness % of the inducer attains a negative value for the first three operating conditions, which in turn suggests that the volume of vapour phase in the inducer increases with the use of the inducer.

For the next four operating conditions, which tend towards the design conditions, there is a steady increase in the effectiveness % of the inducer. This suggests that the inducer is able to decrease substantially the amount of vapour phase in the impeller under these conditions. Thus, it can be concluded that the inducer is extremely effective in reducing cavitation when the pump is operated under the design operating conditions.

It is seen from Fig. 13 that for majority of the operating conditions the net positive head under which the pump can operate without undergoing cavitation increases with the use of an inducer. We can observe that for first three operating conditions where the amount of cavitation is higher with the application of the inducer, their corresponding

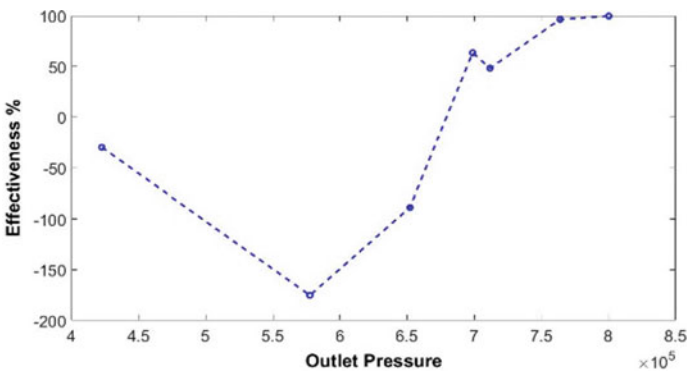


Fig. 12 Variation of effectiveness of the inducer

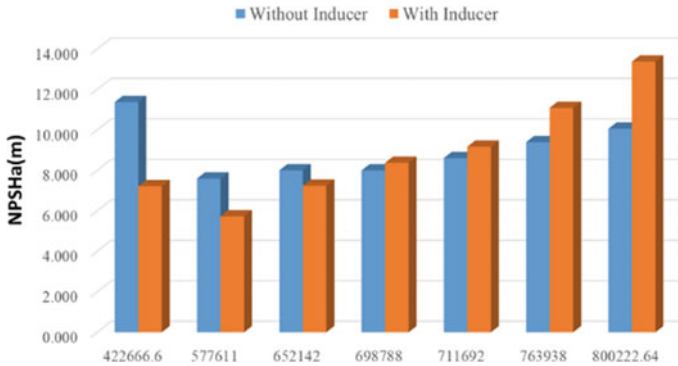


Fig. 13 Variation in NPSHa

NPSHa is lesser. As we move towards the designed operating conditions, we find that there is a steady increase in the value of NPSHa, in the presence of an inducer. A maximum increase of 3.3 m is observed.

From Table 4 (supplementary information), it is observed that the amount of vapour phase in the impeller, in the presence and absence of the inducer is of comparable magnitude for the first three cases. Since these conditions are off-design condition, this demonstrates a very important observation that the effectiveness of the inducer is reduced when it is operated under off-design conditions.

For the next four boundary conditions, we observe a drastic decrease of vapour phase in the impeller with the use of the inducer. Since these conditions are in close proximity of the design operating conditions, we find the inducer is able to eliminate the majority of the cavitation volumes, which are formed on the impeller. Thus, inducer is able to maintain high effectiveness at the neighbourhood of the operating conditions.

4 Conclusions

The most important conclusion which is drawn from the simulations is regarding the effectiveness of the inducer. It is seen that the inducer is most effective at the preferred operating range of the pump and tends to lose its purpose if it operated under off-designed condition.

The multiphase analysis provides us with an insight into the effectiveness of the inducer in reducing cavitation occurring in the blades. At the best efficiency point, it is found that the amount of cavitation is almost negligible in the impeller reiterates the fact that the inducer is most effective at BEP.

Another important inference, which can be drawn from the simulated operating conditions is that when the pump is made to operate at off-design conditions the

inducer is unable to reduce the amount of cavitation in the system. Hence, it is advised to operate the inducer at the designed operating conditions.

From the simulation results, it is seen that the pump efficiency reduces by a small margin of around 2% when an inducer is used due to a reduction in flow rate but the efficiency tends to increase at the best efficiency point of the pump.

Another very important aspect which is studied to judge the effectiveness of the inducer is the comparison of NPSHa of the pump. It is found that the inducer helps in increasing NPSHa by a significant amount. The maximum increase seen within the data set is about 3.3 m. This shows that the inducer increases the head under which the pump can safely operate without the risk of running into cavitation conditions.

Acknowledgments We would like to express our gratitude and sincere thanks to Dr. K S Ravichandran, Professor, Department of Mechanical Engineering, PES University for his support and guidance throughout the due course of the project.

Supplementary Information

See Tables 1, 2, 3 and 4.

Table 1 Different domain volumes in the pump assembly

SN	Domains	Volume m ³
1	Suction volume	0.0067904
2	Inducer volume	0.0047943
3	Impeller volume	0.0043051
4	Volute volume	0.0074308
5	Delivery volume	0.0049079
Total volume		0.0282317

Table 2 List of operating conditions

Case No.	Inlet pressure (Pa)	Outlet discharge (m ³ /s)
1	-38,245.935	0.1142
2	-30,400.615	0.1060
3	-22,555.295	0.0958
4	-12,748.645	0.0819
5	-4903.325	0.0703
6	980.665	0.0569

Table 3 List of operating conditions

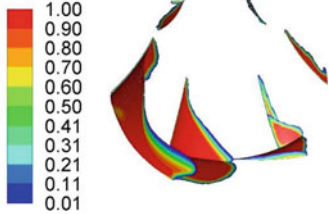
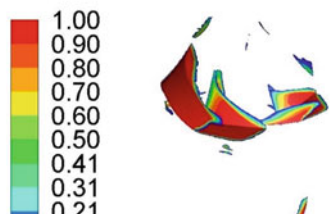
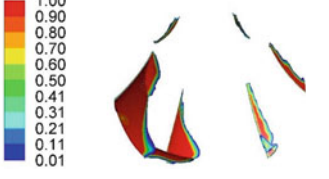
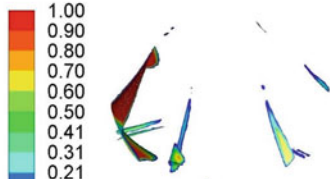
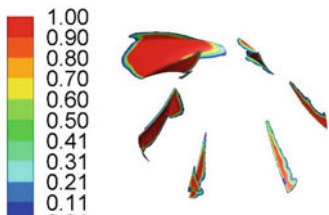
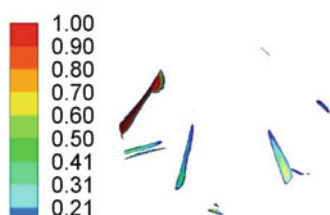
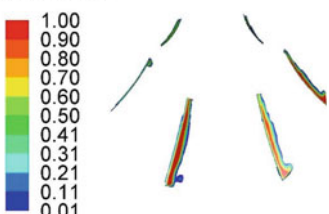
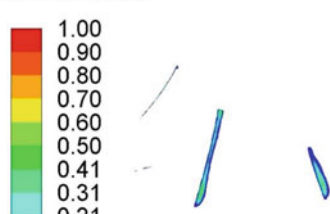
Case No.	Inlet pressure (Pa)	Outlet pressure (Pa)
1	14,709.98	422,667
2	-22,555.00	577,611
3	-18,632.63	652,142
4	-18,632.63	698,788
5	-12,748	711,692
6	-5883	763,938
7	-1961	800,222.6

Table 4 Vapour phase contour plots

Operating conditions	Without inducer	With inducer
Inlet pressure (Pa): 14,709 Outlet pressure (Pa): 422,667	<p>contour-1 Volume fraction (phase-2)</p>	<p>contour-1 Volume fraction (phase-2)</p>
Inlet pressure (Pa): -22,555 Outlet pressure (Pa): 577,611	<p>contour-2 Volume fraction (phase-2)</p>	<p>contour-2 Volume fraction (phase-2)</p>

(continued)

Table 4 (continued)

Operating conditions	Without inducer	With inducer
Inlet pressure (Pa): -18,632 Outlet pressure (Pa): 652,142	contour-1 Volume fraction (phase-2) 	contour-1 Volume fraction (phase-2) 
Inlet pressure (Pa): -18,632 Outlet Pressure (Pa): 698,788	contour-belowcavitation Volume fraction (phase-2) 	contour-1 Volume fraction (phase-2) 
Inlet pressure (Pa): -12,748 Outlet pressure (Pa): 711,692	contour-2 Volume fraction (phase-2) 	contour-2 Volume fraction (phase-2) 
Inlet pressure (Pa): -5883 Outlet pressure (Pa): 763,938	contour-2 Volume fraction (phase-2) 	contour-1 Volume fraction (phase-2) 

(continued)

Table 4 (continued)

Operating conditions	Without inducer	With inducer
Inlet pressure (Pa): -1961 Outlet pressure (Pa): 800,223		

References

1. Binama M, Muhirwa A, Bisengimana E (2016) Cavitation effects in centrifugal pumps—a review. *Binama Maxime. Int J Eng Res Appl* 6(5): 52–63
2. Liu HL, Liu DX, Yong W, Wu XF, Jian WANG, Hui DU (2013) Experimental investigation and numerical analysis of unsteady attached sheet cavitating flows in a centrifugal pump. *J Hydrodyn Ser B* 25(3): 370–378
3. Li XJ, Pan ZY, Zhang DQ, Yuan SQ (2012) Centrifugal pump performance drop due to leading edge cavitation. In: *IOP conference series: earth and environmental science*, vol 15, No. 3, p 032058. IOP Publishing
4. Kim DJ, Sung HJ, Choi CH, Kim JS (2017) Cavitation instabilities of an inducer in a cryogenic pump. *Acta Astronaut* 132:19–24
5. Hong SS, Kim DJ, Kim JS, Choi CH, Kim J (2013) Study on inducer and impeller of a centrifugal pump for a rocket engine turbopump. *Proc Inst Mech Eng Part C J Mech Eng Sci* 227(2):311–319
6. Coutier-Delgosha O, Morel P, Fortes-Patella R, Reboud JL (2005) Numerical simulation of turbopump inducer cavitating behavior. *Int J Rotating Mach* 2005(2):135–142
7. Ning C, Wang Y, Zhu ZT, Xie SF, Zhao LF, Liu ZC (2015) Numerical calculation for cavitation flow of inducer. In: *IOP conference series: materials science and engineering*, vol 72, No. 3, p 032025. IOP Publishing
8. Mejri I, Bakir F, Kouidri S, Rey R (2005) Influence of peripheral blade angle on performance and stability of axial inducers. *Proc the Inst Mech Eng Part A J Power Energy* 219(4):289–301
9. Mejri I, Bakir F, Kouidri S, Noguera R, Rey R (2006) Hub shape effects on the inducers performance under cavitation. *Proc Inst Mech Eng Part A J Power Energy* 220(3):217–237
10. Pumpsense Fluid Engineering Pvt. Ltd. Pump Test Certificate, 01/06/16

Influence of Mass Flow Rate and Concentration of Al₂O₃ Nanofluid on Thermal Performance of a Double Pipe Heat Exchanger



Vikas Gulia and Anirban Sur

Abstract Heat transfer is a very important process for industrial purposes. While there has been a constant change in the design of heat exchangers over the years which has made it more compact and efficient than ever, the area of modifications in the heat transfer fluid itself has not seen many breakthroughs. Apart from changing the design of the heat exchanger, another method is to use heat carrier fluids which have higher thermal conductivity and heat capacity. Some nanofluids (colloidal solutions of nano-sized particles suspended in a suitable base fluid) of metal oxides show superior thermal properties as compared to water. In this paper, numerical and experimental analyses have been performed to find the improvement in the overall heat transfer coefficient of a double pipe heat exchanger when Al₂O₃ nanofluid of 0.25% concentration is used of variable mass flow rate. Here Al₂O₃ nanofluid's result has been compared with normal water are used to calculate. The overall heat transfer coefficient has been calculated by the measured value of hot and cold fluids inlet–outlet temperatures. First simulation of temperature variation has been observed in ANSYS, and then simulated result has been compared with experimental results. The experimental result shows that the overall heat transfer coefficient increases with the increase of flow rate. At 120 LPH, 240 LPH, and 320 LPH, an improvement of 44.58, 26.37, and 2.78% in the heat transfer coefficient has been observed.

Keywords Nanofluid · Mass flow rate · Concentration · Thermal performance · Heat exchanger

Abbreviations

U	Overall heat transfer coefficient (W/m ² °C)
Q	Average heat transfer rate (W)
A	Heat transfer surface area (m ²)

V. Gulia · A. Sur (✉)

Symbiosis International (Deemed University), Symbiosis Institute of Technology, Pune, India 412115

e-mail: anrban.sur@sitpune.edu.in

© Springer Nature Singapore Pte Ltd. 2021

P. Pant et al. (eds.), *Advances in Mechanical Processing and Design*, Lecture Notes in Mechanical Engineering, https://doi.org/10.1007/978-981-15-7779-6_3

ΔT_{lm}	Logarithmic mean temperature difference ($^{\circ}\text{C}$)
T_{Hi}	Hot water inlet temperature
T_{Ho}	Hot water outlet temperature
T_{Ci}	Cold water inlet temperature
T_{Co}	Cold water outlet temperature
m	Mass flow rate (Kg/s)
C_p	Specific heat (KJ/KgK)
ΔT	Temperature difference
w	Weight fraction of nanoparticles

1 Introduction

Heat exchangers are used for heating and cooling of fluids in the chemical, electrical, heat recovery, cryogenic, production, transportation, manufacturing, refrigeration and air-conditioning industries. Researchers proved that mixing of suspending metal or metal oxides with conventional fluids can improve the thermophysical properties of the fluid. The particles are generally micro-sized and though their addition improves the thermal conductivity, they also have a few drawbacks.

1. Sedimentation of particles (large size) in the base fluids,
2. Clogging in pipeline flow occurs,
3. Large-sized particles in the base fluid also have much higher mass, hence kinetic energy, which results in damage on the wall surfaces,
4. Erosion of pipelines occurs due to the continuous striking of the massive particles which enhance greatly when the flow velocity increases,
5. Due to higher viscosity, the pressure drop goes significantly high in fluids.

To eliminate these restrictions and enhancing the thermal conductivity of heat transfer fluids, nano-sized particles were first introduced by Choi et al. [1] in 1995 with heat exchanger fluid. They observed increment of thermal properties (long time-standing capabilities, thermal conductivity) and uniform fluid having very less obstruction in flow pipes and channels as a result of very minute dimensions and their large surface area.

Nanofluids are stable colloidal suspensions of nanoparticles (Al_2O_3 , CuO, SiC, AlN, SiN, Al, Cu, graphite, carbon nanotubes, etc.) in a base fluid (Water, Ethylene Glycol, Engine Oil, Propylene Glycol, Paraffin, Biofluids) [2–5]. The main aim of nanofluids preparation is uniform dispersion and suspension of the lowest possible concentrations nanoparticles in a suitable base fluid. The ability of nanofluids to enhance heat transfer properties and maintain the lowest possible concentrations nanoparticles in base fluids has been researched widely [6–8]. Researchers proved that nanometer-sized particles show better stability and heat transfer properties when suspended in a base fluid as compared to micrometer and millimeter size particles because of their large relative surface area [9–12]. The scientist noticed that the

nanofluids friction factor raises with concentration due to the increase in viscosity, but friction factor decreases with raises in Reynolds number which leads to raising in heat transfer rate. So a combination of low concentration of nanofluid with a high Reynolds number is most desirable for high heat transfer rates [13, 14]. The scientist also noticed that rate of heat transfer raises with an increase in volumetric flow rate and concentration of nanoparticle and the thermal conductivity of Cu-water and Al-Water nanofluid show good result [15, 16]. So above literature review concluded that for heat transfer rate of nanofluids is depending on Reynolds number, nanoparticle shape and size and inlet temperature of nanofluid [17–20]. The demand for nanofluids is going to increase for heat transfer application [21–25] day by day especially in fuel cells, pharmaceutical processes and refineries.

After going through the above literature review, this worked is aimed at studying the heat transfer enhancement and flow characteristics of Al₂O₃–water nanofluids at a low concentration flowing in a horizontal double pipe heat exchanger in laminar flow condition. It has been decided that the thermal performance of a double pipe heat exchanger using nanofluids and water would be compared first numerically and then numerical result would be validate by experimental result. The results of this study can prove to be beneficial and successfully help to improve the rate of heat transfer.

2 Nanofluid Preparation

For preparing the Al₂O₃ nanofluid, two-step method was used. The nanoparticles of 99.9% purity were purchased from Ultrananotech Pvt. Ltd, Bangalore. The alpha phase Al₂O₃ nanoparticles are of density 3.9 g/cm³ and the particle size ranges between 30 and 50 nm. The nanofluids were prepared in the Material Research Lab of Symbiosis Institute of Technology. Mass of nanoparticle required per unit mass of water calculate in Table 1. Snapshot of the Excel Sheet is attached below. By changing the amount of water and/or the volume concentration, the number of grams of nanoparticles required for that amount of water can calculate.

Mass of nanoparticles was calculated by following equation:

$$\text{Volume concentration} = \frac{(M_n/\rho_n)}{[(M_w/\rho_w) + (M_n/\rho_n)]} \quad (1)$$

Table 1 calculates that 98.9975 g of the nanoparticles requires to prepare 10 L of nanofluid of 0.25% concentration. Nanoparticles are added to the distilled deionized water according to the values obtained in Table 1. Using the magnetic stirring apparatus from the Material Science lab, the solution stirrers at a high rpm for 10 min. Due to the absence of any surfactant, nanofluid remains 100% stable for 30 min, and then the particles gradually start settling thereafter.

Table 1 Nanofluid calculation

Nanofluid concentration calculation sheet		
Al ₂ O ₃		
Mass of base fluid	10	kg
Density of base fluid	1	kg/L
Density of nanoparticle	3.95	g/cc
Percentage calculation	0.25	%
Mass of nanoparticle required	98.9975	g
Mass of base fluid	10	kg
Density of base fluid	1	kg/L
Density of nanoparticle	3.95	g/cc
Percentage calculation	0.1	%
Mass of nanoparticle required	158.635	g
Mass of base fluid	10	kg
Density of base fluid	1	kg/L
Density of nanoparticle	3.95	g/cc
Percentage calculation	0.1	%
Mass of nanoparticle required	39.5395	g

3 Experimental Setup

The Experimental Setup (Fig. 1) consists of double pipe concentric heat exchanger (Fig. 1). Hot water (Fluid 1) obtained from an electric heater, flows through the inner pipe while the nanofluid (Fluid 2) flows through the annulus of the two pipes. The



Fig. 1 Double pipe heat exchanger experimental setup

nanofluid stored in a tank is pumped using a submersible water pump. Ball valves are fitted to control the water and the nanofluid flow rates. These flow rates are recorded and measured with the help of Hall effect water flow meters (YF-S201) which run on an Arduino-based program. A counter flow between the two fluids is established in the double pipe heat exchanger. Once the heat exchange is completed, the water returns to the heater and the nanofluid after passing through which cools it, returns to the reservoir, and the cycle continues. The inlet and outlet temperatures of the fluids are observed by digital thermometer. Since magnetic Hall effect sensor is used here, a circuit is used to convert the electrical pulses into flow rate in LPH. The rotor has a magnet, and there is a Hall effect sensor which senses how many times the magnet crosses the sensor per second. Components used for this setup are: YF S201 Flow Meter × 2, Atmega328p Controller, 16 × 2 LCD Module, 16Mhz Crystal, 22pF Capacitor.

Flowrate has been calculated by using Eq. 2.

$$\text{Flow Rate (LPH)} = (\text{Frequency of hall effect sensor} * 60) / 7.5 \quad (2)$$

Firstly, Bootloader of Arduino has to be programmed onto the Atmega controller. After that, Atmega controller acts like an Arduino. After that, program is uploaded onto the controller and the connections are made between the flow meter and the 16 × 2 LCD display.

4 Experiment Procedure

Heat transfer between hot water–cold water and hot water–nanofluid performed separately. For hot water, normal water is heated in the heater first. Before entering the heater, flow of water is controlled using a ball valve. Flow is measured using magnetic Hall effect flow meter. After heat exchange by hot water inside the heat exchanger, the water flows out to the drainage. For cold water loop, water is stored in the evaporator of refrigeration test rig. Here, water is cooled using R134a coolant. Then this cold water is pumped to the heat exchanger. The flow of water is controlled by ball valve. To ensure the safe operation of the pump, a bypass valve also provides. For nanofluids loop, first nanofluid is cooled in refrigerator. Then the nanofluids is pumped to the heat exchanger and flow valve is used to control the flow. The flowrate of the nanofluid is measured using the flow meter.

In the first experiment, the hot water loop and cold water loop run simultaneously. While doing so, inlet outlet temperatures of hot and cold fluids are measured. These reading are used for to calculate overall heat transfer coefficient.

In the second experiment, the hot water loop and nanofluid loop run simultaneously. While doing so, inlet and outlet temperatures of two fluids are measured. From these reading, overall heat transfer coefficient is calculated and then compares it with the value obtained in the previous experiment.

$$\Phi = \frac{m_p / \rho_p}{(m_p / \rho_p) + (m_f / \rho_f)}$$

5 Result and Analysis

By the help of measured inlet and outlet temperatures of hot and cold fluid, the overall heat transfer coefficient calculates to estimate the thermal performance of heat exchanger. It is also calculated to determine the enhancement of heat transfer rate on replacement of water with nanofluid. Amount of heat transfer between two fluid is calculated by Eq. 3

$$Q = U A \Delta T_{lm} \quad (3)$$

Equation 4 is used for calculating Overall heat transfer

$$U = \frac{Q}{A \Delta T_{lm}} \quad (4)$$

where,

Logmean temperature is calculated by Eq. 5

Here,

$$\Delta T_{lm} = \frac{(T_{Hi} - T_{Co}) - (T_{Ho} - T_{Ci})}{L_n \frac{(T_{Hi} - T_{Co})}{(T_{Ho} - T_{Ci})}} \quad (5)$$

Amount of heat carried by hot and cold fluid is calculated by Eq. 6.

$$Q = m C_p \Delta T \quad (6)$$

Heat capacity (C_p) value for nanofluid is calculated using Eq. 7.

$$C_p(\text{nanofluid}) = w * C_p(\text{Al}_2\text{O}_3) + (1 - w) * C_p(\text{Water}) \quad (7)$$

Weight fraction (w) of nanofluids is calculated by Eq. 8

$$w = \frac{\text{weight of nanoparticles}}{\text{weight of nanoparticles} + \text{weight of base fluid}} \quad (8)$$

Table 2 Condition of fluids

	Flow rate (LPH)	Inlet temp (°C)	Outlet temp (°C)	Velocity (m/s)	Parameter	Diameter (mm)
Hot water	120	51	45	0.3848	Copper tube	12.5
Cold water	120,240,320	28	32	0.18855	GI tube	33.8
Nanofluid	120,240,320	21	25	0.0707	Nanofluid inlet	12.7
					Nanofluid outlet	12.7
					Hot water inlet/Outlet	10.5

6 Simulated Result

Before experimental analysis, simulation of fluid temperature variation along the heat exchanger is done by ANSYS 19.2. For modeling, SCDM is used. Table 2 shows the parameter used for numerical analysis. Thermo-physical properties are calculated by the help of above equations and shown in Table 2. Hybrid initialization is done because it solves the Laplace equation to determine the pressure and velocity parameters. Pressure-based solver is used with absolute velocity formulation. The pressure-based solver solves this equation in an implicit manner. It is generally used for incompressible flow simulations. For this heat exchanger, steady-state analysis is used and calculations are performed for 1000 iterations at reporting interval of 1. For CFD post, all the cell zone conditions, boundary conditions, material properties will remain same. Analysis was carried out at 3 different flow rates. Flow rate of hot water was maintained at 120 LPH, and the flow rate of cold water and nanofluid was varied from 120 to 320 LPH. With the respective pipe diameters, we found out the velocities at required flow rate and the results are shown in Figs. 2,3,4,5, 6, and 7 (Table 3).

7 Experimental Result

Results obtained experimentally show that the overall heat transfer coefficients for the water–water experiment at 120 LPH, 240 LPH, and 320 LPH are 0.323, 1.058, and 1.976 kW/m² °C, respectively. Similarly, the overall heat transfer coefficients for the nanofluid–water experiment at the same flow rates are 0.467, 1.337, and 2.031 kW/m² °C, respectively (Figs. 8 and 9).

Results obtained from ANSYS show that the overall heat transfer coefficients for the water–water experiment at 120 LPH, 240 LPH, and 320 LPH are 0.469, 1.058, and 1.976 KW/m² °C, respectively. Similarly, the overall heat transfer coefficients

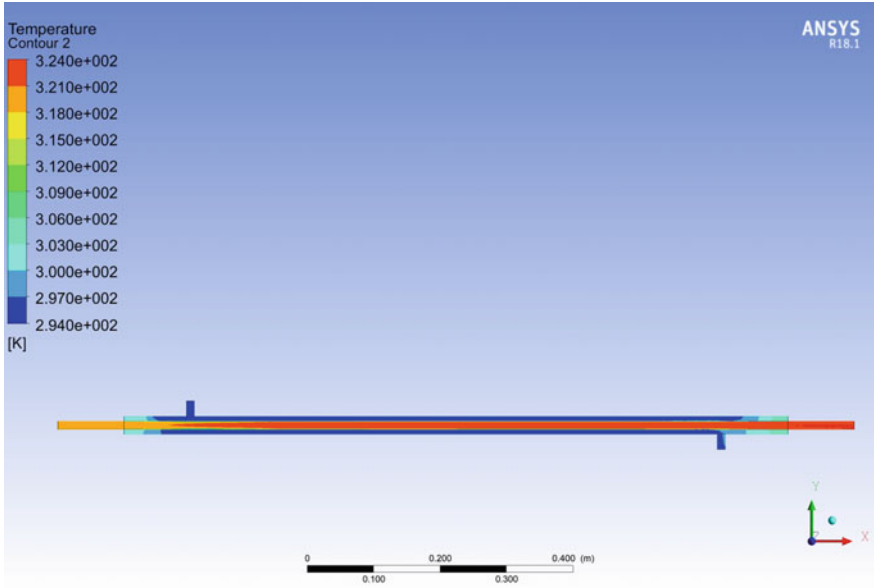


Fig. 2 Observation table of water at 120 LPH

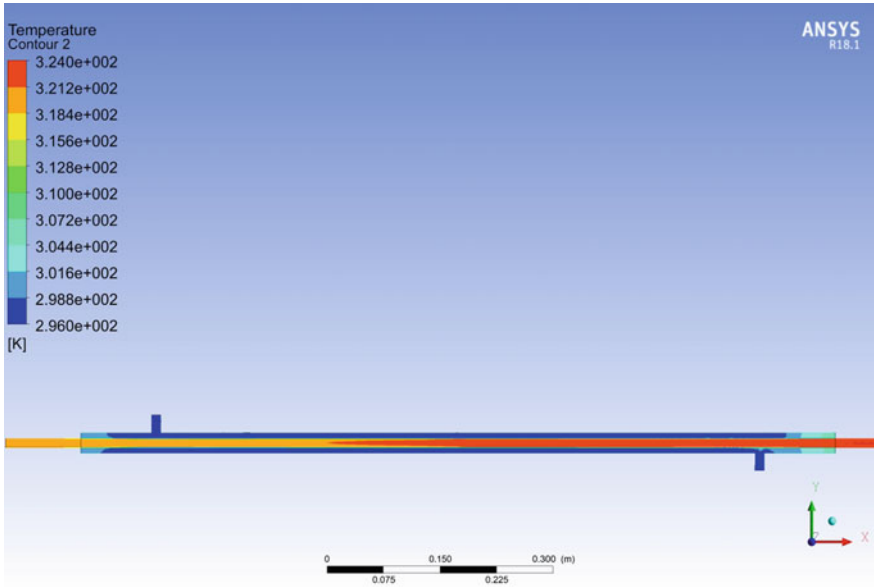


Fig. 3 Observation table of water at 240 LPH

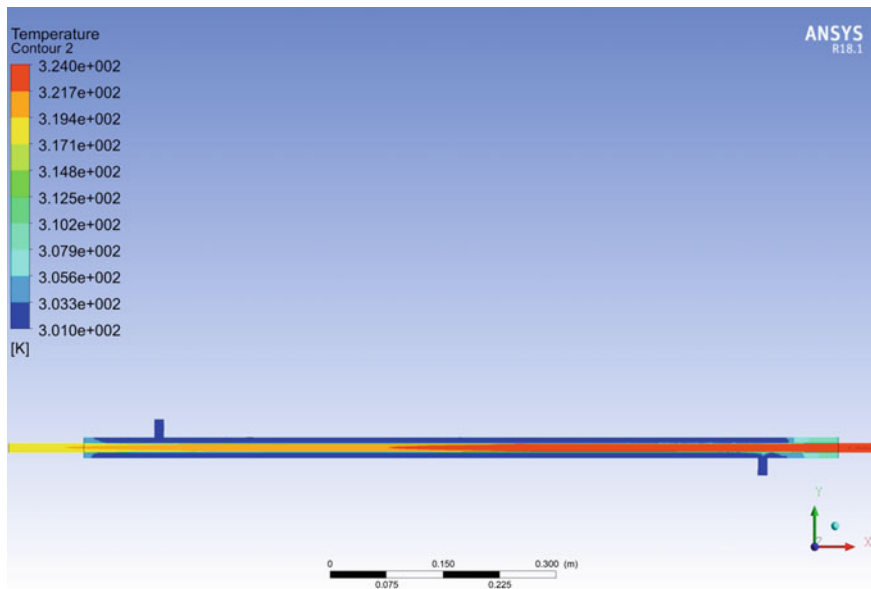


Fig. 4 Observation table of water at 320 LPH

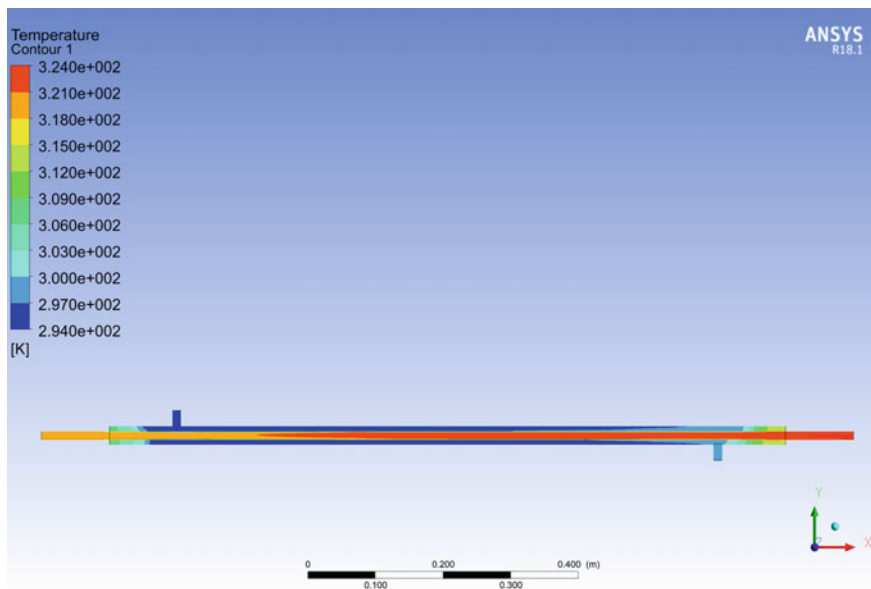


Fig. 5 Observation table for nanofluid Al₂O₃ at 120 LPH

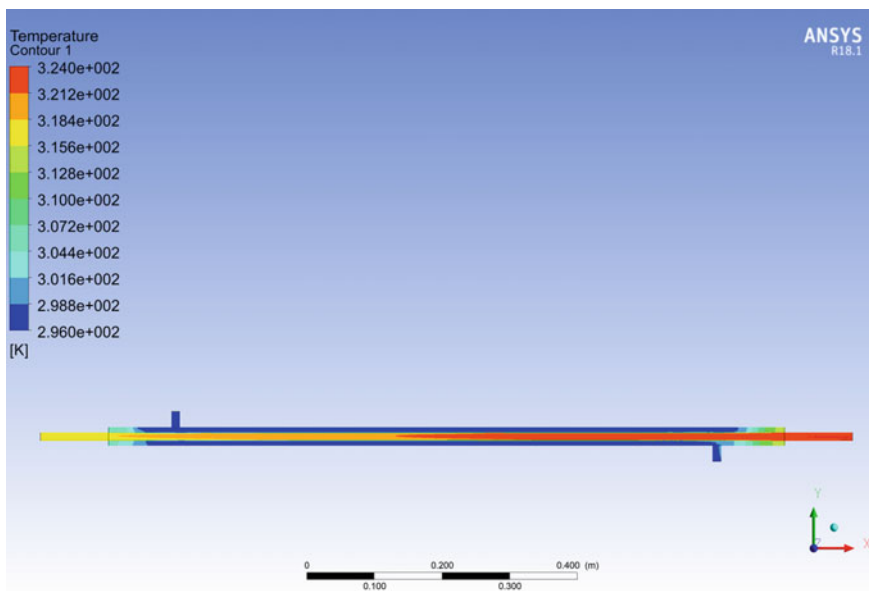


Fig. 6 Observation table of nanofluid Al_2O_3 at 240 LPH

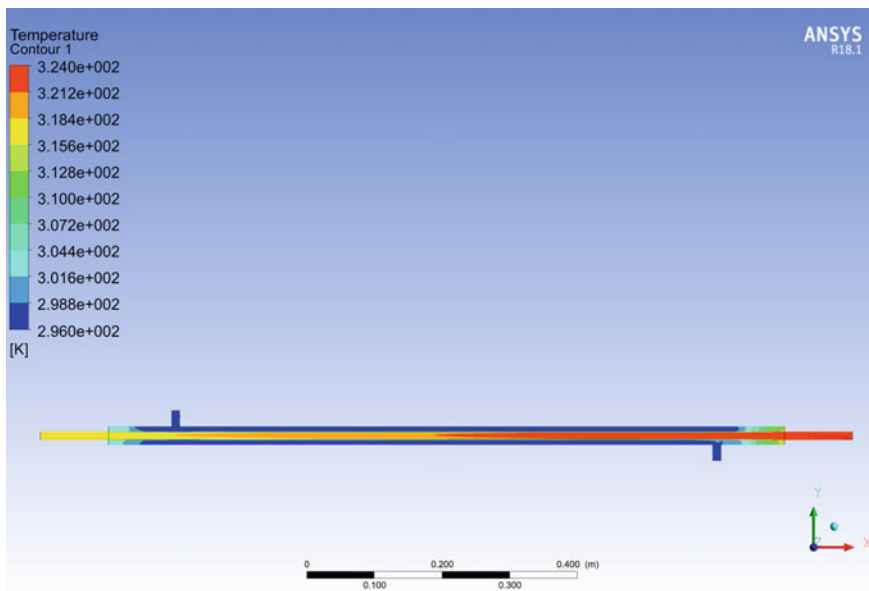


Fig. 7 Observation table of nanofluid Al_2O_3 at 320 LPH

Table 3 Thermo-physical properties

Material	Density (kg/m ³)	Specific heat(J/kg K)	Th. conductivity (W/m K)	Viscosity (kg/m s)
Copper	8978	381	387.6	
GI	2719	871	202.4	
Water–liquid (fluid)	998.2	4182	0.6	0.001003
Nanofluid 0.25%Al ₂ O ₃ (fluid)	1038	3806	0.7	0.001582
Nanofluid 0.75%Al ₂ O ₃ (fluid)	1121	5490	0.8	0.001762

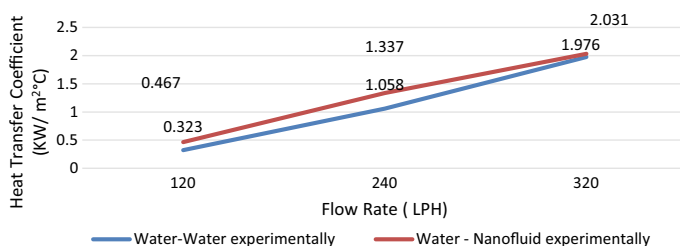


Fig. 8 Experimental values of overall heat transfer coefficient variation for different flow rate

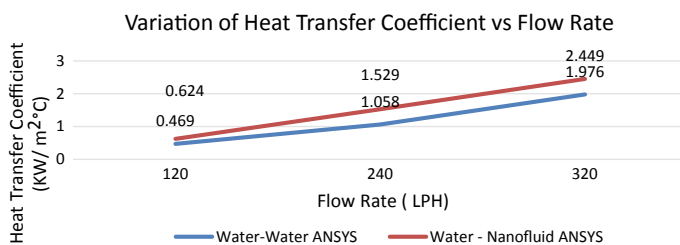


Fig. 9 Simulated values of overall heat transfer coefficient variation for different flow rate

for the nanofluid–water experiment at the same flow rates are 0.624, 1.529, and 2.446 KW/m² °C, respectively.

8 Conclusion

The results obtained show that, at 120 LPH, 240 LPH, and 320 LPH an improvement of 44.58, 26.37, and 2.78% in the heat transfer coefficient. After analysis of above result, it can conclude that the overall heat transfer coefficient increases with increase in flow rate. At the same flow rate, the heat transfer coefficient is enhanced when

nanofluids are used. At 320 LPH, the heat transfer was found to be maximum. Experimental temperature difference was found to be 7°C , and analytical value was 8°C . Overall heat transfer coefficient at 320 LPH was maximum. However, the increase in heat transfer coefficient after using nanofluid was the least. Overall heat transfer coefficients calculated from ANSYS are slightly higher than actual values owing to heat lost. In ANSYS, we have considered the heat exchanger to have an adiabatic wall; however, the actual insulation provided is not 100% efficient.

It has been also observed that the higher concentrations of nanofluids enhance the thermal properties of the nanofluids; however, heat transfer coefficient would increase with increase in concentration only up to a certain limit. Adding a surfactant to the nanofluid will most likely increase the stability and improve the thermal properties of the nanofluid. Shape and size of the nanoparticles also affect the thermal and mechanical properties of the nanofluids.

An example where nanofluids can be used is in photovoltaic solar panels. Owing to the ever fluctuating energy prices, the need for energy recovery systems is rapidly increasing. Photovoltaic systems harness the solar energy and convert it into electrical energy. However, a major drawback of this system is that only the light energy is used in photovoltaic cells to generate electricity. The remaining energy which is in the form of heat is wasted. Along with that, due to higher temperatures, efficiency of photovoltaic cells reduces, and cooling is required. This waste heat can be extracted using heat recovery units where our nanofluids can act as a working fluid to carry heat more efficiently as compared to water.

References

1. Choi SUS, Eastman JA (1995) Eastman enhancing thermal conductivity of fluids with nanoparticles. In: ASME international mechanical engineering congress & exposition, 12–17 Nov, San Francisco, CA
2. Thakre PB, Pachghare PR (2017) Performance analysis on compact heat exchanger. *Mater Today Proc* 4(8):8447–8453
3. Bhosle BB, Hatkar DN (2018) Experimental investigation of heat transfer co-efficient in nanofluids. *Int Res J Eng Technol (IRJET)* 05(03). e-ISSN: 2395–0056
4. Anil Kumar Naik B, Venu Vinod A (2018) Heat transfer enhancement using non-Newtonian nanofluids in a shell and helical coil heat exchanger. *Exp Thermal Fluid Sci* 90:132–142
5. Tiwari AK, Ghosh P, Sarkar J (2013) Performance comparison of the plate heat exchanger using different nanofluids. *Exp Thermal Fluid Sci* 49:141–151
6. Bahiraei M, Rahmani R, Yaghoobi A, Khodabandeh E, Mashayekhi R, Amani M (2018) Recent research contributions concerning use of nanofluids in heat exchangers: a critical review. *Appl Therm Eng* 133:137–159
7. Han D, He WF, Asif FZ (2017) Experimental study of heat transfer enhancement using nanofluid in double tube heat exchanger. *Energy Procedia* 142:2547–2553
8. Zhu HT, Zhang CY, Tang YM, Wang JX (2007) Novel synthesis and thermal conductivity of CuO nanofluid. *J Phys Chem C* 111(4):1646–1650
9. Kwak K, Kim C (2005) Viscosity and thermal conductivity of copper oxide nanofluid dispersed in ethylene glycol. *Korea-Australia Rheol J* 17(2):35–40
10. Liu M-S, Lin MC-C, Huang I-T, Wang C-C (2006) Enhancement of thermal conductivity with CuO for nanofluids. *Chem Eng Technol* 29(1):72–77

11. Agarwal R, Verma K, Agrawal NK, Duchaniya RK, Singh R (2016) Synthesis, characterization, thermal conductivity and sensitivity of CuO nanofluids. *Appl Therm Eng* 102:1024–1036
12. Vajjha RS, Das DK, Namburu PK (2010) Numerical study of fluid dynamic and heat transfer performance of Al₂O₃ and CuO nanofluids in the flat tubes of a radiator. *Int J Heat Fluid Flow* 31(4):613–621
13. Fotukian SM, Nasr Esfahany M (2010) Experimental study of turbulent convective heat transfer and pressure drop of dilute CuO/water nanofluid inside a circular tube. *Int Commun Heat Mass Transfer* 37(2):214–219
14. Usri NA, Azmi WH, Mamat R, Abdul Hamid K, Najafi G (2015) Thermal conductivity enhancement of Al₂O₃ nanofluid in ethylene glycol and water mixture. *Energy Procedia* 79:397–402
15. Yu W, Xie H, Li Y, Chen L, Wang Q (2012) Experimental investigation on the heat transfer properties of Al₂O₃ nanofluids using the mixture of ethylene glycol and water as base fluid. *Powder Technol* 230:14–19
16. Syam Sundar L, Venkata Ramana E, Singh MK, Sousa ACM (2014) Thermal conductivity and viscosity of stabilized ethylene glycol and water mixture Al₂O₃ nanofluids for heat transfer applications: An experimental study. *Int Commun Heat Mass Transfer* 56:86–95
17. Naseema, Nawazish Mehdiya S, Manzoor Hussain M, Khader Basha S, Abdul Samad M (2018) Heat enhancement of heat exchanger using aluminium oxide (Al₂O₃), copper oxide (CuO) nano-fluids with different concentrations. *Mater Today Proc* 5(2):6481–6488
18. Hashemabadi SH, Hoseini SM, Seifi Jamnani M (2015) Experimental study of heat transfer enhancement using water/ethylene glycol based nanofluids as a new coolant for car radiators. *Int J Autom Mech Eng* 12:2857–2865
19. Kumar N, Sonawane SS, Sonawane SH (2018) Experimental study of thermal conductivity, heat transfer and friction factor of Al₂O₃ nanofluid. *Int Commun Heat Mass Transfer* 90:1–10
20. Venkata Raman E, Singh M, Sousa ACM, Sundar S (2014) Thermal Conductivity and viscosity of stabilized ethylene glycol and water mixture Al₂O₃ nanofluids for heat transfer applications: an experimental study. *Int Commun Heat Mass Transfer* 56:86–95
21. Narendar G, Gupta AVSKS, Krishnaiah A, Satyanarayana MG (2017) Experimental investigation on the preparation and applications of Nano fluids. *Mater Today Proc* 4(2):3926–3931
22. Somasekhar K, Malleswara Rao KND, Sankararao V, Mohammed R, Veerendra M, Venkateswararao T (2018) A CFD investigation of heat transfer enhancement of shell and tube heat exchanger using Al₂O₃—water nanofluid. *Mater Today Proc* 5(1):1057–1062
23. Naraki M, Pegyhambarzadeh SM, Hasembadi SH, Vermahmoudi Y (2013) Parametric study of overall heat transfer coefficient of CuO/water nanofluid in a car radiator. *Int J Thermal Sci* 66:82–90
24. Tijani AS, bin Sudirman AS (2018) Thermos-physical properties and heat transfer characteristics of water/anti-freezing and Al₂O₃/CuO based nanofluid as a coolant for car radiator. *Int J Heat Mass Transfer* 118:48–57
25. Agarwal R, Verma K, Agrawal NK, Singh R (2017) sensitivity of thermal conductivity for Al₂O₃ nanofluids. *Exp Thermal Fluid Sci* 80:19–26

Impact of Inlet Angle on Cooling of a Continuously Variable Transmission in a BAJA SAE Vehicle



Amitabh Das, Tarashekhar Padhy, and Kannan Chidambaram

Abstract Continuous operation of the CVT or continuously variable transmission results in enormous generation of heat and thermal gradient within the transmission unit. This can lead to substantial damage of the rotating belt and pulleys in contact eventually affecting its performance. This reduces the torque transfer capacity of the CVT. CVT can be cooled with the assistance of air inlet on its cover. This paper analyzes the various angle of air inlet for CVT cover and determines the ideal inlet geometry for maximum cooling effect using CFD simulation in ANSYS Fluent. Based on benchmarking, the dimensions of the Gaged GX9 are used, and the cover is designed using the appropriate dimensions from the BAJA SAE Rulebook 2018. Different inlet geometries are simulated for constant heat generation rates, and the resultant heat flux, outlet temperature and internal temperatures are calculated for each of them using ANSYS. The outcome is a well-defined angle of inlet for the given CVT cover model, which enables better cooling and yields satisfactory results. CVT, heat transfer, inlet angle, CFD

Keywords CVT · Heat transfer · Inlet angle · CFD

1 Introduction

Automotive aerodynamics has become an indispensable part of the automotive industry owing to several factors like vehicle performance, comfort, stability and cooling of components. Drag reduction is a paramount requirement for aerodynamic research. However, the necessity for cooling of components by providing adequate interfacing with air is also indispensable. Air cooling is still a major engineering practice employed in automobile components to keep parts in ideal running temperatures for ensuring maximum efficiency and reducing wear and tear. CVT or continuously variable transmission has two clutches; primary and secondary. The primary clutch is attached to and powered by the engine, and the secondary clutch receives torque

A. Das (✉) · T. Padhy · K. Chidambaram
Vellore Institute of Technology, Vellore 632014, India
e-mail: amitabh.dash51@gmail.com

from the primary via a belt. The belt is manufactured with reinforced kevlar rubber and generates heat while running. The heat increases the belt stiffness and belt slip-page resulting in loss of transmission. Furthermore, overheating of the belt may result in melting and burning of it causing massive inconvenience and creating a hazard in the C-section of the car. Therefore, proper cooling is crucial not only to get maximum performance but also to reduce the probability of mechanical failures in the transmission components. Heat generation rate (by conduction) is given by Eq. (1)

$$Q = hA(T_2 - T_1) \quad (1)$$

where

Q = heat transferred (W).

h = Convective heat transfer coefficient ($\text{W m}^{-2} \text{K}^{-1}$ or $\text{W m}^{-2} \text{°C}^{-1}$).

A = Surface area (m^2).

2 Theory

The governing equation used in thermal analysis involves Navier–Stokes equation which defines the momentum conservation.

$$\underbrace{\rho \left(\frac{\partial \mathbf{u}}{\partial t} + \mathbf{u} \cdot \nabla \mathbf{u} \right)}_1 = \underbrace{-\nabla p}_2 + \underbrace{\nabla \cdot (\mu(\nabla \mathbf{u} + (\nabla \mathbf{u})^T)) - \frac{2}{3}\mu(\nabla \cdot \mathbf{u})\mathbf{I}}_3 + \underbrace{\mathbf{F}}_4 \quad (2)$$

where \mathbf{u} is the fluid velocity, p is the fluid pressure, ρ is the fluid density, and μ is the fluid dynamic viscosity. The different terms correspond to the inertial forces (1), pressure forces (2), viscous forces (3) and the external forces applied to the fluid (4).

The continuity equation defines the mass conservation as

$$\frac{\partial \rho}{\partial t} + \nabla \cdot (\rho \mathbf{u}) = 0 \quad (3)$$

Both Navier–Stokes equation and continuity equation are solved together to get the results.

The literature review has been carried out to understand the scope and limits of CVT cooling. Vaishya et al. [1] confirmed that the majority of cooling in a scooter's CVT is carried out by convection and attempted to increase its rate by increasing the mass flow rate in it. With modified air inlets and outlets, they were able to reduce the temperature by 15 °C and belt temperature by 20 °C. Dhongde and Chandran [2] carried the experimental study of CVT cooling in a 110 cc scooter and modified the outlet, insulator plate and fan blades to improve cooling of the belt and the clutches.

They obtained the best results after modifying the fan blades (about 14% cooling) as compared to insulator blade (8%) and modified outlet (4%). Wurm et al. [3] have done a comparative study of CVT cooling in snowmobiles and investigated the rate of cooling in the system with different fan blades at different RPMs for the same rate of heat generation. The thickness of the pulley was also varied, and instead of fans, nubs were used in one simulation for the same boundary conditions and came to the conclusion that the ribs are more efficient in convective cooling. Patil et al. [4] have done more modifications in CVT to improve cooling. Introduction of holes, changing the material of the pulleys and using the fins on the rotary parts are the ones which improved the performance. The papers signify that the temperature of the CVT can go as much as 150 °C during operation under maximum load. Analysis showed the modifications in the design showed 10.4% in secondary and 8.55% in primary pulley of the CVT. Steady state thermal analysis done by Sivakumar et al. [5] in ANSYS WORKBENCH showed an approximate 33% increase in the surface areas of the pulleys reduces the temperature by 21.8% in case of rectangular fins and 5.67% in case of cylindrical fins. Also, the overall mass of the pulleys increase by 0.47 and 6.16% in case of rectangular fins and cylindrical fins, respectively. This shows that the cooling rate can be increased extensively by using rectangular pulley. CVT efficiency can also dictate the fuel economy of the vehicle as shown in the study and testing by Yu Long Lei et al. [6]. The bench testing of the CVT drivetrain of a test car was carried out by Yu Long et al. using softwares like AVL Cruise using a 4 drum chassis dynamometer. They tried to validate the CVT efficiency impact on fuel economy using real-time experimental setup. Karthikeyan et al. [7] proposed the design of partition plate inside the CVT housing can direct the flow into belt and prevent the fluid around driven and drive pulley from mixing, and can further decrease the temperatures of the belt and pulley.

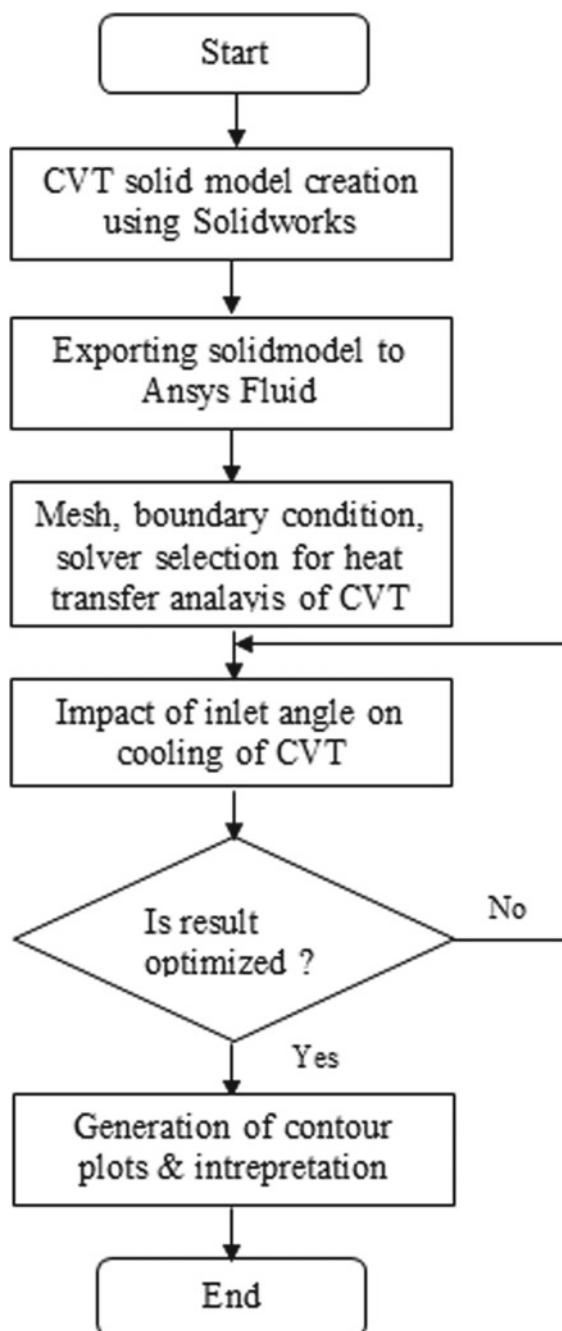
3 Methodology

The flowchart for the adopted simulation work in this research is presented in Fig. 1.

3.1 Modeling

The modeling is done using SOLIDWORKS 17.0, and the dimensions of the Gaged GX9 for the CVT and dimensions of the cover are taken from clearances as stated in BAJA SAE Rulebook 2018. The material for the cover is aluminum for ease in manufacturing, and it is lightweight. The CVT cover has three parts (this particular design): the front cover, the back plate and the curved part. The back plate is toward the engine, and the front cover is toward outside and can be opened in order to remove the CVT. The center-to-center distance of the primary and secondary clutches are 10inches(254 mm) as per benchmarked model of Gaged GX9, and the diameters of

Fig. 1 Flowchart for the adopted simulation work



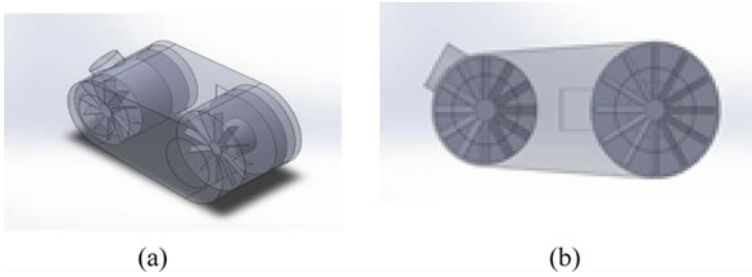


Fig. 2 a and b CAD model of CVT

primary and secondary clutches are 5.5in and 6.5in (the dimensions are primarily in inches because Gaged is a company in the USA and the BAJA SAE rules are US-based only). On top of that, a minimum of 8 mm clearance is given between the outer edge of the clutches and the inner walls of the curved part of the CVT cover. Furthermore, the thickness of the CVT cover at the curved part is 3 mm (as stated in the rulebook) and is manufactured out of aluminum. The isometric and front views CVT CAD models are shown in Fig. 2a, b, respectively.

3.2 Meshing

Conversion from physical domain to computational domain is done using tetrahedral mesh in ANSYS Fluent. Tetrahedron meshing is selected as it is the default meshing provided in ANSYS Fluent. It is convenient to mesh complex geometries. Since the model used for CFD analysis is a 2-D model, distortions are minimum and hence enable tetrahedron to be a comfortable choice than the more accurate hexahedron. The meshing parameters are presented in Table 1, while the meshed solid model is shown in Fig. 3.

Table 1 Meshing parameters of the model

Global mesh size	6 mm
Curvature normal angle	1°
Growth rate	1.2
Cell type	Tetrahedron
Smoothing	High

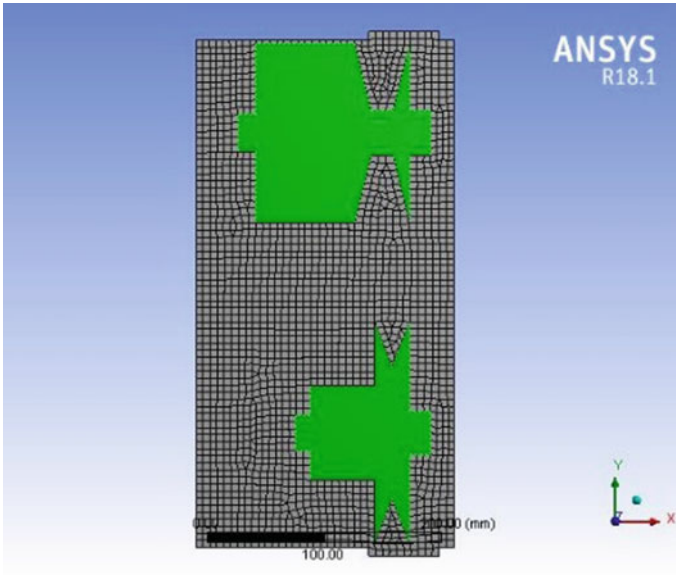


Fig. 3 Tetrahedron meshing of 2-D model

Table 2 Solver details

Scheme	Simple
(a) Gradient	Least square cell
(b) Pressure	Second order-based
(c) Momentum	Second-order upwind
(d) Turbulent kinetic energy	Second order upwind
(e) Turbulent dissipation rate	Second-order upwind

3.3 Numerical Method and Solver

The model is imported into ANSYS Fluent solver for setup (parallel). The solver, material properties and discretization schemes are chosen. After that, the boundary conditions are given as per the calculated approximations. The detailing of solver and boundary conditions adopted in this work are presented in Tables 2 and 3, respectively.

4 Results and Discussions

The source of heat generation in the CVT is the region where the sheaves and the belt come in contact with each other. Within 10–15 min of operation, the temperature reaches to almost 353 K. Fins are often attached to the rotating clutches which

Table 3 Boundary condition

Angle of air inlet (deg.)	Inlet x-velocity (m/s)	Inlet y-velocity (m/s)
15°	2.58	-9.65
30°	5.00	-8.66
45°	7.07	-7.07
60°	8.66	-5.00
75°	9.65	-2.58

Table 4 Heat transfer rates

Angle of air inlet (deg.)	Heat transfer rate (W/m ³ /s)
15°	2433.052
30°	2192.764
45°	1965.037
60°	1725.638
75°	802.998

circulate the air and cool the system and/or an air inlet if given to the curved region of the CVT cover in order to facilitate airflow inside the cover for cooling. The heat transfer rate for different angles of air inlet is presented in Table 4.

It can be observed from the table that for an inlet angle of 15° the heat transfer rate is the maximum. At this angle, the minimum internal temperature and pressure drop at outlet are observed. The pressure drop increases with increase in inlet angle. This can be attributed to the geometry of the CVT cover. The variation of heat transfer rate with respect to inlet air angle is shown in Fig. 4.

Contours for Temperature, Velocity and Pressure across the mid-plane:

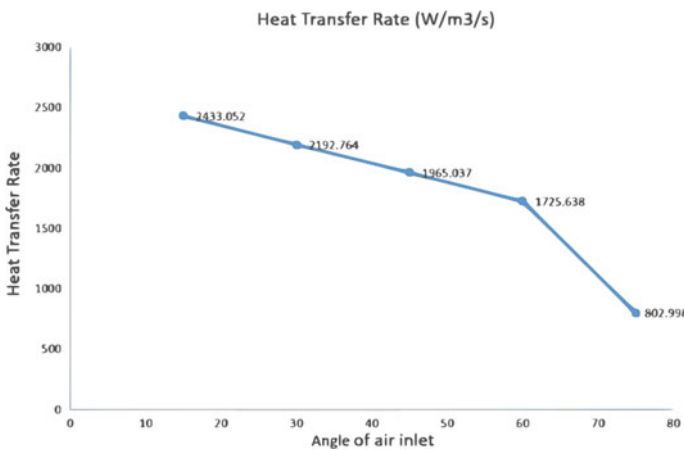


Fig. 4 Graph showing the variation of heat transfer rate with respect to angle of inlet air

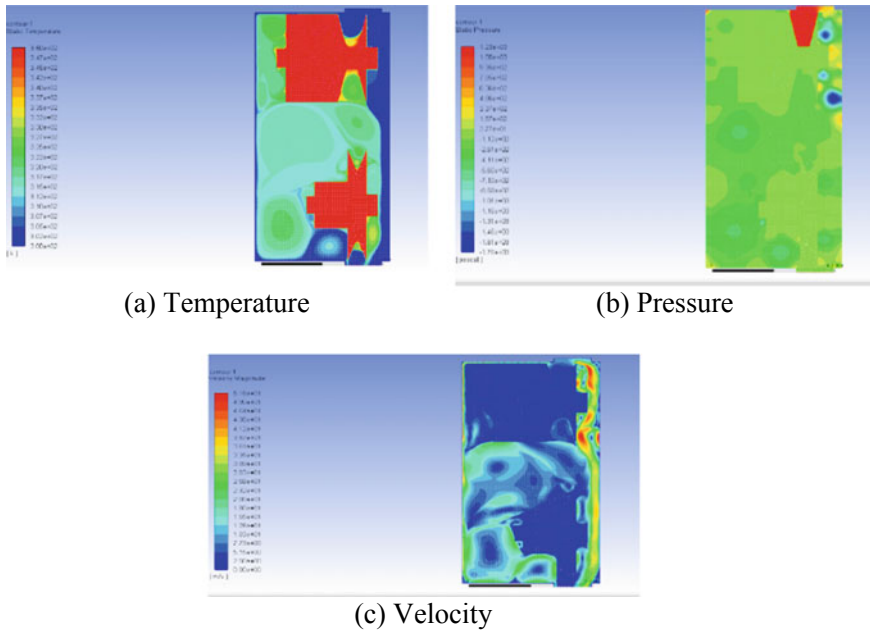


Fig. 5 Contour plot of temperature, pressure and velocity for an air inlet angle of 15°

There is continuous increase in the temperatures in the corresponding angles increasing from 15° to 75° , which can be inferred from Figs. 5, 6 and 7. The inlet angle and heat transfer rate have an inverse proportional relationship. The pressure drop at the outlet is directly proportional to the inlet angle. The inlet angle cannot be reduced to 0° because it violates rules defined in BAJA SAE rulebook (if the angle is 0° , the inlet will be facing the firewall of the vehicle; on the event of a mechanical failure of the CVT, the rotating parts should not hit the firewall as it is a hazard for the driver).

5 Conclusion

Cooling of the drivetrain components is extremely important for maintaining performance and ensuring higher transmission efficiency. In case of CVT, cooling can be done by increasing the surface area of the clutches, adding fins, increasing surface area of inlet and outlet, inducing fans to increase mass flow rate through inlet and outlet and as seen in this paper, the angle of inlet. Angle of inlet with respect to the horizontal is inversely proportional to the rate of heat transfer, and hence, cooling increases as we decrease the angle. Also, the correct combination of the above modifications will help in the ideal cooling of the Continuously Variable transmission. Most of the scooters and two-wheelers use similar inlet–outlet layout and can also change the inlet angle

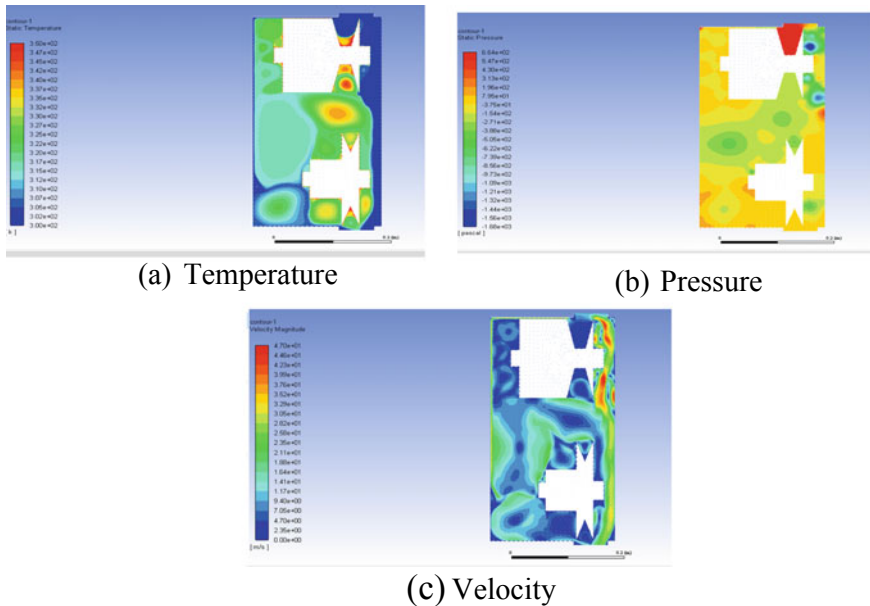


Fig. 6. Contour plot of temperature, pressure and velocity for an air inlet angle of 30°

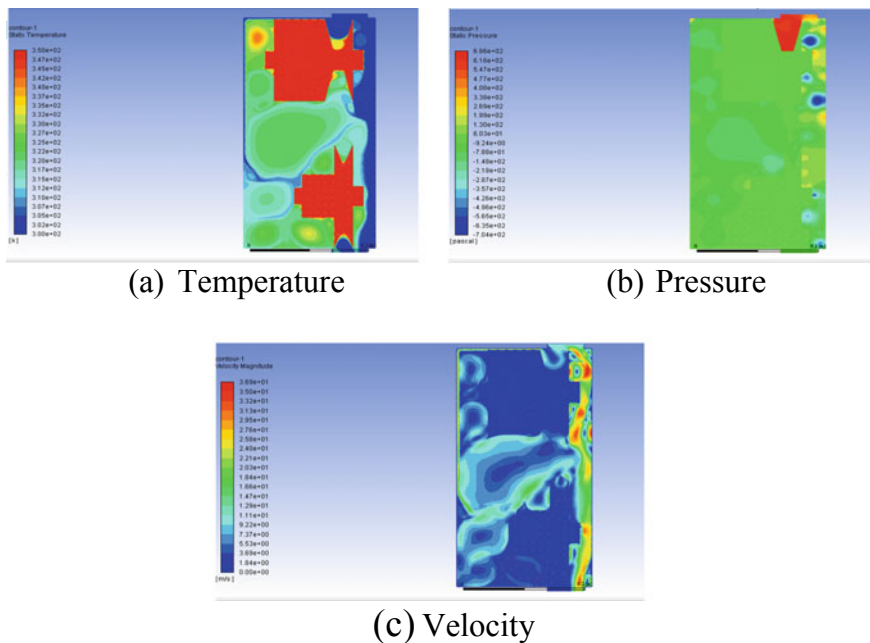


Fig. 7. Contour plot of temperature, pressure and velocity for an air inlet angle of 45°

to enhance the cooling effect. However, there can be several other modifications from the materials aspect as well which can induce higher cooling characteristics. A holistic approach for CVT design incorporating all the above factors can be implemented considering optimized input angle has been accomplished through numerical simulation to get the best results.

References

1. Vaishya AL, Phadnis S (2013) Experimental investigations of forced air cooling for continuously variable transmission (CVT). No. 2013-32-9073. SAE Technical Paper
2. Dhongde S, Chandran V (2014) Experimental study of cooling of continuously variable transmission (CVT) in scooter. No. 2014-01-2003. SAE Technical Paper
3. Wurm J, Hochenauer C, Väisänen E, Hurtig E, J Mähönen (2017) Advanced heat transfer and underhood airflow investigation with focus on continuously variable transmission (CVT) of snowmobiles. SAE Int J Commercial Veh 10(2)
4. Patil M, Bharadwaj K, Sathwick S (2016) A study of cooling of continuously variable transmission (CVT)
5. Sivakumar P, Appalaraju P, Srikar CH, Sanjeevkumarreddy T, Jayendrakumar Y, Vishnuvardhan Babu K (Apr 2018) Steady state thermal analysis of continuous variable transmission with extended surfaces. Int Journal of Mechanical and Production Engineering Research and Development (IJMPERD) ISSN (P): 2249-6890; ISSN (E): 2249- 8001 8(2), 1147–1156
6. Lei YL et al (2018) Car fuel economy simulation forecast method based on CVT efficiencies measured from bench test. Chin J Mech Eng 31(1):83
7. Karthikeyan N, Gokhale A, Bansode N (2014) A study on effect of various design parameters on cooling of clutch for a continuously variable transmission (CVT) system of a scooter. SAE Technical Paper 2014-01-2595. <https://doi.org/10.4271/2014-01-2595>

Coaxial Thermal Probe as a Heat Flux Sensor: An Analytical, Numerical, and Experimental Approach



Anil Kumar Rout, Niranjana Sahoo, and Pankaj Kalita

Abstract Measurement of transient heat flux values is a challenging task as it requires fast response sensors. The standard heat flux sensors cannot satisfy the requirement for transient measurement due to more response time. Therefore, a thermal probe has been prepared in-house for capturing transient response in high speed flows especially in aerodynamics studies. The probe has been fabricated from bare chromel and constantan thermoelements named as “coaxial surface junction thermocouple (CSJT).” Experiments are carried out for heat flux calibration with the help of a laser unit to access the capability of the probe in measuring heat flux values. The inferred experimental temperature signal is used to estimate the surface heat flux values analytically. Similarly, a numerical simulation has been performed to validate the results. The values are found to have a matching with the applied heat flux in terms of trend and magnitude in a timescale of 0.4 s.

Keywords Thermocouple · Transient temperature · Coaxial thermal probe · Surface heat flux · Laser

1 Introduction

Information regarding transient temperature history and surface heat flux values is having enormous importance for efficient design of many engineering equipment and systems, e.g., I.C. Engine design, reentry vehicles, etc. Sensors used for capturing average heat flux values are incapable for capturing transient temperature signals. To do so, there is a requirement of fast response sensors (~ microsecond response time). Generally, heat flux value is estimated from transient temperature history using well-adopted processes. The transient surface heat flux values can be predicted from temperature signals captured by many useful sensors like null point calorimeter, thin-film sensors, different gauges, and coaxial thermocouples. Specific advantages and disadvantages are always associated with different sensors with respect to sensing

A. K. Rout (✉) · N. Sahoo · P. Kalita
Centre for Energy, Indian Institute of Technology Guwahati, Guwahati, Assam 751039, India
e-mail: anil.rout@iitg.ac.in

capability and applicability. Coaxial surface junction thermocouple is superior to other sensors used for short duration studies due to its instant responsive nature and robustness. Different researchers have adopted various design techniques and predicted the heat flux values from transient temperature signals [1, 2]. An initial study by Sanderson and Sturtevant [3] provided an inference regarding the tapered fit model among the thermoelements which resulted in imparting a response time in the order of $1 \mu\text{s}$ and was quite capable in measuring transient heat flux values in wind tunnel experiments. Similarly, a straight and simple design was used by Mohammed et al. [2, 4], which provided a decent information regarding a low-cost K-type CSJT. It also explained the difficulties during fabrication process, the effect of scratch technique, and efficient estimation of thermal product values. The work by Kumar and Sahoo [5] focused regarding design and fabrication of a K-type CSJT and simple laboratory calibration techniques. Some similar methods were adopted by Kumar et al. [6]. The techniques for convective surface heat transfer measurement in aerodynamic structures were discussed by Sahoo and Peetala [7]. Similarly, Agarwal et al. [1] have presented about the thermal “product” determination in millisecond time durations, for CSJT using laboratory experiments. Modifying the work by Sanderson and Sturtevant, Desikan et al. [8] fabricated and tested a tapered type K-type coaxial in a shock tunnel at free stream Mach no of 5.75. The response time obtained was $\sim 3 \mu\text{s}$.

As inferred from the literature, most of the studies focus on the usage of such coaxial probes for few milliseconds. There is no such evidence of usage of such probes for any extended scale of measurement. Therefore, the present study focuses on finding out the behavior of such probes for an extended timescale of measurement. In addition, it is aimed to access the capability of the thermal probe to measure surface heat flux values and hence its usability as a heat flux probe. To achieve this objective, an E-type thermal probe has been fabricated in the laboratory scale from its constituent thermoelements (Chromel–Constantan). The probe is calibrated for finding the linearity of output voltage with temperature for the measurement temperature range which also provides the sensitivity value of the probe. Then, the correctness of the heat flux values have been analyzed through experimental, analytical, and numerical method. This type of analysis will help in justifying the correctness of recovered heat flux values measured with the help of this probe which at a later part can help for routine use of such probes in unsteady temperature measurements.

2 Fabrication of CSJT

The fabrication was carried out with bare E-type thermocouple materials (chromel and constantan). The process was carried out by coaxially placing the constantan wire (diameter 0.91 and 15 mm length) inside the chromel wire (3.25 mm diameter and 10 mm length) with a thin layer of epoxy in between them throughout the length. The junction between two thermoelements was created with abrasion method which forms a contact between them in the form of cold welds. Lead wires with 0.25 mm

diameter having similar material composition were spot welded to the sensor which was used for the data acquisition purpose. More details regarding fabrication are explained by Mohammed et al. [2]. The schematic of the probe is similar to the computational domain as presented in Fig. 3.

3 Static Calibration of CSJT

The direct output from the acquisition system is in the form of voltage. However, for the estimation of heat flux, temperature history is an inherent requirement. Therefore, to find a correlation between the voltage and temperature, a calibration setup is designed which consists of oil bath setup, CSJT, heater, and data acquisition system (Fig. 1a). A beaker containing silicone oil was placed on a heated along with a scientific thermometer to measure the temperature of the oil. The thermometer was used along with CSJT and placed up to the same depth to have a similar sensing environment. The DAS was used for recording the voltage. The rise and fall in temperature values were noted from the thermometer and the corresponding voltage values from DAS. The cold junction temperature was achieved through the use of an ice bath. The voltage and temperature values were plotted to find a relationship between them which resulted in the form of a constant slope for a temperature range greater than 100 °C (Fig. 1b). Referring to Eq. 1, the value of average sensitivity was calculated to be 59 μV/°C for three sets of experiments.

$$\text{Sensitivity, } S = \frac{\Delta V}{\Delta T} \tag{1}$$

$$\dot{q}_s(t) = \frac{\beta}{\sqrt{\pi}} \int_0^t \frac{1}{\sqrt{t-\tau}} \frac{d\{T_s(\tau)\}}{dt} d\tau; \quad \beta = \sqrt{\rho c k} \tag{2}$$

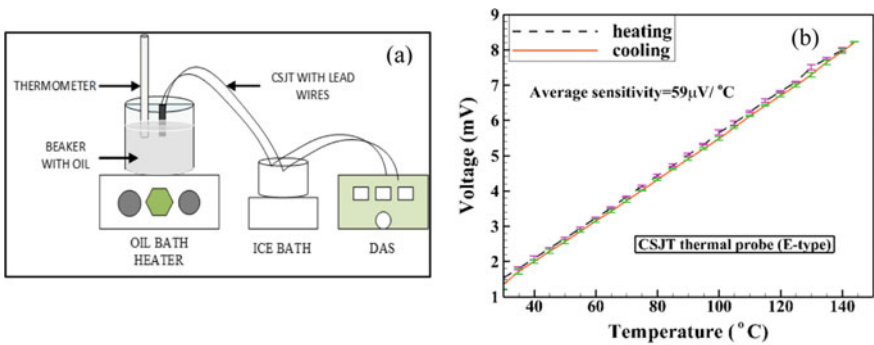


Fig. 1. Static calibration setup (a) oil bath setup for static calibration (b) static calibration plot

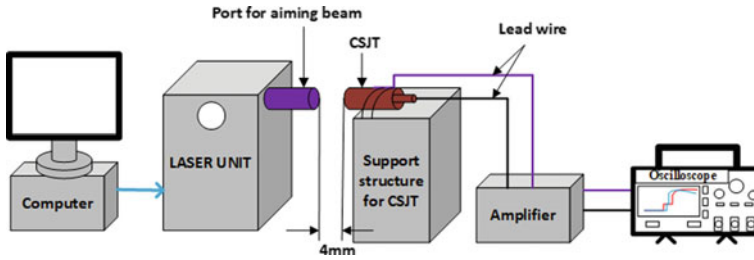


Fig. 2 Laser-based experimental setup

4 Experimentation with LASER Unit

One of the major aims of the present work is to check the correctness of the surface heat flux values obtained from the transient signals of the thermal probe. Therefore, it is quite legitimate to compare or calibrate the inferred heat flux values against a known heat flux reference. A laser light due to its coherence nature can be used as a heating source to provide a constant wattage on the probe. A CW Laser of 2 W is allowed to fall (as step load) on the sensor for 1.5 s. The wattage was managed through a computer operated software interface. The sensor surface was insulated and mounted on a support. The sensor was placed in an appreciable distance from the laser source so to confirm the coverage of entire sensing surface area of the sensor (Fig. 2). Before acquisition, the voltage signals need to be amplified as the output voltage from CSJT is less. Therefore, the voltage is amplified to a gain of 500 and captured in an oscilloscope for a sampling frequency of 5 kHz. From the knowledge of sensitivity value, temperature response is calculated from the voltage response. The schematic of the experimental setup is presented in Fig. 2. Heating the thermal probe by laser is governed by radiation mode of heat transfer. Due to the small timescale of experimentation, the view factor between the source and sink is assumed to be unity. The experimental transient voltage signal and corresponding temperature signal is plotted in Fig. 4.

5 Surface Heat Flux Estimation

Due to the non-availability of any direct formula for the estimation of surface heat flux values in short duration studies, these are predicted analytically through conventional techniques. In the analytical method, the basic heat transfer equations are solved with appropriate boundary conditions involving many assumptions. With the advancement of computational techniques, the heat flux values can be obtained through numerical analysis also.

5.1 *Experimental Heat Flux*

The experimentation is carried out by allowing the laser light of known wattage (2 W) on the thermal probe for 1.5 s, and transient response is recorded. Due to monochromatic nature of the laser light and the experimentation is for a short duration, the inferred wattage on the thermal probe can be assumed to be constant throughout the experiment. The heat flux value imposed on the probe can be calculated from the knowledge of laser wattage and sensor surface area. Assuming a step response from the laser heating, the heat flux value can be taken as a reference value. The transient temperature signals captured from the experiment are utilized to extract the surface heat flux values both analytically and experimentally.

5.2 *Analytical Heat Flux*

The transient temperature captured from experiment is utilized for heat flux prediction through classical heat transfer analysis by assuming one-dimensional heat conduction in a semi-infinite body. The supporting assumptions for the analysis are: (i) Thermal properties of the substrate material are constant and (ii) no lateral heat conduction. With proper assumptions, the basic heat conduction equations can be framed into the form as mention in Eq. 2. A MATLAB code has been used to extract the heat flux values from using Eq. 2. A spline fitted polynomial curve is framed to the discretized set of data obtained from the equation. The detailed description regarding discretization is explained by Taler [9]. Referred to Eq. 2, value of Thermal product (β) for a sensor is an important factor for the accuracy of the heat flux values. Different researchers used different techniques for the determination of thermal product values. It is quite difficult to quantify the exact share from each thermoelement in the junction formation. Therefore, for the present case, the thermal product value is taken with 50% share from each element and the value obtained is $8650.2 \text{ J m}^{-2} \text{ K}^{-1} \text{ s}^{-0.5}$. The extracted heat flux values are plotted in Fig. 5.

5.3 *Numerical Heat Flux*

With the advancement of numerical computations, the fact can be cross-verified numerically. Commercially available software package (ANSYS) has been used for the heat flux estimation. The individual properties of thermoelements are used for respective thermoelements, whereas the average property was used at the junction for simulation purpose. The thermal properties are taken as per the literature [10]. A grid-independent study was carried out to find out the mesh independency with number of nodes as 1,555,647, 1,626,896, and 1,714,609. The results are almost matching with each other. To have minimum computational time, the minimum number of

nodes was used for simulation. The experimental temperature signals are used as input for heat flux prediction along with other boundary conditions as mentioned in Fig. 3. Additionally, the simulation was carried out with heat flux as step input and the temperature signals were compared with experimental signal (Fig. 4). The numerically simulated heat flux values show a nice match with analytical heat flux value (Fig. 5). However, the peak magnitudes are not having an exact match with the experimental heat flux values. Referring to Fig. 4, the temperature trends are having

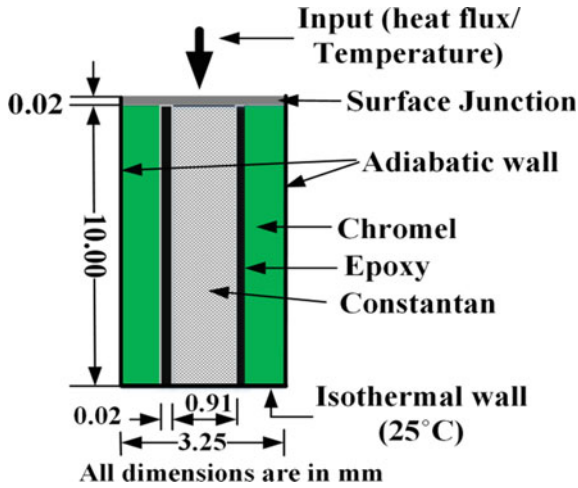


Fig. 3 Computational domain

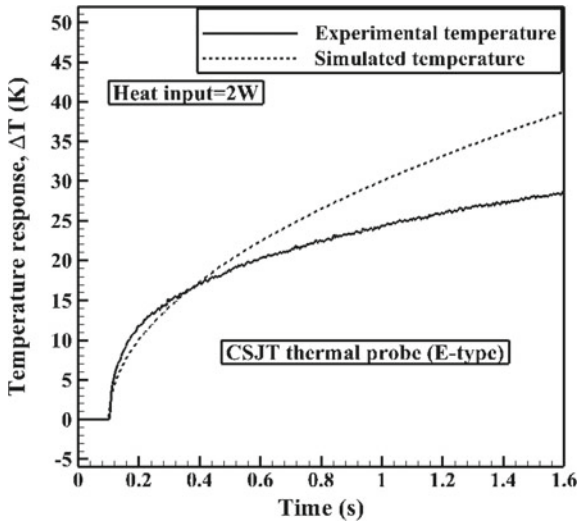


Fig. 4 Comparison of temperature

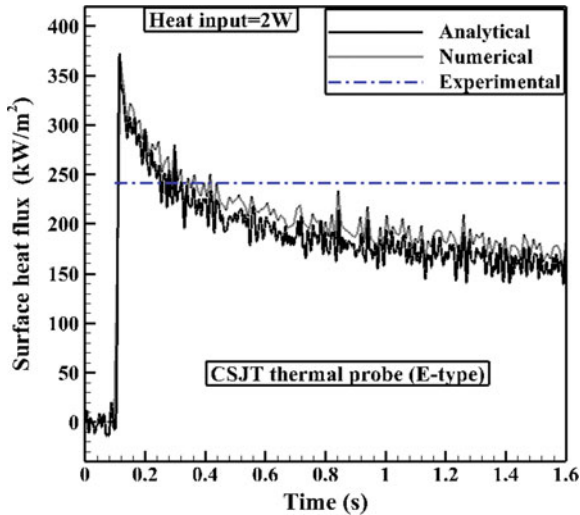


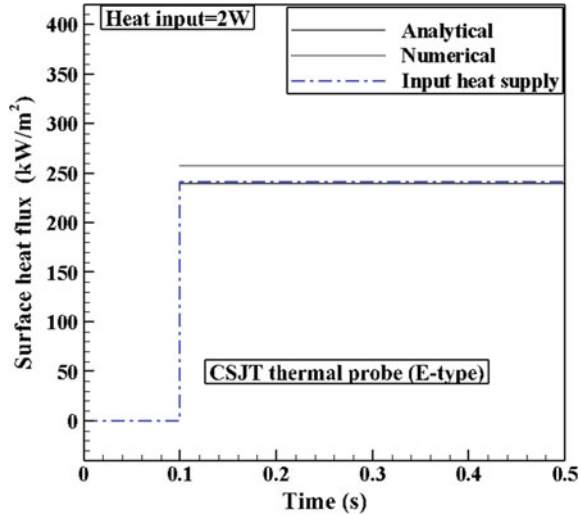
Fig. 5 Comparison of heat flux values

a nice match up to 0.4 s after rise. Therefore, the heat flux values are compared for a timescale of 0.4 s.

6 Comparison of Heat Flux Values

As inferred from the temperature response plots, a nearly matching trend of temperature is observed up to 0.4 s after rise (Fig. 4). Therefore, average heat flux plots are compared for 0.4 s as plotted in figure and found to have a nice match within an error band of $\pm 10\%$. From the analysis made so far using the experimental, analytical, and numerical simulations, it can be concluded that there is a nice match in the trend and magnitude of heat flux values obtained analytically and numerically. However, they do not exactly replicate the step nature of heat load as assumed in case of experimental heat flux. It can be visualized from the temperature signals that after 0.4 s, the signals start deviating, whereas the experimental temperature is observed to be decaying in magnitude as well as in slope compared to the numerical temperature. This nature may be due to penetration of heat towards the distal end of the sensor or a lateral heat transfer may have occurred violating the exact one-dimensional heat transfer assumption. However, these probes can be used effectively in a timescale of 0.4 s (Fig. 6)..

Fig. 6 Comparison of heat flux values for 0.4 s timescale



7 Error Analysis

The uncertainties associated with the current experiments are mainly the combined effect of instrumental errors from the instruments used for experimental purpose. As per the specification from the manufacturer, the errors are ± 0.01 °C, $\pm 0.015\%$, $\pm 0.02\%$, $\pm 0.01\%$, and $\pm 0.12\%$ for thermometer, data acquisition system, amplifier, oscilloscope, laser unit, respectively. The overall uncertainty in the for heat flux estimation is calculated using sequential perturbation method [11], and the estimate range of uncertainty is $\pm 0.5\%$.

8 Conclusion

A coaxial thermal probe has been fabricated in-house from its bare constituent elements (chromel–constantan). The static sensitivity value for the sensor was calculated using an oil bath setup. For heat flux estimation, the sensor was exposed to a CW laser light of known wattage, and temperature signals were noted. Later, surface heat flux was extracted from the temperature signals analytically and numerically. All the heat flux values are compared with experimental heat flux value. The average value of numerically and analytically obtained heat flux values for 0.4 s after rise is found to have a nice match with the experimental heat flux. These experiments provide an inference regarding the usage of such probes as heat flux sensors. However, using it for any particular application requires further investigation.

Acknowledgements The authors would like to acknowledge the financial support received from DRDO, New Delhi (India), for this experimental work.

References

1. Agarwal S, Sahoo N, Singh RK (2016) Experimental techniques for thermal product determination of coaxial surface junction thermocouples during short duration transient measurements. *Int J Heat Mass Transfer* 103:327–335
2. Mohammed H, Salleh H, Yusoff MZ (2008) Design and fabrication of coaxial surface junction thermocouples for transient heat transfer measurements. *Int Commun Heat Mass Transfer* 35(7):853–859
3. Sanderson SR, Sturtevant B (2002) Transient heat flux measurement using a surface junction thermocouple. *Rev Sci Instrum* 73(7):2781–2787
4. Mohammed H, Salleh H, and Yusoff MZ (2011) The effect of scratch technique on the thermal-product value of temperature sensors. *Thermophys Aeromech* 18(1):51–64
5. Kumar R, Sahoo N (2013) Dynamic calibration of a coaxial thermocouples for short duration transient measurements. *J Heat Transfer* 135:1245021–1245027
6. Kumar R, Sahoo N, Kulkarni V (2010) Design, fabrication and calibration of heat transfer gauges for transient measurement. In: *Processing and engineering applications of novel materials*. In: IMECE 2010-40253, pp 17–23
7. Sahoo N, Peetala RK (2011) Transient surface heating rates from a nickel film sensor using inverse analysis. *Int J Heat Mass Transf* 54(5–6):1297–1302
8. Desikan SLN, Suresh K, Srinivasan K, Raveendran PG (2016) Fast response co-axial thermocouple for short duration impulse facilities. *Appl Therm Eng* 96:48–56
9. Taler J (1996) Theory of transient experimental technique for surface heat transfer. *Int J Heat Mass Transfer* 39(17):3733–3748
10. Rout AK, Sahoo N, Kalita P (2019) Effectiveness of coaxial surface junction thermal probe for transient measurements through laser based heat flux assessment. *Heat Mass Transfer* 1–12
11. Moffat RJ (1988) Describing the uncertainties in experimental results. *Exp Thermal Fluid Sci* 1(1):3–17

Thermo-economic and Environmental Analyses of Full Site Repowering Through Coal Gasification and Carbon Capture by Downstream MCFC Integration



Samiran Samanta and Sudip Ghosh

Abstract This study reveals thermodynamic, economic and environmental evaluation of full site-repowering proposal of coal-fuelled thermal power station through integrated gasification combined cycle (IGCC) technology with downstream MCFC integration for CO₂ capture. High-ash Indian coal is mixed with petroleum coke and then gasified in conventional Shell gasifier. The syngas is used to run the integrated gasification combined cycle. Then at the downstream of the combined cycle, natural gas-fired MCFC unit is integrated for CO₂ capture. The findings suggest that the repowering results in 6% capacity increase, 9.2% point efficiency enhancement with a 90% capture of emitted CO₂ from the plant. The cost of electricity becomes high as 108 \$/MWh. Once the cost of MCFC price would go down, it would go down further.

Keywords Repowering · IGCC · MCFC · Carbon capture · Efficiency · Cost of electricity

1 Introduction

Electricity utilization is increasing more and more with time to satisfy the thirst of rapid growth in urbanization, industrialization and economic development. A major portion (about 40%) of world's total electricity is generated by coal-fuelled power plant; however, even more large percentage of electricity comes from coal in several countries like China (79%), India (69%), USA (49%) and many more [1]. It is forecasted that from 2010 to 2040 time periods there would be 46% increase in total CO₂ emission of the world, associated with electricity generation [2]. Among others, conventional coal-fired power plants (CFPPs) are bulk emitters of CO₂ into

S. Samanta (✉)

School of Mechanical Engineering, Kalinga Institute of Industrial Technology (KIIT), Deemed To Be University, Bhubaneswar, Odisha 751024, India
e-mail: samirankgec@gmail.com

S. Ghosh

Department of Mechanical Engineering, Indian Institute of Engineering Science Technology, Shibpur, Howrah 711103, West Bengal, India

© Springer Nature Singapore Pte Ltd. 2021

P. Pant et al. (eds.), *Advances in Mechanical Processing and Design*, Lecture Notes in Mechanical Engineering, https://doi.org/10.1007/978-981-15-7779-6_6

the environment and CO₂ is the major contributor in global warming. In recent COP-21 summit, a worldwide target has been set to restrict the increase in atmospheric temperature within 1.5 °C by cutting down the CO₂ emission into the atmosphere. For this reason, the researchers are giving attention to such methods that would generate electricity efficiently with lesser CO₂ emission into the environment in spite of using coal as fuel. So now the questions come in front of the nations, those who contribute more in total CO₂ emission of the world due to their dependency on coal, which technology should be used to set up new plants or refurbish old plants that has come to its end of life span or abandoned. Setting up new greenfield power station may perhaps not possible all the time because of associated problems regarding land acquiring, other legal clearance, etc. In this situation, full site repowering of an old discarded power station is an interesting option to set up a coal-based power station with improved capacity, efficiency and specific CO₂ emission. Site repowering calls for blowing up the existing plant set-up, except the cooling water system and switchyard and other auxiliary systems. Site repowering is advantageous because there is no need to compromise in adapting the recent advanced technology to existing system components. In comparison with set-up a new plant on a new site, the repowering route is better because there would be savings in both time and cost for the permitting process, transmission access and socio-economic considerations for the local area. Full site repowering is commonly applied to the plant that has almost covered its entire specified life span. Full repowering calls for new technology, new materials, new set-up and new plant components which help to get an improved overall performance from the power station. There is very little study available regarding full site-repowering analysis. Naserabad et al. [3] did thermodynamic analysis of full site repowering of a 320 MW old steam power plant through integrating gas turbine and heat recovery steam generator (HRSG). The results indicated that the repowered power plant can have a maximum efficiency of 52.04%. Ahmadi et al. [4] did energetic and exergetic investigations of full repowering of 200 MW unit of Montazeri Steam Power Plant in Iran by using 400 MW gas turbine. The energy and exergy efficiencies increased by 76.8% and 73%, respectively, due to repowering. In the earlier studies, various methods of repowering had been addressed. Those studies mostly proposed partial repowering. Full site repowering is also talked about by very few researchers. Those site-repowering schemes were based on natural gas-fired GT and HRSG technology. The novelty of present site-repowering scheme is gasification of high-ash Indian coal mixed with petroleum coke to run gas turbine plant with downstream CO₂ capture by molten carbonate fuel cell (MCFC). In this paper, full site-repowering method for an aged sub-critical power station is conceptualized. The aged power station has come to its end of estimated life span and is going to be discarded. It has a capacity of 750 MW (3 × 250 MW). After full site repowering, the new proposed plant would be consisted of an integrated gasification combined cycle (IGCC) with a downstream incorporation of molten carbonate fuel cell (MCFC) unit for CO₂ separation and capture. In this paper, thermodynamic, economic and environmental performance analyses of the proposed repowered plant are being done and compared with the old existing plant performances.

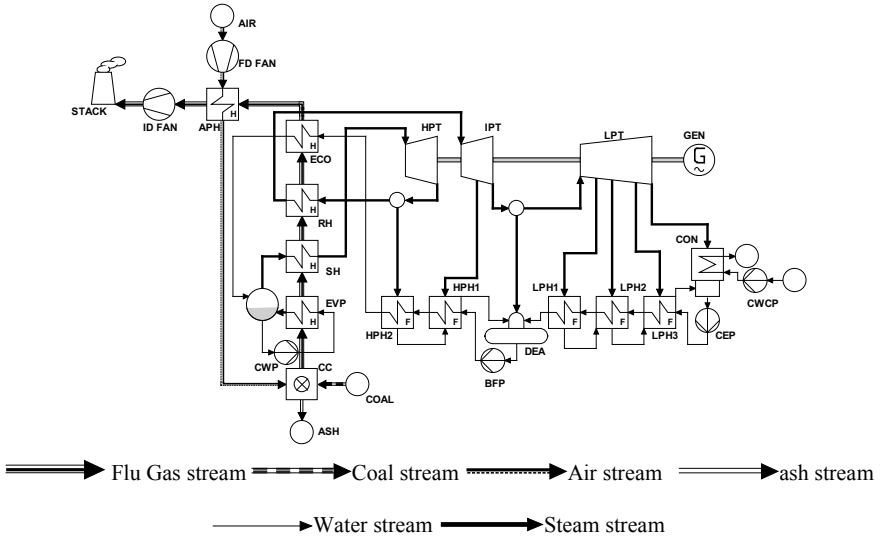


Fig. 1 Illustration of a single unit of old plant created in Cycle Tempo simulation software

2 Description of the Existing Plant

The existing plant consists of three similar separate units of 250 MW each. The total capacity of the old plant is 750 MW. Figure 1 shows the schematic diagram of each single unit of existing plant. The extensive description of each unit is illustrated in earlier study of present authors [5]. However, the major components of the plant are high-pressure turbine (HPT), intermediate-pressure turbine (IPT), low-pressure turbine (LPT), high-pressure feedwater heater (HPH), low-pressure feedwater heater (LPH), deaerator (DEA), condenser (CON), condensate extraction pump (CEP), boiler feed pump (BFP), cooling water circulation pump (CWCP), circulation water pump (CWP), combustion chamber (CC), evaporator (EVP), superheater (SH), reheater (RH), economizer (ECO), air preheater (APH), induced draft fan (ID FAN), forced draft fan (FD FAN) and generator (GEN).

3 Description of New Plant Configuration

Figure 2 depicts the block diagram of proposed new plant configuration. A coal-based integrated gasification combined cycle (IGCC) power plant is considered. The plant is developed in Cycle Tempo taking similar working thermodynamic parameters from a running plant given in a published literature [6]. Sub-bituminous coal mixed with pet coke is gasified in Shell coal gasifier which operates at a temperature of 1600 °C. The produced syngas is cooled up to 250 °C for gas cleaning purpose. The cleaned syngas

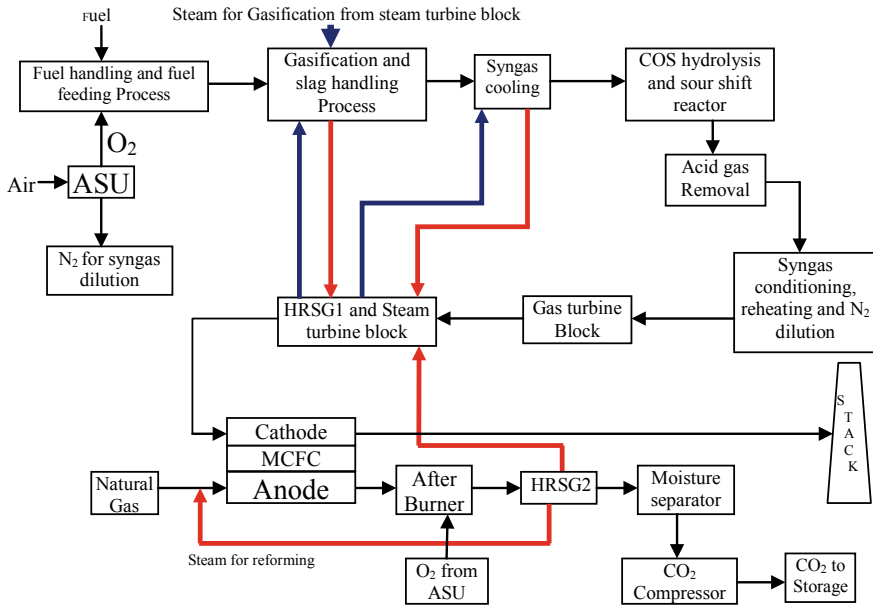


Fig. 2 Schematic diagram of IGCC power plant integrated with MCFC (red colour for steam and blue colour for water)

is fed to run a gas turbine (GT) power generating unit. The GT exhaust, which has a considerable amount of thermal energy, is directed through a heat recovery steam generator (HRSG1) for generating steam to run a steam cycle. A high-temperature MCFC unit is positioned after HRSG1 and steam turbine unit of the IGCC plant. The cathode side of MCFC is fed with flue gas coming out of HRSG1 associated with the steam cycle. Natural gas with steam, generated in HRSG2 situated at the downstream of the MCFC unit, is supplied to cathode. Anode exhaust is sent to afterburner where it is combusted with pure oxygen coming from air separation unit (ASU). The exhaust from afterburner goes through downstream HRSG2 associated with MCFC and moisture separator. After moisture separator, CO₂ stream goes through a multistage compression unit for compression up to 110 bar for storage. The excess steam generated at HRSG2 is also sent to steam turbine unit for power generation. In this configuration also, the plant is configured in such a way so that it would give a net power output of 800 MW with a specific CO₂ emission of 0.092 ton/MWh. Running an IGCC power plant with high-ash coal is a big challenging issue. Running an IGCC with high-ash low-grade coal is not preferable due to its low performance. As the ash content goes higher, the gasifier consumes more oxidant, steam as the gasifying agent. Also, the gas composition and heating value of the syngas produced from the gasification of high-ash low-grade coal are poor. As a result, the overall efficiency of the IGCC plant becomes lower. In many previous studies [7–13], high-ash coal gasification mixed with pet coke or biomass is talked about to minimize the effect of high ash percentage in coal. Keeping in view on those published literatures, here

we consider high-ash Indian coal and pet coke produced from petroleum refineries to be mixed at 1:1 ratio to run the IGCC plant.

4 Thermodynamic Analysis of the Plant

The assumptions used during thermodynamic analysis of both old and new plants are listed below. These data are used as input for Cycle Tempo simulation. The coal has a lower heating value (LHV) 17000 kJ/kg. Isentropic efficiencies of turbines, pumps, fans and generator are 88%, 86%, 86% and 95%, respectively. There are 34.46% carbon, 2.43% hydrogen, 0.69% nitrogen, 6.97% oxygen, 0.45% sulphur, 12% moisture and 43% ash in coal by mass [14]. There are 89% methane, 7% ethane, 1% propane, 0.1% normal butane, 2% carbon dioxide and 0.89% nitrogen in natural gas by mole [15]. Natural gas has a LHV of 46.502 MJ/kg [15]. Composition of pet coke is taken as follows: 82% C, 6.9% S, 2.55% H, 8% H₂O, 0.55% ash (by mole), and calorific value is 8500 kcal/kg [10]. Seventy-five percentage of fuel utilization, 83% CO₂ utilization, 1500 A/m² of current density, 0.7 V of cell voltage and 650° C of cell temperature for MCFC are considered [15]. In reforming process, 3.5 kg of steam for 1 kg of carbon is used [15]. The energetic performances of the plants are done by following first law of thermodynamics. Net output from each unit of the old plant ($W_{\text{net, st}}$) is estimated by the following equation

$$(W_{\text{net}})_{\text{st}} = W_{\text{HPT}} + W_{\text{IPT}} + W_{\text{LPT}} - W_{\text{CEP}} - W_{\text{BFP}} - W_{\text{CWP}} - W_{\text{CWCP}} - W_{\text{IDFan}} - W_{\text{FDFan}} \quad (1)$$

The overall efficiency of old plant (η_{st}) is expressed by the following equation

$$\eta_{\text{st}} = \frac{(W_{\text{net}})_{\text{st}}}{m_{\text{coal}} \times \text{LHV}} \times 100\% \quad (2)$$

The thermodynamic calculations to estimate electrical power generated from MCFC unit ($W_{\text{MCFC Unit}}$) are given in detail in previous publications of the present authors [5]. For the sake of simplicity, the detailed thermodynamic calculations of the MCFC unit are not rewritten here. Net output of new plant (W_{new}) is given as:

$$W_{\text{new}} = (W_{\text{Gross}})_{\text{GT Cycle}} + (W_{\text{Gross}})_{\text{Steam Cycle}} + (W_{\text{Gross}})_{\text{MCFC Unit}} - (W_{\text{auxiliary}})_{\text{GT Cycle}} - (W_{\text{auxiliary}})_{\text{Steam Cycle}} - (W_{\text{auxiliary}})_{\text{MCFC Unit}} - W_{\text{CO}_2 \text{ Compressor}} \quad (3)$$

Overall efficiency of new plant (η_{new}) is estimated by the following equation.

$$\eta_{\text{new}} = \frac{W_{\text{net}}}{Q_{\text{in}}} \times 100\% \quad (4)$$

where Q_{in} is the total heat input to the MCFC integrated IGCC plant and is estimated as follows:

$$Q_{in} = m_{Coal} \times LHV_{Coal} + m_{Petcoke} \times LHV_{Petcoke} + m_{Natural\ Gas} \times LHV_{Natural\ Gas} \quad (5)$$

Total mass flow rate of emitted CO_2 (m_{CO_2}) is estimated by the following equation.

$$m_{CO_2} = \frac{m_{gas\ going\ to\ stack}}{M_{gas\ going\ to\ stack}} \times \text{molar\% of } CO_2 \times \text{Molar weight of } CO_2 \quad (6)$$

where ' m ' is mass flow rate.

CO_2 coming out from the plant per unit produced electricity (ξ_{CO_2}) is given as:

$$\xi_{CO_2} = \left(\frac{m_{CO_2}}{W_{net}} \right)_{Power\ plant} \quad (7)$$

5 Economic Analysis of the Plant

The assumptions used during economic analysis of both old and new plants are listed below. Life of old plant is 30 years. The life of repowered power plant is assumed to be 35 years. The plants are in operating condition for 8000 h in a year. Discount rate is 12%; 1000 \$/kW is the specific capital cost of old plant [13]. Capacity utilization factor is 85%. Cost of coal is 3.2 \$/GJ, and cost of natural gas is 4.8 \$/GJ [16]. Cost of pet coke is taken as INR 7.6/kg [17]. Auxiliary loss due to transmission is 10%. Total operation and maintenance cost is estimated by assuming it as 4% of total capital cost. MCFC stack is assumed to be replaced after each 5 years. Cost associated with CO_2 transportation is neglected.

Total generated units of electricity (E_{old}) of old plant in a year are given as follows.

$$E_{old} = (W_{net})_{st} \times 8000 \times CUF \times (1 - A_t) \quad (8)$$

where 'CUF' is capacity utilization factor and ' A_t ' is transmission loss.

Total annual capital cost of old plant is determined using the following equations.

$$Z_{CAP} = TONC \times CRF \quad (9)$$

where 'TONC' is total overnight cost and 'CRF' is factor for capital recovery.

Total overnight capital cost (TONC) of old plant is determined using the following equation.

$$\text{TONC} = \text{CC} \times W_{\text{net}} \quad (10)$$

where 'CC' is specific capital cost of the old plant.

Capital recovery factor (CRF) is determined using the following equations.

$$\text{CRF} = \frac{\text{DR}}{(1 - (1 + \text{DR})^{-n})} \quad (11)$$

where 'DR' is discount rate and 'n' is life of old plant.

The annualized cost of fuel for old plant is given as:

$$Z_{\text{FUEL}} = C_{\text{FUEL}} \times m_{\text{Fuel}} \times \text{LHV} \times \text{Yearly operating hour} \quad (12)$$

where 'C' is the fuel cost.

Levelized cost of electricity delivered by old plant (LCOE_{old}) is given as:

$$\text{LCOE}_{\text{old}} = \frac{(Z_{\text{CAP}})_{\text{old}} + (Z_{\text{O\&M}})_{\text{old}} + (Z_{\text{FUEL}})_{\text{old}}}{E_{\text{old}}} \quad (13)$$

The economic assessment of the repowered plant is done by the 'bottom-up' approach. Here, capital cost of each separate component is estimated and then they are added up to calculate the total capital cost. Then, operational and maintenance costs of components are calculated and the fuel cost is estimated. Finally, levelized cost of electricity delivered by new plant (LCOE_{new}) is calculated. Economic analysis is done based on results obtained from Cycle Tempo simulation; data are obtained from the literatures and some rational assumptions which are already mentioned earlier. Scaling methodology is adapted to estimate the capital cost of different components of IGCC block of the new plant. Then, the individual component cost is added together to estimate the total capital cost of the IGCC block. The typical cost scaling formula is as follows:

$$Z_C = C_0 \times \left(\frac{S}{S_0} \right)^f \quad (14)$$

where ' Z_C ' is the component cost of present study, ' C_0 ' is the reference component cost, ' S ' is the scaled parameter of the component, ' S_0 ' is the referenced scaled parameter and ' f ' is the exponential factor. Capital cost of air separation unit (Z_{ASU}) is determined by the following equation [18].

$$\begin{aligned} Z_{\text{ASU}} = & 0.8 \times (\text{Cost})_{\text{reference plant}} \\ & \times \left(\frac{\text{O}_2 \text{ production rate of the plant}}{\text{O}_2 \text{ production rate of the reference plant}} \right)^{0.7} \\ & + 0.2 \times (\text{Cost})_{\text{reference plant}} \end{aligned}$$

$$\times \left[\frac{(\text{Compressor power})_{\text{this study}}}{(\text{Compressor power})_{\text{reference plant}}} \right]^{0.54} \quad (15)$$

Total equipment cost of the IGCC plant is given as follows:

$$TOC_{\text{Components of IGCC plant}} = \sum Z_{\text{component}} \quad (16)$$

All the components including ASU are listed in Table 1. The value of reference cost and other parameters used to calculate the component cost of the IGCC block are listed in Table 1 [18]. The annualized capital cost for the IGCC block ($Z_{\text{CAP, IGCC}}$) is given by:

$$Z_{\text{CAP, IGCC}} = TOC_{\text{Components of IGCC}} \times \text{CRF} \quad (17)$$

For repowering purpose, various components of MCFC unit are added with the IGCC. The capital cost for MCFC unit is illustrated below. All the components related to MCFC stack including the CO₂ capture system are assumed to be called as MCFC unit in this paper. Gas compressor cost (Z_C) is given as:

Table 1 Component cost-related data of IGCC block [18]

Name of the component	Scaling parameter	Reference cost (\$)	Reference parameter	Exponential factor
Coal handling system	Coal flow rate	15,271,000	246 ton/h	0.62
Coal feeding system	Coal flow rate	113,635,000	246 ton/h	0.66
Gasifier, syngas cooler and auxiliaries	Coal flow rate	177,839,000	246 ton/h	0.66
Acid gas removal	Syngas flow rate	34,171,000	11,246 m ³ /h	0.79
Sour shift reactor	Syngas flow rate	7,788,000	416 ton/h	0.59
COS hydrolysis	Syngas flow rate	2,912,000	338 ton/h	0.78
Slag handling	Ash/slag flow rate	15,999,000	17 ton/h	0.3
GT unit	Power	85,752,000	223 MW	1
HRSRG	Input heat capacity	32,735,000	700 MW	0.7
Steam turbine and accessories	Generated power	28,830,000	272 MW	0.7
Transformer	Power	15,101,000	752 MW	0.71
Stack	Gas flow rate	3,449,000	4539 ton/h	0.7

$$Z_C = \frac{39.5 \times m_a}{0.9 - \eta_{AC}} \times \left(\frac{P_{\text{Delivery}}}{P_{\text{Suction}}} \right) \times \ln \left(\frac{P_{\text{Delivery}}}{P_{\text{Suction}}} \right) \quad (18)$$

where ' m ' is mass flow rate through compressor, ' P ' is pressure and ' η ' is isentropic efficiency of the compressor.

Fuel compressor cost (Z_{FC}) is determined by the following equation.

$$Z_{FC} = 91562 \times \left(\frac{W_{FC}}{445} \right)^{0.67} \quad (19)$$

where ' W ' is work input into the compressor.

Heat exchanger's cost (Z_{HX}) is given by the following equation.

$$Z_{HX} = 2290 \times (A_{HX})^{0.6} \quad (20)$$

where ' A_{HX} ' is heat exchanger's area.

The cost of MCFC stack ($Z_{MCFC \text{ Stack}}$) is determined by using the following equation [5]

$$Z_{MCFC \text{ stack}} = 1500 \times W_{MCFC} \quad (21)$$

where ' W ' is capacity of MCFC. Cost of inverter attached with MCFC stack ($Z_{Inverter}$) is determined by the following equation.

$$Z_{Inverter} = 10^5 \times \left(\frac{W_{MCFC,DC}}{500} \right)^{0.7} \quad (22)$$

where ' W ' is DC power output from MCFC.

Combustion chamber's cost (Z_{CC}) is determined by the following equation.

$$Z_{CC} = \frac{46.08 \times m_{\text{oxidant}}}{0.995 - \frac{P_{\text{out}}}{P_{\text{in}}}} \times [1 + \exp(0.018 \times T_{\text{out}} - 26.4)] \quad (23)$$

where ' m ' is oxidant flow rate, ' T ' is outlet temperature of after combustion gas and ' P ' is pressure of stream going in/out of the combustion chamber.

Cost of HRSG unit (Z_{HRSG}) is determined by the following equation.

$$Z_{HRSG} = 6570 \times \left[\left(\frac{Q_{ec}}{\Delta T_{LMTD,ec}} \right)^{0.8} + \left(\frac{Q_{ev}}{\Delta T_{LMTD,ev}} \right)^{0.8} \right] + 21276 \times m_w + 1184.4 \times (m_g)^{1.2} \quad (24)$$

where ' Q_{ec} ' and ' Q_{ev} ' are amount of heat transfers at economizer and evaporator part, respectively. The cost of air separation unit (Z_{ASU}) is determined by the following Eq. [18]

$$\begin{aligned}
Z_{ASU} &= 0.8 \times (\text{Cost})_{\text{reference plant}} \\
&\times \left(\frac{O_2 \text{ production rate of the plant}}{O_2 \text{ production rate of the reference plant}} \right)^{0.7} \\
&+ 0.2 \times (\text{Cost})_{\text{reference plant}} \\
&\times \left[\frac{(\text{Compressor power})_{\text{this study}}}{(\text{Compressor power})_{\text{reference plant}}} \right]^{0.54}
\end{aligned} \tag{25}$$

CO₂ compression and condensation unit cost (Z_{CO_2}) is given as follows [19]

$$Z_{CO_2} = n \times C_0 \times \left(\frac{\text{Compressor Power}}{n \times \text{Compressor power of reference plant}} \right)^{0.67} \tag{26}$$

where 'n' is the number of unit and 'C₀' is the reference plant cost.

The total equipment cost of all integrated components of MCFC unit is determined as:

$$Z_{\text{Equipment}} = \left(\sum Z_{\text{Components}} \right)_{\text{MCFC Unit}} \tag{27}$$

Total direct plant cost (TDPC) for MCFC unit is given as:

$$(Z_{\text{TDPC}})_{\text{MCFC Unit}} = Z_{\text{Equipments}}(1 + f_{\text{INST}}) \tag{28}$$

where 'f_{INST}' is installation correction factor [20].

Engineering procurement and construction cost (EPC) for MCFC unit is determined as:

$$(Z_{\text{EPC}})_{\text{MCFC Unit}} = (Z_{\text{TDPC}})_{\text{MCFC Unit}} \times (1 + f_{\text{EPC}}) \tag{29}$$

where 'f_{EPC}' is EPC correction factor [20].

Total overnight cost (TOC) for MCFC unit is given as:

$$(Z_{\text{TOC}})_{\text{MCFC Unit}} = (Z_{\text{EPC}})_{\text{MCFC Unit}} \times (1 + f_{\text{OCC}}) \tag{30}$$

where 'f_{OCC}' is commissioning correction factor [20].

Finally, the capital cost of the MCFC unit ($Z_{\text{CAP, MCFC unit}}$) is given as:

$$Z_{\text{CA, MCFC Unit}} = (Z_{\text{TOC}})_{\text{MCFC unit}} \times \text{CRF}_{\text{MCFC Unit}} \tag{31}$$

O&M cost for MCFC unit ($Z_{\text{O\&M, MCFC Unit}}$) is taken equal to 2.5% of its capital cost [20]. At the same time, further a maintenance cost equal to 5% of fuel cell stack is taken into account the stack replacement after each 5 years [20]. So, 30% of the fuel cell stack cost is added for total life of the new plant. Thus, O&M cost of the

MCFC unit ($Z_{O\&M, MCFC \text{ unit}}$) is given as:

$$Z_{O\&M, MCFC \text{ Unit}} = 0.025 \times (Z_{CAP})_{MCFC \text{ Unit}} + 0.3 \times (Z_{CAP})_{MCFC \text{ stack}} \quad (32)$$

Fuel cost associated with MCFC unit ($Z_{Fuel, MCFC \text{ unit}}$) is given as:

$$Z_{Fuel, MCFC \text{ unit}} = CF \times m_{NG, MCFC \text{ Unit}} \times LHV_{NG} \times H \times 3600 \quad (33)$$

where 'CF' is specific fuel cost, 'm' is fuel flow rate and 'H' is yearly operating hours.

The capital cost ($Z_{CAP, IGCC \text{ with MCFC}}$) and O&M cost of the IGCC plant with MCFC ($Z_{O\&M, IGCC \text{ with MCFC}}$) are estimated by the following equations

$$Z_{CAP, IGCC \text{ with MCFC}} = Z_{CAP, IGCC \text{ plant}} + Z_{CAP, MCFC} \quad (34)$$

$$Z_{O\&M, IGCC \text{ with MCFC}} = Z_{O\&M, IGCC \text{ plant}} + Z_{O\&M, MCFC} \quad (35)$$

The O&M cost for IGCC plant is determined assuming the O&M cost will be 4% of the capital cost. For the MCFC integrated IGCC plant, three types of fuel are used: coal and pet coke are used for the IGCC plant, and fresh natural gas is used to run the MCFC plant. So, total yearly fuel cost for the IGCC plant integrated with MCFC ($Z_{FUEL, IGCC \text{ with MCFC}}$) is given as follows:

$$Z_{FUEL, IGCC \text{ with MCFC}} = Z_{coal} + Z_{Petcoke} + Z_{Natural \text{ Gas}} \quad (36)$$

where ' Z_{coal} ', ' $Z_{Petcoke}$ ' and ' $Z_{Natural \text{ Gas}}$ ' represent the annualized fuel cost for using coal, pet coke and natural gas, respectively. These are estimated as follows individually by using Eq. (12) separately for each type of fuel. Finally, LCOE of IGCC plant integrated with MEA carbon capture is estimated as follows:

$$LCOE_{IGCC \text{ with MCFC}} = \frac{Z_{CAP, IGCC \text{ with MCFC}} + Z_{O\&M, IGCC \text{ with MCFC}} + Z_{FUEL, IGCC \text{ with MCFC}}}{E_{IGCC \text{ with MCFC}}} \quad (37)$$

where ' $E_{IGCC \text{ with MCFC}}$ ' is total generated units of electricity of new plant in a year and determined by the following equation.

$$E_{IGCC \text{ with MCFC}} = W_{net} \times \text{Operating Hour} \times CUF \times (1 - A_t) \quad (38)$$

where ' W_{net} ' is net output of new plant.

6 Results and Discussion

Table 2 shows key performance indicators (both thermodynamic and economic) of a single unit of old plant.

From the results of Table 2, it is concluded that the existing steam power plant has a net capacity of 750 MW ($250 \text{ MW} \times 3 \text{ units}$) with a net efficiency of 35.7% and specific CO₂ emission of 0.92 ton/MWh and the LCOE of old plant is 57.41 \$/MWh. Table 3 shows important working parameters used for IGCC plant [21]. The IGCC plant is scaled up as per the requirement of this study and integrated with MCFC unit.

Now IGCC plant is simulated with carbon capture by integrating MCFC. Table 4 shows important performance indicators of IGCC plant integrated with MCFC.

It can be noticed from Table 4 that the new plant has a capacity of 800 MW and efficiency of 43.1%, and specific emission of 0.09 ton/MWh. LCOE of the plant becomes 108 \$/MWh. The cost of MCFC has a great influence on LCOE of the proposed repowered plant because currently there is uncertainty in the cost of MCFC. Earlier researches [20–24] had reported a range of cost of MCFC which depends on the size of the production volume per year. All the previous studies projected that the

Table 2 Key thermodynamic and economic performance indicator of old plant

Name of the parameters	Value	Units
Energy input	700,740	kW
Gross output	260,920.69	kW
Auxiliary power	10,910.71	kW
Net power	250,009.98	kW
Net plant efficiency	35.67	%
Specific CO ₂ emission	0.92	ton/MWh
LCOE	57.41	\$/MWh

Table 3 Key working parameters used in IGCC plant

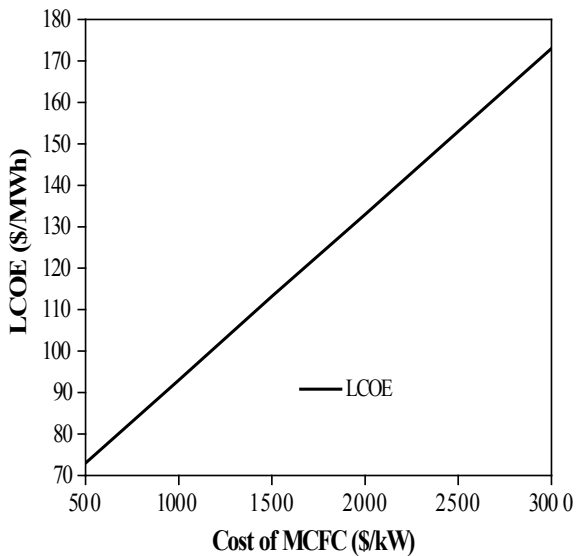
Items	Value	Items	Value
Gasifier operating pressure	26.2 bar	Air compressor discharge pressure	15 bar
Gasifier operating temperature	1600 °C	Combustor pressure	14 bar
Oxygen/carbon ratio	0.825	GT inlet temperature	1200 °C
Steam/carbon ratio	0.064	GT outlet temperature	600 °C
Slag ash: fly ash	80: 20	HP steam pressure	120 bar
Syngas cooler inlet temperature	800 °C	IP steam pressure	29 bar
Syngas cooler outlet temperature	235 °C	LP steam pressure	4 bar
HP steam temperature	510 °C	LP steam temperature	255 °C
IP steam temperature	510 °C	Generator efficiency	96%

Table 4 Major performance parameters of IGCC plant with MCFC carbon capture

Items	Unit	Value
Area of MCFC	m ²	442 × 10 ³
Mass flow rate of coal	kg/s	26
Mass flow rate of pet coke	kg/s	26
Mass flow rate of natural gas to MCFC	kg/s	11.25
Gross output from GT	MW	590
Gross output from steam cycle	MW	230
Gross output from MCFC	MW	341
Auxiliary power consumption	MW	361
Net power of new plant	MW	800
Total input energy	MW	1856
Overall efficiency	%	43.1
Specific CO ₂ emission	t/MWh	0.09
LCOE	\$/MWh	108

cost of MCFC could go down than the present one. It could even go down to 1000 \$/kW or beyond which is also projected by the Department of Energy of United States of America. Looking into this uncertainty in MCFC cost, a sensitivity study is done for showing the effect of cost of MCFC on LCOE of repowered plant. Figure 3 shows the change in LCOE of repowered plant with the variation of MCFC cost. LCOE of the MCFC integrated plant is getting reduced as MCFC capital cost decreases. Not only that the COE of the MCFC integrated plants is approaching near to the

Fig. 3 Variation of LCOE of repowered plant with MCFC cost



existing power plants. So once lowest cost of MCFC would be achieved, the choice of plant configuration would depend largely on thermodynamic performances rather than economic performance.

7 Conclusion

This paper presents thermodynamic economic and environmental analyses of full site repowering of a 750 MW sub-critical steam power station through IGCC integrated with downstream MCFC for carbon dioxide separation and capture. The projected site-repowering method results in a growth in plant capacity by 6.67% and net plant efficiency by 7.43% points with a 90% reduction in specific CO₂ emission. However, the LCOE of the proposed new plant is 108 \$/ MWh. LCOE of the new plant is about 88% higher compared to the old plant. This study shows that once DOE target of specific cost of MCFC would be achieved then the LCOE of the repowered plant would be slightly higher than the old plant but within a comparable limit which is very much better than the LCOE of a coal-based steam power plant with conventional MEA-based carbon dioxide capture route. Keeping on view of present environmental situation, the government should implement this type of power plants with giving some subsidiaries to make this more economically acceptable and thermodynamically and economically as well.

References

1. Hanak DP, Biliyok C, Yeung H, Bialecki R (2014) Heat integration and exergy analysis for a supercritical high-ash coal fired power plant integrated with a post-combustion carbon capture process. *Fuel* 134:126–139
2. U.S. Energy Information Administration (2013) International Energy Outlook 2013. DOE/EIA-0484
3. Naserabad SN, Mobini K, Mehrpanahi A, Aligoodarz MR(2015) Exergy-energy analysis of full repowering of a steam power plant. *Front Energy* 9(1): 54–67
4. Ahmadi GR, Toghraie D, Azimian A, Akbari O (2016)Evaluation of synchronous execution of full repowering and solar assisting in a 200 mw steam power plant, a case study. *Appl Thermal Eng* 112:111–123
5. Samanta S, Ghosh S (2016) A thermo-economic analysis of repowering of a 250 MW coal fired power plant through integration of molten carbonate fuel cell with carbon capture. *Int J Greenhouse Gas Control* 51:48–55
6. Promes EJO, Woudstra T, Schoenmakers L, Oldenbroek V, Thattai AT, Aravind PV (2015) Thermodynamic evaluation and experimental validation of 253 MW integrated coal gasification combined cycle power plant in Buggenum, Netherlands. *Appl Energy* 155:181–194
7. Rich Jr JW, Hoppe R, Choi GN, Hennekes RJ, Heydenrich R, Hooper M (2003) WMPI—waste coal to clean liquid fuels. In: Proceedings of the gasification technologies 2003, San Francisco, California, 12–15 Oct 2003
8. Wang P, Massoudi M (2011) Effect of coal properties and operation conditions on flow behavior of coal slag in entrained flow gasifiers: a brief review. Report number: DOE/NETL-2011/1508 (2011)

9. Wang P, Massoudi M (2013) Slag behavior in gasifiers. Part I: Influence of coal properties and gasification conditions. *Energies* 6:784–806
10. Mathew T (2013) Coal/petcoke gasification and reliance's Jamnagar gasification project. https://teqip.jdvu.ac.in/for_website/Program%2026.07.2013/Presentation_Thomas_Mathew.pdf. Accessed on 19/12/2016
11. Ghassemi H, Mostafavi SM, Markadeh RS (2016) Modeling of high-ash coal gasification in an entrained-flow gasifier and an IGCC plant. *J Energy Eng* 142(4):1–8
12. Thattai AT, Oldenbroek V, Schoenmakers L, Woudstra T, Aravind PV (2016) Experimental model validation and thermodynamic assessment on high percentage (up to 70%) biomass co-gasification at the 253 MW integrated gasification combined cycle power plant in Buggenum, the Netherlands. *Appl Energy* 168:381–393
13. Ali DA, Gadalla MA, Abdelaziz OY, Hulteberg CP, Ashour FH (2017) Co-gasification of coal and biomass wastes in an entrained flow gasifier: Modelling, simulation and integration opportunities. *J Nat Gas Sci Eng* 37:126–137
14. Suresh MVJJ, Reddy KS, Kolar AK (2010) 3-E analysis of advanced power plants based on high ash coal. *Int J Energy Res* 34:716–73.
15. Campanari S, Chiesa P, Manzolini G (2010) CO₂ capture from combined cycles integrated with Molten Carbonate Fuel Cells. *Int J Greenhouse Gas Control* 4:441–451
16. Banerjee R (2014) Coal-based electricity generation in India
17. Reliance Industries Limited (2016) Price of petcoke
18. Park SH, Chung SW, Lee SK, Choi HK, Lee SH (2015) Thermo-economic evaluation of 300 MW class integrated gasification combined cycle with ash free coal (AFC) process. *App Thermal Eng* 89:843–852
19. Manzolini G, Macchi E, Gazzani M (2013) CO₂ capture in natural gas combined cycle with SEWGS. Part B: Economic assessment. *Int J Greenhouse Gas Control* 12:502–509
20. Campanari S, Chiesa P, Manzolini G, Bedogni S (2014) Economic analysis of CO₂ capture from natural gas combined cycles using Molten Carbonate Fuel Cells. *App Energy* 130:562–573
21. Najafi B, Shirazi A, Aminyavari M, Rinaldi F, Taylor RA (2014) Exergetic, economic and environmental analyses and multi-objective optimization of an SOFC-gas turbine hybrid cycle coupled with an MSF desalination system. *Desalination* 334:46–59
22. Mamaghani AH, Najafi B, Shirazi A, Rinaldi F (2015a) 4E analysis and multi-objective optimization of an integrated MCFC (molten carbonate fuel cell) and ORC (organic Rankine cycle) system. *Energy* 82:650–663
23. Mamaghani AH, Najafi B, Shirazi A, Rinaldi F (2015b) Exergetic, economic, and environmental evaluations and multi-objective optimization of a combined molten carbonate fuel cell-gas turbine system. *App Thermal Eng* 77:1–11
24. Ahmadi GR, Toghraie D (2015) Parallel feed water heating repowering of a 200 MW steam power plant. *J Power Technol* 95(4):288–301

Vortex Formation During Liquid Draining from a Cylindrical Tank with Conical Bottom—A Numerical Study



K. Sreenath, Mahadev Prabhu, R. Ajith Kumar, J. S. Jayakumar, and P. J. Joshy

Abstract This paper deals with a numerical study on the Rankine vortex formation during liquid draining from cylindrical tanks with conical base. ANSYS-Fluent was used for the numerical simulation. A liquid column contained in a cylindrical tank with conical bottom is rotated and then drained through a centrally located drain port situated at the base of the tank. For this, various values of initial rotation of liquid (n rpm) were considered. For each ' n ', angle of the bottom base (Φ) and drain port diameters (d_p) were varied over a broad range in an attempt to suppress the vortex formation. Results indicate that as ' Φ ' is increased, the critical height decreases (h_c); i.e., vortex is more suppressed. Also, higher vortex suppression occurs at larger port diameters for a given Φ . Reynolds number and Froude number are found to significantly influence the vortex formation, whereas Weber number is found to be non-influential.

Keywords Vortexing · Air core · Conical bottom · Draining · Critical height · Suppression

1 Introduction

As a liquid drains off through a drain port, a dip occurs on the free surface of the draining fluid. The dip formed instantly transforms into an axially slender pillar-like structure and penetrates through the liquid column through the free surface reaching the drain port, which is called as vortex air core. The time at which the air core reaches the drain port is termed as critical time (t_c), and the free surface height of the fluid at that instance of time is termed as critical height (h_c). Air core vortex formation is a spotted topic in many engineering applications such as hydraulic engineering, metal

K. Sreenath · M. Prabhu · R. Ajith Kumar (✉) · J. S. Jayakumar
Department of Mechanical Engineering, Amrita Vishwa Vidyapeetham, Amritapuri, India
e-mail: amritanjali.ajith@gmail.com

P. J. Joshy
Department of Mechanical Engineering, Cochin University of Science and Technology, Kerala, India

casting, and aerospace engineering. Therefore, an understanding on the mechanism of air core generation and its disappearance is important.

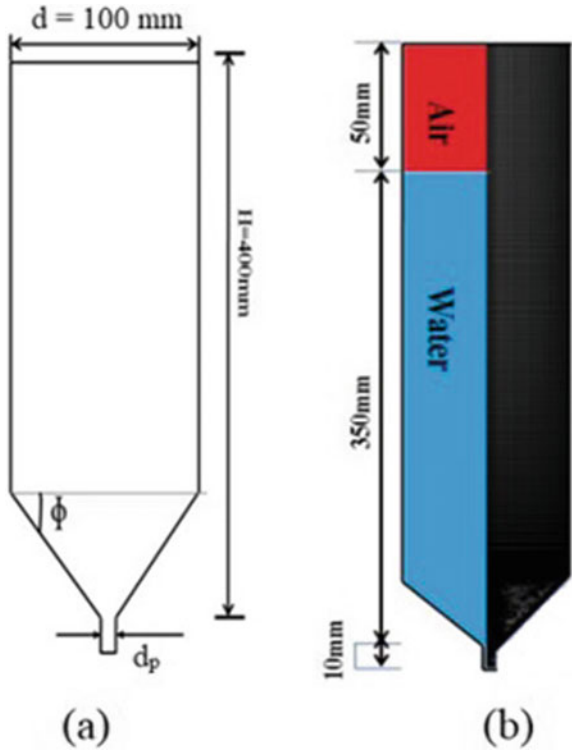
Experimental study conducted by Lubin and Springer [1] observed vortexing during draining process from cylindrical tanks. Even though water was the draining fluid in the experiments, various fluids were placed above the water. Investigators came up with an important finding that critical height can be written as a function of density ratio and drain rate.

The aforementioned studies were applicable only for an initially quiescent fluid. Tank rotation provided to the fluid prior to draining will enhance the vortexing phenomenon. Numerical study conducted by Sohn et al. [2] on draining of liquids from a cylindrical tank revealed that the tank rotation speed, tank diameter, and drain port diameter significantly influence the critical time. To characterize the air core generation phenomenon, authors had proposed a correlation between several non-dimensional parameters. Experimental study conducted by Kumar et al. [3] shows that critical height can be greatly influenced by changing the values of eccentricity and drain port diameter. They observed that, when the eccentricity is zero, the air core is suppressed when the drain port-to-tank diameter ratio is less than 0.3. Kumar et al. [4] observed that, the value of the drain port-to-tank diameter ratio required to suppress the air core is a strong function of eccentricity. Experimental study conducted by Ramamurthi and Tharakan [5] revealed that stepped drain ports are very efficient in arresting the vortexing phenomenon as compared to bell mouth and circular drain ports.

Mechanism of air core formation is well-described by Nazir and Sohn [6, 7]. They found that axial velocity and swirl velocity will greatly influence the mechanism of air core formation. Experimental and numerical investigations carried by the same group of authors found that vortexing phenomenon can be controlled by changing the values of initial height [6] and temperature of draining fluid [7]. Prabhu et al. [8] conducted experiments with two drain ports at equal eccentricity and found that vortexing can be suppressed when the diameters of both the ports are equal. They also found and explained the phenomenon of unusually fast-draining process. Prabhu et al. [9] found that octagonal drain port can efficiently suppress the vortex formation compared to the traditionally used circular geometry.

In all the previous works, flat bottom tanks were considered to study Rankine vortex formation. But in most of the practical applications (pressure vessels, cryogenic propellant tanks, etc.), tanks having curved base are employed which will enhance air core vortex formation. Hence, it is felt that alternate geometric modifications of tanks should be thought of to investigate possible vortexing suppression strategies. With this objective in mind, vortex formation during draining from a cylindrical tank with rotated liquid column is numerically investigated. Figure 1 illustrates the present study configuration. Present investigation is intended to bring to light the influence of base angle (Φ) and port diameter (d_p) on critical height of vortex formation. For this purpose, numerical simulations were carried out considering a broad range of base angle and port diameter values. Flow structures associated with vortex formation were also analyzed in detail to provide a better understanding of the formation of Rankine vortex. In real engineering systems such as liquid propellant

Fig. 1 Configuration of the present study



tanks, vortex generation occurs and creates undesirable effects. This warrants novel suppression vortex strategies like the one adopted in the present study.

2 Numerical Methodology

In this investigation, 2D axisymmetric numerical simulations are performed to analyze the mechanism of vortexing phenomenon during draining of water from cylindrical tanks.

Equation set for continuity, represented by Eq. (1), radial and axial momentum conservation equations represented by Eqs. (2) and (3), respectively, are solved to describe the swirling and draining flow in tank. Air core phenomenon studied by the numerical analysis can be satisfactorily captured using this axisymmetric assumption.

$$\frac{\partial \rho}{\partial t} + \frac{1}{r} \frac{\partial}{\partial r} (r u_r) + \frac{\partial (u_z)}{\partial z} = 0 \quad (1)$$

$$\rho \left(\frac{\partial u_r}{\partial t} + u_r \frac{\partial u_r}{\partial r} + u_z \frac{\partial u_z}{\partial z} \right) = - \frac{\partial P}{\partial r} + \mu \left[\frac{1}{r} \frac{\partial}{\partial r} \left(r \frac{\partial u_r}{\partial r} \right) - \frac{u_r}{r^2} + \frac{\partial^2 u_r}{\partial z^2} \right] \quad (2)$$

$$\rho \left(\frac{\partial u_z}{\partial t} + u_r \frac{\partial u_z}{\partial r} + u_z \frac{\partial u_z}{\partial z} \right) = -\frac{\partial P}{\partial r} + \mu \left[\frac{1}{r} \frac{\partial}{\partial r} \left(r \frac{\partial u_z}{\partial r} \right) + \frac{\partial^2 u_z}{\partial z^2} \right] + \rho g_z \quad (3)$$

Here, z is the axial component of the coordinate system, r the radial coordinate component, u_r the radial velocity component, ρ the density, and μ the dynamic viscosity, t the time variable, g_z is the component of acceleration due to gravity in axial direction.

To track interface between two phases, VOF method has been employed. Park and Sohn [10] assumed flow to be laminar; hence, authors are employing laminar viscous model for simulating the flow field. The top open end of the tank was specified as pressure inlet, the bottom draining end of the drain port as pressure outlet. The wall of the tank was assumed to be stationary with surface tension coefficient 0.073 N/m and contact angle 90° . Before iterations began, initial swirls were imparted to the liquid column using custom field functions. An initial height of 350 mm, i.e., from the top end of the drain port till the surface of the water column, the region was initialized with water phase and the region above and below this was initialized with air phase. The pressure-implicit with splitting of operators (PISO) scheme was employed for pressure-velocity coupling to run the pressure-based solver. Pressure staggering option (PRESTO!) employs a staggered grid or mesh, apart from the main mesh to find face pressure value by means of pressure interpolation. It is comparatively efficient and can be employed with structures as well as unstructured meshes. Non-iterative time advancement (NITA) formulation is also employed to reduce the truncation errors.

Numerical simulations were conducted in a cylinder with diameter (d) of 100 mm and height of 400 mm. To find a suitable mesh for the investigation, a grid independency study was performed for all cases. A typical case of drain port diameter ($d_p = 10$ mm), initial rotation (n) = 200 rpm, and the base angle (Φ) = 15° is shown in Fig. 2. The selected geometry and mesh are shown in Fig. 3a, b, respectively. Grid

Fig. 2. Grid independency test

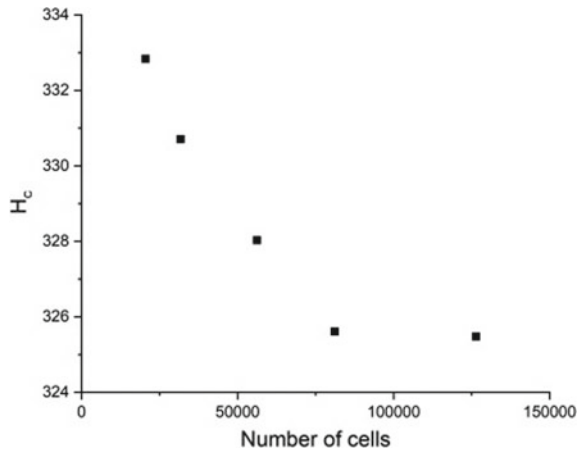
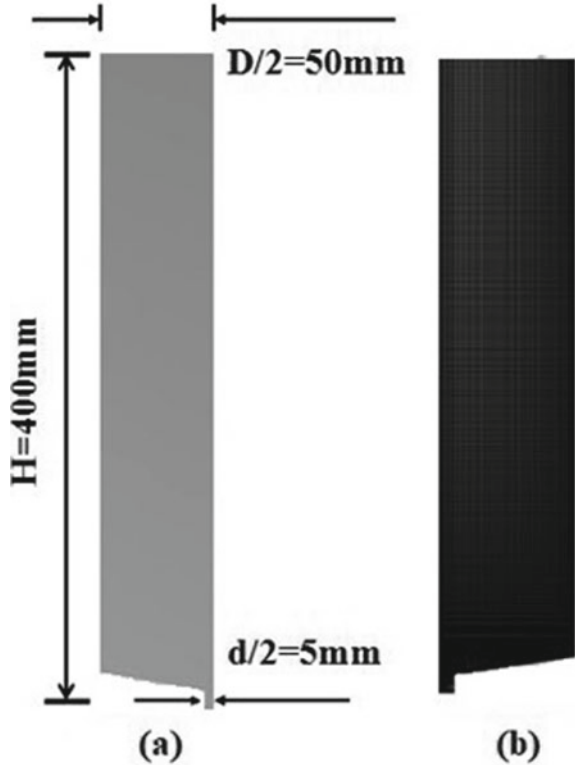


Fig. 3 a Geometry, b mesh



independency study suggests that a mesh with 81,121 cells is appropriate to conduct numerical simulations.

Figure 4 shows the validation plot for validating the numerical solver. It is a plot between non-dimensional critical height ($H_c = h_c/h_i$) versus initial rotation. This study is conducted by the authors on flat bottom cylindrical tank with port diameter (d_p) = 10 mm for a range of initial rotation (n) ranging from 40 to 200 rpm with a step size of 40 rpm. Experiments were conducted with rotating cylinder setup as shown in Fig. 5 in which a cylinder filled with water up to an initial height ($h_i = 350$ mm) is kept on the rotating disk. RPM controller maintains the required initial rotation for a specified time. A rotation for 2 min was applied to the cylinder. After 2 min, cylinder rotation was stopped and fluid was allowed to drain. In this process, an initial dip was generated at the free surface which subsequently penetrated the free surface of the liquid to form a complete air core. Height of the free surface when the tip of air core touches the drain port (critical height, h_c) was measured using a graduated scale vertically attached to the outer surface of the tank. Experimental and numerical results are in good agreement with each other as evident in Fig. 3a the error being below 5%.

Fig. 4 Validation

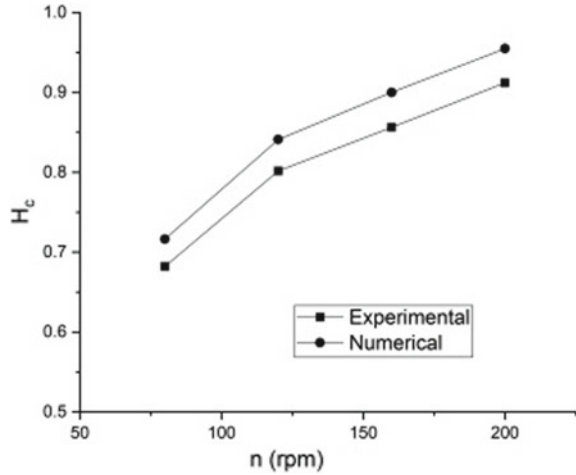
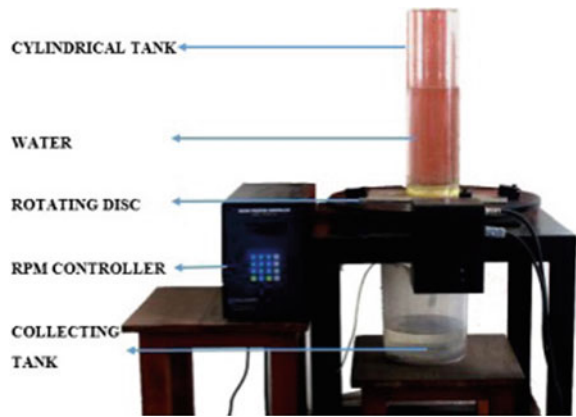


Fig. 5 Experimental setup



For studying the effect of base angle on vortexing phenomenon, values of angle ranging from 0° to 60° were selected with a step size of 15°. For each value of base angle, simulations were performed for values of port diameters (d_p) varying from 4 to 12 mm with a step size of 2 mm. Effect of non-dimensional numbers, viz. Reynolds number, Froude number, and Weber number on vortexing phenomenon, was also investigated in this study. These non-dimensional numbers were obtained using Buckingham π -theorem as a part of this study as follows.

Rotational Reynolds number = $\frac{\rho d^2 \omega}{\mu}$, rotational Froude number = $\omega \sqrt{\frac{d}{g}}$ and rotational Weber number = $\frac{d^3 \omega^2 \rho}{\sigma}$, where ρ is density, μ is dynamic viscosity, σ is surface tension coefficient, g is gravitational acceleration, and ω is the angular velocity.

3 Results and Discussion

Numerical results on the effect of base angle and diameter on vortexing phenomenon are presented in this section. Critical height is used to quantify vortexing phenomenon and is non-dimensionalized with respect to the initial height of the liquid column ($H_c = h_c/h_i$). Figure 6 is a plot between H_c and non-dimensional initial fluid rotational speed ($N = n * 1 \text{ min}$) for a typical non-dimensional port diameter ($D = d_p/d$) value of 0.1. For all other port diameters tested, trend is nearly the same as shown in Fig. 6 and hence, not presented here. Authors have attempted to study the effect of port diameter for a conical bottom shaped tank. It is observed from Fig. 7 that, critical height of vortex formation decreases when value of port diameter is increased. This observation is in agreement with the numerical simulation results of Sohn et al. [2] with base angle zero. It is also observed from Figs. 6 and 7 that, H_c is augmented with initial rotation which is in agreement with the results reported [3, 4]. It could be noted from Fig. 6 that, for a particular port diameter $d_p = 10 \text{ mm}$, at a given initial rotation value, H_c reduces with increase in base angle. This means by employing a conical bottom, efficient suppression of vortexing is possible.

Percentage suppression is computed for various values of liquid initial rotation and base angles and is presented in Fig. 8. Percentage suppression is calculated using Eq. (4) as given below

$$\%S = \left(\frac{(\{H_c\}_{D=0.04} - \{H_c\}_{D=0.12})}{\{H_c\}_{D=0.04}} \right) * 100 \tag{4}$$

From Fig. 8, it could be noted that for all value of base angles, air core is efficiently suppressed at the lower values of N . This means that a tank with conical bottom is

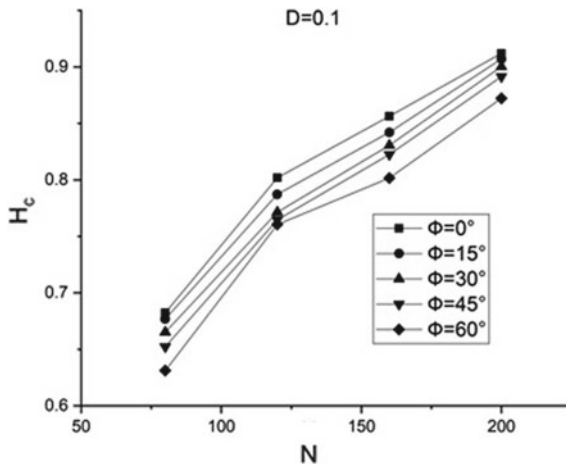


Fig. 6 H_c and N for various Φ

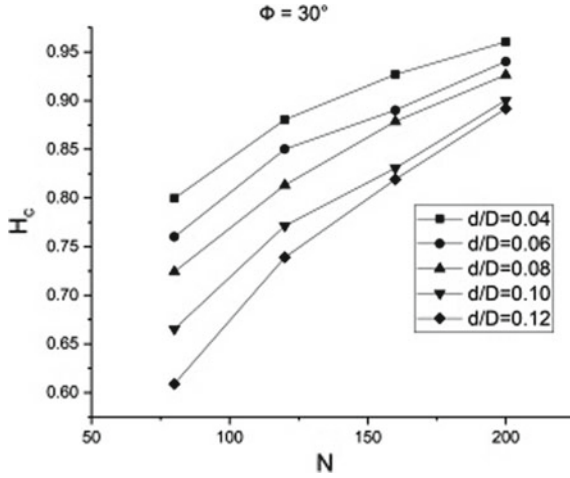
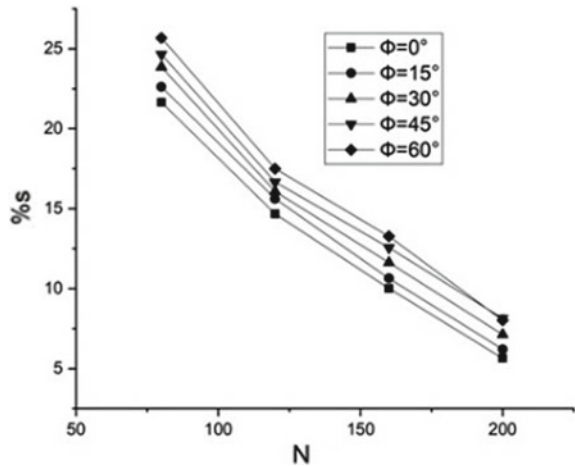


Fig. 7 H_c and N for various D

Fig. 8 %s versus N



efficient in suppressing the vortex when the disturbances in the system are very small. As the value of N increases, efficiency in suppressing the air core goes down. Another important observation is that at a given value of N , maximum vortex suppression occurs at the highest value of base angle tested, i.e., at $\Phi = 60^\circ$.

It is important to know the physics behind the arrest of the air core vortex in conical bottom tanks. For this, static pressure contours near the vicinity of the drain port for a typical case are obtained and presented in Fig. 9. It is obtained for all base angles with port diameter (d_p) = 10 mm, $n = 200$ rpm and at a time instance of $t = 2$ s after draining of fluid. It is observed that for cylindrical tanks ($\Phi = 0^\circ$), the drain port is almost in a low pressure zone which attracts air core from free surface. However,

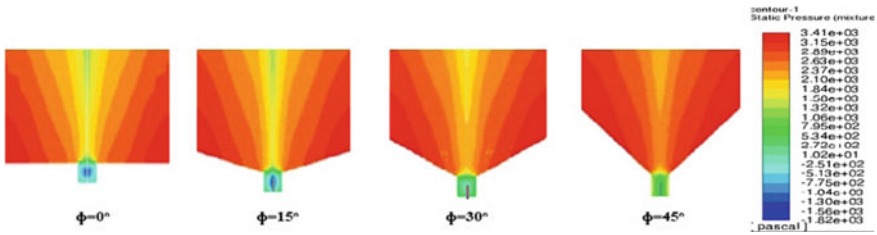


Fig. 9 Static pressure contours at time instance $t = 2$ s

at the same instance of time, as base angle (Φ) is increased, the static pressure around the drain port increases as evident in Fig. 9. High pressure zones will not attract air core and hence vortex is suppressed.

Authors have also attempted to study the effect of non-dimensional parameters on vortexing phenomenon. This is carried out at $\phi = 45^\circ$ and $d_p = 10$ mm. For this, H_c is plotted against Reynolds number (Re), Froude Number (Fr), and Weber number (We). It should be specifically noted that, value of each non-dimensional parameter is varied by keeping other non-dimensional parameters constant.

In Fig. 10, the variation in Re without altering other non-dimensional parameters is numerically obtained by changing the value of dynamic viscosity of the fluid (μ). It is observed that non-dimensional critical height enhances with Re . Trend-wise, this complies with numerical results obtained by Sohn et al. [7] when they studied the effect of fluid temperature on vortexing. Figure 11 represents the change in H_c with respect to Fr . The variation in Fr is numerically obtained by changing the value of acceleration due to gravity (g) unlike changing the d_p as in Gluck et al. [11]. After a slight increase in H_c with Fr in the range $0 < Fr < 4$, H_c drops significantly at high Fr values reaching negligibly small critical height values at $Fr \sim 8.5$. This trend is in very good agreement with the numerical results reported by Agarwal et.al

Fig. 10 H_c versus Re

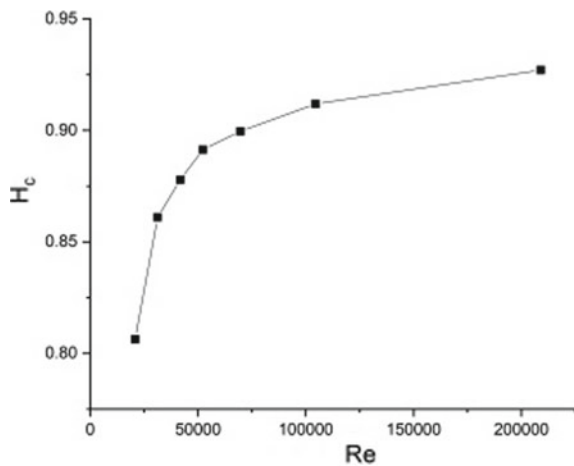


Fig. 11 H_c versus Fr

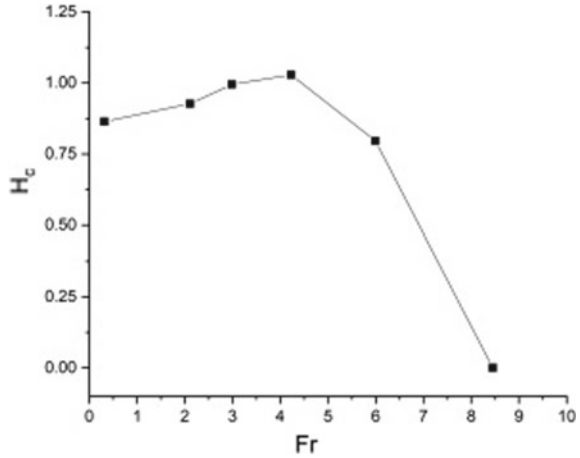
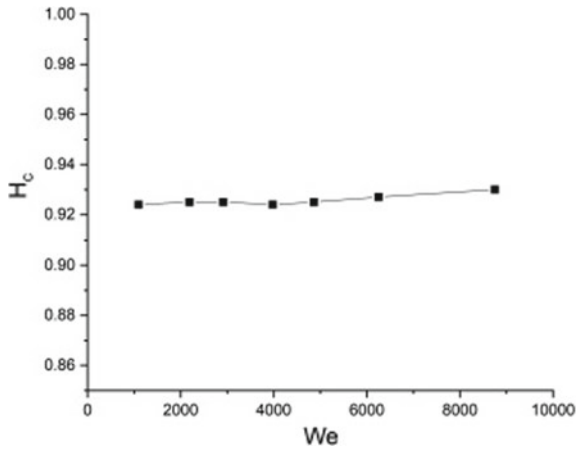


Fig. 12 H_c versus We



[12]. Figure 12 represents the variation of H_c with respect to We . The variation in We without altering other non-dimensional parameters is numerically obtained by changing the value of surface tension of the fluid (σ). As evident in Fig. 12, We has no significant influence on air core vortex formation, which is in line with the numerical results obtained by Sohn et al. [7].

4 Conclusions

In the current study, effect of base angle on vortex formation was numerically investigated. It was found that by increasing the base angle, vortexing phenomenon can be arrested efficiently. Results reveal that conical bottom tanks are effective in arresting

air core vortex formed particularly at lower values of initial rotation. The study of static pressure contours at the same instance of time for various base angles showed that as base angle increases, low pressure inside the drain port vanishes, and this ultimately reduces the formation of air core. Effect of port diameter was also studied by keeping base angle constant. It is found that, as diameter increases, the critical height of vortexing decreases. Reynolds number and Froude number are found to substantially influence the air core formation, whereas Weber number does not seem to have any impact on the vortexing phenomenon.

References

1. Lubin BT, Springer GS (1967) The formation of a dip on the surface of a liquid draining from a tank. *J Fluid Mech* 29:385–390
2. Sohn CH, Hyeon SJ, Park IS (2013) Numerical analysis of vortex core phenomenon during draining from cylinder tank for various initial swirling speeds and various tank and drain port sizes. *J Hydrodyn* 25:183–195
3. Kumar A, Joykutty J, Shaji RK, Srikrishnan AR (2016) Vortex suppression through drain port sizing. *J Aerosp Eng* 29:06016002
4. Kumar A, Nair RR, Prabhu M, Srikrishnan AR (2017) Vortex formation during draining from cylindrical tanks: effect of drain port eccentricity. *J Aerosp Eng* 30:06017001
5. Ramamurthi K, Tharakan TJ (1992) Shaped discharge ports for draining liquids. *J Spacecraft Rockets* 30:786–788
6. Nazir K, Sohn CH (2017) Study of air core phenomenon and influence of water height during liquid draining. *J Mech Sci Technol* 31:3831–3837
7. Nazir K, Sohn CH (2018) Effect of water temperature on air core generation and disappearance during draining. *J Mech Sci Technol* 32:703–708
8. Prabhu M, Kumar A, Gopikrishnan TH, Deshpande PJ, Anandkrishnan U, Kiran AS, Govindu RP (2020) Rankine vortex formation during draining: a new twin port suppression strategy. *J Appl Fluid Mech* 13:147–160
9. Prabhu M, Kumar A, Nair RR, Anith TA (2019) Liquid draining through polygonal ports: an investigation on gas entraining vortices. *J Spacecr Rock* 56:1651–1657
10. Park IS, Sohn CH (2011) Experimental and numerical study on air cores for cylindrical tank draining. *Int Commun Heat Mass Transfer* 38:1044–1049
11. Gluck DF, Gillie JP, Zukoski EE, Simikin DJ (1966) Distortion of a free surface during tank discharge. *J Spacecr Rockets* 3:1691–1692
12. Agarwal D, Basu P, Tharakan TJ, Salih A (2014) Prediction of gas-core vortices during draining of liquid propellants from tanks. *Aerosp Sci Technol* 32:60–65

Evaluation of Noise and Air Pollution During Diwali in Berhampur City, India: An Inclusive Annoyance Study



A. K. Sahu, S. K. Nayak, J. K. Mohanty, P. K. Pradhan, and C. R. Mohanty

Abstract Diwali is one of the main cultural festivals in India. Goddess ‘Kali’ is worshiped and people celebrate with light and fireworks on that day. There are two types of fireworks: one being producing sound and the other producing illumination and lot of smoke. Burning of different fireworks generates acute noise and toxic fumes which lead to noise and air pollution in ecosystems. The present paper deals with noise pollution and air pollution during Diwali in Berhampur city, India. The present study focuses on noise level and air pollution level in three different areas of the city. Compare to normal days, on Diwali, the average equivalent continuous noise level has been increased. The ambient air tested on Diwali day’s shows significant rise of SO₂, NO₂ and PM₁₀ level compared to normal days. The authors feel it obliged to propose few suggestions earned during study period.

Keywords Noise pollution · Air pollution · Fire crackers · Noise climate · Equivalent continuous noise level

1 Introduction

Noise is unwanted and undesirable sound. Home appliances and ventilation systems are the sources of noise in living house. In community areas, noise comes from nearby road traffic, rail, construction works, religious functions (and temple prayers), and social celebrations. During social celebration, using of drums, electronics loud speaker, fireworks are the major sources of community noise. Though these community noise last for short duration, but its effects cannot be ignored. Use of fire crackers is not only in Diwali festival (in India) but also in several functions like New Year

A. K. Sahu · J. K. Mohanty · P. K. Pradhan (✉)
Mechanical Engineering Department, VSSUT, Burla, India
e-mail: prasant2001uce@gmail.com

S. K. Nayak
Civil Engineering Department, VSSUT, Burla, India

C. R. Mohanty
Civil Engineering Department, PMEC, Berhampur, India

celebration and celebration of joy after winning games in throughout the world. So, celebration of Diwali with fireworks is not an exception to it. Diwali is one of the important festivals in India. Celebration of Diwali is mentioned in different scriptures and mythological mentions. The earlier celebrations were limited to capital of the kingdoms but with passage of time, the same was celebrated in all areas in India. Goddess 'Kali' is worshiped and people celebrate with light and fireworks on that day. There are two types of fireworks: one being producing sound (i.e., fire cracker) and the other producing illumination and lot of smoke (i.e., fire illumine). Bursting of fire crackers brings noise and air pollution to ecosystems where as fire illumine produce only colorful light and smoke. Fireworks contain chemicals like aluminum, arsenic, sulfur, manganese, sodium oxalate, potassium perchlorate, barium nitrate, etc. Burning and bursting of different fire crackers generate acute noise and toxic fumes.

Exposure of noise reduces psychological and physiological wholeness of humans. The impacts of physiology are blood pressure, heart ailments, obesity, and many more [1]. The impacts of psychological are sleep disturbance, annoyance, irritation, loss of concentration, and many more [2]. High noise for longer period may bring temporary/permanent hearing problem (i.e., NITTS, noise-induced temporary threshold shift, and NIPTS noise-induced permanent threshold shift). Sometimes, ear drum gets damaged due to impact of sudden noise.

Berhampur is a rapidly growing city and having highest number of district- and state-level establishment. It is treated as capital of southern Odisha. The city is growing day by day as is becoming a business hub in Odisha. Due to its commercial nature with dominating business community, all festivals are being celebrated with much fanfare. Attention on noise and air pollution was given specifically to residential areas in view of the historic judgment given by Honorable Supreme Court of India to permit green crackers with time limit of two hours (8 pm to 10 pm). The present study focuses on measurement and analysis of noise pollution and air pollution during Diwali in Berhampur city.

2 Literature Review

Restrictions on the use of horns and use of old vehicles reduce the noise level and reduce the annoyed persons in Cairo city [3]. WHO report [4] says that the adverse health effects like disturbance in sleep, mental health, and performance reductions are because of high noise in community areas. In a study, Singh and Davar [5] observed that females are more affected than males because of community/religious noise. Holi celebration and immersion of idol in various puja pollute the water but Diwali pollute both the noise and air [6]. Noise level increases at commercial and residential areas in Haridwar city during Diwali [7]. Besides noise and air pollution, Diwali celebration generates huge amount of solid waste [8]. Rao et al. [9] found that the concentration of $PM_{2.5}$ and PM_{10} in air increases three times on Diwali day compare to normal days in Nagpur city. Noise at all areas like commercial, silence, residential, and industrial

areas in Kohlapur city enhanced during Diwali due to bursting of fire crackers [10]. Similarly, all residential, commercial, and silence areas are of Raipur city are affected because of Diwali [11]. In another study in New Delhi [12], it is found that residential areas are more affected than commercial areas during Diwali. Also, noise level and level of SO_2 in air are increased significantly in New Delhi during Diwali [13].

Though the celebration of Diwali is for a short period, it is enough to affect human health. In Diwali, the suspended particulate matter and respirable particulate matter are high and it remains in air for a longer time in cold metrological condition. It remains at lower height in atmosphere and causes lot of bronchitis problem [14]. The environmental effects and to tackle any mishap during Diwali due to bursting and lightening of illumine are known to less numbers of citizens in rural and urban areas. The health effects of fireworks also have same score among masses. In a study, it is mentioned that People in Vishakhapatnam city are less aware of the health consequences of pollutants emanating from fireworks during Diwali [15]. Fatality in Delhi due to fire crackers and its toxicity in the air are reported and precaution measures are suggested by Tondon et al. [16] and Murty [17].

3 Methodology and Experimentation

The present study was conducted in Berhampur city to evaluate the noise and air pollution during Diwali. The geographical and sociological features of Berhampur city are shown in Table 1. The recommended noise standards by Central Pollution Control Board (CPCB, New Delhi) for different category areas are mentioned in Table 2.

Though there is a restriction of Diwali celebration (with fire work) timing 8 pm–10 pm, but practically, the fire crackers are bursted from 6 pm in evening and continued up to 11 pm. So, readings were taken from 6 to 11 pm at three locations. Locations were chosen like Tulsi Nagar as residential area, MKCG campus (Medical college-cum-Hospital) as silence area, and Giri market as commercial area (shown in Fig. 1). The suitable study points were chosen to avoid echo and obstruction of sound. The readings were recorded on hourly basis in each location. Noise indices as L_{10} , L_{50} , L_{90} , equivalent continuous noise level (L_{eq}), L_{np} , and noise climate (NC) were calculated to measure the noise pollution level at all three locations.

Table 1 Geographical features of Berhampur city

S. No.	Specifications	Recorded value
01	Population (2011 census)	3.6 Lakh
02	Geographical area	86.82 km ²
03	Population density	4100 per km ²
04	Latitude	19° 32' N
05	Longitude	84° 78' E

Table 2 Recommended noise standards in different areas by CPCB, New Delhi

Area code	Category of area	Environmental noise standards L_{eq} (dB(A))	
		Working time/Day time (6.00 am–10.00 pm)	Night time (10.00 pm–06.00 am)
A	Industrial area	75	70
B	Commercial area	65	55
C	Residential area	55	45
D	Silence area	50	40

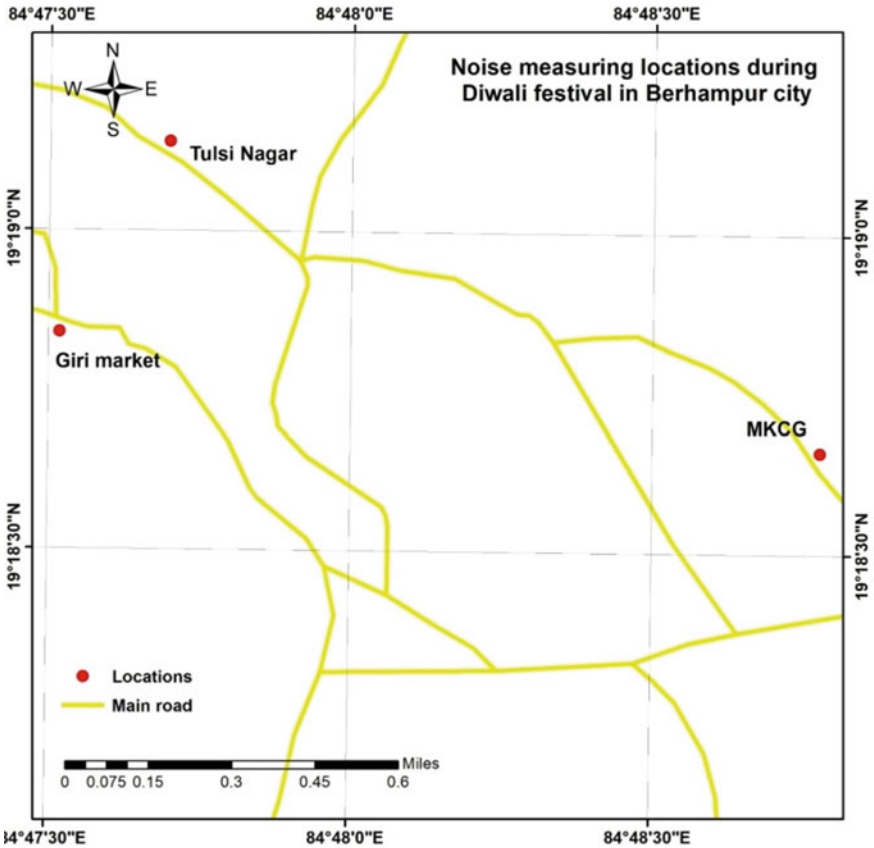


Fig. 1 Three study locations in Berhampur city

The noise levels were measured at all three locations with help of sound-level meter-cum-hand-held analyzer (Bruel and Kjaer make). The ordinarily used frequency weight is A-weighting, which implies that it resembles the human ear's response. The range of the instrument is 0–130 dBA. Calibration of the instrument was made before taking readings. On Diwali, at a time, three instruments are used simultaneously for the measurement of noise at three different locations.

3.1 Noise Measurement

Observations were carried out on Diwali day (i.e., 7th Nov. 2018) and a normal day after a week. Noise was monitored from 6 to 11 pm. The percentile values as L_{10} , L_{50} and L_{90} were recorded in each reading locations for determination of noise climate (NC) and noise pollution levels. The values of noise indices are calculated as

$$(i) \text{ Noise Climate (NC)} = L_{10} - L_{90} \quad (1)$$

$$(ii) \text{ Noise Pollution Level (} L_{NP} \text{)} = L_{eq} + \text{NC} \quad (2)$$

where L_{10} is the level of sound exceeding for 10% of total time of measurement, L_{50} is the level of sound exceeding for 50% of total time of measurement, and L_{90} is the level of sound exceeding for 90% of total time of measurement.

3.2 Air Pollution Measurement

Air (high volume) sampler-cum-analyzer (Envirotech 415) was used to estimate the contents of total suspended particulate matter (TSPM). As the dust concentration in air was more, duration of sampling time is short (apx. 10 min). Proper procedures were followed for installation of glass fiber filter paper. The distilled water was filled up to zero mark on meter scale of orifice meter. Particulate concentrations were made by weighing filters and volume of air passed through the same. Laboratory analysis was carried out by UV spectrophotometer to measure the concentrations of SO_2 and NO_2 . Experimental results and their analysis of the present work are presented and discussed in the next section.

4 Results and Discussion

The results and discussion of the present work mainly consist of the following;

- (i) Assessment and analysis of noise pollution,

- (ii) Assessment of air pollution,
- (iii) Social survey on Diwali celebration.

4.1 Assessment and Analysis of Noise Pollution

The L_{10} , L_{50} , and L_{90} values obtained from the observations were used to calculate the NC, and L_{np} . The equivalent noise levels (L_{eq}) obtained from the instrument directly. The L_{10} , L_{50} , L_{90} , NC and L_{np} are presented in Table 3. The comparisons of L_{eq} at different locations are presented in Figs. 2, 3 and 4 for better visualization (Fig. 5).

On Diwali day, the noise levels at all locations were compared with normal day and CPCB standard. The highest L_{eq} at Tulsi Nagar, MKCG, and Giri market are 85.6 dB, 77.5 dB, and 89.8 dB, respectively. At all places, the highest noise level timing is in between 8 and 9 pm as it is peak time of celebration with fire cracker bursting.

4.2 Assessment and Analysis of Air Pollution

After testing the air with help of analyzer Envirotech-415 and spectrometer, the concentrations of SO_2 , NO_2 , and PM_{10} per m^3 of air are measured and are presented in Table 4. A significant difference was noted between the study locations between Diwali and non-Diwali day. This is shown in Fig. 5. PM_{10} was measured by mass collected on filter and volume of air sampled. All the measured pollutants (in air) are compared with prescribed limit.

The air quality analysis indicates the concentration of PM_{10} during Diwali increase and it exceeds the NAAQ Standards. Though concentration of SO_2 and NO_2 are within prescribed limit, but it significantly increases compare to normal days.

4.3 Social Study

The excessive use of fireworks (both crackers and illumine) on Diwali day increases the noise and air pollution levels. The pollution levels exceed the CPCB standard and NAAQS standards which have an impact on the residents in the area as well adjoining. As it is celebrated in whole the city, the scenario shall remain same irrespective of all study areas. The health risks from fire crackers are very high as it contains sodium, potassium chlorate, arsenic, nitrates, etc. Its presence in higher amount in atmosphere shall definitely cause respiratory problems and shall multiply the already existing ones.

Table 3 Noise levels at study locations on Diwali and normal day from 6 to 11 pm

	Timing	Noise levels in dB													
		Diwali day							Normal day						
		L ₁₀	L ₅₀	L ₉₀	L _{eq}	NC	L _{np}	L ₁₀	L ₅₀	L ₉₀	L _{eq}	NC	L _{np}		
Tulsi Nagar (res area)	6-7 pm	84.5	76.9	66.8	78.6	16.7	97.3	70	62.3	58.2	63.2	11.8	77		
	7-8 pm	86.6	70.9	67.8	77.9	19.8	97.7	75.2	67.3	60.2	69.2	15	86.2		
	8-9 pm	90.2	83.9	77.1	85.6	13.2	100.8	82.3	72.4	63.5	75.8	18.8	96.6		
	9-10 pm	85.5	75.8	66.3	78.2	19.2	99.4	71.8	63.2	54.2	61.4	17.6	81		
	10-11 pm	85.2	70.4	66.4	75.2	19.8	97.1	62.1	56.3	50.2	56.6	11.9	70.5		
MKCG campus (silence area)	6-7 pm	79.2	72.1	65.2	73.9	14	89.8	71.6	62.2	52.4	65.8	19.2	87		
	7-8 pm	77.5	70.2	63.5	71.8	14	87.8	73.2	64.1	53.2	67.7	20	89.7		
	8-9 pm	85.2	77.4	68.3	77.5	16.9	96.4	67.3	62.2	55.3	62.1	12	76.1		
	9-10 pm	80.2	71.6	64.3	73.8	15.9	91.7	69.4	60.2	55.2	61.4	14.2	77.6		
	10-11 pm	72.1	65.1	61.2	67.2	10.9	78.1	66.8	58.3	59.5	59.2	7.3	68.5		
Giri market (comm area)	6-7 pm	93.4	81.3	77.4	85.6	16	104.6	88.4	80.4	74.3	79.1	14.1	97.2		
	7-8 pm	94.8	82.3	77.8	87.5	17	106.5	90.6	80.6	76.3	81.2	14.3	99.5		
	8-9 pm	98.7	85.4	78.8	89.8	19.9	114.7	89.6	80.5	74.6	81.3	15	100.3		
	9-10 pm	94.6	82.4	78.2	86.5	16.4	104.9	85.4	78.4	71.8	78.2	13.6	95.8		
	10-11 pm	84.3	78.2	70.4	78.7	13.9	94.6	82.3	72.4	63.1	72.2	19.2	95.4		

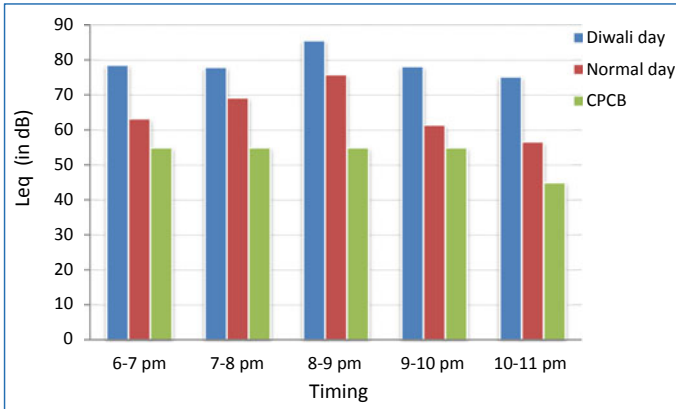


Fig. 2 Comparisons of L_{eq} at Tulsi Nagar (residential area)

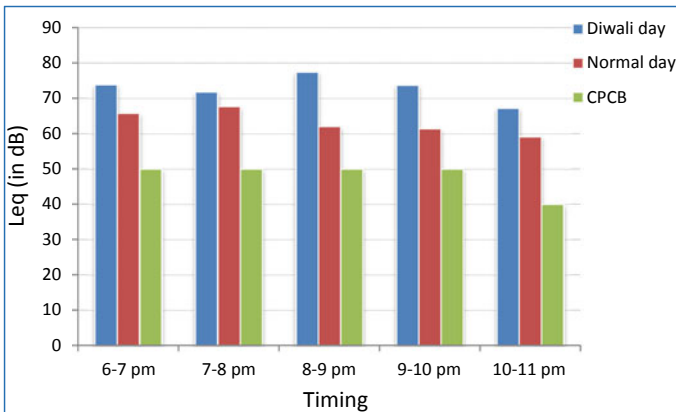


Fig. 3 Comparisons of L_{eq} at MKCG campus (silence area)

A social study was undertaken after Diwali at study locations. The respondents were intimated personally with questionnaires. The total numbers of respondents were 314. The questionnaires were based on (i) awareness on pollution, (ii) awareness on health effects, and (iii) awareness on risk and safety measures. The details of the data collected are shown in Table 5.

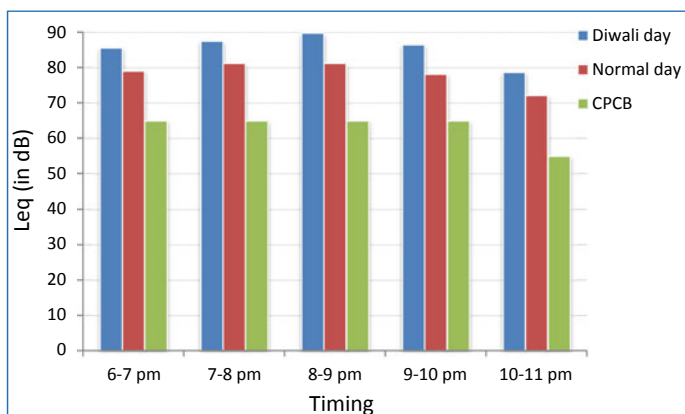


Fig. 4 Comparisons of L_{eq} at Giri market (commercial area)

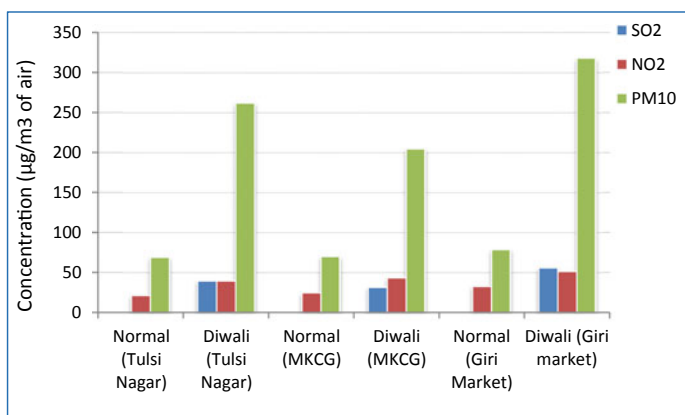


Fig. 5 Air quality at all three locations during Diwali and normal days

Table 4 Concentration of SO₂, NO₂ and PM₁₀ at study locations

Locations	Normal day			Diwali day		
	Concentration (µg/m ³ of air)			Concentration (µg/m ³ of air)		
	SO ₂	NO ₂	PM ₁₀	SO ₂	NO ₂	PM ₁₀
Tulsi Nagar (residential area)	BDL	21.5	69	39.7	39.8	262
MKCG medical (silence area)	BDL	24.9	70	31.9	43.6	205
Giri market (commercial area)	BDL	32.8	79	56.2	51.8	318
NAAQ standards	80	80	100	80	80	100

Where NAAQ National Ambient Air Quality Standards and BDL below detectable level

Table 5 Social survey on Diwali celebration

Subjects	Tulsi Nagar (residential)	MKCG (silence)	Giri market (commercial)
Numbers of respondents (male + female)	108 (96 + 12)	102 (91 + 11)	104 (97 + 7)
Awareness on pollution (%)	21.3	36.3	26
Awareness on health effects (%)	15.75	23.5	11.5
Awareness on risk and safety measures (%)	10.2	17.64	13.46
Annoyed and against the use of fireworks (%)	31.5	36.2	27.9
Annoyed but in favor of fireworks use (%)	24.7	19.6	29.8
Not annoyed but against the use of fireworks (%)	14.8	22.5	8.65
Not annoyed and in favor of fireworks use (%)	29.6	21.5	33.65

5 Conclusion

Due to growth of population, the noise pollution and air pollution became intolerable due to various sources and in addition to social celebration like Diwali. It is definitely a cause of concern to every stake holders of the society.

The study represents the noise situation during Diwali day and a normal day after a week in Berhampur city. The following observations are obtained at the end of study.

1. At all places, the highest noise level timing are in between 8 and 9 pm as it is peak time of celebration with fire cracker bursting.
2. The highest L_{eq} at Tulsi Nagar (residential area), MKCG (silence area), and Giri market (commercial area) are 85.6 dB, 77.5 dB, and 89.8 dB, respectively.
3. The air quality analysis indicates the concentration of PM_{10} during Diwali increases significantly and it exceeds the NAAQ standards.
4. Though concentrations of SO_2 and NO_2 are within prescribed limit, but, it is increased compare to normal days.

In spite of stricter guidelines by Honorable Supreme Court of India, people cannot control themselves from using fire cracker. Control measures have to be adopted to protect the citizens from exposure. The authors feel to suggest research outputs for public awareness and for mitigation measures.

- i. Use of fireworks (both cracker and illumine) should be minimized.
- ii. Use of electric illumination should be encouraged instead of using fire illumine.

- iii. Fire crackers should not be used within 500 m of hospitals.
- iv. Public awareness programme should be held much before Diwali to educate them about the environmental impact because of using cracker.

References

1. Berlund B, Lindvall T (1995) Community noise. Centre for sensory research, Stockholm, Sweden. ISSN 1400-2817
2. Kim M, Chang SI, Seong JC, Holt JB, Park TH, Ko JH, Holt JB (2012) Road traffic noise annoyance, sleep disturbance, and public health implication. *Am J Prevent Med* 43(4):353–360
3. Ali SA, Amura A (2003) Road traffic noise levels, restrictions and annoyance in Greater Cairo, Egypt. *Appl Acoust* 64:815–823
4. Berglund B, Lindvall T, Schwela DH (1999) Guidelines for Community Noise Geneva. World Health Organization. <https://whqlibdoc.who.int/hq/1999/a68672.pdf>
5. Singh N, Davar SC (2004) Noise pollution—sources, effects and control. *J Hum Ecol* 16(3):181–187. <https://doi.org/10.1080/09709274>
6. Shivhare P, Rastogi D (2016) Environmental impact assessment due to festivals. *Int J Eng Technol Sci Res* 3(5):166–172
7. Sharma V, Joshi BD (2010) Assessment of noise pollution during Deepawali festival in a small township of Haridwar city of Uttarakhand, India. *Environmentalist* 30:216–218
8. Verma C, Deshmukh DK (2014) The ambient air and noise quality in India during Diwali festival: a review. *Recent Res Sci Technol* 6(1): 203–21
9. Rao PS, Gajghate DG, Gavane AG, Suryawanshi P, Chauhan C, Mishra S, Gupta N, Rao CVC, Wate SR (2012) Air quality status during Diwali festival of India: a case study. *Bull Environ Contamin Toxicol* 89:376–379
10. Lad RJ, Patil VN, Raut PD (2012) Study of noise pollution during Deepawali festival in Kolhapur city of Maharashtra, India. *Indian Streams Res J* 1(v):1–5
11. AHIRWAR AV, Bajpai S (2015) Assessment of noise pollution during Deepawali festival in Raipur City of Chhattisgarh, India. In: International conference on chemical, environmental and biological sciences (CEBS-2015), 18–19 Mar, Dubai (UAE), pp 88–90
12. Mandal P, Prakash M, Bassin JK (2012) Impact of Diwali celebrations on urban air and noise quality in Delhi City, India. *Environ Monitor Assess* 184:209–215
13. Singh DP, Gadi R, Mandal TK, Dixit CK, Singh K, Saud T, Singh N, Gupta PK (2010) Study of temporal variation in ambient air quality during Diwali festival in India. *Environ Monitor Assess* 169:1–13
14. Hooper LG, Young MT, Keller JP, Szpiro AA, OBrien KM, Sandler DP, Vedal S, Kaufman JD, London SJ (2018) Ambient air pollution and chronic bronchitis in a cohort of US women. *Environ Health Perspect* 1–9. <https://doi.org/10.1289/EHP2199>
15. Manoj KK, Saritha V, Kavitha Dwarapureddi B (2017) Doctrines, environmental and health impacts of Deepawali. *J Basic Appl Res Int* 20(2):113–121
16. Tandon R, Agrawal K, Narayan RP, Tiwari VK, Prakash V, Kumar S, Sharma S (2012) Fire-cracker injuries during Diwali festival: the epidemiology and impact of legislation in Delhi. *Indian J Plast Surg* 45(1):97–102
17. Murty OP (2000) Diwali toxicity. *J Forensic Med Toxicol* 17(2):23–26

Performance and Analysis of Phase Change Material by Using Hybrid Nanofluid (Zinc Cobalt Iron Oxide) on Thermal Energy Storage Device



Harish Kumar Sharma, Satish Kumar, and Mani Kant Paswan

Abstract This paper displays that effectiveness of latent heat storage device is expanded by diminishing charging time of PCM by utilizing the blend of nanofluid (Cobalt Zinc Iron Oxide) and water as heat transfer fluid. By utilizing nanofluids, it is discovered that the charging time for paraffin wax is diminished to about 24% and releasing time is additionally decreased to about 21%. Release of heat utilizing nanofluid is not so recipient since it lessens the hour of releasing which is commonly not required in this way it is encouraged to utilize nanofluid for charging reason and basic water for releasing reason to get most extreme effectiveness of the framework.

Keywords Thermal energy storage · PCM · Nanofluid

1 Introduction

The fundamental goal of this investigation is to build the effectiveness of LHESS by decreasing the charging time of PCM. This is finished by utilizing the blend of Zinc Cobalt Iron Oxide, which fills in as HTF.

LHESS is a type heat exchanger, the space among shell and cylinder is stacked up with PCM, and HTF is allowed to course through the cylinder in order to move energy.

In this test study, the storage capacity of LHESS is gotten by utilizing PCM and hybrid HTF. The thermal attribute, i.e., conductivity is recorded by shifting volume fixation inside the scope of 0.24–1.4% at an interim of 0.24% and HTF temperature inside the scope of 55–80 °C at an interim of 5 °C. The exhibition factors, for example, charging, releasing, exergy, and by and large effectiveness are caught.

Some well-known investigations on thermal energy stockpiling framework acted in the past are introduced underneath.

H. K. Sharma (✉)

Department of Mechanical Engineering, GLA University, Mathura 281406, India

e-mail: harish.sharma@gla.ac.in

S. Kumar · M. K. Paswan

Department of Mechanical Engineering, NIT Jamshedpur, Jamshedpur 831014, India

Feldman et al. [1], overviewed a few natural materials and estimated the dissolving focuses, freezing focuses, thermal properties, progress temperature, and inactive thermalth of combination in the groups of unsaturated fat like capric corrosive, palmitic corrosive, lauric corrosive, and their paired blend, esters, ethers, blends of direct alcohols and sulfur mixes in the scope of temperature 15–60 °C and idle temperature of change 152–181 kJ/kg.

Abhat [2] explored the dormant thermalth of combination of various stockpiling materials like natural materials (paraffin, unsaturated fats), inorganic salt hydrates, eutectic mixes, and he additionally researched the softening and cementing attributes of materials, various strategies for thermal investigation, freezing and liquefying conduct of substances, thermal cycling test, and erosion testing in the temperature run between 0 and 125 °C.

Lacroix [3] performed different analyses to get with the impact of the different thermal and geometric parameters on the thermalth move process numerically and built up an enthalpy-based technique model to ponder heat move conduct of LTES with utilizing various kinds of balances.

Velraj et al. [4], improved the thermalth move rate in an idle thermal energy stockpiling framework comprising of longitudinal blades on a round and hollow vertical cylinders, miniaturized scale embodiment of PCM, embeddings metal lattice in the PCM, and lessing rings by utilizing paraffin RT60 to defeat the downsides of poor thermal conductivity of LHSM.

Banaszek et al. [5] examined transient conduct of PCM experiencing a non-isothermal stage change and progress thermal attributes of paraffin wax in vertical winding thermalth exchanger utilizing paraffin PPW20 as a PCM in the temperature scope of 21–85 °C and found tentatively during thermaling and cooling of PCM an example of convection and conduction dominants separately.

Sari et al. [6], tried myristic corrosive, and after that, thought about the thermal presentation just as thermalth move attributes based on parameters like change time, temperature range, and proliferation through strong fluid interface in the temperature scope of 40–60 °C. He found that thermalth move from the thermalth exchanger to PCM is to a great extent affected by regular convection.

Dimaano et al. [7], researched thermal qualities of C–L corrosive (capric and lauric) with pentadecane in various volume proportion utilizing differential examining calorimetry examination by utilizing stockpiling case of length 420 mm, internal measurement 30 mm, and found that 50:50 of C-L and pentadecane has most elevated thermalth charged and 90:10 has vastest softening band.

Zalba et al. [8] investigated the material of PCM and thermalth move with strong fluid connection and its different applications. She portrayed additionally about material strength, thermo-physical properties, and epitome issues of PCM.

Alkan et al. [9] built up the strategy to expand the enthalpy of dissolving and cementing of paraffin to build its LHTES limit by sulfonation at ionomer level in the temperature scope of 44–56 °C. Different thermal properties were acquired and showed that the enthalpy of liquefying and hardening of docosane and hexacosane could be stretched out by sulfonation.

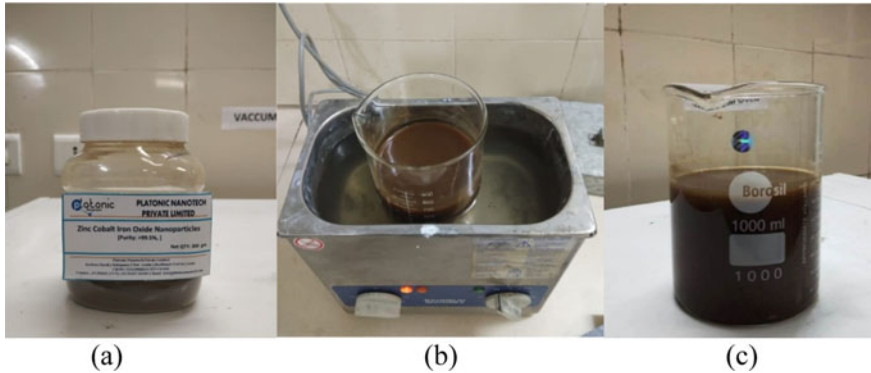


Fig. 1 HTF sample preparation for the heat storage system, **a** hybrid nanoparticles, **b** HTF preparation by sonication, **c** HTF sample ready to use

The obstruction of low conductivity of paraffin can be improved by including high conductivity nanoparticles. Execution of solar water heater joining PCM is noted; similarly as nonattendance of research in structure change of LHESS using nanoparticles is moreover noted.

2 Materials

Hybrid nanomaterial was acquired with immaculateness of over 99.4%. These nanoparticles are about circular with a normal molecule size of 35–45 nm (nanometers). It is showed up as dull dark colored in shading as demonstrated as follows (Fig. 1).

These nanoparticles are dispersed in distilled water to prepare nanofluid to be used as heat transfer fluid. Nanofluid was set up by including wanted centralization of nanoparticles to water by ultrasonic shower sonication process, in which energy is moved from the base of sonicator as ultrasonic waves to the mix of water and nanoparticles for an impressive time as appeared previously.

3 Experimental Setup

The goal of the examination is to enhance storage capacity by utilizing PCM. There are distinctive PCMs and the framework is intended to perform try different things with in any event two PCMs independently. PCMs are kept in the tempered steel chambers to stay away from heat move to the environment. Winding sort heat exchangers are introduced in the chamber for charging and releasing (putting away or extricating of thermal) purposes.

Various pieces of the framework are associated with G.I channels of ½ inch size. To coordinate the HTF according to the prerequisite, a few entryway valves are there in the proper areas. To quantify various factors like temperature, stream rates, and so on, particular sensors are put at the focused on focuses.

Water is utilized as a thermal move liquid (HTF) in the framework. During the charging procedure, high temp water from the thermal exchanges thermal to the PCM. In the releasing procedure, the virus water gets heat from the PCM. To supply water for various purposes, three tanks are there in the framework.

The working of the structure begins with filling the cold HTF. The high temp water offers thermal to the PCM by the procedure of conduction and convection while spilling out of one finish of the thermal exchanger to the next. This phase where the PCM procure energy from the high temp water is known as the boiling water and is known as the charging stage. To discharge the PCM, cold water is sent through the exchanger of the PCM chamber from the HTF source tank.

4 Results and Discussion

The temperatures of PCM at various areas in the capacity tank are recorded during liquefying and during cementing under the HTF temperature 90 °C. The examination of the consequences of utilizing deionised water as HTF and nanofluid concentrated water as HTF is finished. Paraffin wax is taken as PCMs for trial reason.

4.1 Charging

At first, the paraffin wax is at starting temperature (33 °C). During charging procedure of paraffin wax utilizing water as HTF at 95 °C, the most extreme temperature spans to 59.22 °C. The mass stream rate is taken as 8 LPM. As appeared in Fig. 2, at first, the temperature of PCM rises quickly on the grounds that the temperature contrast between temperature of PCM and HTF is high, so there is high addition of thermal during this period. After which as the temperature contrast decreases, the PCM begins to become balance out which totally reaches to liquefying temperature in 115 min. So, time taken for the charging stage at 85 °C temperature is about 115 min. Figure 3 likewise shows temperature advancement during charging procedure of paraffin wax utilizing nanofluid 85 °C. In this, the readings of thermocouple are set on a diagram regarding time. The greatest temperature spans to 61.05 °C in around 88 min. The time taken for the accusing period of nanofluid at 85 °C temperature is about 88 min.

From above chart, it is unmistakably obvious that the time during the charging stage is decreased by 28 min which shows that the exhibition of the framework is improved by utilizing nanofluids during charging stage for paraffin. By the utilization of nanofluids, it is unmistakably found from the outcomes and appeared in Fig. 2 that the charging time for paraffin wax is decreased by about 24%.

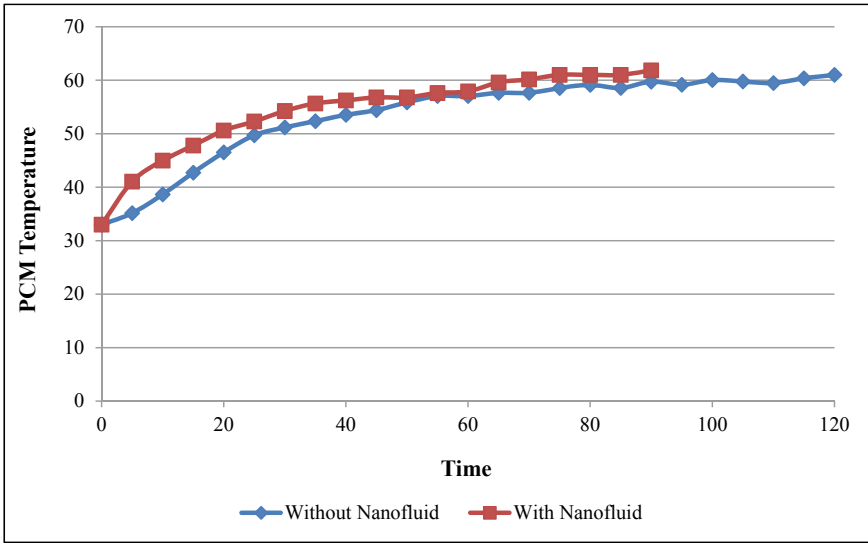


Fig. 2 Charging with and without using nanomaterial

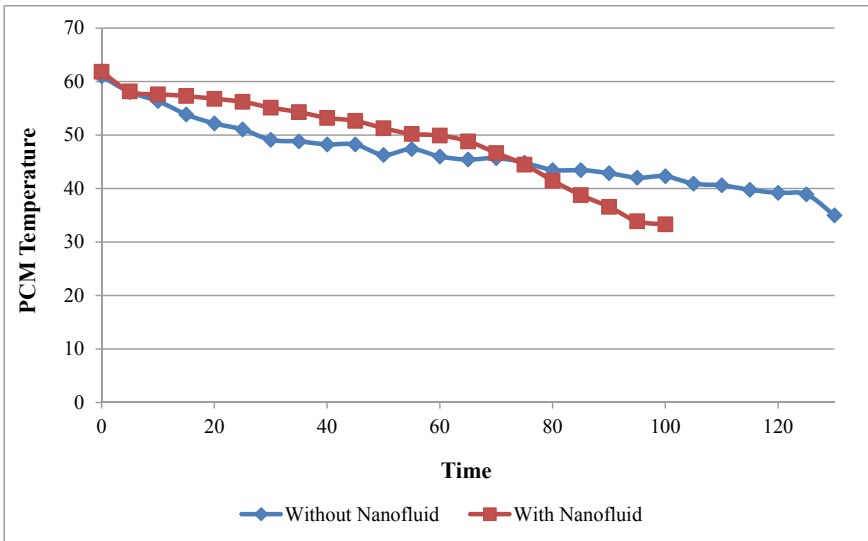


Fig. 3 Discharging with and without using nanofluid

4.2 Discharging

After the charging system is done, the discharging technique is started expeditiously bypassing cold HTF. During this procedure, the PCM in the annulus is in liquid stages. Figure 3 exhibits the temperature of the PCM during the test unit with time in hardening. It is seen that the temperature of the PCM is decreased rapidly near the HTF pipe until it accomplishes a beginning temperature of the PCM (around 33 °C). During solidifying of the PCM, the thermal energy is released. The temperature is decreased rapidly once all the PCM have solidified. The time taken for the releasing stage utilizing water is about 125 min. Figure 3 likewise shows the temperature of the PCM as paraffin wax utilizing nanofluid. The time taken for the releasing stage with nanofluid is about 102 min to accomplish a beginning temperature of the PCM (around 34 °C).

It is likewise unmistakably portrayed from the investigation and appeared in Fig. 3 that the releasing time is additionally diminished by utilizing nanofluids. For paraffin wax, releasing time is decreased to about 21%.

5 Comparison with Earlier Work

To approve the dependability of results, the examinations between the present readings and writing results were performed under the identical geometric parameters. Figure 4 exhibits a correlation of normal temperature profile of PCM while charging using water as HTF versus time between two works.

Results of present examination is in great simultaneousness with that of Jesumathy et al. [10]. The normal charging time blunder is about 5.48% and the most extreme charging time mistake is about 8.21% at 80 min. These blunders are inside the acceptable extent of mistakes. In this way, it portrays that the physical model results in the present paper are adequate.

6 Conclusions

It can be seen from above outcomes that release utilizing nanofluid is not so recipient since it lessens the hour of releasing which is commonly not required along these lines; it is encouraged to utilize nanofluid for charging reason and straightforward water for releasing reason to acquire greatest effectiveness of the framework. By the utilization of nanofluids, it is obviously found from the outcomes that the charging time for paraffin wax is upgraded by approx. 24%. It is likewise plainly delineated from the investigation that the releasing time is additionally decreased by utilizing nanofluids. For paraffin wax, releasing time is decreased to about 21%. The decrease in liquefying time of PCM is compulsory so it could get charged in less time or we

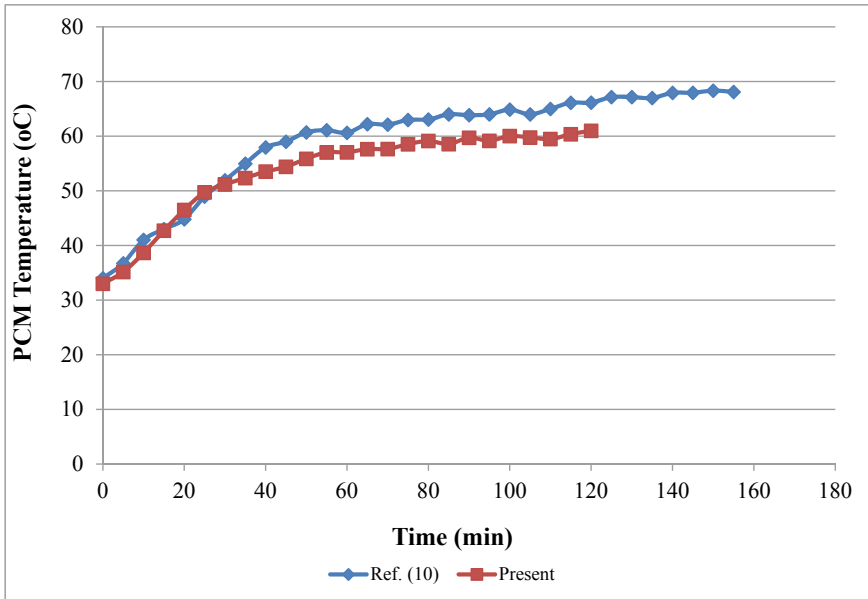


Fig. 4 Results concurrence between the present study and the results of Ref. [10]

can say that by the utilization of nanofluid, the measure of thermal energy required by the PCM to reach to its softening time is less.

References

1. Feldman D, Shapiro MM, Banu D (1986) Organic phase change materials for thermal energy storage. *Solar Energy Mater.* 13:1–10
2. Abhat A (1983) Low temperature latent heat thermal energy storage: heat storage materials. *Solar Energy* 30:313–332
3. Lacroix M (1989) Computation of heat transfer during melting of a pure substance from an isothermal wall. *Numer Heat Transf Part B* 15:191–210
4. Velraj R, Seeniraj RV, Hafner B, Faber C, Schwarzer K (1997) Experimental analysis and numerical modelling of inward solidification on a finned vertical tube for a latent heat storage unit. *Sol Energy* 60:281–290
5. J. Banaszek, R. Domański, M. Rebow, F. El-Sagier, Experimental study of solid–liquid phase change in a spiral thermal energy storage unit, *Appl. Thermal Eng.* 19 (1999) 1253–1277.
6. Sari A, Kaygusuz K (2001) Thermal energy storage system using some fatty acids as latent heat energy storage materials. *Energy Sour* 23:275–285
7. Dimaano MNR, Watanabe T (2002) The capric–lauric acid and pentadecane combination as phase change material for cooling applications. *Appl. Thermal Eng.* 22:365–377
8. Zalba B, Man JM, Cabeza LF, Mehling H (2003) Review on thermal energy storage with phase change: materials, heat transfer analysis and applications. *Appl Therm Eng* 23:251–83

9. Alkan C, Sarı A, Karaipekli A, Uzun O (2009) Preparation, characterization, and thermal properties of microencapsulated phase change material for thermal energy storage. *Sol Energy Mater Sol Cells* 93:143–147
10. Jesumathy SP, Udayakumar M, Suresh S, Jegadheeswaran S (2014) An experimental study on heat transfer characteristics of paraffin wax in horizontal double pipe heat latent heat storage unit. *J Taiwan Inst Chem Eng* 45:1298–1306

A Numerical Experiment on Thermo-fluidic Transport of Third-Grade Fluid Flow Through a Porous Microchannel Under the Influence of Combined Electromagnetohydrodynamic Effect



Motahar Reza, Amalendu Rana, and Raghunath Patra

Abstract A theoretical investigation is done to analyze the thermo-fluidic transport features of (electromagnetohydrodynamic) EMHD flow of third-grade fluid in a microchannel through a porous medium. The viscous dissipation and Joule heating are considered to analyze the thermal characteristics for this flow through microchannel with porous medium impregnated by third-grade fluid. The reduced governing equations which are becoming highly nonlinear due to considering third-grade fluid are solved numerically to obtain the solutions for velocity and temperature distributions. The novel results show that the unknown Nusselt number (Nu) has been derived from bulk mean temperature to control the rate of heat transfer by applying suitable strength of the magnetic field and electric field. The significant effects of momentum and thermal transport phenomenon within the porous microchannel for various physical factors such as Hartmann number, Darcy number, transverse electric field, non-Newtonian parameter are elaborated in this work.

Keywords EMHD flow · Porous medium · Third-grade fluid · Joule heating · Microchannel

1 Introduction

Microfluidics is used by engineers to design small-scale systems in modern science and technology. In various micro-devices have been utilized in biomedical devices, lab-on-chip devices, and MEMS. The electrolyte solution gets hold on walls of

M. Reza (✉)

Department of Mathematics, GITAM Deemed to be University, Hyderabad 502329, India
e-mail: motaharreza90@gmail.com

M. Reza · A. Rana

Department of Mathematics, National Institute of Science and Technology, Berhampur 761008, India

A. Rana · R. Patra

Department of Mathematics, Berhampur University, Berhampur 760007, India

© Springer Nature Singapore Pte Ltd. 2021

P. Pant et al. (eds.), *Advances in Mechanical Processing and Design*, Lecture Notes in Mechanical Engineering, https://doi.org/10.1007/978-981-15-7779-6_10

a microchannel, and the chemical reaction with solid–liquid interface cogenerates an electric double layer (EDL) about the rampart of the microchannel. In most of technology, enrapture of non-Newtonian fluid via microchannel is found, and this transport mechanism is characterized by mathematically to considering the material behavior on nonlinear relation between stress and strain rate. Recently, many theoretical investigations by various flow problem have been examined by many researchers to analyze the non-Newtonian characteristic. Many theoretical and experimental studies on microfluidics are done by so many researchers and engineers because of its broad area of applications in various areas like biomedical devices, lab-on-chip devices, micropump, EMHD micropump, heat exchanger, etc. [1–4]. In the last two decades, many researchers investigated the experimental and theoretical work on EMHD flow in microfluidics. First, Jang and Lee [5] examined the pumping mechanism in a microchannel by applying a magnetic field and demonstrated this result by experimental observation. Chakraborty et al. [6] analyzed the electrokinetic effect on flow through microchannel under constant wall heat flux conditions. Recently, Buren et al. [7] studied the EMHD flow through a micro parallel channel with the corrugated wall by perturbation technique. Very recently, Rashid et al. [8] investigated the EMHD effects on porous microchannel with the corrugated wall of a non-Newtonian second-grade fluid by using the perturbation technique. An analytical solution of the third-grade fluid flow through the microchannel in presence of electrokinetic and magnetic field effect is examined by Wang et al. [9].

From the above motivational investigations, it is remarkable to examine the flow transport and heat transmit phenomenon of third-grade fluid through the porous microchannel. The main objective of this study is to find the approximation solutions of the third-grade fluid flow using numerical technique inside a porous microchannel with combined electromagnetohydrodynamic (EMHD) effects. The constitutive governing equation is modified from the Navier–Stokes equation by using constitutive relations of third-grade fluid model. The flow velocity distribution is obtained by applying for the fourth-order Runge–Kutta method. The heat transfer phenomenon is also analyzed in the presence of viscous dissipation, Darcy dissipation and Joule heating effects. Further, the Nusselt number is obtained by finding bulk mean temperature numerically. The graphical representation of the computed results of this flow problem with several pertinent dimensionless parameters will be discussed in this work.

2 Formulation of the Mathematical Model of the Problem

Consider a steady, laminar, fully developed viscous flow of an incompressible non-Newtonian third-grade fluid in a microchannel through porous medium with combined electromagnetohydrodynamic effects. The flow is assumed to be thermally fully developed through the microchannel of height $2h$, width W ($2h \ll W$) and length L ($2h \ll L$). Also, consider the electrolyte solution with viscosity μ , electrical conductivity σ and density ρ . The origin of the microchannel is fixed at the

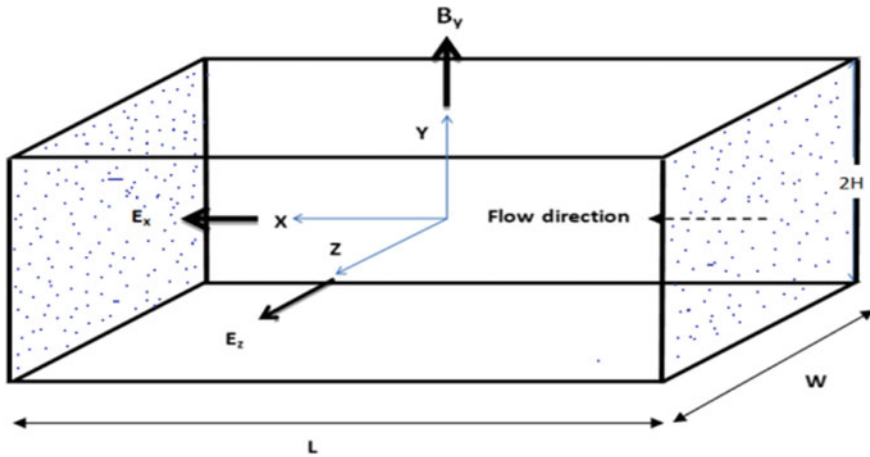


Fig. 1 Physical sketch of the problem

middle of the channel with the unit base vector (e_x, e_y, e_z) , in the Cartesian coordinate system. And the electric field E_x is acted along the x -axis. The uniform magnetic field B_y is along the transverse direction of the flow. The transverse electric field E_z is generated along the z -direction (Fig. 1).

For incompressible third-grade fluid, the Cauchy tensor τ is described as [10]

$$\tau = -pI + \mu A_1 + \alpha_1 A_2 + \alpha_2 A_1^2 + \beta_1 A_3 + \beta_2 (A_1 A_2 + A_2 A_1) + \beta_3 (tr A_1^2) A_1 \tag{1}$$

where p is the pressure and $\alpha_1, \alpha_2, \beta_1, \beta_2$ and β_3 are material constants of the third-grade fluid. A_1, A_2 and A_3 are the Rivlin–Ericksen tensors which can be expressed as

$$A_1 = \text{grad}(V) + \{\text{grad}(V)\}^T \tag{2}$$

$$A_n = \frac{dA_{n-1}}{dt} + A_{n-1}\{\text{grad}(V)\} + \{\text{grad}(V)\}^T A_{n-1}, \quad n = 2, 3. \tag{3}$$

Assuming a one-dimensional velocity in x -direction for the microchannel is given by $V = [u(y), 0, 0]$. In this case, the simplified form of the momentum conservation equation assuming a hydrodynamically fully developed flow through the porous medium for potential field within the electric double layer (EDL) is written as

$$\begin{aligned} \frac{\partial p}{\partial x} = & \mu \frac{d^2 u}{dy^2} + 2(\beta_2 + \beta_3) \frac{d}{dy} \left\{ \left(\frac{du}{dy} \right)^3 \right\} \\ & + \rho_e E_x - \mu \frac{u}{K} - \sigma_e B_y^2 u + \sigma_e B_y E_z \end{aligned} \tag{4}$$

$$\frac{\partial p}{\partial y} = (2\alpha_1 + \alpha_2) \frac{d}{dy} \left\{ \left(\frac{du}{dy} \right)^2 \right\}. \quad (5)$$

$$\frac{\partial p}{\partial z} = 0 \quad (6)$$

If the modified pressure is defined as

$$p^* = p - (2\alpha_1 + \alpha_2) \left\{ \left(\frac{du}{dy} \right)^2 \right\} \quad (7)$$

Since from Eqs. (5) and (6), the pressure is only a function of x and i.e., $p^* = p^*(x)$. Therefore, in Eq. (4), the pressure gradient is constant. Then, Eq. (4) is written as

$$\frac{dp^*}{dx} = \mu \frac{d^2 u}{dy^2} + 2(\beta_2 + \beta_3) \frac{d}{dy} \left\{ \left(\frac{du}{dy} \right)^3 \right\} + \rho_e E_x - \mu \frac{u}{K} - \sigma_e B_y^2 u + \sigma_e B_y E_z \quad (8)$$

The net charge density ρ_e in the EDL depends on the EDL potential ψ , and it is given by

$$\rho_e = -\varepsilon \kappa^2 \psi \quad (9)$$

The EDL potential ψ is well constructed by the linearized Poisson–Boltzmann equation

$$\frac{d^2 \psi}{dy^2} = \kappa^2 \psi \quad (10)$$

The boundary conditions for the EDL potential distribution are

$$\psi = \zeta \quad \text{at} \quad \psi = -h, \quad \frac{d\psi}{dy} = 0 \quad \text{at} \quad y = 0 \quad (11)$$

where $\kappa = ez \left(\frac{2n_0}{\varepsilon k_B T} \right)^{\frac{1}{2}}$ is Dybye–Hückle parameter and $1/\kappa$ be the thickness of the EDL. Here, ζ be the constant zeta potential. By introducing the dimensionless variables $\psi^* = \psi/\zeta$, $y^* = y/h$, $\omega = \kappa h$, and finally, one can obtain the non-dimensional ψ^* as:

$$\psi^* = \cosh(\omega y^*) / \cosh(\omega). \quad (12)$$

Then, the simplified dimensionless form of the Eq. (8) is

$$\frac{d^2 u^*}{dy^{*2}} + 6\beta \left(\frac{du^*}{dy^*} \right)^2 \frac{d^2 u^*}{dy^{*2}} + \omega^2 \psi^* - \left(\text{Ha}^2 + \frac{1}{\text{Da}} \right) u^* + \text{Ha}S + P = 0 \quad (13)$$

The dimensionless variables and parameters are given by

$$\begin{aligned} y^* &= \frac{y}{h}, \quad u^* = \frac{u}{u_{\text{HS}}}, \quad P = \frac{\left(-\frac{dp}{dx}\right)h^2}{\mu u_{\text{HS}}}, \\ u_{\text{HS}} &= -\frac{\varepsilon \zeta E_x}{\mu}, \quad \text{Ha} = B_y h \sqrt{\frac{\sigma_e}{\mu}}, \quad \text{Da} = \frac{h^2}{K}, \\ S &= \frac{E_z h}{u_{\text{HS}}} \sqrt{\frac{\sigma_e}{\mu}}, \quad \beta = \frac{(\beta_2 + \beta_3)u_{\text{HS}}^2}{\mu h^2} \end{aligned}$$

where u_{HS} is the steady Helmholtz-Smoluchowski velocity, Ha is the Hartman number, Da be the Darcy number, respectively. S is the transverse electric field which indicates the strength of the electric field in x -direction, and P is described as the constant dimensionless pressure gradient. β is the non-dimensional parameter related to the non-Newtonian behavior of the third-grade fluid. The dimensionless boundary conditions for the Eq. (13) is given by

$$u^*(-1) = 0, \quad \frac{du^*(0)}{dy} = 0 \quad (14)$$

The energy equation for thermally fully developed flow of third-grade fluid through a porous microchannel is expressed as

$$\rho C_P u \frac{\partial T}{\partial x} = k_{\text{Th}} \frac{\partial^2 T}{\partial y^2} + 2(\beta_2 + \beta_3) \left(\frac{du}{dy} \right)^4 + \Omega + S_j \quad (15)$$

Here, Ω and S_j are the volumetric heat generation due to viscous dissipation and Joule heating, respectively. Here, $\Omega = \mu \left\{ \left(\frac{du}{dy} \right)^2 + \frac{u^2}{K} \right\}$, $S_j = \sigma_e (E_x^2 + B_y^2 u^2 - 2E_z B_y u)$, k_{Th} is the thermal conductivity of the fluid, C_P is the specific heat of the liquid at constant pressure, and T is the local temperature of the liquid. Introducing the non-dimensional temperature $T^* = \frac{k_{\text{Th}}(T - T_w)}{q_w h}$ where T_w is the channel wall temperature and q_w is the constant wall heat flux. Further, for thermally fully developed flow under imposed constant wall heat flux, one may write $\frac{\partial T}{\partial x} = \frac{dT_w}{dx} = \frac{dT_b}{dx} = \text{constant}$ and $\frac{d^2 T}{dx^2} = 0$ in which T_b is the bulk mean temperature. The overall energy balance of an elementary control volume of the fluid with the length of duct dx gives the following expression:

$$\rho C_P h u_m \frac{dT_b}{dx} = q_w + \int_0^h \Omega dy + \int_0^h S_j dy \quad (16)$$

Then, the bulk mean temperature gradient can be obtained as

$$\frac{dT_b}{dx} = \frac{M}{\rho C_P} = \text{constant.} \quad (17)$$

where

$$M = \frac{q_w}{u_m} + \frac{\sigma_e E_x^2 h}{u_m} + \frac{\sigma_e B_y^2 G}{u_m} + \frac{\mu}{u_m} \left(F + \frac{G}{K} \right) - 2E_z \sigma_e B_y, \quad G = \int_0^h u^2 dy, \quad F = \int_0^h \left(\frac{du}{dy} \right)^2 dy, \quad u_m = \int_0^h u dy.$$

The following dimensionless parameters are introduced to make dimensionless the Eq. (15),

$$\gamma = \left(\frac{M u_{HS} h}{q_w} + 2\text{HaSB}r \right), \quad \text{Br} = \frac{\mu u_{HS}}{h q_w}, \quad S_J = \frac{\sigma_e E_x^2 h}{q_w}.$$

where γ is the ratio of the heat generated by the interaction of the electric and magnetic fields to heat conduction, Br is the Brinkman number which describes the ratio of heat produced by viscous dissipation and heat transport by molecular conduction, S_J is the Joule heating due to heat conduction. Then, by using (16), the non-dimensional form of the Eq. (15) is obtained as

$$\frac{d^2 T^*}{dy^*} = \gamma u^* - \text{Br} \left(\text{Ha}^2 + \frac{1}{\text{Da}} \right) u^{*2} - \text{Br} \left(\frac{du^*}{dy^*} \right)^2 - 2\beta \text{Br} \left(\frac{du^*}{dy^*} \right)^4 - S_J \quad (18)$$

The corresponding non-dimensional boundary conditions are expressed as

$$T^*(-1) = 0, \quad \frac{dT^*(0)}{dy^*} = 0 \quad (19)$$

By taking the advantage of the velocity and temperature distribution, the non-dimensional bulk mean temperature can be written as

$$T_b^* = \frac{k_{Th}(T_b - T_w)}{q_w h} = \frac{\int_{-1}^1 u^* T^* dy^*}{\int_{-1}^1 u^* dy^*} \quad (20)$$

Then, the rates of heat transfer at the wall are expressed in the form of the Nusselt number which is obtained as

$$\text{Nu} = \frac{2h q_w}{k_{Th}(T_w - T_b)} = -\frac{2}{T_b^*}. \quad (21)$$

3 Results and Discussions

The velocity Eq. (13) and the temperature Eq. (18) are solved numerically with the corresponding boundary conditions (14) and (19), respectively. These nonlinear equations are solved numerically using the shooting method based on fourth-order Runge–Kutta method in Matlab. Further, the Nusselt number is obtained numerically by using the numerical integration methods.

This study deals the numerical solutions of the velocity and temperature profiles of third-grade fluid under the influence of combined EMHD effects through a porous microchannel. The variation of dimensionless velocity and temperature distributions with different parameter values of the flow is discussed in this section. The interactive influences of different non-dimensional parameters on velocity and temperature are examined. The impacts of electromagnetic effect, the effect of porous medium and the influence of non-Newtonian parameter are discussed on the flow velocity and temperature distribution. The influence of viscous dissipation effect and Joule heating effect is also examined on the temperature distribution. Further, the variation of heat transfer rate is also discussed with various non-dimensional parameters.

The non-dimensional velocity profiles for $\omega = 10$, $Da = 0.1$, $P = 0.5$, $\beta = 0.02$ at different values of Hartmann number are shown in Fig. 2. Due to the absence of transverse electric field (i.e., $S = 0$), the velocity profile is decreasing when the applied magnetic field (i.e., Hartmann number) is increasing which is illustrated in Fig. 2a. But in the presence of the transversed electric field (i.e., $S = 3$), it gives an increasing trend on the velocity profile with an increase of Ha which is shown in Fig. 2b. It can be noted that when $S = 0$ velocity becomes slower than the velocity when $S = 3$. However, the flow velocity is always fully developed for both the cases with the variation of applied magnetic field.

Figure 3a depicts the velocity distribution for several value of Darcy number. In the presence of transverse electric field when the Darcy number is increasing, then

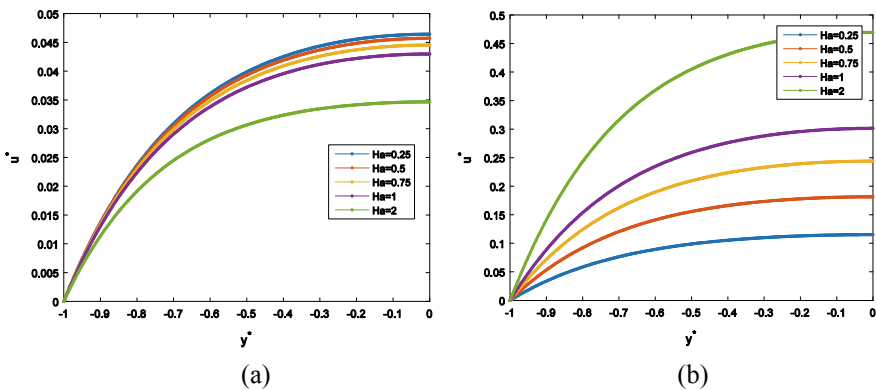


Fig. 2 Variation of velocity distribution for several value of Hartmann number **a** $S = 0$, **b** $S = 3$ for parameter values $\omega = 10$, $Da = 0.1$, $P = 0.5$, $\beta = 0.02$

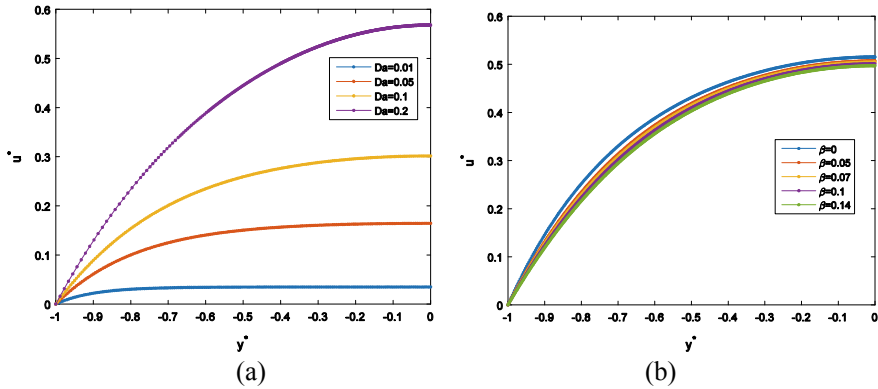


Fig. 3 a Variation of velocity distribution for several value of Darcy number, b variation of velocity distribution for several value of non-Newtonian parameter for parameter values $S = 3$, $\omega = 10$, $Ha = 1$, $P = 0.5$.

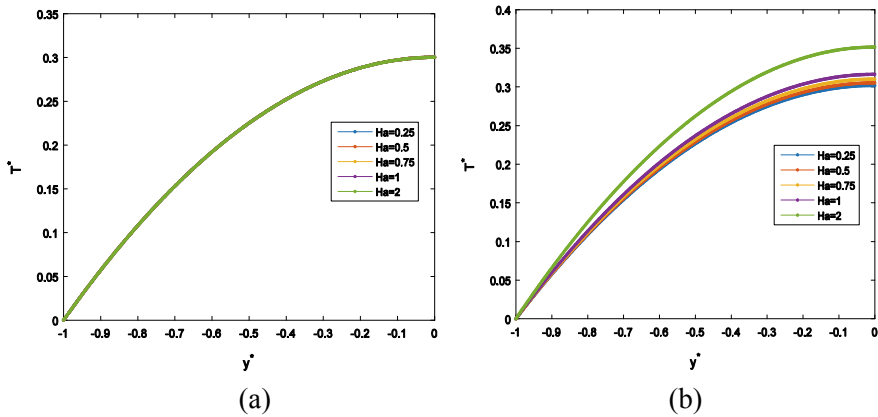


Fig. 4 Variation of temperature distribution for several value of Ha . a $S = 0$, b $S = 3$

the flow velocity is also increasing which is represented in Fig. 3b. So, it is very interesting to know that the velocity of the fluid always increases in high porous medium, but it is slower than the velocity when there exist both components ‘flow aiding’ and ‘flow opposing’ ($\sim \sigma_e B_v^2 u$) due to the imposed electromagnetic field.

The dimensionless velocity distribution for different non-dimensional parameters $Ha = 1$, $Da = 0.1$, $P = 0.5$, $S = 3$ at different values of non-Newtonian parameter is illustrated in Fig. 3b. From this figure, it can be observe that the velocity is increased when the non-Newtonian parameter value increases. Also, it can be noted that when $\beta = 0$, then the fluid is a Newtonian fluid, and for the other values of β , it behaves the non-Newtonian fluid characteristics.

The temperature distribution of the flow is described in Fig. 4 for the parameter values $\omega = 10$, $Da = 0.1$, $P = 0.5$, $\beta = 0.02$, $Br = 0.04$, $\gamma = 0.008$, $S_J = 0.6$ with variation of the applied magnetic field which embodied by Hartmann number. In the absence of transverse electric field, i.e., when $S = 0$, it is failed to trigger any apprehensible change in the associated temperature distribution with the increasing magnitude of Ha which is delineated in Fig. 4a. But in the presence of transverse electric field, the temperature profile is increasing when the Hartmann number increases which is illustrated in Fig. 4b. From both figures, it can be observed that the temperature rises due to enhancement of flow aiding component of the imposed applied electromagnetic field.

Figure 5 exhibits the influences of the dimensionless temperature distributions with different Debye–Hückel parameters and Darcy numbers, respectively. Figure 5a depicts that when Debye–Hückel parameter is enhanced, then the temperature is reduced. The temperature profile has an increasing trend when the Darcy number is increasing which is shown in Fig. 5b. So, it was found that the temperature becomes high in high porous medium. The influence of non-Newtonian parameter is analyzed in Fig. 6a. From this figure, it is noted that the temperature profile is decreasing with the increase of non-Newtonian parameter. But the temperature becomes greater when $\beta = 0$, i.e., when it is a Newtonian fluid.

The viscous dissipation and Joule heating effects are playing very important role in thermal transport characteristics. The viscous dissipation effect which is represented by Brinkman number (Br) and Joule heating effect, represented by (S_J), is shown in Figs. 6b and 7a. It can be observed that the temperature increases when there is an increasing trend on Brinkman number (see Fig. 6b). It is very interesting to know that when the viscous dissipation effect is negligible ($Br = 0$), then the temperature is lower than the temperature due to viscous dissipation effect. Figure 7a illustrates

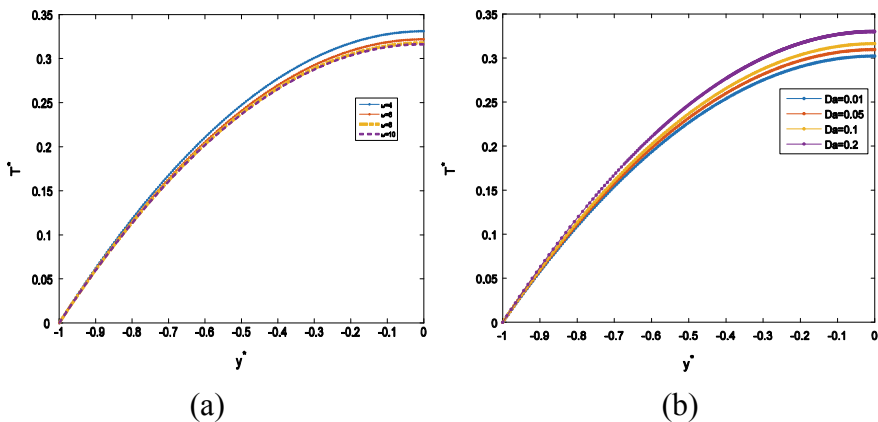


Fig. 5 a Variation of temperature distribution for several value of Debye–Hückel parameter. **b** Variation of temperature distribution for several value of Darcy number for parameter values $P = 0.5$, $\beta = 0.02$, $Br = 0.04$, $\gamma = 0.008$, $S_J = 0.6$

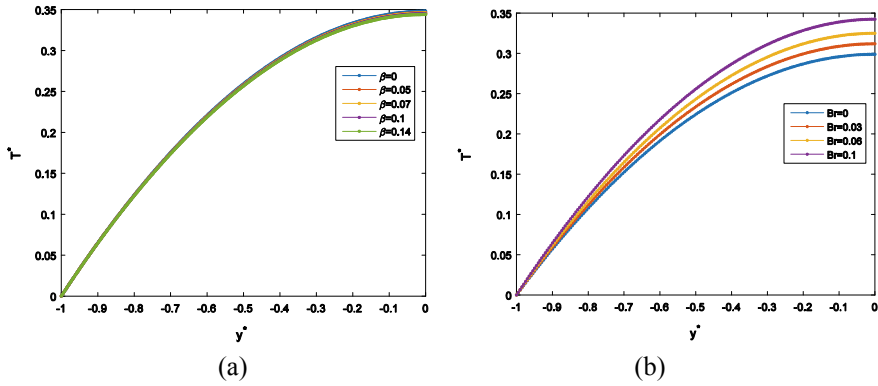


Fig. 6 a Variation of temperature distribution for several value of non-Newtonian parameter. **b** Variation of temperature distribution for several value of Brinkman number for parameter values $\omega = 10, Ha = 1, Da = 1, P = 0.5, \gamma = 0.008, S_j = 0.6$

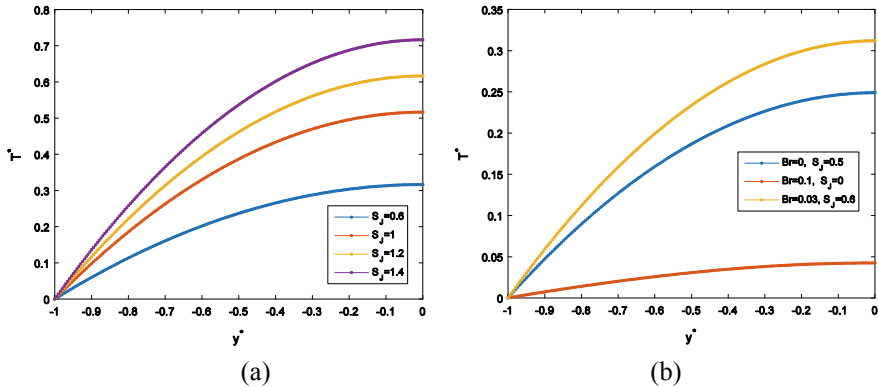


Fig. 7 a Variation of temperature distribution for several value of Joule heating parameter for parameter values $\omega = 10, Ha = 1, Da = 1, P = 0.5, \gamma = 0.008, Br = 0.04, \beta = 0.02$. **b** Comparison of temperature distribution with dissipation and Joule heating effects

the influence of Joule heating effect on the temperature profile. It is seen that the temperature profile is increasing when the dimensionless Joule heating parameter increases. As depicted in Fig. 7b, the dimensionless temperature of the fluid is higher for $Br = 0.03, S_j = 0.6$ compared to the other cases, and the temperature is lower for $Br = 0, S_j = 0.5$.

The effects of porous medium and the effect of non-Newtonian parameter on the Nusselt number are delineated in Fig. 8a, b, respectively. For all cases, the Nusselt number is increasing with increases of other parameters. But for non-Newtonian parameter, it increases rapidly which are shown in Fig. 8b. Also, it can be observed that for low porous medium, the Nusselt number is low.

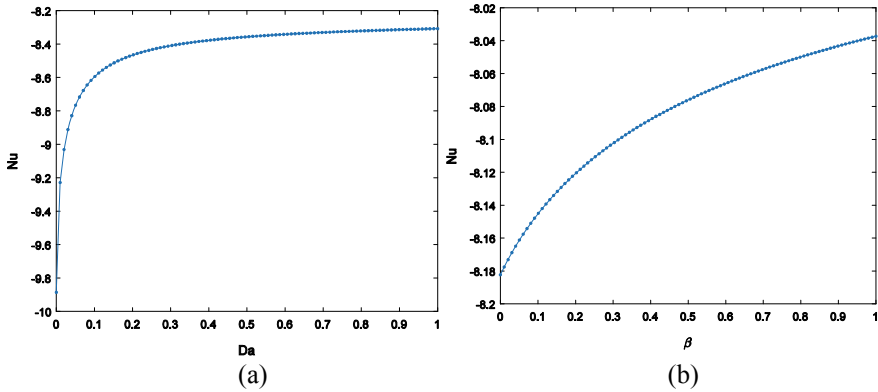


Fig. 8 Variation of Nusselt number **a** with varying magnitude of Darcy number, **b** with varying magnitude of non-Newtonian parameter

4 Conclusions

In this present study, the velocity and temperature distribution are investigated numerically for the third-grade fluid flow through a porous microchannel with EMHD effects. The following observations can be drawn from this numerical study:

- Due to the absence of trigger any apprehensible change in the associated temperature distribution with Hartmann number.
- The velocity and temperature both are proportional to the Darcy number. That means both are increasing in high porous medium.
- The velocity and temperature both are decreased for increase of the given non-transverse electric field, and the applied magnetic field (represented by Hartmann number) is inversely proportional to the velocity profile. Whereas the velocity and temperature both are proportional to Hartmann number in the presence of transverse electric field.
- The velocity and temperature both are decreased for the increase of the given non-Newtonian parameter.
- The Nusselt number increases rapidly for the influence of the non-Newtonian parameter.

Acknowledgements This work was supported by SERB , Govt of India (Grant File No. EMR/2016/006383). The authors would like to acknowledge this support.

References

1. Stone HA, Stroock AD, Ajdari A (2004) Engineering flows in small devices microfluidics toward a lab-on-a-chip. *Ann Rev Fluid Mech* 36:381–411
2. Laster DJ, Santiago JG (2004) A review of micropumps. *J Micromech Microeng* 14:R35–R64
3. West J, Karamata B, Lillis B, Gleeson JP, Alderman JK (2002) Application of magnetohydrodynamic actuation to continuous flow chemistry. *Lab Chip* 2:224–230
4. Weston MC, Gerner MD, Fritsch I (2010) Magnetic Fields for Fluid Motion. *Anal. Chem.* 82:3411–3418
5. Jang J, Lee SS (2000) Theoretical and experimental study of MHD (magnetohydrodynamic) micropump. *Sensor Actuat A Phys* 80:84–89
6. Chakraborty R, Dey R, Chakraborty S (2013) Thermal characteristics of electromagnetohydrodynamic flows in narrow channels with viscous dissipation and Joule heating under constant wall heat flux. *Int J Heat Mass Transf* 67:1151–1162
7. Buren M, Jian Y, Chang L (2014) Electromagnetohydrodynamic flow through a microparallel channel with corrugated walls. *J Phys D Appl Phys* 47:425–501
8. Rashid M, Shahzadi I, Nadeem S (2018) Corrugated walls analysis in microchannels through porous medium under Electromagnetohydrodynamic (EMHD) effects. *Res Phys* 9:171–182
9. Wang L, Jian Y, Liu Q, Li F, Chang L (2016) Electromagnetohydrodynamic flow and heat transfer of third grade fluids between two micro-parallel plates. *Colloids Surfaces A Physicochem Eng Aspects*
10. Ellahi R, Hayat T, Mahomed F M, Asghar S (2010) Effects of slip on the non-linear flows of a third grade fluid. *Nonlinear Anal-Real* 11, 139–146

Experimental Investigation of Performance and Emissions of Single-Cylinder Diesel Engine Enriched by Hydroxy Gas for Various Compression Ratios



Manoj Dahake, Shrishant Patil, and Dileep Malkhede

Abstract The hydroxy gas due to its carbonless structure is considered as a potential supplement fuel for IC engines. It reduces the burden of energy imports and reduces carbon containing tailpipe emission. Hydroxy gas has unique properties due to the absence of carbon which is considered as better alternative fuel compared to other options such as LPG and CNG. In the current study, a single-cylinder VCR research engine was used with constant flow of hydroxy gas in the intake manifold and the performance is compared with baseline diesel performance at varying compression ratios. Hydroxy gas is produced by means of conventional electrolyzer and consumed to eliminate the requirement of storage device. According to experimental results, the brake thermal efficiency increases by 7.36%, 7.68% and 9.25% and BSFC reduces by 10%, 10.71% and 15% at full load condition at compression ratio of 16, 17 and 18, respectively. Improvement is seen in performance parameters as well as in emissions also, and HC reduces by 6%, 8% and 33% and CO reduces by 10%, 12% and 23% at full load condition on same compression ratios, respectively. However, at higher compression ratio, NO_x emissions rise could not be prevented. The increase in compression ratio resulted in reduction of smoke opacity. It was observed that the enrichment of hydroxy gas has resulted in complete combustion with lesser emissions at all compression ratios. It is observed that enrichment technique has potential of getting maximum benefit at higher compression ratios.

Keywords CI engine · Hydroxy gas · Emissions

M. Dahake (✉) · S. Patil
Mechanical Engineering Department, AISSMS's College of Engineering, Pune, India
e-mail: mnjdahake@gmail.com

D. Malkhede
Mechanical Engineering Department, College of Engineering Pune, Pune, India

1 Introduction

The petroleum crude reserves usage is at high rates in developed nations. The potential threat due to uncertainty of petroleum products is an important contemplation for research and development of alternate fuels for transportation and power generation in the future. Hydroxy (HHO) gas is reviewed as the best clean and green alternative fuel among all gaseous fuels by the researchers. The price controlling and the uncertain reserves are major inducement to pursue energy threat. Fossil fuel usage which is one of the reasons for global warming and air pollution is major notable environmental and societal problem [1]. The hydroxy gas needed the strong research and development along with expositions of it for the use in diesel engine. The carbon-less structure of hydroxy gas has the advantage of hardly harmful emissions with higher thermal efficiency. Also, it can be used in a dual fuel mode in combination with other fuels. This study helps to investigate the performance characteristics and enhancement in engine performance using hydrogen as supplement fuel. Addition of hydroxy gas in diesel engines results in improving the thermal efficiency and specific fuel consumption and lessening in HC and CO emission [2].

The fuel is considered suitable for internal combustion engines when the tailpipe emission relating to local pollution norms is less, its cost should be less, practicality to use and acceptance by customer. Hydroxy gas is well thought-out as clean burning fuel due to its carbon less structure. Hydroxy gas contains the mixture of oxygen and hydrogen at 1:2 ratio, and after combustion, the byproduct is only water. It is a non-odorant, non-toxic, gaseous matter and burns entirely. On burning with hydrogen, combustion process does not generate toxic products like hydrocarbons, carbon monoxide, carbon dioxide, oxide of sulfur and organic acids except for the formation of NO_x . Many researchers have investigated that the use of hydrogen in premixed charge in engines gives more fuel efficiency and less emissions. Pre-mixing of hydrogen with air in intake manifold of engines resolves the problem, as the diesel injection timings can be varied to control ignition by giving additional substantial advantage of improving combustion with the use of hydroxy gas. Poor or varying ignition characteristic fuels can be used in diesel engine by pre-mixing. However, this enrichment technique makes less acceptable for transport applications because of the requirement for two fuel supply, storage and injection systems. But, a better option is onboard generation of the hydroxy gas for transport vehicles which makes it popular. Also, the hydroxy gas-based internal combustion engines are cheaper than hydrogen fuel cell vehicles in terms of fuel cost, while hydrogen fuel cell vehicles achieve highest fuel efficiency and hence, can serve bridge for development of infrastructure for hydrogen fuel. Hydrogen has a wide flammability range and high autoignition temperature which makes it extremely popular for lean-burn engines operating at higher compression ratio, and due to high flame speed, knocking of engine can be prevented to greater extent. The flame velocity of hydrogen is much faster than other fuel which allows oxidation with minimum heat transfer which improves thermal efficiency. However, particularly at high loads, hydrogen operated engines prone to pre-ignition firing as the ignition energy is significantly lower than

that of conventional fuels. Hydroxy gas has the ability to burn particularly at lean equivalence ratios. Efficiency may improve due to small quenching gap which allows fuel to burn completely. The main drawback of hydrogen use as a fuel is volume of hydrogen which contains less energy irrespective of higher heating value than hydrocarbon fuel due to its lesser density [1–3].

2 Hydrogen Combustion Characteristics

Hydrogen or hydroxy gas combustion is mostly unlike than that of combustion of hydrocarbon fuel. Hydrogen has large flammability range of 4–75% by volume in air compared to that of diesel of 0.7–5%. The least ignition energy (i.e., 0.02 mJ) enables hydrogen engine to run on lean A-H-F mixtures confirming timely ignition. But, the hot spots present in the cylinder create the issues such as backfiring and premature ignition which can be extinguished by avoiding hot spots in the intake manifold and combustion chamber which acts as an ignition source for combustion and by exhaust gas recirculation or water injection techniques. The lighter density of hydrogen (i.e., 0.0837 kg/m³) compared to air enables it to disperse into the atmosphere fastly. The hydrogen diffusivity is 0.63 cm²/s. Hydrogen contains the highest energy-to-weight ratio among all fuels. The highest flame velocity of hydrogen (i.e., 270 cm/s) results in a rapid rise in cylinder pressure. The higher autoignition temperature of hydrogen (i.e., 585 °C) permits it to be used in IC engine at larger compression ratio [3]. The hydrogen can be used in dual fuel mode in diesel engine. It has been observed that the small horsepower diesel engines converted on hydrogen diesel operation are working efficiently. Addition of hydroxy gas into diesel engine can reduce harmful emissions, but increase in NO_x could not be prevented because of high temperature induced during combustion within the combustion chamber. The oxygen combines with the nitrogen in the air forming oxides of nitrogen at this high temperature [4].

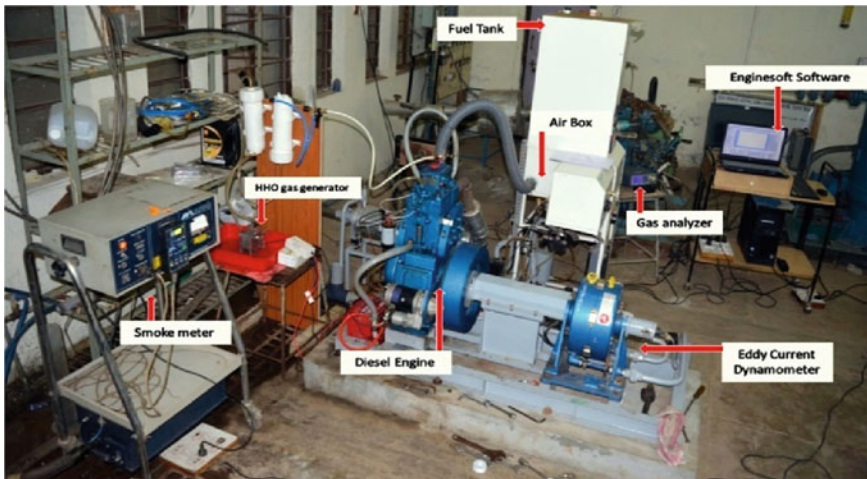
Table 1 gives comparison of combustion characteristics of diesel, petrol and hydrogen.

3 Experimental Procedure

The diesel engine setup enriched with hydroxy gas which is generated through dry cell hydroxy (HHO) gas generator used for the experimentation of presented work is shown in Fig. 1. The experimental investigation was carried out by varying compression ratio on VCR research engine at invariable hydroxy gas flow rate. Table 2 shows the engine specifications of diesel engine used for the study which is connected to eddy current dynamometer for varying the load and measured data is stored in computer. The AVL DiGas444 emission gas analyzer is used to measure emissions and AVL 437 diesel smoke meter is used to measure smoke opacity, respectively.

Table 1 Comparison in combustion characteristics of diesel, petrol and hydrogen [3–6]

Properties	Diesel	Petrol	Hydrogen
Autoignition temperature (°C)	257	260–460	585
Least ignition energy (mJ)	–	0.24	0.02
Flammability range (vol% in air)	0.7–5	1.4–7.6	4–75
Stoichiometric air–fuel ratio	14.5	14.6	34.3
Limits of flammability (equivalence ratio)	–	0.7–3.8	0.1–7.1
Density at 16 °C and 1.01 bar (kg/m ³)	833–881	721–785	0.0838
Calorific value (J/kg)	42,500	43,900	119,930
Flame velocity (cm/s)	30	37–43	265–325
Quenching gap in NTP air (cm)	–	0.2	0.064
Diffusivity in air (cm ² /s)	–	0.08	0.63
Research octane number	30	92–98	130

**Fig. 1** Experimental setup used with hydroxy gas generation

Firstly, the benchmarking for diesel was done. Here, we considered the compression ratio 16, 17 and 18 for experimentation work. The engine is started by setting to compression ratio 16. The base readings were taken for compression ratio 16 at constant speed of 1500 rpm for different loading conditions ranging from 4 kg, 8 kg and 12 kg. Then, measurements were taken for different loading conditions considered at constant speed of 1500 rpm by enriching the intake air with hydroxy (HHO) gas at constant flow rate of 1 lpm through intake manifold, and the same approach was adopted for compression ratio of 17 and 18. The measured performance data is recorded in computer using engine soft engine software, and emissions and smoke were recorded.

Table 2. Diesel engine specification used for experimentation

Engine specifications	
Engine model	TV1
Make	Kirloskar diesel engine
Brake power (kW)	3.5
Maximum speed (rpm)	1500
Bore (cm)/stroke (cm)	11/8.75
Connecting rod length (cm)	23.4
Compression ratio (VCR)	12–18
Stroke	4
Number of cylinder	Single
Swept volume (L)	0.6615

4 Result and Discussion

The baseline diesel operation is compared for different compression ratios with hydroxy (HHO) gas addition for combustion, performance and emission characteristics.

4.1 Combustion

The cylinder pressure variation with respect to crank angle for considered different compression ratio is shown in Fig. 2. The baseline diesel operation results are compared with hydroxy gas enrichment at various compression ratios. The high rate

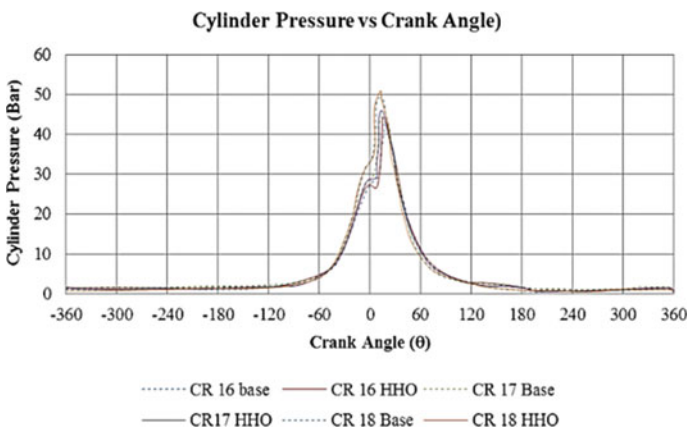


Fig. 2 Variation of cylinder pressure with crank angle for various compression ratios

of pressure rise results in attaining peak pressure close to TDC. The peak pressure at full load condition increased by 1.47 bar from 42.83 to 44.25 bar for compression ratio 16, by 1.65 bar from 44.31 to 45.96 bar for compression ratio 17 and by 1.76 bar from 49.19 to 50.90 bar for compression ratio 18 after enrichment with hydroxy gas. The advancement in peak pressures while inducting hydroxy gas is due to instantaneous combustion of diesel along with hydroxy gas. For CR 16, the peak pressure 1.416 bar is achieved at 15° after TDC when enriched with hydroxy gas. For CR 17, the peak pressure 1.647 bar is achieved at 13° after TDC. For CR 18, the peak pressure 1.715 bar at 12° after TDC can be seen when enriched with hydroxy gas.

4.2 Performance

4.2.1 Brake Thermal Efficiency

The brake thermal efficiency for baseline diesel and after enrichment of hydroxy (HHO) gas was compared for various CR of 16, 17 and 18 as shown in Fig. 3. The brake thermal efficiency of diesel engine after enrichment with hydroxy (HHO) gas at all various compression ratios was found higher compared to diesel operation due to increased calorific value of A-H-F mixture, and homogeneous mixing of hydroxy (HHO) gas with air results in complete combustion of fuels. Hydroxy gas instantly starts to break the heavier hydrocarbon molecule of diesel fuel initiating the chain reaction and also results in efficient combustion and higher brake thermal efficiency than baseline diesel operation.

For compression ratio 16, there is 7.36% increase in thermal efficiency from 28.68 to 30.96%, whereas, for compression ratio 17, an increase of 7.68% in thermal

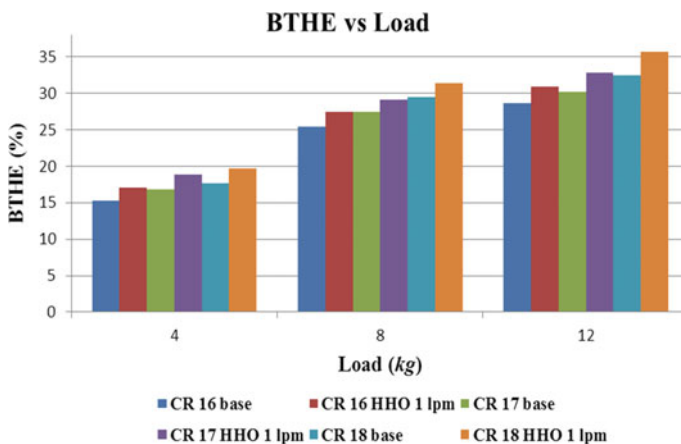


Fig. 3 Variation of brake thermal efficiency for various compression ratios

efficiency from 30.26 to 32.78% is observed. The thermal efficiency for compression ratio 18, an increase from 32.44 to 35.75%, increases by 9.25% compared to baseline diesel operation is observed. The brake thermal efficiency is higher at compression ratio 18 at full load condition after enrichment with hydroxy (HHO) gas.

4.2.2 Specific Fuel Consumption

The variation in the specific fuel consumption for baseline diesel operation and hydroxy gas enrichment for compression ratios 16, 17 and 18 is as shown in Fig. 4. The maximum specific fuel consumption is observed at 4 kg load for all compression ratios, and then, it reduces subsequently toward full load operation. The reduction in specific fuel consumption has been seen after enrichment for each compression ratio.

The homogeneous mixing of hydroxy (HHO) gas along with air reduces SFC which results in complete burning of overall mixture inside the combustion chamber. The wider flammability range and higher flame speed of hydroxy gas help the mixture to be burned completely at faster rate at constant speed conditions. Lower ignition energy of hydrogen in mixture assists diesel fuel to be burned under lean-burn condition also. The specific fuel consumption is reduced for all compression ratios 16, 17 and 18 by 10%, 10.71% and 15%, respectively, a maximum of 15% reduction in specific fuel consumption can be seen at compression ratio 18. Higher compression ratio needs to be preferred to reduce the specific fuel consumption because hydrogen can be compressed at higher compression ratio. At load 4 kg, the reduction in specific fuel consumption is 10.71%, 9.8% and 8.1% for all compression ratios of 16, 17 and 18, respectively.

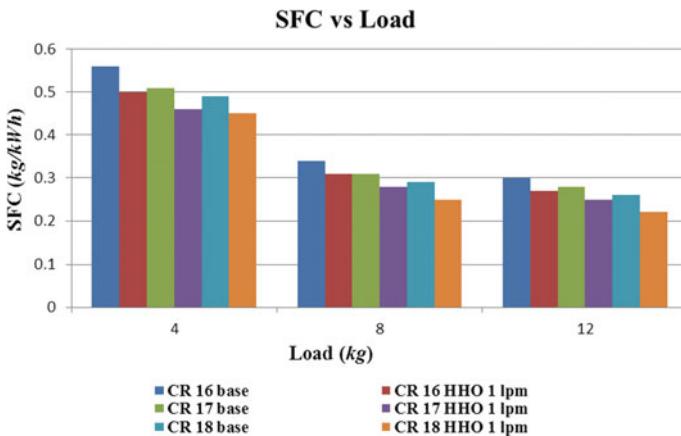


Fig. 4 Variation of specific fuel consumption for various compression ratios

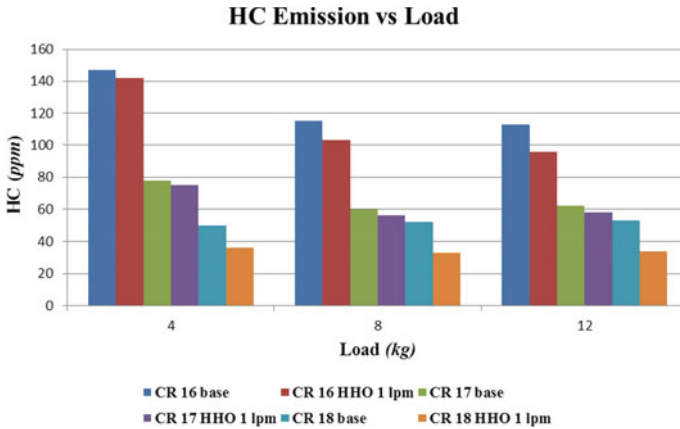


Fig. 5 Variation of hydrocarbon emission for various compression ratios

4.3 Emissions

4.3.1 Hydrocarbon Emission

Figure 5 shows the variation in HC with and without hydroxy gas enrichment which is compared with diesel baseline operation for all considered compression ratios. As hydrogen is carbon-free fuel, hydroxy gas burning with diesel results in reduction in hydrocarbons, and due to high temperature in the cylinder, the carbon particles in main fuel and in lubricating oil will oxidize and convert into carbon dioxide.

The HC emission reduction is observed as the compression ratio increases for both with and without enrichment of HHO. The shorter quenching gap and wider flammability limits of hydrogen produces less hydrocarbon emissions. For compression ratio 18, due to better combustion with hydrogen, the hydrocarbon emission is reduced by 33%, whereas the average percentage of HC emission reduction of 6% and 8% for compression ratio of 16 and 17 is observed. This is due to low compression ratio yielding in rise of HC emission. The hydrocarbons were reduced from 53 to 34 ppm at full load for 18 compression ratio with 37% maximum reduction as compared to neat diesel operation.

4.3.2 Carbon Monoxide Emission

Figure 6 shows that carbon monoxide varies with and without hydroxy gas enrichment at different compression ratios. It has been seen that CO was reduced with addition hydroxy gas for all considered compression ratios. With the increase in compression ratio, the CO emission decreases for both baseline and hydroxy enriched combustion. The absence of carbon in fuel is the main reason for reduction in CO emission. An average of 10%, 12% and 23% reduction in CO emission can be observed when

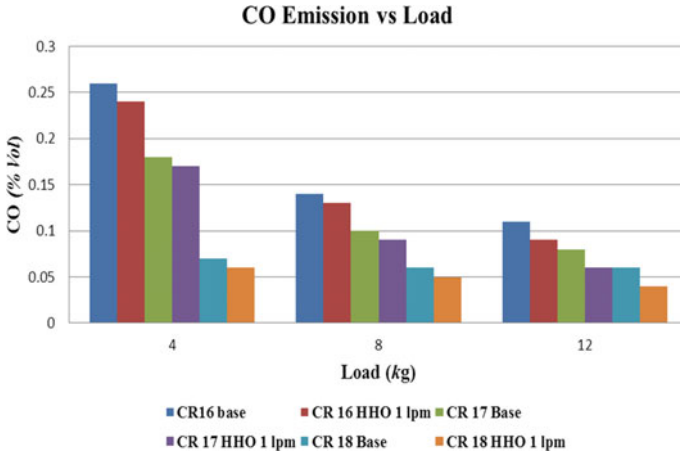


Fig. 6 Variation of CO emission for various compression ratios

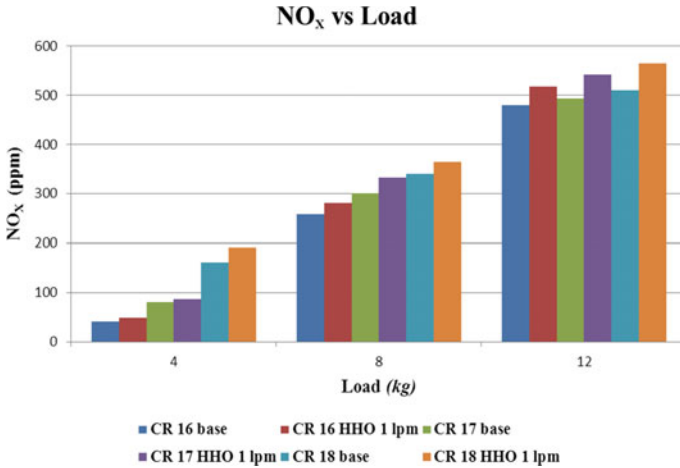


Fig. 7 Variation of NOx for various compression ratios

enriched with hydroxy gas, for all considered compression ratio. It has been seen that for 18 compression ratio, the CO emission is decreased more compared to compression ratio 16 and 17. For 18 compression ratio, CO emission reduced from 0.06% to 0.04% by volume, with 33% highest reduction at full load condition.

4.3.3 Oxides of Nitrogen Emission

Figure 7 shows that the nitrogen oxide varies with respect to the load on engine with and without enrichment for all considered compression ratio. The reasons for formation of nitrogen oxides are the peak combustion temperature, the oxygen concentration and the residual time of higher temperature gas inside the cylinder. The higher calorific value of hydroxy gas causes rapid rise in temperature in combustion chamber because combustion leads to increase in NO emission. It has been found that NO increases with hydroxy gas enrichment for all considered compression ratio. It is observed that NO increases from 510 to 565 ppm, from 493 to 542 ppm and from 480 to 518 ppm and for CR 18, 17 and 16, respectively at fully loading condition.

4.3.4 Smoke Emission

The smoke by the test engine when operated with pure diesel fuel and hydroxy (HHO) gas enriched at 1 lpm at various load ranges of the engine for all considered compression ratios is compared as shown in Fig. 8.

When hydroxy (HHO) gas is enriched, the smoke reduces substantially. The main reason for formation of smoke is incomplete combustion of the air–fuel mixture. The hydroxy (HHO) gas enrichment helps in complete combustion of air–fuel mixture in combustion chamber resulting in lesser smoke. When hydroxy gas at 1 lpm is introduced during full load operation, the smoke opacity reduced to 8% as that of 10% for neat diesel operation for 18 compression ratio. Also, the smoke opacity is decreased from 4.1 to 3.8% and from 7 to 5% and for compression ratio 16 and 17, respectively.

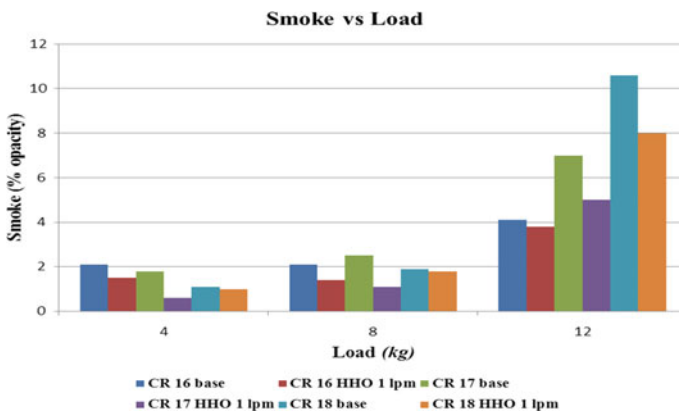


Fig. 8 Variation of smoke for various compression ratios

5 Conclusion

The improvement in performance and reduction in emissions was observed with the enrichment of hydroxy gas at higher compression ratio except the exhaust gas temperature and ultimately NO_x . The result from the experiment shows that hydroxy gas enrichment worked best at compression ratio 18.

From the experiments we conclude the following

- The maximum peak pressure observed for compression ratio 18. The peak pressure rise of 1.715 bar from 49.188 bar to 50.903 bar is observed for compression ratio 18 when enriched with hydroxy gas at full load condition.
- The higher thermal efficiency is obtained for CR 18, an increase of 9.25% compared to baseline diesel operation of engine.
- The marginal decrease in specific fuel consumption was observed which was reduced by 15% for compression ratio 18 at fully loaded condition.
- The increase in exhaust gas temperature is seen at all three compression ratios with enrichment of hydroxyl gas.
- The better combustion due to hydroxy gas enrichment at higher compression ratio leads to reduction in HC by 33%.
- The CO was decreased marginally with an average of 23% at all compression ratios.
- The increase in NO could not be prevented with hydroxy gas enrichment for all compression ratios, and for compression ratio 18, the NO found to be increased from 510 to 565 ppm.
- The smoke opacity obtained was found to be less, i.e., 8% as that of 10%, for neat diesel operation for compression ratio 18 and reduces with decrease in compression ratio.

The NO emissions were found to be increased with increasing compression ratios; the exhaust gas recirculation technique can be implemented to decrease NO emission. The CO_2 emission may increase at higher flow rate of hydrogen due to complete conversion of CO in CO_2 . After-treatment devices should be used to reduce CO_2 emission. The enrichment of hydroxy gas for various flow rates can be further studied to improve the performance and reduction the emission from diesel engine.

References

1. Verhelst S, Wallner T (2009) Hydrogen-fueled internal combustion engines. In: Progress in energy and combustion science, vol 35, 490–527
2. Sun Z, Liu F-S (2012) Research and development of hydrogen fuelled engines in China. Int J Hydrogen Energy 37:664–681
3. Ciniviz M, Köse H (2012) Hydrogen use in internal combustion engine: a review. Int J Autom Eng Technol 1(1):1–15
4. White CM, Steeper RR, Lutz AE (2006) The hydrogen-fueled internal combustion engine: a technical review. Int J Hydrogen Energy 31:1292–1305

5. Saravanan N, Nagarajan G, Dhanasekaran C, Kalaiselvan KM (2007) Experimental investigation of hydrogen port fuel injection in DI diesel engine. *Int J Hydrogen Energy* 32, 4071–4080
6. Yilmaz AC, Uludamar E (2010) Effect of hydroxy (HHO) gas addition on performance and exhaust emissions in compression ignition engines. *Int J Hydrogen Energy* 30, 1–7

Biomethanation of Aloe Vera Waste for Energy Production



Diksha Srivastava, Deepak Sharma, and Nafisa Ali

Abstract The study deals with the use of waste produced by *Aloe vera* processing plants as alternate feed in biogas plant. The waste consists of *Aloe vera* leaf peel, tentacles, gel froth, etc., which is non-edible by ruminants and on composting produces foul smell, creating environmental pollution. An *Aloe vera* waste-based 2 cum modified KVIC biogas plant, having a mechanical hand-driven mixing unit to solve the problem of chocking of biogas plant, has been developed and installed at user's site. The study reveals that the average monthly gas production from *Aloe vera* was 238.58 L/kg dm, and the average methane and carbon dioxide percentage were 57.67 and 36.82%. Therefore, *Aloe vera* waste can be used as adduct and substrate for increased biogas production as compared to cattle dung.

Keywords *Aloe vera* waste · Biomethanation · Modified KVIC biogas plant · Renewable energy

1 Introduction

The renewable energy sources are being considered as an alternative to solve energy needs and reduce environmental problems. Compared with other renewable energy, biomass from different production processes is an interesting alternative. Biogas technology seems promising to attain sustainable energy yields without damaging the environment only when it is produced through anaerobic digestion (AD) and recovered properly. The term “anaerobic” suggests that the process occurs in the absence of free oxygen and produces CH₄ through decomposition of waste in nature and reduces environmental pollution.

Various forms of agro-wastes, industrial waste and their by-products and animal dung are providing safe and convenient sources of energy in the form of biogas and liquid fuel. These wastes create much nuisance in the environment if disposed without processing. *Aloe vera* (*Aloe barbadensis* Miller) is a perennial evergreen

D. Srivastava (✉) · D. Sharma · N. Ali
Department of Renewable Energy Engineering, Udaipur, India
e-mail: dkshme@gmail.com



Fig. 1 Waste generated by *Aloe vera* processing plant

plant with fleshy leaves. The botanical genus of *Aloe vera* has always been classified in the family called *Liliaceae* [1]. Economically, *Aloe vera* had found importance by being an important ingredient in many of the medicinal, cosmetic and food products [2–4]. Among all the product-type segments, *Aloe vera* whole leaf extracts will continue to grow at a relative higher rate, representing 41% volume share of the market in 2016 [5]. The major areas under *Aloe vera* cultivation in India are Alwar in Rajasthan, Satnapalli in Andhra Pradesh and Rajpipla in Gujarat. It is also cultivated in the dry areas of states of Maharashtra and Tamil Nadu [6].

Present study deals with the problem of waste disposal produced by the *Aloe vera* processing plant. The waste generated consists of leaf peel, tentacles, froth of gel, etc. (Fig. 1). The produced *Aloe vera* processing waste cannot be used as cattle feed; whereas, on composting it produces foul smell leading to environmental pollution and problem for the nearby residents. Although, previously, research has been done for alcohol production which has also been reported, but using it as biofuel for energy purposes is not techno-economically feasible process [7].

Therefore, the best strategy is to manage and utilize such waste to use them as “biomass” resources rather than disposing of as “waste” for serving not only energy and economic benefits but also environmental benefits. The produced biogas provides energy for heating, cooking and lighting; whereas, the digested slurry can be directly used as manure for agriculture. Therefore, biomethanation of such waste is a better solution for their disposal.

2 Experimental

Aloe vera used for the study was collected from College of Technology and Engineering campus. The leaves were peeled to remove the gel, leaving the waste. Biochemical analysis of *Aloe vera* waste was done using standard methods of APHA and compared to that of fresh cattle dung to check its feasibility to be used as feed for biogas plant. The results are shown in Table 1.

Table 1 Biochemical analysis of *Aloe vera* and cattle dung (fresh)

Substrates	TS%	MC%	VS%	C %	N %	P%	K%	pH
<i>Aloe vera</i>	3.91	96.09	81.00	46.98	6.5	0.29	0.68	6.1
Cattle Dung	18.84	81.16	82.67	47.55	1.93	0.63	0.17	7.2

TS total solids; MC moisture content; VS volatile solids; C carbon; N Nitrogen, P phosphorus, K potassium

Table 2 Treatments with different ratio of *Aloe vera* and cattle dung

Treatment	Alv. (g)	CD (g)	Ratio	BSS (ml)	Water (ml)	Gas in L kg ⁻¹ dm ⁻¹
T ₁	400	–	100:0	60	500	214.82
T ₂	200	200	50:50	60	500	220.23
T ₃	100	300	25:75	60	500	258.23
T ₄	300	100	75:25	60	500	240.44
T ₅	–	400	100:0	60	500	225.32

Alv. *Aloe vera*, CD cattle dung, BSS biogas spent slurry

Laboratory study was done using batch-type digester, and the gas was collected using water displacement method. Total five sets with three replications were prepared having different ratio of cattle dung and Aloe vera waste. Table 2 shows the treatments with different ratio of *Aloe vera* and cattle dung along with the gas produced by each of them. The results are the calculated average of the three replications taken of each treatment. Maximum gas production was observed in the set having cattle dung to Aloe vera ratio 1:3, i.e., 258.23 L/Kg dm.

Field study was carried out on an *Aloe vera* waste-based modified KVIC biogas plant of 2 cum capacity, which has been developed and installed successfully at user's site, Sh. Heera Lal Meena, Gram: Padla, Panchayat Samiti: Devpura, Distt.: Udaipur (Rajasthan) in Padla village. Following parameters were considered in designing of biogas plant:

W = Weight of waste/substrate fed per day (kg/day).

G = Gas production rate (m³/day).

V_s = Active slurry volume in the digester (m³).

V_d = Dome volume (m³).

H = Height of cylindrical portion of the digester up to the top edge of the outlet opening (m).

D = Diameter of the digester (m).

d_h = Height of the dome (m).

r = Radius of the dome (m).

A suitable size of inlet and outlet was provided at the opposite ends of digester for feeding and removing the slurry. Figure 2 shows the developed dome/gas holder of modified KVIC biogas plant based on *Aloe vera* waste. A mechanical hand-driven mixing unit was developed and kept outside the plant perpendicular to the flow of feed material for ease in rotation. Single worker rotated the handle, at speed of 4 rpm

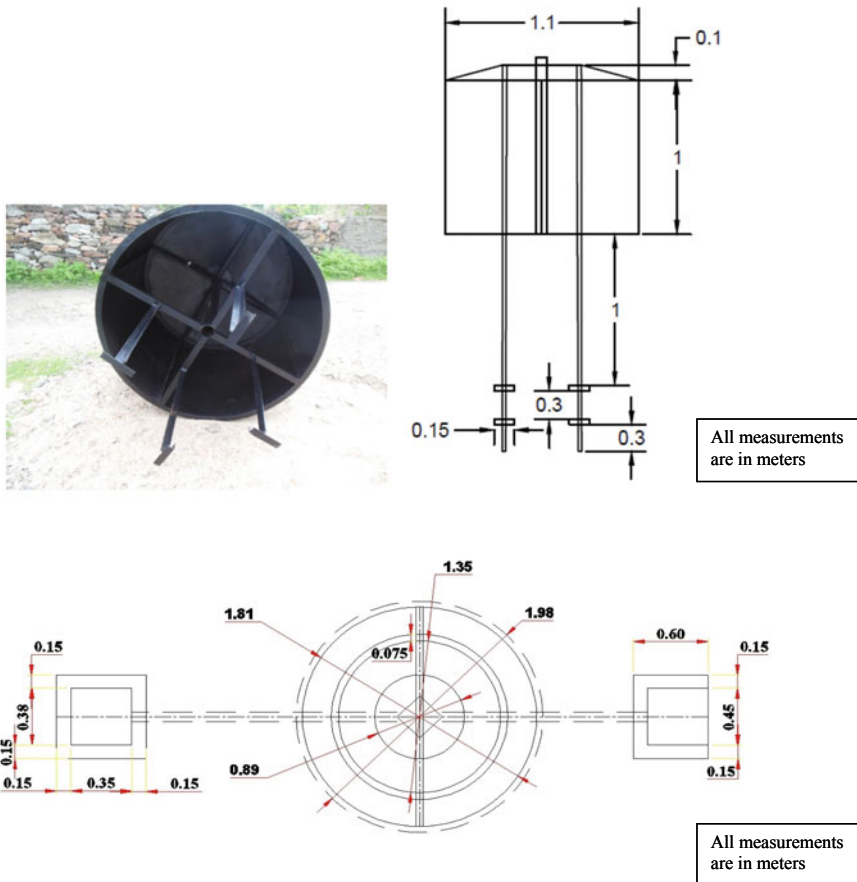


Fig. 2 Dome/gas holder of modified biogas plant

for 5–10 min, during the feeding time intermediately to ensure agitation of biogas slurry in the plant. The top view of modified biogas plant has been shown in Fig. 3. Figure 4 shows the modified KVIC biogas plant installed at user’s site.

Initially, the plant was charged with 100% cattle dung mixed and water in 1:1 ratio. After stabilization of the plant, cattle dung was replaced by 10 kg of *Aloe vera* waste in 15 days interval. Thus, gradually 100% cattle dung was replaced with *Aloe vera* waste. The *Aloe vera* waste was predigested by soaking in water for 2 days along with 20% biogas spent slurry before feeding it to the plant and later mixed in the mixing tank with remaining amount of water to make 1:3 ratio.

After complete replacement by *Aloe vera* wastes, daily biogas production was noted using wet biogas flow meter in liters (least count = 0.05 L). The results have been reported as biogas yield in liters per kg of dry matter (L/kg dm). Methane and carbon dioxide contents in produced biogas were also measured monthly by using a GASBOARD-3200P portable biogas analyzer.



Fig. 3 Top view of modified biogas plant



Fig. 4 Modified KVIC biogas plant for *Aloe vera* waste installed at beneficiary site

3 Result and Discussion

Biochemical analysis of *Aloe vera* waste showed that it has all the essential properties in accepted range for biogas generation such as volatile solids, carbon, nitrogen, potassium and phosphorus (Table 1). From the laboratory study, it was inferred that maximum biogas production was obtained from the set having *Aloe vera* to cattle dung ratio 1:3, i.e., 258.23 L/kg of dry matter.

In the field study, a simple mixing unit was developed for the KVIC biogas plant to solve the problems of choking experienced when using lignocellulosic material as its feedstock in conventional biogas plants. Previous research work showed that silting of substrate was a major constraint in the long duration application of lignocellulosic

material-based biogas plant. To overcome this problem and also to provide facilities such as easy evacuation of slurry from the plant, a mechanical stirring may be helpful. The view of the commissioned biogas plant is given in Fig. 4.

After complete replacement of cattle dung by *Aloe vera* waste, recording of observations was started. Observations of biogas generation were taken daily. The maximum biogas production from *Aloe vera* waste was recorded 296.79 L/Kg dm. Minimum biogas production was 158.84 L/Kg dm. Average monthly gas production from *Aloe vera* was 238.58 L/Kg dm. It was observed that the average methane and carbon dioxide percentage were 57.67 and 36.82% (Table 3). Monthly biochemical analysis of undigested and digested slurry of the biogas plant showed increase in nitrogen and phosphorus percentage in the digested *Aloe vera* slurry as compared to that of undigested slurry, as shown in Table 4.

The total cost of installing the biogas plant based on *Aloe vera* waste was Rs. 40,100/-. The modified KVIC biogas plant based on *Aloe vera* waste is successfully working at the user's site. The generated biogas is supplied to the kitchen of the beneficiary, and the gas is being used for cooking purpose as shown in Fig. 5.

4 Conclusions

Production of biofuel from plant materials is a major step toward providing energy security to the world. Process of converting waste biomass into biogas fuel promises a cheaper way to go green. Based on the biochemical analysis, it was suggested that *Aloe vera* waste can be used for biomethanation process. It is being found that alternative feedstock generates biogas much faster than conventional feed of cattle dung (Medors, 2007). It can be concluded from the study that it is a unique and novel approach, wherein *Aloe vera* waste is used for biogas production. Biogas is an efficient renewable fuel thereby allowing its safe disposal, and its effluent slurry provides good organic manure with have rich manurial properties. The laboratory study reveals that 1:3 ratio of *Aloe vera* to cattle dung (T3 treatment) gives best results. In field, a modified KVIC biogas plant was designed to solve the problems of choking experienced while using lignocellulosic material such as *Aloe vera*. The plant was installed at user's site at Udaipur District of Rajasthan and is running successfully.

Table 3 Monthly biogas production from *Aloe vera* waste

Month	March	April	May	June	July	August	September	October	November	Average
Biogas produced (L/kg dm)	158.84	240.08	250.64	293.93	296.79	279.07	270.55	180.23	177.14	238.58
CH ₄ %	58	58	57	59	60	56	57	56	58	57.67
CO ₂ %	37	37	37	35	35	39	38	38	37	36.82

Table 4 Biochemical analysis of fresh and digested slurry

No	Month	Undigested slurry						Digested Slurry					
		TS%	N %	VS%	P %	K%	pH	TS%	N %	VS%	P %	K%	pH
1	March	9.95	4.60	78.5	2.50	0.76	6.6	7.58	5.40	66.6	3.03	1.01	7.2
2	April	10.03	4.80	79.0	2.34	0.70	6.7	7.00	6.30	55	3.58	1.80	7.2
3	May	10.12	4.75	78.5	2.60	0.71	6.5	6.82	7.89	55.4	3.68	1.09	7.4
4	June	8.62	4.36	78	2.73	0.80	6.6	6.45	7.90	56.0	3.89	1.50	7.4
5	July	9.87	3.81	79.5	2.24	0.64	6.6	7.07	6.58	57.5	2.87	1.05	7.3
6	August	9.85	4.06	80.4	1.95	0.73	6.7	7.43	7.28	58.0	2.35	1.02	7.4
7	September	10.40	3.90	81.0	2.60	0.65	6.5	7.58	7.80	58.6	2.25	1.02	7.3
8	October	8.35	0.56	81	0.50	0.48	6.5	7.32	1.30	65.2	1.03	1.00	7.2
9	November	9.02	0.80	80	0.48	0.50	6.6	7.48	1.25	65	1.02	1.01	7.3
Average		9.65	3.51	82.1	2.06	0.66	6.6	7.22	5.56	61.15	2.90	1.24	7.31



Fig. 5 Biogas being used for cooking at user's site

Acknowledgements We are highly thankful to the Coordinator, Indian Council of Agricultural Research (ICAR), for providing financial assistance and Head, Department of Renewable Energy Engineering, College of Technology and Engineering, Udaipur, for providing all sorts of required facilities for the study.

References

1. Anonymous (2006) Database on important medicinal and aromatic plants. Government of India, Ministry of Commerce, Directorate General of Foreign Trade
2. Bhargava S (2006) An analysis of medicinal and cosmetic properties of *Aloe vera* and its biotechnology. National seminar on Biodiversity, conservation, cultivation, processing and marketing of medicinal and aromatic plants, pp 113–114
3. Briggs C (1995) Herbal medicine: Aloe. Canadian. Pharm J 128:48–50
4. Chandegara VK, Varshney AK (2007) Effect of temperature on gel extraction from *Aloe vera* leaves. In: 41st ISAE annual convention and symposium, 29–31 Jan 2007, CAET, JAU, Junagadh, India, 3.71
5. <https://www.iasc.org/>
6. http://agritech.tnau.ac.in/horticulture/horti_medical%20crops_aloe.html
7. Nagaraju M, Ramulla S, Murthy NYS (2010) Production of biogas and alcohol from *Aloe barbadensis* Miller. Asian J Chem 23(4):1863–1864
8. ICAR, Tribals earn respectable income from *Aloe vera* processing unit. www.icar.org.in/en/node/1206

Heat Transfer and Pressure Drop Assessment of a Vortex Generator Supported Fin-And-Tube Heat Exchanger



Shailesh Kumar Sarangi, Nikhil Anand, Kushagra Srivastava, Pankaj Chamoli, Dipti Prasad Mishra, and Lakhbir Singh Brar

Abstract This paper aims at enhancing the thermo-fluid performance of a plain fin-and-tube heat exchanger. Influence of the height of rectangular type vortex generator on the heat exchanger performance has been analysed. In dimensionless form, the heat transfer is expressed as Colburn factor (j) and pressure drop in terms of the friction factor (f). The arrangement of all the vortex generators follows a “common-flow-up” configuration which tends to counter-rotate the vortices in the wake region of the tubes, thereby, enhancing the thermal mixing to improve the heat transfer. Another parameter, called quality factor (a ratio of j and f), is also evaluated to compare the results between different heights of the winglets. It has been observed that the j factor is the highest for the height 2.8 mm and f factor is the lowest for the height 0.7 mm, whereas the quality factor suggests the height of 0.7 and 1.4 mm to be the appropriate ones.

Keywords Vortex generators · Fin-and-tube heat exchanger · Heat transfer enhancement · Rectangular winglet

1 Introduction

Compact plain fin-and-tube heat exchangers find numerous applications such as in domestic and commercial cooling systems, petrochemical industries and for cooling of several electronic equipment. However, the heat transfer surface area is reduced in the compact heat exchangers compared to the conventional heat exchangers. Also, the low heat transfer coefficient (h) of air makes the air side thermal resistance substantially high. Therefore, to make these devices more efficient, the air side thermal resistance needs to be lowered. An effective way of increasing heat transfer coefficient is to place the winglets in the channel (guiding the flow)—this diverts the flow towards the wake region behind the tubes, thereby minimizing the tube wake region and increases the effective surface contact of the fluid. Several orientations

S. K. Sarangi · N. Anand · K. Srivastava · P. Chamoli · D. P. Mishra · L. S. Brar (✉)
Mechanical Engineering Department, Birla Institute of Technology, Mesra, Ranchi 835215,
Jharkhand, India
e-mail: brarlsb@gmail.com

© Springer Nature Singapore Pte Ltd. 2021

P. Pant et al. (eds.), *Advances in Mechanical Processing and Design*, Lecture Notes in Mechanical Engineering, https://doi.org/10.1007/978-981-15-7779-6_13

149

and types of winglets have been studied to improve the performance parameters of heat exchangers, viz. the pressure drop and heat transfer coefficient.

The concept of increasing heat transfer performance using VGs is not new, and many researchers have investigated the potential of different VG shape and location. Edward and Alker [1], after investigating the effect of steam wise vortices on heat exchanger performance, reported that delta winglets performed superior to cubes placed on a flat plate. Generally, two types of VG configurations are used, i.e. “common-flow-up” and “common-flow-down”. Earlier literature [2–4] reveals that in “common-flow-down” configuration, pair of VGs is placed downstream to the tube to introduce turbulence in the flow for greater thermal mixing. For “common-flow-up” configuration [5–7], the placements of VGs are slightly upstream of the tube forming a narrow passage and accelerating the fluid near the tube. This leads to delay in separation and minimization of the wake. Previous literature reports that common-flow-down configuration is more efficient with in-line tube geometry than with staggered-tube geometry under identical conditions [8]. VGs enhance the heat transfer, but on the other hand, it also increases pressure drop—this means that more pumping power is required with VGs. Russell et al. [9] compared the in-line rectangular and delta winglets with staggered arrangements and concluded that the effectiveness of rectangular winglets improves in staggered arrangement with two rows. Delta and rectangular wing and winglets were examined experimentally by Fiebig et al. [10] from heat transfer viewpoint and they found the delta winglet to be more effective. Torii et al. [11] examined the in-line and staggered arrangement of tubes at $Re = 350\text{--}2200$ and reported the maximum enhancement of 40% in heat transfer, whereas the associated penalty of pressure drop was about 50% in case of staggered arrangement. Joardar and Jacobi [12] employed delta winglets in “common-flow-up” configuration with Re ranging from 220–960 and reported that the air side performance of heat transfer improved by 44% and 69%, respectively, for single and three-row VG pairs. Few researchers [13, 14] also used the concept of punched triangular and rectangular vortex generators to enhance the heat transfer performance. Agarwal and Sharma [15] used rectangular winglets at different roll angle and reported the optimized roll angle of 15° that increased the heat transfer by 17.5%. Sarangi and Mishra [16] worked on the location of rectangular winglet pairs and presented optimum stream and span wise locations. On increasing the winglet number and attack angle, they reported an increase in the heat transfer as well as pressure drop. In their recent work [17], they also investigated the effect of locations of plain and wavy rectangular winglets for improved thermo-fluid performance.

In view of the above, it becomes apparent that no study, based on the effect of height of winglets (corresponding to the channel height), on heat transfer and pressure drop has been performed. Thus, the objective of the present work is to investigate the impact of winglet height on the thermo-fluid performance of the heat exchanger.

2 Mathematical Formulation

A model of plain fin-and-tube type heat exchanger is numerically investigated in this paper. Figure 1 shows the schematic diagram of the flow domain. The assembly of heat exchanger is such that the tubes are expanded within the collars. Since the tubes and collars have very high thermal conductivity, the temperature is maintained constant there.

2.1 Governing Equations

The fluid is Newtonian with constant properties, and the flow is in laminar regime where Re ranges from 200–1000. The continuity, momentum, energy and conduction equations according to flow conditions are shown below.

Continuity equation:

$$\frac{\partial}{\partial x_i}(\rho u_i) = 0 \tag{1}$$

Momentum equation:

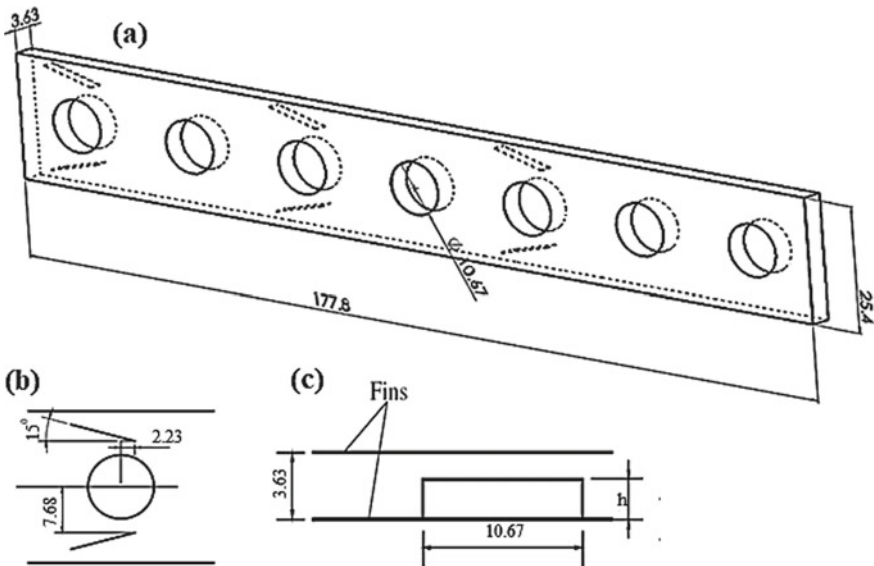


Fig. 1 Winglet orientation (a) computational domain, (b) top view, and (c) side view (dimensions shown are in mm)

$$\frac{D}{Dt}(\rho u_i) = \frac{\partial}{\partial x_i} \left(\mu \frac{\partial u_k}{\partial x_i} \right) - \frac{\partial p}{\partial x_i} \quad (2)$$

Energy equation:

$$\frac{D}{Dt}(\rho T) = \frac{\partial}{\partial x_i} \left(\frac{k_a}{C_p} \frac{\partial T}{\partial x_i} \right) \quad (3)$$

Conduction equation:

$$\frac{\partial^2 T}{\partial x_i^2} = \frac{1}{\alpha} \frac{\partial T}{\partial t} \quad (4)$$

where

$$\alpha = \frac{k_{al}}{(\rho_{al} C)} \quad (5)$$

2.2 Boundary Conditions

The boundary conditions are described as follows and also represented in Fig. 2:

- At the inlet surface of the flow domain, Dirichlet boundary condition is applied for both velocity as well as temperature:
- $U = U_{in} = \text{constant}$, $v = 0$, $w = 0$; $T_{in} = 310.6 \text{ K}$.
- On top and bottom surfaces, periodic boundary condition is applied:
- $u_{up} = u_{down}$ and $T_{up} = T_{down}$.
- On the side surfaces, we use the symmetry boundary condition:

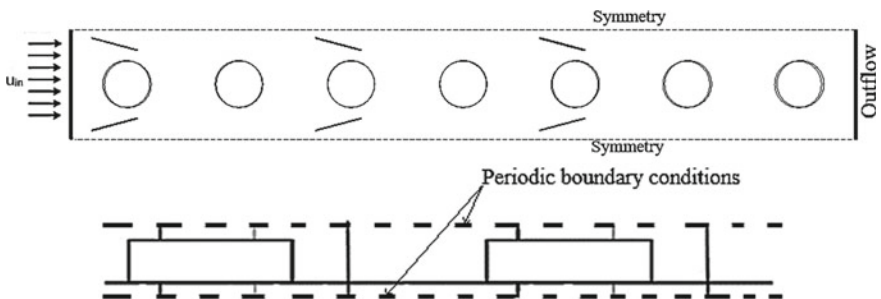


Fig. 2 Boundary conditions applied on the computational domain

$$\frac{\partial u}{\partial y} = \frac{\partial w}{\partial y} = 0, v = 0, \frac{\partial T}{\partial y} = 0$$

- At the outlet boundary, Neumann boundary condition is applied:

$$\frac{\partial u}{\partial x} = \frac{\partial v}{\partial x} = \frac{\partial w}{\partial x} = \frac{\partial T}{\partial x} = 0$$

- At the fin, tube and winglet surfaces, we use

$$T_{\text{tube}} = 291.77 \text{ K}, u = v = w = 0, \text{ (no slip) and coupled boundary condition.}$$

2.3 Numerical Method

The fluid domain was discretized using hexahedral cells (Cartesian mesh, in particular) using ANSYS workbench 16.2. Three levels of mesh were evaluated; Fig. 3 presents the (level 1) mesh over a small section of the heat exchanger consisting of 385,542 hexahedra in total. Level 2 and level 3 mesh consisted of 548,664 and 872,382 hexahedra.

CFD code Fluent is utilized to compute the governing equations with the prescribed boundary conditions. The second-order upwind scheme is applied to discretize the convective terms appearing in the governing equations. The SIMPLE algorithm is used for the pressure–velocity coupling. The convergence is attained when residuals fall below 10^{-6} for energy and 10^{-3} for momentum and continuity. For all the cases, the pseudo-transient approach was adopted for the simulations. These settings are consistent with most of the studies reported in the literature [16, 17].

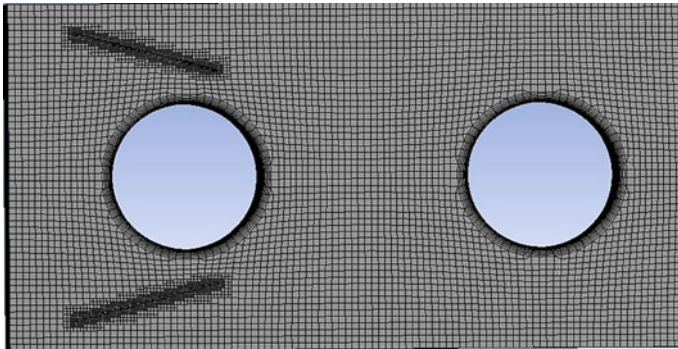


Fig. 3 Top view of the generated mesh

2.4 Parameter Definitions

The following parameters are evaluated to assess the heat exchanger's performance [14].

Total heat transfer

$$Q = \dot{m}C_p(\dot{T}_o - \dot{T}_{in}) \quad (6)$$

Here, $Q \equiv$ heat transfer, $\dot{m} \equiv$ inlet mass flow rate, $\dot{T}_o \equiv$ outlet temperature, $C_p \equiv$ specific heat capacity, and $\dot{T}_{in} \equiv$ inlet temperature.

Hydraulic diameter,

$$D_h = 4(A_{min}L)/A_T \quad (7)$$

A_T and A_{min} are the total heat transfer surface area and minimum free flow area, and L is the flow length.

$$Re = \rho U_{in} D_h / \mu \quad (8)$$

where ρ and μ are the fluid density and dynamic viscosity, respectively. U_{in} is the frontal velocity.

Colburn factor,

$$j = St \cdot Pr^{2/3} \quad (9)$$

Stanton number,

$$St = \frac{h}{\rho C_p V_m} \quad (10)$$

h is the heat transfer coefficient, and Pr is the Prandtl number.

Friction factor,

$$f = \frac{\Delta p}{\frac{\rho V_m^2}{2} \frac{A_T}{A_{min}}} \quad (11)$$

Δp is the pressure drop.

3 Validation of Model and Numerical Method

Validation is an important part in simulations as one justifies the numerical settings used and also evaluates the effect of the grid density on the results. Simulations are

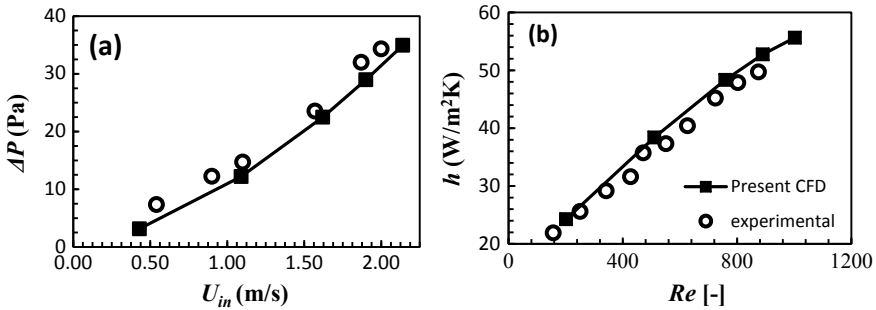


Fig. 4 Validation of (a) pressure drop and (b) heat transfer coefficient with experimental data [12] for fin-and-tube heat exchanger without winglets

performed on a model of a fin-and-tube heat exchanger having the same dimension as described in [12]. The velocity at the inlet ranges from 0.54–2.14 m/s, corresponding to Re ranging from 200–1000. The validation results are compared for the pressure drop (ΔP) and the heat transfer coefficient (h) with the experimental results [12], as shown in Fig. 4a, b, respectively (with level 1 mesh). The CFD predictions are in good agreement with the experimental results. Furthermore, level 2 and level 3 mesh were also evaluated, and the maximum deviations observed were 3.73% in ΔP and 4.13% in h values. Hence, the solution can be considered to be independent of the grid size. For all the cyclone variants, we opt for level 1 mesh to reduce computational overheads.

4 Results and Discussion

This paper attempts to study the influence of winglet height on thermo-fluid characteristics. The winglet height is varied with a step size of 0.7 mm ranging from 0.7–2.8 mm for a fixed winglet length of 10.67 mm. The results are plotted for pressure drop and heat transfer coefficient against Re . Also, an optimizing factor, called quality factor (E), is plotted against Re to summarize the overall performance.

4.1 Effect on Heat Transfer Coefficient

Figure 5 shows the variations in h values against Re for various winglet heights. The height for delta winglets without any reduction is 3.5 mm, and the height is reduced with a step size of 0.7 mm. The heat transfer coefficient is maximum for a height of 2.8 mm (i.e. 20% reduction), and it decreases by further reducing the height of

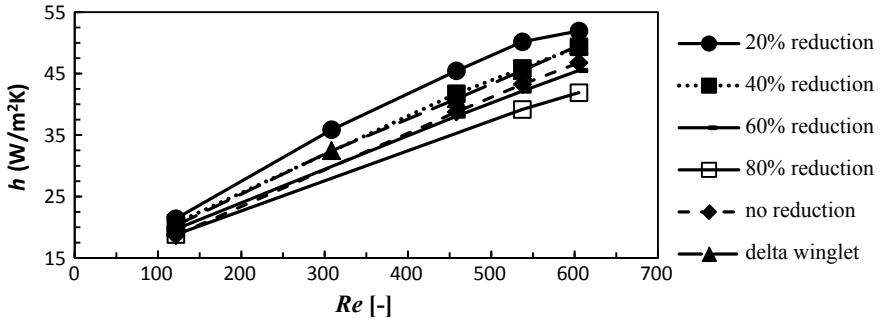


Fig. 5 Influence of Re on h for different height of winglets and comparison with baseline case

winglets. The results are also compared with the experimental results of the three-delta-winglets model, and they were very closely associated at 2.1 mm height of winglets.

Figure 6 presents the temperature distribution over the cut section, which indicates that the greater winglet height helps in providing enriched thermal mixing in the regions of poor heat transfer and thereby enhances local heat transfer coefficient downstream of tubes. With a reduction in the winglet height, a part of the incoming flow does not get diverted towards the thermally isolated region, and relatively lower heat transfer effect is obtained.

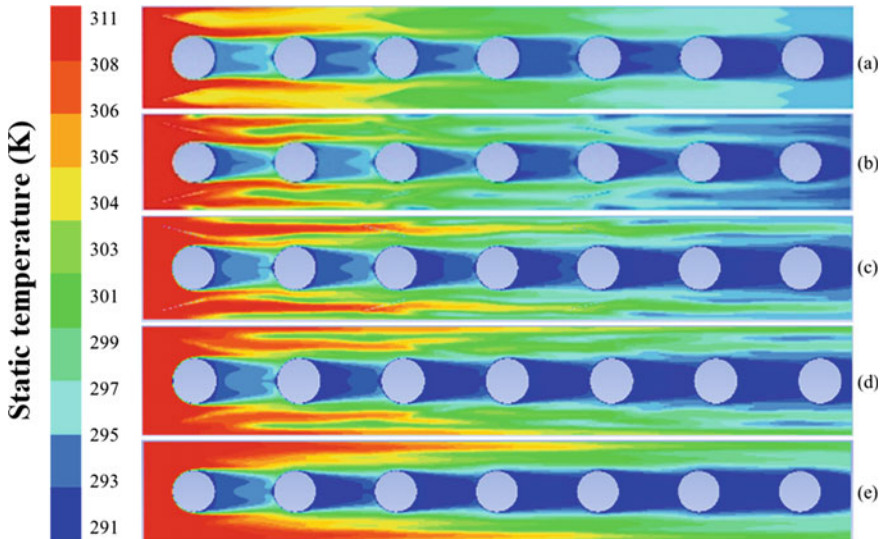


Fig. 6 Temperature contours (unit: K) for different winglet heights at $Re = 1002$. (a) 3.5 mm (No reduction), (b) 2.8 mm (20% reduction), (c) 2.1 mm (40% reduction), (d) 1.4 mm (60% reduction), (e) 0.7 mm (80% reduction)

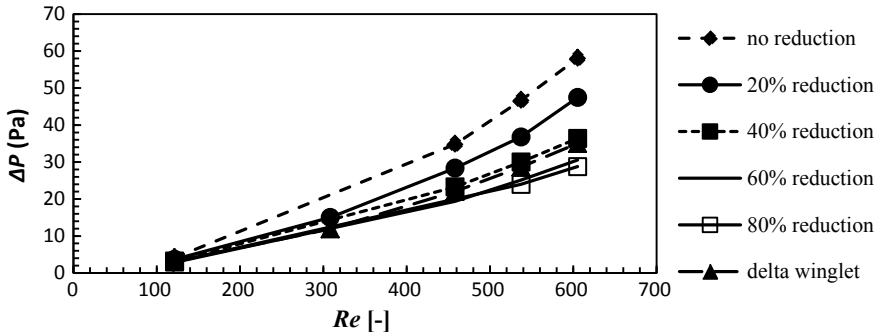


Fig. 7 Effect of Re on pressure drop for different height of winglets and comparison with baseline case

4.2 Pressure Drop

Figure 7 presents the pressure drop values as a function of Re . It represents the power required to pump and maintain the flow along the channel. Two types of drags are associated with pressure drop, i.e. pressure drag and friction drag. Pressure drag dominates when the fluid is restricted to flow due to additional oblique surfaces. Friction drag dominates when surface over which the fluid flows is rough, where friction is the main cause of restriction. Pressure drop for 0.7 mm (80% reduction) and 1.4 mm (60% reduction) height of winglets is very close and minimum of all other reductions. Further changes in height of the winglets lead to an increase in pressure drop. This increase in pressure drop is due to enhanced flow restriction with increasing height of the winglets over a certain channel height.

4.3 Quality Factor

The ratio of Colburn factor to the friction factor is termed as the quality factor. Higher the quality factor, the more will be the effectiveness of the heat exchanger. It becomes apparent from Fig. 8 that the quality factor came out to be maximum for 1.4 mm height of winglets (60% reduction). Therefore, corresponding to this height of winglets, an optimum balance between heat transfer and pressure drop will be achieved.

5 Conclusions

The objective of this paper was to assess the influence of winglet height on thermo-fluid characteristics of a fin-and-tube heat exchanger. An in-line configuration, with

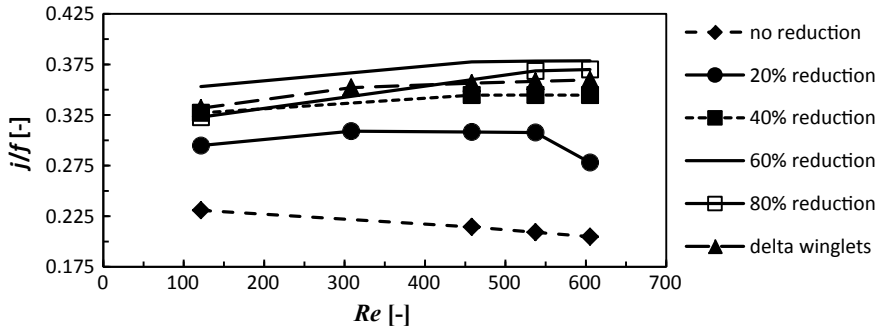


Fig. 8 Quality factor as a function of Re for different height of winglets and comparison with baseline case

seven tubes supported with winglets of different heights, was numerically investigated at different Re . The overall performance of the heat transfer surface has been presented in terms of quality factor. Major findings, in reference to the experimental results of delta winglets, have been listed below:

1. The pressure drop increased with increase in height of winglets. For the winglet height of 1.4 mm, the pressure drop decreased by 12%. For a winglet height of 0.7 mm, the reduction in the pressure drop by 20% was observed.
2. The increased winglet height enhanced the heat transfer performance, and it came out to be the maximum for a height of 2.8 mm. For this height, the heat transfer was raised up to 39% at high Re .
3. Quality factor came out to be maximum for the winglet height of 1.4 mm which was enhanced by 6%, and this height was taken as the optimum winglet height. Height of 0.7 mm also showed an increase in quality factor by 2.8% at higher Re .

References

1. Edwards FJ, Alker GJR (1974) The improvement of forced convection surface heat transfer using surface protrusions in the form of (a) cubes and (b) vortex generators. In: Proceedings of the fifth international heat transfer conference Tokyo, vol 2, pp 2244–2248
2. Vasudevan R, Eswaran V, Biswas G (2000) Winglet type vortex generators for plate fin heat exchangers using triangular fins. *Numer Heat Transfer Part A* 38:533–555
3. Sohankar A, Davidson L (2001) Effect of inclined vortex generators on heat transfer enhancement in a three-dimensional channel. *Numer Heat Transfer Part A* 39:433–448
4. Gentry MC, Jacobi AM (2002) Heat transfer enhancement by delta-wing-generated tip vortices in flat-plate and developing channel flows. *J Heat Transfer (ASME)* 124:1158–1168
5. Song K, Xi Z, Su M, Wang L, Wu X, Wang L (2017) Effect of geometric size of curved delta winglet vortex generators and tube pitch on heat transfer characteristics of fin-tube heat exchanger. *Expt Therm Fluid Sci* 82:8–18
6. Jain A, Biswas G, Maurya D (2003) Winglet-type vortex generators with common-flow-up configuration for fin-tube heat exchangers. *Numer Heat Transfer Part A* 43:201–219

7. Biswas G, Torii K, Fujii D, Nishino K (1996) Numerical and experimental determination of flow structure and heat transfer effects of longitudinal vortices in a channel flow. *Int J Heat Mass Transfer* 38:3441–3445
8. Lemouedda A, Breuer M, Franz E, Botsch T, Delgado A (2010) Optimization of the angle of attack of delta-winglet vortex generators in a plate-fin-and-tube heat exchanger. *Int. J. Heat Mass Transf.* 53:5386–5399
9. Russell CMB, Jones TV, Lee GH (1982) Heat transfer enhancement using vortex generators. In: *Proceedings of the seventh international heat transfer conference, Munchen, Germany, vol 3*, pp 283–288
10. Fiebig M, Kallweit P, Mitra NK (1986) Wing-type vortex generators for heat transfer enhancement. *IHTC* 6:2909–2913
11. Torii K, Kwak KM, Nishino K (2002) Heat transfer enhancement accompanying pressure-loss reduction with winglet-type vortex generators for fin-tube heat exchangers. *Int J Heat Mass Transfer* 45:3795–3801
12. Joardar A, Jacobi AM (2008) Heat transfer enhancement by winglet type vortex generator arrays in compact plain-fin-and-tube heat exchangers. *Int J Refrig* 31:87–97
13. Wu JM, Tao WQ (2008) Numerical study on laminar convection heat transfer in a rectangular channel with longitudinal vortex generator part B; parametric study of major influencing parameter. *Int J Heat Mass Transfer* 51:3683–3692
14. He YL, Han H, Tao WQ, Zhang YW (2012) Numerical study of heat-transfer enhancement by punched winglet-type vortex generator arrays in fin-and-tube heat exchangers. *Int J Heat Mass Transfer* 55:5449–5458
15. Agarwal S, Sharma RP (2016) Numerical investigation of heat transfer enhancement using hybrid vortex generator arrays in fin-and-tube heat exchangers. *J Therm Sci Eng Appl* 8:0310071–0310079
16. Sarangi SK, Mishra DP (2017) Effect of winglet location on heat transfer of a fin-and-tube heat exchanger. *Appl Therm Eng* 116:528–540
17. Sarangi SK, Mishra DP, Mishra P (2019) Numerical analysis of thermofluid performance of fin-and-tube heat transfer surface using rectangular winglets. *J Heat Transfer* 141(10)

Computational Modeling to Investigate the Heat Transfer Enhancement by Using Ethyl Glycol–Water–MWCNT Nanofluid Through Corrugated Pipe



Prakash Ghose and Rishitosh Ranjan

Abstract A computational model has been developed to study the heat transfer augmentation by using nanofluid flow through a hot corrugated pipe. Multi-walled carbon nanotube (MWCNT) is used as nanoparticles. Ethyl glycol–water solution is used as base fluid at a ratio of 30:70 by volume. A semicircular wavy corrugated wall is maintained at 315 K temperature. Eight numbers of nozzle holes are provided on corrugated wall at 60° apart along circumference. The nanofluid at various volume fractions has been supplied through the main duct. From the study, it has been observed that Nusselt number increases almost linearly along with increase in Reynolds number; whereas, pumping power varies nonlinearly along with increase in Reynolds number. Moreover, at the lowest duct Reynolds number, a recirculation zone has been observed.

Keywords Nanofluid · Corrugated · MWCNT · Ethyl glycol–water

1 Introduction

There are various methods employed to increase the heat transfer through forced convection from hot pipe surface has been found in pipe flow systems. Pipe with internal fin, insertion of twisted plate or by making dimples on pipe surfaces, etc., are various methods used to increase the heat transfer. Heat transfer enhancement through corrugated pipe is an area of research on which work has been performed by [1–3] various researchers. Application of nanofluid has also been observed to increase the heat transfer by increasing the conductivity of the fluid. Enhancement of heat transfer by using various nanofluids such as Al_2O_3 -water, CuO-water and SiO_2 -water are studied by various researchers through corrugated channel [1–3]. However, Al_2O_3 and CuO are found to be the most common nanoparticles and water, and engine oil is the common fluid used as base fluid. Ethyl glycol-based nanofluid is preferred because of its lower freezing point temperature. Therefore, in this work, EG-water

P. Ghose (✉) · R. Ranjan

Kalinga Institute of Industrial Technology, Deemed To Be University, Bhubaneswar, India

e-mail: pghosefme@kiit.ac.in

© Springer Nature Singapore Pte Ltd. 2021

P. Pant et al. (eds.), *Advances in Mechanical Processing and Design*, Lecture Notes in Mechanical Engineering, https://doi.org/10.1007/978-981-15-7779-6_14

161

mixture is used as base fluid to maintain very low temperature of hot surface [4]. From the literature, it has been observed that numerical investigation of a forced convective system by using MWCNT + water ethyl glycol nanofluid along with jet impingement cooling through a corrugated surface is very rare. Therefore, in this work, the heat transfer from a corrugated pipe by using ethyl glycol–water + MWCNT as a flowing fluid is investigated.

2 Thermophysical Properties

The thermophysical properties of water-EG mixture at different volumetric ratio are found in the Ref. [5]. The thermophysical properties of MWCNT depend upon the number of walls, lattice arrangement or chirality, length to diameter ratio, surface area and purity [5–7]. In this work, the MWCNT with average diameter of 30–50 nm, length of 10–20 μm , specific surface area of 60 m^2/g and of 95% purity has been considered. The base fluid is used as the mixture of 70% water and 30% EG by volume. The individual properties of base fluid and nanoparticles at room temperature are given in Table 1.

Hamilton–Crosser model [8] is an established model to determine the thermal conductivity of nanofluid. This model predicts better for ratio of the conductivity of nanoparticle to base fluid is greater than 100. However, Bhattacharya et al. [9] model predicted with a better accuracy for thermal conductivity of EG-water/MWCNT nanofluid when compared with the experimental results of Kumaresan et al. [10]. Mathematically, temperature-independent Bhattacharya model is

$$k_{\text{eff}} = \phi k_{\text{np}} + (1 - \phi)k_{\text{bf}} \quad (1)$$

Two models are broadly used to calculate the temperature-independent specific heat. First model is much similar to ideal gas mixing theory [11]. This is a straight average relation and specific heat of nanofluid is a function of specific heat of base fluid, nanoparticle and the volume fraction of nanoparticle. The second model which is based on classical mechanism by assuming that the nanoparticles and base fluid are in thermal equilibrium [12]. Mathematically, the temperature-independent model for specific heat used is expressed as;

Table 1 Thermophysical properties of nanoparticle and base fluid

Properties	Nanoparticle	Base fluid (water + EG)
Density (kg/m^3)	2100	1039
Thermal conductivity (W/mK)	15	0.49
Specific heat ($\text{J}/\text{kg K}$)	470	3930
Viscosity ($\text{kg}/\text{m s}$)	–	Non-Newtonian

$$c_{p,nf} = \frac{\varnothing(\rho c_p)_{np} + (1 - \varnothing)(\rho c_p)_{bf}}{\varnothing\rho_{np} + (1 - \varnothing)\rho_{bf}} \quad (2)$$

To evaluate density of nanofluid, at reference temperature, the following correlation is used

$$\rho_{nf} = (1 - \varnothing)\rho_{bf} + \varnothing\rho_{np} \quad (3)$$

This correlation is used to determine the density of nanofluid at different concentration of nanoparticles (Al_2O_3 , CuO) for water-based nanofluid [1]. For natural convection, the above relation is used by Esfe et al. [13] to calculate the density of water-EG/MWCNT nanofluid at different concentration of MWCNT particles.

Viscosity is an important property of fluid which causes the pressure drop inside the system. Water-EG-based nanofluid with MWCNT nanoparticles exhibits pseudo-plastic rheological behavior and following power law. Therefore, power law model is used to incorporate the non-Newtonian behavior of the fluid.

3 Computational Modeling

In this work, the nanoparticles are fine and assumed to be well dispersed. Therefore, the slip velocity between base fluid and nanoparticles is assumed to be negligible. For that reason, single-phase approach has been considered for the simulation. Time-averaged continuity, momentum and energy equations are solved in Eulerian frame. In order to calculate turbulent quantities in governing equations, SST $k-\omega$ turbulent model [14] is used in this work. SST $k-\omega$ model predicts well at far from and near the boundary as well. The governing equations are solved through commercial CFD software ANSYS Fluent 19.0. All the terms are discretized using second-order upwind scheme. Appropriate boundary conditions are chosen for all the boundaries. SIMPLE algorithm method has been followed for pressure velocity coupling. Appropriate convergence criteria are used for various governing equations.

4 Physical Model

Physical model of the present study has been given in Fig. 1. Diameter of the inlet and outlet duct is 0.04 m, lengths of wall inlet and wall outlet are 0.27 m and 0.26 m, respectively, length of heated wall zone is 0.14 m, protrusion is of semicircular cross section of diameter 0.02 m, and there are total eight number of nozzle inlet through heat wall of diameter of 0.005 m. To obtain fully developed flow through heat wall zone, the wall inlet zone is created. Ethyl glycol-water as base fluid at a ratio of 30:70 has been used. MWCNT has been added within a range of volume fraction of

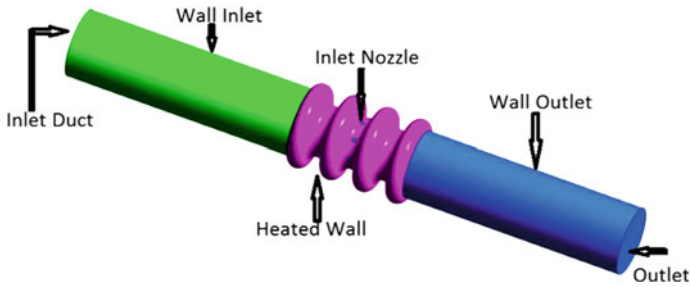


Fig. 1 Physical model of computational domain

0–0.045%. The simulation has been conducted with Reynolds number at duct inlet varying from 6000 to 8000; whereas, nozzle Reynolds number is kept as 6000 in each nozzle hole. The entire computational domain is discretized with 330,485 number of unstructured hexahedral mesh. Fine mesh has been generated near the curvature and small boundaries to simulate various gradients correctly.

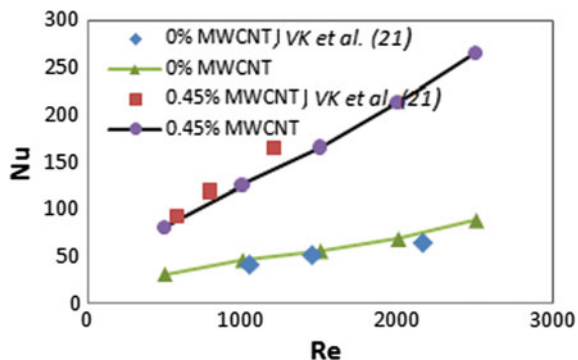
5 Results and Discussion

The computational model is validated with Kumaresan et al. [10]. In their experiment, they used ethyl glycol–water as base fluid at a ratio of 30:70. From Fig. 2, it has been observed that the model fairly predicted the Nusselt number. The area-weighted average Nusselt numbers are evaluated with the help of following expression.

$$\overline{Nu}_{Dh} = \frac{1}{A} \int Nu_{Dh} dA \tag{8}$$

In Eq. 8, dA is the cell surface area of corrugated part and A is the total surface area of the hot corrugated part. The local Nusselt number Nu_{Dh} is calculated as follows:

Fig. 2 Nusselt number at different Reynolds number [10]



$$Nu_{Dh} = \frac{h_w D_h}{k} \tag{9}$$

where D_h is the hydraulic diameter of the duct at outlet. The local heat transfer coefficient is $h_w = q_w / (T_w - T_b)$, where q_w is the corrugated wall heat flux. The bulk mean temperature T_b is the area-weighted average temperature at outlet, and it is evaluated as follows:

$$T_b = \frac{1}{A} \int T dA \tag{10}$$

In Eq. 10, dA represents the cell surface area at outlet plane and A is the total surface area at the outlet plane.

Velocity inlet boundary condition (BC) is used at duct and nozzle inlet. The velocities at duct inlet and nozzle inlet are calculated from Reynolds number expression as follows: $Re_{duct} = \rho_{nf} u_{duct} D_{h_{duct}} / \mu_{nf}$ and $Re_{nozzle} = \rho_{nf} u_{nozzle} D_{h_{nozzle}} / \mu_{nf}$, respectively. Pressure outlet BC is used at outlet plane where the gradient of all variable is considered as zero. All the walls are considered as no slip boundary. At inlet, turbulent intensity and hydraulic diameter BC are used. The turbulent intensity is calculated from the empirical correlation given as follows: $I = 0.16 (Re_D)^{-8}$. Standard wall function condition is used as the boundary condition for k and ω . Temperature boundary condition is set to all boundary except inlet and outlet duct wall, where zero wall heat flux condition is used.

6 Effect of Duct Reynolds Number

Average Nusselt number variation with different duct Reynolds number (Re_{duct}) at a fixed nozzle Reynolds number (Re_{nozzle}) is depicted in Fig. 3. It is observed that Nusselt number increases with increase in duct Reynolds number irrespective of percentage of nanoparticles present in the fluid. It is because with the increase in fluid

Fig. 3 Nusselt number versus duct Reynolds number ($Re_{nozzle} = 6000$)

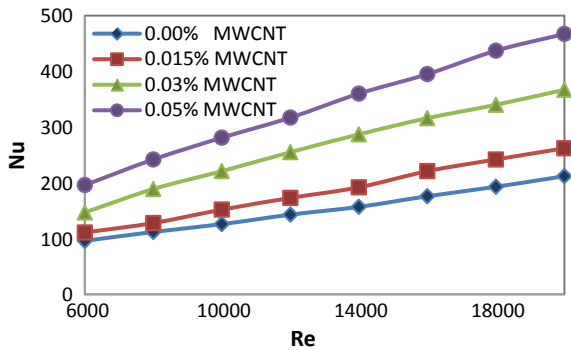
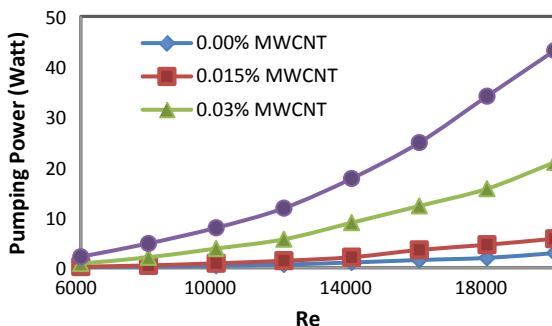


Fig. 4 Pumping power versus duct Reynolds number ($Re_{\text{nozzle}} = 6000$)



velocity, heat transfer rate increases. Amount of heat conducted through nanofluid from heated wall is moving out at a faster rate carrying more heat. Moreover, with higher percentage of nanoparticles present in nanofluid, Nusselt number increases. This is because as conductivity of nanofluid increases with increase in nanoparticles, heat conducted from heated wall too occurs at a faster rate. It causes augmentation of convective heat transfer.

Figure 4 shows the pumping power required to the flow at various Reynolds number and volume fraction of nanoparticles in nanofluid at a fixed nozzle Reynolds number. Pumping power is calculated as follows: Pumping power (watt) = $\Delta P \times Q$, where ΔP is the area-weighted average pressure difference in between duct inlet plus nozzle inlet and outlet of the model. Q is the total discharge. Discharge is calculated as the product of cross section at outlet and area-weighted average velocity at outlet.

From the figure, it has been depicted that pumping power increases with increase in duct Reynolds number irrespective of amount of nanoparticle present in nanofluid. This is due to huge pressure drop caused by friction at higher velocity as well as the losses due to stronger vortex formation in the protrusion region as Reynolds number increases as shown in Fig. 5. Moreover high pumping work is required with higher percentage of nanoparticles present in nanofluid, because as the percentage of nanoparticles increases, the viscosity of the nanofluid increases which causes a higher viscous resistance.

Figures 5 and 6 depicts the effect of quantity of nanoparticles present in nanofluid on the velocity field. A sectional view (heated wall zone) of superimposed velocity vector with velocity contour at a nozzle Reynolds number of 6000 and duct Reynolds number of 6000 has been shown in figure at various percentage of nanoparticles in nanofluid. Figure 5a shows a recirculation zone at the center exposed to nozzle fluid without nanoparticles. In this case, nozzle fluid obstructs the main flow through duct. But with higher percentage of nanoparticles for same Reynolds number, inlet velocity of main stream is higher which somehow removed that flow obstructions but strong recirculation zones are present in the protrusion region. Moreover, velocity of the fluid after the nozzle plane increases centrally due to additional mass addition through nozzle inlet. With very high Reynolds number flow ($Re = 20,000$) shown in Fig. 6, there is no obstruction present in the nozzle section due to higher inlet

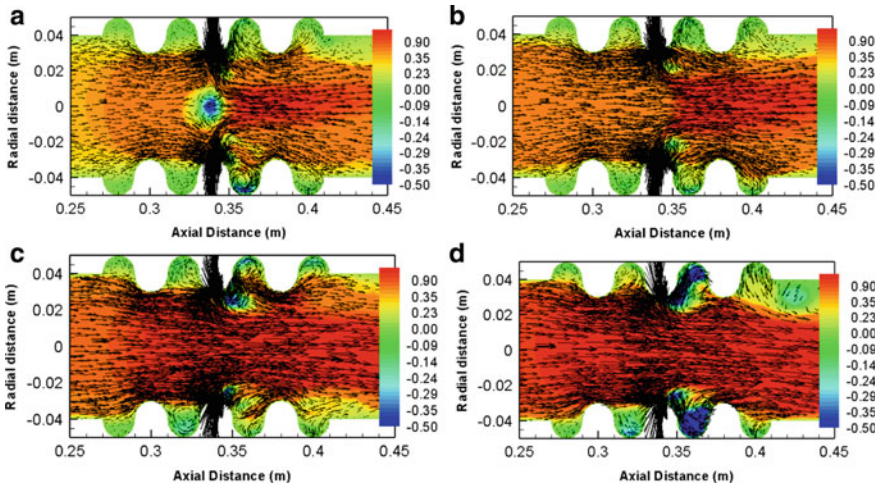


Fig. 5 Sectional view of velocity contour with superimposed velocity at ($Re_{nozzle} = 6000$) and duct ($Re_{duct} = 6000$) with **a** 0%, **b** 0.015%, **c** 0.03%, **d** 0.045% v.f. of MWCNT

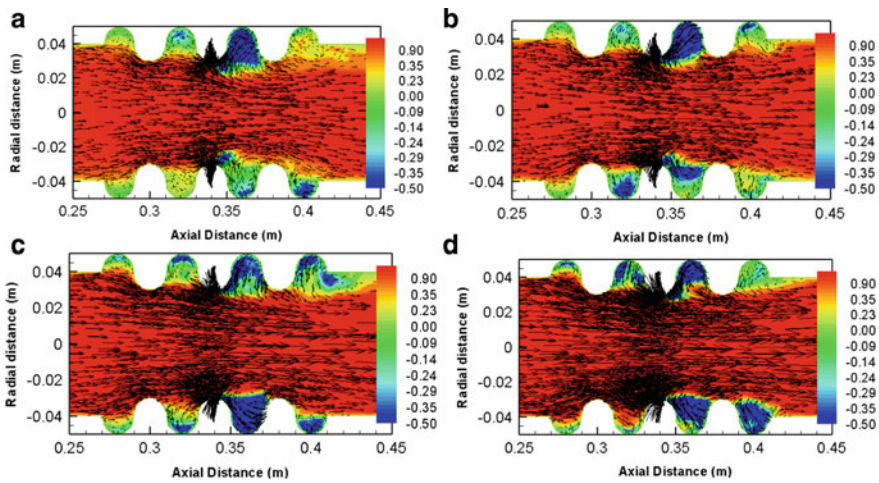


Fig. 6 Sectional view of velocity contour with superimposed velocity at ($Re_{nozzle} = 6000$) and duct ($Re_{duct} = 20,000$) with **a** 0%, **b** 0.015%, **c** 0.03%, **d** 0.045% v.f. of MWCNT

velocity. But the recirculation zone in the protrusion region becomes stronger with higher Reynolds number which causes energy losses during the flow.

Figures 7 and 8 depict the effect of quantity of nanoparticles present in nanofluid on the temperature field at different Reynolds number. The temperature range is decreased in these figures for the better visualization of temperature gradient in the

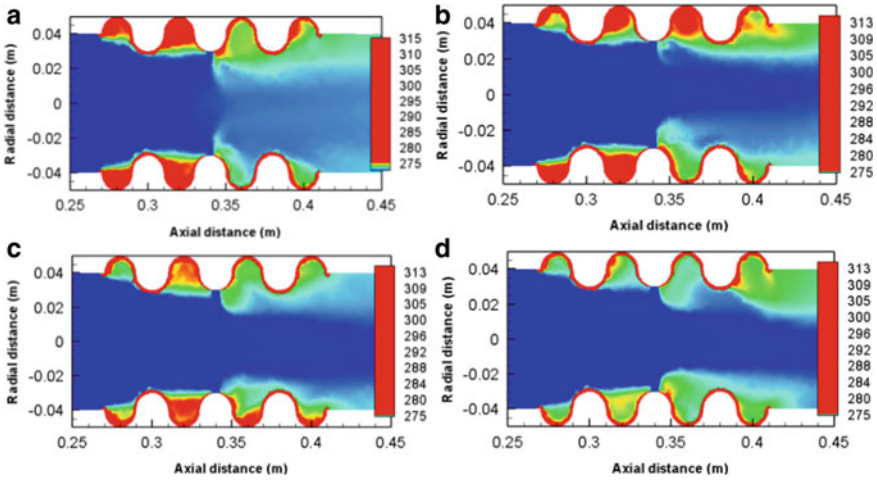


Fig. 7 Sectional view of temperature contour at ($R_{e_{nozzle}} = 6000$) and duct ($R_{e_{duct}} = 6000$) with **a** 0%, **b** 0.015%, **c** 0.03%, **d** 0.045% vol fraction of MWCNT

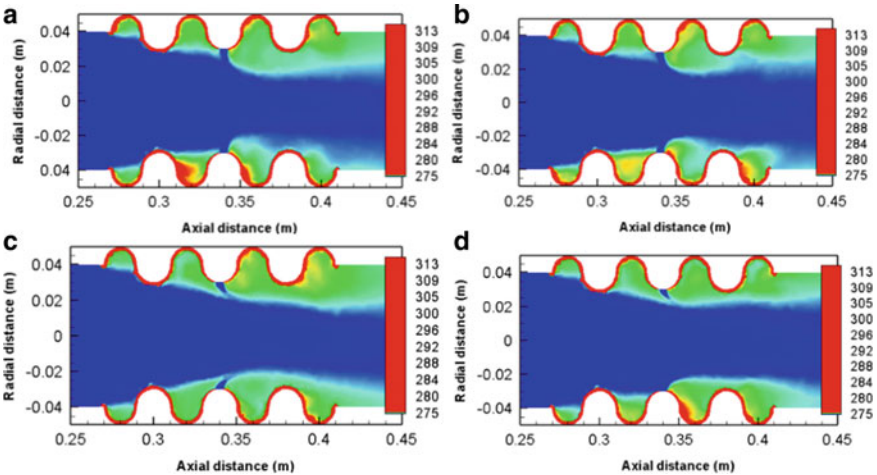


Fig. 8 Sectional view of temperature contour at ($R_{e_{nozzle}} = 6000$) and duct ($R_{e_{duct}} = 20,000$) with **a** 0%, **b** 0.015%, **c** 0.03%, **d** 0.045% vol fraction of MWCNT

flow field. From Fig. 7, it has been observed that with higher percentage of nanoparticles present in nanofluid, the temperature gradient near the portusion region is higher. This is due to the higher conductivity with higher percentage nanoparticles conducted significant amount of heat through fluid. With lower percentage of nanoparticles, low-temperature gradients have been observed.

From Fig. 8 ($Re = 20,000$), it has been observed that with higher percentage of nanoparticles present in nanofluid, the temperature gradient near the portusion

region is higher. This is due to the higher conductivity with higher percentage nanoparticles conducted significant amount of heat through fluid. With lower percentage of nanoparticles, low-temperature gradients have been observed.

7 Conclusion

A computational model has been developed to study the heat transfer augmentation by using ethyl glycol-MWCNT flow through a heated corrugated pipe. A semicircular wavy corrugated surface is heated and maintained at a constant temperature of 315 K. The nanofluid at various volume fractions with a range of 0–0.045% has been supplied through the main duct along with eight nozzle holes at different velocities. The effect of duct Reynolds number and volume fraction of nanoparticles in nanofluid on Nusselt number and pumping power are studied. It has been observed that Nusselt number increases almost linearly along with increase in Reynolds number; whereas, pumping power varies nonlinearly along with increase in Reynolds number. Moreover, at the lowest duct Reynolds number, a recirculation zone has been observed.

References

1. Abed AM et al (2015) Enhance heat transfer in the channel with V-shaped wavy lower plate using liquid nanofluids. *Case Stud Thermal Eng* 5:13–23
2. Al-Shamani AN et al (2015) Enhancement heat transfer characteristics in the channel with Trapezoidal rib–groove using nanofluids. *Case Stud Thermal Eng* 5:48–58
3. Ahmed MA et al (2015) Numerical investigations on the turbulent forced convection of nanofluids flow in a triangular-corrugated channel. *Case Stud Thermal Eng* 6:212–225
4. <https://webserver.dmt.upm.es/~isidoro/bk3/c07sol/Solution%20properties.pdf>
5. Mantena KV (2009) Electrical and mechanical properties of MWCNT filled conductive adhesives on lead free surface finished PCB's. University of Kentucky Master's Theses. Paper 613. https://uknowledge.uky.edu/gradschool_theses/613
6. Laurent C, Flahaut E, Peigney A (2010) The weight and density of carbon nanotubes versus the number of walls and diameter. *Carbon* 4(8):2989–2999
7. Hepplestone SP et al (2006) Size and temperature dependence of the specific heat capacity of carbon nanotubes. *Surf Sci* 600(18):3633–3636
8. Hamilton RL, Crosser OK (1962) Thermal conductivity of heterogeneous two-component systems. *IEC Fund* 1(3):187–191
9. Bhattacharya P, Saha SK, Yadav A, Phelan PE, Prashar RS (2004) Brownian dynamics simulation to determine the effective thermal conductivity of nanoparticles. *J Appl Phys* 95:6492–6494
10. Kumaresan V, Mohaideen Abdul Khader S, Karthikeyan S, Velraj R (2013) Convective heat transfer characteristics of CNT nanofluids in a tubular heat exchanger of various lengths for energy efficient cooling/heating system. *Int J Heat and Mass Transf* 60:413–421
11. Smith JM, Van Ness MC (1987) Introduction to chemical engineering thermodynamics. McGraw-Hill, New York
12. Buongiorno J (2006) Convective transport in nanofluids. *J Heat Transfer* 128(3):240–250

13. Esfe MH et al (2016) Natural convection in a trapezoidal enclosure filled with carbon nanotube–EG–water nanofluid. *Int J Heat Mass Transf* 92:76–82
14. Menter FR (1994) Two-equation Eddy-viscosity turbulence models for engineering applications. *AIAA J* 32(8):1598–1605

Numerical Analysis of a Steady Turbulent Flow Over a Backward-Facing Step with Varying Step Angles Using OpenFOAM



R. S. Sarath and K. Arunkumar

Abstract The research work studies the effect of varying step angle in the flow through a backward-facing step geometry. The work was done using OpenFOAM solver. The step angles were varied in the range 10° to 80° . The solution was obtained using simpleFoam inside the OpenFOAM solver. The variation of velocity magnitude, pressure and turbulent kinetic energy was observed for the varying step geometries. At 80° , a standalone highly turbulent vortex was observed near the nozzle region, which is also evident from the pressure and velocity contours.

Keywords Backward-facing step · OpenFOAM · SimpleFoam

1 Introduction

Backward-facing step flow is considered as a standard reference for the analysis of many engineering applications. Large separation of flow near surface whose cross-sectional area increases suddenly is an interesting aspect of this study. Large flow separations and vortices created are of great excitement when it comes to comparison with real-life applications such as airfoils and spoilers. The model was well studied by Chen et al. [1] and he observed large recirculation near the sudden area changing sections. The model is very much available as a standard reference in Comsol [2] and NASA [3] directories. The present study aims to investigate steady turbulent flow over a backward-facing step. The problem description is taken from one used by Pitz and Daily [4] in an experimental investigation against which the computed solution can be compared. The domain is two dimensional, consisting of a short inlet, a backward-facing step and converging nozzle at the outlet. The numerical methodology used in the present analysis was taken from the works of Sarath et al. [5] and Chandar et al. [6].

In the present work, the conventional backward-facing step was modified by varying the step angles. The step angles were varied by 10° , 20° , 30° , 40° , 50° ,

R. S. Sarath (✉) · K. Arunkumar

Department of Mechanical Engineering, Amrita Vishwa Vidyapeetham, Amritapuri, India
e-mail: contactmesarathrs@gmail.com

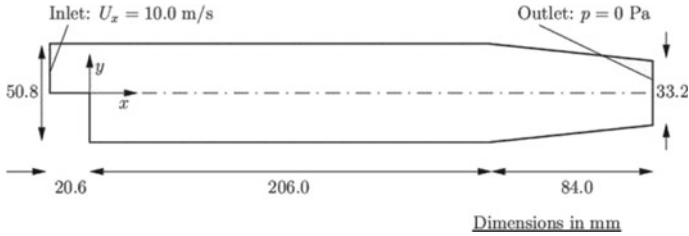


Fig. 1 Numerical model

60°, 70°, 80° with respect to the vertical. The numerical model considered for the study is as follows Fig. 1.

2 Governing Equations

The governing equations used for the analysis are

- Mass continuity for incompressible flow

$$\partial u / \partial x + \partial v / \partial y + \partial w / \partial z = 0 \quad (1)$$

- Steady-state flow momentum equation

$$\nabla(U \cdot U) - \nabla(v_{\text{eff}} \nabla U) = -\nabla p \quad (2)$$

3 Methodology

The flow analysis was carried out using the following methodology. The initial and boundary conditions applicable to the study are:

Initial conditions: $U = 0$ m/s, $p = 0$ Pa.

Boundary conditions:

Inlet (left) with fixed velocity $U = (10, 0, 0)$ m/s;

Outlet (right) with fixed pressure $p = 0$ Pa;

No-slip walls on other boundaries.

Transport properties: kinematic viscosity of air $\nu = \mu / \rho = 14.0 \mu\text{m}^2/\text{s}$.

Turbulence model: Standard $k - \epsilon$;

Coefficients: $C_\mu = 0.09$, $C_1 = 1.44$, $C_2 = 1.92$, $\alpha_k = 1$, $\alpha_\epsilon = 0.76923$.

Solver:

The solver used for the study is simpleFoam. SimpleFoam deals with an incompressible, steady, viscous flow. It has full access to all the turbulence models

in the incompressible turbulence models library and the non-Newtonian ones in incompressible transport models library implemented in OpenFOAM.

The $k-\epsilon$ model needs initial conditions to be set. The following hypothesis was used for the simulation of the backward-facing step case:

1. Isotropic initial turbulence;
2. Initial turbulence fluctuation intensity: 5%;
3. Turbulent reference length scale: 10%.

The correspondent parameters set-up is then resulting: $u' = v' = w' = 5\%$

4 Computational Domain and Meshing

The computational domain and meshing were done using the BlockMesh utility in OpenFOAM. The geometries and meshes (Fig. 2a, b) are as shown below for the varying step inclinations from 0° to 80° .

5 Results

The variation of the following parameters was considered for comparing the various models used for the study.

- (a) Velocity magnitude along the x-direction;
- (b) Variation of turbulent kinetic energy;
- (c) Streamlines.

The variation of velocity and pressure (Fig. 3a–d) along the streamwise direction was also plotted graphically.

5.1 Velocity Magnitude Along the x-Direction

From the velocity magnitude contour for a backward-facing step, it is evident that as expected, the flow has high velocities nearer to the top wall region. Due to the particular geometry of the backward step, the flow will have low velocities near the lower wall. Sufficient amount of vorticity was also observed in these regions with high rotationality. The velocity profiles looked almost the same for most cases up to step angle of 60° . After a step angle of 60° , the flow velocity near the lower wall is seen to increase. The vortex formation near the lower walls seems to get shortened in diameter. At a step angle of 80° , the flow is almost having uniform velocity in the mid-region with a slight vortex formed near the end of the step inclination.

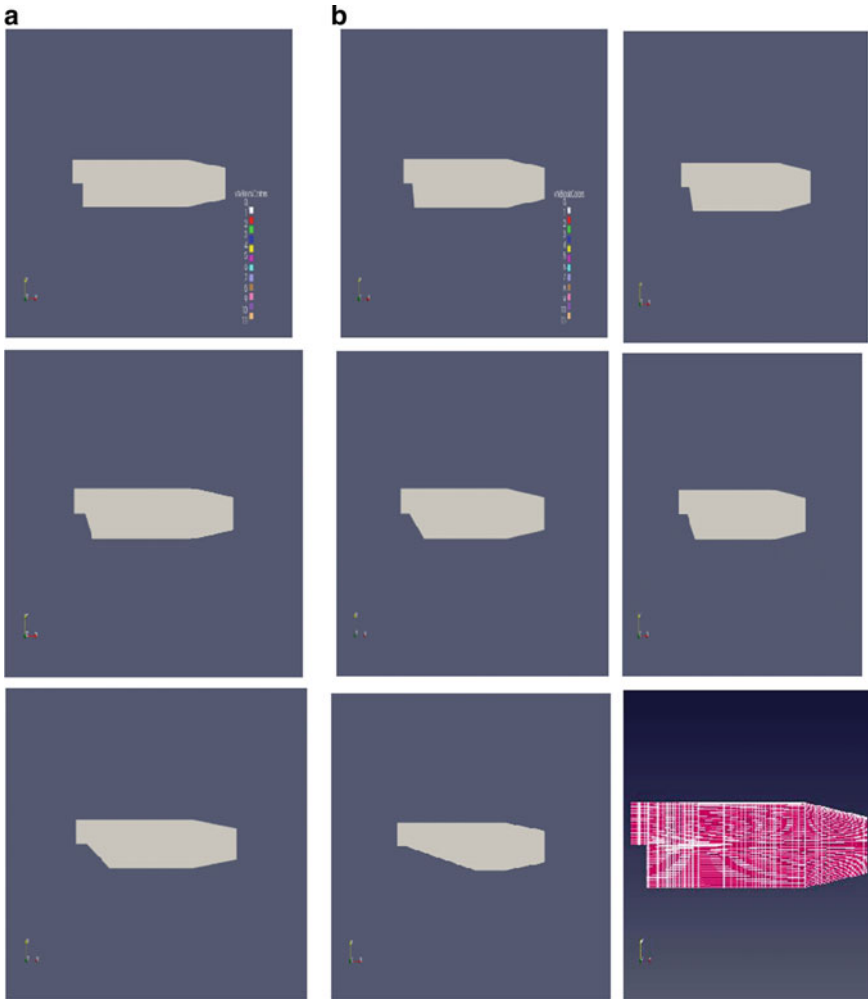


Fig. 2. **a** Step geometries (0° to 80°), **b** mesh generated for 0°

5.2 Variation of Turbulent Kinetic Energy

The turbulent kinetic energy distribution near the bottom wall up to 60° inclination is because of the high vorticity created in this region. High vorticity is always associated with high level of turbulence which is evident from the plots. After 70° , high turbulence was observed near the start of the step. This may be because of the step inclination that small vortices will be formed in these regions. At 80° , we can observe a standalone highly turbulent vortex near the nozzle region, which is also observed from the pressure, and velocity contours as shown in Fig. 4a, b.

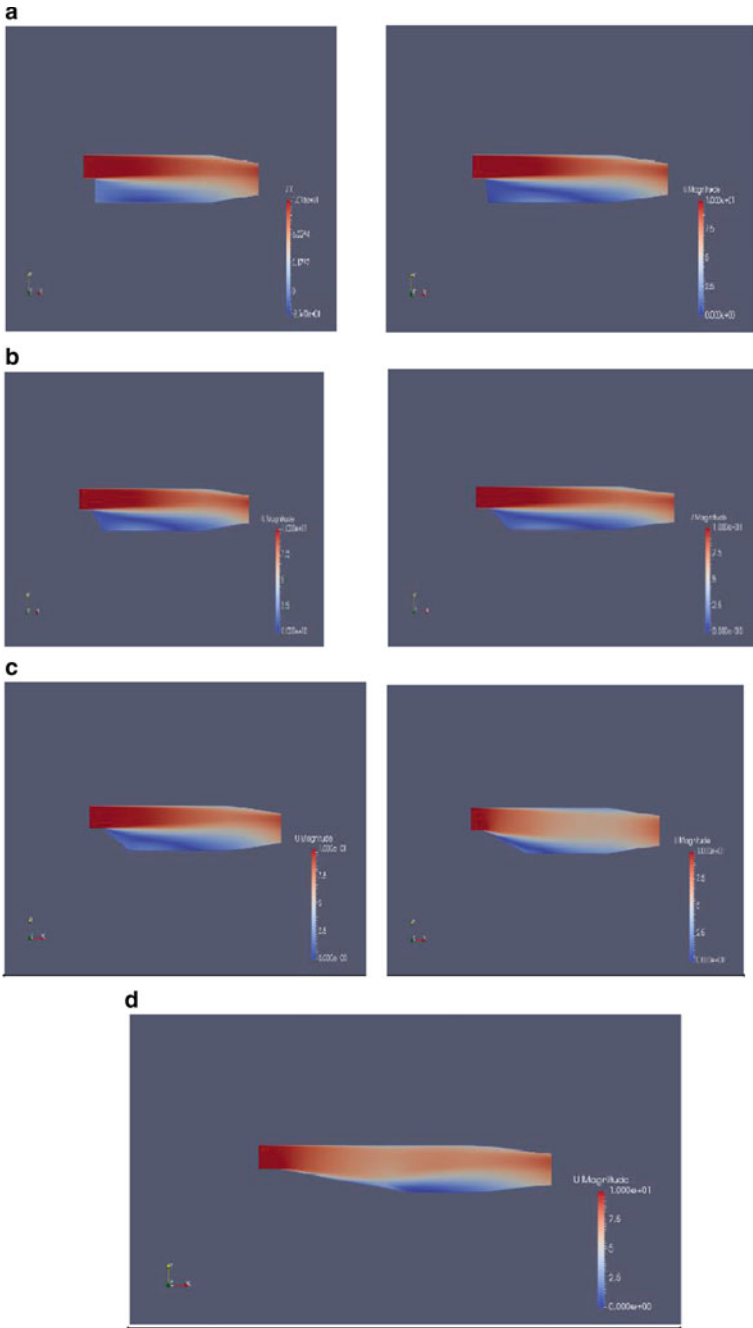


Fig. 3. **a** Velocity magnitude along x -direction for 0° and 10° , **b** velocity magnitude along x -direction for 40° and 50° , **c** velocity magnitude along x -direction for 60° and 70° , **d** velocity magnitude along x -direction for 80°

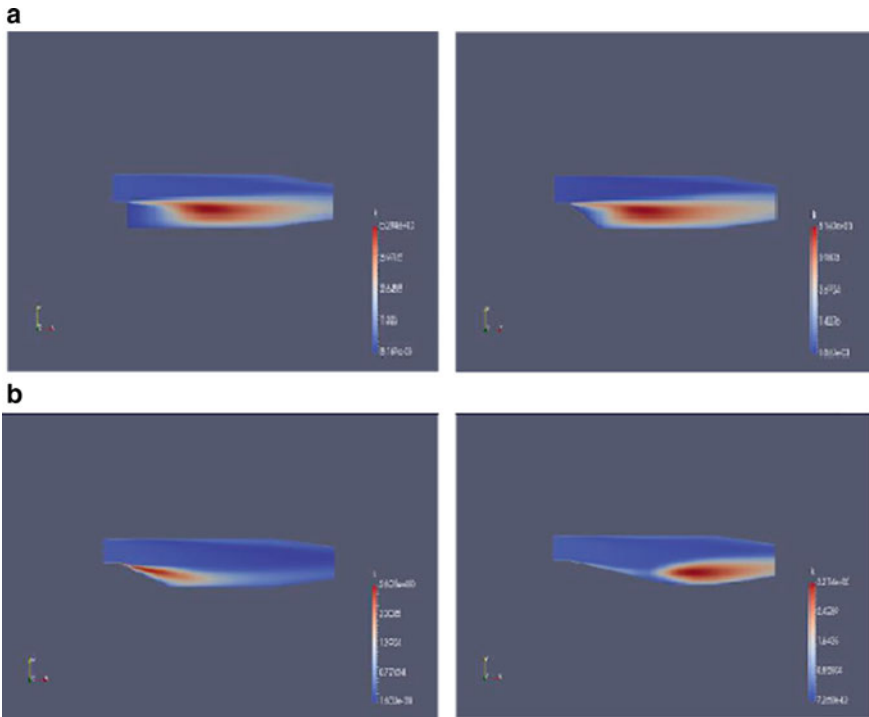


Fig. 4. **a** Turbulent kinetic energy along x -direction for 0° and 60° , **b** turbulent kinetic energy along x -direction for 70° and 80°

5.3 Streamlines

The streamlines (Fig. 5a–c) also take us to the conclusion that the flow loses its vorticity when the step inclination increases. For the highest step inclination, no vorticity is observed near the upstream region. A standalone vortex is observed near the nozzle through the streamline plot also.

The results in the above plots (Fig. 6a, b) support the observations made with the help of velocity, pressure contours and streamlines. As the step inclination increases, the upstream region will have high-pressure zones. This is because as the step inclination increases, the influence of step geometry is decreasing. The flow becomes more uniform. The influence of vorticity created near the lower wall because of step is reducing. The pressure plot for 80° step inclination shows two pressure peaks near the nozzle inlet. This is because of the strong standalone vortex that is formed at this region which is evident from the streamlines also.

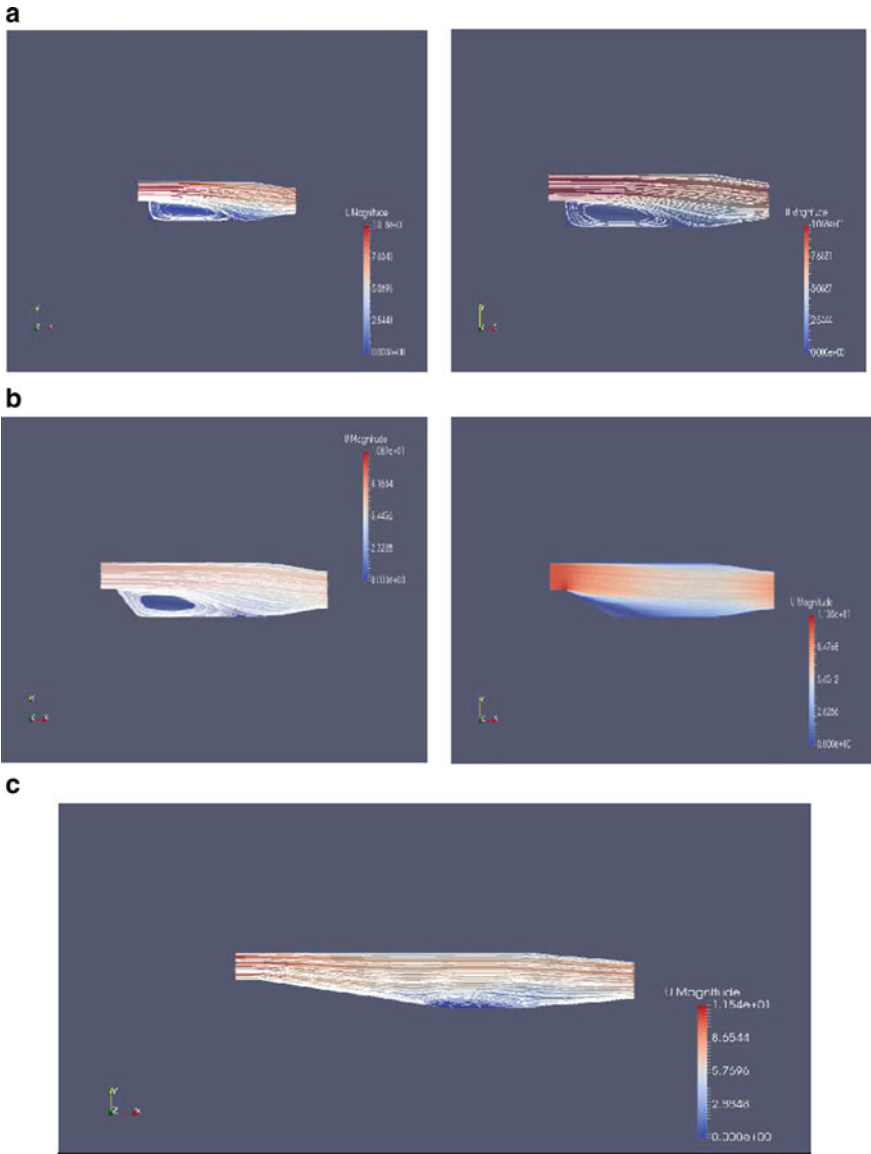


Fig. 5. **a** Streamlines for 0° and 10°, **b** streamlines for 50° and 70°, **c** streamlines for 80°

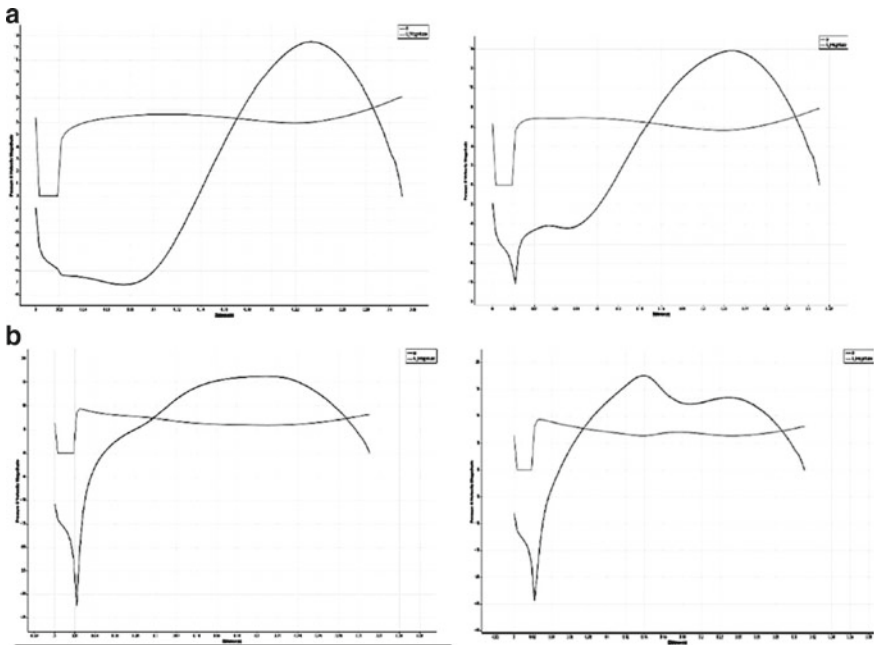


Fig. 6. **a** Pressure and velocity magnitude versus distance (x) for 0° and 60° , **b** pressure and velocity magnitude versus distance (x) for 70° and 80°

6 Conclusions

The numerical analysis revealed the influence of backward-facing step with varied step angles on the fluid flow. Predominant recirculation's and vortices are characteristics of such flows. Standalone vortices observed in the case of higher step angles are a key area which needs to be examined in the coming research works.

Acknowledgements Authors would like to thank all the members of Mechanical Engineering Department, Amrita School of Engineering, Amritapuri campus and to all others who have directly or indirectly helped us in carrying out this work.

References

1. Chen L, Asai K, Nonomura T, Xi G, Liu T (2018) A review of backward-facing step (BFS) flow mechanisms, heat transfer and control. *Thermal Sci Eng Progr* 194–216
2. COMSOL Multiphysics® Modeling Software. <https://www.comsol.com>
3. NASA. <https://www.grc.nasa.gov/www/wind/valid/backstep/backstep.html>

4. Chandar SV, Sarath RS, Kumar RA (2017) Aerodynamic characteristics of a square section cylinder: Effect of corner arc. In: 2017 2nd international conference for convergence in technology (I2CT). IEEE Apr 2017. Available from: <https://doi.org/10.1109/i2ct.2017.8226241>
5. Sarath RS, Ajith Kumar R, Prasad BVSSS, Srikrishnan AR (2016) Numerical analysis of effects of turbine blade tip shape on secondary losses. Lecture notes in mechanical engineering. Springer, India, pp 871–879
6. Chandar SV, Sarath RS, Kumar RA (2017) Aerodynamic characteristics of a square section cylinder: effect of corner arc. In: 2017 2nd international conference for convergence in technology (I2CT), Apr 2017

Investigation of Flow Structures Around a Circular Cylinder with Notch: A Flow Visualization Analysis



K. Arunkumar and R. S. Sarath

Abstract In this paper, the results of flow visualization study and the numerical analysis on the flow around a circular cylinder with notch are presented. The notch angle is varied from 15° to 140° . All the tests are conducted in a water channel having a test section width (w) of 350 mm. Test cylinder model has a diameter of 30 mm and a depth of 180 mm. The numerical analysis is conducted using ANSYS Fluent. The Reynolds number value of 2100 is taken for both experimental and numerical analysis. Results indicate that the variation in notch angles bring notable changes in the near wake flow structures of a circular cylinder. The variation in notch angles brings considerable changes in Strouhal number and coefficient of drag. The coefficient of drag increases from 15° to 30° and then it decreases till 45° . Afterward, the C_d value shows a constant increase till 140° . Wake width and vortex formation length considerably influence the drag coefficient. In view of marine structures and building sections with similar geometry, the present study carries considerable practical significance.

Keywords Strouhal number · Coefficient of drag · Wake width · Pressure coefficient

1 Introduction

Flow past a bluff body is omnipresent both in nature and many engineering applications. Because of its practical importance in engineering community and significance of understanding fundamental fluid mechanics, flow around a circular cylinder has attracted intensive study interests. When exposed to flow, a circular cylinder is characterized by flow separation and alternating vortex shedding downstream in the near wake [1]. If the circular cylinder is free to oscillate, vortex-induced vibrations (VIVs) may take place when its vortex shedding frequency approaches the structure's natural frequency. Engineering structures or equipment with cylindrical cross sections, such

K. Arunkumar (✉) · R. S. Sarath
Department of Mechanical Engineering, Amrita Vishwa Vidyapeetham, Amritapuri, India
e-mail: akmallasseril@gmail.com

as cables of cable-stayed bridges, towers, offshore structures, heat exchangers, are usually immersed in moving fluids (air, water, etc.), and thus VIVs are likely to occur. Vortex-induced vibrations (VIVs) may lead to catastrophic damages to the structures [2]. Very few studies have concentrated on the vortex shedding behind modified circular cylinders. Literatures reports some studies in the effect of modifications on the flow characteristics around a circular cylinder by imparting different modifications like axial slit and concave rear notch, etc. [3, 4]. However, a complete flow visualization study on modified circular cylinder is not done yet. Hence, this has been taken up in the present investigation. The current work is motivated for performing a qualitative study on the flow structures around a circular cylinder with varying notch angles, and the results are taken at a Reynolds number value of 2100 (based on D). Though the flow visualization is a qualitative study, to verify the results a numerical analysis using ANSYS Fluent was performed at the same Reynolds number.

2 Experimental Setup: Flow Visualization Water Channel

The experiments were conducted in a flow visualization water table (Fig. 1), which is essentially a recirculating water channel as shown in Fig. 1. It is a tank having a dimension of 2.5×1.5 m with a depth of 150 mm. At one end of the table, two sets of aluminum disks (vanes) are located with suitable spacing between them and are rotated using a variable speed DC motor. They act as paddles and when they are rotated, they create a flow which is suitably guided to the test section where the models are placed and studied. Two guides made of fiber reinforced plastic with a height of 0.15 m are placed at a certain distance to guide the flow properly to the test section where the models are placed. The distance between the guides, i.e., the test section width was set to 350 mm. A wire mesh was placed between the guides to eliminate possible unwanted vortices present in the incoming flow. A wide range of flow speeds can be achieved in the test section by varying the speed of the DC motor. The fluid in the tank is water and fine aluminum powder particles of size 80 μm are used as tracer medium. The water bed is illuminated using powerful lamps, after dispersing aluminum particles on the water surface. Aluminum particles reflect the light enabling visualization of flow (Fig. 2).

Flow visualization pictures are captured using SONY high definition camera (Make: SONY DSR-PD150) and the video was recorded at 25 frames per second. Flow is analyzed frame-by-frame to capture the finer details of the phenomena. Water channel flow is calibrated with the rotational speed of the motor. To determine the flow velocity, a lightweight small particle was introduced on the flow bed and the time taken for it to travel 50 cm was noted. Flow velocity can be found by dividing the distance travelled by the time taken by the particle. Ten sets of readings were taken and average of these velocities were taken as the flow velocity. This was repeated for each of the rpm readings. It was found that without any wavy oscillations at the water bed, the flow velocity (U) can be obtained in the range of 0.05–0.09 m/s. Reynolds

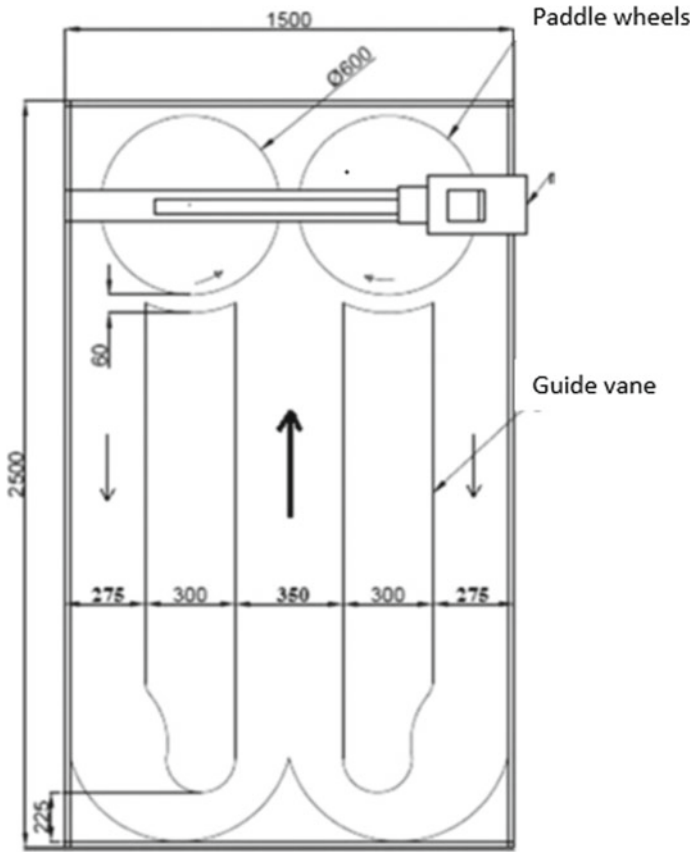


Fig. 1 Flow visualization water channel

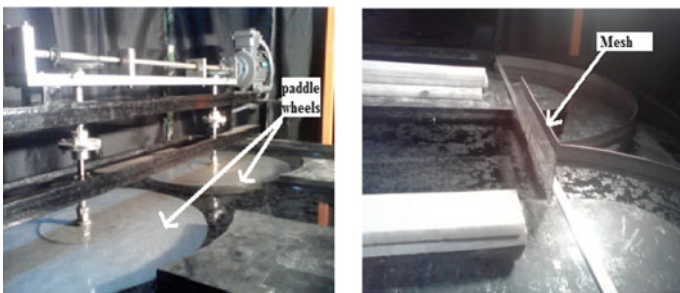


Fig. 2 Motor, paddle wheels and mesh

number is defined based on the side dimension of the test cylinder. Reynolds number range for this experimental set up is from 600 to 2800. In this Re range, flow in the test section of the channel is quiet and steady. The channel blockage ratio is 8.5% (<10%).

2.1 Models Used for the Experiment

The models used for the experiments are shown below. Six cylinders were considered with different angles for the rectangular notches. The angles considered for the notches were 15°, 30°, 45°, 90°, 120° and 140°. The diameter of the cylinder is 30 mm and the depth is 180 mm (Figs. 3 and 4).

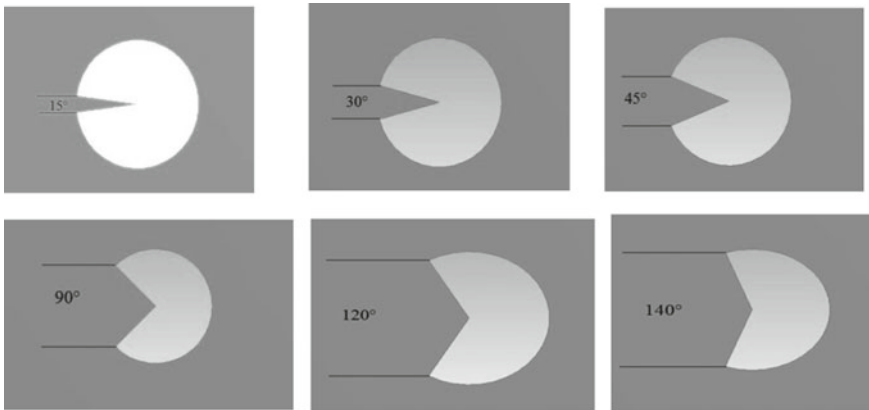


Fig. 3 Model geometry

Fig. 4 Models used for visualization



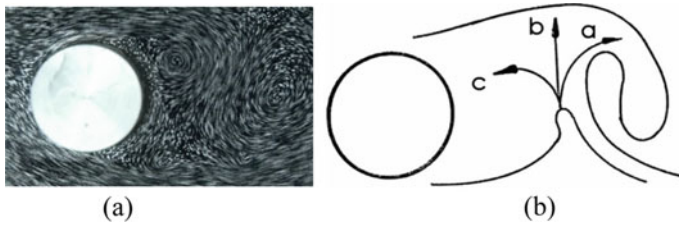


Fig. 5 Visualization image of circular cylinder and its schematic sketch

2.2 Validation: Flow Over Circular Cylinder

Before going directly into the problem of present investigation, flow over a circular cylinder is visualized and analyzed as given in Fig. 5.

Flow over a circular cylinder of diameter 30 mm is visualized at a Reynolds number of 2100. The Strouhal number was found to be 0.195 which is matching with the value reported by Troesch and Kim [5]. For this geometry, the visualized vortex shedding mechanism (Fig. 5a, b) is same that of described by Gerrard [6]. From the visualized flow pattern, salient hydrodynamic characteristics such as coefficient of drag, vortex formation length and total circulation (contained in a vortex) are found out as given in the subsequent sections.

2.3 Parameters Estimated from Flow Structures

By carefully analyzing the video frames, the l_f (vortex formation length) is calculated by the empirical relations proposed by Bearman [7]

$$l_f = C/Cpb \quad (1)$$

where C is an empirical constant varying from 1.6 to 1.8 in the Reynolds number range 1000–9000. From $(-Cpb)$, the base pressure parameter can be calculated as

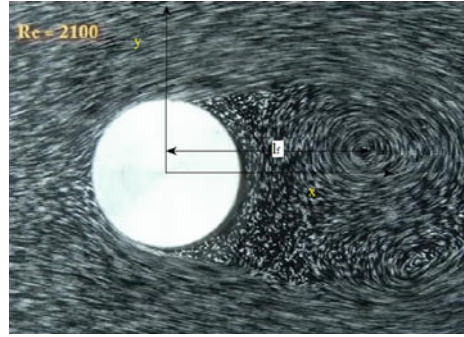
$$K = \sqrt{(1 - Cpb)} \quad (2)$$

From the value of k and Strouhal number ($St = fd/U$), the coefficient of drag (C_d) can be estimated from the following relationship

$$CD \cdot S = 0.4777K - 0.45167 \quad (3)$$

Figure 6 shows the picture of a vortex just shed from a circular cylinder at $Re = 2100$. In Fig. 6, the non-dimensional vortex formation length (l_f) is measured using MATLAB.

Fig. 6 Vortex formation length from the visualization image



Accordingly, the non-dimensional vortex formation length (l_v) is measured to be 1.2333. From that, the following values were obtained using the above-mentioned empirical relations.

Base pressure coefficient = -1.29729

Base pressure parameter = 1.51

Coefficient of drag = 1.3.

From the above results, the value of drag coefficient is matching with that of the previous experimental results.

3 Computational Details

ANSYS Fluent 14.0 was used for the computational analysis. The mesh flexibility of turbulent flow is analyzed by SST $k-\omega$ model. Second-order upwind scheme is used for convective and diffusive terms (Fig. 7 and Table 1).

Validation of the present geometry (smooth circular cylinder) has been done for coefficient of drag and Strouhal number and found to be matching with the previous experimental results [8, 9].

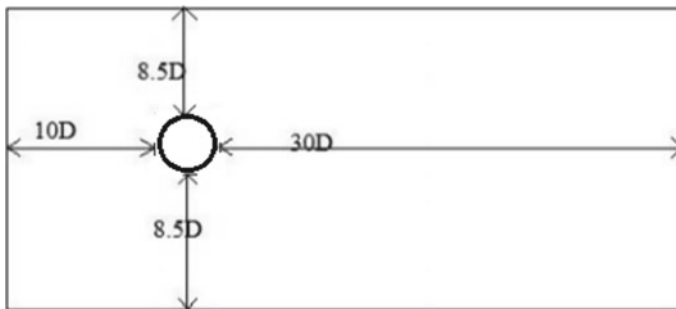


Fig. 7 Flow domain for numerical analysis

Table 1 General setup for the numerical simulation

Type	Pressure based
Time	Transient
2D space	Planar
Models	Viscous SST $k-w$, turbulence 5%
Solution methods	Scheme—SIMPLE
Gradient	Green gauss cell based
Momentum	Second order upwind
Turbulent kinetic energy	First order upwind
Specific dissipation rate	First order upwind
Time formulation	First order implicit

4 Results and Discussion

4.1 Flow Visualization Results

A close inspection into the flow structures around the new models reveals some interesting features. When compared to the smooth circular cylinder, the separation point will be delayed when the notch is introduced. The size and strength of the convected vortex are found to depend on the notch angle as well. When the separation point is varied, it is well known that it will affect the flow structure and hence the drag lift characteristics and also the wake width. The visualization images of the models with notch are given in Fig. 8.

From Fig. 8, it is clearly seen that the vortex formation length is entirely different for 45 and 140° notch angles and it can be inferred that negative pressure and wake width will be maximum for the 140° model compared to 45.

4.2 Strouhal Number Variation

From Fig. 9, the Strouhal number for a circular cylinder is 0.2. Thus, it can be inferred that the St value decreases when a notch is introduced. In experimental analysis, the Strouhal number decreases from 15° to 30° due to lower wake width. Afterward, it increases till 45°. Then, it again decreases from 45° to 140°. It is evident that the non-modified circular cylinder produces vortices with more strength compared to the other modified cylinders. Also, it can be seen that the thickness of the boundary layers from the separation point is also increases with notch angle. Interestingly, the wake width of the cylinder with 30° notch angle is found to be higher compared to the non-modified circular cylinder. For the cylinders with 90°, 120° and 140° with notch angles, flow seems to be separated at the leading edge itself. For all

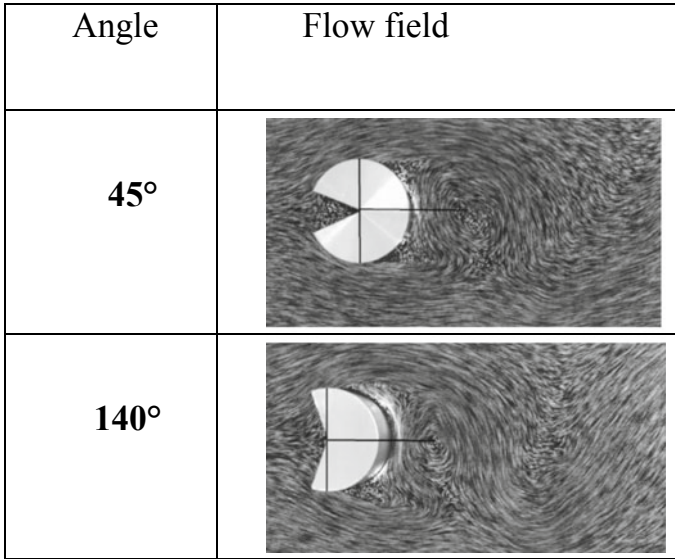


Fig. 8 Flow structure behind notch angle 45 and 140

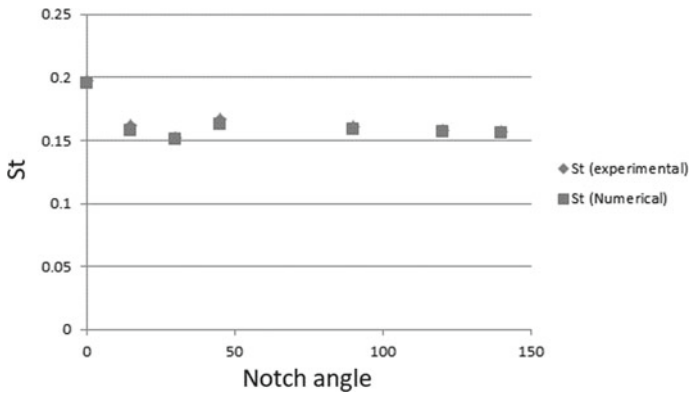


Fig. 9 Strouhal number variation

the cylinders, Gerrard’s mechanism seems to be in operation for vortex shedding. In ANSYS analysis, it shows the same trend when compared to the experimental results.

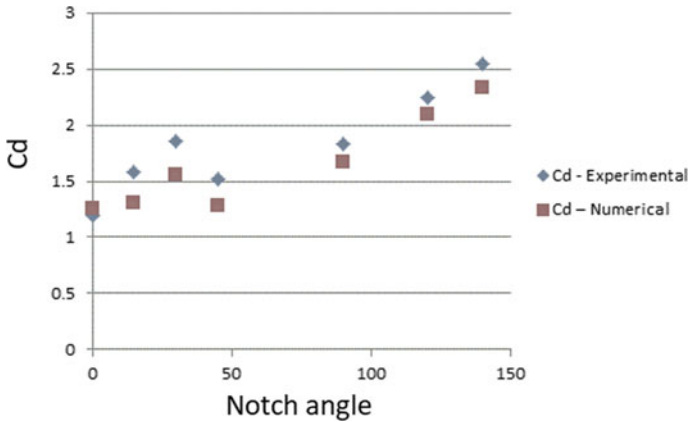


Fig. 10 Drag variation

4.3 Variation in Coefficient of Drag

The C_d value for a circular cylinder from experimental and numerical results are 1.2 and 1.26, respectively, which is lesser than that of cylinders with notches. It can be inferred that the introduction of notch increases the drag coefficient. In experimental analysis, the value of C_d first increases and then decreases. From 45° to 140° , C_d value shows a steady increase. The minimum of C_d among the six given angles is at 45° and the maximum value is at 140° . It is evident from both Figs. 9 and 10 that both C_d and St shows an inverse relationship w.r.t notch angle, obeying conventional bluff body physics.

5 Conclusions

1. Both the experimental and numerical results show a similar pattern for Strouhal number as well as coefficient of drag. When a notch is introduced in a circular cylinder, the drag increases. When the notch angle is close to the separation point, it effectively reduces the drag.
2. Wake width is lowest in 45° cylinder. As a result, negative pressure is lowest in this cylinder, so it has the lowest drag coefficient. When the vortex formation length increases, the location of shedding moves away from the cylinder and decreases the drag coefficient.
3. In the analysis, the St value decrease 15° – 30° and it increases till 45° . Then, the value decreases till 140° . The highest Strouhal number is for 45° and the lowest value is for 140° .

References

1. Krishnamoorthy S, Price SJ, Paigdoussis MP (2001) Cross-flow past an oscillating circular cylinder: synchronization phenomena in the near wake. *J Fluids Struct* 15:955–980
2. Baek H, Karniadakis G (2009) Suppressing vortex-induced vibrations via passive means. *J Fluids Struct* 25:848–866
3. Olsen JF, Rajagopalan S (2000) Vortex shedding behind modified circular cylinders. *J Wind Eng Ind Aerodyn* 86:55–58
4. Ferreira RL, Vieira EDR (2005) Flow around modified circular cylinders. *J Engenharia Termica (Therm Eng)* 5:62–67
5. Troesch AW, Kim SK (1991) Hydrodynamic forces acting on cylinders oscillating at small amplitudes. *J Fluids Struct* 5:113–126
6. Gerrard JH (1966) The mechanism of the formation region of vortices behind bluff bodies. *J Fluid Mech* 25:401–413
7. Bearman PW (1984) Vortex shedding from oscillating bluff bodies. *Ann Rev Fluid Mech* 16:195–222
8. Ajith Kumar R, Nair AK, Many HC (2015) Effect of dissimilar leading edges on the flow structures around a square cylinder. *J Pressure Vessel Technol* 137:061301–061311
9. Kwok KCS (1986) Turbulence effect on flow around circular cylinders. *J Eng Mech* 112:1181–1197

Comparative Study on Gasoline and Methanol in a Twin Spark IC Engine



A. S. Divakar Shetty, Debjyoti Sahu, J. Arthur Davis, and Ravi Kumar

Abstract In search of a viable alternative to petrol and diesel, methanol, ethanol and biodiesel play an important role. Methanol and ethanol are traditional alternatives to petrol (gasoline) because of better engine performance and reduced emission of carbon monoxide, oxides of nitrogen (NO_x), unburnt hydrocarbon (UBHC) and other harmful gases. This work represents the result of four sets of spark timings on engine performance and engine emissions when run on methanol and petrol. Exhaustive investigations are carried out on a variable compression ratio DTSi engine for both methanol and gasoline. Engine was run at full throttle and at a constant speed of 1600 RPM. The efficiency of the engine found to be enhanced with methanol fuel which has higher octane number and high laminar flame speed. Maximum efficiency was found to be $\sim 25.45\%$ and $\sim 28.7\%$ at compression ratio 10 for gasoline and methanol fuel, respectively. This is observed at $26^\circ\text{--}24^\circ$ BTDC (before top dead center) spark advance combination. Optimum compression ratio for gasoline and methanol is found to be 6.8 and 7.4, respectively, at this spark advance angle combination. Moreover, methanol fuel eventually emits lesser amount of CO, UBHC and NO_x than gasoline under all experimental combinations.

Keywords Methanol fuel · DTSi engine · Spark advance angle · Variable compression ratio

A. S. Divakar Shetty · J. Arthur Davis
Engineering Department, Ibri College of Technology, Ibri, Sultanate of Oman

D. Sahu (✉)
School of Mechanical Engineering, Kalinga Institute of Industrial Technology (KIIT), Deemed to be University, Bhubaneswar 751024, India
e-mail: debjyoti.sahufme@kiit.ac.in

R. Kumar
Department of Mechanical Engineering, Christ University, Bengaluru 560029, India

1 Introduction

Many a times methanol or ethanol shows better combustion characteristics in regular gasoline engine [1]. Unlike petroleum products, alcohol resources are mostly renewable. The alcohols such as methanol and ethanol are biologically processed using various live stocks that have starch content. Fermentation, distillation and partial distillation processes are conveniently used for this purpose. The crude methanol can also be derived from synthesis gas. Gasification of wood, straw, coal, garbage, plant stalks, etc., can produce synthesis gas (syngas) cheaply. Syngas can be availed by decomposing natural biomass. Upon chemical reaction, syngas is converted to methanol and ethanol [2]. Another tested biological way of getting methanol is the gasification of rice husk subjected to partial oxidation followed by separation and purification [3].

Methanol and ethanol have similar research octane number of 109 (ideally 100 for gasoline) but motor octane number of 90 and 89, respectively (85–88 for commercial gasoline). Methanol– or ethanol–gasoline blend can readily (100% soluble) be used in internal combustion engine in any proportion [4, 5]. However, ignition timing is a very important parameter in achieving complete combustion, and ignition timing can be optimized. Dubey et al. reported performance of single spark, twin spark and triple spark engine [6]. They claimed that multiple spark shows better efficiency than a single spark engine due to faster flame speed. However, placing more number of spark plug is not feasible if the engine size is small. Khan and Shaikh emphasized that increase in efficiency is noticeable only at higher load in case of a multiple spark engine [7]. Zareei and Kakaee studied spark advance from 40° BTDC to 10° ATDC (after top dead center) on a high speed engine (3400 RPM) [8]. They found optimum spark advance angle of 31° BTDC for a single spark.

In case of a two spark plug engine, spark is initiated in two different locations, few microseconds apart, within the combustion chamber. Revolution of crankshaft for one cycle is 720° ; at the end of compression stroke, ideally, the spark should happen (at 360°). However, spark is advanced by $20\text{--}40^\circ$ (i.e., instead of 360° , it happens at $320\text{--}340^\circ$ rotation of the crankshaft) to provide sufficient time for combustion and also to avoid autoignition [9–12]. If combustion is advanced before TDC, compression (stroke) work requirement increases. If combustion process is delayed by retarding the spark timing, peak cylinder pressure achieved is less; hence, net power output is less. Thus, the optimum timing to produce maximum brake torque occurs when spark is advanced by $20\text{--}40^\circ$. In this effort, an electronic circuit to manage the spark timings is employed; it is an addition to the existing engine system [13–15]. Many in the research community have thought through the usage of methanol and gasoline in pure form as fuel for Otto cycle engine [16, 17]. Many showcased superior results for twin spark ignition in terms of performance and exhaust emissions [17, 18]. However, finding the effect of compression ratio in twin spark engine is crucial. Here, the engine was tested for four different spark advance angles between 32° and 20° at compression ratio 6, 8 and 10 to obtain the optimal spark timing for best performance and least emission. Here, methanol combustion is

compared to gasoline combustion in the same engine vis-à-vis its emission as gasoline is the most popular petroleum fuel. Now, to change from gasoline to methanol, the effect of compression ratio and spark advancement is presented in this work. This paper would show a simple methodology for optimizing compression ratio as well as spark advance angle for a twin spark engine vis-à-vis its efficiency.

2 Experimental Methodology

The performance of the engine and emission pattern was measured on a computerized, four-stroke, single-cylinder engine at compression ratio of 6:1, 8:1 and 10:1. The engine was run at the constant speed of 1600 RPM under full throttle condition. Here, the cylinder head is remodeled by the supplier to vary the compression ratio. Specifications of the engine are shown in Table 1. The engine setup was developed with tunable spark timing and twin spark plug arrangements. Photograph of this setup is shown in Fig. 1. It is observed in the literature that methanol consumption is higher than gasoline near full load [4, 5]. So, it was needed to modify the carburetor main jet for methanol fuel operation [19]. Ethanol is a regulated item hence not considered in this work for trial. This work is aimed to attain homogeneous combustion process at different compression ratios (6:1, 8:1 and 10:1) and generate the performance characteristics curves and exhaust emission pattern. This twin spark ignition was enabled by an electronic circuit which is already reported [19].

Engine emission was measured using an exhaust gas analyzer. Commercial gasoline is used for which calorific value is assumed to be 44 MJ/kg. Reagent grade methanol is used without purification for which calorific value is assumed to be 23 MJ/kg.

Table 1 Engine specifications

S. No.	Particulars	Details
1	Make	KIRLOSKAR
2	Type	Four stroke, single cylinder
3	Displacement	330 cc
4	Bore and stroke	76 mm, 72.6 mm
5	Rated power	6.02 kW at 1800 rpm
6	Compression ratio	6:1–12:1
7	Ignition	Twin spark
8	Spark plug	12 mm × 1 mm



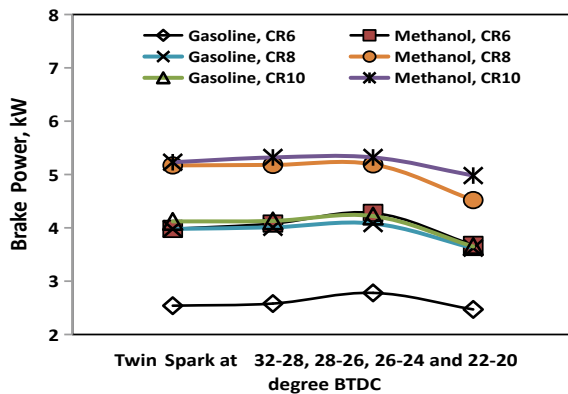
Fig. 1 Engine test rig with water cooling and computer-based data acquisition system

3 Results and Discussion

3.1 Engine Performance

Towards the end of the compression, spark initiates the combustion in gasoline engine. Two spark plugs in Digital Twin Spark ignition (DTSi) system are located strategically to result fast and efficient combustion. Higher the speed of the engine, higher should be the spark advance angle to avail optimum combustion duration [16]. Here, the brake power developed by the engine for different spark advance angle sets at three different compression ratios is as shown in Fig. 2. Overall trend emphasizes that higher compression ratio yields more power, and methanol can generate more power than gasoline in the same engine. Interestingly, at compression ratio

Fig. 2 Variation of brake power with respect to spark timings



6, gasoline yields least power (average ~2.59 kW) but methanol yields ~54% more power (average ~4 kW). However, increasing compression ratio from 8 to 10 does not enhance the power output in case of gasoline. The reason can be similar level of completeness in combustion [8]. It can be ensured by measuring the unburnt hydrocarbon emission from the engine.

The brake power values at different sets of spark timings show a trend. It indicates that maximum BP occurs at compression ratio of 10 for gasoline fuel. Maximum BP generated is ~4.13 kW while twin spark initiated at 28°–26° BTDC. When methanol is the fuel, it provides higher power of 5.32 kW at the same pair of spark timings. At 26°–24° BTDC, power output maximizes to 5.38 kW. These results show that maximum brake power is generated if twin spark is initiated between 28° and 24° BTDC. Power output declines if spark is initiated at 22°–20° BTDC. Few reasons can be attributed to high power output at the 26°–24° BTDC combination. Advancing spark up to 32° is not helpful because the compression is incomplete [7]. Now, if the advancement is ~26°, combustion duration is sufficient to yield maximum power. Thus, balancing the work required during the compression stroke in a spark advanced environment might be another reason to generate optimum brake power.

Interestingly, methanol and gasoline respond differently to change in spark advance angle. Brake-specific fuel consumption variation is represented in Fig. 3. Minimum fuel consumption is observed for gasoline fuel when run at high compression ratio of 10 (average ~383 g/kWh). Therefore, at high compression ratio, high thermal efficiency is expected [11]. Interestingly, SFC is hardly changing by the change in the spark advance angle. If the compression ratio is 8, then gasoline consumption increases when the advance angle is down to 22°–20° BTDC combination.

Predictably, fuel consumption is maximum for methanol when run at low compression ratio of 6. Because despite running at low compression ratio, methanol yields substantial amount of power (average ~4 kW) as shown in Fig. 2. At this compression ratio, fuel consumption decreases when ignition advance is reduced from 32° to 28°

Fig. 3 Variation of brake-specific fuel consumption with respect to spark timings

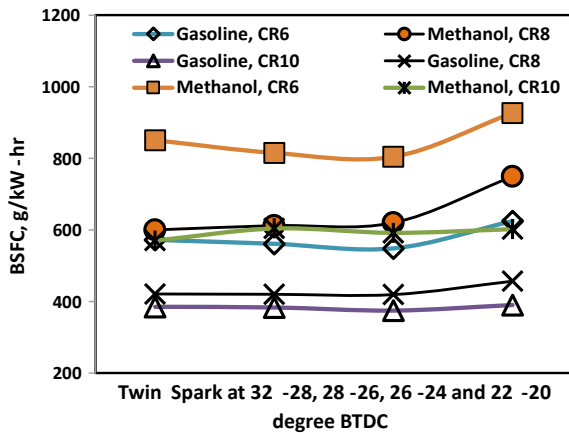
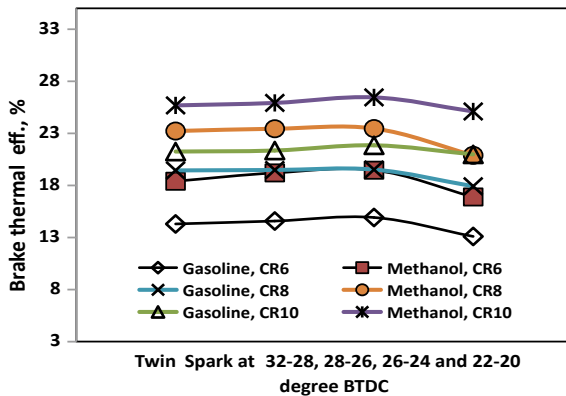


Fig. 4 Variation of BTE with respect to spark timings



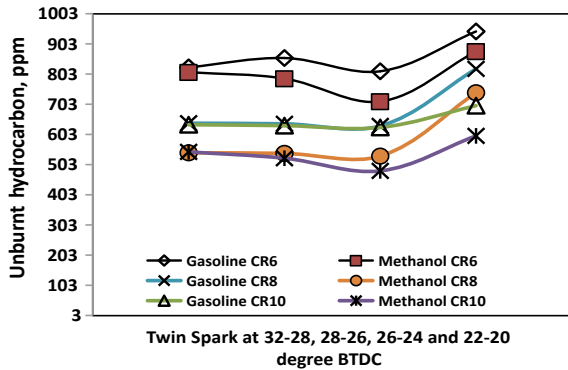
BTDC combination to a lower value. Therefore, both 28° – 26° and 26° – 24° BTDC combinations are advantageous. However, if the ignition advance is brought to 22° – 20° BTDC combination, then the trend is changed. When the compression ratio is increased to 8, then the methanol consumption decreases than compression ratio 6; hence, better efficiency can be expected at high compression ratio. When compression ratio is raised to 10, both methanol and gasoline fuel consumption decrease further. Moreover, at compression ratio ~ 10 , specific fuel consumption does not change much even though the spark advance angle is changed between 32° and 20° (Fig. 3).

Brake thermal efficiency (BTE) can be considered as actual efficiency as it denotes the actual power available at the shaft with respect to the energy content of the fuel [11]. Variation in spark timing is affecting brake thermal efficiency of engine. The pattern is shown in Fig. 4. For gasoline, the highest BTE value is 14.92%, 19.52% and 21.85% at compression ratio 6, 8 and 10, respectively. This is obtained in this engine at 26° – 24° BTDC spark advance combination. Therefore, increasing compression ratio from 6 to 10 increases the BTE value by $\sim 45\%$. While methanol is used as fuel in the same engine, the highest brake thermal efficiency observed are 19.46%, 23.46% and 26.45% at compression ratio 6, 8 and 10, respectively (at 26° – 24° BTDC). Therefore, increasing compression ratio from 6 to 10 enhances the brake thermal efficiency by $\sim 36\%$. Practically, there is huge effect of compression ratio in combustion and power output.

3.2 Engine Emission

To establish the superiority of methanol over gasoline, it is important to measure its emission along with power output. Measurement of unburnt hydrocarbon can enlighten on completeness of combustion. If methanol can be efficiently burnt using a DTSi engine, it will also lessen the probability of aldehyde formation, which anyway

Fig. 5 Variation of UBHC with respect to spark timings



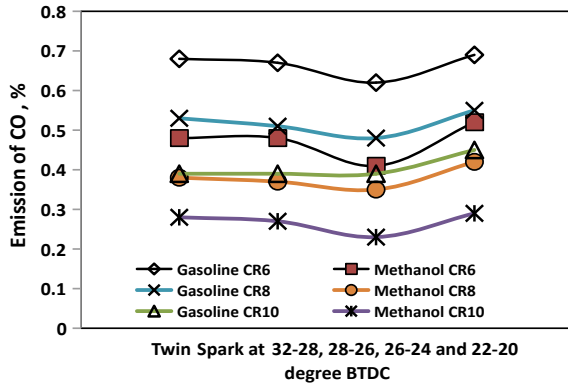
is very less [16]. Gasoline once combusted at compression ratio 6 yields least power which might be due to incomplete combustion. As seen in Fig. 5, UBHC emission is maximum at this compression ratio. For methanol fuel also, this trend is visible.

Unburned hydrocarbon (UBHC) is a pollutant coming out in exhaust because there is insufficient time available for combustion or that portion of fuel did not come in contact of a flame. Comparisons of gathered experimental results are clearly indicating that combustion at 22°–20° BTDC spark timings generates higher amount of UBHC at all compression ratios. Initiating combustion process near TDC is not beneficial because the required pressure inside the combustion chamber might not be favorable when the piston is completing compression stroke [20, 21]. Enhanced combustion chamber temperature and likely uniform heat distribution can reduce HC emission for the compression ratio 8 and 10, respectively. At compression ratio 10 for gasoline, there is hardly any change in UBHC emission with respect to spark advance angle. For the same reason, it shows less variation in brake thermal efficiency (Fig. 4). From efficiency and power output point of view, both 28°–26° and 26°–24° BTDC spark advance combinations seem to result the same. Now, the UBHC emission result shows that the spark ignition pairs of 26°–24° BTDC are marginally better than 28°–26° BTDC. Therefore, 26°–24° BTDC combination is optimum spark initiation time for this engine.

As per emission norms, the most significant combustion gas is carbon monoxide (CO). The role of spark timings on CO emission at different compression ratios for gasoline and methanol is as shown in Fig. 6. Similar to UBHC emission, CO emission is highest for gasoline combustion at compression ratio 6, whereas the minimum CO emission happens at compression ratio 10. Probable reasons for less CO emission are combustion of fuel in homogeneous mixture and supply of correct amount of air required for combustion reaction [16–18].

When twin spark is generated at 26°–24° BTDC, CO emission recorded is 0.41% for methanol and 0.62% for gasoline fuel, respectively (compression ratio 6). Methanol (CH₃OH) fuel emits lesser CO in all combinations than gasoline, and the pattern is shown in Fig. 6. Predictably, the least CO emission is visible if methanol is burnt at compression ratio 10. On an average scale, CO emission is reduced from

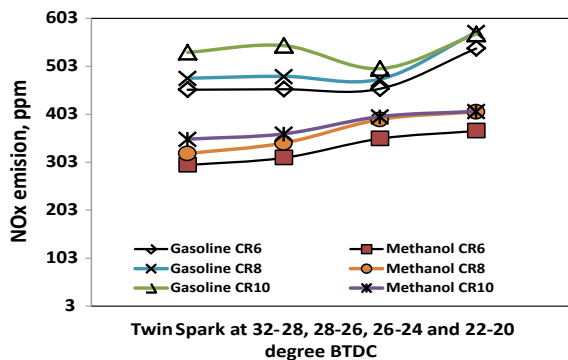
Fig. 6 Variation of CO with respect to spark timings



~0.47 to ~0.27% when compression ratio is hiked from 6 to 10. However, for gasoline when compression ratio is hiked from 6 to 10, the CO emission reduces from ~0.66 to ~0.4% on average. Comparing gasoline and methanol fuel, it is obvious that methanol is a cleaner fuel than gasoline [21–23].

Emission of NO_x is highly dependent on the temperature and pressure surge inside the combustion chamber of the engine. Variation of the NO_x emission at different spark timing combinations is plotted together and presented in Fig. 7. Therefore, if the compression ratio is high, NO_x emission will also be high. Here, both methanol and gasoline are burnt at similar compression ratio, but uneven temperature rise due to incomplete combustion might have a dominant effect here. NO_x emission significantly dropped for methanol compared to gasoline for all twin spark combinations (Fig. 7). Flame velocity of methanol (0.492 m/s at 300–600 K and 100 kPa) is higher than gasoline (for isoctane 0.465 m/s at 300–600 K and 100 kPa) [24]. Methanol has high heat of vaporization ~1104 kJ/kg (for gasoline ~350 kJ/kg) which might be the reason for low cylinder temperature and reduction in NO_x emission [22, 25]. Maximum NO_x emission is observed at 22°–20° BTDC spark combination under all test conditions. Initiating spark very close to TDC might lead to uncontrolled

Fig. 7 Variation of NO_x with respect to spark timings



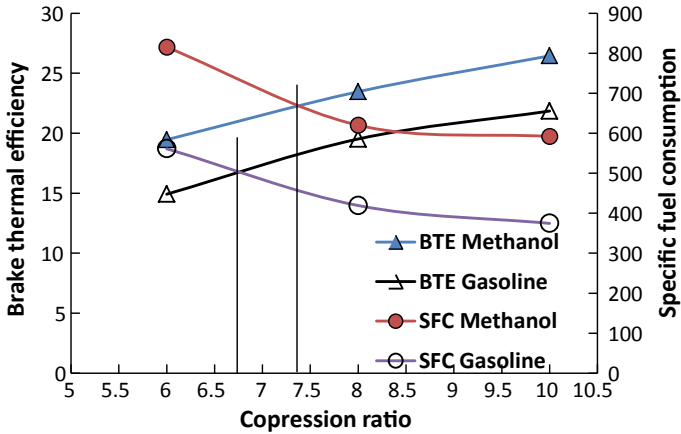


Fig. 8 Variation of efficiency and fuel consumption with respect to compression ratio

cylinder temperature and subsequent increase in NO_x emission [17, 18, 20]. Therefore, reducing the spark advance angle may cause harm to the engine especially if gasoline is used as fuel.

Finally, it is important to decide on the compression ratio at which the engine should be running if methanol is the alternative fuel. Since twin spark at 26°–24° BTDC results the best efficiency and lowest emission, optimization of compression ratio is executed at this spark timing. In Fig. 8, both brake thermal efficiency and specific fuel consumption are plotted. For methanol, this DTSi engine can be run at compression ratio of 7.4, whereas for gasoline, the engine can be run at compression ratio 6.8. Theoretically, better compression ratio leads to higher efficiency which is the case here. Methanol combustion results in lower emission even at higher compression ratio; thus establishes methanol as a competitive alternative fuel.

4 Conclusion

The effect of spark timings on engine performance and emission characteristics is recorded and analyzed at three compression sets in an electronically controlled twin spark IC engine. Engine was run on commercial gasoline and reagent grade methanol in laboratory. The engine performance parameters and emission characteristics are observed at several twin spark combinations between 32°–28° and 22°–20° BTDC. By spark advancement engine is found to be more efficient and emission of carbon monoxide, unburnt hydrocarbon and oxides of nitrogen decreased to a considerable level. But this trend did not continue when the engine had twin spark at 22°–20° BTDC combination. Analyzing the results at all spark angles 26°–24° BTDC combination can be considered as optimum spark timing with maximum efficiency and minimized emission of harmful gases. Comparing the efficiency and fuel

consumption, optimum compression ratio for gasoline and methanol is found to be 6.8 and 7.4, respectively.

References

1. Vancoillie J, Demuynck J, Sileghem L, de-Ginste MV, Verhelst S, Brabant I (2013) The potential of methanol as a fuel for flex-fuel and dedicated spark ignition engines. *Appl Energy* 102:140–149
2. Nakagawa H, Harada T, Ichinose T, Takeno K, Matsumoto S, Kobayashi M (2007) Biomethanol production and CO₂ emission reduction from forage grasses, trees and crop residues. *Jpn Agric Res Q* 41:173–180
3. Li J, Gong CM, Su Y, Dou HL, Liu XJ (2010) Effect of injection and ignition timings on performance and emissions from a spark-ignition engine fueled with methanol. *Fuel* 89:3919–3925
4. Yousufuddin S, Mehdi SN (2008) Effect of ignition timings, equivalence ratio, and compression ratio on the performance and emission characteristics of variable compression ratio SI engine using ethanol-unleaded gasoline blends. *IJE Trans B Appl* 21:97–106
5. Canakci M, Ozsezen AN, Alptekin E, Eyidogan M (2013) Impact of alcohol-gasoline fuel blends on the exhaust emission of an SI engine. *Renew Energy* 52:111–117
6. Dubey A, Pareta A, Sharma P (2014) Study of multiple spark ignition engines with single spark ignition engines on the basis of engine efficiency and emission characteristics size. *Int J Curr Eng Technol* 2014(3):14–17
7. Khan TA, Shaikh R (2016) Performance and emission analysis of two stroke dual sparkplug SI engine. *IOSR J Mech Civ Eng* 2016:50–53
8. Zareei J, Kakaee AH (2013) Study and the effects of ignition timing on gasoline engine performance and emissions. *Eur Transp Res Rev* 5:109–116
9. Wu X, Daniel R, Tian G, Xu H, Huang Z, Richardson D (2012) Duel-injection: the flexible, bi-fuel concept for spark-ignition engines fueled with various gasoline and biofuel blends. *Appl Energy* 88:2305–2314
10. Chen RH, Chiang LB, Wu MH (2010) Gasoline displacement and NO_x reduction in an SI engine by aqueous alcohol injection. *Fuel* 89:604–610
11. Elfasakhany A (2015) Investigations on the effects of ethanol-methanol-gasoline blends in a spark-ignition engine: performance and emission analysis. *Eng Sci Technol* 18:713–719
12. Otto NA (1887) Gas motor engine. US patent application US 365701
13. Antony AJ, Shetty DAS (2017a) Performance and emission characteristics of digital twin spark ignition engine working on gasoline–methanol blends. *Int J Res Eng Appl Manag* 3(9):87–92
14. Antony AJ, Shetty DAS (2017b) Methanol as alternative fuel in high compression ratio twin spark ignition SI engine. *Int J Mech Eng Technol* 8(12):1172–1179
15. Wani MM (2018) Thermodynamic evaluation of methanol as an alternative fuel to gasoline in a single cylinder spark ignition engine. *Energy Power* 8(2):35–45
16. Kowalewicz A (1993) Methanol as a fuel for spark ignition engines: a review and analysis. *Proc Inst Mech Eng* 207:43–52
17. Fortea C, Bianchi GM, Corti M, Fantoni S (2015) Evaluation of the effects of a twin spark ignition system on combustion stability of a high performance PFI engine. *Energy Procedia* 81:897–906
18. Li WY, Li Z, Xie KC (2009) The development of methanol industry and methanol fuel in China. *Energy Sources Part A* 31:1673–1679
19. Antony AJ, Shetty DAS (2018) Combustion analysis of single cylinder twin spark ignition engine at different gasoline-methanol blends. *Pollut Res* 37(1):155–159
20. Olah GA, Goepfert A, Prakash GKS (2006) *Beyond oil and gas: the methanol economy*. Wiley-VCH

21. Ward PF, Teague JM (1996) Fifteen years of fuel methanol distribution. In: XI international symposium on alcohol fuels. www.energy.ca.gov/papers/CEC-999-1996-017.PDF
22. Richard L, Bechtold MB, Goodman, Timbario TA (2007) Use of methanol as a transportation fuel. Prepared for The Methanol Institute. www.methanol.org/wp-content/uploads/2016/06/Methanol-Use-in-Transportation.pdf
23. Ramtilak A, Joseph A, Sivakumar G, Bhat S (2005) Digital twin spark ignition for improved fuel economy and emissions on four stroke engines. SAE Tech Pap 26. <https://doi.org/10.4271/2005-26-008>
24. Gulder OL (1983) Laminar burning velocities of methanol, isoctane and isoctane/methanol blends. *Combust Sci Technol* 33:1–4, 179–192
25. Jessup RS (1935) Heats of vaporization of eight gasolines. https://nvlpubs.nist.gov/nistpubs/jres/15/jresv15n3p227_A1b.pdf
26. Peng Z (2008) New orientation and new progress of fuel methanol industry in China, and new thinking on the industry. In: 17th international symposium on alcohol fuels, Taiyuan

Coal Water Slurry Flow in Pipelines Using Homogeneous Equilibrium Model



Anupama Routray, Aditya Abinash, M. K. Padhy, and Sudhansu S. Sahoo

Abstract This work is focused on the computational analysis of coal water slurry (CWS) flow in pipelines, mostly encountered in power plant sectors. Homogeneous equilibrium model has been adopted for two phase flow analysis for this slurry flow presented in this paper. The best bimodal mix having a coal concentration in the range of 58–70% by weight has been considered in the numerical simulation. Different diameters of the tube, velocity in pipelines are varied as well to obtain pressure drop. Velocity contours are obtained and analyzed for the mention parameters variation.

Keywords CWS · Homogeneous equilibrium model · Coal concentration · Velocity contours

1 Introduction

Consequent on depletion of oil reserve, alternate source of energy production from biomass [1] and biodiesel [2] has been taken up. But the availability and efficiency of all these resources in comparison with coal are not economical and aplenty. Hence, industries opt for coal as cheap a source of energy production, and extensive research has been taken up in the field of CWS [3].

Low viscosity and high coal loading of coal particles are the main guiding factors for the efficiency of CWS [4]. High concentrated CWS involves inter-particle interaction which leads to high viscosity and creates problem during the pipeline transportation [5]. In order to reduce the interaction between the particles, different additives like natural additive [6, 7] have been tried to increase the rheological behavior of CWS [8]. Many researchers used chemical additives [9–13], and also, few researchers used mixture additive [14, 15] in CWS for enhancing the stability and reducing the viscosity of the slurry. After the preparation of CWS, a computational fluid behavior

A. Routray (✉)
ITER, SOA Deemed to be University, Bhubaneswar, Odisha, India
e-mail: anupamaroutray@soa.ac.in

A. Abinash · M. K. Padhy · S. S. Sahoo
College of Engineering and Technology, Bhubaneswar, Odisha, India

through the pipeline has been studied by some researchers to know the pressure drop effect by varying the diameter of the pipe as well as varying the velocity of the slurry [16–18].

In the present study, data has been taken from the rheological behavior of bimodal CWS mixture additive. The slurry has attained a concentration range of 58–70% by weight with a viscosity range of 0.05–1.12 Pa s [15]. An Euler–Lagrange single phase homogeneous equilibrium model is used to numerically simulate the flow of slurry by varying diameter of pipe as well as varying the velocity of slurry for analyzing the pressure drop and velocity distribution. Velocity contours are obtained and analyzed for the mention parameters variation.

2 Mathematical Modeling and Simulation Approach

2.1 Homogeneous Equilibrium Model (HEM)

HEM model considers the two fluids to be mixed intimately such that they can be considered as a homogeneous fluid with suitable average properties. Variation in these three potential variables will promote momentum, energy and mass transfer between the phases so that equilibrium is reached. Thus, the single phase equations for continuity, momentum and energy can be applied to the two-phase mixture by merely replacing the fluid properties with the mixture properties.

Mathematical $k-\varepsilon$ Realizable function model consists of continuity equation and momentum equation. Based on the applications, commercial CFD Ansys Fluent 16.0 code is implemented to solve Navier–Stokes equation as well as other auxiliary equations.

The set of assumptions related to governing Hagen–Poiseuille Flow are:

- Steady Flow ($\partial/\partial t = 0$)
- Swirl component of the fluid velocity is zero ($v_\theta = 0$)
- The flow is axisymmetric ($\frac{\partial}{\partial \theta} = 0$).

Continuity equation

$$\frac{1}{r} \frac{\partial(r v_r \cdot \rho_r)}{\partial r} + \frac{\partial(v_z \cdot \rho_z)}{\partial z} = 0 \quad (1)$$

Momentum equation

$$\begin{aligned} v_r \frac{\partial(v_r \cdot \rho_r)}{\partial r} + v_z \frac{\partial(v_r \rho_r)}{\partial z} &= \rho_r g_r - \frac{\partial p}{\partial r} \\ &+ \frac{\partial}{\partial r} \left(\frac{1}{r} \frac{\partial r v_r \cdot \mu_r}{\partial r} \right) + \frac{1}{r^2} \frac{\partial^2(v_r \cdot \mu_r)}{\partial \theta^2} + \frac{\partial^2(v_r \cdot \mu_r)}{\partial z^2} \end{aligned} \quad (2)$$

$$\begin{aligned}
v_r \frac{\partial(v_z \rho_z)}{\partial r} + v_z \frac{\partial(v_z \rho_z)}{\partial z} &= \rho_z g_z - \frac{\partial p}{\partial z} \\
+ \frac{1}{r} \frac{\partial}{\partial r} \left(r \frac{\partial v_z \cdot \mu_z}{\partial r} \right) + \frac{1}{r^2} \frac{\partial^2(v_z \cdot \mu_z)}{\partial \theta^2} + \frac{\partial^2(v_z \cdot \mu_z)}{\partial z^2} &
\end{aligned} \quad (3)$$

Darcy's equation

$$\Delta p = \frac{f \cdot L \cdot V^2}{2gD} \quad (4)$$

2.2 Geometrical Details and Modeling

Flow characteristics of CWS with high solid concentrations in pipelines are investigated using commercial computational fluid dynamics (CFD). CFD tool ANSYS Fluent 16.0 is used to carry out the simulations with three different pipes diameters 50 mm, 100 mm and 150 mm having fixed 3 m length of pipe. Average specific gravities are 1.3, 1.33, 1.38 and 1.39 having viscosities 0.05747, 0.1261, 0.5885 and 1.12 Pa s, respectively. Homogeneous equilibrium model (HEM) is used for the performance of flow characteristics of mixture in pipelines. $k-\varepsilon$ scheme with realizable wall function model is used for solving transport equations and various model constants. First-order upwind scheme is implemented for solving pressure correction and momentum, turbulent dissipation rate and turbulent kinetic energy. Simulation of CWS can be done by using AMG segregated solver. Pressure-velocity coupling is carried out by using SIMPLE scheme. Convergence criteria of solution parameter are considered as 10^{-6} .

2.3 Rheological Properties of CWS

High-ash coal sample used for the CFD analysis. The particle size used for this study is the mixture of fine and coarse particle. Coarse particle size is $-300 \mu\text{m} + 212 \mu\text{m}$, and fine particle size is $<38 \mu\text{m}$. Density of high-ash coal sample is considered as 1.6 g/cc. Rheological behavior of the CWS has been carried out using HAAKE rheo-stress rheometer. At low concentration, the slurry behaves Newtonian behavior, and at higher concentration, the flow behavior is non-Newtonian behavior.

Concentration to density equation

$$C_w = \frac{\rho_f(\rho_m - \rho_w)}{\rho_m(\rho_f - \rho_w)} \quad (5)$$

Table 1 Detail data of high-ash coal with concentration, viscosity and density

High-ash coal	Concentration (%)	Viscosity (Pa s)	Density (kg/m ³)
(212–300 μm) + (<38 μm)	58	0.05747	1300
	62	0.1261	1330
	68	0.5885	1380
	70	1.12	1390

where C_w concentration of the slurry in percentage

ρ_f Density of coal

ρ_w Density of water

ρ_m Density of slurry

2.4 Numerical Simulation

Simulations can be done by using commercial CFD tool Ansys Fluent 16.0. Various pipe diameters such as 50, 100 and 150 mm are considered for simulations with a fixed 3 m pipe length. The solid concentrations (by weight) of the coal are taken as 58, 62, 68 and 70% with viscosities 0.05747, 0.1261, 0.5885 and 1.12 Pa s. The densities of the slurry having the above solid concentrations are 1300, 1330, 1380 and 1390 kg/m³. Single phase homogeneous $k-\varepsilon$ Realizable function model is implemented for flow characteristics of CWS in pipeline. This is selected for calculation of eddy viscosity and transportation equation.

2.5 Boundary Conditions

Boundary conditions are considered at inlet, outlet and wall. Inlet boundary conditions are applied for getting fully developed flow in horizontal pipeline. Outlet boundary condition is applied at 3 m apart from inlet. The diameters are 50, 100, 150 mm, and velocities are varied from pressure–velocity coupling is done by using from 2 to 5 m/s in each of the pipe diameters. Inlet pressure is assumed to be same as atmospheric pressure. No slip condition is used on the wall of pipe. Roughness constant of inner part of pipe is considered as 0.5 during simulation. *First-order upwind* scheme is applied for pressure correction and for solving of turbulent dissipation rate and turbulent kinetic energy (Fig. 1).

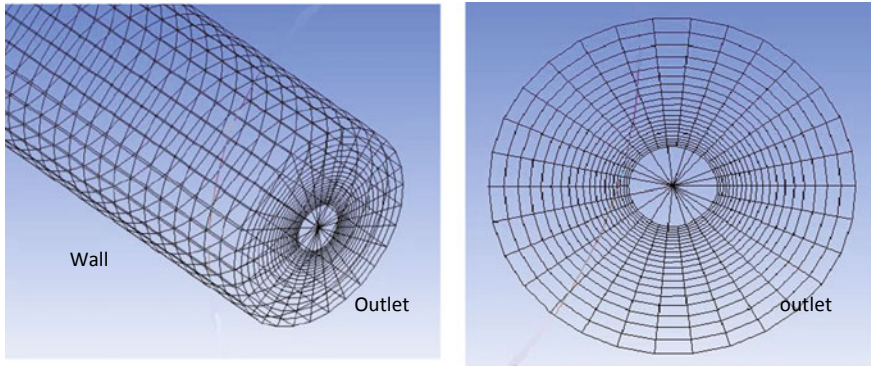


Fig. 1 Mesh contour of the pipe (isometric and side view)

3 Results and Discussion

Numerical simulations are carried out on 50, 100 and 150 mm diameter pipe. Velocity of the flow is varied from 2 to 5 m/s in 3 m length of pipeline. The solid concentrations of slurry are 58, 62, 68, 70% with particle size in the bimodal sample, i.e., (212–300 μm) and $-38 \mu\text{m}$ [15]. Mostly, pressure drop is obtained for the mentioned parameters and analyzed in this section.

3.1 *Effect of Velocity and Diameter Variation on Pressure Drop*

Figure 2 shows the variation of pressure drop with the velocity for varying pipe diameters, i.e., 50, 100 and 150 mm. According to Darcy's equation, it is seen that pressure drop falls with increase in pipe diameter. Minimum pressure drop is observed as 2377.47 Pa for a velocity 2 m/s with 150 mm pipe diameter, whereas maximum pressure drop is observed as 49,204.2 Pa for a velocity of 5 m/s with 50 mm diameter. From the equation, it is seen that as the solid concentration increases, the slurry density increases. Pressure drop in pipeline also rises nonlinearly with rise in velocity and density for all different pipe diameters. Therefore, pressure drop in pipeline rises with rise in solid concentration for varying the pipe diameter. In Fig. 2a, the percent reduction in pressure drop is found to be 66.8% and 28.89% for pipe diameter 50–100 mm and 100–150 mm at velocity, respectively, 5 m/s. The percentage reduction in pressure drop increases at higher velocity as compared to lower velocities whereas decreases with increase in diameter. From Fig. 2b, pressure variation for 50 mm diameter indicates a steady increase in pressure as the inlet velocity increases in between 2 and 4 m/s range. But a sudden increase is observed when velocity increases

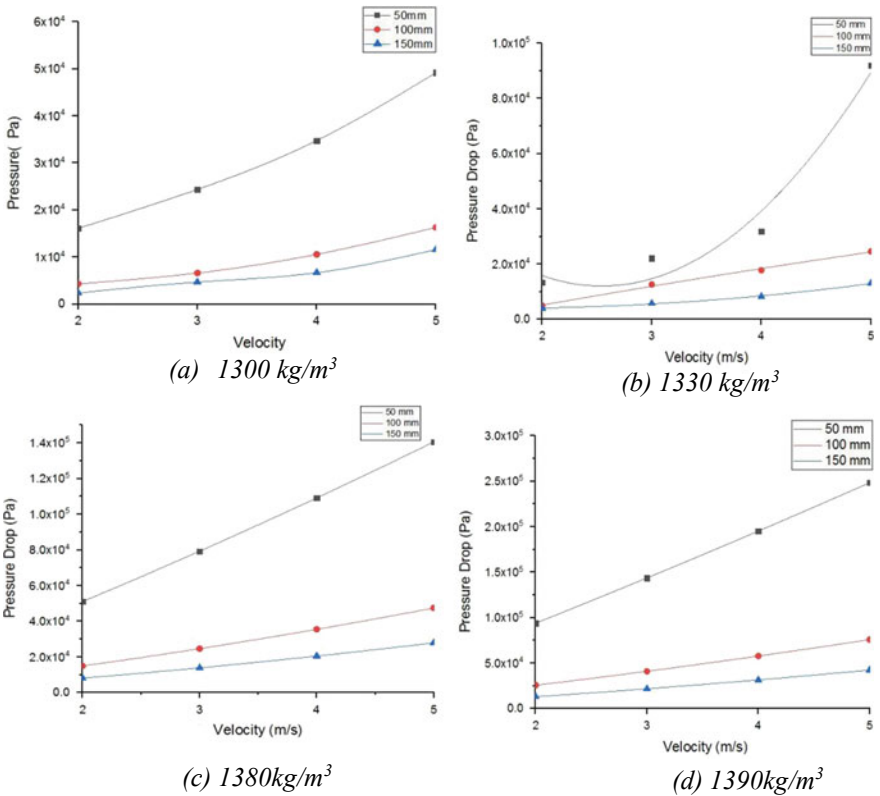


Fig. 2 Variation of pressure drop with velocity at various diameter

to 5 m/s. This is because of the increase in velocity at constant viscosity results increase in Reynold’s Number and it exceeds beyond the laminar range.

From Fig. 2, it is seen that pressure drop increases with increase in slurry density. This is because of the rise in viscosity which results in decrease in Reynold’s number as well as increase in shear stress. Increase in value of shear stress results in increase in pressure drop.

Figure 3 explains the variation of pressure drop depends upon certain parameters such as density, diameter and velocity. As the diameter increases, according to Darcy’s equation, pressure drop decreases. Similarly, as the inlet velocity increases, pressure drop is observed to be increasing at a steady rate. But in case of density 1330 kg/m^3 (Fig. 3b), for velocity range 2–4 m/s, steady rise in pressure drop is maintained. But, as described above, when the velocity increases from 4 to 5 m/s, there is a sudden increase in pressure drop observed due to increase in Reynold’s number. This is because as the Reynold’s number increases, shear stress induced at the wall also increases and causes increase in pressure at the wall. Also, density

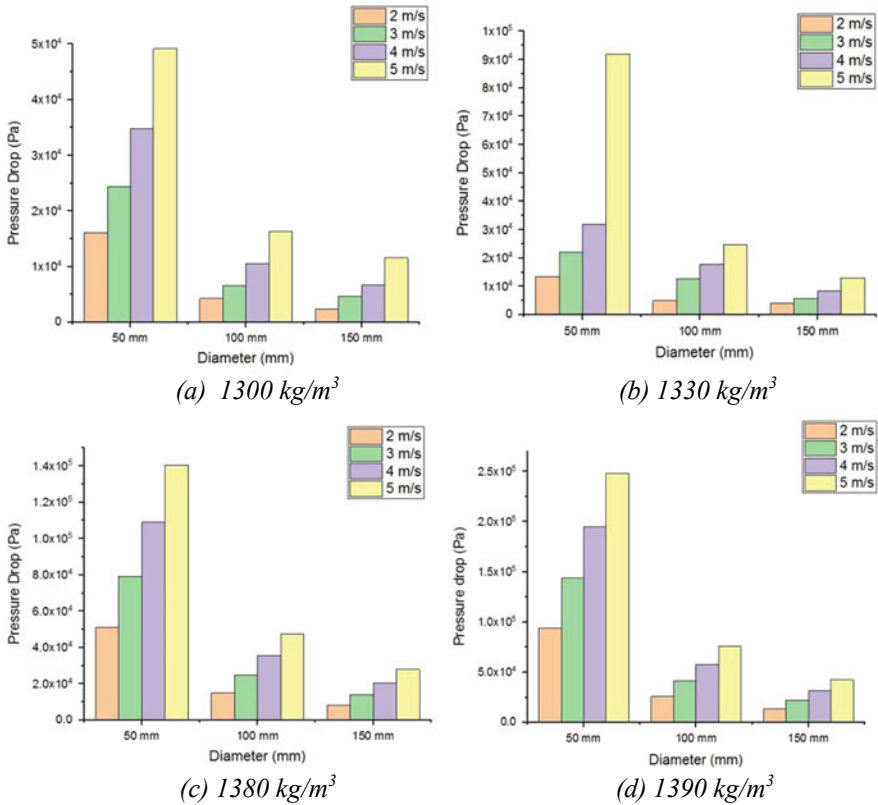


Fig. 3 Effect of various diameters with increase in velocity on pressure drop

plays an important role in increase in pressure drop, as it increases with increase in density.

3.2 Concentration Distribution Effects on Velocity

Figure 4 explains the velocity contour formed due to the variation of concentration on constant diameter 50 mm and constant inlet velocity 5 m/s. From Fig. 4, it is seen that, in case of homogeneous flow model, the velocity profile satisfies the Poiseuille flow condition, which explains maximum velocity is observed at the axis of the pipe and velocity decreases toward the wall of pipe. As the concentration increases, magnitude of maximum velocity is observed to be increasing in the range of 6.06–9.36 m/s. But as the concentration increases to 1380 and 1390 kg/m³, maximum velocity zone is observed to be confined around the axis, and low velocity zone is found near the pipe walls. This is because of variation of Reynolds numbers. In case of concentration 58

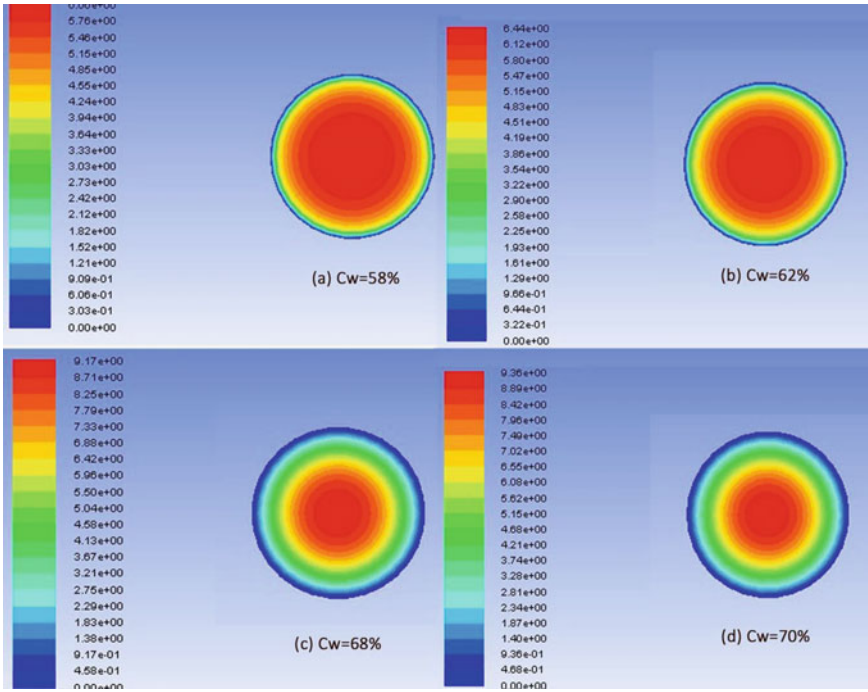


Fig. 4 Effect of variation of concentration on velocity 5 m/s for constant diameter 50 mm

and 62%, the viscosities are very low, so the Reynolds number is more than laminar range, hence their velocity profile follows the logarithmic nature. But as in case of concentration 68 and 70%, due to very high viscosity, the Reynolds number falls in the laminar range. Therefore, it follows the parabolic velocity profile. This explains more velocity at the axis of the pipe.

3.3 Diameter Variation Effects on Velocity

Figure 5 represents the variation of diameter on velocity contour at constant density 1300 kg/m^3 . It is seen that the velocity profile is almost logarithmic in nature for all diameters in homogeneous flow model. But there is a slight decrease in velocity from 2.6 to 2.38 m/s observed as the increase in diameter. This occurs due to increase in diameter causes decrease in velocity for a constant Reynolds's number. As the diameter increases, the Reynolds's number rises, the slope of logarithmic velocity gradient becomes steeper; hence at any vertical cross section of pipe, irrespective of decrease in magnitude, maximum velocity zone extends toward the walls.

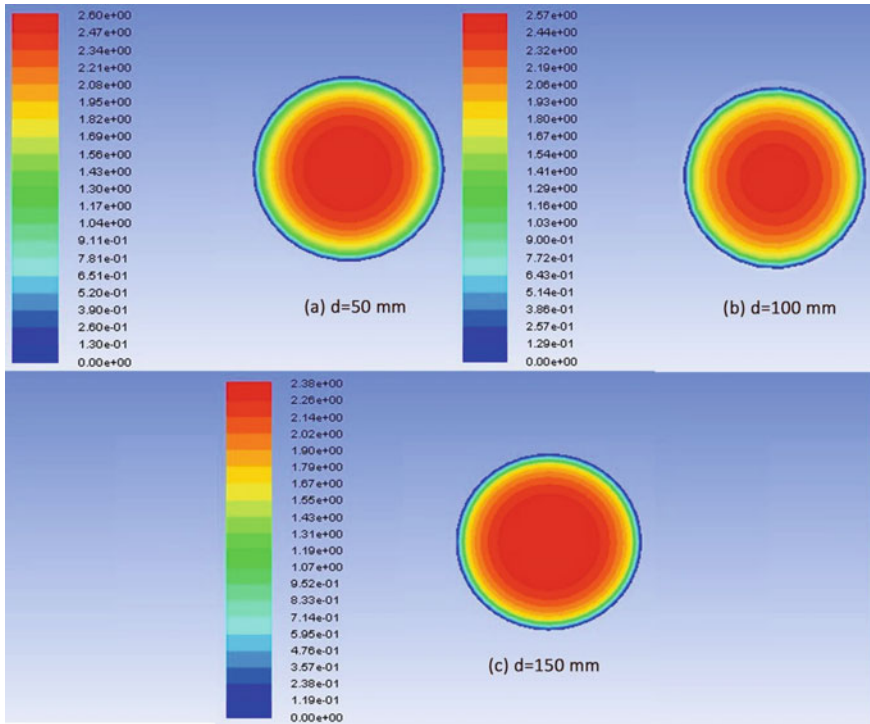


Fig. 5 Effect of variation of diameter on velocity at constant density of 1300 kg/m³

4 Conclusions

In this study, Euler–Lagrange homogeneous approach with realizable $k-\varepsilon$ turbulent scheme is used to analyze the two-phase flow behavior of coal slurry at high concentration for a particular particle size in 50, 100 and 150 mm diameter pipeline. The numerical simulation results are analyzed to predict the pressure drop in the pipeline with velocity and concentration distributions. The increase in pressure drop is observed with the increase in solid concentration and velocity for a particular pipe diameter, whereas reduction in pressure drop is observed with increase in pipe diameter. Pressure drop along the length is highest in 50 mm diameter and lowest in 150 mm diameter. But, while considering in lateral direction, velocity distribution, in a particular cross section, is found highest in case of 150 mm diameter and lowest in 50 mm diameter. Future work may be carried out considering different two phase flow models apart from HEM model presented here for probable better results. More parametric studies may be done as well in this area.

References

1. Manganaro J, Chen B, Adeosun J, Lakhapatri S, Favetta D, Lawal A (2011) Conversion of residual biomass into liquid transportation fuel: an energy analysis. *Energy Fuels* 25:2711–2720
2. Chen H, Chen GQ (2011) Energy cost of rapeseed-based biodiesel as alternative energy in China. *Renew Energy* 36:1374–1378
3. Mishra SK, Kanungo SB (2000) Factors affecting the preparation of highly concentrated coal-water slurry (HCCWS). *J Sci Ind Res* 59:765–790
4. Das D, Panigrahi S, Misra PK, Nayak A (2008) Effect of organized assemblies. Part 4. Formulation of highly concentrated coal–water slurry using a natural surfactant. *Energy Fuels* 22:1865–1872
5. Lee S (2007) Handbook of alternative fuel technologies. In: Lee S, Speight JG, Lyalka SK (eds) Chap 4. Coal slurry fuel. CRC Press, pp 125–152
6. Senapati PK, Dass D, Nayak A, Mishra PK (2008) Studies on preparation of coal water slurry using a natural additive. *Energy Sources Part A* 30:1788–1796
7. Routray A, Das D, Parhi PK, Padhy MK (2018) Characterization, stabilization, and study of mechanism of coal-water slurry using Sapindous Mukorrosi as an additive. *Energy Sources Part A*
8. Shen W, Li Z, Liu Y (2008) Surface chemical functional groups modification of porous carbon. *Recent Pat Chem Eng* 1:27–40
9. Das D, Dash U, Nayak A, Misra PK (2010) Surface engineering of low rank Indian coals by starch-based additives for the formulation of concentrated coal-water slurry. *Energy Fuels* 24:1260–1268
10. Yi F, Gopan A, Axelbaum RL (2014) Characterization of coal water slurry prepared for PRB coal. *J Fuel Chem Technol* 42(10):1167–1171
11. Zhu J, Zhang G, Liu G, Qu Q, Li Y (2014) Investigation on the rheological and stability characteristics of coal water slurry with long side-chain polycarboxylate dispersant. *Fuel Process Technol* 118:187–191
12. Zhu J, Zhang G, Miao Z, Shang T (2012) Synthesis and performance of a comb like amphoteric polycarboxylate dispersant for coal water slurry. *Colloids Surf A* 412:101–107
13. Das D, Dash U, Meher J, Misra PK (2013) Improving stability of concentrated coal-water slurry using mixture of natural and synthetic surfactants. *Fuel Process Technol* 113:41–51
14. Das D, Panigrahi S, Senapati PK, Misra PK (2009) Effect of organized assemblies. Part 5: study on the rheology and stabilization of a concentrated coal-water slurry using Saponin of the *Acacia concinna* plant. *Energy Fuels* 23:3217–3226
15. Routray A, Senapati PK, Padhy MK, Das D, Mohapatra R (2019) Effect of mixture of a non-ionic and a cationic surfactant for preparation of stabilized high concentration coal water slurry
16. Singh MK, Kumar S, Ratha D (2017) Computational analysis on disposal of coal slurry at high solid concentrations through slurry pipeline
17. Fluent 6.1. (2006) User's guide. Fluent Inc.
18. Duan Y, Chen L, Pu W, Zhao C (2009) CFD simulation of coal-water slurry flowing in horizontal pipelines. *Korean J Chem Eng* 26(4):1144–1154

Two-Phase Flow Analysis in Elbow Bend Pipe Used in Oil Extraction Process: A Computational Approach



Aditya Abinash, Sudhansu S. Sahoo, and Raj Kumar Saini

Abstract To predict and analyze the mechanical fatigue and other damages in pipelines, caused by slug flow in petrochemical industry, large amounts of research have been assigned in understanding and prognosis of slug flow transition in straight and bend pipes. Accurate predictions of liquid hold up, pressure distribution and velocity are imperative for uninterrupted operation of the facility before actual work being carried out. With the above-mentioned motivation, this paper focuses on investigation of oil–water and oil–air two-phase flow formation in straight pipes and bend pipes and its associated pressure drop, maximum velocity and volume of fraction. Mixture model has been adopted in this computational analysis. Newtonian behavior of oil–air and oil–water interface is obtained from the model through a vertical 90° elbow with 50.2 mm pipe diameter. Four different oil velocities such as 5, 10, 15 and 20 m/s along with three air and water velocities 0.5, 1 and 2 m/s, respectively, are used in this study. Velocity distribution and pressure profile at six sections of 90° elbow are obtained and compared in order to analyze the flow pattern behavior. CFD analysis results under mixture model show a decreasing trend in pressure as mixture exits the elbow. Furthermore, it also shows a larger decrease in pressure at higher oil velocities. There is an increase in mixture velocity as the oil velocity rises as well as the water/air velocity increases. Similarly, for increase in VOF from 0.25 to 0.5, there is a significant decrease in pressure as well as increase in velocity is observed. The model can be helpful in designing pipeline and piping systems for oil extraction as well as oil refineries.

Keywords Two-phase flow · CFD · Mixture model · VOF

A. Abinash (✉) · S. S. Sahoo
College of Engineering and Technology, Bhubaneswar 751003, India
e-mail: adityaabinash539@gmail.com

R. K. Saini
Indian Institute of Technology Bombay, Mumbai 400076, India

1 Introduction

“Oil extraction” is the process in which usable crude petroleum is extracted from beneath the earth surface. In this process, geologists survey the ocean floor by gravitometer and magnetometer for potential oil storage. Holes are made on surface by drill well in which oil is suctioned onto the surface. A set of pressure regulatory valves are fitted to regulate flow rate.

Oil extraction process is of three types:

Primary Recovery—Petroleum is trapped in the reservoir mixed with natural gases, water and other impurities. When a well is drilled into the depth of reservoir, oil is gushed toward surface due to a difference in concentration in the form of pressure gradient. Factors are responsible for the pushing out of petroleum such as gravity, water and gas pressure and concentration. Around 30% of the oil is recovered in this method. However, after continuous extraction, the pressure gradient decreases and it becomes difficult for extraction. Then, external energy is provided to the production zone.

Secondary Recovery—In this method, fluids are re-injected externally into the production zone which alters the density and viscosity of the oil and increases the pressure gradient to lift it up to the surface. One of the most common methods is “Water flooding.” In those flooding wells, water is directly injected into the production zone for better recovery. This water injected goes into the oil trapped in the earth crusts and works as a pusher liquid toward outside of the production zone. The primary and secondary recovery process extracts up to 60% of the reservoir capacity.

Tertiary Recovery—This method includes the use of oils, heated fluids or other chemicals, e.g., steam flooding, CO₂ flooding, methane flooding, LPG gas injection, surfactant (soap, detergent) flooding, etc. By now, most promising method in CO₂ injection is followed by water injection which combine to form carbonic acids which gets dissolved in the petroleum and increases the volume and decreasing the overall viscosity, thereby breaking the rock entrapment through and pushing forward in the pipeline. At the surface, the CO₂ is extracted from the mixture and is ready to be used again. This method can extract up to 80% of the reservoir content.

During this extraction, the oil mixes with water/air and causes complex multiphase flow in pipeline [1, 2]. Two-phase flow is the mostly occurring case of multiphase flow whose flow behavior is difficult to predict due to insufficient classical equations which are only to study single-phase flow pattern [3]. For straight as well as curved pipes, single-phase pressure profile and velocity distribution can be predicted with accuracy. However, for two-phase flow, flow behavior becomes complex due to variation in fluid viscosities, phase transformations, densities and their interaction with encircling walls [4].

Among different applications, straight pipes with elbow bend (90°) are commonly used for oil rigs and refineries. This two-phase flow causes mechanical fatigue to the pipelines. Hence, this work is dedicated to understand and predict the variation on pressure and velocity distributions in straight pipe as well as its elbow bends [5].

Computational Fluid Dynamics (CFD)-based approach has been employed to inspect and study the velocity profiles and pressure distributions along with variation in fractions in phase materials 0.25 and 0.5 in elbow bend considering oil–water and oil–air two-phase flow [6]. The two-phase phenomenon is reasonably complex which includes single-phase fluid flow parameters, such as pressure force, viscous force and inertia force. Moreover, properties of two-phase flow such as forces occurring at interface, mass transfer, momentum, contact angle and heat are also influenced on flow behavior [6]. The two-phase flow is affected by void fraction of the oil and water/air present in the section of pipe, superficial velocity of individual phases, interaction of variables of the fluids and geometric design of the pipelines. Among these, two major variables responsible are flow pattern and void fraction [7].

CFD models have been employed to predict oil–water two-phase flow pattern with Eulerian approach and $k-\varepsilon$ turbulence model [4, 8]. The stratified oil–water flow behaviors are also studied by computational method using volume of fluid (VOF) scheme and level-set method [4, 9, 10]. The frictional two-phase pressure reduction at the elbow is higher as compared to single-phase flow [11, 12]. Increased resistance, energy dissipations, circulation, frictional losses and phase interactions in the elbow bend are major factors for total pressure drop in the bends [5].

The aim of the present study is to carry out the CFD analysis of two-phase flow in 90° elbow pipes used in oil extraction process. Oil–water and oil–air type's fluids have been considered for the present study. Mixture model has been utilized for the present two-phase analysis. The velocity and pressure drop in a 90° elbow pipe for oil–air and oil–water types of two-phase flow with varying VOFs 0.25 and 0.5 are obtained using computational approach.

2 System Description

Oil industry uses pipelines carrying oil most of the time. However, due to leakage or related cases, water or air enters in pipeline and flows along with oil. The work presented here focuses on two-phase type flow in bend pipes used in oil extraction process. For the present analysis, pipe having 50.2 mm diameter, 90° elbow bend pipe having a constant radius/diameter ratio of 1.5 has been considered. Oil–air and oil–water having volume fraction 0.25 and 0.5 are used as working fluid in bend pipe. Six different locations are chosen along the pipeline for obtaining results (Fig. 1). Distance between each section in the pipeline is 200 mm. Location 1 and 6 are inlet and outlet of the pipeline and location 3 and 4 are mentioned as the inlet and exit of the elbow bend.

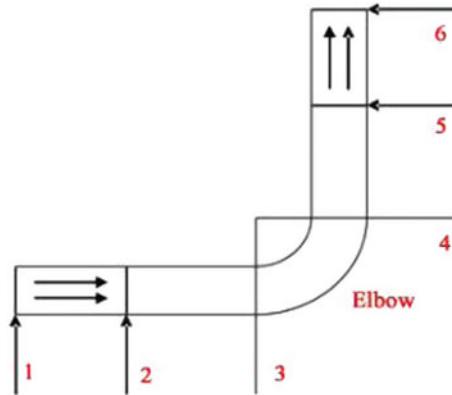


Fig. 1 Elbow geometry with horizontal and vertical pipe sections

3 CFD Approach

3.1 Modeling Basics

Numerical analysis and data structures are used to analyze and solve fluid flow problems using Computational Fluid Dynamics (CFD) approach in which interaction of two different fluids with surfaces is defined by boundary conditions. One of the most prominent turbulence models in which turbulence is modeled using transport equations “ k ” and “ ε ” is found in single-phase flow equation. A simplified model is used for modeling of multi-phase flows where phases flow at it as well as different velocities with strong coupling and slip velocities between phases. It is a promising alternative of Eulerian multiphase model as it can solve with less numbers of variables.

3.2 Validation of Mixture Model Results

The CFD mixture model experiments of Mazumder and Siddique [5] are replicated and validated for nine separate compositions of water and air velocities (Table 1).

In order to analyze the effects of air and water superficial velocities, the results of the above combinations are presented and analyzed. Figure 2 shows the comparison between the data given in the journal and the validated data of the effect of different air superficial velocities for constant water velocity 0.1 m/s on absolute pressure. In between sections 1 and 2, there is a slight pressure decrease observed due to frictional drop. As the phase mixture enters the elbow at section 3, a slight increase in pressure is observed due to bending loss. Pressure decreases as fluid passes through sections 5 and 6. This magnitude of variation in pressure is more at higher air velocities. The

Table 1 Compositions of water and air velocities considered for the CFD mixture model validation

Velocity of air: 15.24 m/s Velocity of water: 0.1 m/s	Velocity of air: 30.48 m/s Velocity of water: 0.1 m/s	Velocity of air: 45.72 m/s Velocity of water: 0.1 m/s
Velocity of air: 15.24 m/s Velocity of water: 1.0 m/s	Velocity of air: 30.48 m/s Velocity of water: 1.0 m/s	Velocity of air: 45.72 m/s Velocity of water: 1.0 m/s
Velocity of air: 15.24 m/s Velocity of water: 10.0 m/s	Velocity of air: 15.24 m/s Velocity of water: 10.0 m/s	Velocity of air: 45.72 m/s Velocity of water: 10.0 m/s

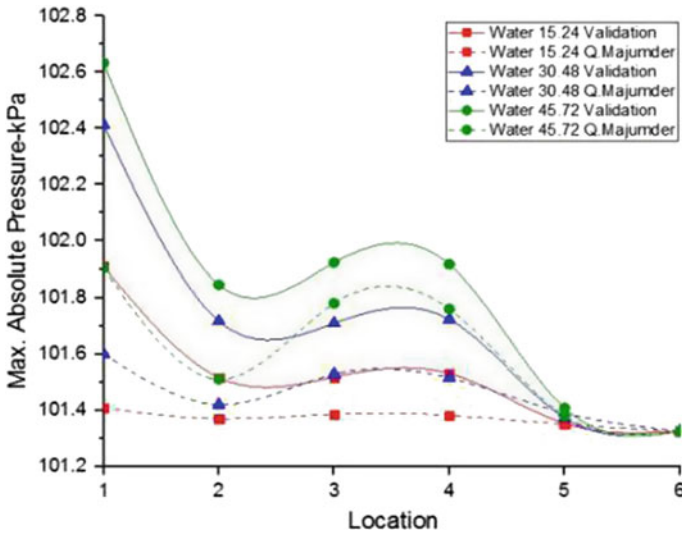


Fig. 2 Pressure profiles considering different air velocities and maintaining constant water velocity of 0.1 m/s

effect of increased air superficial velocities at constant superficial velocity of water is presented in Fig. 3. In between sections 1 and 3, the entrance of the elbow, an increase in the overall mixture velocities is observed. The flow velocity remains impartially constant with a minute reduction in between sections 3 and 6 as fluid leaves the elbow into the vertical pipe section.

4 Two-Phase Modeling and Simulation for Elbow Bend Pipe

4.1 Geometrical Details and Modeling

CFD simulation was performed to evaluate the effect of phases and materials on velocity distribution and pressure profiles of two-phase flow in a 50.2 mm diameter,

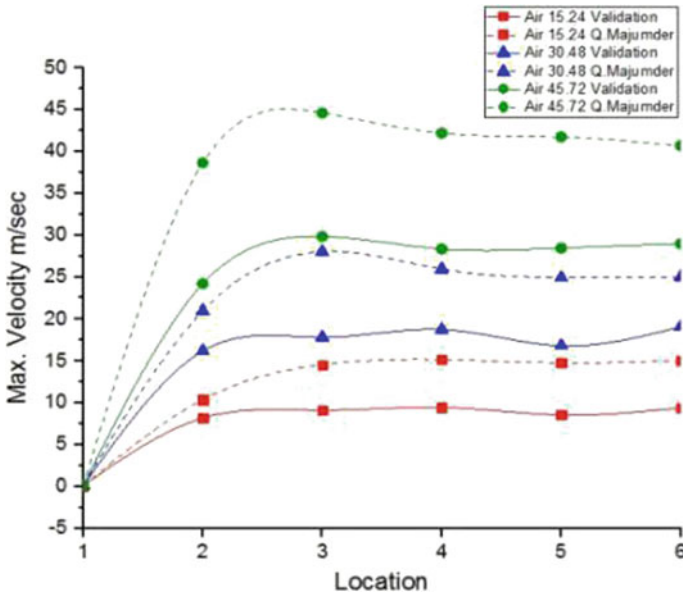


Fig. 3 Maximum mixture velocities considering different air velocities and maintaining constant water velocity of 0.1 m/s

90° elbow bend with a constant radius/diameter ratio of 1.5, as this is the typical elbow bend generally used in oil extraction processes. Results at six locations in vertical and horizontal sections of the elbow are taken to analyze the study (Fig. 1). Distance between each section in the vertical as well as horizontal pipe section is 200 mm.

The geometry was created using the design modeling which is the preprocessor used in Ansys Fluent 16.0 [12]. The number of nodes was found to be 140,833 with 142,767 numbers of cells in the model. Employment of finer grid is advisable in the neighboring region of the wall which has sharp velocity gradients. The geometry of the flow domain was divided into three parts: upstream, downstream and central parts consisting of elbow bend for effective discretization. The water bubbles in the oil are assumed to be spherical having 1 mm diameter. For coupling between pressure and velocity fields, the SIMPLE algorithm is used. To stabilize the converged solutions, under-relaxation technique is used. The residuals are taken as 10^{-6} .

4.2 Boundary Conditions

The CFD mixture model experiments are done for four oil velocities 5, 10, 15 and 20 m/s along with three water/air velocities 0.5, 1 and 2 m/s with variations in volume of fraction 0.25 and 0.5 (Table 2). The air velocities are raised by multiplying factors

Table 2 Combinations of oil-air and oil-water velocities used in the CFD mixture model

Water		Air														
		0.5						0.25						0.5		
Oil-5 m/s	Oil-5 m/s	Oil-5 m/s	Oil-5 m/s	Oil-5 m/s	Oil-5 m/s	Oil-5 m/s	Oil-5 m/s	Oil-5 m/s	Oil-5 m/s	Oil-5 m/s	Oil-5 m/s	Oil-5 m/s	Oil-5 m/s	Oil-5 m/s	Oil-5 m/s	Oil-5 m/s
Water-0.5 m/s	Water-1.0 m/s	Water-2 m/s	Water-1.0 m/s	Water-0.5 m/s	Water-1.0 m/s	Water-2 m/s	Water-1.0 m/s	Water-0.5 m/s	Water-1.0 m/s	Water-2 m/s	Water-1.0 m/s	Water-0.5 m/s	Water-1.0 m/s	Water-2 m/s	Water-1.0 m/s	Water-0.5 m/s
Oil-10 m/s	Oil-10 m/s	Oil-10 m/s	Oil-10 m/s	Oil-10 m/s	Oil-10 m/s	Oil-10 m/s	Oil-10 m/s	Oil-10 m/s	Oil-10 m/s	Oil-10 m/s	Oil-10 m/s	Oil-10 m/s	Oil-10 m/s	Oil-10 m/s	Oil-10 m/s	Oil-10 m/s
Water-0.5 m/s	Water-1.0 m/s	Water-2 m/s	Water-1.0 m/s	Water-0.5 m/s	Water-1.0 m/s	Water-2 m/s	Water-1.0 m/s	Water-0.5 m/s	Water-1.0 m/s	Water-2 m/s	Water-1.0 m/s	Water-0.5 m/s	Water-1.0 m/s	Water-2 m/s	Water-1.0 m/s	Water-0.5 m/s
Oil-15 m/s	Oil-15 m/s	Oil-15 m/s	Oil-15 m/s	Oil-15 m/s	Oil-15 m/s	Oil-15 m/s	Oil-15 m/s	Oil-15 m/s	Oil-15 m/s	Oil-15 m/s	Oil-15 m/s	Oil-15 m/s	Oil-15 m/s	Oil-15 m/s	Oil-15 m/s	Oil-15 m/s
Water-0.5 m/s	Water-1.0 m/s	Water-2 m/s	Water-1.0 m/s	Water-0.5 m/s	Water-1.0 m/s	Water-2 m/s	Water-1.0 m/s	Water-0.5 m/s	Water-1.0 m/s	Water-2 m/s	Water-1.0 m/s	Water-0.5 m/s	Water-1.0 m/s	Water-2 m/s	Water-1.0 m/s	Water-0.5 m/s
Oil-20 m/s	Oil-20 m/s	Oil-20 m/s	Oil-20 m/s	Oil-20 m/s	Oil-20 m/s	Oil-20 m/s	Oil-20 m/s	Oil-20 m/s	Oil-20 m/s	Oil-20 m/s	Oil-20 m/s	Oil-20 m/s	Oil-20 m/s	Oil-20 m/s	Oil-20 m/s	Oil-20 m/s
Water-0.5 m/s	Water-1.0 m/s	Water-2 m/s	Water-1.0 m/s	Water-0.5 m/s	Water-1.0 m/s	Water-2 m/s	Water-1.0 m/s	Water-0.5 m/s	Water-1.0 m/s	Water-2 m/s	Water-1.0 m/s	Water-0.5 m/s	Water-1.0 m/s	Water-2 m/s	Water-1.0 m/s	Water-0.5 m/s

of 2, 3 and 4, whereas water/air velocities are raised by a multiplying factor of 2 from initial condition.

5 Results and Discussion

These combinations are analyzed and the effect of variation in superficial velocities of oil and air/water and the effect of change in VOF on velocity distribution and pressure drop in six different sections of the elbow are compared.

5.1 Effect of Oil Velocity on Pressure Profile

The effect of different oil velocities for constant water velocity 0.5 m/s and constant air velocity 0.5 m/s, respectively, on max absolute pressure is represented in Fig. 4a, b, respectively. Due to friction in the horizontal pipe between sections 1 and 2, a slight drop in pressure is observed. As the oil–water/oil–air mixture flows through the elbow at section 3, a slight increase in pressure is observed in between sections 3 and 4. These two sections 3 and 4 represent the entry and exit of the elbow bend. When the mixture exits the elbow and passes through vertical sections 5 and 6, the pressure again continues to decrease due to increase in datum head. When the oil velocity increases, the pressure also increases. And when VOF of water/air increases from 0.25 to 0.5, a significant decrease in the pressure at all locations is observed. This reduction in pressure occurs due to increase in mass fraction of water/air in the mixture which causes increase in superficial momentum of water/air and decrease in pressure.

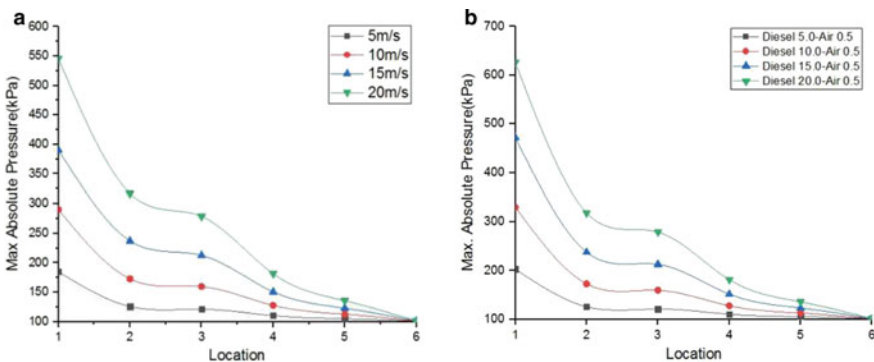


Fig. 4 **a** Pressure profiles at different oil velocities at constant water velocity 0.5 m/s and VOF 0.25. **b** Pressure profiles at different oil velocities at constant air velocity 0.5 m/s and VOF 0.25

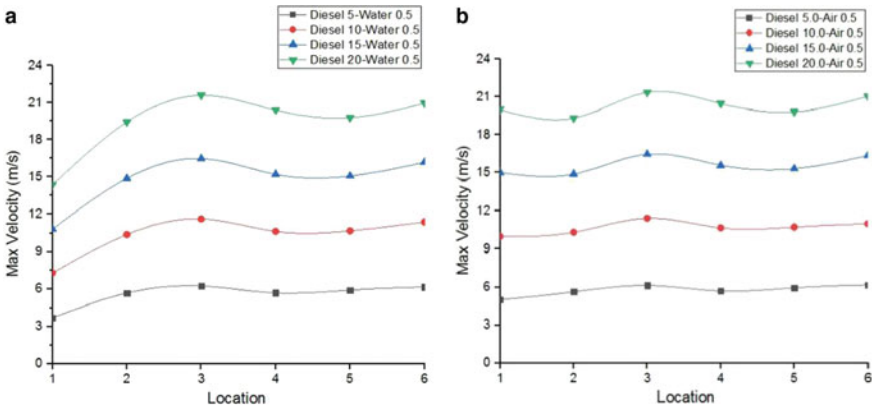


Fig. 5 a Maximum mixture velocities for different oil velocities at constant air velocity 0.5 m/s and VOF 0.25. **b** Maximum mixture velocities for different oil velocities at constant water velocity 0.5 m/s and VOF 0.25

5.2 Effect of Oil Velocity on Velocity Profile

Figure 5(a), (b) shows the effect of increase in oil velocities from 5 to 20 m/s at constant water/air velocity 0.5 m/s on the mixture velocity distribution in the elbow pipe. When fluid enters the elbow between sections 1 and 3, there is an increase in the max mixture velocities observed. When the mixture passes the elbow, a slight decrease in velocity is observed between sections 3 and 4. Then, finally, the flow velocity remains almost constant with a minimal decrease followed by slight increase between sections 4 to 5 and 5 to 6, respectively, as the mixture exits the elbow portion and flows in the vertically upward pipe section. As the VOF increases, a decrease in velocities at all locations is observed.

5.3 Effect of Volume of Fraction (VOF)

In Fig. 6a, the effect of increase in VOF results in decrease in absolute pressure at all the locations in the pipe is shown. This is because, as the viscosity of the oil is greater than water, when the VOF is less, amount of oil is more. So, overall viscosity is more. As the overall viscosity increases, shear stress increases which ultimately increases pressure holdup. Hence, for higher VOF, pressure holdup decreases. From Fig. 6b, it is proved that as the VOF of water/air increases from 0.25 to 0.5, there is a prominent decrease observed in both pressure and velocity profiles., This is because of increase in overall viscosity causes slower flow of the fluid in the pipeline. Hence, as the VOF decreases, velocity of pipeline increases.

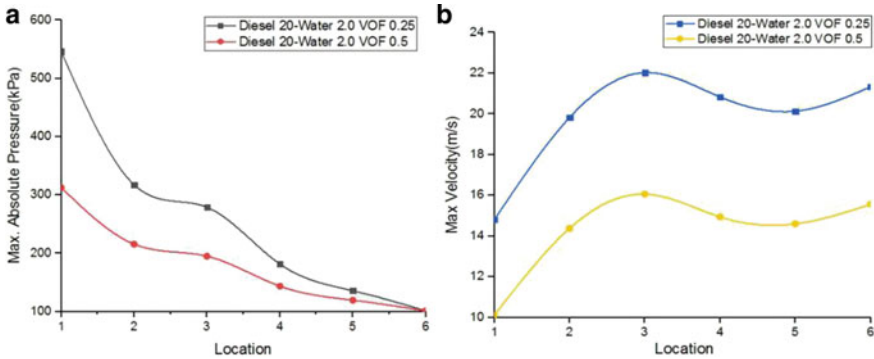


Fig. 6 **a** Pressure profiles at different locations at VOF 0.25 and 0.5. **b** Maximum mixture velocities at different locations at VOF 0.25 and 0.5

6 Contour Analysis

Figure 7a, b shows the cross-sectional absolute pressure contour maps of VOF 0.25 and 0.5 for different oil velocities 5, 10, 15 and 20 m/s for constant water velocity 0.5 m/s at six locations of the elbow pipe. Each row of contour figure shows a single oil–water velocity. At the location 2 for the oil superficial velocity 5 m/s, the pressure profile follows the general trend, i.e., maximum at the central axis and gradually decreases toward the outer wall. However, as the oil velocity increases to 10 m/s, the flow pattern changes to slug flow. Similarly, as the oil velocity increases to 15 and 20 m/s, there is an annular flow observed. As the mixture flows through elbow at location 3, it maintains a non-uniform distribution of pressure with higher pressure at the inner wall and lower toward the outer wall. In this location as the oil velocity increases, the maximum pressure zone shifts toward the inner side of the wall. As the mixture leaves the elbow at section 4, the phase separation is observed along with formation of negative pressure zone near the central axis of the pipe due to rotational flow and recirculation. Maximum pressure accumulation is observed to be at the outer walls of the pipe as the two-phase mixture passing through the elbow bend, strikes the elbow’s outer side and the flows vertically. After passing through location 4, in the vertical pipe, pressure accumulates in the inner wall of the pipe. However, as the oil velocity increases, pressure increases toward the outer wall.

7 Conclusion

CFD analysis is carried out for two-phase flow considering oil–air and oil–water in a 90° elbow. 48 separate flow conditions with four different oil velocities and three water velocities and four oil velocities with three different air velocities were taken into consideration in this study. To solve continuity and momentum equations

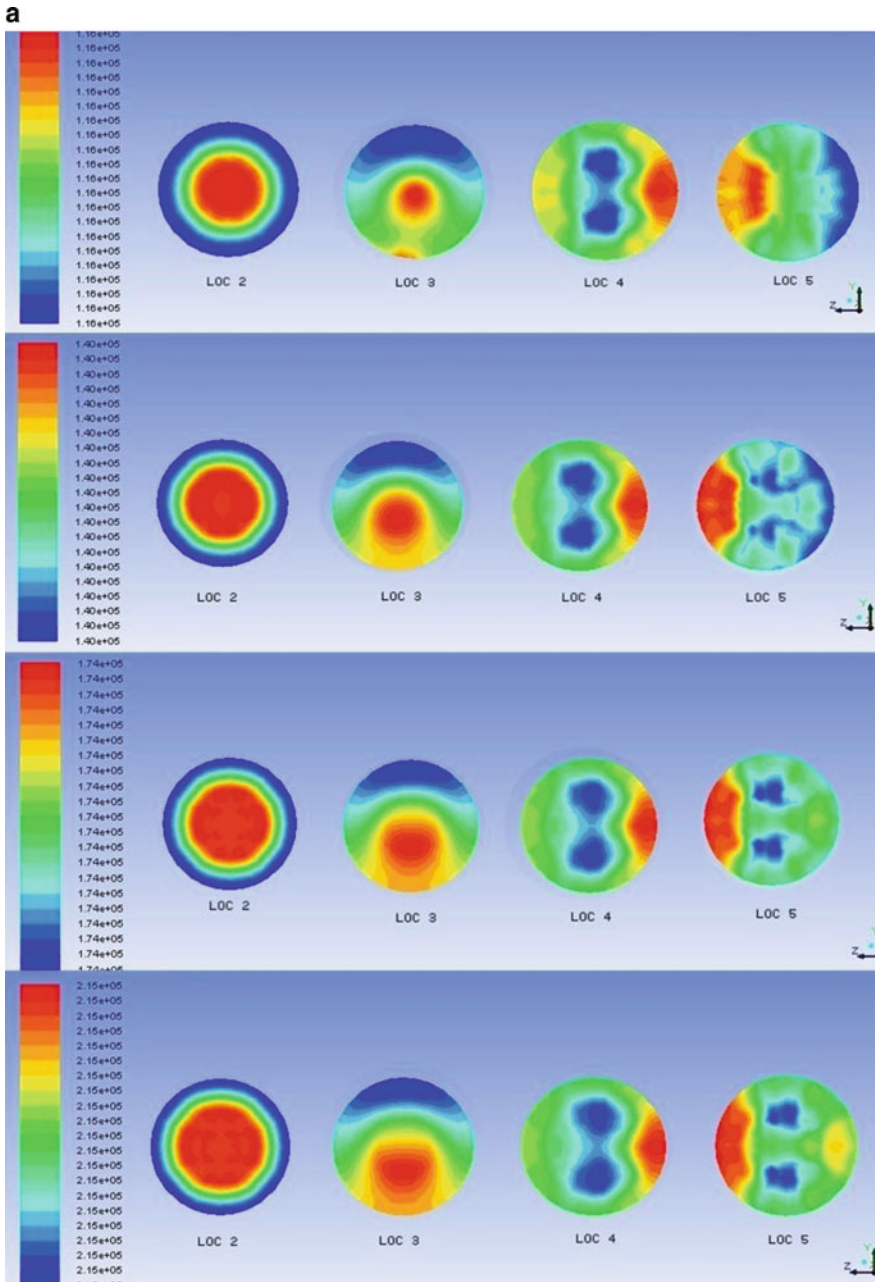


Fig. 7 a Absolute pressure at different locations of elbow for water velocity of 0.5 m/s and VOF 0.5. b Absolute pressure at different locations of elbow for water velocity of 0.5 m/s and VOF 0.25

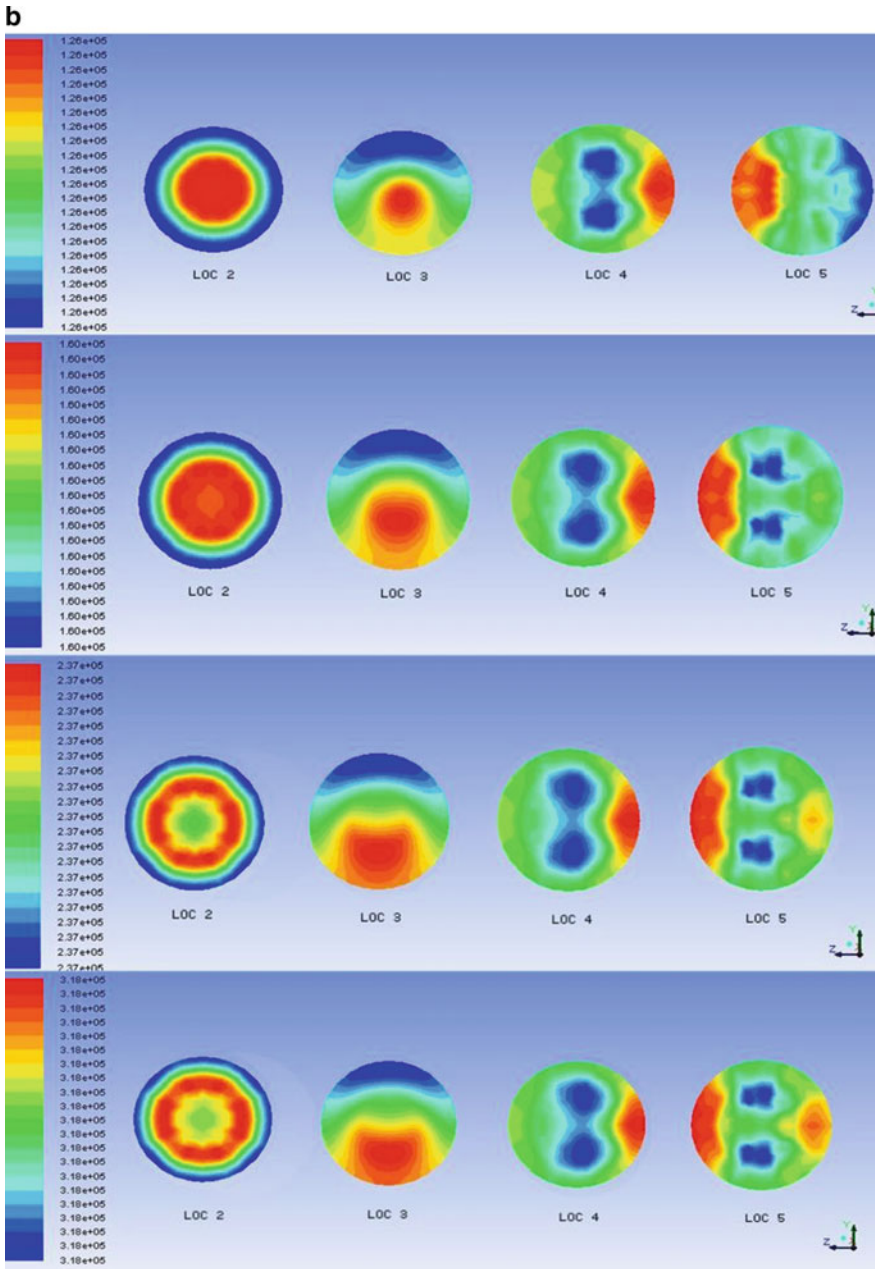


Fig. 7 (continued)

for different oil–air and oil–water velocities, the mixture model was used. Pressure distribution and velocity profiles at six sections at upstream and downstream of the elbow were presented. The analysis shows the following variations at different locations of the elbow, such as:

- Reduction in pressure from 1 to 2 due to friction loss. Then, a slight increase is seen in between entry of elbow 3 and exit of elbow 4. Finally, after the exit of elbow, there is a decrease in pressure between 5 and 6. As the superficial velocity of the oil increases, the max pressure at all locations also increases simultaneously. However, there is minute change in pressure with variation in superficial velocity of oil/water.
- As VOF increases, pressure decreases due to decrease in overall viscosity. Similarly, for oil–air flow, pressure is found to be higher than that of oil–water flow.
- For velocity profile, as the superficial velocity of oil increases, max velocity of the flow also increases. There is a sudden increase in between 1 and 2 which is observed. But then, velocity of flow remains steady throughout the elbow. But, in case of oil–air flow, a slight decrease in velocity in between 1 and 2 is observed with the increase in oil velocity. This velocity reduction is found to be higher at higher oil velocities in VOF 0.5. However, the variation in superficial velocity of air/water has little effect on the velocity profile.
- As on increase in VOF, overall viscosity increases. Hence, there is a significant decrease in the velocity observed at all locations of the elbow.
- Near the inner wall (downstream) of the elbow, rotational flow and recirculation are observed with formation of negative pressure zone.
- It was found that, for lower secondary phase velocities, liquids were accumulated near the center of the pipe with air on the outer diameter of the secondary flow vortex. However, as the air/water velocity was increased, oil–air and oil–water mixtures were observed with more water towards the outer diameter of the secondary flow vortex, thus creating higher pressure on the outer wall of the pipe.

References

1. Piroozian A, Hemmati M, Ismail I et al (2017) An experimental study of flow patterns pertinent to waxy crude oil-water two-phase flows. *Chem Eng Sci* 164(8):313–332
2. Mukhaimer A, Al-Sarkhi A, El Nakla M, Ahmed WH, Al-Hadhrani L (2015) Pressure drop and flow pattern of oil–water flow for low viscosity oils: role of mixture viscosity. *Int J Multiphase Flow* 73:90–96
3. Spedding PL, Benard E, McNally GM (2004) Fluid flow through 90 degree bends. *Dev Chem Eng Min Process* 12:107–128
4. Benbella S, Al-Shannag M, Al-Anber ZA (2009) Gas-liquid pressure drop in vertical internally wavy 90 degree bend. *Exp Therm Fluid Sci* 33:340–347
5. Mazumder QH, Siddique SA (2011) CFD analysis of two-phase flow characteristics in a 90 degree elbow
6. Ban S, Pao W, Nasif MS (2018) Numerical simulation of two-phase flow regime in horizontal pipeline and its validation
7. Sohem O (1982) Flow pattern transition and characterization in liquid-gas two-phase flow in inclined pipes. Tel-Aviv University
8. Kaushik VVR, Ghosh S, Das G et al (2012) CFD simulation of core–annular flow through sudden contraction and expansion. *J Petrol Sci Eng* 86–87:153–164
9. Chenoweth JM, Martin MW (1955) Turbulent two-phase flow. *Pet Ref* 34(10):151–155
10. Lockhart RW, Martinelli RC (1949) Proposed correlation of data for isothermal two-phase two-component flow in pipes. *Chem Eng Prog* 45(1):39–48
11. Spedding PL, Benard E (2007) Gas–liquid two phase through a vertical 90 degree elbow bends. *Exp Therm Fluid Sci* 31:761–769
12. Fluent I (2002) *Fluent 6.3 user guide*. Fluent Inc., Lebanon. NH-03766

Aspects of Heat Transfer Augmentation Using Nanofluids as Coolant in Fusion Reactors: A Brief Review



Sayantana Mukherjee, Purna Chandra Mishra, Sayan Jana, Paritosh Chaudhuri, and Shanta Chakrabarty

Abstract Nanofluids, engineered suspensions of nanosized non-organic particles in base fluids have shown some interesting thermo-physical properties and heat transfer augmentation in various cooling systems. A gigantic number of research works is documented so far, and it is going on to explore various aspects of nanofluids such as their formulation, physical properties, and their utility in various engineering applications. Various investigations report that this class of fluid shows remarkable enhancement in various thermophysical properties such as thermal conductivity, viscosity, heat capacity, density, and surface tension. Enhancement in convective heat flow, critical heat flux enhancement (CHF) enable them as a special class of coolant for high-temperature applications including automobile, micro-electromechanical systems (MEMS), defense and power sectors. To explore the significance of such investigations, the application of nanofluids as coolants in fusion reactors is a very good aspect of this technology. Research agencies around the globe have already initiated research works to explore the potential of nanofluids in fusion reactors. The present contribution revises the theoretical and experimental studies reported on nanofluids, and their potential as future generation coolant for fusion reactors is featured presenting the current status of research.

Keywords Nanofluids · Coolants · Fusion reactors · Thermal conductivity · Heat flux

S. Mukherjee (✉) · P. C. Mishra · S. Jana · S. Chakrabarty
Thermal Research Laboratory (TRL), School of Mechanical Engineering, Kalinga Institute of Industrial Technology (Deemed to be University), Campus-8, Patia, Bhubaneswar, Odisha 751024, India
e-mail: sayantana2210@gmail.com

P. Chaudhuri
Institute for Plasma Research (IPR), Bhat, Gandhinagar, Gujarat 382428, India
Homi Bhabha National Institute, Anushaktinagar, Mumbai 400094, India

1 Introduction

In the present era of fusion engineering, reactor cooling devices constantly encounter high heat flux generated during fusion reaction. Therefore, the development of efficient and safe cooling technology is a big challenge. Further, it is necessary to develop new material and cooling agents to face ever-increasing power density. Besides this, new generation cooling systems should possess techno-economic feasibility without ignoring the safety factors becoming more restrictive due to the occurrence of several mishaps like Fukushima accident.

Among the current technologies, nanofluids are emerging out as promising for high heat flux removal and heat transport in fusion reactors [1]. Nanofluids and its application in heat transfer enhancement are currently a very popular topic of research with rapid increase of scientific papers. A recent search in scientific indexing providers such as Scopus and Web of Science has shown a tremendous rise in publication on the topic of nanofluids which is presented in Fig. 1. The statistics reveals the importance of nanofluids in the present era.

Various research publications reveal that nanofluids show interesting thermophysical properties regarding their ability to heat transfer. The mostly executed application areas of nanofluids are micro–nano–electronic systems, automobile systems, machining, solar thermal systems, and photovoltaic cells [2–5] etc. Researchers are working on utilizing nanofluids as future working fluid or as emergency cooling fluids to avoid accidents. However, the present investigations are still focused on the in-depth knowledge of nanofluids and their thermophysical properties. Simultaneously, heat transfer as well as heat removal capacity of nanofluids is being investigated.

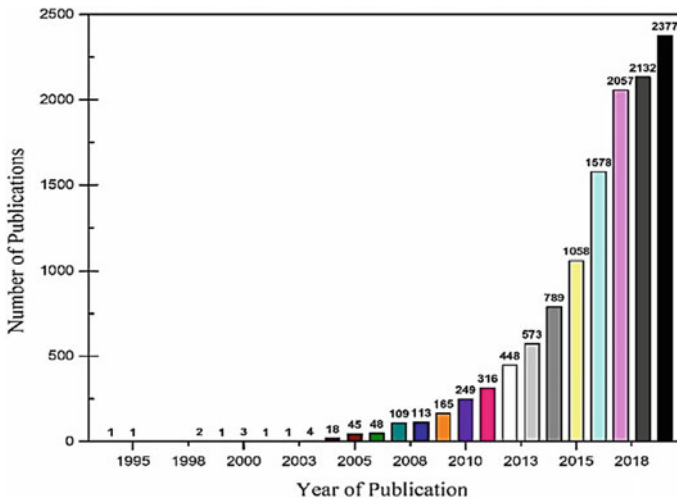


Fig. 1 Year-wise publications related to nanofluids research

The application of nanofluids in heat transfer processes depends on the thermofluidic behavior of the system. Therefore, in order to describe them, important thermophysical properties such as thermal conductivity, viscosity have been reviewed here. Some important results of previous investigations on heat transfer capability, pressure drop, and pumping power characteristics of nanofluids as working fluid in various thermal equipment have been discussed here.

2 Thermo-Physical Properties

As the nanofluids are prepared suspending high-density solid nanoparticles into the base fluids, thus they are having higher viscosity than the viscosity of base fluids and demand greater pumping power to provide the same thermal performance. There is an impressive amount of thermal conductivity that can be obtained with nanofluids which can be counter balanced by the increase in viscosity and decrease in specific heat capacity of these fluids. The flow properties and behavior of nanofluids are found similar to that of base fluids and therefore can be used in place of conventional base fluids in practical engineering applications. But these nanofluids also cause little to moderate amount of turbulent pressure loss. Thus, preparation and characterization of nanofluids are very important to design them as potential heat transfer fluids regarding particle size, shape, materials, and concentrations. It also ensures the utilization of increased heat transfer capability of nanofluids, minimizing the pressure loss to obtain satisfactory results. In nuclear reactors, there are emissions of ionizing radiation; thus, implementing the nanofluids in reactors as coolants require special characteristics, e.g., high heat transfer capability, sustaining stability at very high temperature, having low activation characteristics to minimize the radiation, etc.

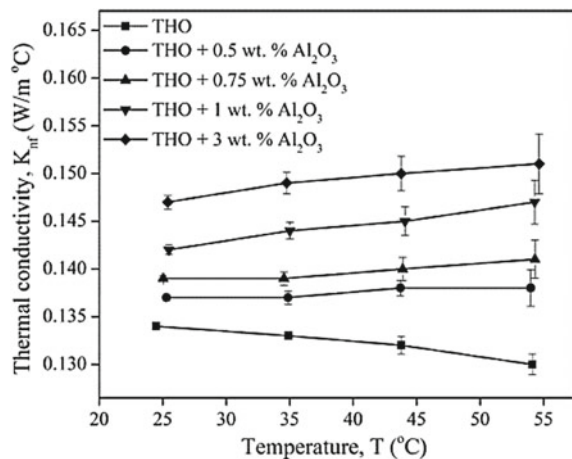
Investigations performed in the fusion engineering showed that the nanofluids behave as Newtonian fluids. Concentration and hydrodynamic size of dispersed-nanoparticles are both considerable factors because not only they affect the physical and chemical stability but also determine the thermal performance. There are findings which describe the viscous stresses by nanofluids differ abruptly when the nanoparticle volume fraction becomes more than a certain quantity. This is called as the dilution limit. Therefore, substantial enhancement in thermal performance and stabilization of nanofluids is obtainable by determining the dilution limit of particular nanofluids and keeping the concentration of particles lower than that limit. Increasing concentrations above this limit, induces agglomeration and sedimentation of nanoparticles, disrupts Brownian motions resulting in a lesser stable nanofluid with no further increase in thermal conductivity.

2.1 Thermal Conductivity of Nanofluids

The most impressive characteristic of nanofluids is its enhanced thermophysical and heat transfer properties compared to the base fluids. Hence, the study of those inherent properties of nanofluids along with the ways of augmentation of those is the primary aim of the researchers. Some important findings in thermal conductivity enhancement with nanofluids have been reviewed below.

In a very recent study of Xu et al. [6] selected Al_2O_3 -water-based nanofluids with concentrations 0.2, 0.5, and 1 wt% to measure the thermal conductivities and informed increment of thermal conductivities by 10.5%, 16.7%, and 22.8%, respectively, compared to water. Yıldız et al. [7] performed numerical investigation on natural convection using Al_2O_3 -water, SiO_2 -water nanofluids along with their hybrid combinations for different Rayleigh numbers ($\text{Ra} = 10^4$ and $\text{Ra} = 10^5$) and different volume concentrations (1, 2, and 3 vol%) and found that available theoretical models for thermal conductivity underestimated the heat transfer performance, SiO_2 -water nanofluid showed deterioration in heat transfer performance and using hybridized nanoparticles, the same amount of enhancement in heat transfer can be obtained at lower volume fractions. Ilyas et al. [8] investigated with alumina-thermal oil-based nanofluid with different concentrations from 0 to 3 wt% and found that nanofluids having high nanoparticle concentrations enhanced the coefficient of heat transfer compared to that of pure thermal oil (shown in Fig. 2). Zarifi et al. [9] presented a thermal-hydraulic analysis of nanofluids in a nuclear reactor core (VVER-1000) as coolant perspective, using the porous media approach, in which Al_2O_3 -water and TiO_2 -water nanofluids with 0–5 vol% were used in the reactor core for the analysis of their study. In modeling part, the nonlinear algebraic equations were solved by FORTRAN language. Finally, the results were compared with the results of pure water. They stated that, temperature of nanofluid coolants increased with the concentration of nanoparticles. Due to the higher heat transfer coefficient, flow

Fig. 2 Temperature versus thermal conductivity of alumina-based nanofluids [8]



rate of nanofluids could be reduced to get the same cooling effect compared to pure water. Buongiorno [10] studied the heat transfer through convection with Cu-ethylene glycol nanofluids in different volume fractions and showed that the nanofluid with 0.3 vol% provided an improvement 40% in the thermal conductivity. One of the oldest studies conducted by Koblinski et al. [11] in which they discussed problems of synthesizing processes, rheology and stability of nanofluids, the heat transfer in static, flow, convection and boiling cases, the dependency of thermal conductivity of nanofluids on various factors, e.g., concentration of nanoparticles, temperature, particle size, and heat flux also about the controversial and out of predicted results of thermal performance in various experiments.

The easiest models for the explanation of improved thermal conductivity require some assumptions such that the particles are spherical in shape, while the particle–base fluid interface effects are not taken into account. In other words, the finite thermal conductance of interface particle–base fluid is not considered. Overall these theories and solutions are valid for nanofluids with the limit of low particle concentrations, but in higher concentrations, there are no considerable theories presented yet.

2.2 Viscosity

Most of authors presented a number of conclusions about the viscosity of nanofluids, which is undoubtedly a major parameter concerning convective heat transfer and power consumption for the flow of nanofluids in pipes, channels, or any other hydraulic circuits. Khodadadi et al. [10] calculated the viscosities of MgO–Water nanofluid ranging from volume fraction 0.07 to 1.25%, from 25 to 60 °C, and found that while water exhibited Newtonian behavior, the nanofluid samples showed non-Newtonian behavior. The viscosity increased with the increase in volumetric concentration of nanoparticles and reduced with the increase in temperature. Their experimental results have been presented in Fig. 3. Alawi et al. [11] investigated for thermal conductivity and viscosities of a number of nanofluids. They selected four metallic oxides, Al₂O₃, CuO, ZnO, and SiO₂ suspended in water in concentrations ranging from 1 to 5 vol% at temperatures of 300–320 K and found the rise in viscosity with the increase of particle concentration.

2.3 Heat Transfer Capacity

Several studies show that for the laminar flow convection heat transfer process, the coefficient of heat transfer of some nanofluids increases rapidly with Reynolds number (Re). In a review work, Sarkar et al. [12] stated that the hybrid nanofluids might be very promising for heat transfer enhancement as shown in Fig. 4.

Bang et al. [13] studied to design nuclear safety systems using nanofluids as coolants applicable for generation III/III+ reactors, based on the axiomatic design

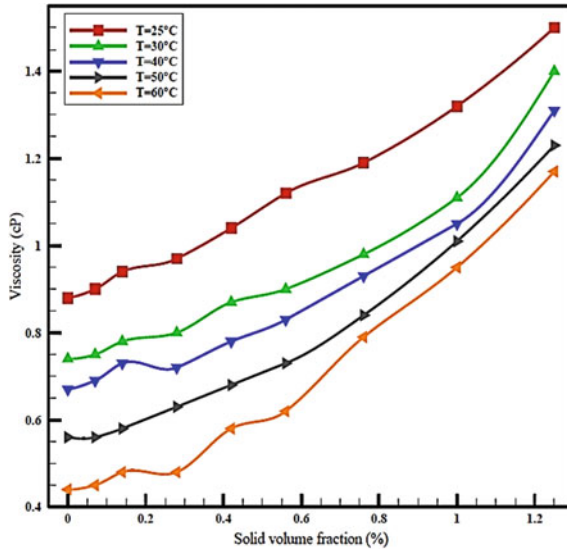


Fig. 3 Dynamic viscosity versus solid volume fraction [10]

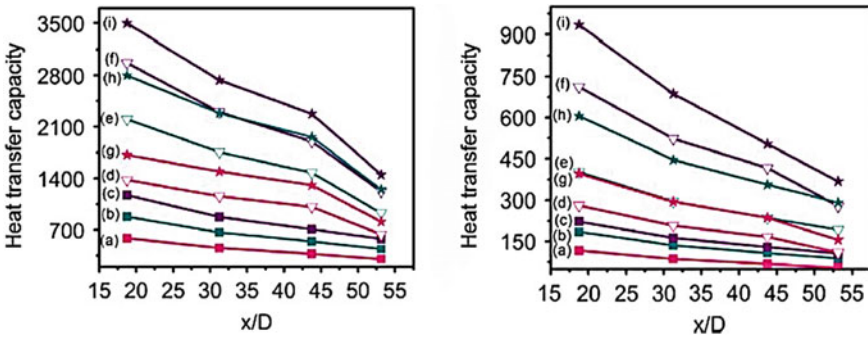


Fig. 4 Variation in heat transfer capacity with x/D coefficient in different Reynolds numbers [12]

theory. They suggested that nanofluids with enhanced heat transfer capability can make the nuclear system more secure and more economic. There are a number of research works related to nuclear applications conducted at the Massachusetts Institute of Technology (MIT) which revealed that CHF of nanofluids depend on the heating surface microstructure and topology change due to particle deposition and the CHF could be enhanced much above than pure water [14, 15]. From the study regarding pool boiling and CHF improvement using Al_2O_3 -water, ZrO_2 -water and SiO_2 -water nano-dispersions, Kim et al. [16] stated that a significant improvement in CHF could be obtained at lower nanoparticle concentrations (<0.1% by volume). Due to the porous layer built up by nanoparticle deposition over the surfaces used with

nanofluids, consequently reduced the contact angle and enhanced surface wettability. Investigations carried out by Buongiorno et al. [17, 18], emphasizing to boiling behavior of nanofluids, including the limitation of CHF and quenching phenomenon particularly for nuclear reactor coolant applications. They stated that nanofluids could be used to enhance the critical heat flux (up to 200%) and to accelerate the quenching heat transfer, which might be helpful for attaining improved safety margins and significant economic gains.

2.4 Pumping Power

Nanofluids can provide exceptional thermal performance with one major drawback of pumping power enhancement. In most of the experimental cases, the implementation of nanofluid as working liquid causes a rise in pumping power which may become one of the obstacles to develop an efficient thermal system using nanofluids.

For example, in a study on heat transfer performance and pumping power by adding hybrid nanoparticles (MgO-MWCNT) ranging from 0.25 to 2 wt% in thermal oil, Asadi et al. [19] stated that the nanofluids caused a certain penalty in pumping power for both the internal laminar and turbulent flows, which increased the energy consumption. But the increase in pumping power for turbulent flow seemed lower than that of laminar flow as shown in Fig. 5.

In their review work related to the effect of concentration of nanoparticles and temperature on the nanofluid properties, heat transfer enhancement, and pumping power, Vajjha and Das [20] informed that nanofluids were efficient enough to replace the convective fluids for both laminar and turbulent flows and a modest concentration of the Al₂O₃ nanofluid have the best combination of properties to yield superior heat transfer at a lower pumping power.

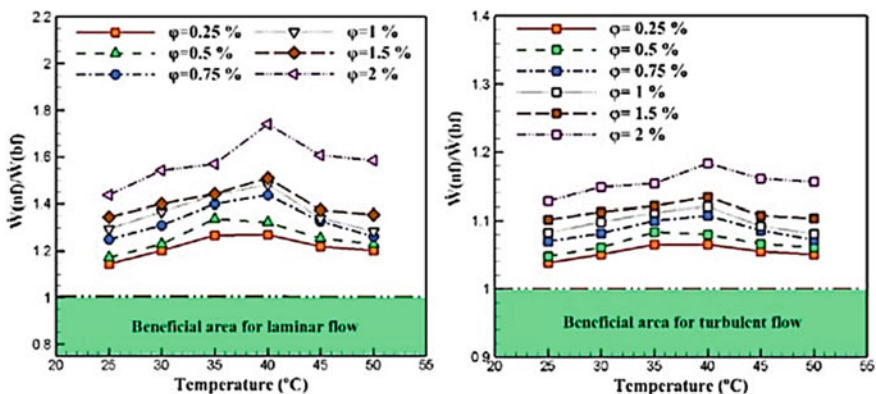


Fig. 5 Variation of pumping power in both the laminar and turbulent flow regimes in different temperatures and particle concentrations [19]

3 Discussion and Future Outlook

Evidently, the choice of suitable nanofluid based on the aspect of enhancements in thermal conductivity and critical heat flux must be accomplished as reported previously. Buongiorno et al. [18] described that the best thermal performance from a nuclear reactor is obtainable using nanofluids under the circumstance which includes a safe and cost-effective approach with minimum impact of the nanoparticles on the neutronic behavior of reactor core. Dilute nanofluids have low impact on neutron transport in reactor core. Selection of nanomaterial is important. Nanoparticles should be non-radioactive in nature or it will not be influenced by radioactivity. Nanofluids should have compatibility with the chemical and radioactive environment of fusion reactors. Regarding that case, the pH and chemical stability of nanofluids are important and complex molecular structures are incompatible with reactor system. Therefore, surfactant stabilized nanofluids are forbidden in fusion reactors. Physical stability of nanofluids is very important. Sedimented nanoparticles block the flow passage resulting in pumping power enhancement. Thermally unstable (unstable at high temperatures) nanofluids are not suitable as the working fluids have to encounter tremendous amount of heat flux continuously. Increase of viscosity due to the addition of nanoparticles is the main drawback of nanofluids. The enhanced viscosity is also responsible for pumping power enhancement which penalizes the running cost of the system. Cost of the nanofluids is important. Economic analysis shows that the cost of nanoparticles is very high which is the main reason for which nanofluids are still not applied for industrial applications.

Deeper understanding of enhanced thermophysical properties of nanofluids in contrast to their base fluids in connection to the enhanced heat transfer capability, in-depth knowledge of nanofluids behavior under high heat flux conditions, knowledge of nanofluids' behavior in fusion reactors, economic feasibility, and security for future generation fusion reactors are very important. These are some desired outcomes which are reckoned as the most propitious aspects of nanofluids in fusion engineering and material science.

4 Conclusion

A brief overview on nanofluids, their properties, and their applications in fusion reactors have been carried out aiming to present the current status of research and development. The paper also indicates the emerging research areas of nanofluid technology.

Important thermophysical properties of nanofluids such as thermal conductivity, viscosity, and their characteristics under several changing parameters such as concentration, temperature, material, and nanoparticle morphology have been reviewed. Heat transfer and its enhancement with nanofluids have been demonstrated.

Stability of nanofluids is a big disadvantage of such technology. To overcome such problems, new methodology should be invented. Moreover, an optimization study is very important to find the best concentration with greater stability and maximum heat transfer rate minimizing pumping power loss.

Acknowledgements The authors cordially acknowledge the financial support provided by the Board of Research in Nuclear Sciences (BRNS), Department of Atomic Energy, Government of India (sanction no: 39/14/04/2017-BRNS/34301).

References

1. Barrett TR, Robinson S, Flinders K, Sergis A, Hardalupas Y (2016) Investigating the use of nanofluids to improve high heat flux cooling systems. *Fusion Eng Des* 88(2013):2594–2597. <https://doi.org/10.1016/j.fusengdes.2013.03.058>
2. Zhang H, Tay AAO, Xue Z (2009) Feasibility study of nanofluid cooling techniques for micro-electronic systems. In: Proceedings of electronics packaging technology conference (EPTC). <https://doi.org/10.1109/EPTC.2009.5416474>
3. Xian HW, Sidik NAC, Najafi G (2019) Recent state of nanofluid in automobile cooling systems. *J Therm Anal Calorim*. <https://doi.org/10.1007/s10973-018-7477-3>.
4. Sharma AK, Tiwari AK, Dixit AR (2015) Progress of nanofluid application in machining: a review. *Mater Manuf Process*. <https://doi.org/10.1080/10426914.2014.973583>
5. Kasaeian A, Eshghi AT, Sameti M (2015) A review on the applications of nanofluids in solar energy systems. *Renew Sustain Energy Rev*. <https://doi.org/10.1016/j.rser.2014.11.020>
6. Xu G, Fu J, Dong B, Quan Y, Song G (2016) A novel method to measure thermal conductivity of nanofluids. *Int J Heat Mass Transf* 130(2019):978–988. <https://doi.org/10.1016/j.ijheatmasstransfer.2018.11.014>
7. Yıldız Ç, Arıcı M, Karabay H (2019) Comparison of a theoretical and experimental thermal conductivity model on the heat transfer performance of Al₂O₃-SiO₂/water hybrid-nanofluid. *Int J Heat Mass Transf* 140:598–605. <https://doi.org/10.1016/j.ijheatmasstransfer.2019.06.028>.
8. Ilyas SU, Pendyala R, Narahari M (2017) An experimental study on the natural convection heat transfer in rectangular enclosure using functionalized alumina-thermal oil-based nanofluids. *Appl Therm Eng*. <https://doi.org/10.1016/j.applthermaleng.2017.08.088>
9. Zarifi E, Jahanfarnia G, Veysi F (2016) Thermal-hydraulic modeling of nanofluids as the coolant in VVER-1000 reactor core by the porous media approach. *Ann Nucl Energy* 51(2013):203–212. <https://doi.org/10.1016/j.anucene.2012.07.041>
10. Khodadadi H, Toghraie D, Karimipour A (2018) Effects of nanoparticles to present a statistical model for the viscosity of MgO-water nanofluid. *Powder Technol*. <https://doi.org/10.1016/j.powtec.2018.09.076>
11. Buongiorno J (2005) Convective Transport in Nanofluids. *J Heat Mass Transf* 128 (3):240–250. <https://doi.org/10.1115/1.2150834>.
12. Keblinski P, Eastman JA, Cahill DG (2015) Nanofluids for thermal transport. *Mater Today* 8 (6):36-44(2005). [https://doi.org/10.1016/S1369-7021\(05\)70936-6](https://doi.org/10.1016/S1369-7021(05)70936-6)
13. Seon Ahn H, Hwan Kim M (2012) A review on critical heat flux enhancement with nanofluids and surface modification. *J Heat Transfer* 134:1–13. <https://doi.org/10.1115/1.4005065>
14. Kim SJ, Bang IC, Buongiorno J, Hu LW (2006) Effects of nanoparticle deposition on surface wettability influencing boiling heat transfer in nanofluids. *Appl Phys Lett* 89:2016. <https://doi.org/10.1063/1.2360892>
15. Kim HD, Kim J, Kim MH (2007) Experimental studies on CHF characteristics of nano-fluids at pool boiling. *Int J Multiphase Flow*. <https://doi.org/10.1016/j.ijmultiphaseflow.2007.02.007>

16. Bang IC, Heo G, Jeong Y, Heo S (2008) An axiomatic design approach of nanofluid-engineered nuclear safety features for generation III+ reactors. *Nucl Eng Tech* 41. <https://doi.org/10.5516/NET.2009.41.9.1157>.
17. Buongiorno J, Hu LW, Kim SJ, Hannink R, Truong B, Forrest E (2008) Nanofluids for enhanced economics and safety of nuclear reactors: an evaluation of the potential features issues, and research gaps. *Nucl Technol* 162:80–91. <https://doi.org/10.13182/nt08-a3934>
18. Buongiorno J, Hu LW (2010) Nanofluid heat transfer enhancement for nuclear reactor applications. In: *Proceedings of ASME micro/nanoscale heat & mass transfer international conference 2009, MNHMT2009*, vol 3, pp 517–522. <https://doi.org/10.1115/MNHMT2009-18062>
19. Asadi M, Asadi A, Aberoumand S (2018) An experimental and theoretical investigation on the effects of adding hybrid nanoparticles on heat transfer efficiency and pumping power of an oil-based nanofluid as a coolant fluid. *Int J Refrig* 89:83–92. <https://doi.org/10.1016/j.ijrefrig.2018.03.014>
20. Vajjha RS, Das DK (2012) A review and analysis on influence of temperature and concentration of nanofluids on thermophysical properties, heat transfer and pumping power. *Int J Heat Mass Transf* 55:4063–4078. <https://doi.org/10.1016/j.ijheatmasstransfer.2012.03.048>

Investigation on Ranque–Hilsch Vortex Tube Using Different Turbulence Models



Satpreet Singh, K. P. Sinhamahapatra, and Nilotpala Bej

Abstract The objective of this study is to find out an appropriate numerical model that would be computationally less expensive and capable of producing a result with the least deviation from the experimental investigation. To verify the prime objective of this paper, a comparison study is performed between the most commonly used turbulence models such as RNG $k-\varepsilon$ model and standard $k-\varepsilon$. In standard $k-\varepsilon$ turbulence model, all the calculations of turbulent diffusion are performed on the same scale. Thus, a single turbulence length scale is responsible for the production of eddy viscosity. Whereas in RNG $k-\varepsilon$ turbulence models, the turbulent diffusion is calculated for a large span of the scale of motion. Performance study of both the models has been carried out using software tool ANSYS FLUENT™ 15.0. It is found that the results obtained due to standard $k-\varepsilon$ method depict closer agreement towards experimental study.

Keywords Thermodynamics properties study · Numerical models · Second law efficiency

1 Introduction

The vortex tube was invented by Georges J. Ranque in the year 1933 and brought to the attention of researchers by Rudolf Hilsch. It has a cylinder-like body. It contains a number of tangentially mounted nozzles. Compressed gas enters the vortex tube through these nozzles. The strong swirling motion produced due to very high pressure flow splits the gas into two zones of gases: the outer zone of hotter gas and an inner zone of cold gas. Vortex tubes are used in many industrial applications for its cooling capability. It is used for separation of the gas mixtures, solidifying polymers,

S. Singh · N. Bej (✉)

School of Mechanical Engineering, Kalinga Institute of Industrial Technology (KIIT), Deemed to be University, Bhubaneswar 751024, India
e-mail: nilotpala2002@gmail.com

K. P. Sinhamahapatra

Indian Institute of Technology, Kharagpur, Kharagpur 721302, India

© Springer Nature Singapore Pte Ltd. 2021

P. Pant et al. (eds.), *Advances in Mechanical Processing and Design*, Lecture Notes in Mechanical Engineering, https://doi.org/10.1007/978-981-15-7779-6_21

237

liquefaction of the gases, purification and dehydration of multiphase gas mixtures, etc.

The study on Ranque–Hilsch vortex tube also known as RHVT deals with the analysis of the qualitative as well as quantitative properties of the working fluid. Quantitative values are mainly the temperature of the cold fluid and hot fluid, total outlet energy. The qualitative study comprises the direction of fluid flow and propagation of energy from the axial layer towards the outer peripheral layer of the device. However, in this era of research and innovation, the selection of numerical models and computational methods plays a vital role to estimate the cost and time of completion of a project. The literature review [1–4] on the vortex tube reveals few important aspects of the device such as performance enhancement based on geometrical optimization, mathematical models closure to results obtained through experimental investigation. Various mathematical studies reported in open literature are CFD code (Star-CD) by Behera et al. [5], large eddy simulation (LES) model by Farouk [6], RNG $k-\varepsilon$, Reynolds stress model (RSM) and LES by Secchiaroli et al. [7], algebraic stress model (ASM) by Eiamsa-ard and Promvonge [8], CFD analysis using STAR-CCM+ by Matveev and Leachman [9]. However, the notion of reversible work and exergy plays a vital role when a real device with similar inlet and outlet conditions compared to an ideal one. In exergy study, thermal irreversibility caused by heat transfer, exergy destruction associated with turbulence, viscosity and pressure drop are taken into consideration. Therefore, exergy study gives an idea about the maximum possible work can be obtained in a given working condition. Outcomes of standard $k-\varepsilon$ and RNG $k-\varepsilon$ models are validated against the results due to experimental investigation by Dincer et al. [10].

2 Computational Domain and Boundary Conditions

The dimensional details of the geometry created for this study are presented in Fig. 1. An axis-symmetric model is created using commercial CFD package ANSYS FLUENT™ 15.0. A grid independence study has been performed to reduce the errors due to the generation of grid extended within a range of 5000–30,000 cells. The grid independence study reports marginal changes in temperature separation due to the change of grid size from 20,000 to 30,000. So, a mesh size of 25,660 has been generated to carry out the numerical study.

The pressure and temperature of the inlet fluid are 730 kPa and 293.15 K respectively. The pressure at the cold exit is maintained as 100 kPa while the hot exit pressure is operated between 200 and 520 kPa to achieve different values of the cold fraction. All solid boundaries are considered as adiabatic in nature without slip.

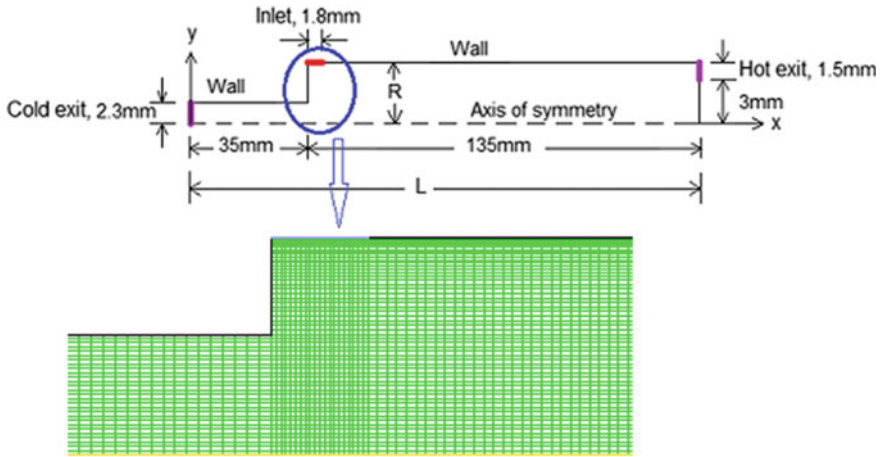


Fig. 1 Dimensional details and mesh of the geometry

3 Mathematical Formulations

The mathematical equations involved in this study are as follows:

$$\frac{\partial}{\partial x_i}(\rho u_i) = 0 \tag{1}$$

$$\frac{\partial}{\partial x_j}(\rho u_i u_j) = -\frac{\partial p}{\partial x_i} + \frac{\partial}{\partial x_j} \left[2\mu S_{ij} - \frac{2}{3}\mu \delta_{ij} \frac{\partial u_i}{\partial x_i} \right] + \frac{\partial}{\partial x_j} (-\rho \overline{u'_i u'_j}) \tag{2}$$

$$\frac{\partial}{\partial x_i} [u_i (\rho E + p)] = \frac{\partial}{\partial x_j} \left[\kappa_{\text{eff}} \frac{\partial T}{\partial x_j} + u_i (\tau_{ij})_{\text{eff}} \right] \tag{3}$$

where $(\tau_{ij})_{\text{eff}}$

$$(\tau_{ij})_{\text{eff}} = \tau_{\text{viscous}} + \tau_t = \mu_{\text{eff}} \left(\frac{\partial u_j}{\partial x_i} + \frac{\partial u_i}{\partial x_j} \right) - \frac{2}{3} \mu_{\text{eff}} \frac{\partial u_k}{\partial x_k} \delta_{ij} \tag{4}$$

$$-\rho \overline{u'_i u'_j} = \mu_t \left(\frac{\partial u_i}{\partial x_j} + \frac{\partial u_j}{\partial x_i} \right) - \frac{2}{3} \delta_{ij} \left(\rho k - \mu_t \frac{\partial u_k}{\partial x_k} \right) \tag{5}$$

$$p = \rho RT \tag{6}$$

Considering steady state, the rate of dissipation and turbulent kinetic energy calculated for standard $k-\varepsilon$ model is presented in Eqs. (7) and (8), respectively

$$\frac{\partial}{\partial x_i}(\rho \varepsilon u_i) = \frac{\partial}{\partial x_j} \left[\left(\mu + \frac{\mu_t}{\sigma_\varepsilon} \right) \frac{\partial \varepsilon}{\partial x_j} \right] + C_{1\varepsilon} \frac{\varepsilon}{k} (P_k + C_{3\varepsilon} P_b) - C_{2\varepsilon} \rho \frac{\varepsilon^2}{k} + S_\varepsilon \quad (7)$$

$$\frac{\partial}{\partial x_i}(\rho k u_i) = \frac{\partial}{\partial x_j} \left[\left(\mu + \frac{\mu_t}{\sigma_k} \right) \frac{\partial k}{\partial x_j} \right] + P_k + P_b - \rho \varepsilon - Y_M + S_k \quad (8)$$

μ_t stands for turbulent viscosity and is calculated as

$$\mu_t = \rho C_\mu \frac{k^2}{\varepsilon} \quad (9)$$

Various constants used in standard $k-\varepsilon$ model

$$\text{Pr}_t = 0.85, C_\mu = 0.09, C_{1\varepsilon} = 1.44, C_{2\varepsilon} = 1.92, C_{3\varepsilon} = -0.33, \sigma_\varepsilon = 1.3, \sigma_k = 1.0.$$

Transport equations involved in RNG $k-\varepsilon$ model

$$\frac{\partial}{\partial x_i}(\rho k u_i) = \frac{\partial}{\partial x_j} \left[\left(\mu + \frac{\mu_t}{\sigma_k} \right) \frac{\partial k}{\partial x_j} \right] + P_k - \rho \varepsilon \quad (10)$$

$$\frac{\partial}{\partial x_i}(\rho \varepsilon u_i) = \frac{\partial}{\partial x_j} \left[\left(\mu + \frac{\mu_t}{\sigma_\varepsilon} \right) \frac{\partial \varepsilon}{\partial x_j} \right] + C_{1\varepsilon} \frac{\varepsilon}{k} P_k - C_{2\varepsilon}^* \rho \frac{\varepsilon^2}{k} \quad (11)$$

where

$$\eta = Sk/\varepsilon \text{ and } S \equiv \sqrt{2S_{ij}S_{ij}} \quad (12)$$

and

$$C_{2\varepsilon}^* = C_{2\varepsilon} + \frac{C_\mu \eta^3 (1 - \eta/\eta_0)}{1 + \beta \eta^3} \quad (13)$$

Various constants used in RNG $k-\varepsilon$ model

$$C_{1\varepsilon} = 1.42, C_{2\varepsilon} = 1.68, C_\mu = 0.0845, \sigma_k = 0.7194, \sigma_\varepsilon = 0.7194, \eta_0 = 4.38, \beta = 0.012.$$

4 Results and Discussion

The simulations are performed in ANSYS FLUENT™. The configuration of the system is as follows: Intel® Core™2 Quad CPU Q8300 @2.5 GHz processor. Exergy calculated at the inlet, cold exit, and hot exit using both the turbulence models are

compared and discussed in this section. The outcomes of the numerical models are validated against experimental results available in the literature [10].

1. Total inlet exergy

Exergy available at the inlet of the vortex tube is calculated as follows:

$$\sum E_i = E_{i,PH} + E_{i,KN} \tag{14}$$

Total exergy calculated using standard $k-\varepsilon$ and RNG $k-\varepsilon$ model is plotted against the experimental results given by [10]. Due to similar boundary conditions at the inlet, exergy calculated by both the turbulence models at the inlet gives the same values of 3770.3 W. The outcomes due to both the numerical models are validated against the experimental results. It is found from Fig. 2 that the experimental data underpredicts by around 0.04% of the CFD models.

2. Exergy study at the hot exit

Exergy available at the hot outlet is calculated as $\sum E_h = E_{h,PH} + E_{h,KN} + E_{h,PT}$. Hot exergy data available due to experimental study by [10] and numerical models are plotted in Fig. 3. It is observed that results due to both the numerical models overpredict at lower cold fractions. However, the discrepancy in numerical and experimental data becomes less like the cold fraction increases. Subsequently, it is noticed that the standard $k-\varepsilon$ model predicts results almost similar to the experimental one as the cold fraction approaches 0.3. On the other hand, the discrepancy in results is more significant in RNG $k-\varepsilon$ model. It is also observed that with the rise in values of cold fraction from 0.4 to 0.8, the hot exergy calculated by RNG $k-\varepsilon$ model gives the surplus of the values of 78–9 W.

3. Cold exergy

Fig. 2 Total exergy at the inlet

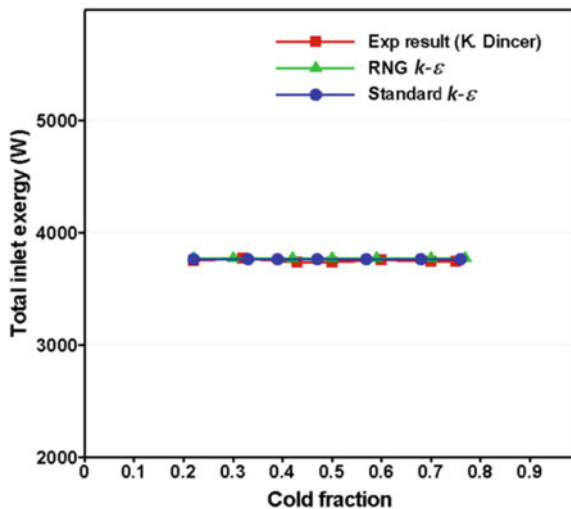
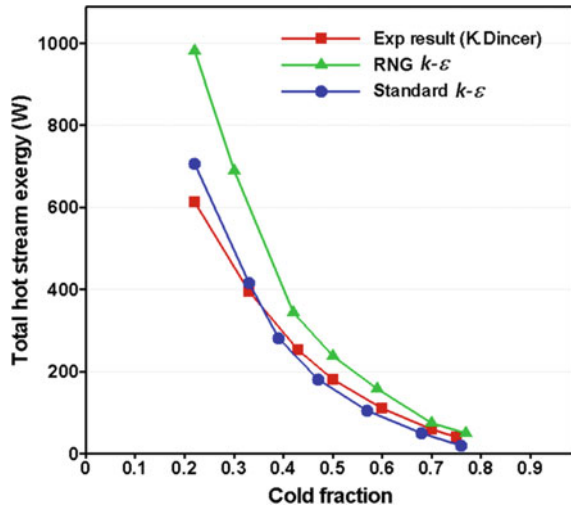


Fig. 3 Hot outlet exergy



Cold exergy is calculated as $E_c = E_{c,PH} + E_{c,KN}$. The comparison study among the numerical models with the experimental results is given in Fig. 4. The standard $k-\epsilon$ model accorded well with the experimental observations. The curve plotted by standard $k-\epsilon$ model very nearly coincides with the experimental observation for cold fraction 0.3–0.6. Nevertheless, at higher values of cold fraction such as 0.6, a significant deviation from the experimental study is observed in standard $k-\epsilon$ curve. The maximum value is 345 W when the cold fraction becomes 0.8. A linear curve is obtained by RNG $k-\epsilon$ model. At cold fraction 0.5, the highest discrepancy from the experimental value (280 W) is noticed.

Fig. 4 Exergy calculated at cold exit

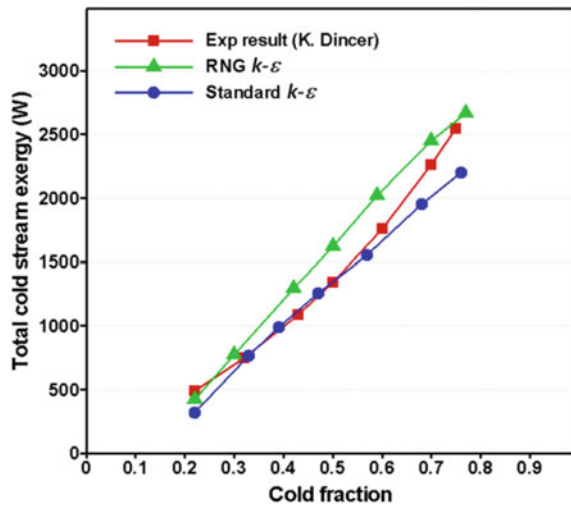
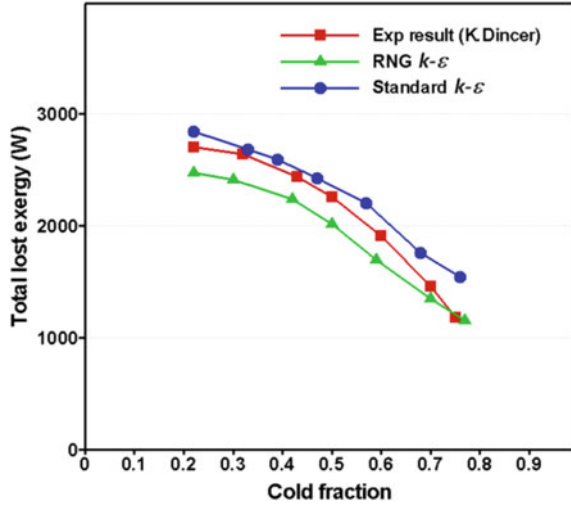


Fig. 5 Exergy lost



4. Total lost exergy

The difference of exergy calculated at the inlet and outlet gives exergy lost. It is calculated using the equation $\sum E_{lost} = \sum E_i - (\sum E_h + \sum E_c)$. The lost exergy due to numerical models and experimental study is plot in Fig. 5. Though very similar qualitative results are noticed by both the numerical models, standard $k-\epsilon$ model produces results closer to the experimental one. The standard $k-\epsilon$ model predicts almost the same values of the lost exergy as that of experimental data up to a cold fraction 0.5. The lost exergy obtained by RNG $k-\epsilon$ model under predicts consistently for cold fraction 0.3–0.65. However, neither the turbulence models could explain satisfactorily the cause of lower intensity in lost exergy as cold fraction increases.

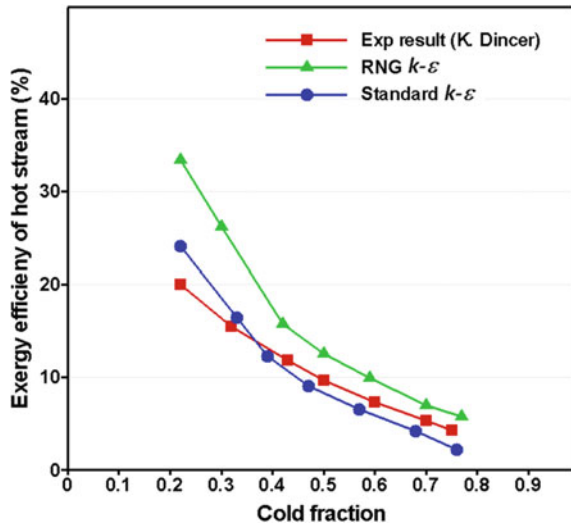
5. Hot exergy efficiency

The comparison study is further extended to hot exergy efficiency. The hot exergy efficiency is calculated as $\eta_{II,h} = \frac{\sum E_h}{\sum (1-\xi)E_i}$. It is obvious from Fig. 6 that within the span of 0.3–0.76, standard $k-\epsilon$ model predicts better than RNG $k-\epsilon$ model. The standard $k-\epsilon$ model deviates from the experimental data by only 2.1% as a whole. The exergy study carried by standard $k-\epsilon$ model and RNG $k-\epsilon$ model too confirms that the standard $k-\epsilon$ model views accorded well with the experimental observations.

5 Conclusions

This paper addresses a comparison study between the standard $k-\epsilon$ and RNG $k-\epsilon$ turbulence models. Exergy available at various sections such as inlet and both the outlets is calculated and compared against the experimental results [10]. The study confirms that standard $k-\epsilon$ model overall performs better than RNG $k-\epsilon$ model.

Fig. 6 Hot exergy efficiency



References

1. Eiamsa-ard S, Promvong P (2008) Review of Ranque-Hilsch effects in vortex tubes. *Renew Sustain Energy Rev* 12:1822–1842
2. Xue Y, Arjomandi M, Kelso R (2010) A critical review of temperature separation in a vortex tube. *Exp Therm Fluid Sci* 34:1367–1374
3. Yilmaz M, Kaya M, Karagoz S, Erdogan S (2009) A review on design criteria for vortex tubes. *Heat Mass Transf* 45:613–632
4. Thakare HR, Patil YR, Parekh AD (2013) A review of computational studies of temperature separation mechanism in vortex tube. *Bonfiring Int J Ind Eng Manag Sci* 3:74–80
5. Behera U, Paul PJ, Dinesh K, Jacob S (2008) Numerical investigation on flow behaviour and energy separation in Ranque-Hilsch vortex tube. *Int J Heat Mass Transf* 51:6077–6089
6. Farouk T, Farouk B (2009) Simulation of gas species and temperature separation in the counter flow Ranque-Hilsch vortex tube using the large eddy simulation technique. *Int J Heat Mass Transf* 52:3320–3333
7. Secchiaroli A, Ricci R, Montelpare S, D'Alessandro V (2009) Numerical simulation of turbulent flow in a Ranque-Hilsch vortex tube. *Int J Heat Mass Transf* 52:5496–5511
8. Eiamsa-ard S, Promvong P (2007) Numerical investigation of the thermal separation in a Ranque-Hilsch vortex tube. *Int J Heat Mass Transf* 50:821–832
9. Matveev KI, Leachman J (2019) Numerical investigation of vortex tube with extended vortex. *Int J Refrig* 108:145–153
10. Dincer K, Yilmaz Y, Berber A, Baskaya S (2011) Experimental investigation of performance of hot cascade type Ranque-Hilsch vortex tube and exergy analysis. *Int J Refrig* 34:1117–1124

Materials and Smart Manufacturing Processes

Development of Bio-Material (Tiger Grass-Reinforced Gaur Gum Matrix Composite) for an Alternative Bio-Based Cutlery for Food Service Applications



Rahul Kurdekar, N. R. Banapurmath, S. A. Hallad, Arun Y. Patil, Ravi Guttal, Ashok S. Shettar, and Sachin Arakeri

Abstract Conventional cutleries used in restaurants, food chains and catering services have major drawbacks as they involve petroleum-based chemicals whose disposal has been associated with a widespread harmful effects on environment and its lives. Hence, the use of natural fibre and natural matrix to build an alternative and feasible bio-composite is the need of hour. In view of this, a bio-material consisting of tiger grass fibre and gaur gum powder was prepared by optimizing the filler concentrations in the holding gaur gum powder matrix. Six specimens of bio-specimens were prepared as per ASTM standard D638. The developed bio-composites were characterized in terms of mechanical properties, such as tensile strength and impact strength. Further, the specimens were tested for moisture absorption properties. Mechanical properties of developed bio-composite were comparable to their conventional counter parts. However, further work needs to be done to improve mechanical properties of developed novel bio-composites for practical realization.

Keywords Tiger grass fibre · Gaur gum powder · Bio-composites · FE analysis · Mechanical properties

1 Introduction

Utilization of natural fibre composites in commercial products and components is the need of hour to create sustainable environment in the material industry. The main advantages of the bio-derived composites are that they are renewable in nature

R. Kurdekar · N. R. Banapurmath (✉) · A. Y. Patil · R. Guttal
School of Mechanical Engineering, B.V.B. College of Engineering and Technology, KLE
Technological University, Hubli 580031, India
e-mail: nrbapurmath@gmail.com

N. R. Banapurmath · S. A. Hallad · A. Y. Patil · A. S. Shettar
Centre for Material Science, B.V.B. College of Engineering and Technology, KLE Technological
University, Hubli 580031, India

S. Arakeri
Vibhava Industries, Hubli, India

and provide biodegradation properties and economic viability [1]. However, low-dimensional stability and high moisture sensitivity are their disadvantages. The present work highlights on development of bio-composites using natural fibres, namely tiger grass fibre scientifically known as *Thysanolaena maxima* reinforced in a matrix called as gaur gum scientifically known as *Cyamopsis tetragonoloba*. *Thysanolaena maxima* is a species belonging to the Poaceae or Graminae family. The grass can be grown as a revenue generating crop for its inflorescences which can be used for making brooms. It is commonly called as tiger grass, broom grass and bouquet grass in English. *T. maxima* has been reported growing in most parts of Southeast Asia. Its availability occurs in slopes of hills, damp steep banks along ravines and sandy banks of the rivers. Annual production of broom grass is 68,410 quintals/year and hence the inflorescence and flowering culms of it are used mainly for making broomsticks or brooms. Broom grass is the major crop grown heavily in the Chepurupalli village, Srikakulam District, Arunachal Pradesh.

The guar plant flourishes in extremely drought-resistant and semiarid regions where most plants perish. It grows best in sandy soils. The major processing centres of guar gum are in the north-western states in India. The guar plant grows from 2 to 9 ft high. Guar gum, also known as guarkernmehl, guaran, goma guar, is extracted from the guar beans forms a gel in water, commonly referred to as guar gum.

The first attempt on composite development using broom fibres was reported in the literature and fibres were extracted from broom branches and reinforced in polypropylene matrix, and the developed composites were characterized for their tensile properties [2]. Mechanical properties of composites reinforced with rice straw, bagasse and cotton stalk fibres of different sizes were characterized in terms of tensile strength, deformation and flexure as reported by the investigator [3]. Broom grass fibre has been frequently used by researchers as filler material reinforced in polypropylene and polyester as matrices to study their feasibility for structural applications. However, studies on the use of broom grass fibres for development of bio-composites have not been reported in the literature.

Natural bio-composites with integration of natural fibre and matrix can address the environment issues by way of reducing the rate of pollution. Tiger grass fibre and gaur gum have many ideal properties in food industry as well as other areas [4].

From the exhaustive literature survey carried out on the development of bio-composites for food service applications with an intension to replace plastic cutleries, it is found that very limited work has been reported on the development of bio-composite using tiger grass fibres and the gaur gum, respectively.

The main objective of the present work is to prepare tiger grass fibre–gaur gum blend for synthesis of tiger–gaur bio-composites and evaluate their tensile strength along with its moisture absorbing properties [5]. The present work is an attempt towards development of bio-composites for food service applications namely cutleries [6]. Further, the work involves proof of concept development representing a prototype cutlery.

2 Materials and Methodology

In this section, materials and method used for the development of bio-composites are reported. For the bio-composites development, earlier combination of bagasse and banana fibres was used as fillers in the starch matrix. The developed composites showed lower strength with reduced intermolecular bonding, and the method of composite preparations was cumbersome with higher processing costs involved. In the second case, bio-composites were developed using tiger grass fibres reinforced in gaur gum with water as plasticizer. The developed bio-composites showed good adhesive properties and higher strength with strong intermolecular bonding. The processing of the composites was faster when compared to the previously developed ones. Further, the bio-composites with preferred physical qualities such as durability and biodegradability at an effective cost were observed for the second set of the materials chosen. The developed bio-composite materials were tested for tensile strength followed by impact and water absorption tests.

For these mechanical testing, composites were developed into regular rectangular strips and dumbbell-shaped strips as per ASTM standards.

2.1 Bio-Composites Developed

Figure 1 shows the bio-composite developed in-house.



Fig. 1 Bio-composite developed as per ASTM D638

2.2 Experimental Set-Up

Experimental set-up used for testing tensile strength of the developed composites is as shown in Fig. 2. Table 1 shows specifications and bench mounting details of the micro UTM.

3 Results and Discussion

The developed bio-composites were tested for tensile strength. As mentioned above, the test is carried out for two different shapes, i.e. rectangular-shaped and dumbbell-shaped strips. Thus, three bio-composites were developed as explained below.

Fig. 2 Micro-UTM



Table 1 Specifications and bench mounting details of the micro-UTM

Specification	Range
Force range	10 kN
Displacement resolution	0.000004 in
Speed resolution	0.001 mm/min
Speed accuracy	$\pm 0.005\%$
Load cell confirms to	ISO75001, EN10002, DIN51221, ASTM E4

3.1 Phase I: Variation of Stress and Deformation for Bio-Composite 1

In this phase, the materials tested for tensile strength of rectangular strips.

Dimensions of specimen is given as:

Length = 120 mm

Width = 14 mm

Thickness = 3 mm.

And, the following composition is considered;

Water: tiger grass fibre: gaur gum.

3.1.1 Composition Ratio is Taken as 80:10:10

Maximum load sustained is 106 N

Maximum stress is 1.77 MPa.

By calculations,

Young's modulus = 272.307 MPa

Strain = 0.0065

Change in length = 0.78 mm.

Figure 3 shows variation of stress with strain for the developed bio-composite material. From Fig. 3, it is found that, the maximum ultimate tensile strength recorded was 1.77 MPa with tiger grass reinforcement at 10 wt.%.

Figure 4 depicts the variation of load with deformation for the developed bio-composite material. From Fig. 4, it is found that, the maximum load was recorded as 106 N in particulate tiger grass reinforced at 10 wt.%.

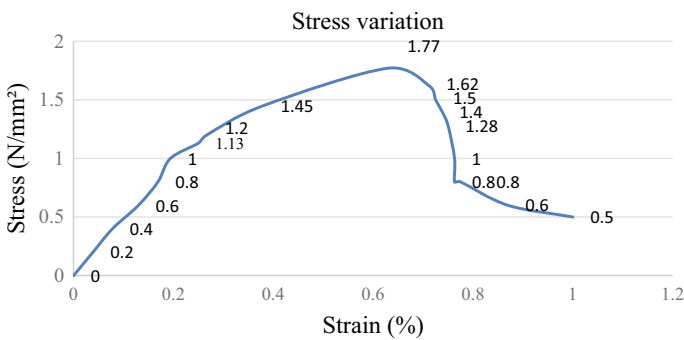


Fig. 3 Variation of stress with strain for bio-composite 1

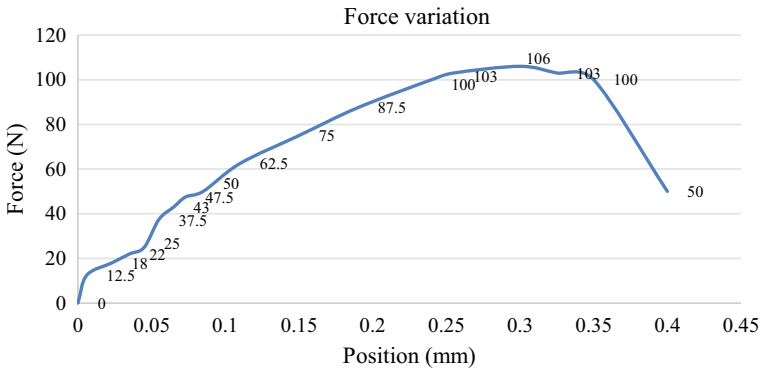


Fig. 4 Variation of force with deformation for bio-composite 1

3.2 Phase II: Variation of Stress and Deformation for Bio-Composite 2

In this phase, material is tested for tensile strength of dumbbell-shaped strips. And, the following compositions are considered,

Water: tiger grass fibre: gaur gum.

3.2.1 Composition Ratio is Taken as 80:10:10

Maximum load sustained is 106 N

Maximum stress is 2.53 MPa.

By calculations,

Young's modulus = 116 MPa

Strain = 0.0218

Change in length = 2.6 mm.

The stress and load results obtained through UTM are as follows:

Figure 5 shows variation of stress with strain for the developed bio-composite material. From Fig. 5, it is found that the maximum ultimate tensile strength was recorded 2.53 MPa in particulate tiger grass reinforced at 10 wt.%.

Figure 6 shows variation of load with deformation for the developed bio-composite material. From Fig. 6, it is found that the maximum load was recorded 106 N in particulate tiger grass reinforced at 10 wt.%.

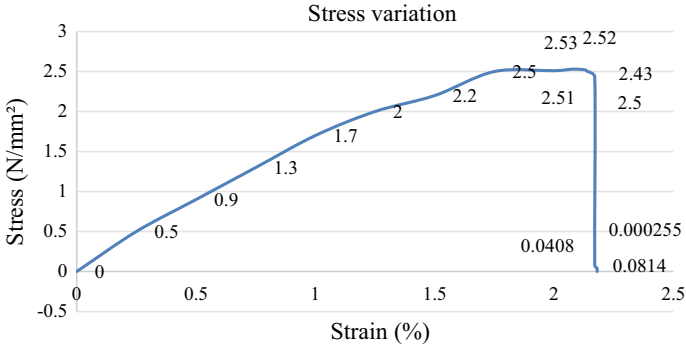


Fig. 5 Variation of stress with strain for bio-composite 2

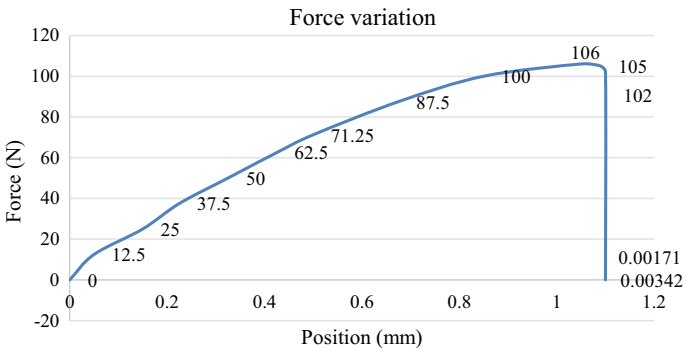


Fig. 6 Variation of force with deformation for bio-composite 2

3.2.2 Composition Ratio is Taken as 80:15:5

Maximum load sustained is 43.6 N
 Maximum stress is 1.04 MPa.

By calculations,

- Young’s modulus = 72.72 MPa
- Strain = 0.0143
- Change in length = 1.71 mm.

The stress and load results obtained through UTM are as follows:

Figure 7 shows variation of stress with strain for the developed bio-composite material. From Fig. 7, it is found that, the maximum ultimate tensile strength was recorded 1.04 MPa in particulate tiger grass reinforced at 15 wt.%.

Figure 8 shows variation of load with deformation for the developed bio-composite material. From Fig. 8, it is found that the maximum load was recorded 43.6 N in particulate tiger grass reinforced at 15 wt.%. The decrease in ultimate tensile strength is due to poor interfacial bonding between hydrophilic fibre and hydrophilic matrix.

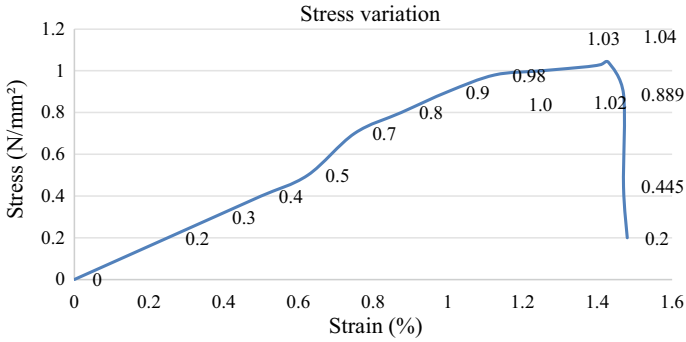


Fig. 7 Variation of stress with strain for bio-composite 3

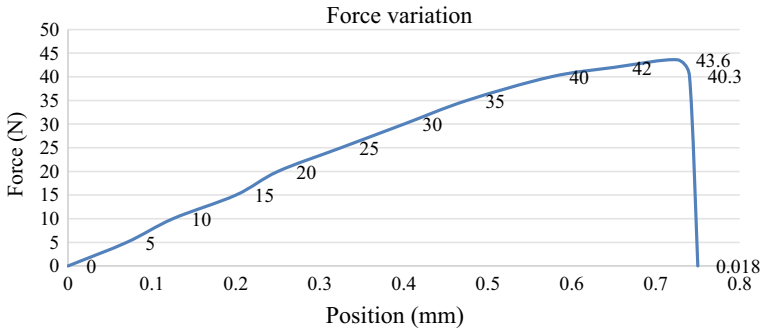


Fig. 8 Variation of force with deformation for bio-composite 3

At 15 wt.%, the fibre-to-fibre contact inside the bio-composite was more. Because of the poor interfacial bonding, effective load transfer could not take place which leads to failure quickly. Considering the intricate points in a cutlery, the values obtained in phase 2 for the dumbbell-shaped strips are suitable to use the mixture composition of ratio 80:10:10 for a durable cutlery.

The Final product as shown in Fig. 9 that we could come up with as a proof of concept.

4 Finite Element Analysis

Finite element analysis is a well-proven simulation method, and currently there are numerous software tools which predict the minimal quantum of error and accurately able to correlate the results. In this analysis, a solid model coupon as per the ASTM D638 was built in ANSYS WORKBENCH 18.2 Version using Design Modeller as



Fig. 9 Final product

a module and then solved using ANSYS Mechanical. The results are correlated with experimental method.

4.1 Solid Model Development

The coupon specimen as per the ASTM D638 was developed in ANSYS WORKBENCH Design Modeller tool [7, 8] and considered for simulation as per experimental method as shown in Fig. 10.

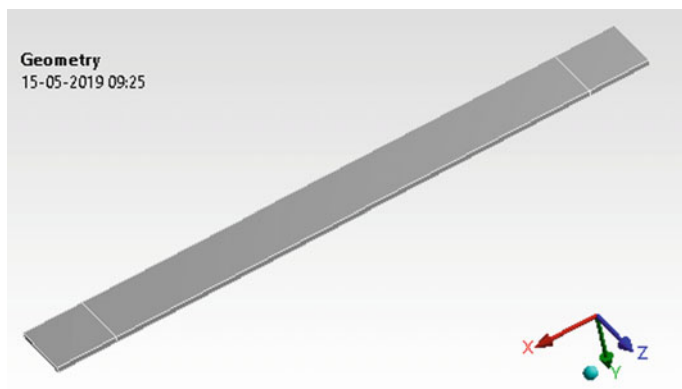


Fig. 10 Coupon modelled in ANSYS WORKBENCH Design Modeller

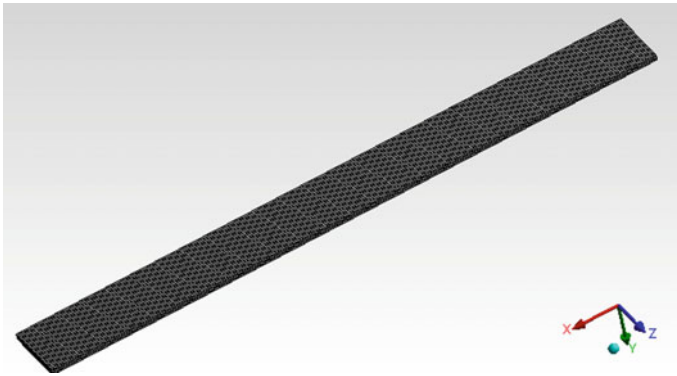


Fig. 11 Coupon mesh generation

4.2 Mesh Generation

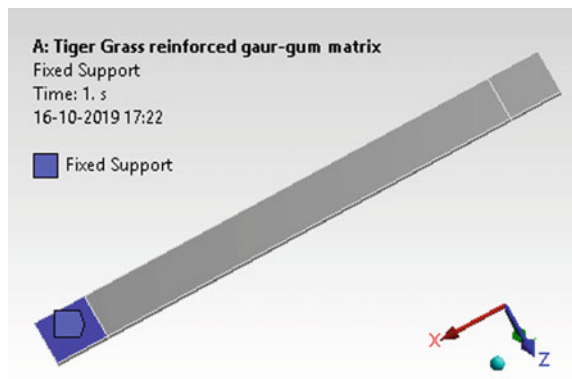
The entire coupon was subjected to a default mesh with mid-node dropped condition. The P-type method was used in this case. The mesh structure had 96,782 nodes and 18,750 elements with hexagonal 8-node SOLID186 element type as shown in Fig. 11.

4.3 Load and Boundary Conditions

The entire model subjected to a real-time experimental set-up boundary condition, one end of the coupon is allowed to be held with micro-gripper and depicted in Fig. 12.

Further, the coupon is subjected to a pull force at the other end with a load of 106 N as shown in Fig. 13.

Fig. 12 Coupon mesh generation



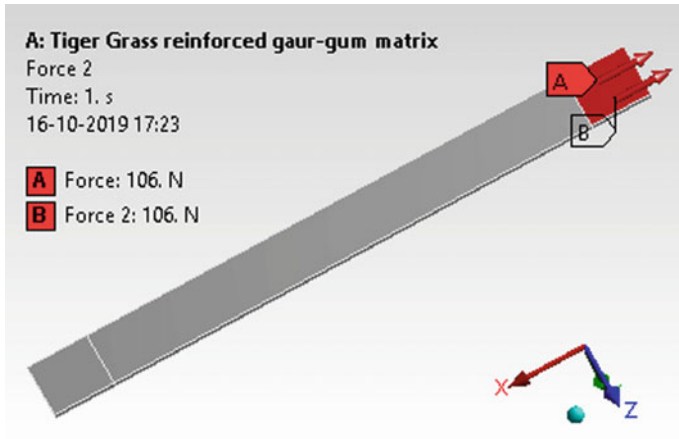


Fig. 13 Load details for coupon of tensile strength test

4.4 FEA Results and Discussion

The coupon was subjected to a tensile strength test, and the results reveal a good correlation with experimental method. From Fig. 14, total deformation of 0.20783 mm was observed and a von Mises stress value of 10.136 MPa is reported [9, 10] (as shown in Fig. 15).

The experimental work and simulation results were correlated for a banana fibre-based bio-material after assigned a particular material properties to the coupon. The details of comparative study were discussed in Table 2.

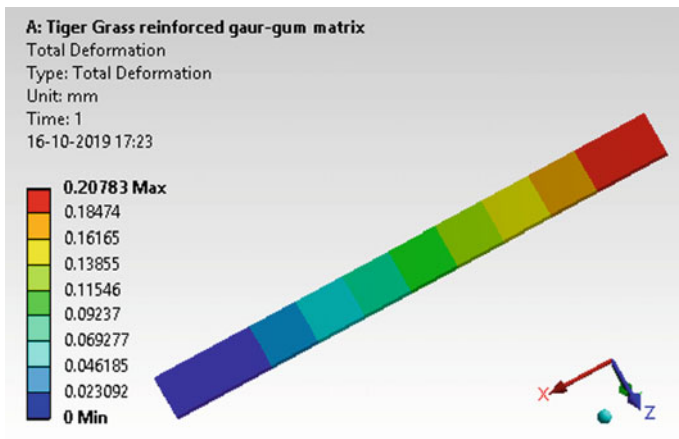


Fig. 14 Total deformation for coupon subjected to tensile strength test

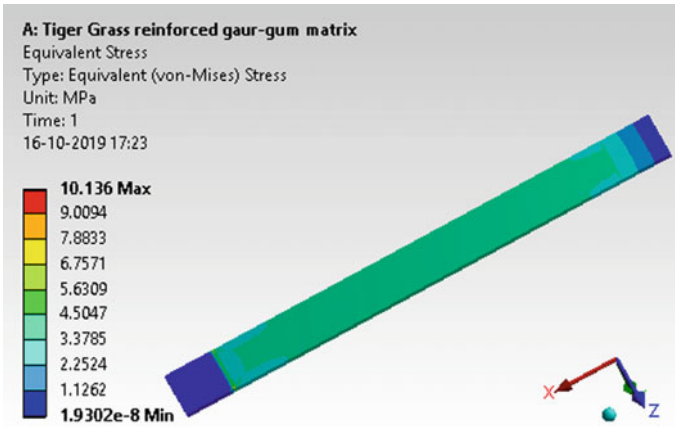


Fig. 15 Load details for coupon of tensile strength test

Table 2 Comparative study of experimental and simulation [8, 10]

Load applied (in Newton)	Experimental tensile strength	Simulation tensile strength	Error (in percentage)
106	2.53	3.37	33.2

5 Conclusions

From the exhaustive experimentation carried on the natural fibre—broom grass—reinforcement in the gaur gum matrix, it can be concluded that the untreated fibres have been able to sustain the loads up to 106 N when mixture is at a balanced ratio. And the load has tremendously gone down to 43.6 N when the mixture is unbalanced with less % of matrix. Also, same is the case with the maximum ultimate stresses which reduces from 2.53 MPa (when mixture ratio is balanced) to 1.04 MPa (when mixture ratio is unbalanced with less % of matrix). The above case is the experimentation carried out on the dumbbell-shaped strips. Results have slightly varied when the experimentation is carried out on the straight rectangular strips. Especially, for the balanced mixture ratio, maximum load it could sustain is 106 N and stress has come down to 1.77 MPa due to stress concentrations.

Hence, it clearly shows that, the mixture with less % of matrix which is used in order to stabilize the moisture absorption property has caused the negative difference in the load-bearing ability of the composite.

Acknowledgements This research was supported by CMS, Centre for Material Science, KLE technological University. We thank our colleagues from KLE Technological University who provided insight and expertise that greatly assisted the research, although they may not agree with all of the interpretations/conclusions of this paper.

We thank Dr. Nagaraj Banapurmath, for assistance in implementing discrete compositions and suggesting standard methodology during testing, and Dr. Ravi Guttal, Director, Centre for Innovation and Product Development for initial inputs that greatly improved the literature survey to proceed with research.

We would also like to show our gratitude to Vibhava Industries for helping us with the raw materials without which the research would not even initiate. And we thank “anonymous” reviewers for their so-called insights. We are also immensely grateful to Kalinga Institute of Technology (KIIT), for their comments on an earlier version of the manuscript, although any errors are our own and should not tarnish the reputations of the esteemed persons.

References

1. Srinivasababu N, Suresh Kumar J, Vijaya Kumar Reddy K (2014) Mechanical and dielectric properties of *Thysanolaena maxima* (broom grass) long fibre reinforced polyester composites. *Procedia Mater Sci*
2. Avella M, Casale L, Dell'ebra R, Focher B, Martuscelli E, Marzetti A (1998) Broom fibers as reinforcing materials for polypropylene-based composites. *J Appl Polym Sci* 68:1077–1089
3. Mohammad Hassan L, Abd-Alla Nada MA (2003) Utilization of lignocellulosic fibers in molded polyester composites. *J Appl Polym Sci* 87:653–660
4. Shellikeri A, Kaulgud V, Yaradoddi J, Ganachari S, Banapurmath N, Shettar A (2018) Development of neem based bioplastic for food packaging application. *IOP Conf Ser Mater Sci Eng*
5. Srinivasababu N, Suresh Kumar J, Vijaya Kumar Reddy K (2014) Mechanical and dielectric properties of *Thysanolaena maxima* (broom grass) long fibre reinforced polyester composites. *Adv Mater Res* 585:311–316
6. Ajith Kumar A, Sreekala KMS, Arun S (2012) Studies on properties of bio-composites from ecoflex/ramie fabric-mechanical and barrier properties. *J Biomater Nanobiotechnol*
7. Patil AY, Umbrajkar Hrishikesh N, Basavaraj GD, Kodancha KG, Chalageri GR (2018) Influence of bio-degradable natural fiber embedded in polymer matrix. *Mater Today Proc* 5:7532–7540
8. Patil AY, Banapurmath NR, Jayachandra SY, Kotturshettar BB, Shettar AS, Basavaraj GD, Keshavamurthy R, Khan Y, Mathad SN (2019) Experimental and simulation studies on waste vegetable peels as bio-composite fillers for light duty applications. *Arab J Eng Sci IF*:1.092
9. Hallad SA, Banapurmath NR, Patil AY, Hunashyal AM, Shettar AS (2015) Studies on the effect of multi-walled carbon nanotube–reinforced polymer based nano-composites using finite element analysis software tool. *Proc IMechE Part N J Nanoeng Nanosyst* 230(4):200–212
10. Hallad SA, Patil AY, Banapurmath NR, Hunashyal AM, Shettar AS, Ayachit NH (2017) Experimental and numerical validation on the utilization of polymer based nano-composites for structural applications using FEA software tool. *Mater Focus* 6(6):685–690

A Concise View Point on Effects of Agro and Industrial Waste as Reinforcement on Characteristic Properties of Aluminum Alloy-Based Metal Matrix Composites



Panda Sasank Shekhar, Senapati Ajit Kumar, and P. Srinivasa Rao

Abstract Aluminum alloy-based metal matrix composites preferred over various conventional materials in aerospace, automotive, electronics, defense and marine applications only to their excellent improved properties. Now, these composites made by adding SiC, Al₂O₃, BN particles into molten Al alloy to make it cost-efficient. Owing to poor wettability of these particulates and the density difference between the particulates and the matrix making the product even costlier. To avoid the above uncommon conditions, researchers have started using industrial waste and agro waste materials as reinforcement which has the potentials of satisfying the demands of advanced engineering applications. Reinforcement materials like fly ash, rice husk ash, coconut shell ash, bagasse ash, eggshell and red mud used to reach optimality in structure and properties of waste materials reinforced metal matrix composite. Many manufacturing techniques have devised over the last three decades. This paper trying to review the various industrial and agro waste reinforcing materials employed in production of aluminum alloy-based metal matrix composites (AMCs). It also explains the way it affects the physical, mechanical and wear properties of the material.

Keywords Aluminum alloy · Stir casting · Metal matrix composites (MMCs) · Mechanical properties · Tribological properties · Industrial and agro waste materials

P. Sasank Shekhar (✉) · P. S. Rao
Centurian University of Technology and Management, Parlakhemundi, Odisha, India
e-mail: sekhar.4206@gmail.com

P. S. Rao
e-mail: psrao@cutm.ac.in

S. Ajit Kumar
GIET University, Gunupur, India
e-mail: senapati.ajit@gmail.com

1 Introduction

Nowadays, aluminum alloys have paying attention of many researchers, designers and engineers as hopeful structural materials for automotive industry and aerospace applications [1–3]. These aluminum alloys have been used as a matrix material by many industries due to its properties like lightweight and moderate strength [4, 5]. The wide uses of aluminum alloys are because of its various desirable properties, with a great variety of shapes and forms [6]. Aluminum alloys became the primary material choice for aircraft applications because of its low density combined with their high strength, where specific strength (strength-to-weight ratio) is a major design consideration [7]. The tribological properties of the aluminum alloys are very poor [3]. Al-Mg-Si alloys termed 6000 series are having medium strength and heat treatable alloys. They also have good formability, medium strength, weldability, low cost comparing to other aluminum alloys and good corrosion resistance characteristics. Aluminum alloy 6000 series is an alloy of magnesium and silicon, which can easily machinable and can hardened by precipitation hardening [8]. Al-Mg-Si alloys are being used broadly in automobiles where tribological property is essential. The life of tribological components adversely affected by the presence of impurities, metallic trash and hard dust particles in lubricant which causes abrasive wear [9]. Al 5056 have nearly all the properties same as that of Al 6061. However, Al 5056 has low temperature specific heat than Al 6061 and less strength-to-weight ratio because of the slightly fewer amount of aluminum than Al 6061. Magnesium is present in Al 5056 instead of silicon [10]. The 6061 Al alloy has used in the automotive industry to fabricate several automobile parts (such as wheels, panels, vehicle chassis, in late case of jet engine, railcars, piping, etc.) [8]. Among all the aluminum alloy series, Al 6061 holds good formability with high hardness and good corrosion resistance [10]. From the 6000 alloy series, Al 6061 is most widely used because of its heat treatable property which can produce precipitation to various degrees. For increasing the strength of this alloy by doing solution heat treatment and quenching, the T6-Al 6061 can be prepared [11]. Al 6061 alloy used in different sectors because of its high specific strength, but it shows inferior tribological properties [12]. T6-Al6061 alloy contains high magnesium and silicon content. It has good mechanical and tribological property and is therefore widely used to fabricate different parts of automobiles and aircrafts [13, 14].

From foregoing given statements, Al or its alloy is good for use as materials except for the cases where it depends on tribological properties. For making use of these Al alloy, nowadays researchers fascinated in fabrication of MMCs with different reinforcements.

2 Fabrication of Aluminum Alloy-Based Metal Matrix Composite

Naher et al. [15] and Sijo and Jayadevan [16] reported three different manufacturing processes available for production of Al-SiC MMC. They are solid, liquid and semi-solid phase. Out of these three types of methods, liquid phase method is widely used because of its advantages like, low cost, ease, flexibility and can be used for mass production. Sevik and Kurnaz [17] and Bharath et al. [18] compared two methods for fabrication of composites by melting (viz. liquid metallurgy and compo-casting). Due to this vortex, the porosity of the MMCs increases. Shanmughasundaram et al. [19] and Admille et al. [20] reported stir casting as a promising route for fabrication of MMCs. The buoyant migration caused in the particles present at the surfaces, because of the gas layer. For getting good quality composites, some important parameters need to consider such as stirring speed, pouring temperature and preheat temperature of the reinforcement metal. Abdizadeh et al. [21] have reported among different types of fabrication processes stir casting and powder metallurgy are two common methods used in different sectors. Due to some advantages like low cost, high production rate, stir casting method is better than powder metallurgy method.

Pal et al. [22] made a comparative study between different production methods and found that melting the alloys by stir casting is a better alternative for fabrication of MMCs. Large-sized parts can also fabricate easily. During fabricating of the MMCs, in stir casting route, the reinforcement material is not damaged. Sedimentation and agglomeration of reinforcement particles occur in the stir casting method. The quality also affected by trapping of aluminum oxide (dross) formed during melting.

From the above discussion of different researchers, we found that stir casting method gives good result in terms of wettability of the reinforcement, cost effective and mass production and hence enhancement of different properties.

3 Types of Reinforcements Used During Manufacturing of AMCs

Anilkumar et al. [23] prepared composite with aluminum alloy and fly ash by stir casting method. Samples of varying fly ash sizes (4–25, 45–50 and 75–100 μm) were chosen for the experiment. The authors reported an enhancement in the mechanical property owing to high dislocation density. Boopathi et al. [24] revealed that fly ash is produced by combustion process in coal formed plants which is available in large amount as solid waste. This is one of the low density and economical reinforcement available for making metal matrix composite.

Behzad [25] revealed rice husk ash (RHA) is a tough material and is thermally stable. It contains 55–97% of silica in the form of crystalline and amorphous. Because of the presence of silica in large amount, these are used as reinforcement for making

composites. Aigbodion [26] prepared a composite with rice husk ash (RHA) as reinforcement. Microscopic study of the prepared composite revealed that, RHA contains around 85–90% amorphous silica. Cristobalite (a crystalline form of silica) obtained from RHA by proper thermal treatment which reduces the corrosion and wear of the composite. Gladston et al. [27] reported that RHA is an imminent reinforcement particle to fabricate aluminum matrix composites (AMCs) cost-effectively.

Usman et al. [28] have studied density of Al-7% Si alloy composite with bagasse ash (BA) as reinforcement produced at 800 °C. BA used as reinforcement with volume percentage from 0 to 30%. The statistical analysis shows there are significant differences among the property of the composites at various levels of BA replacement. Researchers have concluded that the BA can be used as a reinforcement material in making of aluminum matrix composites (AMCs). The produced AMCs can be used in automobile industry for producing engine blocks, pistons, etc.

Debnath et al. [29] used different agro-based materials as reinforcement. The researchers have concluded that coconut shell ash, rice husk ash can be used as reinforcement for making better composites which can be used in different applications. Aku et al. [30] used double stir casting method to fabricate the Al alloy/coconut shell ash particulate composites. The authors revealed that the percentage of coconut shell ash in the composite is inversely proportional to the density of the composite.

From the review on different types of industrial and agro waste reinforcements, researchers have found FA and RHA give better properties than others because of its uniform distribution in the aluminum matrix metal.

4 Properties of Al Matrix Composite (AMCs)

4.1 Mechanical Properties

Haque et al. [31] fabricated A356.2/RHA composites and revealed an enhancement of ultimate strength and compressive strength with the addition of rice husk ash content in the composite. Saravanan and Kumar [32] produced AlSi10Mg/RHA composite and revealed that the tensile strength and hardness increase with the addition of RHA amount. Figure 1 shows a significant increase in the tensile strength of the composite up to 12% of rice husk ash addition. However, further addition of ash decreases the tensile strength of the composite.

Shanmughasundaram et al. [19] investigated the mechanical properties of Al alloy/FA composite. The authors have revealed that with the addition of 1.5 wt% of Mg, the wetting of FA in Al alloy can further improved. The author reported that up to 15% of fly ash content, the tensile strength, hardness and compressive strength increase, and after that, it drops due to particle clustering. Anilkumar et al. [23] produced Al alloy/FA particles and investigated different mechanical properties. The author found that tensile strength of the prepared composite increases with increasing the percentage of reinforcement and decreases with increasing the particle

Fig. 1 Effect of rice husk on tensile strength [32]

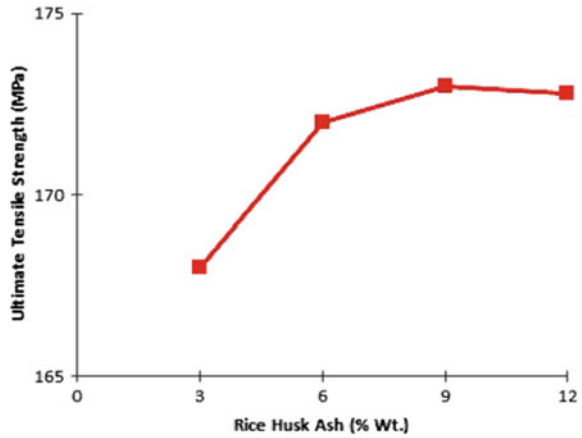
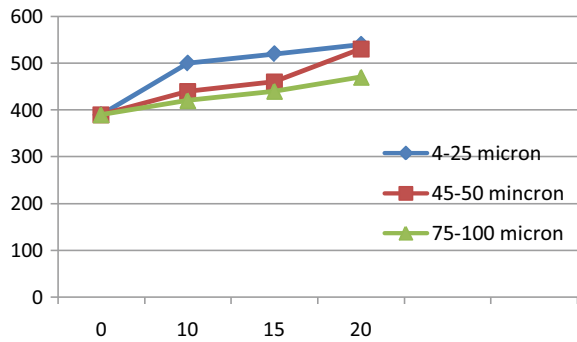


Fig. 2 Tensile strength variation with weight percentage of FA particles [23]



size. Figure 2 shows the increase in the tensile strength of the composite with addition of FA particles.

Suragimath and Purohit [33] investigated different mechanical properties of the LM6-SiC-fly ash composite and revealed the tensile strength is proportional to the weight fraction of fly ash. Senapati et al. [34] fabricated LM6/fly ash composite and made a comparative study between the matrix material and the composite. The authors reported that the hardness is increased by 18.5% over that of the matrix alloy, and the tensile test shows an increase of 20.3% over that of the matrix alloy. Authors reported that rich in carbon percentage (5.6%) may be one of the reasons for enhancement of these mechanical properties. Senapati et al. [35] fabricated a composite using stir casting method with metal matrix as LM6 alloy and reinforcement as treated fly ash (TFA) and untreated fly ash (UFA) with a volume percentage of 12. The authors revealed that mechanical strength of the composite with treated fly ash has better tensile and impact strength than the untreated composite and the matrix metal.

4.2 Tribological Properties

Kumar et al. [36] investigated the wear behavior of MMCs prepared with fly ash as reinforcement in Al matrix. The authors found that, with the increase of wt% of fly ash up to 15%, the specific wear rate decreases. Ramachandra and Radhakrishna [37] fabricated Al-Si/FA composite and studied the wear and friction characteristics by sliding wear test. The authors have found that the wear and frictional force increase with increased normal load and sliding velocity.

Shivaprakash et al. [38] investigated the wear behavior of treated and untreated fly ash reinforced with Al-2024 and observed that the wear characteristics of the treated fly ash composite show better as compared to untreated fly ash composite. Senapati et al. [39] investigated the tribological behavior of the prepared composite with treated and untreated fly ash as reinforcement. The authors found that carbon present in the composite is in graphite form which is responsible for increase in the wear resistance. Response surface methodology (RSM) was used for finding the wear characteristics. A regression equation also developed by taking sliding time, sliding distance while load as input parameter and amount of weight loss and coefficient of friction (COF) as response. It was revealed that sliding velocity and the applied load have the highest influence on the coefficient of friction and weight loss.

Apasi et al. [40] studied the wear behavior of Al-Si-Fe alloy/coconut shell ash composite. The authors also found that increase in the applied load the coefficient friction of friction and wear rate increases significantly. Raju et al. [41] fabricated coconut shell ash particles (CSA) reinforced composites through compo-casting route with different proportion of shell ash. The authors investigated the tribological behavior of the prepared composite at elevated temperature, i.e., (50–150 °C). By using optimization technique, the authors reported that the influence of temperature, sliding distance and sliding speed is more on coefficient of friction and wear.

5 Literature Gap

From the above literatures that we have reviewed, the following gaps we have found:

1. There is scope on high temperature analysis of MMCs prepared with waste reinforcements like fly ash and rice husk ash as these contain different elements which we are getting in the costly reinforcements like SiC, Al₂O₃.
2. Analysis of effect of size of reinforcements has been done but with a contradictory statement and that too at ambient temperature. This can be a good area for focusing by the researchers.
3. Work on optimization of wear for Al-MMCs with waste material reinforcements at elevated temperature is not defined properly.

6 Objectives

From the literature study, the following can be our objective:

1. To prepare an Al-MMCs with agro and industrial waste as reinforcement using stir casting method.
2. To improve different mechanical and physical properties of aluminum.
3. To find the wear behavior of the prepared composite with its effect of sliding speed, sliding distance, time and high temperature.

7 Concluding Remarks

The above review on different method for making the Al-MMCs, different reinforcements concludes as

- Stir casting method is the best alternative for making the aluminum metal matrix composite.
- Many researchers have identified waste materials like fly ash, rice husk ash, bagasse ash, coconut shell ash, eggshell and red mud have potential material as reinforcement.
- Properties of the waste material such as low density, low cost and good wettability attract researchers to use them as reinforcement for making MMCs.
- These waste materials used to improve different properties of the composites and make them high strength, lightweight, good corrosion resistance, improved wear resistance, low density and improved high temperature resistant.
- Improvement in the mechanical properties of the AMCs is shown due to high dislocation density and uniform distribution of the reinforcement particles in the matrix.
- Temperature or heat treatment plays a vital role on wear behavior of the composite.
- Several material parameters such as weight fraction or volume percentage of reinforcement, particulate size, reinforcement distribution, stirring speed and stirring time can influence the physical, mechanical and tribological properties of the metal matrix composites.

References

1. Evancho JW, Kaufman JG (1977) New 6XXX-series alloys for auto body sheet. SAE technical paper no. 770307
2. Altenpohl DG (2012) Materials in world perspective: assessment of resources, technologies and trends for key materials industries. Springer Science & Business Media
3. Lee SH, Saito Y, Sakai T, Utsunomiya H (2002) Microstructures and mechanical properties of 6061 aluminum alloy processed by accumulative roll-bonding. Mater Sci Eng 325(1–2):228–235

4. Dursun T, Soutis C (2014) Recent developments in advanced aircraft aluminium alloys. *Mater Des* (1980–2015) 56:862–871
5. Hirsch J (2014) Recent development in aluminium for automotive applications. *Trans Nonferrous Met Soc China* 24(7):1995–2002
6. Basavaraju S, Arasukumar K, Bendigeri C, Umesh CK (2012) Studies on mechanical properties and tribological characteristics of LM25-graphite-silicon carbide and LM25-flyash-silicon carbide-hybrid MMC's. *Int J Innov Res Sci Eng Technol* 1(1)
7. Murtha SJ (1995) New 6XXX aluminum alloy for automotive body sheet applications. *SAE Trans* 657–666
8. Rezaei MR, Toroghinejad MR, Ashrafizadeh F (2011) Effects of ARB and ageing processes on mechanical properties and microstructure of 6061 aluminum alloy. *J Mater Process Technol* 211(6):1184–1190
9. Shah KB, Kumar S, Dwivedi DK (2007) Aging temperature and abrasive wear behaviour of cast Al–(4%, 12%, 20%) Si–0.3% Mg alloys. *Mater Des* 28(6):1968–1974
10. Demir H, Gündüz S (2009) The effects of aging on machinability of 6061 aluminium alloy. *Mater Des* 30(5):1480–1483
11. Jeyasimman D, Sivasankaran S, Sivaprasad K, Narayanasamy R, Kambali RS (2014) An investigation of the synthesis, consolidation and mechanical behaviour of Al 6061 nanocomposites reinforced by TiC via mechanical alloying. *Mater Des* 57:394–404
12. Lee WS, Tang ZC (2014) Relationship between mechanical properties and microstructural response of 6061-T6 aluminum alloy impacted at elevated temperatures. *Mater Des* 58:116–124
13. Aruri D, Adepu K, Adepu K, Bazavada K (2013) Wear and mechanical properties of 6061-T6 aluminum alloy surface hybrid composites [(SiC+Gr) and (SiC+Al₂O₃)] fabricated by friction stir processing. *J Mater Res Technol* 2(4):362–369
14. Maurya R, Kumar B, Ariharan S, Ramkumar J, Balani K (2016) Effect of carbonaceous reinforcements on the mechanical and tribological properties of friction stir processed Al6061 alloy. *Mater Des* 98:155–166
15. Naher S, Brabazon D, Looney L (2005) Development and assessment of a new quick quench stir caster design for the production of metal matrix composites. *J Mater Process Technol* 166(3):430–439
16. Sijo MT, Jayadevan KR (2016) Analysis of stir cast aluminium silicon carbide metal matrix composite: a comprehensive review. *Procedia Technol* 24:379–385
17. Sevik H, Kurnaz SC (2006) Properties of alumina particulate reinforced aluminum alloy produced by pressure die casting. *Mater Des* 27(8):676–683
18. Bharath V, Nagaral M, Auradi V, Kori SA (2014) Preparation of 6061Al–Al₂O₃ MMC's by stir casting and evaluation of mechanical and wear properties. *Procedia Mater Sci* 6:1658–1667
19. Shanmughasundaram P, Subramanian R, Prabhu G (2011) Some studies on aluminium–fly ash composites fabricated by two step stir casting method. *Eur J Sci Res* 63(2):204–218
20. Admille B, Kulkarni SG, Sonawane SA (2014) Review on mechanical & wear behavior of aluminum-fly ash metal matrix composite. *Int J Emerg Technol Adv Eng* 4(5):863–866
21. Abdizadeh H, Ebrahimifard R, Baghchesara MA (2014) Investigation of microstructure and mechanical properties of nano MgO reinforced Al composites manufactured by stir casting and powder metallurgy methods: a comparative study. *Compos B Eng* 56:217–221
22. Pal MK, Sandhu SS, Kalia R, Ghosh A (2015) Identification of optimum composition and mechanical properties of Al–Ni metal matrix composite. *J Miner Mater Charact Eng* 3(04):326
23. Anilkumar HC, Hebbar HS, Ravishankar KS (2011) Mechanical properties of fly ash reinforced aluminium alloy (Al6061) composites. *Int J Mech Mater Eng* 6(1):41–45
24. Boopathi MM, Arulshri KP, Iyandurai N (2013) Evaluation of mechanical properties of aluminium alloy 2024 reinforced with silicon carbide and fly ash hybrid metal matrix composites. *Am J Appl Sci* 10(3):219
25. Behzad K (2011) Nano filler reinforcement effects on the thermal, dynamic mechanical and morphological behaviour of HDPE/rice husk flour composites. *BioResources* 6:1351–1358
26. Aigbodion VS (2012) Development of Al–Si–Fe/rice husk ash particulate composites synthesis by double stir casting method. *Usak Univ J Mater Sci* 1(2):187–197

27. Gladston JAK, Sheriff NM, Dinaharan I, Selvam JDR (2015) Production and characterization of rich husk ash particulate reinforced AA6061 aluminum alloy composites by compocasting. *Trans Nonferrous Met Soc China* 25(3):683–691
28. Usman AM, Raji A, Waziri NH, Hassan MA (2014) Production and characterisation of aluminium alloy-bagasse ash composites. *IOSR J Mech Civ Eng* 11(4):38–44
29. Debnath S, Lancaster L, Lung MH (2013) Utilization of agro-industrial waste in metal matrix composites: towards sustainability. *World Acad Sci Eng Technol* 1136–1144
30. Aku SY, Yawas DS, Adokma A (2013) Evaluation of cast Al-Si-Fe alloy/coconut shell ash particulate composites. *Gazi Univ J Sci* 26(3):449–457
31. Haque MH, Ahmed R, Khan MM, Shahriar S (2006) Fabrication, reinforcement and characterization of metal matrix composites (MMCs) using rice husk ash and aluminium alloy (A-356.2) 7(3):28–35
32. Saravanan SD, Kumar MS (2013) Effect of mechanical properties on rice husk ash reinforced aluminum alloy (AlSi10Mg) matrix composites. *Procedia Eng* 6(4):1505–1513
33. Suragimath MPK, Purohit GK (2013) A study on mechanical properties of aluminium alloy (LM6) reinforced with SiC and fly ash. *IOSR J Mech Civ Eng (IOSR-JMCE)* 8(5):13–18
34. Senapati AK, Mishra PC, Routray BC, Ganguly RI (2015) Mechanical behavior of aluminium matrix composite reinforced with untreated and treated waste fly ash. *Indian J Sci Technol* 8(S9):111–118
35. Senapati A, Raju SS, Rao GS (2017) Tribological performance of Al-MMC reinforced with treated fly ash using response surface methodology. *Indian J Sci Technol* 10(15)
36. Kumar V, Gupta RD, Batra NK (2014) Comparison of mechanical properties and effect of sliding velocity on wear properties of Al 6061, Mg 4%, fly ash and Al 6061, Mg 4%, graphite 4%, fly ash hybrid metal matrix composite. *Procedia Mater Sci* 6:1365–1375
37. Ramachandra M, Radhakrishna K (2007) Effect of reinforcement of flyash on sliding wear, slurry erosive wear and corrosive behavior of aluminium matrix composite. *Wear* 262(11–12):1450–1462
38. Shivaprakash YM, Basavaraj Y, Sreenivasa Prasad KV (2013) Comparative study of tribological characteristics of AA2024+10% fly ash composite in non-heat treated and heat treated conditions. *Int J Res Eng Technol (IJRET)* 2:275–280
39. Senapati AK, SatyajitPadhy N, Nikhandia P (2014) Investigation on mechanical and tribological properties of Al-Si alloy based MMC. *Int J Recent Innov Trends Comput Commun* 2(9)
40. Apasi A, Madakson PB, Yawas DS, Aigbodion VS (2012) Wear behaviour of Al-Si-Fe alloy/coconut shell ash particulate composites. *Tribol Ind* 34(1):36–43
41. Raju RSS, Panigrahi MK, Ganguly RI, Rao GS (2018) Optimization of tribological behaviour on Al-coconut shell ash composite at elevated temperature. *IOP Conf Ser Mater Sci Eng* 314(1)

A Study on Performance of Hydroxyapatite-Filled Polycarbonate and Polysulfone Composites Under Two-Body Abrasive Wear



Amit Kumar Mehar and Sreekanth Kotni

Abstract In this study, investigation and analysis has been done on two-body grating wear conduct of hydroxyapatite (HAp) fortified polycarbonate (PC) and polysulfone (PSU) composites by the expansion of changing measures of the optional stage (HAp) material. Work has been completed to decide rough wear misfortune to comprehend the grating wear conduct of the composites. The wear obstruction of composites in scraped spot mode is surveyed in dry condition. An adaptive neuro-fluffy induction framework (ANFIS) model is proposed for expectation of rough wear conduct of composites. The wear test was performed on stick on-plate grating wear analyzer (ASTM G99) by utilizing Taguchi's L27 symmetrical cluster to assess the wear misfortune with four control factors, for example, HAp volume rate, load connected, sliding velocity, and track range, each at three levels on 400 grit size water verification silicon carbide (SiC) rough paper at a differing sliding separation. It has been seen that increasingly grating wear misfortune happened in HAp/PC composite when contrasted with HAp/PSU composite. From scanning electron magnifying instrument (SEM) investigation, it is unmistakably apparent that as the volume level of HAp expands, grating wear of the composites likewise builds due to hardness of HAp particles increments in the outside of the polymer network. Because of this expanding of hardness of HAp, scratch is additionally expanded in the polymer network.

Keywords Grit size · Hydroxyapatite · Polycarbonate · Polysulfone · Silicon carbide · Two-body abrasive wear

A. K. Mehar (✉) · S. Kotni
Department of Mechanical Engineering, Raghu Engineering College (Autonomous),
Visakhapatnam, Andhra Pradesh, India
e-mail: amitkumarmehar@gmail.com

S. Kotni
e-mail: sreekanth.kotni@gmail.com

1 Introduction

Wear is a procedure of expulsion of material from either of the two strong surfaces [1]. The two-body rough wear is characterized as a dynamic loss of material when two strong bodies are reached to one another out of which one body is more diligently than the another body which slides or moves along another strong surface [2].

Past written works recommend that different sorts of abrasives are utilized out of which the most elevated wear rate in scraped area is seen with coarse SiC grating paper. It is seen that variables, for example, sliding separation, burden, and grating coarseness size have noteworthy effect on rough wear execution [3]. It is reasoned that wear of a composite increments with increment in the size proportion of HAp particles in the polymer grid. It is considered on impact of silicon carbide (SiC) particulate fillers joining on two-body rough wear conduct of glass fiber-epoxy (GE) composites and presumed that the two-body grating wear execution of GE and GE-SiC composites fundamentally relies upon rubbing separation and coarseness size of the rough paper. The wear misfortune is found to increment in composites with the expansion in scraping separations. The presentation of SiC-filled GE composite is discovered better than unfilled GE composite [4]. It is examined that on impact of molecule size, molecule stacking and sliding separation on the grinding and wear conduct of vinylester composites sliding against solidified ground steel on a stick on-plate wear testing machine and inferred that the submicron particles and small-scale particles can improve both the mechanical and wear obstruction of the cenosphere-filled vinylester composites. The submicron measured particles are progressively successful in improving the wear opposition contrasted and the smaller scale estimated particles. It is seen that the hardness, flexural quality, and compressive quality can be expanded with decrease in cenosphere filled vinylester composite which is a result of solid bond among particles and the grid [5].

In this examination, incorporated hydroxyapatite of $2.248\ \mu\text{m}$ (molecule size) was created by blending calcium hydroxide ($\text{Ca}(\text{OH})_2$) powder (Merck, 96%), orthophosphoric (H_3PO_4) corrosive (Merck, 85%), and smelling salts arrangement (Merck, 25%). Smelling salts arrangement might be added possibly to expand the pH esteem on the off chance that it is not exactly the limit esteems. For the most part, pH worth is kept as 8–10 for this amalgamation.

Polycarbonate ($1.20\ \text{g}/\text{cm}^3$ thickness) is a nebulous polymer is a specific gathering of thermoplastics which are effectively worked, shaped, and thermoformed. Other than this, polycarbonate is a solid material, having high sway opposition and low scratch obstruction. As a result of these one of a kind properties, polycarbonates are utilized in different applications like electronic parts, development materials, car industry, flying machine industry, wellbeing segments, and therapeutic applications, and so forth [6].

Polysulfone ($1.24\ \text{g}/\text{cm}^3$ thickness) is a nebulous polymer whose mechanical properties coordinated with those of the light metals [7]. It has high quality and firmness, protection from oxidation, strength in fluid inorganic acids and bio-idleness properties, which makes it an effective network of a bioactive composite [8].

The aim of the present study is to know the wear loss of HAp/PC and HAp/PSU composites conduct in abrasive wear mechanism because of it is hardly found in the literature earlier.

2 Composite Preparation

Composites with different measures of HAp (0, 10, 20 vol. %) were set up by blending through batch mixer (Rheomix 600, Germany) by following advances like grinding, liquefying, and small-scale infusion shaping. At first, the crude materials were pre-dried in a stove at 120 °C for 4 h. Dried HAp powder is blended with polycarbonate framework with a thickness of 3.15 g/cm³. The blends were then granulated into little granules and after that again pre-dried in a broiler and liquefied through smaller scale compounder (XPLORE, 15 ml, DSM, Netherlands) and formed through miniaturized scale infusion trim machine to deliver standard canine bone molded elastic example (ASTM D638), compressive example (ASTM D695), flexural example (ASTM D790), and effect examples (ASTM D256). The small-scale infusion embellishment machine parameters were infusion weight of 6–7 bar, form temperature of 85 °C, liquefy temperature of 230–240 °C, warming in three front zones just as in three back zones were kept up at a temperature of 210, 220, and 230 °C, rotor speed of 100 rpm, time required for stacking, holding, and cooling is of 5, 30, and 30 s separately, blending time is of 1–2 min, and spout temperature is of 240 °C.

As consistency is excessively high of this composite, it is beyond the realm of imagination to expect to blend HAp in huge sum with PSU polymer in batch blender just as in twin screw extruder. Thusly, composites with different modest quantities of HAp (0, 10, 20 vol. %) were created by blending and softening through micro-compounder (XPLORE, 15 ml, DSM, Netherlands) and formed through micro-infusion embellishment machine straightforwardly to deliver standard canine bone molded tractable example (ASTM D638), compressive example (ASTM D695), flexural example (ASTM D790), and effect examples (ASTM D256). At first, the crude materials (e.g., HAp powder and polymers) were pre-dried at 120 °C for 4 h. Dried HAp powder is blended and dissolved with PSU polymer with a thickness of 3.15 g/cm³ and mean molecule size of 2.248 μm through small-scale compounder and shaped through micro-infusion embellishment machine. The miniaturized scale infusion embellishment machine parameters were infusion weight of 7–8 bar, form temperature of 80 °C, soften temperature of 345–360 °C, warming in three front zones just as in three back zones were kept up at a temperature of 330, 340 and 350 °C, rotor speed of 100 rpm, time required for stacking, holding, and cooling is of 5, 30, and 30 s separately, blending time is of 3–4 min, and spout temperature is of 360 °C.

3 Experimental Details of Two-Body Abrasion Wear Test

Two-body abrasion wear test was conducted on pin-on-disk friction and wear test rig is shown in Fig. 1.

It comprises of stacked switch arm, load cell, steel circle plate of 164 mm distance across, and square stick holder of $8 \times 8 \text{ mm}^2$ with the screw. The length, width, and thickness of the composite stick are kept as 25, 6, and 3.32 mm individually [9]. At first lastly for each test run, the stick is said something gauging machine (Mettler Toledo, 0.001 g exactness) and fixed in stick holder with the assistance of the screw [10]. At that point, it is fixed with the switch arm so that the stick is simply addresses grating paper which is stuck on a steel circle. After that through burden cell, load is connected on the stick with the assistance of the switch arm. The distinction among starting and last weight of the example gives wear loss of the composite [11]. The chose info parameters and their degrees of rough wear for the two composites are appeared in Table 1.

There are four factors; each factor is fluctuated at three levels. A full factorial structure would have required 81 trials. Be that as it may, Taguchi configuration was connected to diminish the quantity of tests [12]. The all out number of exploratory runs is 27 (L27). The yield worth is scraped spot wear misfortune (in gram) which is the distinction among beginning and last weight of the stick. Each analysis was kept running for 5 min. The trial perceptions for scraped area wear misfortune are changed into signal to noise (S/N) proportion. S/N proportion is utilized to decide the exhibition attributes [13]. By and large, S/N proportion utilized is bring down



Fig. 1 Pin-on-disk friction and wear test rig

Table 1 Control parameters and their levels

Control parameters	Symbol	Level			Unit
		1	2	3	
HAp volume	A	0	10	20	%
Load applied	B	10	20	30	N
Sliding speed	C	300	400	500	rpm
Track radius	D	20	30	40	mm

the better, higher the better, and ostensible the best [14]. Since wear misfortune is bothersome trademark, bring down the better trademark is utilized.

4 Results and Discussion

4.1 Abrasive Wear Loss

The experimental data for HAp/PC composite conducted at 400 grit size paper is shown in Table 2. The goal of the exploratory format is to limit the scraped spot wear misfortune [15]. The sign to clamor proportion of lower-the-better execution trademark can be communicated as

$$(S/N)_{LTB} = -10\log \sum y_i^2 \tag{1}$$

where y_i is the output value.

Similarly, the experimental data for HAp/PSU composite conducted at 400 grit size paper is shown in Table 3.

It tends to be seen from Fig. 2 that wear misfortune increments for HAp/PC composite when burden increments from 10 to 30 N though wear misfortune increments for burden from 10 to 20 N and afterward diminishes at 30 N for HAp/PSU composite at 300 rpm and 400 coarseness size paper. It very well may be seen from Fig. 3 that wear misfortune diminishes when burden increments from 10 to 20 N and after that increments at 30 N for both HAp/PC and HAp/PSU composites at 400 rpm and 400 coarseness size paper.

It very well may be seen from Fig. 4 that wear misfortune increments for burden 10–20 N and afterward diminishes at 30 N for HAp/PC composite though wear misfortune diminishes for burden 10–20 N and after that increments at 30 N for HAp/PSU composite at 500 rpm and 400 coarseness size paper. It tends to be seen from Fig. 5 that wear misfortune increments when sliding pace increments for 300–500 rpm for both HAp/PC and HAp/PSU composites at 0 vol. % and 400 coarseness size paper.

Table 2 Experimental data for HAp/PC composite conducted at 400 grit size paper

Exp. No.	Factor A (HAp volume) (%)	Factor B (load applied) (N)	Factor C (sliding speed) (rpm)	Factor D (track radius) (mm)	Wear loss (g)	S/N ratio (lower the better)
1	0	10	300	20	0.017	35.391
2	0	10	300	20	0.015	36.478
3	0	10	300	20	0.016	35.917
4	0	20	400	30	0.059	24.582
5	0	20	400	30	0.060	24.436
6	0	20	400	30	0.061	24.293
7	0	30	500	40	0.084	21.514
8	0	30	500	40	0.083	21.618
9	0	30	500	40	0.085	21.411
10	10	10	400	40	0.297	10.544
11	10	10	400	40	0.296	10.574
12	10	10	400	40	0.296	10.574
13	10	20	500	20	0.251	12.006
14	10	20	500	20	0.253	11.937
15	10	20	500	20	0.252	11.971
16	10	30	300	30	0.119	18.489
17	10	30	300	30	0.117	18.636
18	10	30	300	30	0.118	18.562
19	20	10	500	30	0.106	19.493
20	20	10	500	30	0.107	19.412
21	20	10	500	30	0.108	19.331
22	20	20	300	40	0.059	24.582
23	20	20	300	40	0.061	24.293
24	20	20	300	40	0.060	24.436
25	20	30	400	20	0.100	20.000
26	20	30	400	20	0.102	19.827
27	20	30	400	20	0.101	19.913

It tends to be seen from Fig. 6 that wear misfortune increments when sliding pace increments for 300–400 rpm and after that diminishes at 500 rpm for both HAp/PC and HAp/PSU composites at 10 vol. % and 400 coarseness size paper. It tends to be seen from Fig. 7 that wear misfortune increments when sliding velocity increments for 300–500 rpm for HAp/PC composite though wear misfortune diminishes for sliding pace 300–400 rpm and afterward increments at 500 rpm for HAp/PSU composite at 20 vol. % and 400 coarseness size paper.

Table 3 Experimental data for HAp/PSU composite conducted at 400 grit size paper

Experiment No.	Factor A (HAp volume) (%)	Factor B (load applied) (N)	Factor C (sliding speed) (rpm)	Factor D (track radius) (mm)	Wear loss (g)	S/N ratio (lower the better)
1	0	10	300	20	0.022	33.151
2	0	10	300	20	0.021	33.555
3	0	10	300	20	0.023	32.765
4	0	20	400	30	0.041	27.744
5	0	20	400	30	0.040	27.958
6	0	20	400	30	0.039	28.178
7	0	30	500	40	0.085	21.411
8	0	30	500	40	0.084	21.514
9	0	30	500	40	0.086	21.310
10	10	10	400	40	0.110	19.172
11	10	10	400	40	0.111	19.093
12	10	10	400	40	0.110	19.172
13	10	20	500	20	0.077	22.270
14	10	20	500	20	0.079	22.047
15	10	20	500	20	0.078	22.158
16	10	30	300	30	0.091	20.819
17	10	30	300	30	0.090	20.915
18	10	30	300	30	0.092	20.724
19	20	10	500	30	0.095	20.445
20	20	10	500	30	0.094	20.537
21	20	10	500	30	0.097	20.264
22	20	20	300	40	0.112	19.015
23	20	20	300	40	0.110	19.172
24	20	20	300	40	0.113	18.938
25	20	30	400	20	0.045	26.935
26	20	30	400	20	0.046	26.744
27	20	30	400	20	0.044	27.130

4.2 Prediction of Abrasive Wear Behavior of Composites

4.2.1 ANFIS Methodology Used for HAp/PC Composite

ANFIS is an induction framework which is coupled between neural system and fluffy deduction framework. Essentially, ANFIS is an adjusted type of neural system that depends on Tagaki-Sugeno fluffy derivation framework which maps contributions

Fig. 2 Load versus wear loss (300 rpm on 400 grit size)

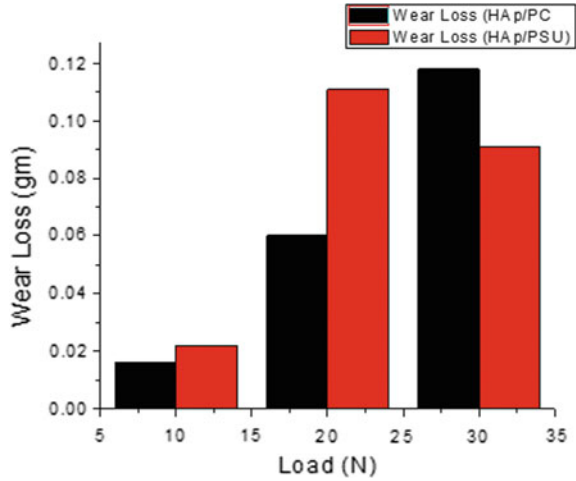
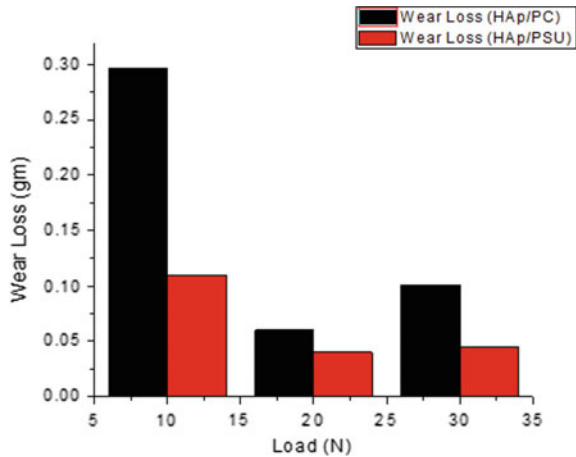


Fig. 3 Load versus wear loss (400 rpm on 400 grit size)



through information participation capacities and yields through yield enrollment capacities. Neural system is difficult to execute the outcomes as it can gain from the information which is available as information and yield matches anyway then again fluffy induction framework are anything but difficult to actualize the outcomes as it requires just IF-THEN runs the show. Along these lines, to foresee the outcomes with a high precision, it is important to manufacture the novel model which depends on both neural system and fluffy induction framework. A run of the mill engineering of ANFIS framework is appeared in Fig. 8. The ANFIS framework is isolated into five layers, for example, input fuzzification layer, fluffy set database development layer, fluffy guideline database development layer, basic leadership layer lastly yield defuzzification layer [16].

Fig. 4 Load versus wear loss (500 rpm on 400 grit size)

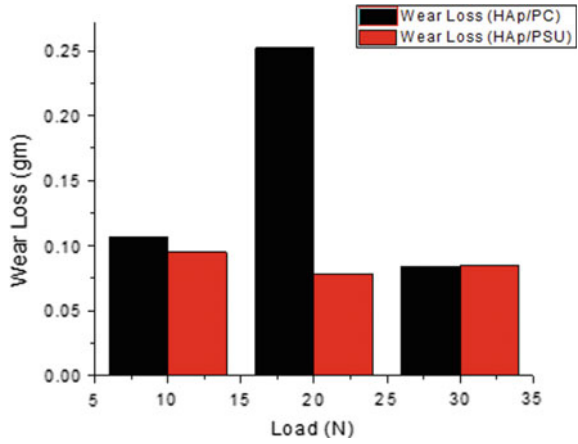


Fig. 5 Sliding speed versus wear loss (0 vol. % and 400 grit size)

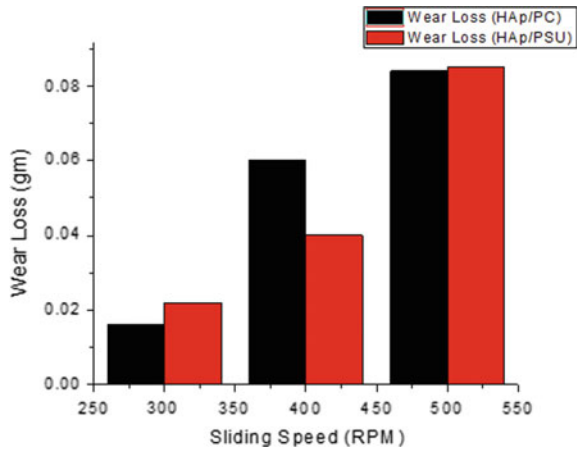
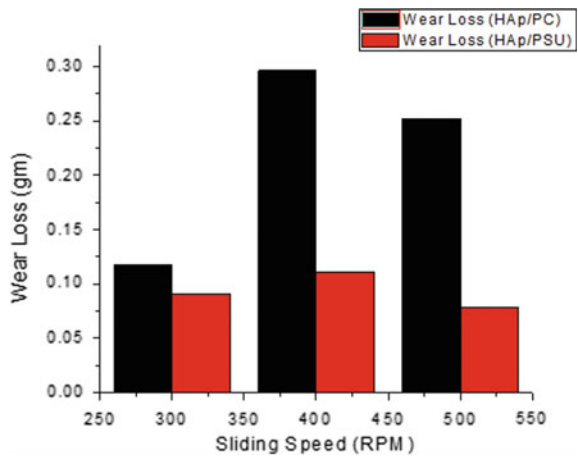


Fig. 6 Sliding speed versus wear loss (10 vol. % and 400 grit size)



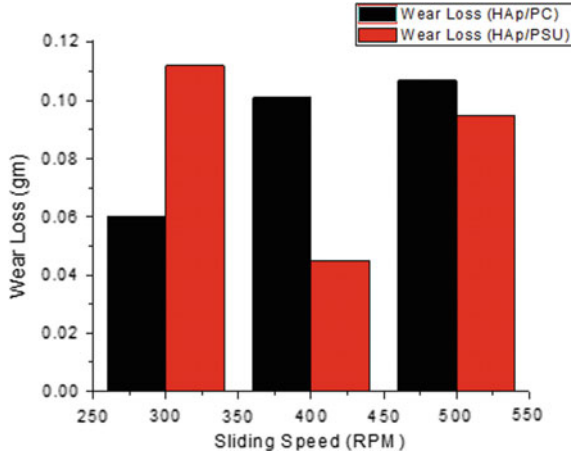


Fig. 7 Sliding speed versus wear loss (20 vol. % and 400 grit size)

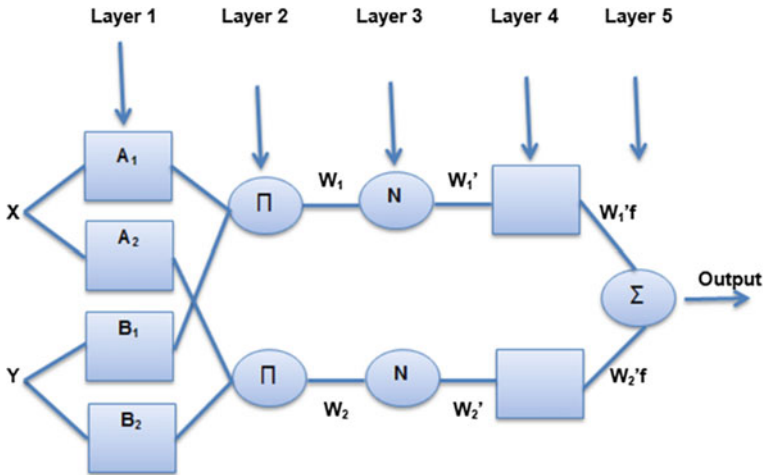


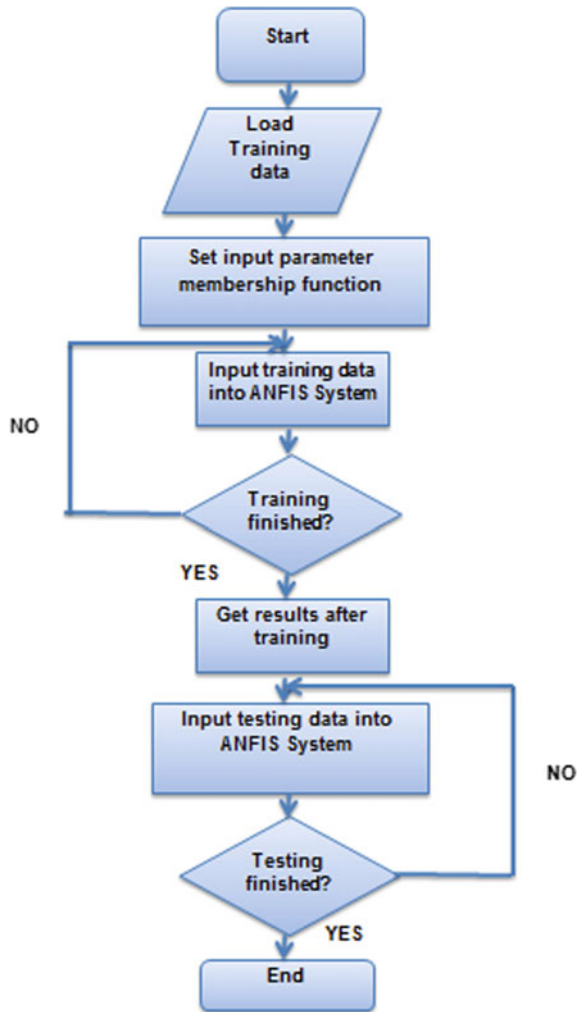
Fig. 8 A typical architecture of ANFIS system

Whole exploratory informational index is partitioned into preparing set and testing set. A sum of 27 informational indexes are utilized out of which 20 are considered as preparing information and 7 as testing information. During preparing, a five-layered ANFIS model is built as talked about. The quantity of hubs in the second layer expanded slowly during preparing beginning with two. It was seen that the mistake is met (diminishing) by expanding the hubs up to three. Thus, the quantity of hubs in second layer is fixed to three and further investigation is done. The five layers are known as one information, three covered up, and one yield layer [17]. The system was kept running on MATLAB stage utilizing HP Compaq LE1902x personal

computer. Three triangular sort participation capacities (trimf) are picked for information and consistent sort enrollment capacity is utilized for yield during producing FIS. The capacity goes consistently because of quicker cross breed learning decide which presumed that the model parameters are coordinated. After that 7 information are utilized for testing to confirm the precision of the proposed model. Figure 9 demonstrates the technique for building up the ANFIS model.

The ANFIS model structure of composites regarding abrasive wear is shown in Fig. 10, while ANFIS editor for both training and testing data of HAp/PC composite is shown in Figs. 11 and 12, respectively.

Fig. 9 Flow chart of ANFIS model



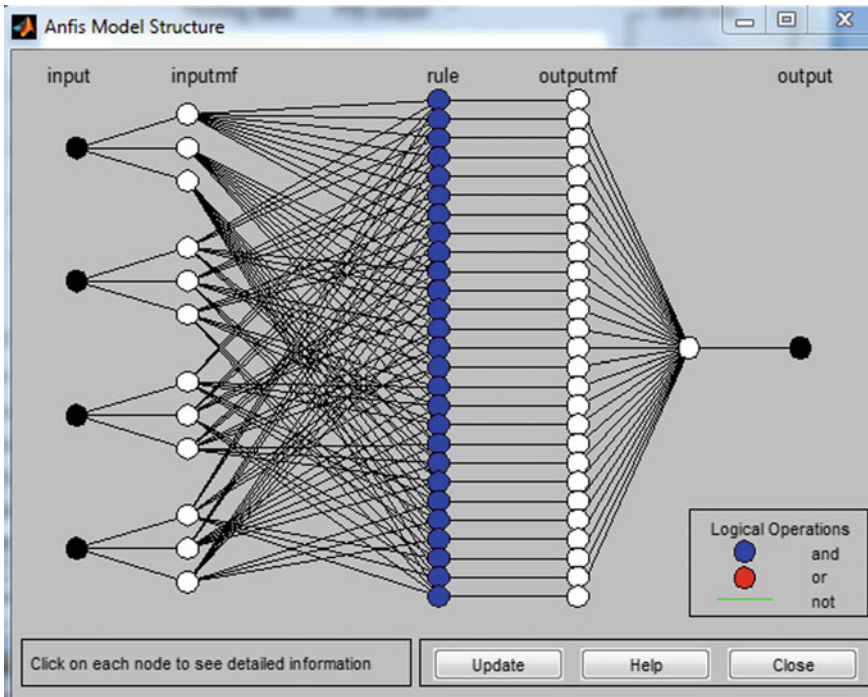


Fig. 10 ANFIS model structure

The input and output experimental values with ANFIS predicted value of HAp/PC composite at 400 grit size for training and testing purpose are shown in Tables 4 and 5, respectively.

By calculating, we get the mean relative percentage error for training and testing of HAp/PC composite conducted at 400 grit size paper is 7.38% and 14.26%, respectively.

4.2.2 ANFIS Methodology Used for HAp/PSU Composite

The ANFIS editor for both training and testing data of HAp/PSU composite is shown in Figs. 13 and 14, respectively.

The input and output experimental values with ANFIS predicted value of HAp/PSU composite at 400 grit size for training and testing purpose are shown in Tables 6 and 7, respectively.

By calculating, we get the mean relative percentage error for training and testing of HAp/PSU composite conducted at 400 grit size paper is 3.80% and 6.30%, respectively.

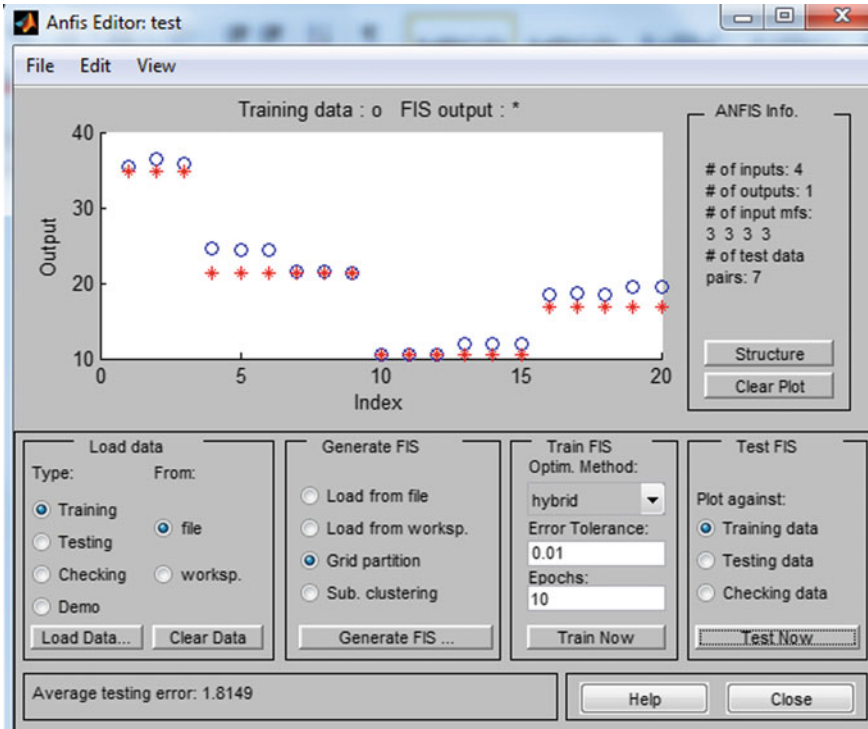


Fig. 11 Distribution of predicted and actual data (training)

4.3 SEM Analysis

It is appeared from Figs. 15, 16, 17, 18, 19, and 20 that as HAp volume rate increments in both HAp/PC and HAp/PSU composites, rough wear additionally increments in the outside of the examples on account of hardness of HAp particles increments in the delicate and smooth surface of the polymer network. Because of this expanding of hardness of HAp, scratch is likewise expanded in the polymer framework.

5 Conclusions

The following are the observations during investigation of the two-body abrasive wear behaviors of HAp/PC and HAp/PSU composites:

- The HAp/PSU composite exhibited the higher wear resistance than HAp/PC composite under different sliding distances.
- From SEM analysis, it is clearly evident that as the volume percentage of HAp increases, abrasive wear of the composites also increases because of hardness of

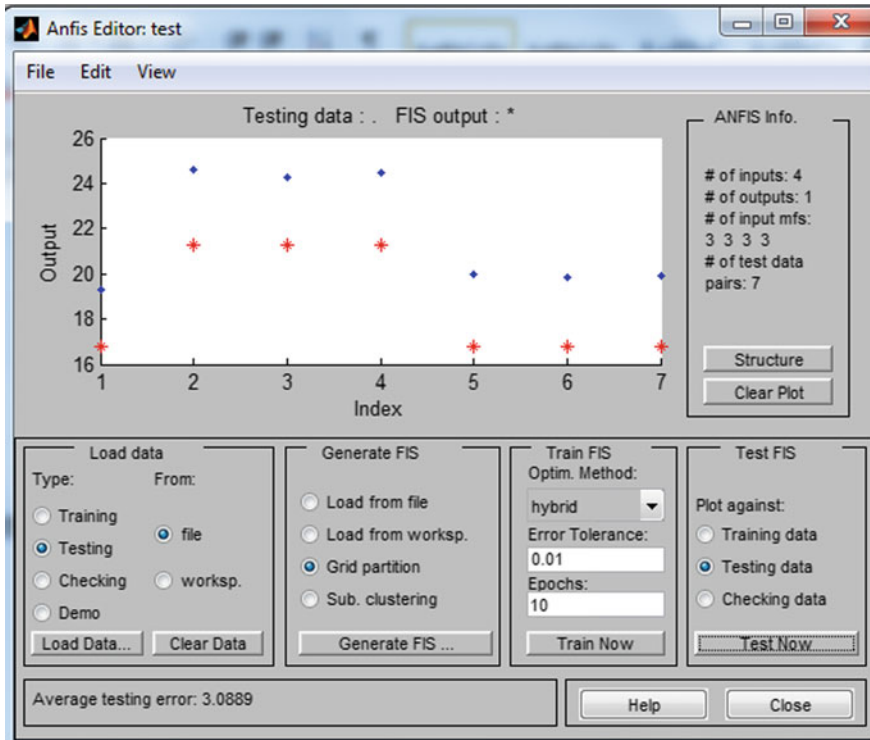


Fig. 12 Distribution of predicted and actual data (testing)

HAp particles increases in the surface of the polymer matrix. Due to this increasing of hardness of HAp, scratch is also increased in the polymer matrix.

- The mean relative percentage error for training and testing of HAp/PC composite conducted at 400 grit size paper is 7.38% and 14.26%, respectively whereas the mean relative percentage error for training and testing of HAp/PSU composite conducted at 400 grit size paper is 3.80% and 6.30%, respectively.
- The performance of HAp/PSU composite is found better than the HAp/PC composite.

Table 4 Input and output data with ANFIS predicted value of HAp/PC composite at 400 grit size

No.	Factor A (HAp volume) (%)	Factor B (load applied) (N)	Factor C (sliding speed) (rpm)	Factor D (track radius) (mm)	Wear loss (g)	S/N ratio of exp. value	ANFIS output predicted value
1	0	10	300	20	0.017	35.391	34.7775
2	0	10	300	20	0.015	36.478	34.7775
3	0	10	300	20	0.016	35.917	34.7775
4	0	20	400	30	0.059	24.582	21.2625
5	0	20	400	30	0.060	24.436	21.2625
6	0	20	400	30	0.061	24.293	21.2625
7	0	30	500	40	0.084	21.514	21.2625
8	0	30	500	40	0.083	21.618	21.2625
9	0	30	500	40	0.085	21.411	21.2625
10	10	10	400	40	0.297	10.544	10.5
11	10	10	400	40	0.296	10.574	10.5
12	10	10	400	40	0.296	10.574	10.5
13	10	20	500	20	0.251	12.006	10.5
14	10	20	500	20	0.253	11.937	10.5
15	10	20	500	20	0.252	11.971	10.5
16	10	30	300	30	0.119	18.489	16.7575
17	10	30	300	30	0.117	18.636	16.7575
18	10	30	300	30	0.118	18.562	16.7575
19	20	10	500	30	0.106	19.493	16.7575
20	20	10	500	30	0.107	19.412	16.7575

Table 5 Input and output data with ANFIS predicted value of HAp/PC composite at 400 grit size

No.	Factor A (HAp volume) (%)	Factor B (load applied) (N)	Factor C (sliding speed) (rpm)	Factor D (track radius) (mm)	Wear loss (g)	S/N ratio of exp. value	ANFIS output predicted value
1	20	10	500	30	0.108	19.331	16.7575
2	20	20	300	40	0.059	24.582	21.2625
3	20	20	300	40	0.061	24.293	21.2625
4	20	20	300	40	0.060	24.436	21.2625
5	20	30	400	20	0.100	20.000	16.7575
6	20	30	400	20	0.102	19.827	16.7575
7	20	30	400	20	0.101	19.913	16.7575

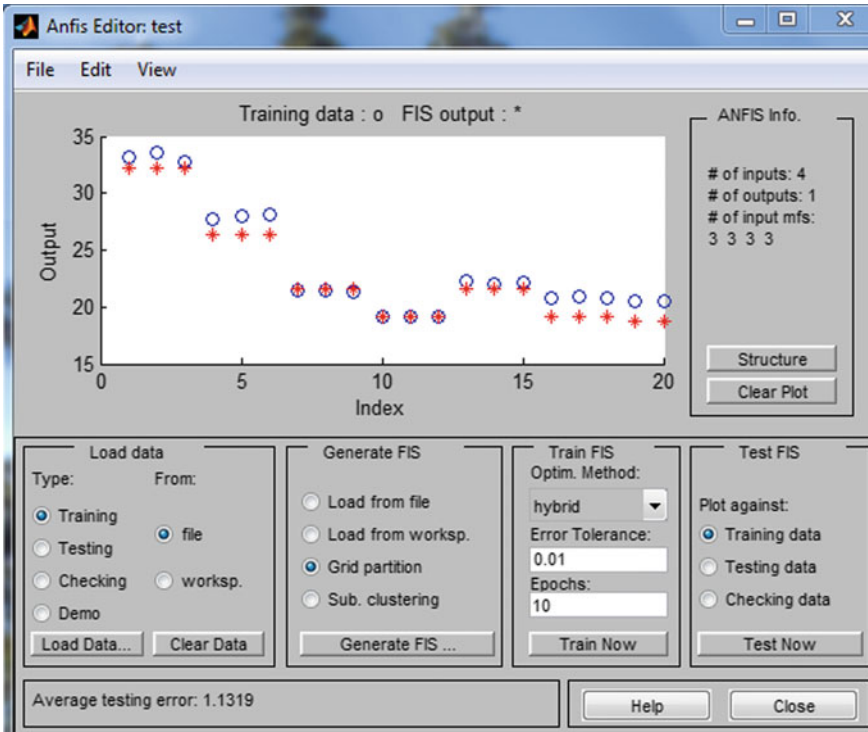


Fig. 13 Distribution of predicted and actual data (training)

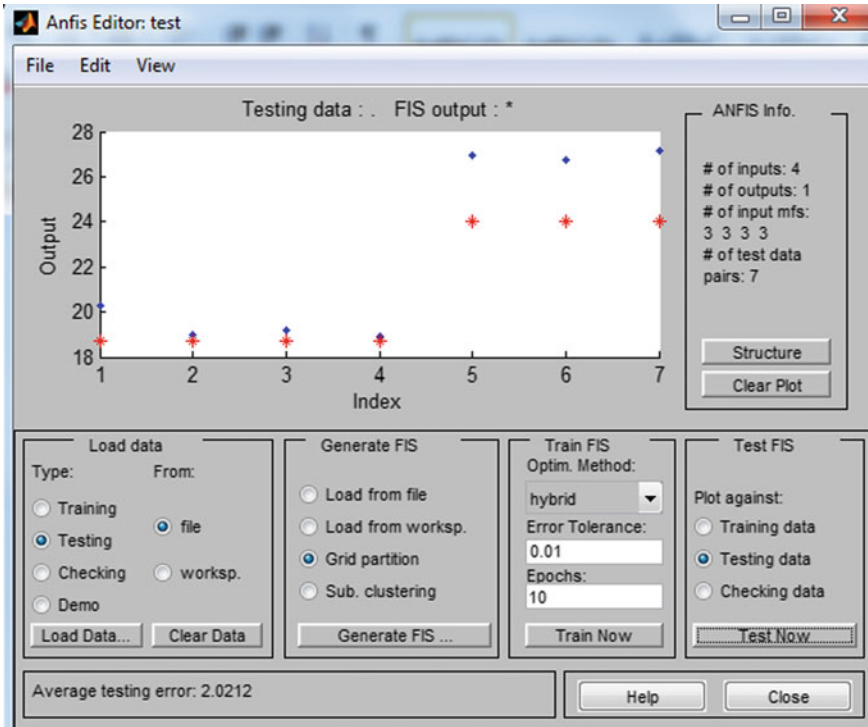


Fig. 14 Distribution of predicted and actual data (testing)

Table 6 Input and output data with ANFIS predicted value of HAp/PSU composite at 400 grit size

No.	Factor A (HAp volume) (%)	Factor B (load applied) (N)	Factor C (sliding speed) (rpm)	Factor D (track radius) (mm)	Wear loss (g)	S/N ratio of exp. value	ANFIS output predicted value
1	0	10	300	20	0.022	33.151	32.2
2	0	10	300	20	0.021	33.555	32.2
3	0	10	300	20	0.023	32.765	32.2
4	0	20	400	30	0.041	27.744	26.4
5	0	20	400	30	0.040	27.958	26.4
6	0	20	400	30	0.039	28.178	26.4
7	0	30	500	40	0.085	21.411	21.6
8	0	30	500	40	0.084	21.514	21.6
9	0	30	500	40	0.086	21.310	21.6
10	10	10	400	40	0.110	19.172	19.2
11	10	10	400	40	0.111	19.093	19.2
12	10	10	400	40	0.110	19.172	19.2
13	10	20	500	20	0.077	22.270	21.6
14	10	20	500	20	0.079	22.047	21.6
15	10	20	500	20	0.078	22.158	21.6
16	10	30	300	30	0.091	20.819	19.2
17	10	30	300	30	0.090	20.915	19.2
18	10	30	300	30	0.092	20.724	19.2
19	20	10	500	30	0.095	20.445	18.7333
20	20	10	500	30	0.094	20.537	18.7333

Table 7 Input and output data with ANFIS predicted value of HAp/PSU composite at 400 grit size

No.	Factor A (HAp volume) (%)	Factor B (load applied) (N)	Factor C (sliding speed) (rpm)	Factor D (track radius) (mm)	Wear loss (g)	S/N ratio of exp. value	ANFIS output predicted value
1	20	10	500	30	0.097	20.264	18.7333
2	20	20	300	40	0.112	19.015	18.7333
3	20	20	300	40	0.110	19.172	18.7333
4	20	20	300	40	0.113	18.938	18.7333
5	20	30	400	20	0.045	26.935	24
6	20	30	400	20	0.046	26.744	24
7	20	30	400	20	0.044	27.130	24

Fig. 15 Wear of 0 vol. % HAp/PC

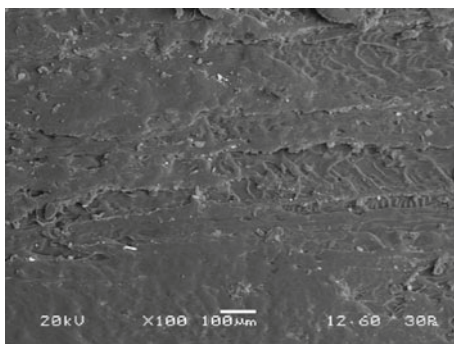


Fig. 16 Wear of 10 vol. % HAp/PC

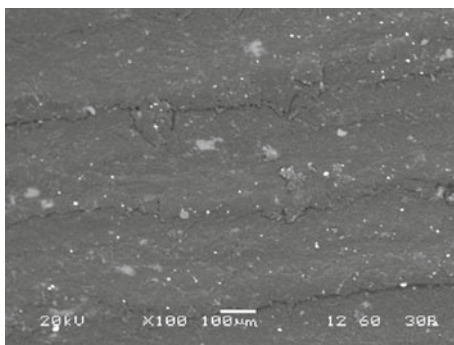


Fig. 17 Wear of 20 vol. % HAp/PC

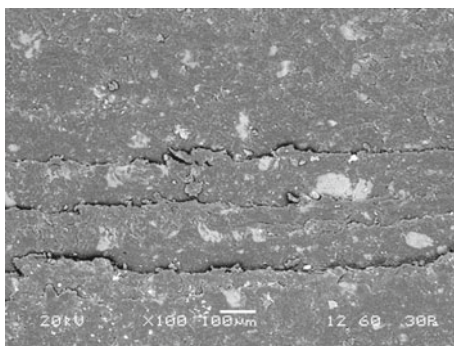


Fig. 18 Wear of 0 vol. % HAp/PSU

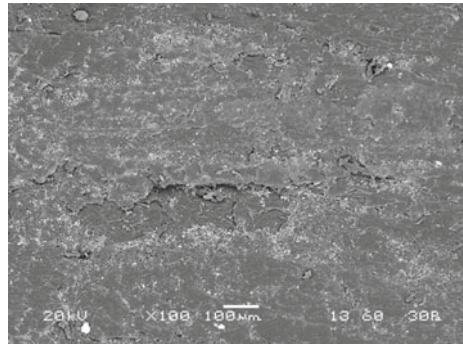


Fig. 19 Wear of 10 vol. % HAp/PSU ($\times 100$)

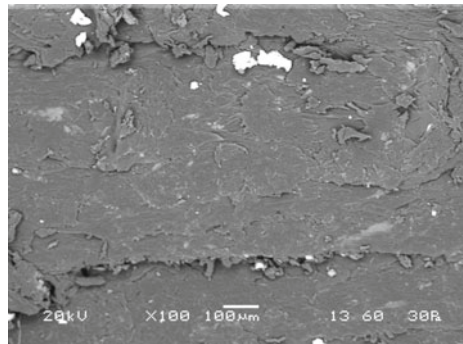
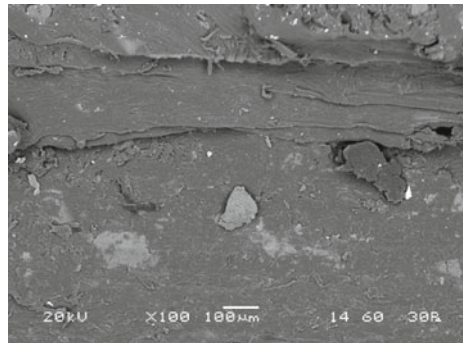


Fig. 20 Wear of 20 vol. % HAp/PSU ($\times 100$)



References

1. Ramakrishna S, Mayer J, Wintermantel E, Leong KW (2001) Biomedical applications of polymer-composite materials: a review. *J Compos Sci Technol* 61(9):1189–1224
2. Donadel K, Laranjeira MCM, Goncalves VL, Favere VT, Machado KD, de Lima JC, Prates LHM (2008) Structural, vibrational, and mechanical studies of hydroxyapatite produced by wet-chemical methods. *J Chem Phys* 1(2):1–10

3. Monmaturapoj N (2008) Nano size HAp powders preparation by wet-chemical precipitation route. *J Met Mater Miner* 18(1):15–20
4. Briscoe BJ, Yoo LH, Stolarski TA (1986) The friction and wear of PTFE-PEEK composites an initial appraisal of the optimum composition. *Wear* 108(1):357–374
5. Friedrich K, Lu Z, Hager AM (1995) Recent advances in polymer composites tribology. *Wear* 190(1):139–144
6. Jia X, Ling R (2007) Two-body free-abrasive wear of polyethylene, nylon 10, epoxy and polyurethane coatings. *Tribol Int* 40(1):1276–1283
7. Sasada T, Emori N, Oike M (1984) The effects of abrasive grain size on the transition between abrasive and adhesive wear. *Wear* 1(1):291–302
8. Gates JD (1998) Two-body and three body abrasion. A critical discussion. *Wear* 214(1):139–146
9. Shipway PH, Ngao NK (2003) Microscale abrasive wear of polymeric materials. *Wear* 255(1):742–750
10. Xu YM, Mellor BG (2001) The effect of fillers on the wear resistance of thermoplastic polymeric coatings. *Wear* 251(1):1522–1531
11. Fouquet S, Rollin M, Pailler R, Bourrat X (2007) Tribological behaviour of composites made of carbon fibers and ceramic matrix in the Si-C system. *Wear*
12. Sole BM, Ball A (1996) On the abrasive wear behaviour of mineral filled polypropylene. *Tribol Int* 29(1)
13. Lancaster JK (1969) Abrasive wear of polymers. *Wear* 14(1):223–239
14. Roy Chowdhury SK, Kulkarni AC, Basak A (2007) Wear characteristic and biocompatibility of some hydroxyapatite-collagen composite acetabular cups. *Wear* 262(11–12):1387–1398
15. Mohan N, Natarajan S, Kumaresh Babu S, Siddaramaiah (2010) Investigation on two-body abrasive wear behavior of silicon carbide filled glass fabric-epoxy composites. *J Miner Mater Charact Eng* 9(3):231–246
16. Singh A, Abhishek K, Datta S, Mahapatra SS (2012) ANFIS based modeling for prediction of surface roughness during machining of glass fiber reinforced epoxy composites. *Int J Mater Manuf Des* 1(1):1–15
17. Sahu M, Singh P, Mahapatra SS, Khatua KK (2012) Prediction of entrance length for low Reynold's number flow in pipe using neuro-fuzzy inference system. *Expert Syst Appl* 39(1):4545–4557

Optimization of Laser Hardening Process Parameters for Cast Iron Using a Design of Experiment Method



Santoshkumar V. Wagh, Dhananjay V. Bhatt, Jyoti V. Menghani,
and Sujit S. Pardeshi

Abstract Laser hardening is one of the economical techniques used to improve surface properties of target materials. This process is easy to use for improving surface properties of a complex shape component with minimum time requirement. The important beauty of this process is that only selective surface area properties can be improved without changing the remaining bulk material surface properties. Cast iron has various important properties like hardness, superior wear resistance, frictional performance, etc. These properties are useful in various industrial applications. The present paper is an attempt to study effect on surface properties by process parameters of laser hardening process (microhardness and microstructure) of cast iron using a design of experiment method. From this investigation, it can be summarized that laser microhardness is maximized by controlling laser power which improves a service life of cast iron laser-treated components. From the comparison of the experimental results and L9 orthogonal array results, it has been found that the percentage error is negligible with a higher co-relation coefficient (r^2) 0.949 which is within the acceptable range.

Keywords Cast iron · Laser hardening · Taguchi's design of experiment method · Microhardness · Microhardness width and depth · Microstructure

1 Introduction

1.1 Background

Cast iron material is used on a large scale for industrial applications in automotive as camshaft lobes, cylinder bore, steering gear housing, cylinder liner, and piston

S. V. Wagh (✉) · S. S. Pardeshi
Department of Mechanical Engineering, College of Engineering Pune, Pune 411005, India
e-mail: waghsv@gmail.com

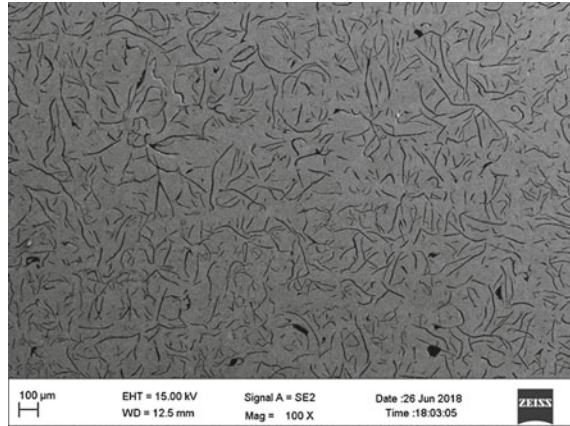
D. V. Bhatt · J. V. Menghani
Department of Mechanical Engineering, Sardar Vallabhbhai National Institute of Technology,
Surat 395007, India

ring, in machinery industry for tool bed, in power generation industry for turbine blade edge, and in railway for diesel engine cylinder. There is maximum utilization of cast iron materials in manufacturing because of their good mechanical properties. The focus in industry, at present, is on material cost, mechanical properties, tribological wear resistance, and thermal properties of materials. The laser source is used for various processes like laser cutting, laser welding, laser bending, laser coating, and laser hardening to improve material surface properties. Laser surface treatments have advantages over the conventional processes like induction hardening, flame hardening, and arc TIG. The selective area can be hardened from the available bulk material, without changing the thermal properties of the rest of the bulk material. The process parameters viz. laser scan speed, focal distance, and laser power are optimized (focal distance between work piece and nozzle tip), and optimization is carried out for a mass production rate [1–3]. Monteiro et al. [1] in their research studied the effects of optimal laser surface treatment process parameters such as laser pulse, laser beam tracks, laser power, laser scan speed, and laser track overlapping on the hardness and wear resistance of laser-treated cast iron material used in the automobile industry on a large scale. Ming-der and Yih-fong [3] discussed the effects of electron-beam hardening process parameters which accelerate voltage, travel speed, electric current and post-heat treatment processes to improve the wear resistance of cast iron by using Taguchi's method. They observed that the most significant process parameter responsible for the wear resistance of cast iron was laser power from the process parameters cited above. Badkar et al. [4] in their research used L9 orthogonal array method for process parameters optimization of laser hardening of pure titanium. They found that the most significant process factor was scanning speed and the remaining followed as laser beam power and standoff distance, which achieved the depth of microhardness, i.e., minimum 0.251 mm and maximum width of microhardness was 1.865 mm, respectively, by optimization. Barka and El Ouafi [5] in their research work studied the impact of laser hardening process on cylindrical shape 4340 steel material harden depth after laser hardening by using a statistical analysis method. They observed that the most significant process factors were laser scan speed, focal position, and laser power which affect the microhardness depth and microhardness of laser-treated samples. Babu et al. [6] studied the impact of the process of laser hardening on microhardness width and microhardness depth of laser-treated EN25 steel by using a response surface method. They observed that the most significant factor was laser power followed by laser scan speed which had effect on microhardness along the depth of the laser-treated samples. They developed a mathematical model to maximize the harden width and to minimize the harden depth to optimize process parameter conditions. Balasubramanian et al. [7] in their research work focused on the impact of process of laser hardening such as laser power and scan speed on the microhardness of different grades steels. Rana et al. [8] conducted experiments to study the effects of laser hardening process parameters on microstructure and hardness of laser-treated carbon steel samples of various carbon percentages. They observed that the most significant process parameter was laser scan speed to maximize the hardness of laser-treated samples. If the carbon percentage increases, the average hardness value increases too, and hardness just below the surface is

slightly higher compared to the top surface hardness. Babu et al. [9] investigated the effects of process parameters of laser hardening on the microstructure and hardness of laser-treated samples of EN25 steel. They experimentally investigated that laser hardening process parameters like laser power and laser scan speed were optimized which obtained microhardness two times the base metal hardness. Roy and Manna [10] used a mathematical model to predict the optimum condition of laser transformation of austempered ductile cast iron. They observed that the hardness depth was directly proportional to the laser power and interaction time. Qiu and Kujanpaa [11] investigated the effects of laser power variations such as lower and higher power density, respectively, on hardness, microstructure, and hardened depth of medium-carbon steel laser-treated samples. Borowski and Bartkowiak [12] investigated the process parameter effect, i.e., laser power 400, 530; and 750 W with a laser scanning speed of 2.8, 3.2; and 5.33 mm/s that do not affect the roughness of the laser-treated samples, so no extra machining work is required after the laser-treated surface. They observed an improvement in hardness after a laser treatment process with uniform microstructure and wear resistance. Gadag et al. [13] studied the effects of laser treatment process factors on microstructure, harden depth, width of harden layer of laser-treated ductile iron materials used in dynamically loaded conditions of components in automobile industry. More et al. [14] used Taguchi's method of experimentation for investigating the significant parameter used for erosion wear study on SS 304. From the literature survey, it has been observed that most of the researchers investigated the effects of laser hardening process parameters on hardness, microstructure, width, and depth of harden layer of different types of target materials. All the above research studies conducted the experimentation in a range for laser power between 400 and 2500 W and for a laser scan speed range from 2.8 to 50 mm/s on various materials except in the study by Balasubramanian et al. [7]. There is a scope in the present investigation of the effects of laser hardening process parameters on the microstructure and microhardness at lower laser power, laser scan speed, and standoff distance undertaken with a minimum range of laser power of 210, 220 and 230 W, laser scan speed of 10, 15, and 20 mm/s, and standoff distance of 250, 275, and 300 mm, respectively. The effects of the process parameters on microstructure and hardness at low laser power and larger lasers scan speed at suitable standoff distance are considered. Hence, to decrease the total cost of laser hardening, the process parameter should be optimized. The purpose of this research work is the laser hardening process that fills in as a solution to low power laser hardening and laser hardening of the selective surface is the advantage over the traditional hardening process. The purpose of this investigation was to improve the surface layer microhardness of particular zone of cast iron specimen by low power laser hardening utilizing optic fiber laser. To evaluate optimum process parameters i.e. laser beam power, laser scan speed and standoff distance, for cast iron laser hardening to optimize microhardness above base metal microhardness and maximize depth of microhardness with low power laser hardening. It improves the components' existence.

Table 1 Elemental composition of cast iron in weight percentage

Elements	C	Si	S	P	Mn
Composition weight %	3.65	1.71	0.067	0.176	0.38

Fig. 1 SEM image of cast iron base material

2 Experimental Details

2.1 Material Used for Experimentation

Nowadays, cast iron is used in automobile industry for manufacturing different components. Therefore, for the present experimental work, cast iron is used as testing material. Table 1 shows the elemental composition in weight percent. SEM image of cast iron is as shown in Fig. 1.

2.2 Experimental Setup and Sample Preparation

Figure 2 shows the image of fiber laser system (CW) of 400 W and 1070 nm laser wavelength. The experiments were conducted on the same laser system. The laser hardening process parameters used laser power of 210, 220, and 230 W, laser scan speed of 10, 15, and 20 mm/s, and standoff distance of 250, 275, and 300 mm as given in Table 2. A laser beam diameter of 1.4 mm and argon gas are used at 10 L/min flow rate as shielding gas. The preparations of the samples were carried out using acetone. The samples were cut by a wire electrical discharge machine into a size of 20 mm × 8 mm × 8 mm.

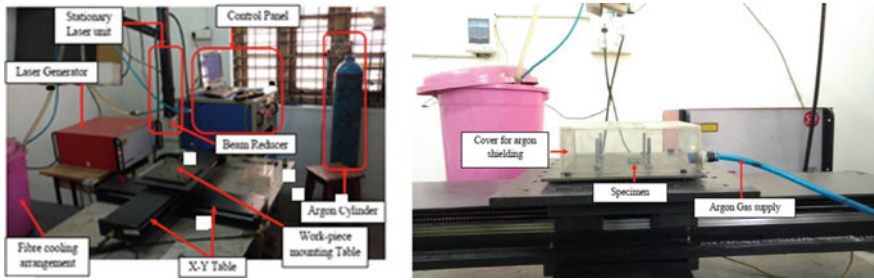


Fig. 2 Fiber laser system (SPI 400 CW, Laser Science Pvt. Ltd. Mumbai)

Table 2 Experimental testing parameters and their levels for laser hardening experiments

S. No.	Laser parameters	Unit	Level		
			1	2	3
1	Laser power (P)	W	210	220	230
2	Laser scan speed (v)	mm/s	10	15	20
3	Standoff distance (f)	mm	250	275	300

2.3 Metallographic and Microstructural Analysis

The optimized process parameters were used to take a laser track on the sample. The laser tracks were taken on the surface of the sample, and laser-hardened cross-sectional area was polished with the help of emery paper of various grades by using etchant as 4% Nital solution (mixing of 4 ml nitric acid and 96 ml methanol), to observe the microstructure of cross section of the laser-treated sample. By using a microscope, the width, depth, and microstructure were studied in the heat-affected area by using a microscope made by Conation Technologies, Pune. A machine was used for microhardness test at 300 g load with 10 s dual time, and microhardness test was conducted on the laser-hardened area of the laser harden sample. Future Tech Corporation Japan, Vickers microhardness testing machine of model number FM700 was used to check the microhardness. The microhardness was checked using HAZ and the base metal along the laser-hardened cross-sectional area.

2.4 Experimental Design

For the analysis of the influencing significant process parameters, the design of experiment technique was used and on the basis of that an output response model was developed. In the process of laser hardening, three input parameters influenced microhardness which has output response. Taguchi’s design of experiment method was

Table 3 Experimental Taguchi L9 matrix for laser microhardness of cast iron

S. No.	Laser power (W)	Laser scan speed (mm/s)	Standoff distance (mm)	Width of HAZ (μm)	Depth of HAZ (μm)	Microhardness HV _{0.3}	S/N ratio
1	210	10	250	1085.80	275.30	727.60	57.2379
2	210	15	275	628.12	207.47	673.30	56.5642
3	210	20	300	918.45	109.80	630.20	55.9882
4	220	10	275	1074.28	293.25	742.10	57.4092
5	220	15	300	1022.81	213.29	699.80	56.8995
6	220	20	250	850.76	167.64	671.90	56.5461
7	230	10	300	737.39	325.33	812.10	58.1922
8	230	15	250	1005.61	254.56	791.20	57.9657
9	230	20	275	827.25	178.47	749.60	57.4966

more flexible to find the effects on microhardness by every process input parameters compared to the other analytical methods.

In this research study, laser power, laser scan speed, and standoff distance are used as cast iron laser hardening process parameters to study the effects on response as a microhardness of laser-hardened cast iron sample. Table 2 shows the levels of process parameters used for the experiment. Table 3 shows process parameters, output response microhardness, width and depth of microhardness, and signal-to-noise ratio of all the run. The output response values are converted to signal-to-noise ratio with the help of Taguchi's L9 design of experiment.

The signal-to-noise (S/N) ratio was calculated for each factor level combination. The formula for the largest is a better S/N ratio using a base 10 log as shown in Eq. (1).

$$S/N = -10 * \log[\Sigma(1/Y^2)/n] \quad (1)$$

where Y is the response for the given factor level combination and n is the number of responses in the factor level combination.

3 Results and Discussion

3.1 Microhardness Analysis by Taguchi's Experimental Design

The results of the present experimental work is analyzed using MINITAB 14. Taguchi's orthogonal array L9 design is used to analyze the experimental work.

Table 4 *S/N* ratio response table using the larger is better characteristics

Level	Laser power	Laser scan speed	Standoff distance
I	56.60	57.61	57.25
II	56.95	57.14	57.16
III	57.88	56.68	57.03
Delta	1.29	0.94	0.22
Level	1	2	3

Table 3 shows details of the experimental parameters and respective results of *S/N* ratio for all the nine sets of experiments. The aim of the present experiment is to increase the value of microhardness. Therefore, ‘the larger the better’ quality characteristic is selected and used for the present Taguchi’s analysis.

Table 4 shows the value of *S/N* ratio response for the present experimental condition and the larger the better quality characteristic. The laser beam power was the most influencing significant control parameter among all the three factors for causing the surface microhardness of cast iron as given in Table 4. The remaining two parameters, namely laser scan speed and standoff distances, are ranked at the second and third positions, respectively, in influencing the surface microhardness of cast iron. The main effects plot for signal-to-noise ratio are graphically shown in Fig. 3. The

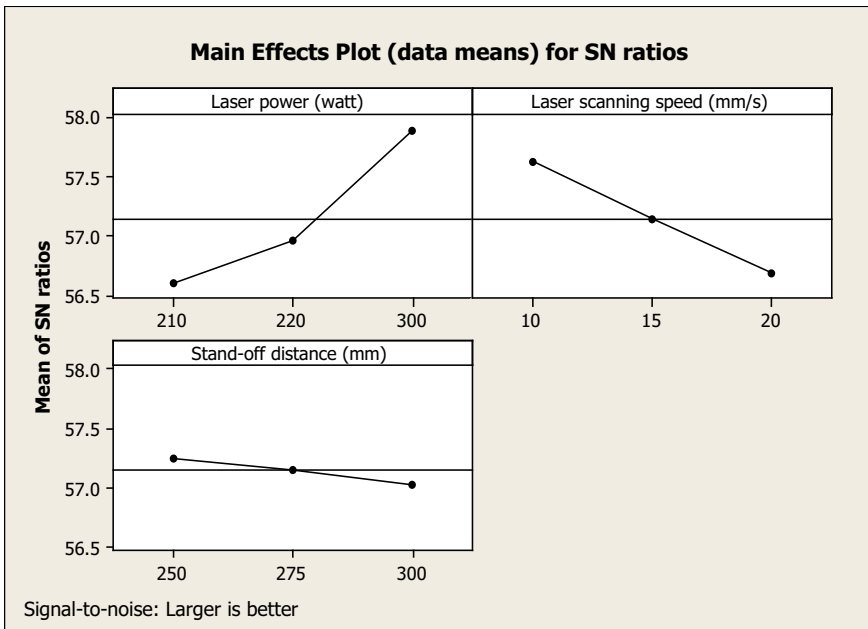


Fig. 3 Main effects plot for *S/N* ratios

microhardness value of laser-hardened sample of cast iron was found maximum at 230 W laser power, 10 mm/s laser scan speed, and 300 mm standoff distance.

3.2 Effect of Laser Power on Hardness

As the laser beam power increases from 210 to 230 W, the value of signal-to-noise ratio and microhardness of laser-hardened sample increases too which is shown in Fig. 3. It is observed from Table 3 that increments in the microhardness are 727.60 HV_{0.3}, 742.10 HV_{0.3}, and 812.10 HV_{0.3}, respectively, of laser-hardened samples of cast iron with variations in the laser beam power of 210, 220, and 230 W at constant 10 mm/s laser scan speed, and the maximum achieved microhardness 812.10 HV_{0.3} was double compared to the base metal microhardness, i.e., 258–327 HV_{0.3}.

3.3 Effects of Laser Scan Speed on Microhardness

The effects on the microhardness value of laser-hardened sample by the process parameter laser scan speed shows that a curve trend graph is inversely proportional as shown in Fig. 3. As the variations in the laser scan speeds are 10, 15 to 20 mm/s at 230 W constant laser beam power is observed. The effects that decrease in the microhardness to 812.10 HV_{0.3}, 791.20 HV_{0.3}, and 749.60 HV_{0.3} and depth of microhardness depth also decreases to 325.33 μm, 254.56 μm, and 178.47 μm, respectively, and decrease in the signal-to-noise ratio values are given in Table 3.

3.4 Surface Morphology Using Microstructure

Figure 4 presents an analysis of microstructures of the nine laser-hardened samples as per Taguchi's sets of experiments and one untreated sample. Figure 4a shows untreated sample, and (b–j) shows nine sets of experiments, respectively, as per Table 3. The effect of change in laser scan speed on microstructure shown is in Fig. 4b–d. The laser scan speed varies from 10, 15, and 20 mm/s at 210 W constant laser power. Figure 4b–d presents a change in microhardness width and decreases the microhardness depth due to the increased laser scan speed and the microhardness decreased. Similar results can be observed in Fig. 4e–g, h–j at laser power 220 W and 230 W, laser scan speed of 10, 15 and 20 mm/s, and standoff distance of 250 mm, 275 mm, and 300 mm, respectively. Figure 4h, b presents maximum microhardness depth and width at 230 W, 10 mm/s, and 300 mm and 210 W, 10 mm/s, and 250 mm, respectively. Figure 4b–d, e–g, h–j depicts constant powers of 210, 220, and 230 W and the variation in the laser scan speed of 10, 15, and 20 mm/s that affects the

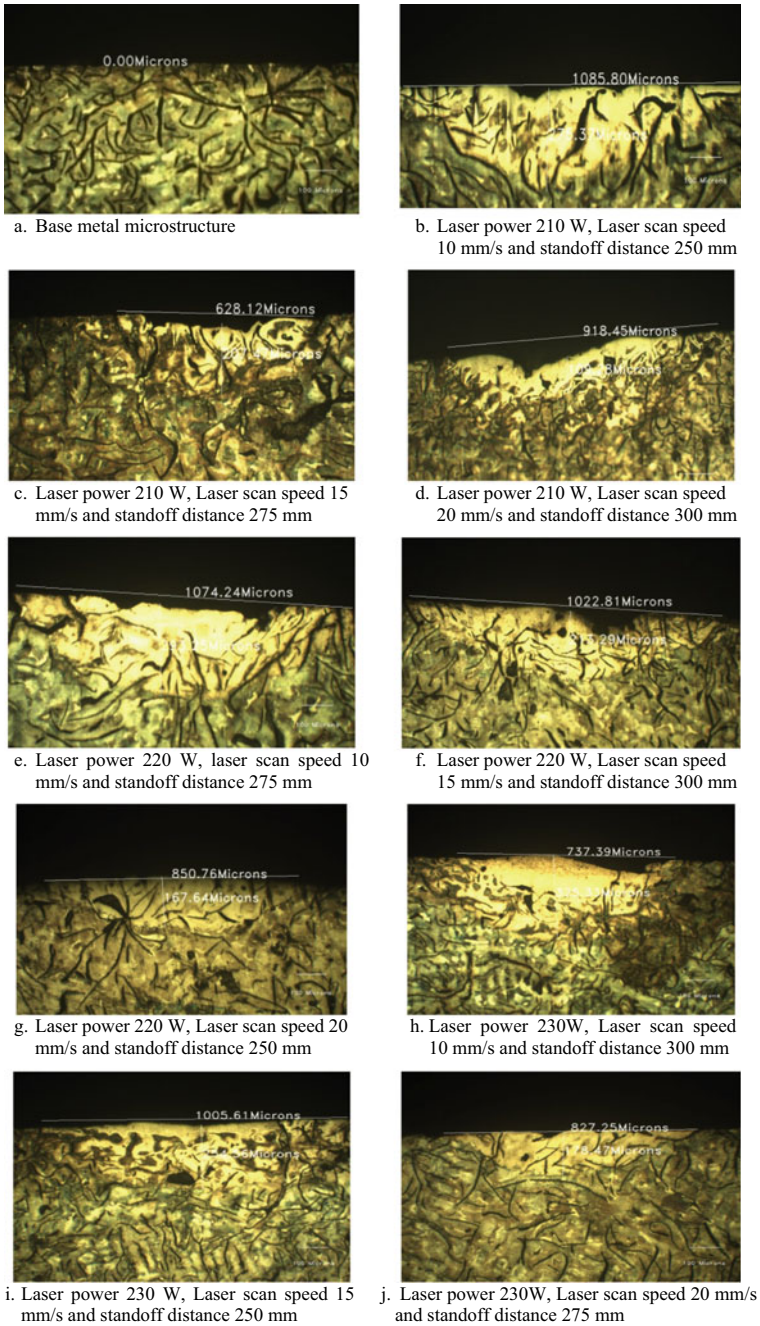


Fig. 4 Microstructure of **a** base metal and **b–j** laser-treated samples as per L9 experiments

microhardness depth, and it decreases that is to say that laser scan speed effects on microhardness.

3.5 Hardness Predication Using Predictive Equation

The microhardness of the laser-treated samples due to laser power was predicted using a nonlinear regression equation for showing the relationship between the microhardness and combination of control parameters. This regression study was carried out by using MINITAB 14 software. The following form of the regression equation was obtained:

$$\text{HV}_{0.3} = -254 + 5.36 (\text{Laser power}) - 7.67 (\text{Laser scan speed}) - 0.324 (\text{Standoff distance}) \quad (2)$$

In Eq. (2), all the constants values are calculated by using MINITAB 14 software. The accuracy of the calculated constants was confirmed because the high correlation coefficient (r^2) of 0.949 was obtained from Eq. (2). The comparison between the hardness obtained from the experimental results and predictive equation is as given in Table 5.

A confirmation test was performed on cast iron sample by considering optimal test parameters such as laser power, laser scanning speed, and standoff distance at which obtained the maximum microhardness value was obtained. The microhardness is obtained in the cast iron material due to the laser hardening process by using both nonlinear regression equation, and confirmation experimental results are given in Table 6. By comparing the experimental results and analytical results, a deviation of about 1.33% was found which is agreeable. Therefore, it is shown that the derived

Table 5 Comparison of experimental and predictive values for microhardness

Expt. No.	Results obtained from experiments	Results obtained from predictive equation	Percentage error (%)
1	727.60	713.60	1.96
2	673.30	675.55	0.33
3	630.20	621.00	1.48
4	742.10	759.40	2.27
5	699.80	712.95	1.84
6	671.90	690.08	2.63
7	812.10	804.90	0.89
8	791.20	782.75	1.07
9	749.60	736.30	1.80

Table 6 Confirmation experimental results for microhardness of cast iron

Laser power (W)	Laser scan speed (mm/s)	Standoff distance (mm)	Hardness in test	Hardness by equation	% error
230	10	250	810.10	821.10	1.33

nonlinear regression equation describes the microhardness of the cast iron material with various control factors with a reasonable degree of approximation.

4 Conclusions

The main conclusions drawn from the research study are summarized as follows:

- From all the three factors, laser power is the most influencing significant factor of laser hardening of cast iron, followed by the laser scan speed and standoff distance, respectively.
- Maximum microhardness achieved is at 230 W laser power, 10 mm/s scanning speed, and 300 mm standoff distance of the metal cast iron to surface laser hardening process.
- Microstructure of laser-hardened sample of cast iron highlights two different zones. The first one is the heat-affected area, and the second one is the base metal area. These are the main characteristics of a laser hardening process.
- The base metal microhardness values are observed between 258 and 327 HV_{0.3}. The microhardness of laser-hardened sample after the laser hardening process was observed between 630.20 and 812.10 HV_{0.3}. The microhardness of laser-hardened sample increased two times to the microhardness of base metal.
- The harden layer depth range is achieved from 109.8 to 325.33 μm for laser-treated sample.
- The deviation in the percentage error between predicted and experimental result was between 3.30 and 2.63%. A higher correlation coefficient value of (r^2) is 0.949 which shows the correctness of the mathematical model used. Therefore, the model is more suitable for future study.
- From this investigation, it can be concluded that the laser surface hardness is maximized by controlling the laser power which improves the service life of the cast iron laser-treated samples equipment.

Acknowledgements The authors thankfully acknowledge the help received from the Department of Mechanical Engineering and Metallurgy and Materials Science Engineering Department, College of Engineering Pune, Maharashtra, India, for experimental facility. The authors also wish to thank the Department of Mechanical Engineering, Sardar Vallabhbhai National Institute of Technology, Surat, Gujarat, India, for their kind support.

References

1. Monteiro WA, Silva EMR, de Rossi W (2009) Evaluation of the laser superficial hardening (LSH) in gray cast iron used in automobile industry. In: 3rd international conference on integrity, reliability and failure, Porto, S2403-P0409, pp 1–11
2. Selvan JS, Subramanian K, Nath AK (1999) Effect of laser surface hardening on En18 (AISI 5153) steel. *J Mater Process Technol* 91:29–36
3. Ming-der J, Yih-fong T (2004) Optimisation of electron-beam surface hardening of cast iron for high wear resistance using the Taguchi method. *Int J Adv Manuf Technol* 24:190–198
4. Badkar DS, Pandey KS, Buvanashakaran G (2011) Parameter optimization of laser transformation hardening by using Taguchi method and utility concept. *Int J Adv Manuf Technol* 52(9–12):1067–1077
5. Barka N, El Ouafi A (2015) Effects of laser hardening process parameters on case depth of 4340 steel cylindrical specimen—a statistical analysis. *J Surf Eng Mater Adv Technol* 5:124–135
6. Babu PD, Buvanashakaran G, Balasubramanian KR (2013) Experimental investigation of laser transformation hardening of low alloy steel using response surface methodology. *Int J Adv Manuf Technol* 67(5–8), 1883–1897
7. Balasubramanian S, Muthukumar V, Sathyabalan P (2017) A study on the effect of process parameters of laser hardening in carbon steels. *Int J Civ Eng Technol* 8(9):201–207
8. Rana J, Goswami GL, Jha SK, Mishra PK, Prasad BVSSS (2007) Experimental studies on the microstructure and hardness of laser-treated steel specimens. *Opt Laser Technol* 39:385–393
9. Babu PD, Buvanashakaran G, Balasubramanian KR (2012) Experimental studies on the microstructure and hardness of laser transformation hardening of low alloy steel. *Trans Can Soc Mech Eng* 36(3):241–257
10. Roy A, Manna I (2000) Mathematical modeling of localized melting around graphite nodules during laser surface hardening of austempered ductile iron. *Opt Laser Eng* 34:369–383
11. Qiu F, Kujanpaa V (2011) Transformation hardening of medium-carbon steel with a fiber laser: the influence of laser power and laser power density. *Mechanika* 17(3):318–323. ISSN 1392-1207
12. Borowski J, Bartkowiak K (2010) Investigation of the influence of laser treatment parameters on the properties of the surface layer of aluminum alloys. *Phys Procedia* 5:449–456
13. Gadag SP, Srinivasan MN, Mordike BL (1995) Effect of laser processing parameters on the structure of ductile iron. *Mater Sci Eng A* 196:145–151
14. More SR, Bhatt DV, Menghani JV (2017) Study of the parametric performance of solid particle erosion wear under the slurry pot test rig. *Int J Ind Tribol* 39(4):471–481

FMECA Analysis and Condition Monitoring of Kneader in Green Anode Plant of an Aluminium Smelter



J. K. Mohanty, I. Hota, P. Sarkar, A. K. Sahu, P. R. Dash, and P. K. Pradhan

Abstract In large plants like aluminium smelters, integrated condition monitoring techniques play an important role as break down of any critical equipment can lead to shut down of the entire plant, which in turn leads to loss of productivity and profits. From economical and operational point of view, it is desirable to ensure optimum level of system availability and reliability. Condition monitoring is implementation of the diagnostic techniques to detect the fault and forthcoming fault in the system. It helps to reduce downtime, increase efficiency and reliability of the system. Nowadays, most of the industries adopted condition monitoring techniques as a part of support system to the basic maintenance strategies. Major techniques that they follow are vibration analysis which can detect faults at a very early stage. But implementation of other techniques like oil analysis or ferrography, thermography, non-destructive testing like ultrasonic tests, magnetic particle testing, etc. can further enhance the data interpretation as they would detect the source of abnormality at much early stage thus provide a longer lead time to plan and take the corrective measures. The present study focuses on FMECA analysis and condition monitoring of the Kneader through vibration analysis and oil analysis.

Keywords Kneader · Condition monitoring · FMECA · Aluminium smelter

1 Introduction

Aluminium is lightweight, high thermal and electrical conductivity, high reflectivity, good corrosion resistance, excellent workability and attractive appearance. Aluminium and its alloys have wider application in aerospace industry, making household utensil and electrical cables, etc.

J. K. Mohanty · A. K. Sahu · P. R. Dash · P. K. Pradhan (✉)
Mechanical Engineering Department, VSSUT, Burla, India
e-mail: prasant2001uce@gmail.com

I. Hota · P. Sarkar
Vedanta Limited, Jharsuguda, India

The prime ore of aluminium is bauxite. Bauxite is converted to aluminium oxide or alumina by the Bayer process. The conversion of alumina to aluminium metal is achieved by the Hall–Heroult process [1], basically an electrolysis process. In this energy-intensive process, a solution of alumina in a molten (950 and 980 °C) mixture of cryolite (Na_3AlF_6) with calcium fluoride is electrolyzed to produce molten metallic aluminium. The liquid aluminium metal sinks to the bottom of the solution and is tapped off, and usually cast into Ingot, Wire rod, Billet, Slab, Bus bar, etc. for further processing.

In electrolysis process, the ions in the aluminium oxide must be free to move so that electricity can pass through it. Aluminium oxide has a very high melting point (over 2000 °C) so it would be expensive to melt it [2]. Aluminium oxide does not dissolve in water, but it does dissolve in molten cryolite. This is an aluminium compound with a lower melting point than aluminium oxide. The use of cryolite reduces some of the energy costs involved in extracting aluminium.

The diagram (Fig. 1) shows an aluminium oxide electrolysis cell. The negative electrodes (cathodes) and the positive electrodes (anodes) are made of graphite, a form of carbon. During electrolysis, (i) positively charged aluminium ions gain electrons from the cathode and form molten aluminium and (ii) oxide ions lose electrons at the anode and form oxygen molecules. The oxygen reacts with the carbon in the anodes, forming carbon dioxide which bubbles off. Carbon is therefore lost from the positive electrodes, so they must be replaced frequently. This adds to the cost of the process.

For production of aluminium, the basic raw materials are alumina from an alumina plant, power from a power plant and the anodes from a carbon plant. The hot metal produced from pot rooms is casted to different products in a cast house. So an aluminium smelter consists of mainly three major units which are carbon plant, pot room and cast house.

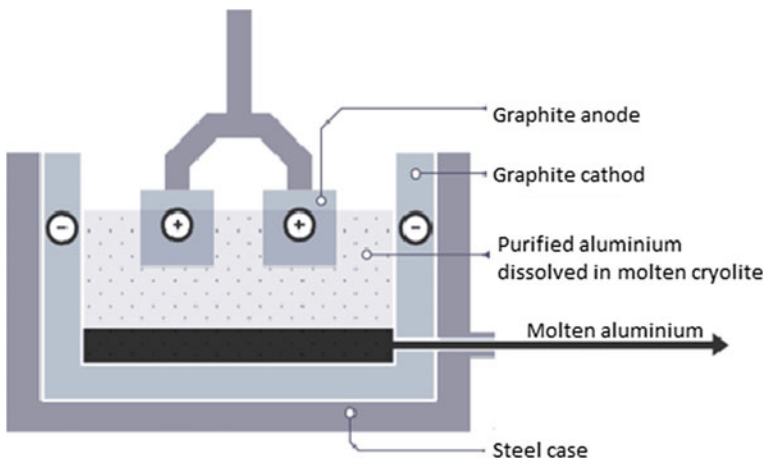


Fig. 1 Sectional view of pot for extraction

Continuous production of aluminium from a smelter depends on the availability of its components and equipment in its three plants. Higher availability of the components and equipment is inherently associated with their higher reliability and maintainability. Since its genesis, the maintenance culture has evolved down, through different types of maintenance techniques [3–6] like

1. Unplanned Maintenance: run to failure or breakdown maintenance.
2. Schedule maintenance.
3. Preventive maintenance.
4. Condition monitoring/predictive maintenance.
5. Reliability centred maintenance.
6. Total productive maintenance.

In earlier days, the main form of maintenance was corrective maintenance instead of predictive maintenance system, resulting to high downtime with reduced production, besides safety and environmental issues. These challenges gave rise to condition-based maintenance (CBM) that actively manages the health and condition of the assets using diagnostic tools and techniques; as maintenance work is only done when really needed.

1.1 Condition Monitoring

Condition monitoring is the periodic or continuous comparative monitoring of parameters which can reflect the condition of a component, subassembly or equipment which on analysis can indicate the item's current condition and the future trend of its possible deterioration. Condition monitoring techniques are used to check equipment while it is in operation to give advance indication of deterioration to plan the maintenance before hand for breakdown prevention. There are different CBM techniques; these are vibration analysis [7], noise analysis, temperature monitoring [8], motor current signature analysis (MCSA) [9], wear debris analysis, etc.

Prior to implementation of CBM of any industry, it is essential to do failure mode, effect and criticality analysis (FMECA) to identify the degree of criticality of various machineries and components of such industry. Based on these, the application of CBM can be decided.

1.2 Failure Mode, Effect and Criticality Analysis (FMECA)

FMECA [10] is a design method used to systematically analyse probable component failure modes of product or process, assess the risk associated with these failure modes and find out the resultant effects on system operations.

The main steps are:

1. Identify the machine(s), item(s) or process(es) to be analysed.
2. Identify the function(s), failure(s), effect(s), cause(s) and control(s) for each item or process to be analysed.
3. Evaluate the risk associated with the issues identified by the analysis.
4. Prioritize and assign corrective actions.

Most analysis of this type also includes some method to assess the risk associated with the issues identified during the analysis and to prioritize corrective actions. There is a common tool used to determine the degree of criticality of the machineries, i.e. risk priority numbers (RPNs).

1.3 RPNs

The RPN is the product of severity (S) \times difficulty to detect (D) \times occurrence (O). With each on a scale from 1 to 10, the highest RPN is $10 \times 10 \times 10 = 1000$. This means that this failure is not detectable by inspection, very severe and the occurrence is almost sure. So, criticality analysis enables to focus on the highest risks.

2 Methodology and Experimentation

The current study is based on Green Anode Plant in Carbon Area of Smelter-1 in Vedanta Limited, Jharsuguda, India, where anodes are produced for use in pot cells for electrolysis process. Carbon area is basically consists of three plants, namely Green Anode Plant (GAP), Bake Oven and Rodding Shop. The anode production process is shown in Fig. 2. In Green Anode Plant, a raw anode is made using coke and pitch. After crushing and screening calcined petroleum coke is mixed with coal tar pitch (as binder) inside Kneader to form semi-solid paste. The paste is filled up in the mould of a vibro compactor to get a solid carbon block (Green Anode) of required density and height. After cooling, it is transferred to storage area and then to Bake Oven for baking. In Bake Oven, the green anodes are baked to release the volatiles to get the required qualities of electrical conductivity, corrosion resistance and mechanical strength suitable for electrolysis process. The Baked anodes are then transferred to Rodding Shop to fuse with aluminium rods, so that they can be connected to the bus bars of pot cells.

Anodes of the electrolysis cell are large carbon blocks of dimension $1600 \times 710 \times 575$ mm and weighing near about 1000 kg. These are used to conduct electricity during the “aluminium reduction process”. Anode is a key constituent in aluminium production because it is good conductor of electricity, capable of withstanding high temperatures (Bath Temp. normally >955 °C), chemically inert to both molten cryolite and aluminium, physically strong and chemically pure and readily available at reasonable cost. These are either baked at the process inside the pot cells or are

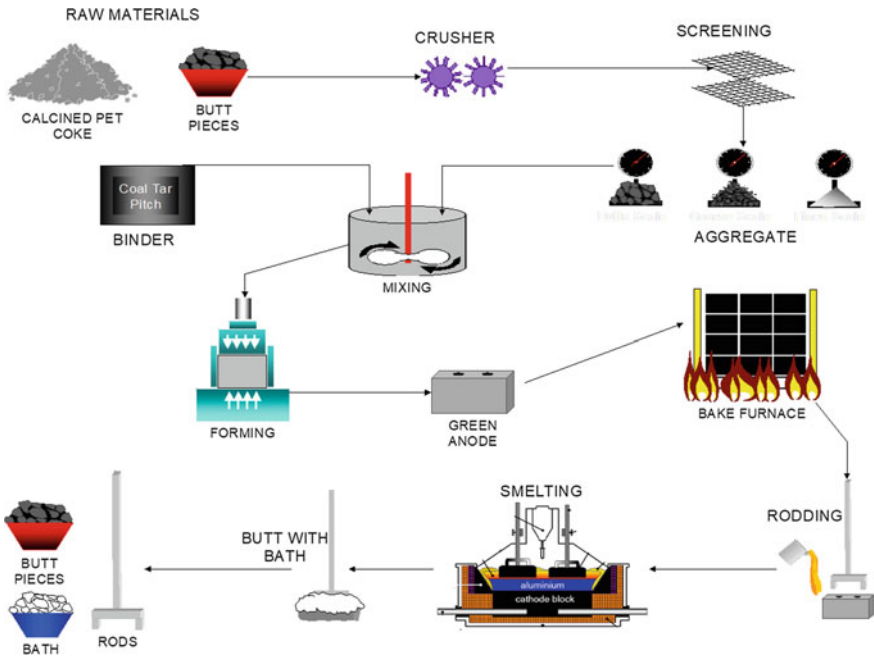


Fig. 2 Overall view of anode production process

prebaked. Despite carbon’s resistivity against corrosion, it is still consumed at a rate of 0.4–0.5 kg per each kilogram of aluminium produced and hence is consumed in the pot in every 28 days. As per the pot design 40 no’s of anodes are used in each pot. So to run pot room with two pot lines each having 304 no’s of pot, daily large numbers of anodes are needed. For anodes, pot room totally depends upon carbon plant. Cathodes are made of anthracite. Cathode is consumed at a rate of 0.02–0.04 kg per each kilogram of produced aluminium. A cell is usually replaced after 2–6 years following a failure of the cathode.

2.1 FMECA of Green Anode Plant

FMECA analysis is done for all individual equipment up to replaceable part and the same is reviewed once in a year which is a normal practice in both Smelter and Captive Power Plant of Vedanta Limited. After taking care of all three parameters, the RPN of all-important equipments are evaluated and presented in Table 1.

The above FMECA analysis says that Kneader’s gear box is the most important equipments of the Green Anode Plant.

Table 1 Criticality analysis for GAP's equipment

S. No.	Equipments	<i>S</i>	<i>O</i>	<i>D</i>	RPN	Remark
1	Belt conveyor	8	2	6	96	Non-critical
2	Crusher	8	4	5	160	Very critical
3	Preheater	8	4	5	160	Very critical
4	Ball mill	7	4	4	112	Critical
5	Cooler	6	4	5	120	Critical
6	Vibrating feeder	8	3	3	72	Non-critical
7	Kneader's gear box	9	4	5	210	Very critical
8	Vibro compacter	7	4	4	112	Critical
9	Power and free	7	4	5	140	Critical
10	Bucket elevator	8	2	6	96	Non-critical

Note For this analysis, (i) RPN ≥ 150 is considered as very critical, (ii) RPN in between 50 and 100 is considered as critical, (iii) RPN < 100 is considered as non-critical

3 Observations and Case Study

Condition monitoring of the Kneader's gear box is done through vibration analysis and oil analysis, which are presented as follows.

3.1 Case Study: Condition Monitoring of Kneader's Gear Box

3.1.1 Equipment Description

1. Kneader is basically a mixer where 87% of calcined petroleum coke with butt is mixed with 13% of coal tar pitch to form a semi-solid paste. The Kneader has been developed to provide a consistent and gentle folding action in order to melt and thoroughly combine materials with a minimum of degradation of the product.
2. Kneader drive details: Motor KW-500, gearbox input RPM: 900 and output RPM: 45 (this is a special type of gearbox having both rotating and reciprocating movement of shafts).
3. The general arrangements of different parts a Kneader are shown in Fig. 3.
4. Kneader specifications: Inner diameter: 600 mm, barrel length: 7232 mm, heating jackets (designed pressure: 6 bar, designed temperature: 300 °C); inlet: 800 × 530 mm; outlet: 1200 × 1200 mm; screw outer diameter: 572 mm; core diameter: 338 mm. It is designed for a rated capacity of 35 tons/hour with minimum and maximum capacities of 21 tons/hour and 40 tons/hour, respectively. Average mixing time takes 120 s with estimated inlet temperature of dry mix coke is

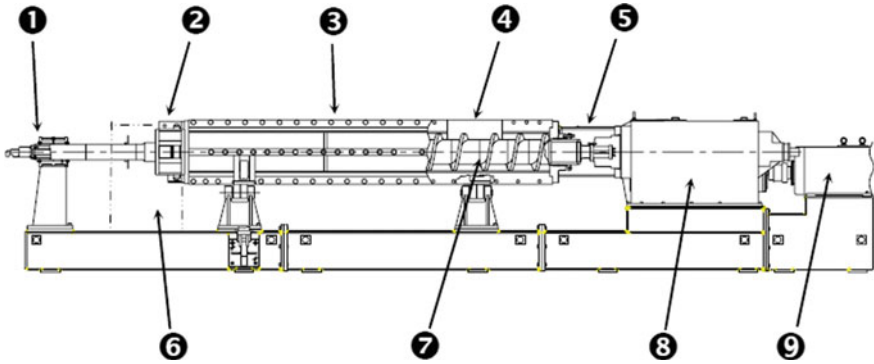


Fig. 3 Kneader and its major components (1) outboard bearing support stand, (2) discharge gate, (3) split barrel, (4) feed inlet, (5) thrust yoke, (6) optional discharge chute, (7) kneading screw, (8) gear box and (9) drive motors

150–160 °C and that of pitch is 180–190 °C. Estimated outlet temperature is maintained at 170–180 °C.

5. Kneader screw rotates and axially reciprocates simultaneously. Screw imparts shear stress to the product by the close interaction of the kneading teeth of the barrel and screw flights. Combined axial and radial mixing contributes to homogenous mixing of the product.
6. In gear box, the gears are designed to produce rotating and reciprocating movement of the kneading screw through a gimbal mechanism. The mixing screw is inserted directly into the output shaft of the constant torque gearbox. The gearbox housing is provided with heavy wall sections. Suitable covers are located in the housing for inspection purposes. The line diagram of kneader gear box is shown in Fig. 4.
7. The lubricating system of Kneader gearbox consists of: (a) Tank mounted oil pump driven by a totally enclosed motor and (b) internally mounted piping directs flow to ensure adequate lubrication reaches all bearings, gears and bushings.
8. Mixing chamber (as shown in Fig. 5) is fabricated of carbon steel utilizing a replaceable abrasion-resistant segmented liner extending the full chamber length. The chamber is constructed of segmented barrels, split along the vertical centre-line and hinged for opening allowing access to the kneading screw, liner sections and replaceable hardened steel kneading teeth. The chamber sections are opened and closed by means of hydraulic cylinders powered by a hydraulic power unit that is complete with a totally enclosed fan cooled electric motor. The chamber halves are bolted together along the top and bottom split lines to ensure a positive seal during operation. The accurate machining tolerances between mixing chamber inner diameter and liner outer diameter provide efficient heat exchange without requiring the use of heat-transfer paste. Barrel sections are jacketed for circulating heat-transfer oil.

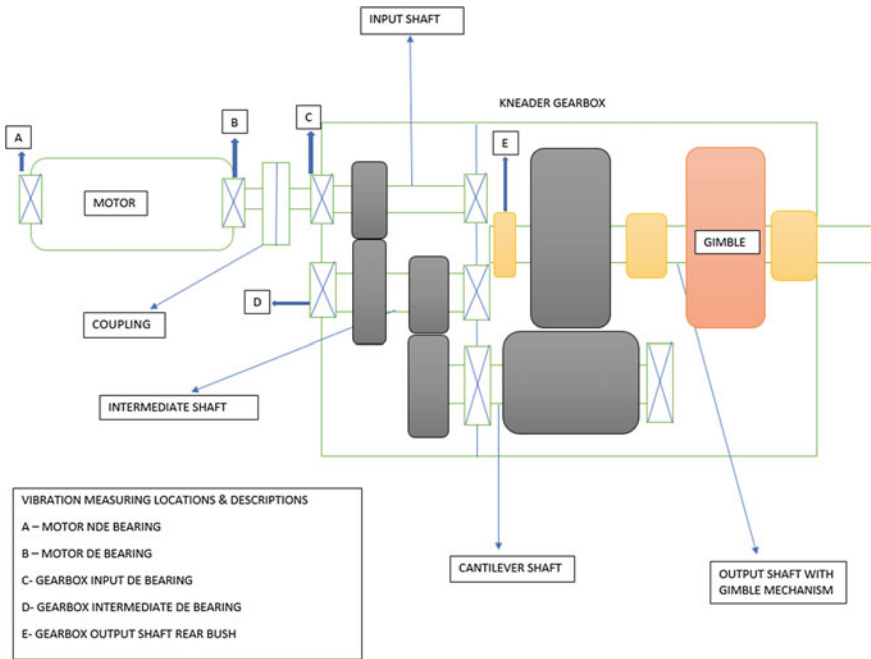


Fig. 4 Line diagram Kneader gearbox drive components

Fig. 5 Kneader mixer screw



3.1.2 Machine Diagnosis Report During Operation

Gear box of Kneader is very critical and single line equipment. Vibration analysis is being conducted on this equipment since 2010. As per ISO 10816, it is a Class III equipment (75 KW drive motor). The vibration limits (RMS) up to 3.5 mm/s in gearbox are considered as normal, in between 3.5 and 5 mm/s is marginal and above 5 mm/s is considered as critical. Also, another parameter PeakVue (G_E) should be less than 1 for good condition. In this system, we are able to cover vibration

measurements at both non-drive and drive-end bearing points of the motor and input and output bearings of gear box. Vibration analyser (CSI make with built-in software) is used for measurement and analysis. The data is captured at 5 averages, Hanning window, 1600 line of resolution (LOR). Vibration readings were taken at bearing C, D and E. The readings are presented in Table 2.

1. Prior to February 2018, vibration trends Kneader-2, were in acceptable limits and maximum amplitude was in range of 2.5–3 mm/s, which is quite acceptable.
2. On 4 February 2018, it was observed that there was oil leakage from Kneader gear box. Since lube oil was contaminated, it was filled and topped up with fresh oil. Kneader was started but an abnormal sound was observed from the gear box. Then, it has been gone for vibration analysis.
3. On 5 February 2018 vibration analysis shows that amplitude of vibration (RMS) increased up to 8.34 mm/s in the intermediate shaft and PeakVue readings were high at 1.25 G_E . Kneader was stopped and gearbox was opened for inspection and it was found that intermediate shaft gear teeth and its drive end bearing were damaged (as shown in Fig. 6). As per recommendation, both the shaft (with integrated gear) and bearing were replaced.
4. On 9 February 2019 vibration measurements showed that PeakVue has decreased to 0.4 G_E but vibration was still more than 7.56 mm/s and still there is little abnormal sound. The assembly was again stopped for inspection and it was

Table 2 Vibration (RMS) readings

	Vibration (in mm/s) on 5 February 2018				Vibration (in mm/s) on 9 February 2018			
	H	V	A	P (G_E)	H	V	A	P (G_E)
Gearbox input DE bearing (C)	1.89	1.66	2.78	0.87	1.23	1.34	1.67	0.34
Gearbox intermediate DE bearing (D)	5.67	5.89	8.34	1.25	3.28	4.53	7.56	0.43
Gearbox rear bush bearing (E)	1.01	1.16	1.27	0.05	0.86	0.92	0.78	0.04
	Vibration (in mm/s) on 5 March 2018				Vibration (in mm/s) on 12 March 2018			
Gearbox input DE bearing (C)	1.39	1.56	1.78	0.43	1.01	1.34	1.21	0.12
Gearbox intermediate DE bearing (D)	3.45	4.36	5.12	0.56	2.13	2.34	2.76	0.12
Gearbox rear bush bearing (E)	0.91	1.01	0.87	0.05	0.83	0.77	0.73	0.05

H, V and A are vibration in horizontal, vertical and axial directions and P is PeakVue

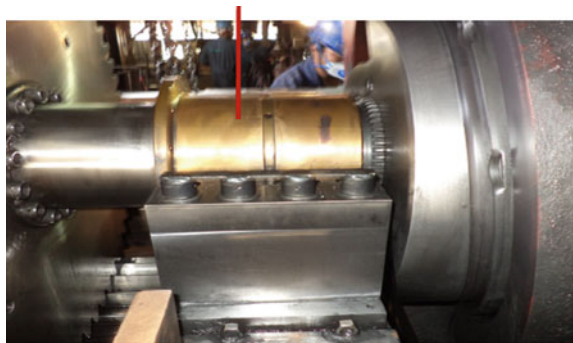


Fig. 6 Damaged intermediate gear and roller bearing

found that intermediate bush clearance was increased (as shown in Fig. 7) due to which abnormal sound was observed. After giving shim packing of 3 mm, clearance was adjusted and sound was reduced.

5. On 5 March 2018, vibration amplitude was still high on intermediate shaft (5.12 mm/s). The time waveform (as shown in Figs. 8 and 9) indicates the irregular impacts, which happens mainly due to bearing looseness, high bearing clearance or other bearing related abnormalities. The impact waves were ranging from +7 to -6 G_s indicating a high alert. The crest factor (peak to RMS) is also as high as 4.25 (against a normal value of 2 to -2 for a good bearing) indicating high impact. Same was being transmitted to input shaft also which showed similar pattern of time waveform.
6. Since already the bearing was replaced along with adjustment of bush, so intermediate bearing housing was removed for checking. After inspection, it was found that housing diameter has increased leading to looseness of bearing in the housing. Bearing housing was repaired with in situ welding and machining to maintain the accurate tolerances.
7. After that on 12 March 2018, vibration readings were found normal, i.e. 2.76 mm/s maximum, which was well within acceptable limits and there is no abnormal sound.
8. The time waveform analysis also showed an excellent improvement in the health of the intermediate and input bearing. There were no fault patterns and impact

Fig. 7 Kneader intermediate bush



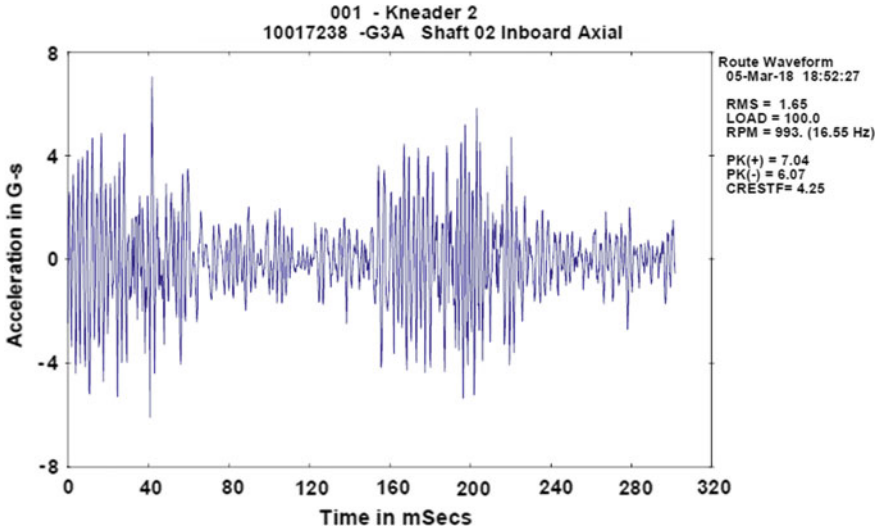


Fig. 8 Time waveform of intermediate shaft during faulty condition

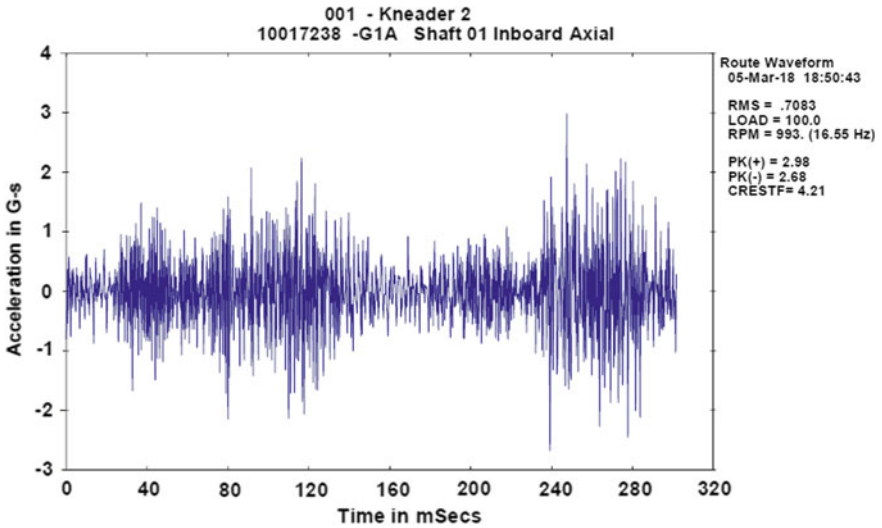


Fig. 9 Time waveform of input shaft during faulty condition

wave ranged from 1.6 G_s to $-1.3 G_s$ indicating normal conditions. The crest factor has also decreased to 2.4 (as shown in Fig. 10).

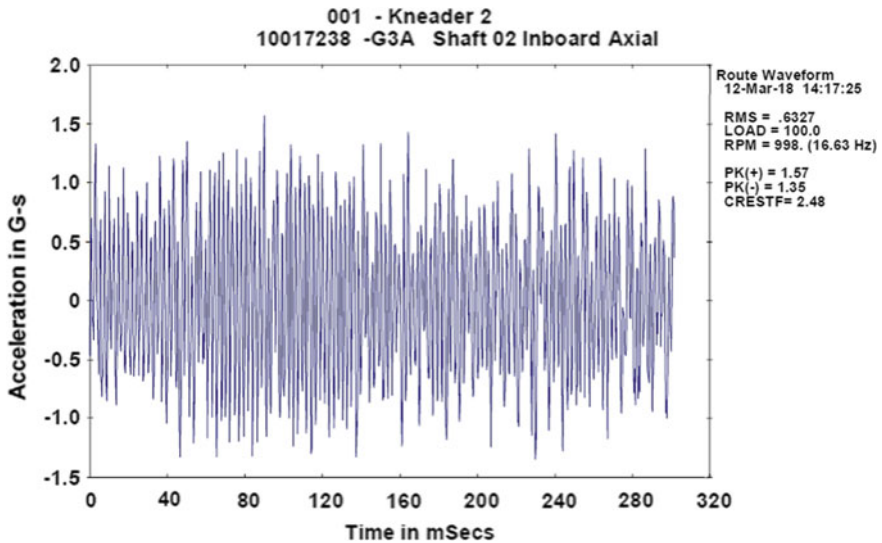


Fig. 10 Time waveform of intermediate shaft after correction

4 Summary

Condition-based maintenance improves the reliability and capability of the system. It avoids accident and so-called sudden failure. Though there are several condition monitoring techniques but vibration analysis is very sensitive and strong technique among those. From this experimental investigation, it can be summarized that

1. This paper concludes that the combined study of time waveform and crest factor can lead us to measure the faults at a very early stage.
2. For the complex drive (similar to Kneader gear box), measurement and analysis of vibration of input and output shaft which may able to give an indication of the internal components health like; condition of intermediate shaft and gear (which are inside cover and not accessible for taking readings).
3. A combination of oil analysis with vibration analysis can detect the gear box-related problem.

References

1. Mandin P, Whrich R, Roustan H (2009) Industrial aluminium production: the Hall-Heroult process modelling. *Electrochem Soc Trans* 19(26):1–10. <https://doi.org/10.1149/1.3247986>
2. Maria A, Ramirez M, Vintila RR, Drew RAL (2019) Morphology of aluminum alloy foams produced with dolomite via partial sintering of precursors. *Materials* 12(10):1691–1699. <https://doi.org/10.3390/ma12101691>

3. Mohanty AR (2014) Machinery condition monitoring: principles and practices. CRC Press, London
4. Williams JH, Davies A, Drake PR (1994) Condition-based maintenance and machine diagnostics. Springer, New York
5. Jardine AKS, Lin D, Banjevic D (2006) A review on machinery diagnostics and prognostics implementing condition-based maintenance. *Mech Syst Signal Process* 20:1483–1510
6. Kim H, Na MG, Heo G (2014) Application of monitoring, diagnosis, and prognosis in thermal performance analysis for nuclear power plants. *Nucl Eng Technol* 46(6)
7. Jayaswal P, Wadhvani AK, Mulchandani KB (2009) Review article on machine fault signature analysis. *Int J Rotating Mach* 1–10. Article ID 583982. <https://doi.org/10.1155/2008/583982>
8. Wong WK, Tan PN, Loo CK, Lim WS (2009) An effective surveillance system using thermal camera. In: International conference on signal acquisition and processing (ICSAP 2009), Kuala Lumpur, 3–5 Apr 2009, pp 13–17
9. Mohanty AR, Kar C (2006) Fault detection in a multistage gearbox by demodulation of motor current waveform. *IEEE Trans Ind Electron* 53(4):1285–1297
10. Srivastava NK, Mondal S (2015) Predictive maintenance using modified FMECA method. *Int J Prod Qual Manag* 16(3)

Effect of Hot Rolling on Physical and Mechanical Properties of Al 6061 Alloy-Based Metal Matrix Composite



Senapati Ajit Kumar, Panda Sasank Shekhar, and Mohanty Gopal Krushna

Abstract The present work is focused on the effect of hot rolling on physical and mechanical properties aluminum metal matrix composite. Aluminum metal matrix composite is reinforced with fly ash and rice husk ash particulate prepared by stir casting technique. The microstructure analysis reveals the uniform distribution of the particulate reinforcement in the matrix. The result shows that the mechanical properties such as hardness and tensile strength of hot-rolled fly ash composite are higher than that of rice husk ash composite and as-cast alloy. The hot-rolled composite shows there is a significant decrease in density when compared to as-cast composite. Morphological study has been done for determining the micro-mechanism of failure and crack growth characteristics.

Keywords Metal matrix composites (MMCs) · Fly ash (FA) · Rice husk ash (RHA) · Stir casting · Rolling · Mechanical properties

1 Introduction

Aluminum alloy composite has been considered as an engineering material, since they possess very good mechanical as well as tribological properties. Those materials have now found their application in automobile, aerospace and general engineering industries [1–3]. Inferable from lower warm coefficient of extension and bearable machinability these materials are picking up notoriety over other ordinary materials [4, 5]. Al 6061 is normally chosen as a matrix for making metal matrix composite because these materials have shown good fatigue strength, corrosion resistance as

S. Ajit Kumar · P. Sasank Shekhar (✉) · M. Gopal Krushna
GIET University, Gunupur, India
e-mail: sekhar.4206@gmail.com

S. Ajit Kumar
e-mail: senapati.ajit@gmail.com

M. Gopal Krushna
e-mail: gk.mohanty787@gmail.com

well as good weld ability [6]. As of late, researchers are shedding exorbitant reinforcement materials, for example, SiC and Al_2O_3 . Typically stir casting method is received to produce segment with aluminum matrix composite (AMC) where there is impressive seepage of exorbitant materials, for example, SiC and Al_2O_3 . So as to bring down the expense of generation, expansion of less expensive support, for example, fly ash (FA), rice husk ash (RHA) and coconut shell ash have been picked [7, 8].

Siva Prasad studied microstructure and mechanical properties of the A356 alloy reinforced with rice husk ash MMCs; they found that the density of the composites is inversely proportional to the rice husk ash content, while hardness of the prepared composite increases with increasing reinforcement amount [9]. Saravanan investigated the tribological behavior of rice husk particle size reinforced with Al alloy. They found better wear resistance in case of coarse particle composites compared to fine reinforcement particle composites. They also reported that the wear rate of the composite decreases with the addition of reinforcement into the matrix [10]. Usman studied the wear behavior of Al-6061 reinforced with rice husk ash particulates and concluded that addition of RHA particles increased the wear resistance of the composite and surface damage has been reduced [11]. Hassan analyzed the effect of microstructure on mechanical properties of AL-6061 alloy reinforced with rice husk ash and they reported a well distribution of reinforcement particles; also addition of these particles increased the hardness and tensile strength of the composite [12]. Madakson fabricated two MMCs using two-step stir casting method; (Al-6061 + Al_2O_3) and (Al-6061/ Al_2O_3 + RHA) made a comparative study on the mechanical properties between these two. They reported that the addition of RHA particles in hybrid MMCs enhanced the mechanical properties then the Al_2O_3 MMCs [13]. Anil Kumar studied more comprehensively the particle size effect on mechanical properties of (Al-6061 + RHA) composite. A clear trend observed that the tensile strength, compressive strength and hardness increased with the increased amount of RHA and decreased with the increase in particle size [14]. Arun Kumar investigated the mechanical behavior of the Al-6061 alloy reinforced with the fly ash and e-glass fiber hybrid metal matrix composite. They also concluded that the tensile strength of the composite increased by 60–70% as compared to the cast alloy [15]. Vivekananda studied the mechanical and wear behavior of an aluminum reinforced with fly ash composite by stir casting they reported that with the addition of fly ash particles in the Al matrix alloy, hardness and wear resistance increased significantly [16]. Sharma studied the influence of the particle size on the wear properties of fly ash reinforced AMC; they have concluded that wear resistance of the fabricated composites increases with the increase in the fly ash contents [17].

In primary manufacturing process, microstructural changes in MMCs induce stiffness in the direction of fiber but to poor in transverse direction due to the weak interface region and this problem is less in the case of particulate MMCs. On the other hand, the specific modulus of MMCs are increased, but reduced in ductility. To overcome this problem, mechanical hardenings like forging, rolling used on MMCs and they enhance both strength and ductility of Al MMCs [18]. It is also reported that with conventional metal working process, e.g., rolling, forging, etc., the mechanical

and wear behavior of the composite material can be enhanced [19–21]. The MMCs depend on the forging process parameters and MMCs composition such as reinforcement content, particulate aspect, particulate and matrix interfacial bonding, impurity/porous and even testing condition [22, 23]. The addition of reinforcement results to low ductility and toughness [24] which are unsuitable for fatigue applications, especially low cycle fatigue machine parts [25, 26].

On the other hand, few research works have been done on hot rolling behavior of Al6061 alloy reinforced with fly ash and rice husk ash metal matrix composites by stir castings method. A secondary hot rolling process was used to enhance the mechanical properties of Al-Mg-Si alloy reinforced with fly ash and rice husk ash metal matrix composites. MMCs are fabricated by low-cost liquid metallurgy stir casting process. In this present work, the effect of hot rolling on the microstructure and physical and mechanical properties of the prepared metal matrix composite were analyzed by scanning electron microscope (SEM).

2 Experimental Details

In this experimental work, matrix material used in current experimentation is Al-6061 aluminum casting alloy. Al-6061 alloy has good workability, excellent corrosion resistance and medium strength. It also has good mechanical properties compared to other Al-alloys. Its composition is given in Table 1. Reinforcement material used in current research work is fly ash (FA—an industrial waste) and rice husk ash (RHA—an agriculture waste). FA generated during the combustion of coal in thermal plants which is hazardous to environment and RHA is waste from agriculture. From the literature, it has reported that these contain some elements, due to which can replace the costly reinforcements like Al_2O_3 , SiC, etc., composition of FA and RHA is given in Tables 2 and 3.

A stir casting setup which is consisting with electrical resistance furnace and a stirrer assembly used to blend the composite. Aluminum ingots are cleaned properly and then cut into proper size. The amount required is weighed before charged in to the melting furnace. Fly ash and rice husk are preheated to 650 °C to remove moisture. Electric resistance furnace is used for melting the aluminum alloy with bottom pouring arrangement (Fig. 1). 1 wt% of Mg is added during the melt to improve the wettability of the reinforcement material. Mechanical mixing is accomplished for blending the Mg in the liquefy Al combination. A vortex is made in the melt with a BN covered treated steel rotor to add the reinforcement uniformly, at a speed of 600–650 rpm for 10 min [27]. The pouring temperature of the liquid metal is kept up at 700 °C. At that point, the liquid composite moved into from crucible to a rectangular shape size of (200 mm × 50 mm × 20 mm). The as-cast composite and alloy samples were hot rolled with a reduction of 20% at a temperature of 450 °C with intermediate heat treating process. Hot rolling details of MMC as shown in Table 4. Hot rolling mill with inline push through preheating oven with a load capacity of

Table 1 Composition of Al-6061 alloy

Chemical composition Wt%	Al	Cr	Cu	Fe	Mg	Mn	Si	Ti	Zn
	95.8–98.6	0.04–0.35	0.15–0.4	Max 0.7	0.8–1.2	Max 0.15	0.4–0.8	Max 0.15	Max 0.25

Table 2 Chemical composition of fly ash (wt%)

Chemical composition	Na ₂ O	CaO	MgO	SiO ₂	Al ₂ O ₃	K ₂ O	Fe ₂ O ₃
Wt%	0.10	1.24	0.58	56.43	13.54	0.59	4.97

Table 3 Chemical composition of rice husk ash (wt%)

Chemical composition	SiO ₂	Al ₂ O ₃	Fe ₂ O ₃	CaO	MgO	SO ₃	K ₂ O	Na ₂ O	Others
Wt%	97.095	1.135	0.316	0.073	0.825	0.146	0.181	0.092	Bal

**Fig. 1** Stir casting setup**Table 4** Hot rolling details of MMC

Metal	Thickness (mm) (in 15 passes)		% of reduction
	Before rolling	After rolling	
Al6061 alloy	9.5	5.5	23
MMC RHA	9.2	4.3	18.7
MMC FA	10	4.6	18.5

14MT is used to reduce the thickness of the samples without any lubricant which is given in Fig. 2.

A roller diameter of 96 mm made from hardened tool steel was adjusted with a speed of 40 rpm for rolling. A water displacement method is used for calculating the density of composite. From the Archimedes principle, the apparent weight of the object immersed in a liquid decreases by an amount equal to the weight of the volume of the liquid that it displaces. Brinell hardness test method is used to measure the hardness of the sample. A 2.5 mm steel ball indenter with 187.5 kg load applied into

Fig. 2 Rolling mill setup

the sample for 30 s. Average hardness value was taken at different point on the cross section of the samples. Five different measurements have taken at different points to find an average value of hardness. According to ASTM standard, the specimens for tensile test were prepared tested using electronic tensometer. Microstructure of the tensile specimens was studied before and after test using SEM.

3 Result and Discussion

3.1 Microstructural Analysis

Hot rolling of as-cast Al6061 alloy, Al6061/RHA AMC, Al6061/fly ash AMC was carried out at 450 °C to avoid matrix hardening. The distribution of rice husk and fly ash particles was examined by microscopic investigation on polished sample. Figure 3 shows better distribution of rice husk ash and fly ash particles is generally obtained by rolling. Microstructure investigation uncovers a noteworthy change in the viewpoint rate with the dispersion of condition of whiskers in the wake of rolling. It was discovered that whiskers having high normal viewpoint proportion are haphazardly appropriated and having normal perspective proportion are directionally dispersed in the hot-rolled condition.

3.2 Density

Table 5 demonstrates the density estimation of three materials before rolling and after rolling of as-cast Al6061 combination, RHA composite and FA composite,

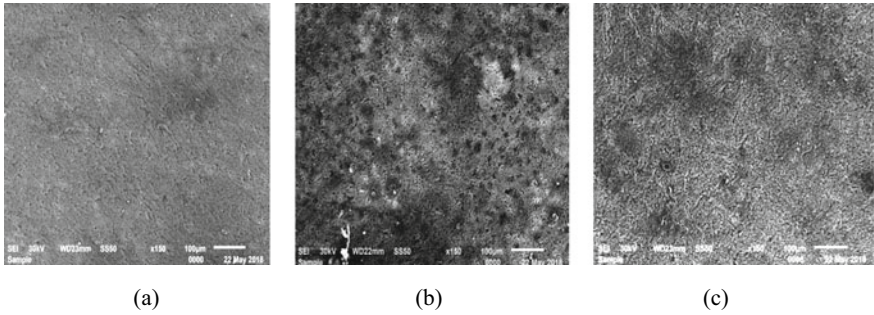
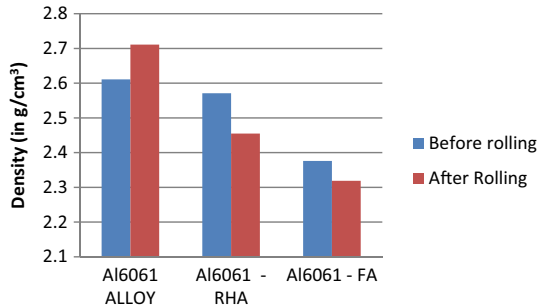


Fig. 3 SEM of rolled as-cast Al6061 alloy (a), rolled rice husk ash composite (b) and rolled fly ash composite (c) at 150×

Table 5 Density of alloy and MMCs

Metal	Cast (before rolling) (in g/cm ³)	After rolling (in g/cm ³)
Al6061 alloy	2.611	2.711
MMC RHA	2.571	2.455
MMC FA	2.376	2.319

Fig. 4 Variation of density before and after rolling



and Fig. 4 demonstrate the variation in the density of the base metal and other two strengthened composites. It was seen that after rolling, density of the base alloy marginally increased, however, the density of the Al6061/RHA composite and Al6061/FA composite is diminished.

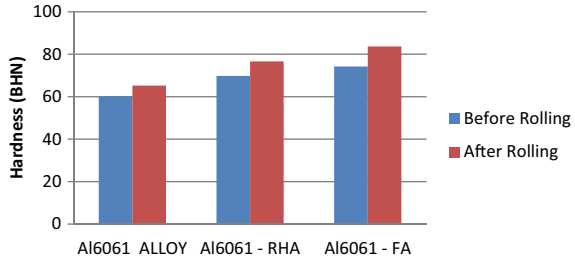
3.3 Hardness

The resistance to penetration or indentation of a material is called as hardness. Hardness of the cast alloy and the composites as shown in Table 6 before and after rolling. The hardness of the Al6061/FA composite is increased compare to as-cast base alloy

Table 6 Hardness of different alloys and MMCs

Metal	Cast (before rolling) (BHN)	After rolling (BHN)	Increase (% age)
Al6061 alloy	60.12	65.23	8.49
MMC RHA	69.78	76.59	9.75
MMC FA	74.25	83.67	12.68

Fig. 5 Variation of hardness before and after rolling



and Al6061/RHA composite. It was found that the hardness of FA/MMC is increased up to 12.68% after rolling. This can be due to the refined grain size and presence of harder reinforcing element, i.e., fly ash. Figure 5 shows the change in the values of hardness before and after hot rolling. It was found that in all the material the hardness is increased after rolling. The reason behind the increase in hardness can be expected to be the hard ceramic particles which act as a barrier to the movement of dislocations in the matrix.

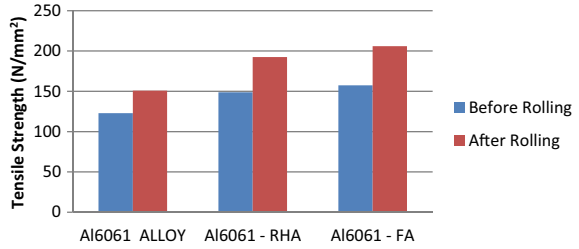
3.4 Tensile Test

Table 7 shows the tensile strength of as-cast 6061 alloy, Al6061/rice husk and Al6061/fly ash composite. It was found that the tensile strength of rolling the three materials was increased after rolling. Al6061 fly ash composite shows better tensile strength compare to other two materials. Due to the presence of hard fly ash particles in the matrix alloy leads to improve in the microstructure which causes increase in the strength. Figure 6 shows the variation in the tensile strength for the three materials.

Table 7 Tensile strength of different alloys and MMCs

Metal	Cast (before rolling) (N/mm ²)	After rolling (N/mm ²)
Al6061 alloy	122.837	150.78
Al6061 RHA	148.81	192.45
Al6061 FA	157.47	205.94

Fig. 6 Variation of tensile strength before and after rolling



3.5 Factography of Selected Composite

Figures 7, 8 and 9 shows the factography images of the fracture surface of Al6061 unreinforced alloy, Al6061/RHA MMC and Al6061/FA MMC of tensile sample for

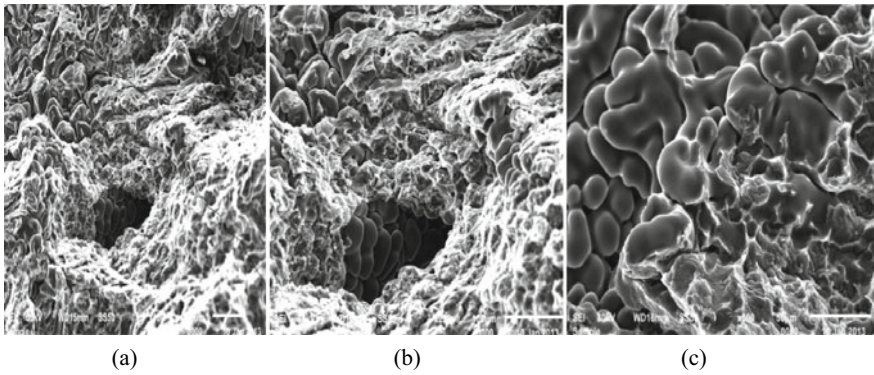


Fig. 7 SEM factography of cast Al6061 alloy **a** at 150 \times , **b** at 250 \times , **c** at 500 \times

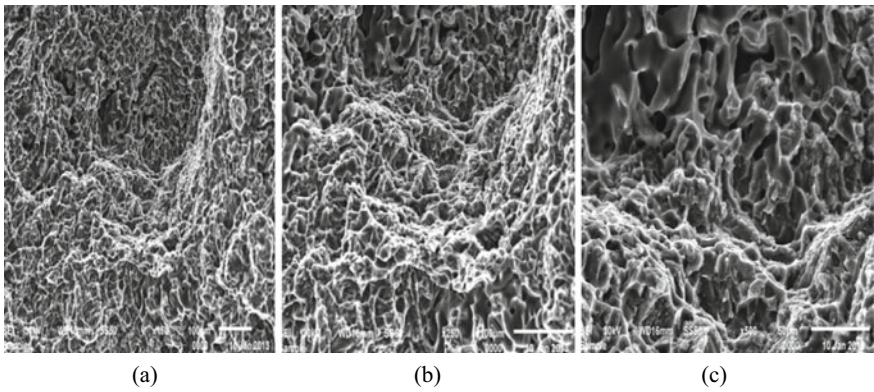


Fig. 8 SEM factography of Al6061/RHA AMC **a** at 150 \times , **b** at 250 \times , **c** at 500 \times

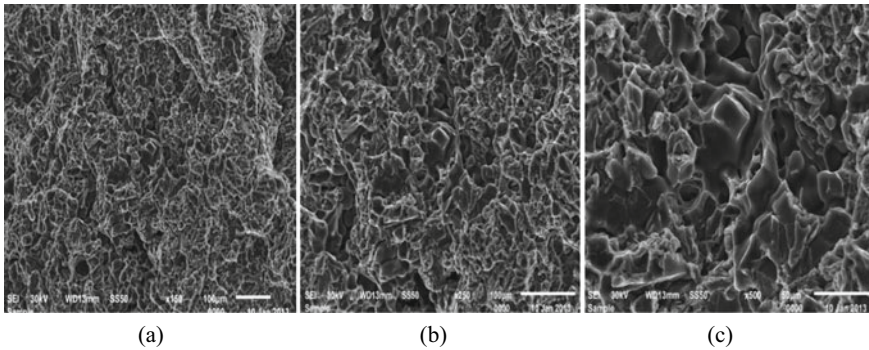


Fig. 9 SEM fractography of Al6061/FA MMC **a** at 150 \times , **b** at 250 \times , **c** at 500 \times

finding the mechanism of failure. Figure 7 reveals the presence of cracks and few dimples in Al 6061 alloy and it shows the ductile type of fracture. Figure 8 shows the fractography image of the Al6061/RHA MMC having less number of dimples and shallower compared to matrix alloy. Figure 9 shows the fractography image of the Al6061/FA MMC which reveals decrease in the number of dimples resulting reduced plastic strain. Tear ridges are observed in the matrix alloy.

4 Conclusion

The following conclusion can be drawn from the experimental work:

- Stir casting technique can be used for fabricating the metal matrix composite with fly ash and rice husk ash as reinforcement.
- The composites with hot-rolled condition exhibit higher strength and higher hardness as compared to ‘as-cast’ composites. The Al6061/fly ash composite in rolled condition shows better tensile strength of 205.94 N/mm² compared to Al6061/RHA and as-cast composites.
- From the microstructure, it was observed that after hot rolling the fine grain size of fly ash particles and their uniform distribution in the matrix element led to increase in the mechanical properties of the composite.
- The density of the fly ash composite decreases where as mechanical properties increases compare to the rice husk ash reinforced composite and base alloy.

References

1. Surappa MK (2003) Aluminium matrix composites: challenges and opportunities. *Sadhana* 28:319–334
2. Singh I, Singh S, Singh A (2013) Conventional and unconventional hole making in metal matrix composites. In: *Mechanical engineering series*, pp 169–193
3. Sahin Y, Acilar M (2003) Production and properties of SiCp-reinforced aluminium alloy composites. *Compos Part A Appl Sci Manuf* 34:709–718
4. Hashim J, Looney L, Hashmi MSJ (2001) The enhancement of wettability of SiC particles in cast aluminium matrix composites. *J Mater Process Technol* 119:329–335
5. Klimowicz TF (1994) The large scale commercialization of aluminium-matrix composites. *J Miner Met Mater Soc* 46:49–53
6. Kumar GBV, Rao CSP, Selvaraj N, Bhagyashekar MS (2010) Studies on Al6061-SiC and Al7075-Al₂O₃ metal matrix composites. *J Miner Mater Charact Eng* 9:43–55
7. Sachin Y (2003) Wear behavior of aluminium alloy and its composites reinforced by SiC particles using statical analysis. *Mater Des* 24:95–103
8. Senapati AK, Panda SS, Mohanty GK (2019) Effect of hot forging on high temperature tribological properties of aluminium composite reinforced with agro and industrial waste. *IJEAT* 8(6):1607–1612
9. Siva Prasad D, Rama Krishna A (2011) Production and mechanical properties of A356.2/RHA composites. *IJAST* 33(51–58):2019–2023
10. Saravanan SD, Senthilkumar M, Shankar S (2013) Effect of particle size on tribological behavior of rice husk ash-reinforced aluminum alloy (AlSi10Mg) matrix composites. *J Tribol Trans* 56(6):1156–1167
11. Usman AM, Raji A, Waziri NH, Hassan MA (2014) Aluminium alloy—rice husk ash composites production and analysis. *Leonardo Electron J Pract Technol* 25:84–98. ISSN 1583-1078
12. Hassan SB (2007) Study the effect of microstructure on mechanical properties of AL-6061 alloy reinforced with rice husk ash. *Mater Sci Eng A* 447(1–2):355–360
13. Madakson PB, Yawas DS, Apasi A (2013) Wear behaviour of rice husk ash—alumina reinforced Al–Mg–Si alloy matrix hybrid composites. *J Mater Res Technol* 2(2):188–194
14. Anil kumar HC, Hebbar HS, Ravi Shankar KS (2011) Mechanical properties of rice husk ash reinforced aluminium alloy (Al6061) composites. *Int J Mech Mater Eng* 41–45
15. Arun Kumar MB, Swamy RP (2011) Evaluation of mechanical properties of Al6061, fly ash and E-glass fiber reinforced hybrid metal matrix composites. *ARPN J Eng Appl Sci* 6(5). ISSN 1819-6608
16. Vivekananthan M, Senthamarai K (2011) Experimental evaluation of aluminium-fly ash composite material to increase the mechanical & wear behaviour by stir casting method. *CARE J Appl Res*. ISSN 2321-4090
17. Sharma K, Singh RC, Chaudhary R (2017) Effect of flyash particles with aluminium melt on the wear of aluminium metal matrix composites. *Eng Sci Technol* 20(4):1318–1323
18. Ahmed S, Haseeb ASMA, Kurny ASW (2007) Study of the wear behaviour of Al–4.5% Cu–3.4% Fe in situ composite: effect of thermal and mechanical processing. *J Mater Process Technol* 182(1–3):327–332
19. Venkata Siva SB, Sahoo KL, Ganguly RI, Dash RR (2012) Effect of hot working on structure and tribological properties of aluminium reinforced with aluminium oxide. *J Mater Eng Perform* 21:1226–1231
20. Prasad T, Chennakesava Reddy A, Jushkumar S (2014) Tensile and fracture behavior of 6061 Al-Si Cp metal matrix composites. In: *International conference on advanced materials and manufacturing technologies (AMMT)*, pp 18–20
21. Reddappa HN, Suresh KR, Niranjan HB, Satyanarayana KG (2014) Effect of aging on mechanical and wear properties of beryl particulate reinforced metal matrix composites. *J Eng Sci Technol* 9(4):455–462

22. Okazaki Y (2012) On the effects of hot forging and hot rolling on the microstructural development and mechanical response of a biocompatible Ti alloy. *Materials* 5:1439–1461
23. Lokesh GN, Ramachandra M, Mahendra KV (2014) Effect of hot rolling on Al-4.5%Cu alloy reinforced fly ash metal matrix composite. *Int J Compos Mater* 4(1):21–29
24. Euh K, Kung SB (2005) Effect of rolling on the thermo-physical properties of SiCp/Al composites fabricated by plasma spraying. *Mater Sci Eng A* 395:47–52
25. Vijay Kumar T, Jayashankar G, Srinivas B, Jithendra J, Sumedh M (2017) Effect of rolling on hardness of aluminium metal matrix composites—an experimental study. *Int J Mech Eng Technol* 8(5):525–530
26. Vasanth Kumar R, Keshavamurthy R, Perugu CS, Koppad PG, Alipoure M (2018) Influence of hot rolling on microstructure and mechanical behaviour of Al6061-ZrB₂ in-situ metal matrix composites. *Mater Sci Eng A* 738:344–352
27. Balasivanandha Prabu S, Karunamoorthy L, Kathiresan S, Mohan B (2016) Influence of stirring speed and stirring time on distribution of particles in cast metal matrix composite. *J Mater Process Technol* 171(2):268–273

Blast Mitigation Analysis of Clay Brick Masonry Wall



P. A. Shirbhate, Jagriti Mandal, and M. D. Goel

Abstract Threats due to terrorism and intensity of blast attacks are increasing across the globe. This not only affects the human lives but also affect structural integrity and its behavior. Majority of undeveloped countries have large numbers of masonry structures which needs research intervention to interpret structural response when subjected to blast load. Moreover, it also demands ways to improve their resistance against such threats. Hence, in the present investigation, a masonry wall under blast loading is numerically investigated using finite element package ABAQUS[®], as it is very difficult to carry out such experiments. ConWep function is used to define blast loading in this study. Analysis of masonry wall with varying standoff distance is performed on the basis of its peak displacement and induced strain. Further, effect of application of polyurea on the clay brick masonry wall against blast loading is investigated. From this investigation, it is observed that application of polyurea results in 15% lower peak displacement of masonry wall with all other parameters being same.

Keywords Masonry wall · Blast loading · ConWep · Polyurea · Numerical simulation

1 Introduction

Terrorist attacks have become a major problem all over the world. An explosion within or nearby a building can cause large damage to structures which include damage of walls and columns leading to progressive collapse of the structure. This leads to loss of precious human lives and properties, thus ultimately affecting a nation to large extent. To overcome such issues, there is a need to design new structures

P. A. Shirbhate (✉) · M. D. Goel
Department of Applied Mechanics, Visvesvaraya National Institute of Technology (VNIT),
Nagpur, Maharashtra 440 010, India
e-mail: payalshirbhate@student.vnit.ac.in

J. Mandal
Department of Mining Engineering, Visvesvaraya National Institute of Technology (VNIT),
Nagpur, Maharashtra 440 010, India

© Springer Nature Singapore Pte Ltd. 2021
P. Pant et al. (eds.), *Advances in Mechanical Processing and Design*, Lecture Notes
in Mechanical Engineering, https://doi.org/10.1007/978-981-15-7779-6_28

and enhancement of strength of the existing ones to improve performance of structures under blast loads. This can be achieved by applying advanced fiber-reinforced polymer (FRP) materials on the surface of wall. Additional reinforcement materials can also be used to increase mass and ductility of wall, if coatings, such as polyurea, are applied.

Way back in 1999, Wong and Karamanoglu presented a numerical model to understand the nonlinear failure criteria of masonry material [1]. Afterward, several researchers studied the behavior of masonry walls susceptible to blast load using polymeric materials. In year 2004, Davidson et al. performed field tests to understand the effectiveness of polymeric materials to increase the flexural resistance of unreinforced masonry walls under blast loads [2]. Later on, in year 2005, Davidson et al. further extended the study to understand the collapse behavior of masonry wall and suggested the application of polymeric material to prevent fragments and failure of the masonry structure [3]. After two years, Buchan and Chen carried out experimental and finite element (FE) analysis for evaluating the blast response of masonry structures retrofitted using FRP or polymer under blast and observed significant reduction in displacement as compared to non-retrofitted wall [4]. In the same year, Malvar et al. reviewed composite materials that can be used to retrofit different structural components [5]. Based on these researches, Crawford et al. proposed the use of composite panels made of metal foam to provide protection from debris and application of polyurea to add tensile strength and ductility to the masonry wall [6]. Later on, Tan and Patoary investigated the effectiveness of FRP in strengthening of masonry wall using experimental blast tests as well as numerical models [7]. Experimental blast load analysis of retrofitted masonry wall using FRP was conducted by Urgessa and Maji, and they presented response of masonry walls due to deformation when subjected to blast load [8]. Irshidat et al. used new polymeric materials to protect and improve the performance of unreinforced masonry structures against blast load, which can be used to replace fiber-reinforced polymer [9]. Afterwards, Ahmad et al. carried out experimental evaluation of behavior of masonry walls under blast loading under varying standoff distances to understand the failure mechanism [10].

In year 2015, Kernicky et al. assessed the performance of conventional masonry building under blast pressure due to internal explosions [11]. Pereira et al. [12] did dynamic out-of-plane blast load analysis to know the response of unreinforced masonry infill wall using underwater blast wave generators. Based on experimental results, numerical model was calibrated using ABAQUS/Explicit® [12]. Later on, Wang et al. analyzed the use of polyurea layer to absorb energy, thereby enhancing the resistance of clay brick masonry. This polyurea layer also minimizes the fragments occurring from collapsed masonry unit, which reduces fatal and injuries [13]. Recently, Alsayed et al. focused on the use of GFRP sheets to retrofit infill masonry walls to provide resistance under blast loads [14]. In the past, most of the investigations were focused on experimental evaluation and few investigations were focused on FE analysis. Further, most of the earlier investigations were done on concrete masonry block walls under blast loads which are different than the typical clay brick masonry wall commonly constructed in many regions of Southeast Asia. Hence,

FE analysis of one brick thick clay brick masonry wall, with and without polyurea retrofitting, under blast loading is presented in this study.

2 Geometry of Wall, Material Properties and FE Modeling

A masonry wall of size 1.01 m × 1.51 m and brick size of 19 cm × 9 cm × 9 cm with mortar thickness 1 cm is considered in this study. The wall thickness is considered as 10 cm including plaster. The wall is fixed at base and free on other three sides, thus depicting a boundary wall, wherein longitudinal deformation is restricted. Commercially available FE software ABAQUS/Explicit® has been used for the analysis [15]. Wall is modeled using deformable extruded solid feature available in ABAQUS/Explicit®. For FE analysis, linear, eight node continuum three-dimensional reduced integration (C3D8R) elements having hourglass control are used in geometric modeling of the wall. Further, a perfect bond between mortar and brick is assumed to exist. In order to compute mesh independent results, three different mesh sizes (i.e., 0.05, 0.03 and 0.01) are used for dynamic response analysis and finally converged mesh; i.e., 0.01 is used for further analysis. To perform dynamic analysis, central difference integration method has been used. Time steps smaller than Courant time limit has been chosen as $\Delta t \leq (l/c)$ where l is the characteristic element dimension and c is speed of sound wave in medium in which it travels to attain conditional stability. Figure 1a shows the FE model of the clay brick masonry wall considered in this study. Brick and mortar is defined using damaged plasticity material model available in ABQUS/Explicit®. This material model provides a general capability to perform analysis of concrete structures under cyclic and/or dynamic loading [15]. When concrete is subjected to low confining pressures, it behaves in a brittle manner, having cracking in tension and crushing in compression as the main failure mechanisms. Whereas when concrete gets exposed to high confining pressure,

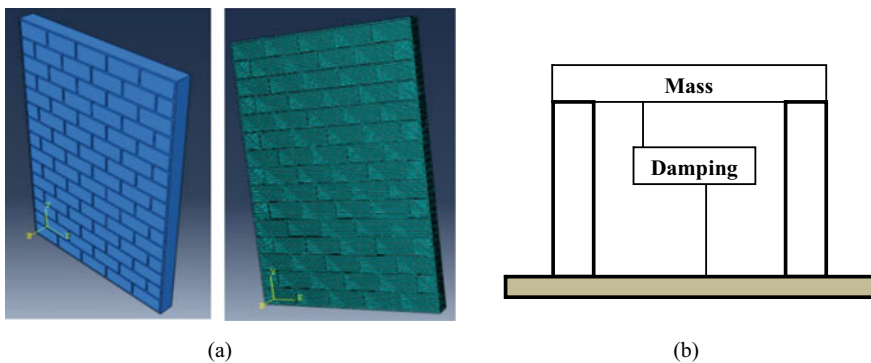


Fig. 1 a CAD and FE model of masonry wall used in the present investigation. b Single-degree-of-freedom (SDOF) model for blast load

the brittle behavior of concrete disappears and the propagation of crack is prevented. Failure of concrete micro-porous microstructure occurs due to consolidation and collapse mechanism; this leads to a macroscopic response that resembles with work hardening in a ductile material.

$$\sigma_t = (1 - d_t)D_0^{el} : (\varepsilon - \varepsilon_t^{pl}) \tag{1}$$

$$\sigma_c = (1 - d_c)D_0^{el} : (\varepsilon - \varepsilon_c^{pl}) \tag{2}$$

where t represents tension and c is the compression behavior. Here, σ_t is the tensile vector and σ_c is compressive stress vectors; ε_t^{pl} and ε_c^{pl} are plastic strains; d_t and d_c are the damage variables which are considered as functions of plastic strain; D_0^{el} is the undamaged initial elastic modulus. The yield function in the considered damaged plasticity model is as

$$F = \left(\sqrt{3/2} \sqrt{\bar{s} : \bar{s}} \right) - 3\alpha \bar{p} + \beta \left\langle \frac{\hat{\sigma}}{\bar{\sigma}_{max}} \right\rangle - \gamma \left\langle -\frac{\hat{\sigma}}{\bar{\sigma}_{max}} \right\rangle - (1 - \alpha)\bar{\sigma}_c = 0 \tag{3}$$

where $\frac{\hat{\sigma}}{\bar{\sigma}_{max}}$ is the maximum principal effective stress; \bar{s} is the deviatoric stress tensor; $\bar{p} = (\bar{\sigma}_1 + \bar{\sigma}_2 + \bar{\sigma}_3)/3$. For nonlinear analyses, it is assumed that the physical properties remain constant only for short increments of time or deformation; accordingly, it is convenient to reformulate the response in terms of the incremental equation of motion. Blast loads are typically analyzed using single-degree-of-freedom (SDOF) model consisting mass and damper (Fig. 1b).

Material properties for brick and mortar, used for the analysis, are reported in Fig. 2. Brick and mortar are connected together using hard contact behavior with a friction coefficient 0.8. Brick and mortar both are modeled using concrete damaged plasticity model, whereas elastic–plastic material model has been used to model polyurea as sheet with thickness of 5 mm. The density of polyurea is 1070 kg/m³ with Young’s modulus of 25.00 × 10⁷ N/m² and Poisson’s ratio of 0.465. Further, Fig. 2 also shows stress–strain behavior of polyurea used in the present investigation

Properties	Brick	Mortar
Density (kg/m ³)	2000	2162
Young’s Modulus (N/mm ²)	20.68 · 10 ⁹	34.47 · 10 ⁹
Poisson’s Ratio	0.1	0.2
Dilation Angle (°)	20	20
Eccentricity (m)	0.1	0.1
f_{bo} / f_{co}	1.15	1.15
k	0.7	0.7

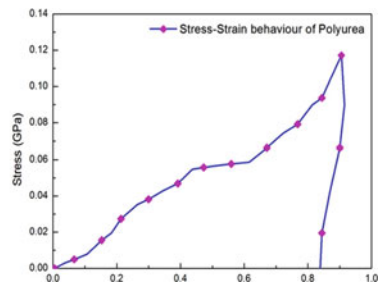
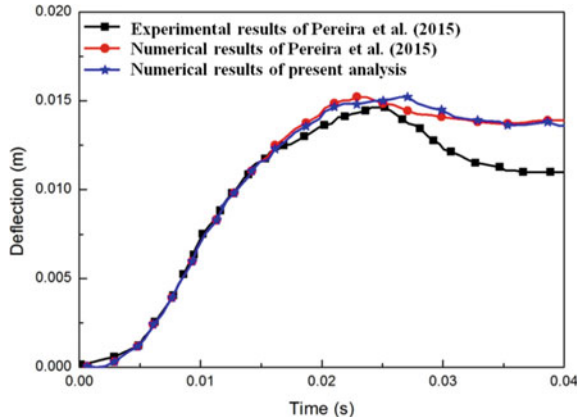


Fig. 2 Stress–strain behavior of polyurea under compression [16, 17]

Fig. 3 Validation of present numerical scheme with numerical and experimental results of Pereira et al. [12]



[16, 17]. This stress–strain curve is converted to true stress–strain curve to be used in ABAQUS/Explicit®.

3 FE Validation of the Present Study

For FE validation of present study, results of the work done by Pereira et al. have been used [12]. In the present investigation, wall is modeled as per Pereira et al. and same material properties are used as reported. The results of present FE analysis are compared with those reported by Pereira et al., in terms of displacement–time history. The percentage error in peak deflection value of experimental analysis and present analysis is 3.44%, whereas for the plastic deformation the difference was found to be approximately 24% between numerically and experimentally obtained results. However, results for the present study agreed well with the numerical results reported in the literature. The difference in the numerical and experimental results could be because of the difference between real material properties and those being defined for the FE simulation. Close agreement in results of numerical model and experimental analysis has been obtained; therefore, it can be said that present FE analysis is validated (Fig. 3).

4 Results and Discussions

Performance of masonry wall under the blast loading resulting from explosion of 1 kg TNT (i.e. W) at the standoff distance (R) of 2, 3 and 4 m is analyzed. Thus, corresponding scaled distance ($Z = R/W^{1/3}$) is $2 \text{ m/kg}^{1/3}$, $3 \text{ m/kg}^{1/3}$ and $4 \text{ m/kg}^{1/3}$, respectively. Figure 4a shows the blast pressure time history for various scaled distances considered in the present investigation as obtained using ConWep function. Figure 4b

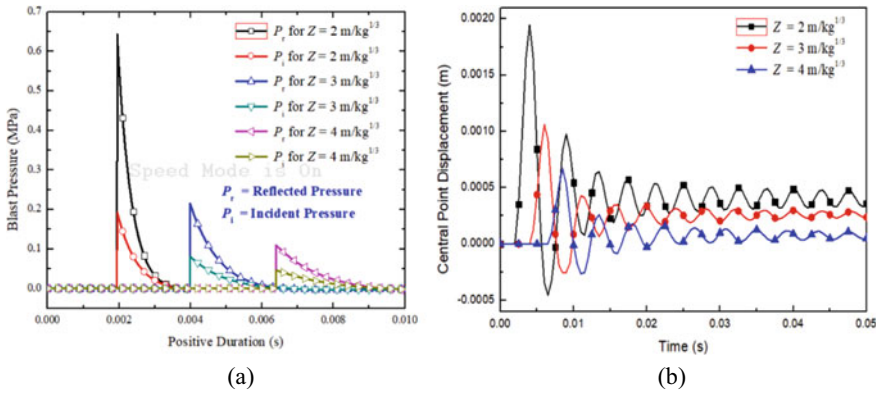


Fig. 4 **a** Blast pressure time history for various scaled distances. **b** Comparison of displacement–time history for 1 kg of TNT at different scaled distances

shows the displacement–time histories of midpoint of wall with three blast loading scenarios as defined earlier. From this figure, it is noticed that peak displacement of the wall decreases, when there is increase in standoff distances. Peak displacement of walls is 1.9 mm, 1.0 mm and 0.07 mm under standoff distances of 2 m, 3 m and 4 m, respectively. Figure 5a shows displacement–time histories of masonry wall with and without polyurea coating at central point under blast loading. It can be observed from this figure that displacement of masonry wall with polyurea is significantly lower than the displacement of the masonry wall without polyurea with all other conditions being same. It has been noticed that maximum displacement of wall is decreased by 15% when polyurea of 5 mm is applied to that of wall without polyurea. Thus, polyurea coating results into increase in enhanced blast performance

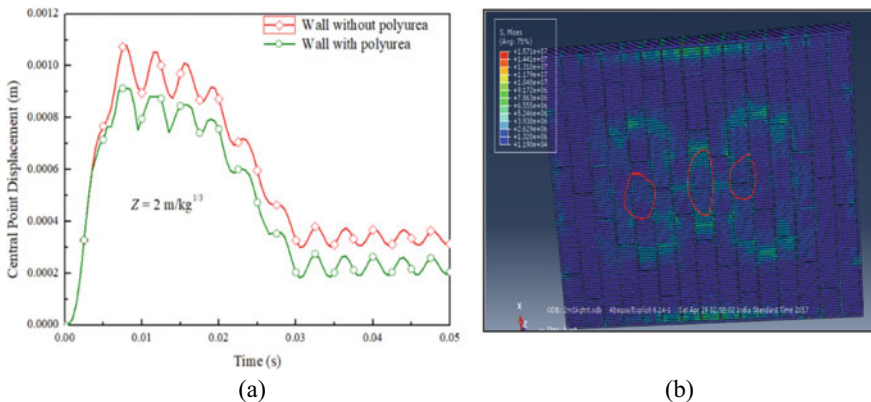


Fig. 5 **a** Comparison of displacement–time history of masonry wall with and without polyurea for scaled distance of 2 m/kg^{1/3}. **b** von Mises stresses on the back face of the wall for 1 kg TNT at 3 m standoff distance

significantly. Further from the deformation analysis, it is observed that application of polyurea prevents the collapse of the wall by imparting additional elasticity, and it also prevents the spread of fragments to the surroundings.

Figure 5b shows the von Mises stress contours at the back side of wall (i.e., face opposite to explosion) for a scaled distance of $3 \text{ m/kg}^{1/3}$. Since the explosive was located centrally with respect to the wall, the maximum displacement and stress was observed in the central portion of the wall, wherein peak von Mises stress (dynamic) was found to be 15.71 MPa. Similar behavior is observed for other scaled distances.

5 Conclusions

In the present investigation, performance of masonry wall under blast loading has been analyzed using ABAQUS[®] finite element package. Displacement–time histories, strain and stresses of wall are analyzed to evaluate the performance of walls under blast loading. The wall is one brick thick and is analyzed under blast loading with and without polyurea coating. From the FE analysis carried out in this study, the following conclusions are drawn,

1. Peak displacement and stresses decreases with the increase in standoff distance of explosive charge from wall.
2. Application of polyurea results in reduction of peak displacement of masonry wall by an extent of 15% with all other parameters being same.
3. Polyurea shows good potential for retrofitting of brick masonry wall against blast loads. The investigation highlighted the effect of application of polyurea for retrofitting of existing masonry walls.
4. Polyurea retrofitting of existing masonry wall is also capable of effectively reducing the flying and scattered debris after explosion.

References

1. Wong CW, Karamanoglu M (1999) Modelling the response of masonry structures to gas explosions. *J Loss Prev Process Ind* 12:199–205. [https://doi.org/10.1016/S09504230\(98\)00058-8](https://doi.org/10.1016/S09504230(98)00058-8)
2. Davidson JS, Porter JR, Dinan RJ, Hammons MI, Connell JD (2004) Explosive testing of polymer retrofit masonry walls. *J Perform Constr Facil* 18:100–106. [https://doi.org/10.1061/\(ASCE\)0887-3828\(2004\)18:2\(100\)](https://doi.org/10.1061/(ASCE)0887-3828(2004)18:2(100))
3. Davidson JS, Fisher JW, Hammons MI, Porter JR, Dinan RJ (2005) Failure mechanisms of polymer-reinforced concrete masonry walls subjected to blast. *J Struct Eng* 131:1194–1205. [https://doi.org/10.1061/\(ASCE\)0733-9445\(2005\)131:8\(1194\)](https://doi.org/10.1061/(ASCE)0733-9445(2005)131:8(1194))
4. Buchan PA, Chen, JF (2007) Blast resistance of FRP composites and polymer strengthened concrete and masonry structures—a state-of-the-art review. *Compos Part B Eng* 38:509–522. <https://doi.org/10.1016/j.compositesb.2006.07.009>

5. Malvar JL, Crawford JE, Morrill KB (2007) Use of composites to resist blast. *J Compos Constr* 11:601–610. [https://doi.org/10.1061/\(ASCE\)1090-0268\(2007\)11:6\(601\)](https://doi.org/10.1061/(ASCE)1090-0268(2007)11:6(601))
6. Crawford JE, Morrill KB, Magallanes JM, Youcai W (2019) Retrofit of masonry walls to enhance their blast resistance. *Struct Congr*, 1–10. [https://doi.org/10.1061/41016\(314\)92](https://doi.org/10.1061/41016(314)92)
7. Tan KH, Patoary MKH (2009) Blast resistance of FRP-strengthened masonry walls. I: approximate analysis and field explosion tests. *J Compos Constr* 13:422–430. [https://doi.org/10.1061/\(ASCE\)1090-0268\(2009\)13:5\(422\)](https://doi.org/10.1061/(ASCE)1090-0268(2009)13:5(422))
8. Urgessa GS, Maji AK (2010) Dynamic response of retrofitted masonry walls for blast loading. *J Eng Mech* 136:858–864. [https://doi.org/10.1061/\(ASCE\)EM.1943-7889.0000128](https://doi.org/10.1061/(ASCE)EM.1943-7889.0000128)
9. Irshidat M, Al-Ostaz A, Cheng AD, Mullen C (2011) Nanoparticle reinforced polymer for blast protection of unreinforced masonry wall: laboratory blast load simulation and design models. *J Struct Eng* 137:1193–1204. [https://doi.org/10.1061/\(ASCE\)ST.1943-541X.0000361](https://doi.org/10.1061/(ASCE)ST.1943-541X.0000361)
10. Ahmad S, Elahi A, Pervaiz H, Rahman AGA, Barbhuiya S (2014) Experimental study of masonry wall exposed to blast loading. *Mater Constr* 64(313):1–12
11. Kernicky TP, Whelan MJ, Weggel DC, Rice CD (2015) Structural identification and damage characterization of a masonry infill wall in a full-scale building subjected to internal blast load. *J Struct Eng* 141:D4014013. [https://doi.org/10.1061/\(ASCE\)ST.1943-541X.0001158](https://doi.org/10.1061/(ASCE)ST.1943-541X.0001158)
12. Pereira JM, Campos J, Lourenço PB (2015) Masonry infill walls under blast loading using confined underwater blast wave generators (WBWG). *Eng Struct* 92:69–83. <https://doi.org/10.1016/j.engstruct.2015.02.036>
13. Wang J, Ren H, Wu X, Cai C (2017) Blast response of polymer-retrofitted masonry unit walls. *Compos Part B Eng* 128:174–181. <https://doi.org/10.1016/j.compositesb.2016.02.044>
14. Alsayed, SH, Elsanadedy HM, Al-Zaheri, ZM, Al-Salloum, YA, Abbas H (2016) Blast response of GFRP-strengthened infill masonry walls. *Constr Build Mater* 115:438–451. <https://doi.org/10.1016/j.conbuildmat.2016.04.053>
15. ABAQUS®/Explicit User's Manual (2011) Dassault systèmes Simulia corporation. France
16. Bahei-El-Din YA, Dvorak GJ, Fredricksen OJ (2006) A blast-tolerant sandwich plate design with a polyurea interlayer. *Int J Solids Struct* 43:7644–7658. <https://doi.org/10.1016/j.ijsolstr.2006.03.021>
17. Blackard B, Mettupalayam, KW: Experimental observations of masonry infilled reinforced concrete frames with openings. *Spec. Publ.* 265:199–222. <https://doi.org/10.14359/51663296>

Interdependence of Morphological, Mechanical and Fracture Behaviour of Toughened Bio-Based Polyamide 11



Saroj Kumar Samantaray, Shushil Kumar Gope,
and Bhabani Kumar Satapathy

Abstract The present study embodies the fabrication of toughened polyamide 11 blends via melt blending route with POE-g-MA (impact modifier) and their characterization. The structural, thermal, mechanical and fracture performance were investigated for the blends in the composition range of 0–30 wt%. The melting point remained unaffected, but the overall crystallinity decreased linearly with elastomer loading. The tensile and flexural properties showed a declining trend with the concentration of elastomer which is accompanied by an increase in ductility. Almost 82% enhancement in impact energy is registered for the blends with 10 wt% of elastomer loading which has a correspondence to the rubber domain size of $\sim 0.22 \mu\text{m}$. The essential work of fracture (EWF) approach was employed to analyse the resistances to crack initiation (w_e) and crack propagation (β_{wp}) under plane stress condition. The w_e as a measure of the resistance to crack initiation increased by $\sim 53\%$ in the blend with 10 wt% of elastomer. The study demonstrates the interdependence of morphological, mechanical and fracture behaviour of toughened bio-based polyamide 11/POE-g-MA blend.

Keywords Polyamide 11 · POE-g-MA · Toughening · Essential work of fracture

1 Introduction

Polyamide 11 is now widely accepted in the automobile sector for its excellent piezoelectric and cryogenic performances, which is beneficial for gas/oil pipeline and oil storage applications [1]. PA 11 is completely a bio-based polymer, whose monomer is derived from renewable castor oil. Above the glass transition temperature, it shows inherent flexibility due to high methylene-to-amide ratio. Like other grades of polyamide, it also has behavioural limitations in terms of notch and strain rate sensitivity at room/low service temperature. Therefore, to enhance toughness, the melt blending with low modulus-high flexible polymer is an economical route and

S. K. Samantaray · S. K. Gope · B. K. Satapathy (✉)
Department of Materials Science and Engineering, Indian Institute of Technology Delhi, Huaz
Khas, New Delhi 110016, India
e-mail: bhabaniks@gmail.com

© Springer Nature Singapore Pte Ltd. 2021

P. Pant et al. (eds.), *Advances in Mechanical Processing and Design*, Lecture Notes
in Mechanical Engineering, https://doi.org/10.1007/978-981-15-7779-6_29

339

hence better choice than other toughening mechanisms, like internal plasticisation, co-polymerisation, etc. In literature, various elastomers with/without compatibiliser were reported with significant improvement in impact strength for various class of polyamide [1–7].

The efficiency of the rubber-toughening process depends largely on the type of elastomer, elasticity-to-viscosity ratio of elastomer, viscosity ratio of matrix and dispersed phase, dispersed phase domain size, the percentage of rubber loading. In-depth analysis and interdependence of toughing parameters were exclusively reported in the article of Bucknall et al. [8]. POE is a cheap elastomer, and it has excellent oil and chemical resistance with low viscosity-to-elasticity ratio [9]. POE is a non-polar, and PA 11 has polar amide linkage; hence, the phase miscibility at the interface cannot be expected. The blending will result in an adverse effect on part performance due to coagulation of dispersed phase on matrix and larger domain size. Hence, the grafting of maleic anhydride (hereafter-MA) which has both polar and non-polar end, to elastomeric phase is the best possible option. Comparative analysis with and without grafted elastomer is comprehensively available in the article literature. It is well established through a series of devoted work that partial phase miscibility at the interface will sufficiently decrease interfacial tension; hence, the toughening efficiency increased [10]. In perspective of the above said, in this study, POE-g-MA (commercially marketed by DuPont in the trade name of Fusabond) was used for blending with PA 11, for toughened PA 11/POE-g-MA blend. The essential work of fracture (EWF) method for analysing the fracture performance of polymeric material by partitioning the total work of fracture into essential (crack initiation) and non-essential (crack propagation) work is useful for highly ductile polymer system. The comprehensive details on EWF are well reported in [11] following the pioneering work of Mai et al. [12].

Bio-based polyamide 11 is currently anticipated that would venture into long-term and heavy-duty automobile applications. However, the behavioural limitations to notch and strain rate sensitivity at room/low service temperature of PA 11 induce no enthusiasm for this. The synergistic effect of improved impact toughness, low moisture absorption and outstanding combination electrical and chemical resistance properties may overcome the limitation. The interdependency analysis of the mechanical-morphological-fracture performance of PA 11/POE-g-MA blends may provide important insights on toughening aspect, which is still un-attempted. In this work, PA 11/POE-g-MA blends with varying content elastomer (wt%) were fabricated by melt mixing route in a twin-screw extruder. For the optimisation of the blends with an overall based compromise in structural, mechanical and fracture properties; blend composition (optimum toughness/stiffness), the morphological parameters (domain size, inter-particle distance), mechanical performances, impact strength and fracture performances of the blends were analysed.

2 Experimental

2.1 Materials and Sample Preparation

The manufacturer, grade and technical details of used PA 11 and POE-g-MA are listed in Table 1. The PA 11 granules were pre-dried for 12 h in a vacuum oven at 80 °C to remove moisture content. The blends of different elastomer wt% were prepared using co-rotating twin-screw extruder at 70 rpm screw speed. The extruded strands were then chopped off and dried for 12 h prior for further processing in injection moulding machine for tensile, flexural, impact and fracture specimen. The temperature profile and process conditions maintained in injection moulding and extrusion process are listed in Tables 2 and 3. The sample designations with the matrix and dispersed phase proportion are given in Table 4.

Table 1 Details of raw material

Raw materials	Grade	Manufacturer	Manufacturer data
PA-11 (granules)	Rilsan	Arkema	Density (ρ) = 1.06 g/cc, MFI (g/10 min) = 28 @ 230 °C, 2.16 kg. T_m = 183 °C
POE-g-MA (granules)	Fusabond N493	Dupont, India	Density (ρ) = 0.87 g/cc T_m = 58 °C, MA content (%) = 0.5, MFI (g/10 min) = 1.6 @ 190 °C and 2.16 kg

Table 2 Extrusion temperature profile (°C)

Die	Zone 9	Zone 8	Zone 7	Zone 6	Zone 5	Zone 4	Zone 3	Zone 2
200	205	205	200	198	195	188	185	180

Table 3 Temperature profile (in °C) and process condition in injection moulding

Nozzle	Zone 3	Zone 2	Zone 1	Feed
198	195	188	185	180
Process parameter			Value	
Injection pressure			25%	
Injection speed			20%	
Cooling time			25 s	
Holding time			6 s	

Table 4 Composition and designation of PA-11/POE-g-MA blends

Designation	PA-11 (wt%)	POE-g-MA (wt%)
NE-0	100	0
NE-10	90	10
NE-15	85	15
NE-25	75	25
NE-30	70	30

2.2 Thermal and Morphological Analysis

The thermal transitions, i.e., melting and crystallisation behaviour of the blends, were measured in Perkins Elmer (Model Pyris 6) instrument at a heating rate of 10 °C/min in a temperature range of 20–225 °C in N₂ atmosphere. The samples were first heated (first heating cycle) up to 200 °C to remove residual stresses and then cooled at 10 °C/min to obtained crystallisation peak. The cooled samples again heated (second heating cycle) at the same heating rate for melting endotherm peak. The percentage of crystallinity is measured from the heat of fusion (ΔH_m) of PA 11/POE-g-MA, the heat of fusion (ΔH_{mo}) for 100% crystalline PA 11 (224.6 J/g) and weight fraction (w) of dispersed phase using the following expression. The melt flow index is very useful for processing perspective because it shows the melt flow behaviour. The MFI of neat polyamide 11 and the blends were estimated using Dynisco MFI setup as per ASTM D1238 test procedure.

$$X_c = \frac{\Delta H_m}{\Delta H_{mo} \times w} \times 100 \quad (1)$$

The POE-g-MA phase distribution over the matrix polyamide phase was investigated in a scanning electron microscope (SEM) Zeiss EVO-50. The blend samples were etched in hot xylene (100 °C) for 24 h for selective removal of the rubber phase. The samples were coated with gold to make conductive. The SEM images were processed in Image J software to evaluate the number average domain size (D_n) and inter-particle distance (IPD). The D_n and IPD were calculated using the following equations.

$$D_n = \frac{\sum Ni Di}{\sum Ni} \quad (2)$$

$$\tau = Dn \left[\left(\frac{\pi}{6\phi} \right)^{1/3} - 1 \right] \quad (3)$$

2.3 Mechanical Properties

The tensile properties of blended samples were measured in a universal testing machine (UTM) (Zwick Z250) at a strain rate of 50 mm/min as per ASTM D638 procedure. The flexural strength and modulus, and Izod impact strengths of PA 11 and PA 11/POE-g-MA blends were evaluated as per ASTM D790 and D256 standard, respectively. All the tests were repeated five times, and an average of the results with standard deviation is reported. Tests were conducted in room temperature (25 ± 2 °C).

2.4 Essential Work of Fracture (EWF) Analysis

Double-edged notched tension (DENT) specimens ($80 \times 20 \times 1$) were prepared from injection-moulded rectangular sheet. The DENT specimen is then subjected to uniaxial tensile load with constant 5 mm/min cross-head speed in ZWICK Z250 universal testing machine with varying ligament length (distance between two notch tips). The load versus displacement curve of at least six ligament lengths was performed to fulfil the basic criteria of self-similarity in EWF concept. Unlike other fracture concepts, EWF conceptually distinguished the total work of fracture in two-zone a) inner fracture process zone, IFPZ, and b) outer plastic deformation zone, OPDZ. As per EWF, the total work of fracture (W) is the sum of W_e (energy dissipated in IFPZ or resistance to crack initiation) and W_p (energy dissipated in OPDZ or resistance to crack propagation) under plane stress condition.

$$W = W_e + W_p \quad (4)$$

$$W = w_e B l + \beta w_p B l^2 \quad (5)$$

B is the thickness of DENT sample, l is the ligament length, and β is the shape factor. Upon dividing the total work of fracture by notched-ligament area ($B \times l$), specific work of fracture (w) is obtained, and the expression is:

$$w = w_e + \beta w_p l \quad (6)$$

w_e and βw_p can be calculated from the slope and intercept of the linear fit between specific work of fracture and ligament length. The schematic of the DENT sample and energy partitioning process and its evaluation is exclusively explained in [11].

Table 5 DSC and MFI data of PA 11 and PA 11/POE-g-MA blends

Designation	T_m (°C)	T_c (°C)	AH (J/g)	Crystallinity (%)	MFI (g/10 min/)
NE 00	184.12	162.45	34.77	15.35	29.5
NE 10	185.73	162.98	31.07	13.72	16.2
NE 15	185.15	161.39	24.59	10.86	6.7
NE 25	185.16	161.16	24.16	10.67	5.3
NE 30	184.91	161.08	24.62	10.87	3.39

3 Results and Discussion

3.1 Thermal Properties and Melt Flow Behaviour

The DSC heating and cooling scan peaks correspond to the melting and crystallisation temperature of the neat polyamide, and PA 11/POE-g-MA blends are presented in Table 5. No marginal changes in both melting and crystalline peaks can be observed irrespective of any wt% of elastomer loading, which sufficiently assures the retention of thermal properties of PA 11 in the blend system.

The percentage of crystallinity (% X_c) is calculated using Eq. (1) and listed in Table 5. The crystallinity decreases with elastomer loading, and it may be due to the physical inter-diffusion of the elastomeric phase in semi-crystalline polyamide. MFI of the blends gradually increases with elastomer loading, as given in Table 5. During melt processing of PA 11 and POE-g-MA, chemical interaction between MA and amide linkage formed a co-polymer at the interface; thus, the viscosity increases with decreasing MFI trend.

3.2 Morphology of Blends

SEM images of cryo-fractured-etched extruded strands are shown in Fig. 1. The selective removal of the rubbery phase from the matrix surface (etching process) shows uniform rubber phase distribution over PA 11. Bi-phase morphology with homogeneous distribution indicates the partial phase miscibility, which is due to the compatibilised rubber. The domain size (No. average diameter, D_n) and inter-particle distance (IPD) are calculated using Eqs. (2) and (3). The domain size increases and IPD decreases with elastomer loading due to the fusion of the rubber phase during high shear processing [6].

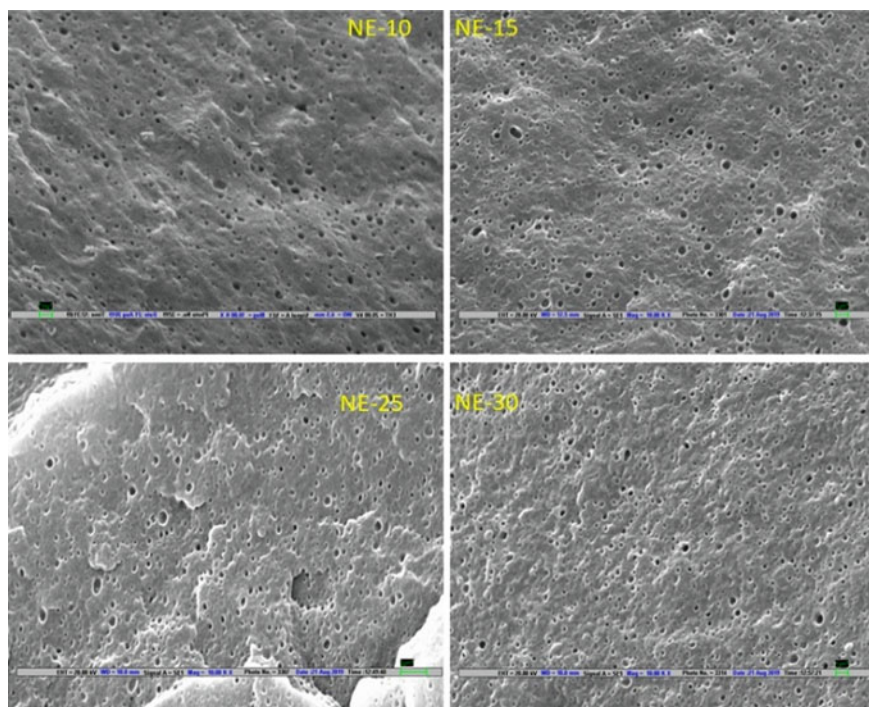


Fig. 1 SEM micrographs of cryogenically fractured and xylene-etched surfaces of PA-11/POE-g-MA blends: Magnification ratio (X 10,000)

3.3 Mechanical Performances

The uniaxial tensile stress versus strain plot is shown in Fig. 2a. The elongation at break increases with 10 wt% of elastomer loading and remains comparatively similar till the extent of elastomer incorporation of up to 25 wt%, and subsequently, it reduced upon further increase in POE-g-MA content to 30 wt%. The area under the stress–strain curve (toughness) systematically increases with elastomer content until 10 wt% and decreases further due to a reduction in modulus and strength without an increase in strain at break, Fig. 2b. The flexural modulus and strength of the blends show an identical trend as tensile properties, Fig. 2c. The similar nature of neat polyamide 11 and PA 11/POE-g-MA blends to both uniaxial and flexing mode of tension indicates the isotropic nature of the multiphase system. The inter-diffusion of amorphous region of elastomer in semi-crystalline PA 11 matrix caused sufficient reduction in stiffness, though the ductility did not improve beyond a critical extent of rubber loading of 10 wt%.

The impact energy dissipated by the PA 11 and the blends under instant high strain load (Izod setup) is shown in Fig. 2d. The impact strength almost increased by almost 82% for 10 wt% rubber incorporation and gradually decreases; further,

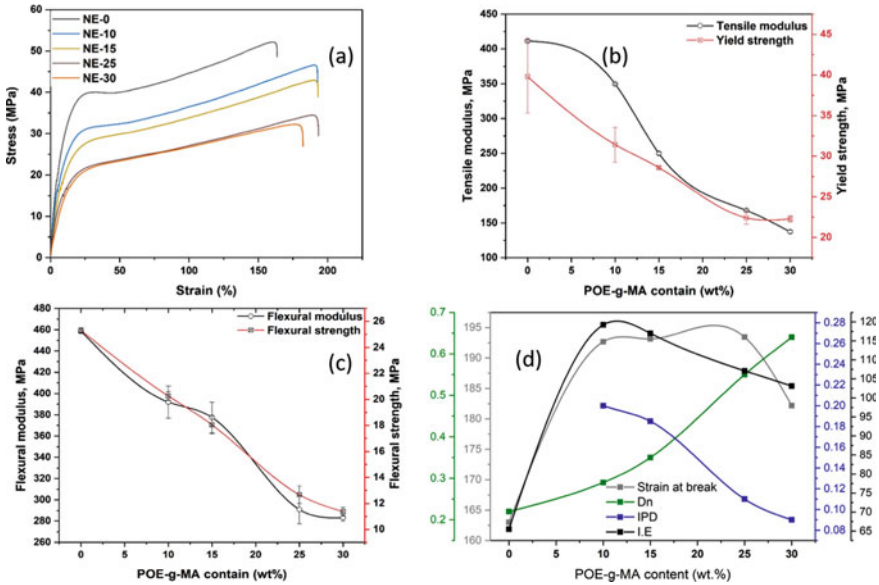


Fig. 2 Mechanical properties and impact strength-morphology-mechanical properties correlation

the reason may be attributed to phase separation. The variation of dispersed phase domain size, inter-particle distance, impact energy and elongation at break as a function of elastomer loading is presented in Fig. 4d. A drop of approximately 3% in impact energy compared to maxima can be observed for 15 wt%. However, in the range of 10–15 wt% loading, the elongation at break and inter-particle distance and impact energy remained comparable with the increase in domain size. The identical (increasing) trend of impact energy, elongation at break and domain size illustrates the cavitation-based toughening process. Based on the observation drawn from Fig. 4d, it is thus safe to report the optimum range of POE-g-MA loading in PA 11 matrix is 10–15 wt%.

3.4 Fracture Behaviour and Its Correlation to Morphology and Impact Behavior

The self-similarity nature of load versus displacement curve can be observed for all blend composition, as shown in Fig. 3. This indicates the applicability of EWF concept as per post-yield fracture mechanics (PYFM) for thin plate/sheet where plane stress condition can easily attain at low strain rate. The variation of specific work of fracture with ligament length is shown in Fig. 4a. The resistance to crack initiation (w_e) and propagation (βw_p) is estimated from the intercept and slope of the linear fit of specific work of fracture (w).

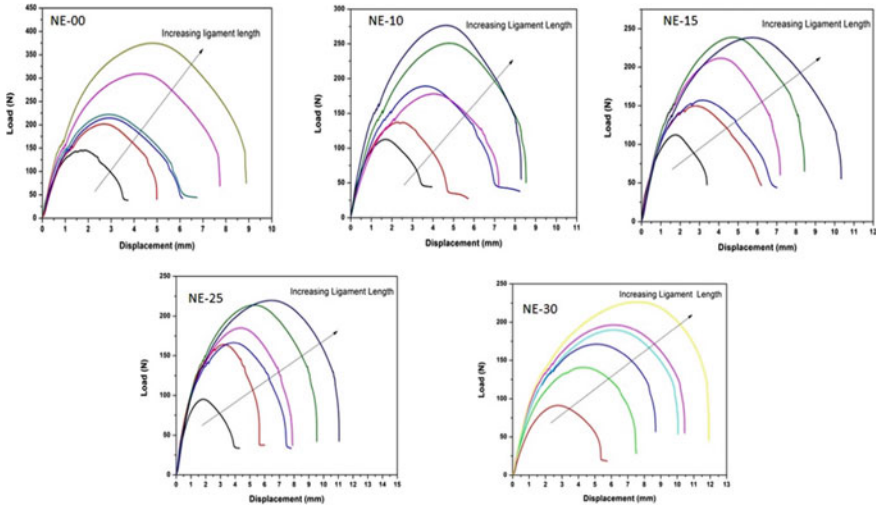


Fig. 3 Self-similarity of load versus displacement curve

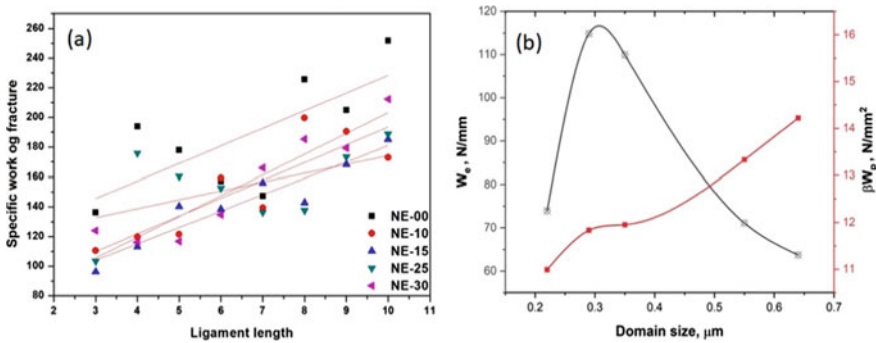


Fig. 4 **a** Variation of specific work of fracture as a function of ligament length and **b** Dependence of w_e and βw_p on the domain size

The dependence of w_e and βw_p on the particle domain size is displayed in Fig. 4b. The w_e increased with domain size up to $\sim 0.22 \mu\text{m}$ and linearly decreased with further elastomer loading. Almost 53% increase is registered for 10 wt% rubber loading in the range of $0.22\text{--}0.29 \mu\text{m}$. In the same range, βw_p and w_e have been observed to be complementing each other, which in turn indicated the attributes of super-toughness for the present system. Such an observation is well in agreement with the findings from Fig. 2d. In the reported range, the toughness may be attributed to the morphology of the dispersed (rubber) phase, where the rubber domains are effectively absorbing the load.

4 Conclusions

The thermal, morphological, mechanical, impact and plane–stress fracture performance of the PA 11 and its blends with POE-g-MA were investigated. The melting temperature of the blends remained unaffected, but the percentage of crystallinity reduced linearly with addition of elastomer, as evidenced from the broadening of the crystalline peaks. The tensile and flexural properties depreciated with substantial enhancement in elongation up to 10 wt% of POE-g-MA and remained in tune with the rubber content in the entire composition range up to ~25 wt%. The critical toughness parameter, i.e., domain size, is found to be 0.22–0.35 μm for 10–15 wt% of elastomer loading with an almost 82% increase in impact strength. In accordance with this, the resistance to crack imitation (w_e) (estimated through EWF process) obtained the maximum in the above composition range. However, the resistance to crack propagation βw_p increases with rubber loading. Based on the obtained results and above discussions, it is noteworthy that PA 11/POE-g-MA blend (90:10–15) with low moisture uptake, dimensionally stable, superior cryogenic and piezoelectric, and improved impact properties may potentially be an emerging material for automotive and industrial application. The study systematically demonstrates the domain size of dispersed rubber phase, i.e., POE-g-MA, controlling not only the extent of influence on the tensile and flexural properties but also the post-yield fracture toughness behaviour of PA 11/POE-g-MA blends.

References

1. Zhou C, Wang K, Fu Q (2009) Toughening of polyamide 11 via addition of crystallizable polyethylene derivatives. *Polym Int* 58(5):538–544
2. Mehrabzadeh M, Burford RP (1996) Impact modification of polyamide 11. *J Appl Polym Sci* 61(13):2305–2314
3. Oono Y, Li Y, Nakayama K, Shimizu H (2006) Impact modification of polyamide 11 by the reactive blending with epoxy group modified polyethylene. *J Nanosci Nanotechnol* 6(12):3915–3918
4. Majumdar B, Keskkula H, Paul DR (1994a) Mechanical behaviour and morphology of toughened aliphatic polyamides. *Polymer (Guildf)* 35(7):1399–1408
5. Majumdar B, Keskkula H, Paul DR (1994b) Morphology development in toughened aliphatic polyamides. *Polymer (Guildf)* 35(7):1386–1398
6. Kumar S, Satapathy BK, Maiti SN (2013) Correlation of morphological parameters and mechanical performance of polyamide-612/poly(ethylene–octene) elastomer blends. *Polym Adv Technol* 24(5):511–519
7. Huang JJ, Keskkula H, Paul DR (2006) Comparison of the toughening behavior of nylon 6 versus an amorphous polyamide using various maleated elastomers. *Polymer (Guildf)* 47(2):639–651
8. Bucknall CB, Paul DR (2009) Notched impact behavior of polymer blends: part 1: New model for particle size dependence. *Polymer (Guildf)* 50(23):5539–5548
9. Xie T, Wu H, Bao W, Guo S, Chen Y, Huang H, Chen H, Lai SY, Jow J (2010) Enhanced compatibility of PA6/POE blends by POE-g-MAH prepared through ultrasound-assisted extrusion. *J Appl Polym Sci* 118(3):1846–1852

10. Yu ZZ, Ou YC, Hu GH (1998) Influence of interfacial adhesion on toughening of polyethylene-octene elastomer/nylon 6 blends. *J Appl Polym Sci* 69(9):1711–1718
11. Bárány T, Czigány T, Karger-Kocsis J (2010) Application of the essential work of fracture (EWF) concept for polymers, related blends and composites: a review. *Prog Polym Sci* 35(10):1257–1287
12. Mai YW, Cotterell B (1986) On the essential work of ductile fracture in polymers. *Int J Fract* 32(2):105–125

Fabrication of Chitosan–Carboxymethyl Cellulose Silver Nanocomposite Films as Antimicrobial Materials



Mamata Das, Ganeswar Sahu, and Jasaswini Tripathy

Abstract This study presents the in situ fabrication of silver nanoparticles through “green” synthetic approach by reducing silver nitrate salt with non-toxic carboxymethyl cellulose. The chitosan and carboxymethyl cellulose-based silver nanocomposite film was fabricated by solution casting method. The samples were characterized by UV–visible spectroscopy, X-ray diffraction (XRD) and FTIR spectroscopy. Scanning electron microscopy (SEM) and transmission electron microscopy (TEM) were carried to evaluate the size and morphology of silver nanoparticles embedded in nanocomposite films. Mechanical testing and thermogravimetry confirmed the improved mechanical strength and thermal stability of chitosan–carboxymethyl cellulose silver nanocomposite (CHCMCNC) films as compared to chitosan–carboxymethyl cellulose blend (CHCMCB). SEM and TEM images clearly indicated the presence of silver nanoparticles with uniform size distribution in CHCMCNC films. The antibacterial activity of fabricated nanocomposite films has been tested against two different pathogenic strains, *E. coli* and *S. aureus*. The chitosan–carboxymethyl cellulose silver nanocomposite films can be explored as antibacterial materials for packaging as well as wound dressing.

Keywords Chitosan · Carboxymethyl cellulose · Antibacterial activity · Polymer nanocomposite

1 Introduction

In recent years, polymer nanocomposites have attracted considerable attention owing to their wide range of applications. They play key role in modern nanotechnologies, due to their unprecedented performance and improved properties. These advanced materials are prepared by dispersing nanoparticles inside polymeric matrix [1, 2] which is an efficient strategy to avoid aggregation of nanoparticles. Recently, there is growing interest in synthesis of natural polymer-based nanocomposites due to

M. Das · G. Sahu · J. Tripathy (✉)
School of Applied Sciences (Chemistry), Kalinga Institute of Industrial Technology (KIIT),
Deemed to be University, Campus-3, Patia, Bhubaneswar, Odisha 751024, India
e-mail: jasaswinitripathy@gmail.com

© Springer Nature Singapore Pte Ltd. 2021
P. Pant et al. (eds.), *Advances in Mechanical Processing and Design*, Lecture Notes
in Mechanical Engineering, https://doi.org/10.1007/978-981-15-7779-6_30

their biocompatibility and biodegradability. Polysaccharides are the natural carbohydrate polymers widely used in food industry and for biomedical applications [3]. Carboxymethyl cellulose (CMC) is a biodegradable and biocompatible polysaccharide extensively used in various fields such as paper industry, drug delivery, oil well drilling, textile industry, detergents and food [4–6]. Chitosan is produced by deacetylation of chitin. It can be readily modified due to the presence of hydroxyl and amine as functional groups and is used in various biomedical applications [3]. Polymer nanocomposite can be fabricated by embedding metal nanoparticles into the polymer matrices which is a facile way to combine the suitable properties of nanoparticles as well as polymers. Among various nanoparticles, silver nanoparticles have attracted considerable research interest as antimicrobial agents to avoid antibiotic resistance caused by overuse of antibiotics [7, 8]. The silver-based materials can be used to treat infections [9], to prevent bacteria colony formation on catheters, [10] prostheses, [11] dental materials, [12] and skin [13] due to the antibacterial activity. Silver containing materials also find applications in water treatment as well as in textile industry to eliminate microorganisms on textile fabrics [14]. These nanoparticles disturb the cell wall permeability of bacterial cells. In spite of the excellent antibacterial properties of silver nanoparticles, the synthetic methodologies mostly rely on the use of toxic organic solvents and reducing agents which pose a major environmental risk. The chemical reduction method opted to synthesize silver nanoparticles often involves use of harsh chemicals which increase the toxicity issues. Moreover, these nanoparticles have tendency of agglomeration. In this regard, the development of science must be integrated with sustainable approaches and “green” synthetic routes. Therefore, the synthesis protocols involving reduction of the silver ions and stabilization process in the presence of polymers and hydrogels are preferred [15]. Earlier reports have dealt with natural polymers as reducing agents as well as stabilizers for synthesis of silver nanoparticles [16]. In the present paper, we report “green approach” for synthesis of chitosan- and CMC-based silver nanocomposite (CHCMCNC). The chitosan/CMC films with or without Ag nanoparticles were prepared and characterized by UV, FT-IR, XRD, FE-SEM, TEM, TGA and tensile tests. In addition, the antibacterial activity of the nanocomposite films was evaluated towards the Gram-negative and Gram-positive bacteria.

2 Experimental Techniques

2.1 Materials

Chitosan (CH) (>75% deacetylated, high Mw) and carboxymethyl cellulose CMC (Mw = 70 kDa) were procured from Sigma-Aldrich. AgNO₃, acetic acid (glacial, 99–100%), glutaraldehyde were purchased from Merck (India). All the reagents and chemicals used were of analytical grade.

2.2 Preparation of Nanocomposite Films

2.2.1 Fabrication of Chitosan–Carboxymethyl Cellulose Blend Films (CHCMCB)

Chitosan–CMC blend was prepared by mixing chitosan solution prepared in 2% acetic acid and CMC solution in 1:1 ratio with 1 wt% of each solution in 250 ml beaker. The obtained solution was stirred at 60 °C for 1 h to get homogeneous solution. Further, 1 ml of 2% glutaraldehyde solution (crosslinker) was added to the Chitosan–CMC solution at room temperature under constant stirring for 1 h. The cross-linked chitosan–CMC blend film (CHCMCB) was obtained by transferring the obtained solution into a petri dish and further drying at room temperature.

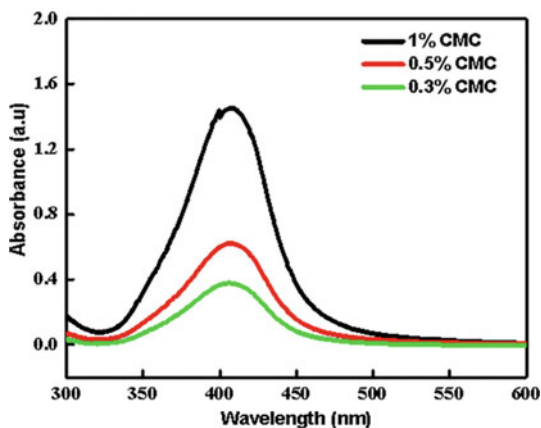
2.2.2 Fabrication of Chitosan–Carboxymethyl Cellulose Silver Nanocomposite Films (CHCMCNC)

50 ml of CMC solution was prepared in three different beakers with varied wt% (0.2%, 0.5% and 1%). To the prepared solutions, 0.1 wt% of AgNO₃ was added separately at 80 °C with continuous stirring. The solutions were stirred for 2 h at same temperature to generate silver nanoparticles. The formation of silver nanoparticles was indicated by transformation of transparent colorless solution into pale yellow and thereafter brownish-black. To all these solutions, 50 ml of 1 wt% chitosan solution (dissolved in 2% acetic acid) was separately added followed by addition of 1 ml of crosslinking agent (2% glutaraldehyde) at room temperature under constant stirring for 1 h. The obtained solutions were poured into petri dishes and dried at room temperature to get chitosan–CMC silver nanocomposite (CHCMCNC) films.

2.3 Characterization

UV–visible spectra of colloidal dispersions were accomplished using Shimadzu FTIR–8400S spectrophotometer at a scanning wavelength between 200 and 600 nm. X-ray diffraction measurements were carried out using XPERTPro, Panalytical JDX-8030, JEOL to know the crystallinity of the nanocomposite films. Morphological variations of blend and nanocomposite film were studied by FEI SERION scanning electron microscope. The thermogravimetric analysis of prepared films was carried by using STA7200 Hitachi under nitrogen atmosphere with a heating rate of 10 °C/min and flow rate 10 ml/min. Transmission electron microscope (TEM) images of silver nanoparticles were obtained using instrument JEM 2100F. Universal mechanical tester (Instron, Model 3382, USA) was used to perform mechanical testing of films. FT-IR spectroscopy was carried from 500 to 4000 cm⁻¹ using Thermoscientific iS5, D1-Transmission.

Fig. 1 UV–visible spectra of silver nanoparticle formed with CHCMCN



3 Results and Discussion

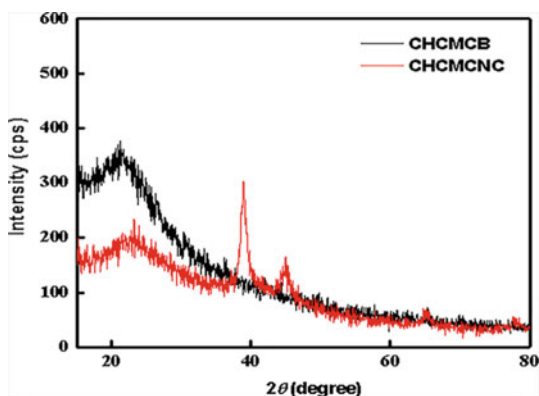
3.1 Fabrication of Chitosan–Carboxymethyl Cellulose Silver Nanocomposite Films

The composition of CMC and chitosan in fabrication of CHCMCB and CHCMCN was optimized by varying the CMC wt%. The solution containing 1 wt% CMC exhibited maximum peak intensity in UV–visible spectra (Fig. 1) as compared to 0.2 wt % and 0.5 wt% CMC. The increased CMC concentration increased reduction and stabilization capacity [16]; however, further increasing the concentration of CMC above 1 wt% resulted in silver nanoparticles aggregates. Thus, for all the experiments and characterizations, 1 wt% CMC was opted, while increased chitosan above 1 wt% resulted into nonuniform and brittle films; hence, 1 wt% of chitosan was taken for film fabrication.

3.2 UV–Visible Spectroscopy

The in situ synthesis of silver nanoparticles in carboxymethyl cellulose solution was confirmed by UV–visible analysis. An intense peak in the wavelength range of 400–410 nm was observed in Fig. 1, which corresponds to surface plasmon absorption peak indicating the formation of silver nanoparticles with narrow size distribution.

Fig. 2 XRD of **a** CHCMCB and **b** CHCMCNC



3.3 X-ray Diffraction

The X-ray diffraction (XRD) studies were carried to determine the crystallographic pattern of films. The X-ray diffraction pattern of blend (CHCMCB) and nanocomposite (CHCMCNC) has been shown in Fig. 2.

The broad diffraction pattern below 30° in CHCMCB and CHCMCNC corresponds to semicrystalline behaviour of chitosan. The diffractogram of the polymeric nanocomposite film CHCMCNC is assigned to 2θ values 38.8° , 43.9° , 64.6° , 77.6° corresponding to face-centred cubic (fcc) planes of silver nanoparticles. In blend film, no such peaks were observed.

3.4 FTIR Analysis

The interactions of silver nanoparticles and the polymeric chains of CMC and chitosan have been confirmed by the FTIR analysis. The difference in FTIR peaks for CHCMCNC as compared to polymeric blend CHCMC has been depicted from Fig. 3.

The blend film showed absorption peak at 2920 cm^{-1} corresponding to C–H symmetrical stretching. A broad band appeared around 3309 cm^{-1} due to OH and NH_2 groups. The carboxylate group contributed to peak at 1411 cm^{-1} . The silver nanocomposite film exhibited shift of amide III band from 1326 to 1310 cm^{-1} . The characteristic peak corresponding to amino group of chitosan at 1572 cm^{-1} for blend film has been shifted to 1563 cm^{-1} in nanocomposite film, whereas the stretching vibration due to OH and NH_2 has been shifted to 3281 cm^{-1} with decreased intensity due to interactions with silver nanoparticles [17].

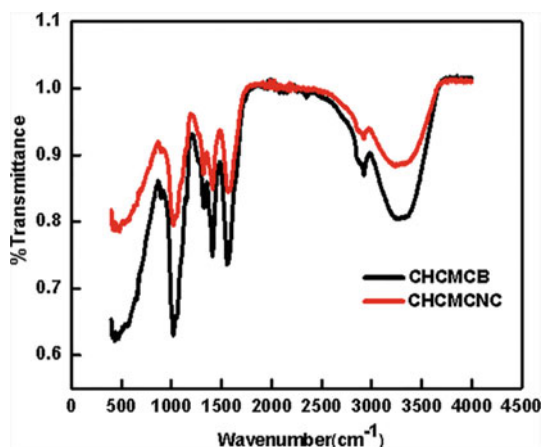


Fig. 3 FTIR spectra of **a** CHCMCB. **b** CHCMCNC

3.5 Electron Microscopic Analysis

The morphological analysis of the prepared films was carried by SEM. The surface morphology of CHCMCB blend (Fig. 4a) clearly showed the homogeneous mixing of CMC and chitosan, whereas nanocomposite film (CHCMCNC) showed rough morphology due to the presence of silver nanoparticles (Fig. 4b). Further, the size of the silver nanoparticles in the CHCMCNC was determined by TEM image. The silver nanoparticles obtained were mostly spherical in shape and dispersed morphology with an average size of 15–20 nm as indicated by TEM image (Fig. 4c).

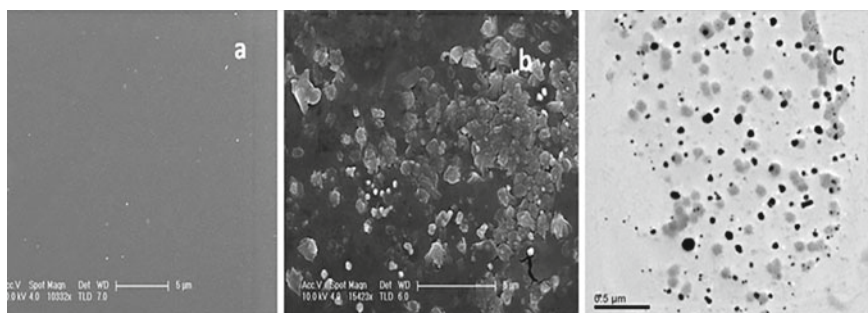
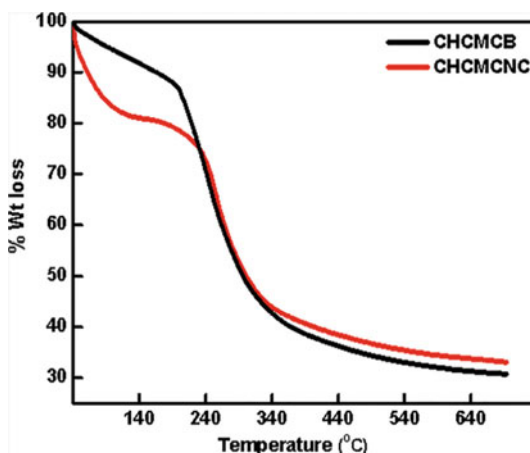


Fig. 4 SEM of **a** CHCMCB. **b** CHCMCNC and **c** TEM of CHCMCNC

Fig. 5 TGA of **a** CHCMCB
b CHCMCNC



3.6 Thermogravimetric Analysis

Figure 5 shows the percentage of thermal degradation of CHCMCB and CHCMCNC films.

TGA curves reveals that the decomposition for CHCMCB blend film started at about 150 °C due to loss of moisture and major decomposition started around 220 °C and continued till 590 °C with weight loss around 67%, whereas in case of CHCMCNC nanocomposite film, the major decomposition started around 240 °C with loss of 63% at same temperature. The result illustrates the enhanced thermal stability of CHCMCNC nanocomposite film due to silver nanoparticles present in the polymeric matrix.

3.7 Mechanical Studies

The tensile parameter, modulus and percentage elongation of films were analysed (Table 1) to get the information of mechanical properties exhibited by both the films. The tensile strength and modulus were found to increase in silver nanoparticles embedded nanocomposite films (CHCMCNC), whereas percentage elongations of the nanocomposite film decreased as compared to blend film.

Table 1 Mechanical properties of (a) CHCMC and (b) CHCMCNC

Sample	Tensile strength (MPa)	Modulus (MPa)	% Elongation
(a) CHCMCB	9.196	430	4
(b) CHCMCNC	16.11	837	2

Fig. 6 Average zone of inhibition of films
a CHCMCB against *S. aureus* **b** CHCMCNC against *S. aureus*
c CHCMCB against *E. coli* **d** CHCMCNC against *E. coli*

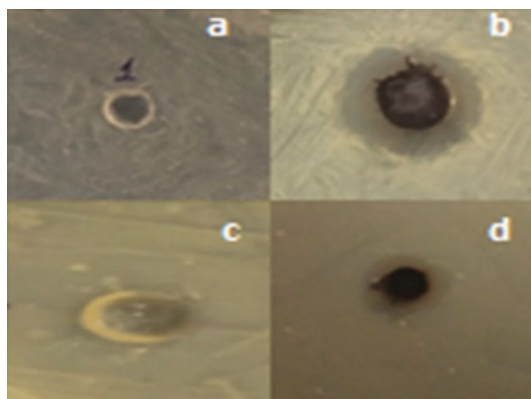


Table 2 Zone of inhibition of (a) CHCMCB and (b) CHCMCNC

Samples	Inhibition zone diameter against <i>E. coli</i>	Inhibition zone diameter against <i>S. aureus</i>
(a) CHCMCB	0 mm	0 mm
(b) CHCMCNC	14–16 mm	18–19 mm

3.8 Antibacterial Activity

The antibacterial activity of the films was evaluated against two bacterial strains *S. aureus* and *E. coli* by disc diffusion method. The antibacterial efficacy of the films has been evaluated from the zone of inhibition as shown in Fig. 6. The inhibition zones on petri dishes showed the extent of antibacterial activities of the silver nanocomposite films (Table 2). The silver containing CHCMCNC exhibited good antibacterial activity with inhibition zone of 14–16 mm and 18–19 mm towards bacterial strains *E. coli* and *S. aureus*, respectively.

4 Conclusions

An eco-friendly in situ synthesis of silver nanoparticles was carried in CMC solution. CMC acted as reducing as well as stabilizing agent. The formation of Ag nanoparticles was confirmed by various characterization techniques. The glutaraldehyde cross-linked chitosan–carboxymethyl cellulose silver nanocomposite films were fabricated by solution casting method. The silver-based nanocomposite films exhibited enhanced mechanical, thermal and antibacterial properties. Thus, these films can find applications in wound dressing and antimicrobial packaging materials.

References

1. Norouzi M, Zare Y, Kiany P (2015) Nanoparticles as effective flame retardants for natural and synthetic textile polymers: application, mechanism, and optimization. *Polym Rev* 55:1–30
2. Shukla MK, Singh RP, Reddy C, Jha B (2012) Synthesis and characterization of agar-based silver nanoparticles and nanocomposite film with antibacterial applications. *Bioresour Technol* 107:295–300
3. Babu RV, Kim C et al (2010) Development of semi-interpenetrating carbohydrate polymeric hydrogels embedded silver nanoparticles and its facile studies on *E. coli*. *Carbohydr Polym* 81:196–202
4. Yadollahi M, Namazi H, Barkhordari S (2014) Preparation and properties of carboxymethyl cellulose/layered double hydroxide bionanocomposite films. *Carbohydr Polym* 108:83–89
5. Barkhordari S, Yadollahi M, Namazi H (2014) pH sensitive nanocomposite hydrogel beads based on carboxymethyl cellulose/layered double hydroxide as drug delivery systems. *J Polym Res* 21:454
6. Wang S, Zhang Q, Tan B, Liu L, Shi L (2011) pH-sensitive poly (vinyl alcohol)/sodium carboxymethylcellulose hydrogel beads for drug delivery. *J Macromol Sci B* 50:2307–2317
7. Panaek A, Kvitek L, Prucek R, Kolar M et al (2006) Silver colloid nanoparticles: synthesis, characterization, and their antibacterial activity. *J Phys Chem B* 110:16248–16253
8. Sambhy V, MacBride MM, Peterson BR, Sen A (2006) Silver bromide nanoparticle/polymer composites: dual action tunable antimicrobial materials. *J Am Chem Soc* 128:9798–9808
9. Ulkur E, Oncul O, Karagoz H, Yeniz E, Celikoz B (2005) Comparison of silver-coated dressing (Acticoat™), chlorhexidine acetate 0.5% (Bactigrass®), and fusidic acid 2% (Fucidin®) for topical antibacterial effect in methicillin-resistant Staphylococci-contaminated, full-skin thickness rat burn wounds. *Burns* 31:874
10. Rupp ME, Fitzgerald T, Marion N, Helget V, Puumala S, Anderson JR, Fey PD (2004) Effect of silver-coated urinary catheters: efficacy, cost-effectiveness, and antimicrobial resistance. *Am J Infect Control* 32:445
11. Gosheger G, Harges J, Ahrens H, Streitburger A et al (2004) Silver-coated megaendoprostheses in a rabbit model—an analysis of the infection rate and toxicological side effects. *Biomaterials* 25:5547
12. Ohashi S, Saku S, Yamamoto KJ (2004) Antibacterial activity of silver inorganic agent YDA filler. *Oral Rehabil* 31:364
13. Gauger A, Mempel M, Schekatz A, Schafer T, Ring J, Abeck D (2003) Silver-coated textiles reduce staphylococcus aureus colonization in patients with atopic eczema. *Dermatology* 207:15
14. Yuranova T, Rincon AG, Bozzi A, Parra S, Pulgarin C, Albers P, Kiwi J (2003) Antibacterial textiles prepared by RF-plasma and vacuum-UV mediated deposition of silver. *J Photochem Photobiol* 161:27
15. Thomas V, Namdeo M, Murali Mohan Y, Bajpai SK, Bajpai M (2008) Review on polymer, hydrogel and microgel metal nanocomposites: a facile nanotechnological approach. *J Macromol Sci Part A Pure Appl Chem* 45:107–119
16. Hebeish AA, El-Rafie MH, Abdel-Mohdy FA et al (2010) Carboxymethyl cellulose for green synthesis and stabilization of silver nanoparticles. *Carbohydr Polym* 82:933–941
17. Vimala et al (2011) Fabrication of curcumin encapsulated chitosan-PVA silver nanocomposite films for improved antimicrobial activity. *J Biomater Nanobiotechnol* 2:55–64

Multi-objective Optimization of EDM Process Parameters on Al-7075-Based Hybrid MMCs



Sudhansu Sekhar Singh, Ashutosh Satpathy, and Sasmita Kar

Abstract In current manufacturing science and engineering application, material selection is an important criterion. Hybrid metal matrix composite (MMCs) has emerged as an important growing demand for manufacturing field like aerospace, automotive and electronic engineering due to its excellent mechanical, physical and thermal characteristics in comparison with convectional materials. The distinctive features of electrodischarge machining (EDM) and high exhaustiveness lead to improve the machining characteristics of MMCs. In this current research work, EDM technique has been applied in order to machine hybrid Al-7075 composite to obtain the high product quality and improve the performance level. The impetus of this research paper is to investigate the optimum parameters to reduce the machining time with high material removal rate (MRR), low surface roughness (SR), low tool wear rate (TWR) and frequency by varying the input parameters such as current, voltage and pulse-on time (T_{on}), pulse-off time (T_{off}) and arc gap. Several experimental runs are conducted by using L16 orthogonal array (OA), and prime parameters were predicted by ANOVA technique with effective parametric contributions. From the result, it is found that Grey–Taguchi method gave better optimization result with error percentage as compared to simple Taguchi method and also found current and voltage, T_{on} gave higher contribution in the time of machining in comparison with other parameters.

Keywords EDM · MMCs · MRR · SR · TWR · Taguchi · ANOVA · Grey–Taguchi

S. S. Singh (✉) · A. Satpathy · S. Kar
Centre for Advanced Post Graduate Studies, BPUT, Rourkela, Odisha, India
e-mail: singhsudhansu16@yahoo.com

S. Kar
e-mail: sasmitakarom@gmail.com

1 Introduction

In the current developing world of manufacturing sector, quality plays significant role. For maintaining the quality and flexible manufacturing of the product, most of the company is focused on advanced machining process. The enhanced mechanical and thermal properties with least residual stresses and good surface finish those are obtained by non-conventional machining process has been mostly appreciated in today's manufacturing field. Nowadays, different advanced materials, depending upon the hardness, are not suitable under conventional machining process. So, EDM is the non-traditional machining mostly preferred, where tool and workpiece are not in contact with each other so this machining process has more attention in many engineering field due to its ability to create any complicated shape. It is an electrical operated electrothermal process, which is applied to produce sparks, and this spark removes metal from the workpiece surface.

Sozhamannan et al. [1] investigated the effect of critical process parameters in continuous stir casting method. When MMCs prepared in stir casting process particle are distributed perfectly and its holding time influence the viscosity of liquid metal, hardness increases or decreases due to increasing the process temperature and holding time. Zhang [2] profoundly investigated on recast layer by using kerosene and deionized water as dielectric fluid and obtained surface roughness were higher in water–oil dielectric as compared to kerosene and deionized water dielectric medium. Auradi and Kori [3] had manufactured Al-based composites with weight percentage variation of B₄C powder. The experimental result proved the enhancement in the properties such as hardness, tensile strength and compression strength of material. Vinoth and Moorthy [4] had adopted stir casting method on Al7075/SiC composite and reported that it was the easy and most economically used technique for casting MMCs. Seo et al. [5] assessed the machinability characteristics of functionally graded SiC-reinforced hybrid Al359-based MMCs by EDM process and they concluded that increase in MRR occurs with similar increase in peak current and pulse-on time. Ndalima et al. [6] made an attempt for water mixed with urea in appropriate proportion as dielectric medium on titanium-based metal. It was interestingly concluded that SR results comparatively better in the medium of water but the urea as dielectric medium enhances the microhardness. Tanjilul [7] beautifully focused on improvement of surface finish by introducing vacuum flushing system and maintaining optimum gap across the electrodes in EDM. Ultimately it improved the MRR and reduced the tool wear rate (TWR). Shehata et al. [8] made an attempt to study the EDM parametric influence mostly current (IP), pulse-on time (T_{on}), duty cycle (DT) and gap voltage (V_g), on aluminium-based hybrid MMCs with 5% and 10% variation of SiC. Mehdi [9] critically experimented on Al–Mg–SiC composed hybrid MMCs to use best variable influence for maximizing MRR and minimizing EWR. The predominant effect on MRR and TWR has deliberated the test results which were less than 6.6 obtained by controlling the current, voltage and pulse on (T_{on}). Kumaran and Suresh [10] critically explored the optimization of EDM process parameters in the time of machining of hybrid aluminium alloy reinforced with silicon carbide and boron carbide-based

composite by GRA method, and the experimental result showed that significant factor on affecting the response was cutting speed followed by feed. Mishra and Routara [11] had analysed on EN-24 alloy machined with EDM by using Taguchi and Grey relation and found that multi-objective optimization for the target of high MRR and low TWR was converted into a single equivalent objective function. Patel et al. [12] found that discharge and duty cycle were most influencing parameters and for multi-performance Grey–Taguchi is a suitable way for getting exact optimized value in a single response.

Apart shining from all literature review it was found that many researchers have previously focused on aluminum based metal matrix composite but very few have investigated on this type of hybrid composite. Machining of this hybrid composite is still very difficult and challenging. According to this research gap, I was getting my objective to fabricate an advance material and used it for machining purpose to get better shape with better machining characteristics; in such a case, the machining of material should produce better surface finish.

1.1 Principle of EDM

It is a metal removal process from workpiece by swiftly electric discharge across electrodes. A suitable gap at range 0.005–1.0 mm range present between the tool and w/p is called spark gap and also can be varied by machining condition. In EDM process, both tool and workpiece are immersed in dielectric medium; most common dielectric medium is kerosene, distilled water and deionized water, etc. The temperature of that spot is raised up to 10,000 °C causing surface to melt and vaporized and ultimately take the form of sphere and quenched by surrounding fluid.

2 Experimental

In this experiment, machining works is conducted by die shrinking-type EDM machine whose model is FORM E350. Here, aluminium-based MMCs at composition of Al7075 + 10%Al₂O₃ + 4%B₄C are used as workpiece which is prepared by stir casting process. The tool material is used as copper tungsten at 16 mm diameter and 95 mm length. The composition of tool is 50% Tungsten + 50% Cu at density 11.85 gm/mm³, and for lubrication and cooling purpose, a commercial grade EDM oil 30 is used whose specific gravity is 0.825 °F and boiling temperature is 300 °F. Here, the machining parameters are current (IP), voltage (V), pulse on (μs), pulse off (μs) and arc gap are considered to obtain the optimized response parameters like MRR, TWR, SR and frequency. The exact factors with its corresponding level are obtained through Taguchi's technique. After completing all the experiment using the data obtained from Minitab software L16 OA, the value of MRR, TWR and

frequency is calculated by following formula.

$$\text{MRR} = [(\pi r^2 h)/T] \quad (1)$$

where $\pi r^2 h$ = Total Volume of (for are circular electrode/cylindrical electrode) material removed mm^3 .

T = Time (minutes), πr^2 = Electrode area/area of cut.

h = Depth of cut = 1.3 mm, r = Radius of electrode = 8 mm.

So, volume of cylindrical specimen = $\pi r^2 h = \pi \times (8)^2 \times (1.3) = 261.380 \text{ mm}^3$

$$\text{TWR} = [(W_{\text{TB}} - W_{\text{TA}})/T] \quad (2)$$

where W_{TA} = Weight of W/P after machining and W_{TB} = Weight of W/P before machining

$$\text{Frequency} = 1000/\text{Total cycle time } (\mu\text{s}) \quad (3)$$

where total cycle time = T_{on} (pulse on) + T_{off} (pulse off).

2.1 Machining Levels

The input factors and their Levels are represented in Table 1, according to which the experiments are conducted and Fig. 1 represents the EDM machine in which all the experiments are done.

3 Results and Discussion

The EDM machine operation is carried out on the manufactured hybrid MMCs specimen, and the results are represented in Table 2.

Table 1 Input factor and their level for analysis

Factors	Units	Symbol	Level 1	Level 2	Level 3	Level 4
Current (I_p)	(Ampere)	<i>A</i>	5	15	25	30
Voltage (V)	(Volt)	<i>B</i>	10	15	20	25
Pulse on (T_{on})	(μs)	<i>C</i>	100	200	300	500
Pulse off (T_{off})	(μs)	<i>D</i>	6	7	8	9
Arc gap	(mm)	<i>E</i>	0.5	0.6	0.7	0.8

Fig. 1 EDMGF FORM E350



3.1 Optimization Using Grey Relation Analysis

Grey relational analysis is a measurement method that analyses uncertain relations among factors and interactions in a given system. It is a prediction and decision-making system. The relation between machining input value and response value can be found out using grey relation analysis, and it is a combination of all performance characteristics and produces its one single value. Three different types of grey relations are observed.

Step-1 Convert the initial value into SN ratio value, and for this purpose, three different equations are used such as larger-is-better, nominal-is-better, smaller-is-better and subsequent these equation analysis were carried out (Tables 3 and 4).

- Smaller-is-better SN ratio = $-10 \log \left[1/n \sum y^2 \right]$ (4)

- Larger-is-better SN ratio = $-10 \log \left[1/n \sum 1/y^2 \right]$ (5)

- Nominal-is-better SN ratio = $-10 \log (s^2)$ (6)

Step-2 In second step, grey relation pre-processing data calculated by three equations larger-is-better, smaller-is-better and nominal-is-better and some reference sequence at range 0–1 are present and this is called grey generation and reference sequence are arranged $x_0^0(k)$ and comparability sequence are $x_i^0(k)$ where $i = 1, 2$ and $3 \dots m$ ($m =$ total no. of experiment) $k = 1, 2, 3 \dots n$ ($n =$ total no. of observation data). The grey relation equation is

$$\text{Larger is better } xi^* (k) = \frac{xi^{\circ}(k) - \min(xi^{\circ}(k))}{\max(xi^{\circ}(k)) - \min(xi^{\circ}(k))} \tag{7}$$

$$\text{Nominal is better } xi^* (k) = 1 - \frac{|xi^{\circ}(k) - q|}{\max\{\max(xi^{\circ}(k) - q, q - \min(xi^{\circ}(k)))\}} \tag{8}$$

Table 2 Observation table

S. No.	Current	Voltage	Pulse on	Pulse off	Arc gap	Time	Depth	MRR	TWR	Surface roughness	Frequency
1	5	10	100	6	0.5	3.12	1.3	83.77	0.114	10.216	9.434
2	5	15	200	7	0.6	2.14	1.3	122.14	0.065	11.944	4.8309
3	5	20	300	8	0.7	2.57	1.3	101.70	0.094	10.472	3.2468
4	5	25	500	9	0.8	3.27	1.3	79.93	0.141	10.216	1.9646
5	15	10	200	8	0.8	1.40	1.3	186.70	0.039	11.997	4.8077
6	15	15	100	9	0.7	1.50	1.3	174.25	0.051	9.587	9.1743
7	15	20	500	6	0.6	3.21	1.3	81.42	0.128	17.476	1.9763
8	15	25	300	7	0.5	4.20	1.3	62.23	0.152	11.845	3.2573
9	25	10	300	9	0.6	1.35	1.3	193.61	0.02	9.153	3.2362
10	25	15	500	8	0.5	2.21	1.3	118.27	0.082	14.577	1.9685
11	25	20	100	7	0.8	3.04	1.3	85.98	0.103	14.772	9.3458
12	25	25	200	6	0.7	5.35	1.3	48.85	0.16	11.889	4.8544
13	30	10	500	7	0.7	18.13	1.3	14.41	0.232	8.406	1.9724
14	30	15	300	6	0.8	19.27	1.3	13.54	0.253	8.123	3.268
15	30	20	200	9	0.5	9.48	1.3	27.57	0.193	7.693	4.7847
16	30	25	100	8	0.6	6.49	1.3	40.90	0.173	4.869	9.2593

Table 3 SN ratio table

SNRA1 (MRR)	SNRA2 (TWR)	SNRA3 (Roughness)	SNRA4 (FRQNCY)
38.4618	18.8619	-20.1856	-19.4939
41.7372	23.7417	-21.5430	-13.6806
40.1464	20.5374	-20.4006	-7.4095
38.0542	17.0156	-20.7843	-5.8655
45.4229	28.1787	-21.5815	-13.6387
44.8235	25.8486	-19.6337	-19.2515
38.2164	17.8558	-24.8488	-5.9171
35.8800	16.3631	-21.4707	-10.2572
45.7386	33.9794	-19.2313	-10.2007
41.4575	21.7237	-23.2734	-5.8708
38.6879	19.7433	-23.3888	-19.4123
33.7773	15.9176	-21.5029	-13.7227
23.1733	12.6902	-18.4918	-5.8999
22.6324	11.9376	-18.1943	-10.2856
28.8087	14.2889	-17.7219	-13.5971
23.2345	15.2391	-13.7488	-19.3316

Table 4 Grey relation generation value

S. No.	MRR	TWR	RA	Frequency
Ref sequence	1.0000	1.0000	1.0000	1.0000
1	0.6850	0.6858	0.5798	
2	0.8268	0.5098	0.7021	0.5734
3	0.7579	0.6098	0.5992	0.3201
4	0.6674	0.7696	0.6338	0
5	0.9863	0.2631	0.7056	0.5703
6	0.9603	0.3688	0.5301	0.9822
7	0.6744	0.7315	1	0.0037
8	0.5733	0.7992	0.6956	0.3222
9	1	0	0.4939	0.31811
10	0.8147	0.5560	0.8580	0.0012
11	0.6948	0.6458	0.8684	0.9940
12	0.4823	0.8194	0.6985	0.5765
13	0.0234	0.9658	0.4272	0.0025
14	0	1	0.4004	0.3243
15	0.2673	0.8933	0.3579	0.5673
16	0.0260	0.8502	0	0.9880

$$\text{Smaller is better } xi^* (k) = \frac{\max(xi^\circ(k)) - \min(xi^\circ(k))}{\max^\circ(xi(k)) - \min^\circ(xi(k))} \tag{9}$$

Step-3 Now $\Delta_{oi}(k)$ is the deviation which is calculated by using the reference sequence $x^\circ(k)$ and comparability sequence $xi^*(k)$. Then, the output data are stored in Table 5 and also minimum and maximum deviations are identified.

$$\Delta_{oi}(k) = |x_o(k) - x_i(k)| \tag{10}$$

Here, the identified maximum and deviation data are presented...

$$\Delta_{\max} = 1.00, \quad \Delta_{\min} = 00$$

Step-4 After the calculated data of pre-processing value, the grey relation coefficient is calculated. It is calculated to correlate the actual experiment. This approach converts a multi-response optimization by calculating overall grey relation grade.

$$\xi_{ik} = \frac{\Delta_{\min} + \xi \Delta_{\max}}{\Delta_{oi}(k) + \xi \Delta_{\max}} \tag{11}$$

Table 5 Deviation response

Deviation sequence expo no.	$\Delta_{oi}(k)$ MRR	$\Delta_{oi}(k)$ TWR	$\Delta_{oi}(k)$ SR	$\Delta_{oi}(k)$ frequency
1	0.3150	0.3142	0.4202	0
2	0.1732	0.4902	0.2979	0.4266
3	0.2421	0.3902	0.4008	0.6799
4	0.3326	0.2304	0.3662	1
5	0.0137	0.7369	0.2944	0.4297
6	0.0397	0.6312	0.4699	0.0178
7	0.3256	0.2685	0	0.9963
8	0.4267	0.2008	0.3044	0.6778
9	0	1	0.5061	0.6819
10	0.1853	0.4440	0.1420	0.9988
11	0.3052	0.3542	0.1316	0.006
12	0.5177	0.1806	0.3015	0.4235
13	0.9766	0.0342	0.5728	0.9975
14	1	0	0.5996	0.6757
15	0.7327	0.1067	0.6421	0.4327
16	0.9740	0.1498	1	0.0120

where $\Delta_{oi}(k)$ is deviation sequence of compatibility sequence $x_i^*(k)$ and reference sequence $x_o^*(k)$. ξ stands for identification coefficients whose value is taken as 0.5 in this current experiment.

Step-5 It determines the averaging of grey relation coefficient into corresponding performance characteristics where $N = \text{no. of level}$ that should be chosen by yourself (Table 6).

$$\gamma_i = \frac{\xi 1(1) + \xi 2(2) + \xi 3(3) + \xi 4(4)}{N} \tag{12}$$

Step-6 Grey relation level is calculated by combination of the entire grade and then divisible by the no of levels (Table 7).

$$\Delta (\text{delta}) = \text{Larger level (max)} - \text{smaller level (min)} \tag{13}$$

$$\text{Mean} = (\text{level 1} + \text{level 2} + \text{level 3} + \text{level 4})/4 \tag{14}$$

After calculating mean relation grade total mean those are $(\gamma_m) = 0.606$.

Step-7 For determination of optimal level of the response parameter, again this grey relation value is used in Taguchi’s method (Fig. 2; Tables 8 and 9).

From this above SN ratio plot for grey grade, it was found that in the combined factor, A2B3C1D1E4 has optimal values (Fig. 3; Table 10).

Table 6 Grey relation coefficient and grade value

Expo No.	Grey relation coefficient				Grey relation grade	Rank
	MRR	TWR	SR	Frequency		
1	0.6134	0.6140	0.5433	1	0.6927	3
2	0.7427	0.5049	0.6266	0.5396	0.6034	7
3	0.6737	0.5616	0.5550	0.4237	0.5535	12
4	0.6005	0.6845	0.5772	0.3333	0.5489	15
5	0.9733	0.4042	0.6295	0.5378	0.6362	5
6	0.9264	0.4420	0.5156	0.9656	0.7124	2
7	0.6056	0.6506	1	0.3341	0.6475	4
8	0.5395	0.7134	0.6215	0.4245	0.5748	10
9	1	0.3333	0.4969	0.4230	0.5633	11
10	0.7296	0.5296	0.7788	0.3336	0.5929	9
11	0.6209	0.5853	0.7916	0.9881	0.7465	1
12	0.4913	0.7346	0.6238	0.5414	0.5978	8
13	0.3386	0.9359	0.4660	0.3338	0.5186	16
14	0.3333	1	0.4547	0.4252	0.5533	13
15	0.4056	0.8241	0.4377	0.5360	0.5508	14
16	0.3392	0.7694	0.3333	0.9765	0.6046	6

Table 7 Grey relation level

Parameter	Symbol	Grey relation grade				Delta	Mean	Rank
		Level 1	Level 2	Level 3	Level 4			
Current	A	0.5996	0.6427	0.6251	0.5568	0.0859	0.606	2
Voltage	B	0.6027	0.6155	0.6245	0.5815	0.0430	0.606	3
Pulse on	C	0.6890	0.5970	0.5612	0.5770	0.1278	0.606	1
Pulse off	D	0.6228	0.6108	0.5968	0.5938	0.0290	0.606	4
Arc gap	E	0.6028	0.6047	0.5955	0.6212	0.0257	0.606	5

Bold indicates desire result

The graphs represented in Figs. 4 and 5 are obtained by Microsoft Excel. It indicates the variation of grey relation grade and the variation of SN ratio values, with respect to experimental runs.

Step-8 To investigate the significant percentage of each factor on multi-wear performance characteristic, an ANOVA grey relation analysis is performed at 95% confidence interval level. Result shows that pulse on has highest effect 61.13% on GRG followed by current 27.02% and voltage 6.24% respectively (Table 11).

Step-9 Confirmation Test After identification of optimal setting, the final step of grey relation analysis leads to the enhancement of response. Confirmation test is conducted by taking the optimal factor, and it is calculated by the help of predicted

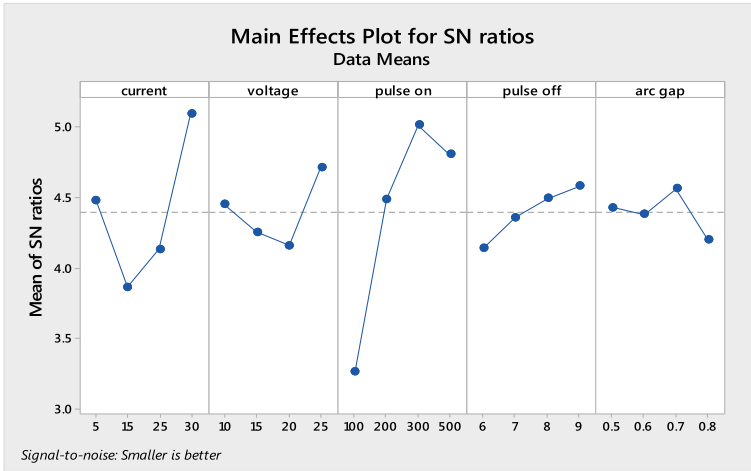


Fig. 2 Main effect plot for grey grade

value and the experimental value. Here, two improvement values are considered such as 0.1287 which is initially designed and 0.0297 which is optimal designed because both case experimental values are much similar to with the predicted value. According to the rule lesser value is more significant, therefore in this experiment 0.0297 improvement value has been used. Simultaneously its predicted percentage value is 3.82% and the experimental value 3.97% are also taken. Those values are shown in Table 12.

$$\text{Predict value } (\gamma \text{ predict}) = \gamma_m + \sum_{i=1}^q (\gamma_0 - \gamma_m) \tag{15}$$

where γ_m = mean of grey grade and γ_0 = maximum average grey relation grade.

4 Conclusion

From the above all calculation, it was found that the optimal parameter where machine provides better performance is current between 15–25 A, voltage between 10–20 V, pulse on 100 μ s, pulse off 7 μ s and arc gap 0.8 mm. From grey relation analysis, it was shown that the confirmation test is good at agreement for value 3.97 with 0.0297 minimum improvement condition. It is also found that Grey–Taguchi method gives better optimization result with lesser percentage of error as compared to simple Taguchi’s method and Current, Voltage, Pulse on time yield higher contribution in the time of machining as compared to other machining parameters.

Table 8 SN ratio for Grey–Taguchi

Expo No.	Grey relation grade	SN ratio	Rank
1	0.6927	3.1891	3
2	0.6034	4.3878	7
3	0.5535	5.1376	12
4	0.5489	5.2101	15
5	0.6362	3.9281	5
6	0.7124	2.9455	2
7	0.6475	3.7752	4
8	0.5748	4.8096	10
9	0.5633	4.9852	11
10	0.5929	4.5403	9
11	0.7465	2.5394	1
12	0.5978	4.4688	8
13	0.5186	5.7033	16
14	0.5533	5.1407	13
15	0.5508	5.1801	14
16	0.6046	4.3706	6

Table 9 Response for SN ratio

Level	Current	Voltage	Pulse on	Pulse off	Arc gap
1	4.481	4.451	3.261	4.143	4.430
2	3.865	4.254	4.491	4.360	4.380
3	4.133	4.158	5.018	4.494	4.564
4	5.099	4.715	4.807	4.580	4.205
Delta	1.234	0.557	1.757	0.437	0.359
Rank	2	3	1	4	5

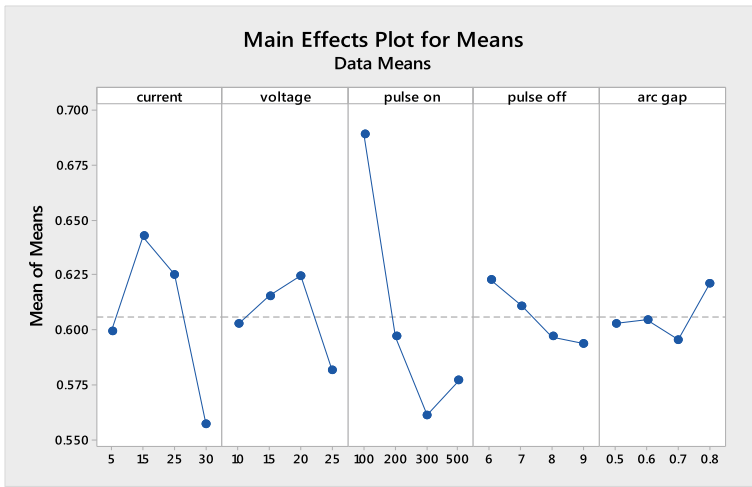


Fig. 3 Main effect plot for grey means

Table 10 Mean response of input parameters

Level	Current	Voltage	Pulse on	Pulse off	Arc gap
1	0.5996	0.6027	0.6891	0.6228	0.6028
2	0.6427	0.6155	0.5971	0.6108	0.6047
3	0.6251	0.6246	0.5612	0.5968	0.5956
4	0.5568	0.5815	0.5770	0.5938	0.6212
Delta	0.0859	0.0431	0.1278	0.0290	0.0257
Rank	2	3	1	4	5

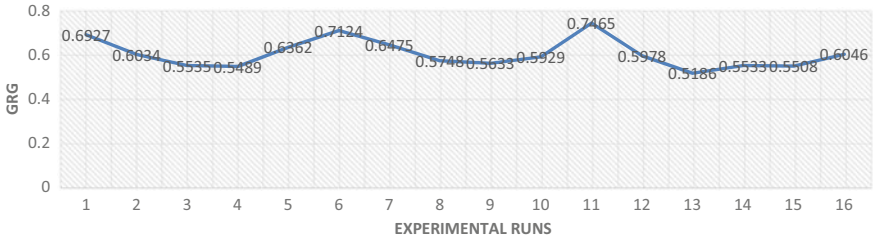


Fig. 4 GRG versus experimental runs

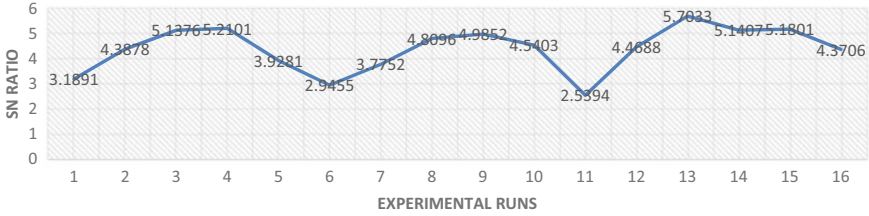


Fig. 5 SN ratio versus experimental runs

Table 11 ANOVA for grey grade

Source	DF	Adj SS	Adj MS	F-value	P-value	Contribution (%)	Remarks
Current	3	0.006854	0.002285	9.62	0.010	27.02	Significant
Voltage	3	0.001583	0.000528	2.22	0.186	6.24	Significant
Pulse on	3	0.015507	0.005169	21.77	0.001	61.13	Significant
Error	6	0.001424	0.000237			5.62	
Total	15	0.025369				100	

$S = 0.0154083$ $R^2 = 94.38\%$ $R^2(\text{adj}) = 85.96\%$ $R^2(\text{pred}) = 60.07\%$

Table 12 Confirmation table

Condition description	Initial design		Optimal design parameter	
	Prediction	Experiment	Prediction	Experiment
Setting level	$A_2B_3C_1D_1E_4$	$A_2B_3C_4D_1E_2$	$A_2B_3C_1D_1E_4$	$A_3B_3C_1D_2E_4$
Grey relation grade	0.7762	0.6475	0.7762	0.7465
Percentage (%)	19.87	16.58	3.82	3.97
Improvement	0.1287		0.0297	

Bold indicates desire result

5 Future Work

- Composite can be prepared by adding different types of adhesive in the time of manufacturing; also, composite can be prepared in the presence of different gaseous environment.
- Study the temperature, stresses and vibration generated in tool and workpiece while working in EDM. Also, calculate the error those are generated from measuring equipment.

Acknowledgements I deem it a privilege to have been a student of mechanical Engineering Stream in “Biju Patnaik University of Technology” (CAPGS), Rourkela. I take this opportunity to express my gratitude to all those who, helped me in my material preparation at IMMT (Institute of Minerals and Materials Technology)-BBSR and for machining operation at CTTC (Central Tool Room and Training Centre), Bhubaneswar. I am also grateful to my Supervisor, “Prof. Sasmita Kar”, and my co-author “Ashutosh Satpathy” for their selfless help for carrying out the thesis work directly or indirectly. Lastly a Special thanks to other members of the department for being so supportive and helpful in every possible way.

References

1. Sozhamannan GG, Prabu GB, Venkatagalapathy VSK (2012) Effect of processing parameters on metal matrix composites: stir casting process. *J Surf Eng Mater Adv Technol* 2(01):11
2. Zhang B, Cai Y (2011) Study of the recast layer of a surface machined by sinking electrical discharge machining using water-in-oil emulsion as dielectric. *Appl Surf Sci* 257(14):5989–5997
3. Auradi V, Kori SA (2014) Preparation and evaluation of mechanical properties of 6061Al-B4Cp composites produced via two-stage melt stirring. *Mater Manufact Process* (accepted)
4. Vinoth N, Moorthy TV (2014) Synthesis and characterization of Al7075/SiC composite by stir casting. *Appl Mech Mater* 592–594:760–764 (Trans Tech Publications)
5. Seo YW, Kim D, Ramulu M (2006) Electrical discharge machining of functionally graded 15–35 vol% SiCp/Al composites. *Mater Manufact Process* 21(5):479–487
6. Ndaliman MB, Khan AA, Ali MY (2013) Influence of dielectric fluids on surface properties of electrical discharge machined titanium alloy. *Proc Inst Mech Eng Part B J Eng Manufact* 227(9):1310–1316
7. Tanjilul M (2018) A study on EDM debris particle size and flushing mechanism for efficient debris removal in EDM-drilling of Inconel 718. *J Mater Process Technol* 255:263–274
8. Shehata HA, Ebeid SJ, Kohail AM (2012) Optimization of EDM process parameters for Al–SiC reinforced metal matrix composite. *Int J Eng Tech Res* 8(2): 2454–4698
9. Mehdi H (2015) Investigating the electrical discharge machining (EDM) parameter effects on Al–Mg₂Si metal matrix composite (MMC) for high material removal rate (MRR) and less EWR–RSM approach. *Int J Adv Manufact Technol* 77(5–8):831–838
10. Kumaran ST, Suresh S (2014) Electrical discharge machining of Al (6351)–SiC–B4C hybrid composite. *Mater Manufact Process* 29(11–12):1395–1400

11. Mishra BP, Routara BC (2017) An experimental investigation and optimization of performance characteristics in EDM of EN-24 alloy steel using Taguchi method and grey relational analysis. *Mater Today Proc* 4(8):7438–7447
12. Patel KM, Pandey PM, Venkateswara Rao P (2010) Optimization of process parameters for multi-performance characteristics in EDM of Al_2O_3 ceramic composite. *Int J Adv Manufact Technol* 47(9–12):1137–1147

Parametric Optimization of CNC Milling of Al-7075 Based MMCs



Ashutosh Satpathy, Sudhansu Sekhar Singh, and Sasmita Kar

Abstract The advantages of flexible modification of machining technology with advanced design for achieving alternate machining, automatic tool changing, varying the working parameters, load modification by the tool mostly influence the numerically assisted machining process. For the CNC milling machining operation, the work piece should be normally economical and efficient. Machining time can be calculated easily by considering detail tool motion during machining and positioning. This paper represents the end milling operation of Al-7075 based metal matrix composites (MMCs) as the work piece due to its high strength and stiffness, less density, high electrical performance and high wear resistance. Taguchi methodology is subjected to minimize the number of experiments. This paper is dealing with the optimization of selected milling process parameter that is spindle speed, feed rate and depth of cut. After conducting the number of experiments using the Taguchi L9 orthogonal array, the surface roughness and material removal rate are optimized with of ANOVA. The parameter contribution for reduction of SR and improvement of MRR was found and error percentage can be validated.

Keywords CNC milling · Surface roughness (SR) · Material removal rate (MRR) · SN ratio · Taguchi design

1 Introduction

Among the conventional machining process, milling is most predominant machining process used in different field for material removal with a multi-point rotating cutter. The primary factors of the milling machining operation are spindle speed, feed rate and depth of cut. Other factor of the milling operation is depending on the tool material and adjusting of the control factor, etc.

A. Satpathy (✉) · S. S. Singh · S. Kar
Centre for Advanced Post Graduate Studies, BPUT, Rourkela, Odisha, India
e-mail: ashutoshsatpathy2017@gmail.com

S. Kar
e-mail: sasmitakarom@gmail.com

In the CNC milling operation is controlled by the computer numerical method. In latest CNC complex, a significant mechanization of CAD and CAM process is preferably used for design of end-to-end components. The coded stipulation procedure by a computer is the most common expression used for systems that control the functions of the machine tool using CNC machine. The part program of the CNC tool improves the propensity of the tool to accomplish repeat functions with outstanding precision. The CNC machine program is coded by G-code and M-code. The G-code is mostly used for tool movements, linear cutting movements. The command for on and off functions in case of machines is usually denoted by M-codes.

The product quality is significantly based on the outstanding evolution of SR, as it generally affects the mechanical components performance additionally the production constants. The static mechanical and functional behaviors like fatigue, corrosion resistance, creep life, friction, wear, light reflection and electrical conductivity, etc. are mostly depend on surface roughness. Surface roughness not only depends upon the machining variables (speed of spindle, feed rate and depth of cut) but also tool geometry (nose radius, tool rake angle, side cutting edge angle and cutting edge), type of work piece and tool materials quality. MRR predominantly depends upon the removed materials volumes per unit time and simultaneously the spindle speed, feed rate and depth of cut. The unit time is calculated by the machining time of the each operation. The MRR values are varying with the machining time.

The research gap is getting from the below literature review and the gaps are previously milling machining done on cast iron, mild steel and different types of alloys but the MMCs are recently used in the modern manufacturing world. The signal to noise ratio is a very simple optimize method and it simplifies the optimization of the responses in shortly with the help of control factor. The objective of the research work is to machining the Al-7075 based MMCs in the CNC milling machine with the help of specify control factor then to optimize the responses (SR and MRR) using signal to noise ratio and to find the optimize value and then to compare the individual responses and the control factor of the each experiment.

Arkiadass et al. [1] calculated the flank wear of end milling of LM25 Al/SiCp and also found the spindle speed. They predicted the surface roughness depends upon the composition of Al/SiCp composite material. Grossi and Scippa [2] explained during machining of Aluminum 6082-T4 alloy; the chatter formation depends upon the cutting force, number of revolution and depth of cut. Samy et al. [3] proposed that it was the cyclic interaction betwixt the tool and the work piece by increasing of chip production depending on the increasing feed rate. The better surface finish occurred due to minimum feed and depth of cut. Vishnu et al. [4] optimized the parameter of EN-31 steel alloy, mainly feed rate, depth of cut, flow rate of coolant by Taguchi optimization method. Arokiadass et al. [5] studied the machining characteristics of LM 25Al/SiCp composite material and found the tool wear by response surface methodology (RSM) and another optimization technique used that was central composite design (CCD) method. Huang [6] profoundly studied the graphical representation of cutting distance, cutting speed and flank wear, and presented the most significant influence of cutting speed on tool wear and flank wear graphically. The tool wear was highly depending upon the increased cutting speed. Chang [7] studied on work piece

S545C medium carbon steel by using as high speed steel tool and it was coated with TiN. For evaluating side milling process, the performance attributes frequently used were roughness of feeding direction, axial direction and waviness. Van de Wouw et al. [8] investigated on stable and unstable chip formation from the SLD diagrammed depending upon the material model and machine model. They concluded that the three model analysis was affected the chip formation and it was based on the surface roughness model. Mustafa [9] experimented on steel composites by CNC milling and optimized the tool wear and temperatures developed due to high speed which cause softening and reduction of the glued material on tool. Baek et al. [10] considered the profile and run out error for explaining the optimal feed rate of typical face milling operation, which was operated on work piece AISI 1041 with milling cutter made by tungsten. Karakaş [11] explained the better performance in the work piece occurred by coated tool as compare to uncoated tool and flank wear gradually decreased with decrease in cutting speed. Sun [12] elaborately explained the dependency of cutting temperature on various cutting speed and also the cutting temperature increased if the cutting speed was increased. A better surface integrity was depending upon the low cutting speed; along with the tool wear was calculated based on wear of rake face and flank of other corner edge. Jayakumar et al. [13] studied the microstructure of Al 356 alloy and Al-SiCp composite material and modeled the cutting force to define the force in X, Y and Z direction, respectively, to calculate cutting depth, cutting speed and feed dimension, etc. Reddy et al. [14] explained the surface integrity depends upon the compatibility, fatigue resistance and surface friction during machining. Microhardness improved with the increase in cutting depth and calculated by grain size from the SEM data. Turgut et al. [15] described the improvement of feed rate and cutting depth with enhancement of cutting force. The rapid decrease of cutting force there was a significant development in the cutting speeds.

2 Experimental Setup

In the current work, vertical CNC milling setup is used to operate on Al 7075 based metal matrix composite materials (MMCs). It is experimented to obtain the best combination of prime values for the designed critical factors to diminish the SR and MRR utilizing Taguchi's Robust Design Strategy. The design of experiments (DOE) for selection of suitable levels and factors is obtained by using L9 (3³) OA. The following CNC milling machine specifications and its image are stated in Table 1 and Fig. 2.

In this present work, Al-7075 based metal matrix composites (MMCs) (Fig. 1) material is used. The dimension of the work piece material is (φ) is 45 mm and height of the material is 20 mm. The percentages of the reinforcement and matrix materials are (Al-7075-97%, Al₂O₃-2%, B₄C-1%). The MMC material is manufactured by stir casting method (Fig. 2).

Table 1 CNC milling machine specification

Machine characteristics	Specification
Name of The CNC machine	SURYA 5
Type of the CNC machine	CNC vertical milling machine
Series of the machine	Fanuc series mate MD
Make of the machining	HFW-BHARAT FRITZ WERNER LTD
Year of commissioning of machine	2013
Axis specification of the milling machine	(800 × 350 × 380) mm
Accuracy of the machine	10 micron
Cost of the machine	1.8 million
Motor power of the milling machine	0.5 HP

Fig. 1 Work piece material

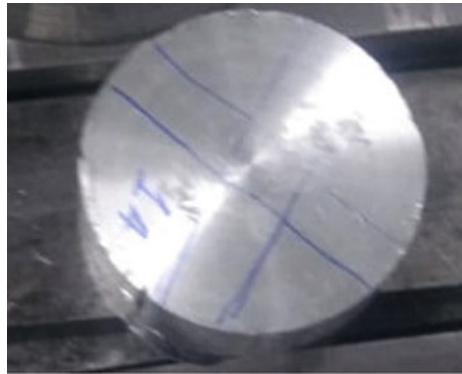


Fig. 2 CNC milling setup



Table 2 Experimental design of the control factors

S. No.	Factors	Symbol	Level-1 (low)	Level-2 (medium)	Level-3 (high)	Unit
1	Spindle speed	A	800	1200	1500	RPM
2	Feed rate	B	200	350	500	mm/min
3	Depth of cut	C	0.4	0.8	1	mm

3 Cutting Tool Material

In the CNC end milling operation, the cutting tool material high speed steel (HSS) is used having the dimensions of diameter—10 mm, helix angle—38°, number of flutes—4, tool length—72 mm, cutting edge length—24 mm. The predominant use of HSS in super alloys and steel alloys is due to its principal hardness and toughness.

4 Selection of Control Factors or Input Parameter

Al-7075 based MMCs are machined by considering the suitable process parameters with three levels and represented in Table 2. The control factor of the experiment is chosen by the above the literature study with the help of CNC machine compatibility. Here, no noise factor is chosen because noise factor is only chosen for uncontrollable sources in the design of experiment but this control factors are controllable sources for the machining process and the work piece.

5 Results and Discussion

This section represents the experimental results of Al-7075 based MMCs optimal SR and MRR which are calculated with the help of distinctive process parameters such as spindle speed (A), feed rate (B) and depth of cut (C) in varying conditions of Taguchi techniques. The SR experimental results are represented in Table 3.

The S/N ratio for SR (i.e.) the smaller is the better is calculated by the formula, Smaller is better SN ratio = $-10 \log [1/n \sum y^2]$.

The S/N ratio of SR is calculated by significant consideration of the three processes parameters by conducting nine experimental runs designed by Taguchi’s methodology on Al-7075 based MMCs. S/N ratio of output response SR is represented in Table 4.

In the graph Fig. 3 it also represents that the means of SN ratio value with respect to the input factors (spindle speed, feed rate and depth of cut). Here, S/N ratio value of the SR is calculated by the smaller is the better condition. This graph represents, when there is increase in speed of spindle from 800 to 1500 rpm, the S/N ratio

Table 3 Output table for the SR

S. No.	Spindle speed (rpm)	Feed rate (mm/min)	Depth of cut (mm)	Surface roughness (μm)
1	800	200	0.4	1.184
2	800	350	0.8	1.115
3	800	500	1	1.493
4	1200	200	0.8	0.618
5	1200	350	1	0.902
6	1200	500	0.4	0.995
7	1500	200	1	0.636
8	1500	350	0.8	0.574
9	1500	500	0.4	0.589

Table 4 S/N ratio output of the SR

S. No.	Spindle speed	Feed rate	Depth of cut	Surface roughness (μm)	S/N ratio (SR)
1	800	200	0.4	1.184	-1.46703
2	800	350	0.8	1.115	-0.9455
3	800	500	1	1.493	-3.4812
4	1200	200	0.8	0.618	4.18023
5	1200	350	1	0.902	0.89587
6	1200	500	0.4	0.995	0.04354
7	1500	200	1	0.636	3.93086
8	1500	350	0.8	0.574	4.82176
9	1500	500	0.4	0.589	4.59769

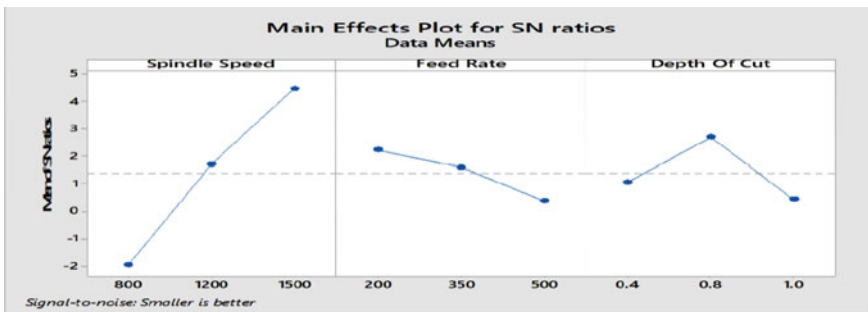


Fig. 3 S/N ratio plot of surface roughness

value is increased from -1.9646 to 4.4501 . The increase in feed rate from 200 to 500 mm/min leads to decrease the value of S/N ratio from 2.2147 to 0.3867 . In the third case, the value of the depth of cut is increased from 0.4 to 1 mm. The S/N ratio value is increased from 1.0581 to 2.6855 and then decreases from 2.6855 to 0.4485 .

From the table, the rank of the input factor is calculated by the corresponding the S/N ratio value. As per the result of S/N ratio of SR, the speed of spindle is the greatest influencing factor as compared to feed rate and depth of cut. The rank is importantly signified by the delta value of the SN ratio value and presented in Table 5.

In this experiment, the material removal rate (MRR) of the Al-7075 is calculated by the ratio between volumes of the material remove per using different level of input parameter and unit time of each experiment. The result of the MRR value of the experiment is shown in Table 6.

The result of the experiment is also optimized by the Taguchi method and the S/N ratio of output response MRR is presented in Table 7.

From the graph (Fig. 4), it is concluded that the performance of S/N value of MRR calculation with respect to the input factor. Here, S/N ratio of MRR is represented by the larger is better condition because when the MRR value is high, the machining time and the machining economy both are less. In the S/N ratio graph, it describes, when the S/N ratio value increase from 800 to 1500 rpm, the mean value of S/N ratio

Table 5 Rank calculation of S/N ratio of SR

Level	Spindle speed	Feed rate	Depth of cut
1	-1.9646	2.2147	1.0581
2	1.7065	1.5907	2.6855
3	4.4501	0.3867	0.4485
Delta	6.4147	1.8280	2.2370
Rank	1	3	2

Table 6 Output table for the MRR

S. No.	Spindle speed	Feed rate	Depth of cut	MRR
1	800	200	0.4	9.45
2	800	350	0.8	27.43
3	800	500	1	41.66
4	1200	200	0.8	18.29
5	1200	350	1	33.088
6	1200	500	0.4	21.22
7	1500	200	1	21.63
8	1500	350	0.8	29.22
9	1500	500	0.4	20.83

Table 7 S/N ratio output of the MRR

S. No.	Spindle speed	Feed rate	Depth of cut	MRR	S/N ratio (MRR)
1	800	200	0.4	9.45	19.5086
2	800	350	0.8	27.43	28.7645
3	800	500	1	41.66	32.3944
4	1200	200	0.8	18.29	25.2443
5	1200	350	1	33.088	30.3934
6	1200	500	0.4	21.22	26.5349
7	1500	200	1	21.63	26.7011
8	1500	350	0.8	29.22	29.3136
9	1500	500	0.4	20.83	26.3738

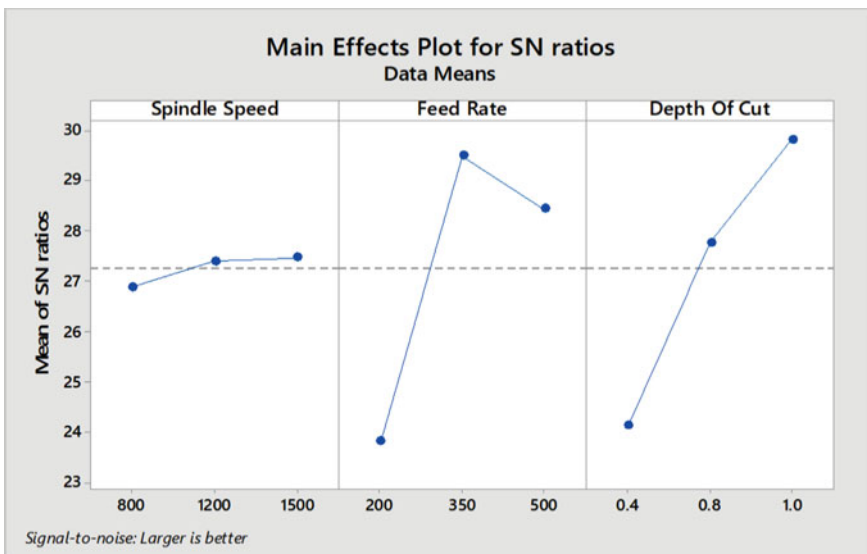


Fig. 4 S/N ratio plot of MRR

gradually increases from 26.89 to 27.46. In the second case, feed rate value increases from 200 mm/min to 500 mm/min. In the third input factor (depth of cut), here value of input factor is gradually increased from 0.4 to 1 mm increasing the S/N value from 24.14 to 29.83 and presented in Fig. 4.

Table 8 represents the rank calculation for corresponding S/N value w.r.t. the MRR responses value and it is concluded that cutting depth exert maximum influence as compared to speed of spindle and feed rate.

Table 8 Rank calculation of S/N ratio of SR

Level	Spindle speed	Feed rate	Depth of cut
1	26.89	23.82	24.14
2	27.39	29.49	27.77
3	27.46	28.43	29.83
Delta	0.57	5.67	5.69
Rank	3	2	1

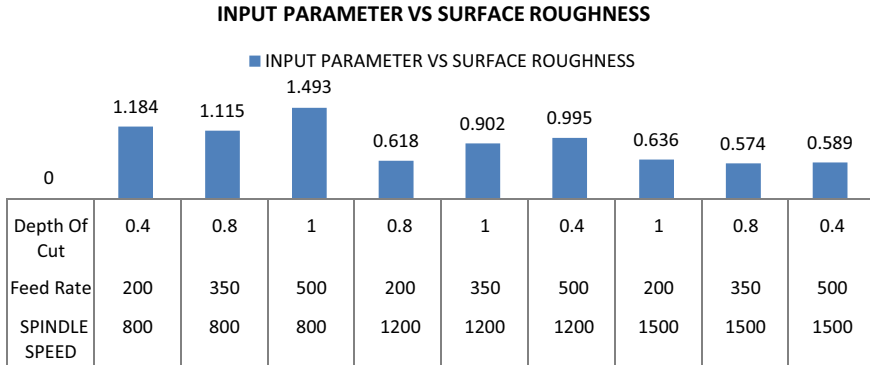


Fig. 5 Histogram graph between input parameter versus surface roughness value

6 Cutting Parameters Influence on Surface Roughness and MRR

From the above histogram representation, the SR frequently depends on cutting depth and speed of spindle, and ultimately, it concludes the inverse relation of SR on spindle speed and depth of cut (Fig. 5).

The above histogram graph represents the increase of MRR by increasing the feed rate and depth of cut when spindle speed remains constant. As the MRR value in the spindle speed of 800 rpm, feed rate of 200 mm/min and depth of cut of 0.4 mm is 9.45 mm³/s and the MRR value of spindle speed 800 rpm, feed rate 500 mm/min and depth of cut 1 mm is 41.66 mm³/s (Fig. 6).

7 Conclusions

From the above present experimental investigations, it is clear that the optimum SR and MRR value of Al-based hybrid MMCs is suitably obtained by CNC operated end milled operation with significant combinations of speed of spindle, depth of cut and feed rate. The optimum value of the SR is based on the combination of the control

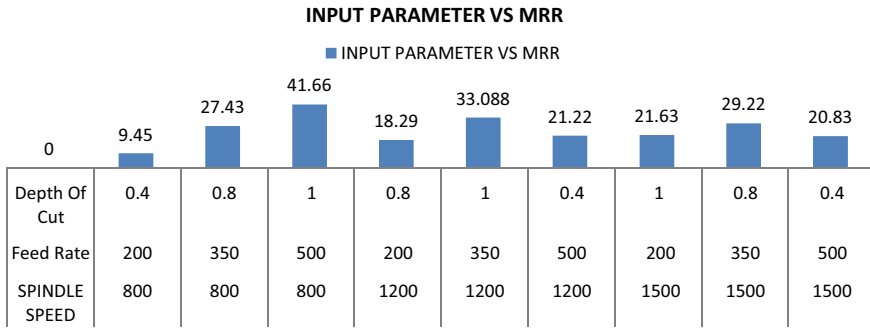


Fig. 6 Histogram graph between input parameter versus surface roughness value

factors mostly cutting speed 1500 rpm, feed rate 500 mm/min and depth of cut 1 mm. The optimum value is predicted by the SN ratio value. From the SN ratio value, it is indicated that the rank of the control factor with respect to SN ratio value. The optimum value of the MRR is based on the combination of the control factors are cutting speed 800 rpm, feed rate 200 mm/min and depth of cut 0.4 mm.

8 Future Scope

In this current investigation, the prime values are obtained by using Taguchi technique. In future work, it can be further optimized by Gray Taguchi and ANN method, and further, the machining time, chip morphology and tool wear of the MMCs can be obtained by varying different control factors. In future, the error analysis of the experiment is calculated with the help of ANOVA study. The error analysis will do between the predicted value and the experimental value.

References

1. Arokiadass R, Palaniradja K, Alagumoorthi N (2012) Prediction and optimization of end milling process parameters of cast aluminium based MMC. *Trans Nonferrous Met Soc China* 22(7):1568–1574
2. Grossi N, Scippa A (2014) Chatter stability prediction in milling using speed-varying cutting force coefficients. *Proc CIRP* 14:170–175
3. Samy GS, Thirumalai KS, Uthayakumar M (2017) An analysis of end milling performance on B4C particle reinforced aluminum composite. *J Aust Ceram Soc* 53(2):373–383
4. Naidu GG, Vishnu AV, Raju GJ (2014) Optimization of process parameters for surface roughness in milling of EN-31 steel material using Taguchi robust design methodology. *Int J Mech Product Eng*. ISSN: 2320-2092
5. Arokiadass R, Palaniradja K, Alagumoorthi N (2012) Tool flank wear model and parametric optimization in end milling of metal matrix composite using carbide tool: response surface

- methodology approach. *Int J Ind Eng Comput* 3(3):511–518
6. Huang ST (2012) Experimental study of high-speed milling of SiCp/Al composites with PCD tools. *Int J Adv Manufact Technol* 62(5–8):487–493
 7. Chang C-K, Lu HS (2007) Design optimization of cutting parameters for side milling operations with multiple performance characteristics. *Int J Adv Manuf Technol* 32(1–2):18–26
 8. Faassen RPH, Van de Wouw N, Oosterling JAJ, Nijmeijer H (2003) Prediction of regenerative chatter by modelling and analysis of high-speed milling. *Int J Mach Tools Manuf* 43(14):1437–1446
 9. Mustafa F (2014) A study on high speed end milling of titanium alloy. *Proc Eng* 97:251–257
 10. Baek DK, Ko TJ, Kim HS (2001) Optimization of feedrate in a face milling operation using a surface roughness model. *Int J Mach Tools Manuf* 41(3):451–462
 11. Karakaş MS (2006) Effect of cutting speed on tool performance in milling of B4Cp reinforced aluminum metal matrix composites. *J Mater Process Technol* 178(1–3):241–246
 12. Sun FH (2004) High speed milling of SiC particle reinforced aluminum-based MMC with coated carbide inserts. *Key Eng Mater* 274–276:457–462 (Trans Tech Publications)
 13. Jayakumar K, Mathew J, Joseph MA (2013) An investigation of cutting force and tool–work interface temperature in milling of Al–SiCp metal matrix composite. *Proc Inst Mech Eng Part B J Eng Manuf* 227(3):362–374
 14. Reddy NS, Kumar S-S, Yang M (2008) Experimental study of surface integrity during end milling of Al/SiC particulate metal–matrix composites. *J Mater Process Technol* 201(1–3):574–579
 15. Turgut Y, Şahin I, Findik T (2011) Study of cutting force and surface roughness in milling of Al/SiC metal matrix composites. *Sci Res Essays* 6(10):2056–2062

Tribo-Behaviour of Tin-Based Dry Bearing Material



Priya S. Gajjal

Abstract Bronze is used widely as a journal-bearing material for copper-based alloys. These materials are good for high electrical and thermal conductivity, good corrosion, self-lubrication, and wear resistance for a long period of time and give good results for use as journal bearings. In this study, wear and friction properties of journal bearings manufactured with different percentage of tin 6%, 8%, and 10% bronze and the effect of PV (pressure \times velocity) parameter have been investigated and examined. Experiments have been carried out for different values of PV under different time domains.

Keywords Bronze materials · Dry sliding · Wear and friction

1 Introduction

Nowadays, use of dry bearing material is almost becoming a routine practice in industry scenario. In fact, in our country we do not have adequate data on Indian-based material of construction. Needless to say, it is essential to have performance data on such materials. Lancaster and others [1–4] discussed and mentioned the performance criteria and testing of dry bearings and its different materials. The main two basic requirements of the dry bearings materials are as follows: (i) The material must be able to support an applied load in the environment apprehensive without significant deformation, distortion, or strength loss and (ii) both the friction coefficient and the rate of wear must be reasonably low. The properties of a variety of materials like polymers, carbon, graphite, solid-film lubricants, etc., are discussed briefly along with their limitations and advantages for dry sliding bearings [5–7]. Wear is the greatest uncertainty associated with the operation of dry bearings. Both numerous experiments and simple theory have shown that once the surface conditions during sliding achieve a steady state, and the volume of wear ‘ v ’ is proportional to the distance of sliding ‘ d ’. The volume of wear per unit sliding distance is directly

P. S. Gajjal (✉)

Mechanical Engineering Department, AISSMS College of Engineering, Pune 4110041, India
e-mail: psgajjal.scoe@gmail.com

© Springer Nature Singapore Pte Ltd. 2021

P. Pant et al. (eds.), *Advances in Mechanical Processing and Design*, Lecture Notes in Mechanical Engineering, https://doi.org/10.1007/978-981-15-7779-6_33

389

proportional to the load if changes in the load applied 'W' do not cause major changes in any other variable [1, 8–11]. The authors felt the need to study bronze bearings having different percentage of tin as far as its tribological properties. By reviewing the literature survey, it is shown that study of different materials is done individually or comparison of different material has been made with metal and plastic or with adding some additives in regular materials. And PV relation is not mentioned in literature. Thus, author felt to study same material with different percentages of Sn with PV parameter.

2 Experimental Procedure

There are various principles used for analysis of friction and wear. Various test rigs like pin-on-disc, ball-on-disc, etc., are available which will give measurement of frictional force between two mating parts and wear measurement subsequently. A photograph of the pin-on-disc friction and wear tester is used as shown in Fig. 1. The machine uses round-shaped specimen which was held in a specially designed holder and tightly pressed into contact with the rotating disc by lever, loaded by dead weights. The experiments are carried out at nominal sliding speed at different range. The pressure varies from 0.2 to 2 N/mm². Each test has been carried out till thermal condition, or the rate of wear is reached at steady-state condition. The friction can be measured by a load sensor attached to the arm and wear by weight difference method.

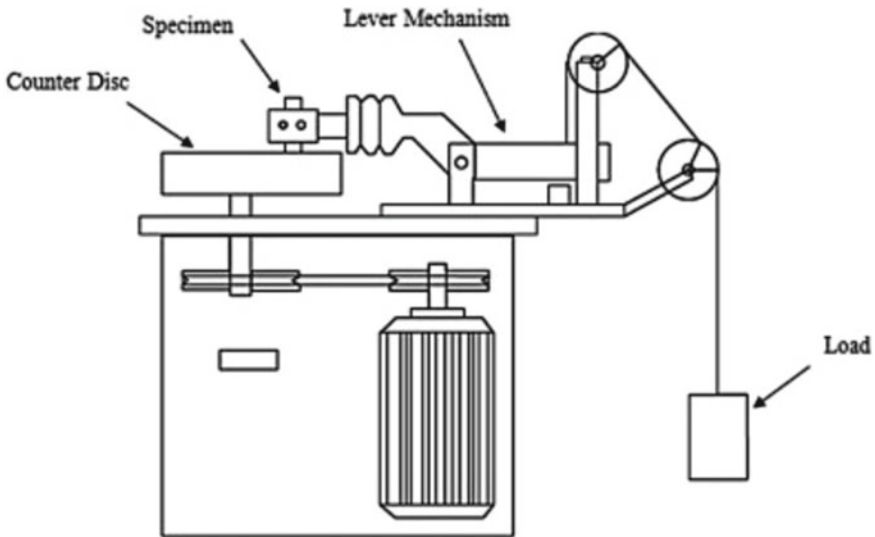


Fig. 1 Pin-on-disc friction and wear machine

3 Results and Discussions

The specimens were tested against rotating disc at different parameters and PV values. Under these conditions, the following results were observed.

Figure 2 shows that coefficient of friction varies against speed for bronze material at different percentage of Sn at pressure 0.5 N/mm^2 . From Fig. 2, it has been observed that as speed rises, coefficient of friction decreases. This has been observed for all the material under pressure at 0.5 N/mm^2 .

Figure 3 represents the coefficient of friction against pressure for bronze material with 6% Sn, 8% Sn, and 10% Sn at a speed 0.732 m/s . As shown in Fig. 3, as there is

Fig. 2 Variation of coefficient of friction versus speed (under pressure 0.5 N/mm^2)

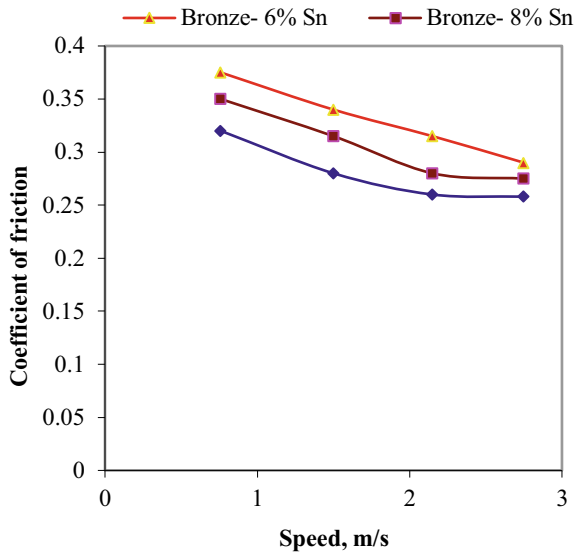
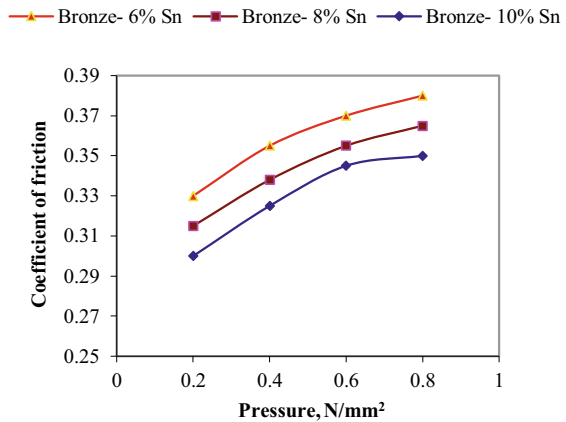


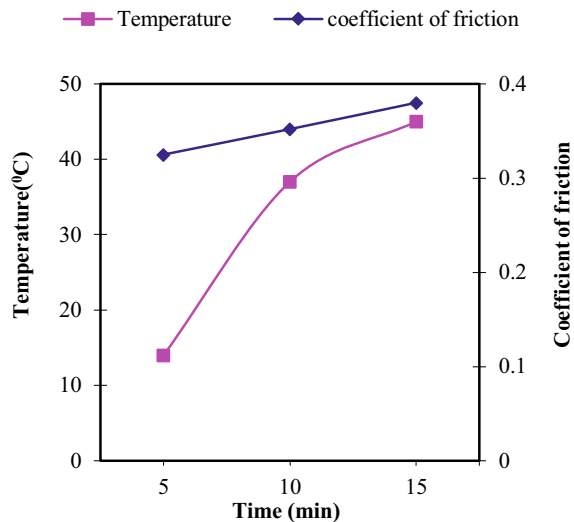
Fig. 3 Coefficient of friction versus pressure (at constant speed: 0.732 m/s)



increase in pressure, the coefficient of friction also rises for all the bronze material. Figure 4 represents the coefficient of friction and temperature against time of sliding for bronze material with 6% Sn at $PV = 0.35 \text{ N/mm}^2 \text{ m/s}$. From Fig. 4, it has been observed that the coefficient of friction and temperature increases as the time increases. It has also been noted that there is a constant rate of change in coefficient of friction, but there is a rapid change in rate in temperature. This is due to the fact that interface undergoes wear and as a result presents rough surface. Figure 5 shows the variation of temperature and friction against time. It has been noticed in Fig. 5 that the coefficient of friction and temperature increases as the time increases for nature with 8% Sn. The rate of change in coefficient of friction and temperature is almost same. Figure 6 represents the temperature and coefficient of friction against time for 10% Sn. From Fig. 6, it has been noticed that as the time increases, the coefficient of friction and temperature increases for 10% of Sn under PV of $0.35 \text{ N/mm}^2 \text{ m/s}$. It has been observed that there is a continuous change in the coefficient of friction and temperature on a period of time.

Figure 7 represents the temperature against PV values. From Fig. 7, it has been observed that temperature increases as PV values increase. This has been observed for all the material under time of 15 min. It has been observed that in case of 10% Sn, temperature increment undergoes a very rapid change, but in case of 6% and 8% Sn, the temperature increment is moderate. This nature of behaviour is due to different values of thermal conductivity and specific heat of the material. PV value plays an important part in the practical use of the bearing. This limiting PV value is determined on the basis of rapid changes in friction, wear, and temperature values. From Fig. 8, it has been shown that as the % of Sn increases, limiting values of PV increase slightly. However on average, it can be said the limiting value of PV is around $0.4\text{--}0.6 \text{ N/mm}^2 \text{ m/s}$ for all materials. Figure 9 shows the variation of wear against

Fig. 4 Variation of temperature and coefficient of friction versus time for bronze -6% Sn (under $PV = 0.35 \text{ N/mm}^2 \text{ m/s}$)



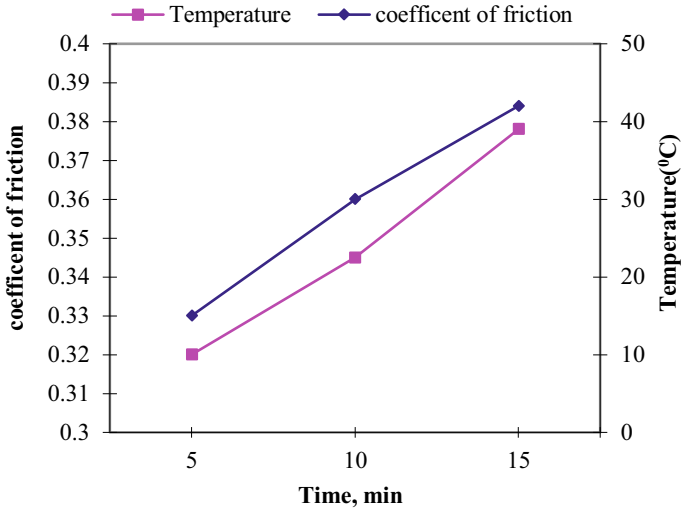
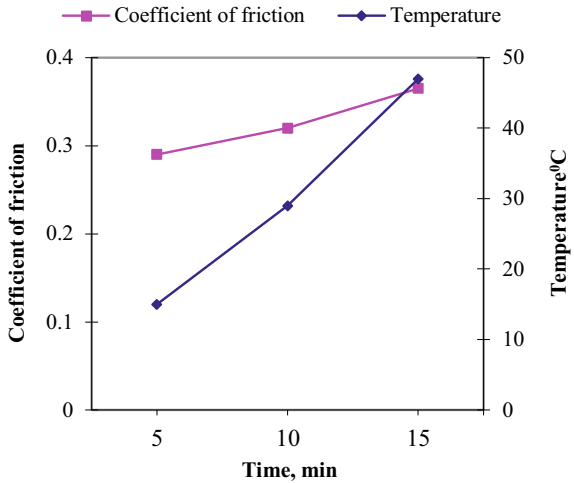


Fig. 5 Variation of temperature and coefficient of friction versus time for bronze -8% Sn (under $PV = 0.35 \text{ N/mm}^2 \text{ m/s}$)

Fig. 6 Variation of temperature and coefficient of friction versus time for bronze -10% Sn (under $PV = 0.35 \text{ N/mm}^2 \text{ m/s}$)



speed. From Fig. 9, it has been observed that in case of 6% Sn, there is constant increase of wear up to speed 1.5 m/s, but there is a sudden change in the wear rate after speed 1.5 m/s under pressure of 0.5 N/mm^2 , and same has been observed for 8% and 10% of Sn. Figure 10 represents variation of wear against pressure. From Fig. 10, it has been deputed that there is increase in wear i as the pressure rises for all material at speed of 0.732 m/s. It has been noted that that in case of 8% Sn, the

Fig. 7 Temperature generation at various PV values (At time 15 min)

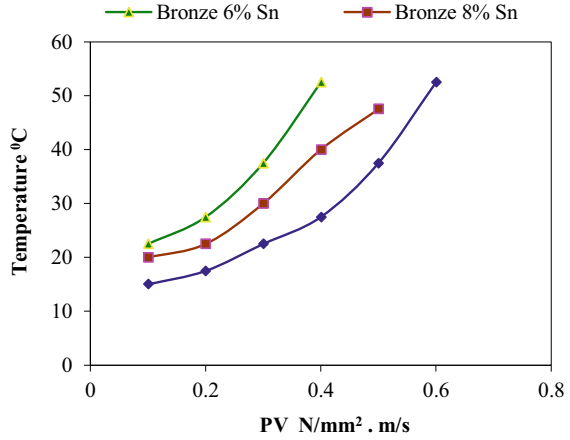


Fig. 8 PV, values of bronze material

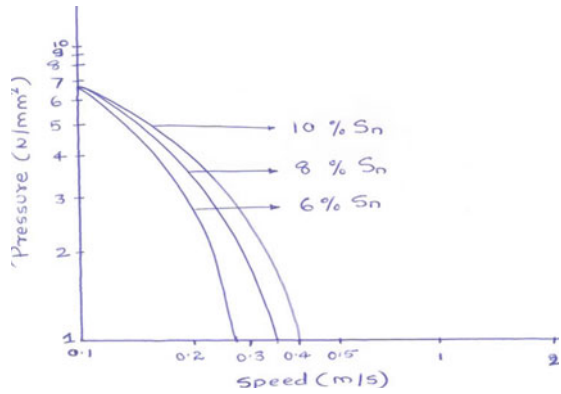
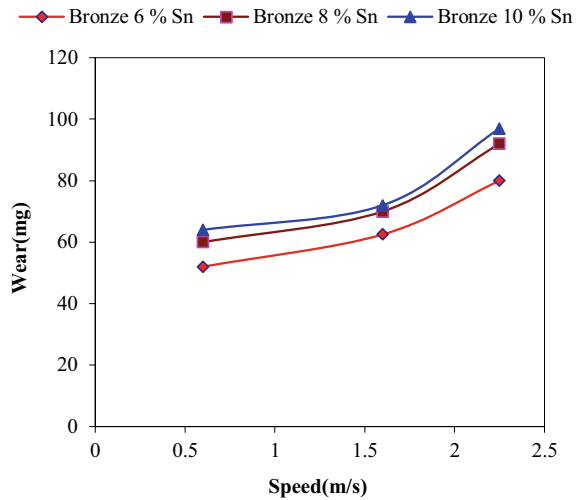


Fig. 9 Variation of wear versus speed (pressure of 0.5 N/mm² and at time 10 min)



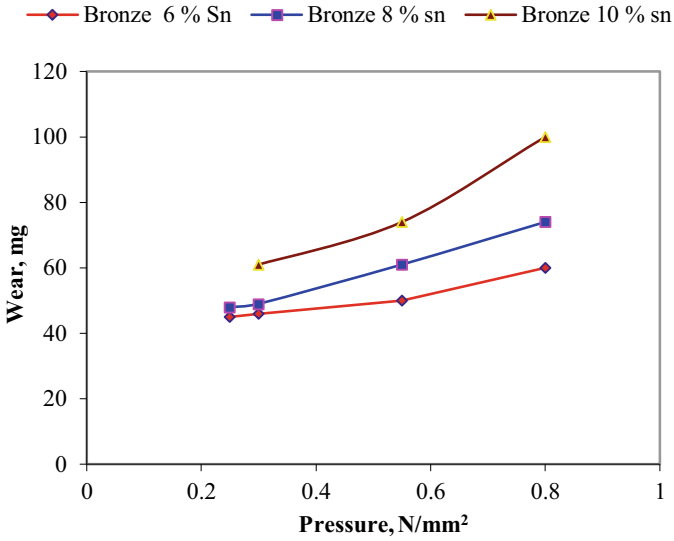


Fig. 10 Variation of wear versus pressure (speed 0.732 m/s and time 10 min.)

wear is increasing at constant rate, but in case of 10% Sn there is sudden increase in wear after a pressure of 0.55 N/mm².

Figure 11 shows wear against time. From Fig. 11, it has been shown that the wear increases as time increases. This has been observed for all the material at PV of 0.4 N/mm² m/s. It has also been noted that in case of 6% Sn, the wear increases

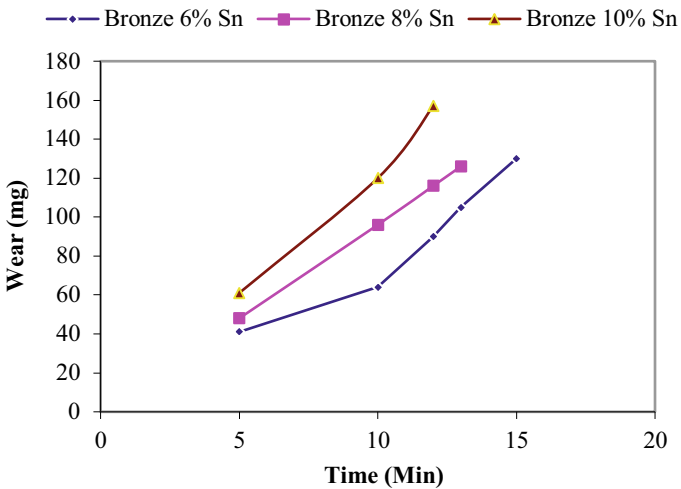


Fig. 11 Wear against time (under PV = 0.4 N/mm² m/s)

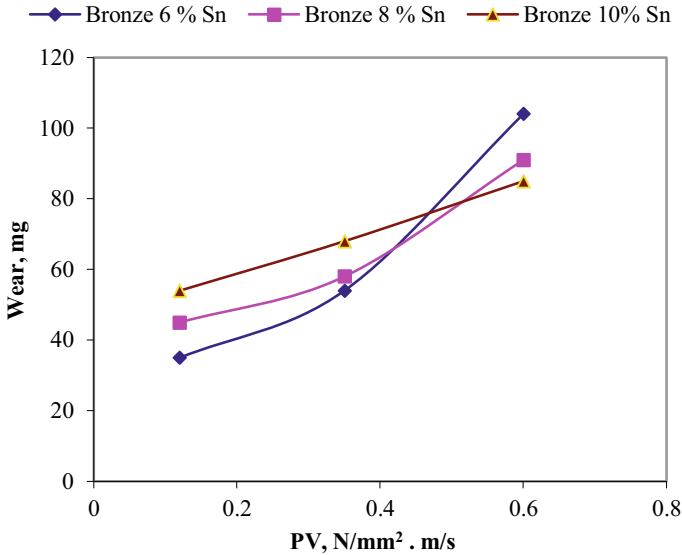


Fig. 12 Wear versus PV (for time 10 min.)

rapidly after 10 min of running and similarly things have not been observed for 10% Sn and 8% Sn. Figure 12 shows the wear rate of different material at different PV values. It has been shown that the wear increases as PV value increases. It has also been noted that for 6% Sn, wear rate rapidly increases at 0.4 N/mm² m/s, but in case of 8% Sn, wear rate increases slightly but in case of 10% Sn, the rate of wear seems to be constant.

4 Conclusion

1. Bronze materials with different percentage of Sn show different tribological behaviours depending on percentage of Sn content.
2. For all bronze material taken under study, friction coefficient is decreasing with respect to speed under experimental condition; friction coefficient is more with lesser percentage of Sn.
3. For bronze materials, coefficient of friction increases with pressure and here also coefficient of friction is highest in case of 6% Sn.
4. Coefficient of friction is affected by time and temperature. Deterioration of surface takes place over a period of time; as a result, coefficients of friction and temperature both increase with respect to time.
5. The temperature generated for all the bronze material is very close and is around 45 °C after 15 min of sliding with a PV = 0.35 N/mm² m/s.

6. Temperature, which is very important parameter that governs PV values, increases with increase of PV value. For example, at 40 °C, PV value for 6% Sn is around 0.3 for 8% and for 10% it is around 0.5 N/mm² m/s.
7. Limiting values of PV for practical application have been noted as in the range of 0.4–0.6 N/mm² for all material under study.
8. Wear of material increases with speed, pressure as well as time.
9. Wear value increases with PV values, and Sn shows less wear with maximum percentage of bronze.

References

1. Lancaster JK (1973) Dry bearings: a survey of materials and factors affecting their performance. *Tribology* 6:219–251
2. Prasad BK (2004) Sliding wear behaviour of bronzes under varying material composition, microstructure and test conditions. *Wear* 257:110–123
3. Lancaster JK (1971) Estimation of the limiting PV relationships for thermoplastic bearing materials. *Tribology* 4:82–86
4. Molesh M, Saka N, Suh NP (2002) A mechanism of high friction in dry sliding bearings. *Wear* 252:1–8
5. Jaeger JC (1942) Moving sources of heat and the temperature at sliding contacts. *Proc R Soc NSW* 76:203–224
6. Glaser WA (1967) High temperature bearing materials. *Metal Eng Quart* 7(2):53.
7. Marx S, Junghans R (1996) Friction and wear of highly stressed thermoplastic bearing under dry sliding conditions. *Tribol Int Wear* 193:253:260
8. Engineering Sciences Data Unit (1962) Dry rubbing bearing—a guide to design and materials selection. In: *Engineering sciences data*, vol 68018. Institution Mechanical Engineers, London
9. ASM handbook vol 2. Properties and selection of non-ferrous alloys and special purpose material. ASM International Handbook Committee
10. So H (1996) Characteristics of wear results tested by pin-on-disc at moderate to high speeds. *Tribol Int* 29(5):415–423
11. ASM (1979) *Metals handbook*, vol 2, 9th edn. ASM, Materials Park, pp 383–394
12. ASM (1992) *Metals handbook*, vol 18, 10th edn. ASM, Materials Park, pp 741–757

Optimization of Process Parameters for Wired Electro-Discharge Machining of Titanium Based Hybrid Compo-Sites Using Response Surface Methodology



Soutrik Bose, Samiran Samanta, Vibhav, Prashant Bharti, and Titas Nandi

Abstract Machining of titanium-based hybrid composites by conventional method is very complicated due to its enhanced strength-to-weight ratio, corrosion resistance, abrasion resistance and fatigue resistance which is extensively used in aerospace, spacecrafts, marine, automobile, sports and biomedical applications. This paper provides an optimization technique of wired electro-discharge machining (WEDM) of titanium-based hybrid composites varying peak current and pulse duration as main input process parameters for machining complicated complex silhouette which is practically unfeasible to develop by conventional machining. In this paper, investigation is done on response surface methodology (2 factors 4 levels) design of experiments (DOE) on output response like surface roughness, and satisfactory results are obtained and authenticated by the confirmatory test. Both the process parameters displayed enormous impact on the output response, and an optimal condition and solution is obtained to achieve the best output response.

Keywords Titanium-based hybrid composite · Response surface methodology · ANOVA · Wired electro-discharge machining · Optimization

S. Bose · Vibhav · P. Bharti
Department of Mechanical Engineering, MCKV Institute of Engineering, 243 G.T. Road (N),
Liluah, Howrah, West Bengal 711204, India

S. Bose · T. Nandi
Department of Mechanical Engineering, Jadavpur University, Kolkata, West Bengal 700032, India

S. Samanta (✉)
School of Mechanical Engineering, Kalinga Institute of Industrial Technology (KIIT), Deemed to
be University, Campus-8, Patia, Bhubaneswar, Odisha 751024, India
e-mail: samirankgec@gmail.com

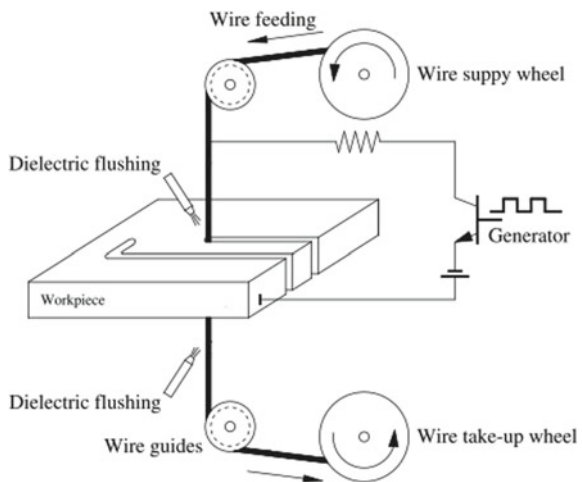
1 Introduction

Titanium-based hybrid composites are light, strong and durable with outstandingly good properties like corrosion resistant, fatigue resistant and exceptional strength-to-weight ratio which is sustained at extremely high temperature. These alloys and composites are highly used in various industries like biomedical applications, automobile, aerospace, chemical, food industries, etc. by Gu et al. [1]. Nowadays, titanium is widely used in medical grounds for its excellent biocompatibility with bone growth and other tissues. Titanium is used in diverse medical purpose like bones, hips, dental problems and knees replacement enucleation and has an assortment of various other surgical instruments by Elias et al. [2]. There are also few limitations like high initial cost, availability and ease of manufacturability by Kumar et al. [3]. Machining these composites by conventional machining methods is extremely difficult because of occurrence of rough surface finish at elevated temperature causing excessive wear. The microstructure, corrosion and fatigue behaviour of titanium varying different environmental conditions were deliberated by Saji et al. [4] and Fleck and Eifler [5]. In biomedical research, machining titanium with maximum precision and in minimum time is an important issue. WEDM uses electrical as well as thermal responses for precision machining of conductive materials. Numerous researchers have endeavoured for the improvement of the performance of WEDM of titanium but have not yet concluded the optimal process parameters. Hence, in this paper, the optimal process parameters for better surface finish and maximum MRR using WEDM of titanium-based hybrid composites are determined experimentally and compared with the past works. There is an increment of temperature throughout the machining of titanium as it is highly reactive to chemical agents and possesses low thermal conductivity influencing the wire breakage at the tool-workpiece interface. The major scope is to compare and analyse the WEDM performance parameters of Ti-based hybrid composites with the input process parameters by optimization of machining parameters like peak current and pulse duration, to acquire the most excellent machining condition in stipulations with surface roughness (Ra). The other objective is to develop novel hybrid titanium composite which can be useful in biomedical applications, automobile, aerospace, chemical, food industries, etc. It can also be used in manufacturing the blades of propeller and wings and can also be used in the automobile sectors in engines and valves manufacturing sections where high thermal and heat generations occur with lesser investments. Therefore, 2 factors 4 levels DOE is premeditated using response surface methodology (RSM) design matrix. A 2^4 combination of run-orders is used in a full quadratic mathematical model depending on the experimental results, and multi-objective optimization is done based on the response surface methodology.

2 Experimental Methodology

The TiNiCu alloy is used as the experimental sample whose main components by wt% are C(0.008), Fe(0.25), Al(2.5), Cu(5.0), Zr(1.5), Cr(0.5), V(0.5), H(0.1), Ni(39.5) and rest Ti of $5 \times 10 \times 15$ mm dimensions. Two types of tool electrodes are used; one being brass wire and the other is of zinc-coated brass wire whose wire diameter is 0.25 mm each. Figure 1 shows the experimental set-up, and Fig. 2 depicts the process flow diagram varying the process parameters. WEDM employs a wire as the tool electrode with electro-thermal mechanism for precision manufacturing. Both the tool electrode and the workpiece are inundated in dielectrics (deionized water and kerosene). The dielectric acts as an electrical insulator, and then machining occurs with the occurrence of the electrical discharge. A gap is created on the wire advancement towards the workpiece, and higher voltage is generated breaking the dielectric and generating the electrical discharge initiating a spark between the wire-workpiece interfaces. The dielectric becomes an ionized gas and turns into plasma bubble. The plasma bubble collapses, vigouring the cutting material to disperse into the dielectric, creating small craters leading to wire failure and rupture. This process continues approximately around 240,000 times per second removing the metal, and a precision cut is formed. A flushing flow of dielectric acts as a coolant of the wire removing the scattered particles. As the wire erodes, a WEDM machine continuously supplies unsullied wire from a reel and dumps the used eroded wire to trash bin for recycling. The main control factors and the two input process parameters taken in the DOE are peak current (A) of four levels 3, 6, 9 and 12 and pulse duration (μ s) of 4, 24, 50 and 100 while the other constraints are fixed. The constraints are dielectric conductivity = 20 mho, open arc voltage = 80 V, servo voltage = 50 V, dielectric flush = 25 kg/cm², wire tension = 18 kgf, finish = 0, polarity = 2 signifying positive polarity and wire feed = 10 mm/min.

Fig. 1 Experimental set-up



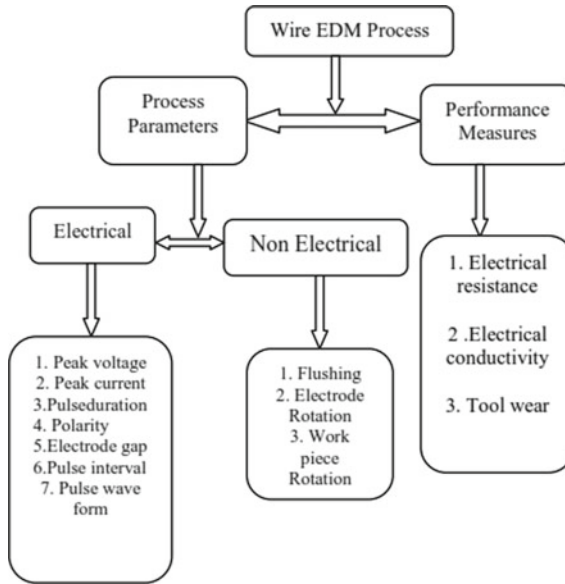


Fig. 2 Process model with process parameters

3 Results and Discussion

3.1 Material Removal Rate (MRR)

MRR is the most noteworthy structure which involves in the productivity of all manufacturing industries. It is the quantity of the removed material from the workpiece under the machining time (3 mm/min); hence, the characteristic efficiency of the machine is determined. From Fig. 3, it is pragmatic that higher MRR is obtained by the positive polarity of the electrode preferably with deionized water than when compared with kerosene. It is primarily because of the adherence of carbon the tool surface which defends the erosion of tool electrode. The increment of MRR is due to the increment of the discharge current (power) as the removal of the material is easily obtained by increasing the density of the current. The MRR increases and reaches a threshold value with increase in pulse on time duration but then decreases. At high pulse duration, increase in the localized temperature decomposes the carbon leading to lower the MRR value. It is also unswervingly proportional to the discharge pulse energy which is again dependent upon the servo voltage and capacitance. Thus, at elevated voltage wider gap is formed, leading to high discharge. The capacitance establishes the frequency, larger crater forms at the lower frequency. MRR is also affected largely by hardness. Lower hardness and melting temperature cause higher MRR which is determined by Sen et al. [6]. According to Lin et al. [7], lower MRR is obtained with high melting temperature and thermal conductivity. With the increment

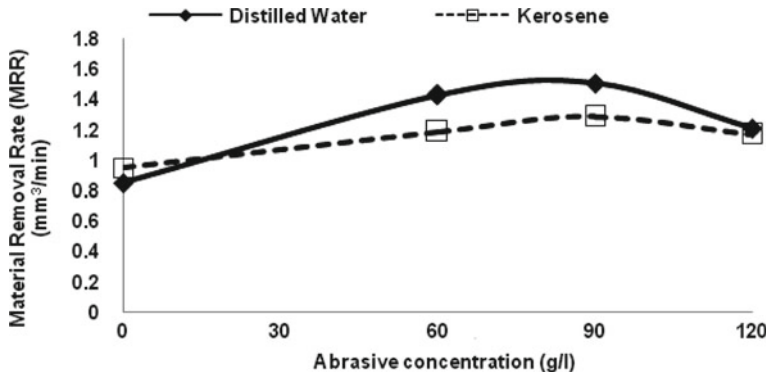


Fig. 3 Effect of SiC concentration on MRR on TiNiCu alloy

in pulse duration, higher MRR is obtained. MRR also augments with the amplification in peak current. The MRR enhances almost linearly with the pulse duration with deionized water, but enhances nonlinearly up to the optimum zone and then reduces when kerosene is used. Electrode wear ratio (EWR) amplifies with the pulse duration with kerosene rather than deionized water as obtained by Chen et al. [8]. This paper also provides a comparative correlation using kerosene and deionized water with silicon carbide (SiC) abrasive concentration as dielectrics. It is observed from Fig. 3, the maximum value of MRR is obtained after using 90 g/l SiC concentration in the dielectric fluid. MRR obtained is greater for distilled water in comparison to kerosene. Figure 4 represents the white layer formation on TiNiCu alloy during WEDM with dielectrics like kerosene and distilled (deionized) water which clearly depicts using distilled (deionized) water as dielectric medium provides a better white layer forming less amount crater on the tool-work piece surface.

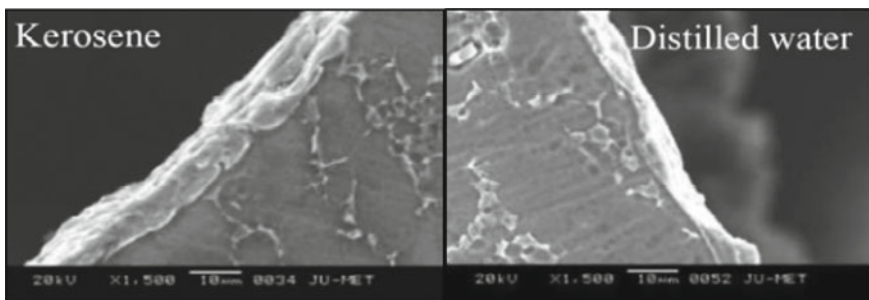


Fig.4 White layer formation on the alloy with kerosene and distilled (deionized) water

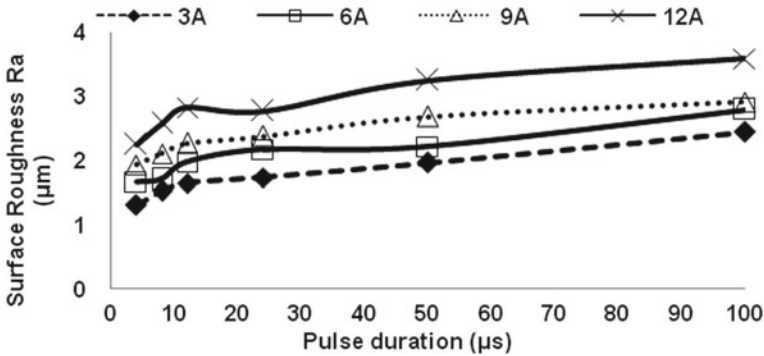


Fig. 5 Surface roughness with variation of pulse duration of different TiNiCu-based alloys

3.2 Surface Roughness (SR)

Surface roughness (Ra value) is another important parameter which has a great impact on the performance characteristics of the machined components. Surface roughness mainly varies with the discharge current followed by pulse duration. Low discharge current and pulse duration result in better surface roughness. Proper selection of tool material is essential as the surface roughness depends on it. The pulse duration also affects the surface roughness. From Fig. 5, it is evident that surface roughness directly depends on pulse duration; higher the pulse duration more is the surface roughness. Increasing the pulse duration enhances the feed rate thus allowing greater discharge energy penetrating into the surface of work-piece material forming deep crater wear. The surface roughness augments with the discharge current for any material of the WEDM electrode. Surface roughness hence enhances with the discharge current. The best 'Ra' value obtained experimentally is 1.31 μm at a peak current of 3 A and pulse duration of 4 μs . Improved surface finish can be accomplished at elevated values of servo speed because of rapid erosion of particles. An augmentation in servo voltage amplifies the surface roughness because of more number of collisions between ions and electrons resulting in higher MRR. Therefore, for the sake of better surface finish, low standard value of servo voltage is required. Increment in the pulse-off time results in the decrement of surface roughness. The higher pulse-off time supplies better cooling effect and sufficient time to flush the unwanted debris. High dielectric pressure results in total removal of particles resulting in better surface finish. Low wire speed causes more melting of material due to higher energy, and hence, high MRR is obtained causing high surface roughness. Therefore, it is necessary for an optimum wire speed selection for better surface finish. Low wire tension is the root cause of amplified vibration during the machining, and high wire tension may result in breakage. The wire feed rate is another important dependant parameter affecting the surface roughness. Improved surface finish can be attained with the inferior machine feed by Alias et al. [9]. Figure 6 represents the different images of the recast layer formation with variation in peak current (3, 6, 9, 12 A)

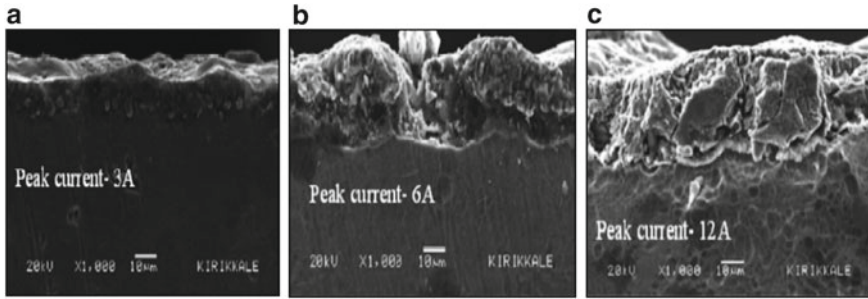


Fig. 6 **a** White layer formation 3A peak current on TiNiCu alloy. **b** White layer formation 6A peak current on TiNiCu alloy. **c** White layer formation 12A peak current on TiNiCu alloy

of TiNiCu alloy which clearly indicates better surface finish at low peak current and lower pulse duration.

4 Optimization

Optimization is done on input process parameters like peak current and pulse duration to obtain the best machining condition depending on the response of surface roughness (Ra). A 2⁴ combination of run-orders in a full quadratic un-coded mathematical model based on RSM is employed for multi-objective optimization [10, 11] of DOE. 16 runs/set of experiments are performed as per RSM on titanium composite where straight slots are cut on the sample to measure the MRR and SR. The contour plots and 3-D response surface of SR have been plotted depending on the fitted model in terms of **Coded Factors**:

$$SR = +2.55 + 0.5397A + 0.5542B + 0.0387AB + 0.0802A^2 - 0.2258B^2 \quad (1)$$

This equation is used for making predictions about the response for specified levels of each factor. By default, the high levels are coded as +1 and the low levels are -1. The coded equation is helpful for recognizing the relative impact of the factors. Again, the contour plots and 3-D response surface of SR have been plotted depending on the fitted model in terms of **Actual Factors**:

$$SR = +1.08255 + 0.051238A + 0.020394B + 0.000179AB + 0.003958A^2 - 0.000098B^2 \quad (2)$$

Table 1 Model terms

Term	Standard error	VIF	R_i^2	Power (%)
A	0.3426	1.04351	0.0417	74.9
B	0.3366	1.01705	0.0168	76.3
AB	0.4478	1.04351	0.0417	52.3
A^2	0.5625	1	0.0000	89.2
B^2	0.5844	1.01705	0.0168	86.9

This above equation is used for making predictions about the response for given levels of each factor. The levels identify in the original entities for each factor. This equation is not used to establish the relative impact of each factor because the intercept is not at the centre of the design space. The evaluation of the above quadratic mathematical model of type polynomial is used in this DOE for output response as surface roughness (Ra values). Table 1 shows the model terms.

The design will better if low standard errors occur. The ideal VIF value is 1.0. Ideal R_i^2 is 0.0. Elevated R_i^2 signifies the terms are correlated with each other, leading to poor models. If the design has multi-linear constraints, then multi-collinearity will exist, which will blow up the VIFs and the R_i^2 , interpreting useless statistics. Therefore, prediction-based metrics are provided in this program via Fraction of Design Space (FDS) statistics. Table 2 depicts model summary statistics of analysis of RSM where the Design Expert 11 software clearly suggests using the quadratic model. Main focus is given on the maximizing the model's Adjusted R^2 and the Predicted R^2 . Table 3 represents the ANOVA table for Surface Roughness.

The F -value of **76.81** entails that the model is significant. Only a 0.01% chance is there for a large F -value due to noise. P -values less than 0.05 indicate model terms are significant. In this case A , B , B^2 are significant model terms. Values greater than 0.1 indicate the model terms are not significant. The **Predicted R^2** of **0.9319** is in reasonable agreement with the **Adjusted R^2** of **0.9619**; i.e. the difference is 0.03. **R^2** is **0.9746** and **Adeq Precision** is **30.4102**. Table 4 depicts the coefficients in terms of coded factors. The coefficient estimate depicts the expected alteration in response per unit change in factor value when the other factors remain constant. When the factors are orthogonal, the VIFs are 1; VIFs greater than 1 indicate multi-collinearity. VIFs less than 10 are tolerable. Adeq Precision computes the signal-to-noise ratio. A ratio greater than 4 is desirable. **30.410** ratio designates a sufficient signal. This model can be developed and used to navigate the design space.

Figure 7 indicates a very near conformity of the actual and predicted values which clearly endow that the results obtained after the experimentation are mitigating with the predicted values. There is a decrement of std error of design whose lower limit is 0.0494867 and upper limit is 0.097679 which is very nominal. Figure 8 represents one optimized solution, where peak current is 4.666 A, pulse duration is 17.092 μ s, surface roughness (Ra value) is 1.742 μ m, StdErr of design is 0.049 and desirability is 0.900. Figure 9 depicts the contour plot of surface roughness which indicates that there is an increment of SR with the increment of peak current and pulse duration

Table 2 Model summary statistics of RSM

Source	Sequential <i>p</i> -value	Lack of fit <i>p</i> -value	Std. dev.	<i>R</i> ²	Adjusted <i>R</i> ²	Predicted <i>R</i> ²	Press	Suggested/aliased
Linear	<0.0001		0.1557	0.9421	0.9332	0.9111	0.4835	
2FI	0.5993		0.1601	0.9434	0.9293	0.9018	0.5341	
Quadratic	0.0182		0.1175	0.9746	0.9619	0.9319	0.3702	Suggested
Cubic	0.0711		0.0806	0.9928	0.9821	0.9337	0.3603	
Quartic	0.5230		0.0821	0.9963	0.9814	0.5016	2.71	Aliased

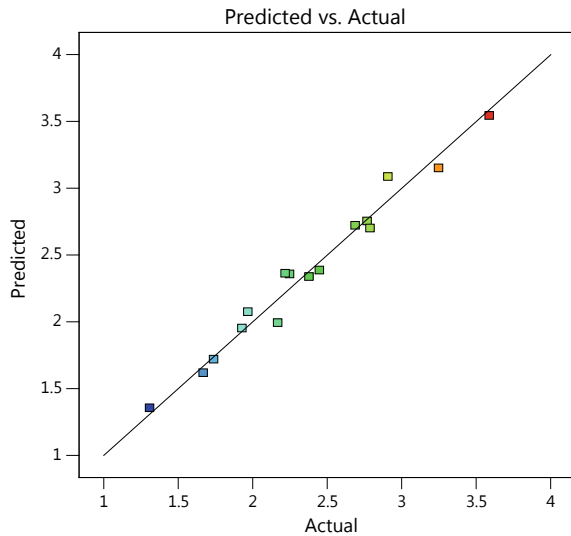
Table 3 ANOVA table for surface roughness

Source	Sum of squares	df	Mean square	F-value	p-value	Significant or not
Model	5.30	5	1.06	76.81	<0.0001	Significant
A-peak current	2.48	1	2.48	179.74	<0.0001	Significant
B-pulse duration	2.71	1	2.71	196.45	<0.0001	Significant
AB	0.0075	1	0.0075	0.5408	0.4790	Not Significant
A ²	0.0203	1	0.0203	1.47	0.2530	Not Significant
B ²	0.1493	1	0.1493	10.81	0.0082	Significant
Residual	0.1380	10	0.0138			
Cor total	5.44	15				

Table 4 Coefficients in terms of coded factors

Factor	Coefficient estimate	df	Standard error	95% CI low	95% CI high	VIF
Intercept	2.55	1	0.0627	2.42	2.69	
A-peak current	0.5397	1	0.0403	0.4500	0.6294	1.04
B-pulse duration	0.5542	1	0.0395	0.4661	0.6423	1.02
AB	0.0387	1	0.0526	-0.0785	0.1559	1.04
A ²	0.0802	1	0.0661	-0.0671	0.2274	1.0000
B ²	-0.2258	1	0.0687	-0.3787	-0.0728	1.02

Fig. 7 Predicted versus actual graph for SR



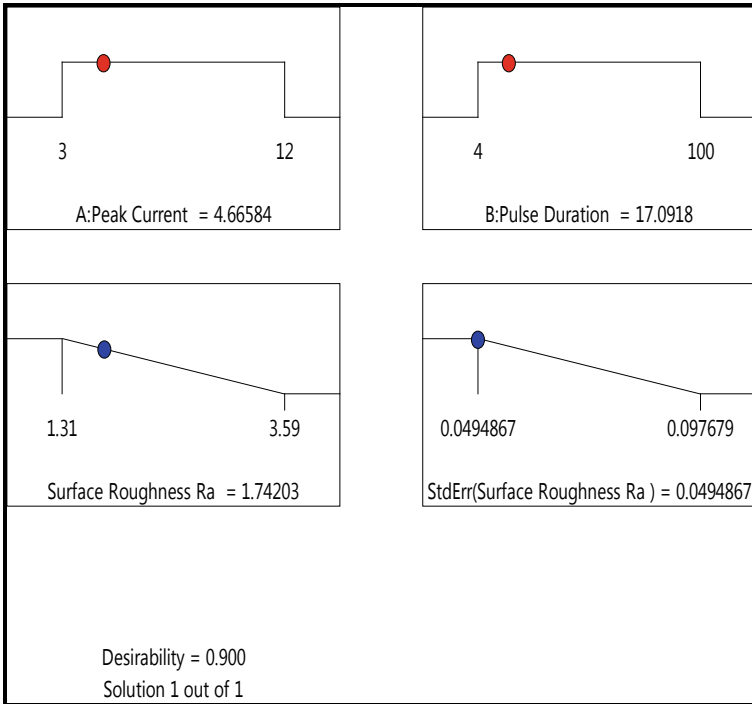


Fig. 8 Optimized result

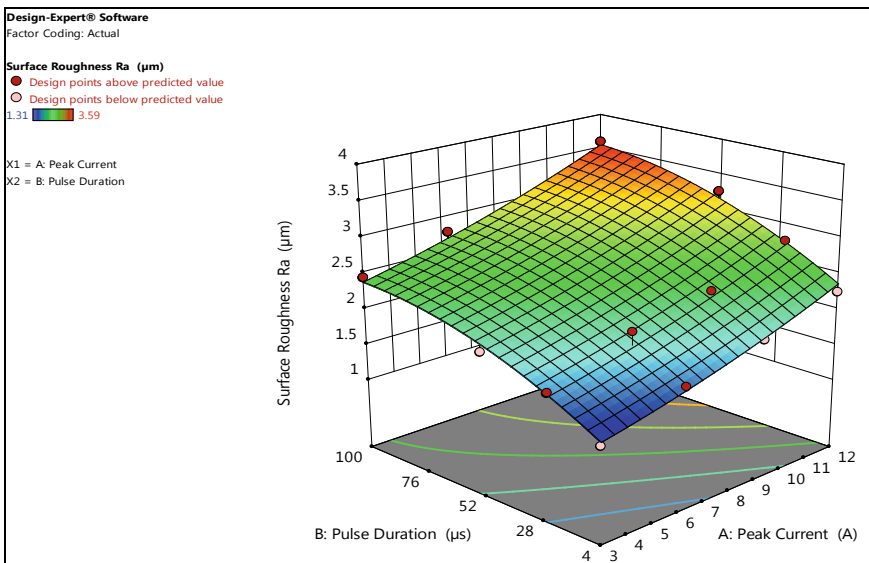


Fig. 9 Response surface and contour plots of surface roughness

which has to be minimized by optimization. After the confirmatory test, the surface roughness predicted mean obtained to be 2.46277 μm , which is 95% two-sided confidence with a 95% PI low of 2.16804 and 95% PI high of 2.7575 with a nominal error of only 0.29473.

5 Conclusion

In this paper, experimental analysis of WEDM of advanced titanium–nickel-based composites materials are done varying different process parameters resulting in optimal solution. Two different wire electrodes like zinc-coated brass and brass wire of 0.25 mm wire diameter are used for the comparative analysis. Higher MRR is obtained by the positive polarity of the zinc-coated brass wire electrode with distilled (deionized) water as dielectric medium compared to kerosene. The MRR is also enhanced with the increment peak current and pulse duration. Surface roughness is inversely proportional to peak current and pulse duration; hence, decrement in surface roughness occurs at low peak current and low pulse duration resulting in better surface finish when tool material of zinc-coated brass wire electrode is applied on WEDM of TiNiCu alloy. The best 'Ra' value obtained experimentally is 1.31 μm at a peak current of 3A and pulse duration of 4 μs . One optimized solution is obtained where peak current is 4.666A, pulse duration is 17.092 μs , surface roughness (Ra value) is 1.742 μm , StdErr of design is 0.049 and desirability is 0.900. The actual vs. predicted graph of the output response of surface roughness depicts an excellent conformity which convinces this research to be on the accurate path. The surface roughness predicted mean is 2.46277 μm after the confirmatory test which is 95% two-sided confidence with a 95% PI low of 2.16804 and 95% PI high of 2.7575 with a nominal error of only 0.29473.

References

1. Gu L, Li I, Zhao W, Rajurkar KP (2012) Electrical discharge machining of Ti6Al4V with a bundled electrode. *Int J Mach Tools Manuf* 53(1):100–106
2. Elias CN, Lima JHC, Valiev R, Meyers MA (2008) Biomedical applications of titanium and its alloys. *Biol Mater Sci* 60(3):46–49
3. Kumar A, Kumar V, Kumar J (2012) An investigation into machining characteristics commercially pure titanium using CNC WEDM. *Appl Mach Mater* 159:56–68
4. Saji VS, Jeong YH, Yu JW, Choe HC (2010) Corrosion behavior of Ti-13Nb-13Zr and Ti-6Al-4V alloys for biomaterial application. *Corros Sci Technol* 9(1):12–15
5. Fleck C, Eifler D (2010) Corrosion, fatigue and corrosion fatigue behavior of metal implant materials, especially titanium alloys. *Int J Fatigue* 32:929–935
6. Sen I, Karthikeyan G, Ramkumar J, Balasubramaniam R (2012) A study on machinability of B-modified Ti-6Al-4V alloys by EDM. *Mater Manuf Process* 27(3):348–354
7. Lin HC, Lin KM, Cheng IS (2000) A study on the machining characteristics of TiNi shape memory alloys. *J Mater Process Technol* 105(3):327–332

8. Chen SL, Yan BH, Huang FY (1999) Influence of kerosene and distilled water as dielectrics on the electric discharge machining characteristics of Ti-6Al-4V. *J Mater Process Technol* 87(1–3):107–111
9. Alias A, Abdullah B, Abbas NM (2012) Influence of machine feed rate in WEDM of Titanium Ti-6Al-4V with constant current (6A) using brass wire. *Proc Eng* 41:1806–1811
10. Nourbakhsh F, Rajurkar KP, Malshe AP, Cao J (2013) Wire electro-discharge machining of titanium alloy. *Proc CIRP* 5:13–18
11. Hsieh SF, Chen SL, Lin HC, Lin MH, Chiou SY (2009) The machining characteristics and shape recovery ability of Ti-Ni-X (X=Zr, Cr) ternary shape memory alloys using the wire electro-discharge machining. *Int J Mach Tools Manuf* 49:509–514

Interaction of Ru-4'-(2-pyridyl)-2,2':6',2''-Terpyridine with Diseased HER2 Protein



Satya Narayan Sahu, Tejaswini Sahoo, Biswajit Mishra,
Subrat Kumar Pattanayak, and Rojalin Sahu

Abstract The development of new approaches to improve screening, diagnosis, prevention and treatment of cancer is an area of intensive research. Breast cancer is one such widespread category of cancer among women which is the world's second leading cause of cancer death universally. The objective of this study is to analyze the structural stability of different diseased mutants of HER2 protein as well as to find out the inhibitory effects of Ru-terpyridine over mutant HER2 protein. To accomplish the study insight, we have carried out using different computational tools. From our *in silico* study, we conclude that, after mutation at positions D769H and V777L in HER2 protein, it was proceeded to cancerous growth and it becomes destabilize, followed by the binding performance of the ruthenium terpyridine over mutant HER2 protein shows the inhibitory effect against HER2 protein-targeted breast cancer.

Keywords Ruthenium-terpyridine · HER2 protein · Molecular docking

1 Introduction

Cancer is a dreadful disease which caused a great threat to mankind. However, there are various cytotoxic chemotherapeutic agents such as 5-fluorouracil, cisplatin, and doxorubicin. [1]. It is still not totally cured due to various loopholes including low targeting, specificity, and number of side effects. This disease involves abnormal cell growth which invades throughout the body, thus spreading throughout the body [2]. This monster disease has hundreds of different wings which have created destruction all over the world [3]. Breast cancer is one such widespread category of cancer among women which is the world's second leading cause of cancer death universally [4]. When the disease is spread, there may be pain in bone, yellowish skin, difficulty in

S. N. Sahu · T. Sahoo · B. Mishra · R. Sahu (✉)
School of Applied Sciences, Kalinga Institute of Industrial Technology (KIIT), Deemed to be
University, Bhubaneswar, Odisha 751024, India
e-mail: rsahufch@kiit.ac.in

S. K. Pattanayak (✉)
Department of Chemistry, National Institute of Technology Raipur, Raipur 492010, India
e-mail: skpiitbbs@gmail.com

breathing, and swelling in lymph nodes [5]. The various factors associated with the development of breast cancer include obesity, lack of physical fitness, consumption of alcohol, late pregnancy or not at all, and in some cases, family history can also be the reason [6]. Few cases are due to genetic inheritance from parents including the genes BRCA1 and BRCA2 [7]. After the diagnosis, test is done to determine the status of the disease whether it has spread to other parts and which treatment will be suitable [8]. Chemotherapy is one of the most widely used treatment technique for various types of carcinoma. However, its accuracy and effectiveness as well as safety and toxicity are a prior concern due to associated side effects. Also resistance to chemotherapy is another matter of worry which creates obstacle in treating various tumors including breast cancer. About 20% of world's breast cancer patients suffer from triple negative breast cancer [9]. In this condition, cells do not have estrogen, progesterone, and HER2 receptors, and this type of breast cancer is very aggressive type. The major obstacle in the metastatic disease treatment is caused by the resistance of these cells to various drugs, thus making the status of the disease more intense [10]. Apart from chemotherapy, other methods for the treatment of cancer include surgery and radiation. But, the latter also has less effectiveness due to their poor targeting. The worldwide clinically approved only metal-based chemotherapeutic drugs with platinum metals, including cisplatin, oxaliplatin, carboplatin, nedaplatin, and lobaplatin [11]. These drugs have been identified as effective agents for treating number of cancers, haunting mankind. But, cisplatin has been found to be associated with number of side effects like allergy, immunity breakdown to other disease, kidney problems, hearing impairment, hemorrhage, gastric disorders, and also drug resistance. Ruthenium (Ru) complexes have been recognized as promising candidates to take place of platinum chemotreatment. Recently, some unique characteristics of Ru-based complexes have been reported such as occupying large number of spatial positions and can exist in oxidation states from II to IV in biological medium. These properties have favored Ru-based complexes to act effective anti-tumour agents. The current study will summarize role of Ru-terpyridine complexes for treating HER2 diseased protein in breast cancer [12]. HER2 is a part of epidermal growth factor receptor of human. Overexpression or multiplication of this gene causes development of various types of highly fatal breast cancer [13]. It is also known as receptor tyrosine-protein kinase or CD340 or proto-oncogene Neu or ERBB2 [14]. HER2 is found in various tumours carrying point mutations. Overexpression caused in other genes can also trigger amplification in HER2. Estradiol and tamoxifen regulate the expression of HER2. When the ratio of co-activator AIB-3 exceeds more than co-repressor PAX2, it leads to tamoxifen-resistant breast cancer. The functional characterization of the genetic alteration associated with cancer has promoted new therapeutic advances which have improved patient's outcome. The examples include lapatinib and trastuzumab for HER2 gene amplification positive breast cancer. This HER2 gene amplification is a wide therapeutic center in breast cancer. Cancer genome sequencing project reported some patients having HER2 somatic mutation in cancer which were lacking HER2 gene amplification. Using in vitro kinase assays and other experiments like protein structure analysis, cell culture, etc., phenotype of this mutation was determined. The three most activating mutations

include D769H, D769Y, and V777L [15]. These somatic mutations are an alternative technique to activate HER2 in breast cancer and authenticate this mutation as drug target for the treatment of breast cancer. Recently, HER2-targeted drugs approved by Food and Drug Administration are trastuzumab, pertuzumab, and lapatinib. Ru-based complexes have recently been identified as potential antimetastatic candidates for various types of cancer [12]. Biphosphine bipyridine Ru-based complexes such as $[\text{Ru}(\text{SO}_4)(\text{dppb})(\text{bipy})]$, $[\text{Ru}(\text{CO}_3)(\text{dppb})(\text{bipy})]$, $[\text{Ru}(\text{C}_2\text{O}_4)(\text{dppb})(\text{bipy})]$, $[\text{Ru}(\text{CH}_3\text{CO}_2)(\text{dppb})(\text{bipy})]\text{PF}_6$ were reported as anti-tumour agent. The most effective among the above-mentioned complexes was the $[\text{Ru}(\text{CH}_3\text{CO}_2)(\text{dppb})(\text{bipy})]\text{PF}_6$. Ruthenium polypyridyl complex with N,N chelating agents such as 2,2 bipyridine, 4,4 dimethyl-2,2' bipyridine, and 1,10-phenanthroline have been reported as important anti-tumor agents in breast cancer [12]. The objective of our study is to analyze the structural stability of different diseased mutants of HER2 protein as well as to find out the inhibitory effects of Ru-terpyridine [16] over mutant HER2 protein.

2 Computational Method

The crystal structure of protein kinase_tyrosine domain of HER2 protein was re-modeled by using modeller 9.21 software. The initial crystal structure of studied protein was retrieved from the Protein databank (PDB) having PDB Id 3PP0, and the universal protein resource (Uniprot) Id is P04626. The studied crystal structure of the HER2 protein covers the amino acid residues from 720 to 976, which is fall in the protein kinase_tyrosine domain having Pfam domain id PF07714. From the previous studies, it is notable that the mutation in the protein kinase domain causes unregulated cell growth and leads to cancer [17]. Therefore, the above-mentioned domain is considered for our study. The native structure of HER2 protein is considered for the structure refinement. Bad contacts are removed by using Pymol visualizing software [18]. The crystal structure of the studied protein was proceeded for the analyzing the structural stability of the protein after mutation by using DUET online server [19]. The negative and positive values of the DUET result show the destabilized and stabilizing performance of the mutant protein structure, respectively. Followed by our next objective of this work, we performed molecular docking study. The molecular docking is the computational process to find out the binding performance between two molecules. The docking was performed by using AutoDock 4.2 software [20]. In the docking process, mutant structure of the HER2 protein was considered as receptor and the ruthenium-terpyridine was taken as ligand. After removal of all the bad contacts from the receptor and ligand, we have calculated Kollman charges and added the hydrogen to the polar contacts of the receptor by using AutoDock tool. During the docking, the autodock tool uses genetic algorithm to perform docking process. For the present studied receptor, we have calculated the grid box size of $126 \times 126 \times 126$ in x , y and z directions and center_x, center_y, center_z are 12.48, 21.717, and 34.045, respectively. The structure preparation and visualization are made by using Pymol and discovery studio visualizing software [21].

3 Results and Discussion

The crystal structure of the HER2 protein was refined by using Pymol software. After the refinement, it proceeds to check the structural stability of the mutant protein by using DUET online server. The DUET analyzing results are -0.617 for D769H mutant structure and -0.096 kcal/mol for V777L mutant structure. From the negative DUET result, the study concludes that the both the mutant structures of the HER2 protein are destabilized. The molecular docking analysis [22, 23] is proceeded to calculate the binding affinity of receptor and ligand. To compute the key features of binding performance between mutant D769H and V777L with ruthenium-terpyridine, molecular docking was performed. The binding performance between D769H and Ru-terpyridine resulting the binding energy -7.77 kcal/mol, in which LEU866, PRO885, LYS883, ALA730, PHE731, and TRP888 residues of HER2 protein interact with Ru-terpyridine in hydrophobic interaction and GLY729 residue binds in hydrogen bonding. The schematic representation of the binding performance is shown in Fig. 1.

The binding residues or binding sides for the V777L mutant structure with Ru-terpyridine were as same as D769H binding sides, but the binding energy between V777L and Ru-terpyridine is -7.78 kcal/mol, and the schematic representation of the binding performance is shown in Fig. 2.

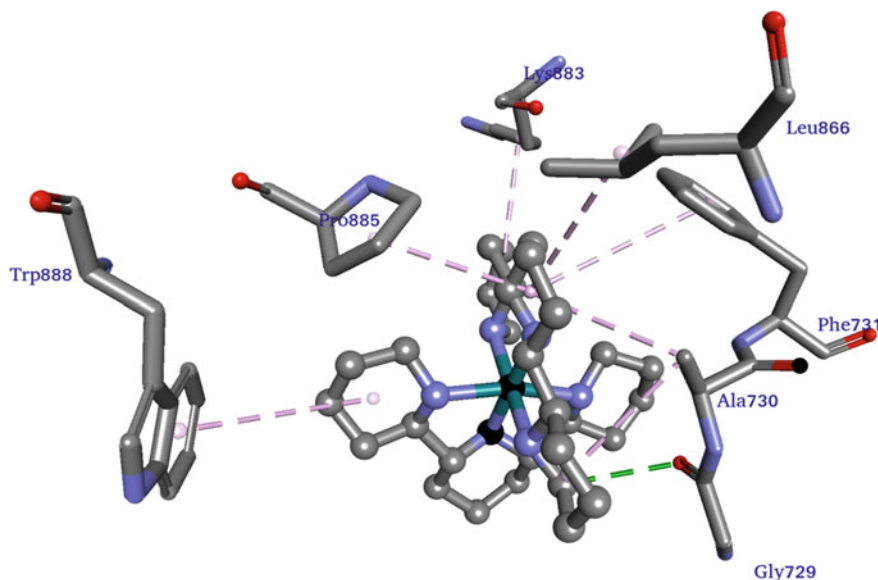


Fig. 1 Schematic representation of interaction between D769H with Ru-terpyridine. The stick models and ball-stick model are representing interacting residues and Ru-terpyridine, respectively. The green, pink color dotted lines are showing hydrogen bond and hydrophobic interactions, respectively

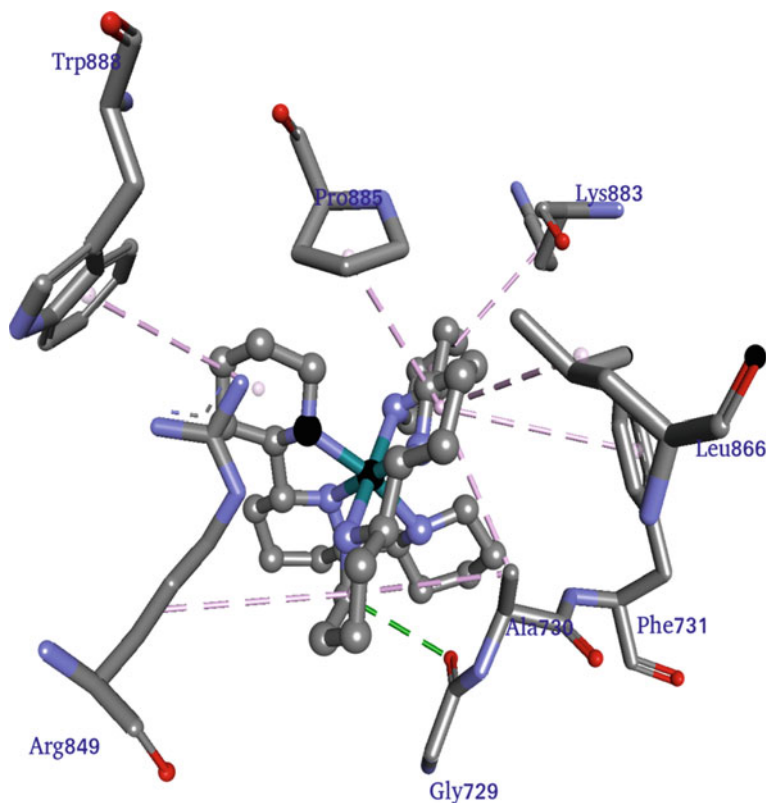


Fig.2 Schematic representation of interaction between V777L with Ru-terpyridine. The stick models and ball-stick model are representing interacting residues and Ru-terpyridine, respectively. The green, pink color dotted lines are showing hydrogen bond and hydrophobic interactions, respectively

The overall results for the binding performance of the above-mentioned molecules are concluded that the drug binding site or binding pocket of the HER2 protein is GLY729, LEU866, PRO885, LYS883, ALA730, PHE731, and TRP888, whereas GLY729 is a potential binding site because of hydrogen bonding in both the cases. The details of the binding results are shown in Table 1.

4 Conclusions

In the present study, we have analyzed the molecular interaction between the mutant structures of protein kinase_tyrosine domain of HER2 protein and Ru-terpyridine, which causes the uncontrolled cell growth and leads to cancer. From our in silico study, we conclude that after mutation at positions D769H and V777L in HER2

Table 1 Binding mechanisms of Ru-terpyridine with mutant HER2 protein

Mutants	Structural stability (kcal/mol)	Binding energy	Ligand efficiency	Binding residues	Nature of the bonds
D769H	-0.617	-7.77	-0.21	GLY729 LEU866 PRO885 LYS883 ALA730 PHE731 TRP888	Hydrogen bond Hydrophobic Hydrophobic Hydrophobic Hydrophobic Hydrophobic Hydrophobic
V777L	-0.096	-7.78	-0.21	GLY729 LEU866 PRO885 LYS883 ALA730 ARG849 PHE731 TRP888	Hydrogen bond Hydrophobic Hydrophobic Hydrophobic Hydrophobic Hydrophobic Hydrophobic Hydrophobic

protein, it was proceeded to cancerous growth and it becomes destabilized. The binding performance of the Ru-terpyridine over mutant HER2 protein shows the inhibitory effect against HER2 protein targeted breast cancer.

References

- Schimmel KJ, Richel DJ, van den Brink RB, Guchelaar HJ (2004) Cardiotoxicity of cytotoxic drugs. *Cancer Treat Rev* 30:181–191
- Leemans CR, Braakhuis BJ, Brakenhoff RH (2011) The molecular biology of head and neck cancer. *Nat Rev Cancer* 11:9
- Eroles P, Bosch A, Pérez-Fidalgo JA, Lluch A (2012) Molecular biology in breast cancer: intrinsic subtypes and signaling pathways. *Cancer Treat Rev* 38:698–707
- Pece S, Tosoni D, Confalonieri S, Mazzarol G, Vecchi M, Ronzoni S, Bernard L, Viale G, Pelicci PG, Di Fiore PP (2010) Biological and molecular heterogeneity of breast cancers correlates with their cancer stem cell content. *Cell* 140:62–73
- Wakabayashi H, Wakisaka S, Hiraga T, Hata K, Nishimura R, Tominaga M, Yoneda T (2018) Decreased sensory nerve excitation and bone pain associated with mouse Lewis lung cancer in TRPV1-deficient mice. *J Bone Miner Metab* 36:274–285
- Patton GC, Olsson CA, Skirbekk V, Saffery R, Wlodek ME, Azzopardi PS, Stonawski M, Rasmussen B, Spry E, Francis K, Bhutta ZA (2018) Adolescence and the next generation. *Nature* 554:458
- Tutt A, Tovey H, Cheang MCU, Kernaghan S, Kilburn L, Gazinska P, Owen J, Abraham J, Barrett S, Barrett-Lee P, Brown R (2018) Carboplatin in BRCA1/2-mutated and triple-negative breast cancer BRCAness subgroups: the TNT Trial. *Nat Med* 24:628
- Halvaei S, Daryani S, Eslami-S Z, Samadi T, Jafarbeik-Iravanian N, Bakhshayesh TO, Majidzadeh-A K, Esmaili R (2018) Exosomes in cancer liquid biopsy: a focus on breast cancer. *Mol Ther Nucl Acids* 10:131–141

9. Guha M, Srinivasan S, Raman P, Jiang Y, Kaufman BA, Taylor D, Dong D, Chakrabarti R, Picard M, Carstens RP, Kijima Y (2018) Aggressive triple negative breast cancers have unique molecular signature on the basis of mitochondrial genetic and functional defects. *Biochim Biophys Acta* 1864:1060–1071
10. Hurvitz SA, Martin M, Symmans WF, Jung KH, Huang CS, Thompson AM, Harbeck N, Valero V, Stroyakovskiy D, Wildiers H, Campone M (2018) Neoadjuvant trastuzumab, pertuzumab, and chemotherapy versus trastuzumab emtansine plus pertuzumab in patients with HER2-positive breast cancer (KRISTINE): a randomised, open-label, multicentre, phase 3 trial. *Lancet Oncol* 19:115–126
11. Bergamo A, Dyson PJ, Sava G (2018) The mechanism of tumour cell death by metal-based anticancer drugs is not only a matter of DNA interactions. *Coord Chem* 360:17–33
12. Popolin CP, Reis JP, Becceneri AB, Graminha AE, Almeida MA, Corrêa RS, Colina-Vegas LA, Ellena J, Batista AA, Cominetti MR (2017) Cytotoxicity and anti-tumor effects of new ruthenium complexes on triple negative breast cancer cells. *PLoS ONE* 12:e0183275
13. Chan A, Delaloge S, Holmes FA, Moy B, Iwata H, Harvey VJ, Robert NJ, Silovski T, Gokmen E, von Minckwitz G, Ejlertsen B (2016) Neratinib after trastuzumab-based adjuvant therapy in patients with HER2-positive breast cancer (ExteNET): a multicentre, randomised, double-blind, placebo-controlled, phase 3 trial. *Lancet Oncol* 17:367–377
14. Hasan R, Bhatt D, Khan S, Khan V, Verma AK, Bharti PS, Anees A, Dev K (2019) Frequency of I655V SNP of HER-2/neu in colorectal cancer: a study from India. *3 Biotech* 9:11
15. Bose R, Kavuri SM, Searleman AC, Shen W, Shen D, Koboldt DC, Monsey J, Goel N, Aronson AB, Li S, Ma CX (2013) Activating HER2 mutations in HER2 gene amplification negative breast cancer. *Cancer Discov* 3:224–237
16. Padhi SK, Sahu R, Manivannan V (2010) Water-chloride 2D-network in 4'-(2-pyridyl)-2,2':6',2''-terpyridine bis-chelates of M(II){M = Fe, Ni, Ru}. *Polyhedron* 29:709–714
17. Aertgeerts K, Skene R, Yano J, Sang BC, Zou H, Snell G, Jennings A, Iwamoto K, Habuka N, Hirokawa A, Ishikawa T (2011) Structural analysis of the mechanism of inhibition and allosteric activation of the kinase domain of HER2 protein. *J Biol Chem* 286:18756–18765
18. DeLano WL (2002) Pymol: an open-source molecular graphics tool. *CCP4 Newslett Protein Crystallogr* 40:82–92
19. Pires DE, Ascher DB, Blundell TL (2014) DUET: a server for predicting effects of mutations on protein stability using an integrated computational approach. *Nucl Acids Res* 14(42):314–319
20. Norgan AP, Coffman PK, Kocher JP, Katzmann DJ, Sosa CP (2011) Multilevel parallelization of AutoDock 4.2. *J Cheminform* 3:12
21. Visualizer DS (2005) Accelrys Software Inc. Discovery studio visualizer, p 22
22. Sahu SN, Moharana M, Sahu R, Pattanayak SK (2019) Impact of mutation on podocin protein involved in type 2 nephrotic syndrome: Insights into docking and molecular dynamics simulation study. *J Mol Liq* 281:549–562
23. Panda J, Sahoo JK, Panda PK, Sahu SN, Samal M, Pattanayak SK, Sahu R (2019) Adsorptive behavior of zeolitic imidazolate framework-8 towards anionic dye in aqueous media: combined experimental and molecular docking study. *J Mol Liq* 278:536–545

Morphology and Mechanical Properties of Polyamide 12/polypropylene/multiwalled Carbon Nanotubes Nanocomposites



Sucharita Sethy and Bhabani K. Satapathy

Abstract Ternary nanocomposites based on PA12/PP-MWCNT have been fabricated and characterized for their microstructural, dispersion morphology, thermo-mechanical and quasi-static tensile mechanical properties. The microstructural attributes were discussed in terms of dispersion nanomorphology and phase-selective micromorphologies based on TEM and SEM investigations. The thermo-mechanical response showed a composition specific shift in the relaxation behaviour of the nanocomposites as indicated from the loss tangent plots obtained from dynamic mechanical analysis. The uniaxial tensile responses of the nanocomposites reiterated the retention of the flexibility of the nanocomposites irrespective of the extent of MWCNT incorporation in the polyamide major phase mixed with MWCNT-embedded PP as the minor phase in the heterogeneous blend. Tensile-fractured surfaces revealed the distinct nature of the failure characteristics manifested on the fractured surfaces, i.e. a matrix dominated ductile failure characteristic in nanocomposites with less than 50 wt% of PP-MWNT masterbatch as the composite filler and a semi-ductile/quasi-brittle type of failed surface topography accompanied with minimum plastic deformation in the composites with more than 50 wt% of PP-MWNT composite filler incorporation. The study illustrated the phase morphological attributes to be primarily controlling the mechanical relaxation and macromechanical failure behaviour of the nanocomposites.

Keywords Polyamide-12 · Multiwalled carbon nanotubes · Nanocomposites · Mechanical · Morphology · Thermo-mechanical

Electronic supplementary material The online version of this chapter (https://doi.org/10.1007/978-981-15-7779-6_36) contains supplementary material, which is available to authorized users.

S. Sethy · B. K. Satapathy (✉)
Department of Materials Science and Engineering, Indian Institute of Technology Delhi, Hauz Khas, New Delhi 110016, India
e-mail: bhabaniks@gmail.com

1 Introduction

Conducting polymer nanocomposites has remained a class of promising materials that could potentially be explored for various multifunctional properties including thermal, electrical, mechanical and thermo-mechanical properties. Conductive polymer composites are being used for a long time for functional applications such as in electronics [1], sensors [2, 3], actuators [4, 5] and optoelectronic devices [6, 7]. Stretchable electronics are gaining attention due to its versatility as it includes flexibility and stable conductive pathways during large strain conditions [8]. It is well known that the properties of neat polymers are improved either by reinforcing it with a filler/fibres as in composite or by blending it with other polymers as in polymer blends. The former is termed as composites while the latter is termed as polymer blends and the combination of both is termed as polymer blend nanocomposites where filler is dispersed in the secondary polymer which in turn is dispersed in the primary matrix polymer. Compatibility/miscibility of the polymers determines the overall combination of properties of the final polymer blend nanocomposites. Fabrication of the multiphase structures depends on the molecular weight, surface energy, polarity and viscosity of the components. Morphology monitors the mechanical and thermo-mechanical properties of any polymer nanocomposite system. As evident, selective distribution of conducting filler such as MWCNT in the polymer blend system alters the morphology affecting the mechanical properties and solid-state relaxation properties [9]. The mechanical properties have observed to increase by the possibility of the MWCNT localization in one of the polymer phases and the interfacial areas between the two polymers [10]. Efficient load transfer during failure depends on the interfacial adhesion or interfacial interaction between the polymers and filler, such as in demonstrated pull-out of MWCNT due to poor interfacial interaction [11]. Additionally, immiscible blends lead to poor mechanical properties because of the phase separation created by the mechano-chemical incompatibility [12]. Reportedly, the mechanical properties increased with increase in MWCNT content. However, further increase in nanotube loading above a critical loading value decreased the mechanical properties which is attributed to heterogeneous distribution of MWCNT in the blend system along with the poor adhesion between the two polymers and between the polymers and MWCNT [13, 14]. Incorporation of MWCNT in polyamide/polypropylene blends has been of intriguing interest as blending of the two polymers gives rise to a co-continuous structure combining the stiffness of MWCNT, mechanical properties and PA and easy processability of PP [15]. However, morphology and mechanical properties of PA-12/PP blends incorporated with MWCNT are less explored. In this regard, PA-12 with high ductility, flexibility and low T_g /melting points may be explored for their mechanical and thermo-mechanical behaviour. Being a commodity thermoplastic, polyolefins possess inferior mechanical properties than polyamides which is a well-known engineering thermoplastic. Polyolefins are easier to process owing to their comparatively lower melting point than polyamides. A common processing window for the two polymers with a low difference of $\sim 15^\circ\text{C}$ (T_m of PA-12: 178°C , T_m of PA-12: 165°C)

Table 1 Compositions and designations of polymer nanocomposites

Sample name	PA-12 (wt%)	PP-MWNT (wt%)	MWNT in the overall composite (wt%)
NPM 0	100	0	0
NPM 6	70	30	6
NPM 8	60	40	8
NPM 10	50	50	10
NPM 12	40	60	12
NPM 14	30	70	14
NPM 20	0	100	20

in their melting points further helps in easy processability of the nanocomposites. So, suitable blending technique is used which combines the properties of both the polymers to produce a polymer blend of improved properties. However, it is well known that to establish a conducting path in such phases, the conducting carbonaceous filler incorporation many at times leads to decrease in ductility (embrittlement), which may lead to a decrease in real-time performance by physically disrupting conducting pathways by structural break-up/failure of such composites.

2 Experimental

2.1 Fabrication of Polymer Composites

The specifications of the selected raw materials selected are presented in Table S1. The polymer nanocomposites were fabricated by melt mixing route at 230 °C and the processing conditions are given in Table S2. The raw and processed polymer granules were dried overnight at 80 °C in a vacuum oven. Table 1 displays the sample designations as per the compositions. A schematic representing the processing route followed along with the possible morphologies is shown in Fig. 1.

2.2 Characterization

The nanomorphology of the ternary nanocomposites was examined in a Tecnai™ G2 20 high-resolution transmission electron microscope (HRTEM). Solid-state relaxation properties for nanocomposite samples of dimensions 17.5 mm × 9.8 mm × 3.9 mm were measured on Q800 (TA Instruments, USA) in single cantilever mode at a heating rate of 5 °C/min from -20 °C to 150 °C at a frequency of 10 Hz. Liquid nitrogen was used to create an inert atmosphere inside the DMA chamber. The uniaxial tensile properties of the fabricated polymer nanocomposites were performed

conforming to ASTM D 638 on a universal testing machine (model Zwick Z250) at a gauge length of 20 mm and cross-head speed of 5 mm/min at room temperature (25 °C).

3 Results and Discussion

3.1 Nanomorphology by TEM

The transmission electron micrographs for the nanocomposites with various compositions are shown in Fig. 2. The presence of three components in the nanocomposites could be clearly revealed by the three different types of contrast in the micrographs attributed to their intrinsic hardness. The tube-like structures showed MWCNTs in the nanocomposites whereas the lighter contrast corresponds to the PA-12 phase and the darker phase corresponds to MWCNT-embedded PP phase. Clearly, MWCNTs were found in specific localized region, i.e. PP phase. This may be attributed to the processing method that involves the use of masterbatch dilution of PP-MWCNT. During processing, nanotubes start to attain flow-assisted mobility from the PP phase

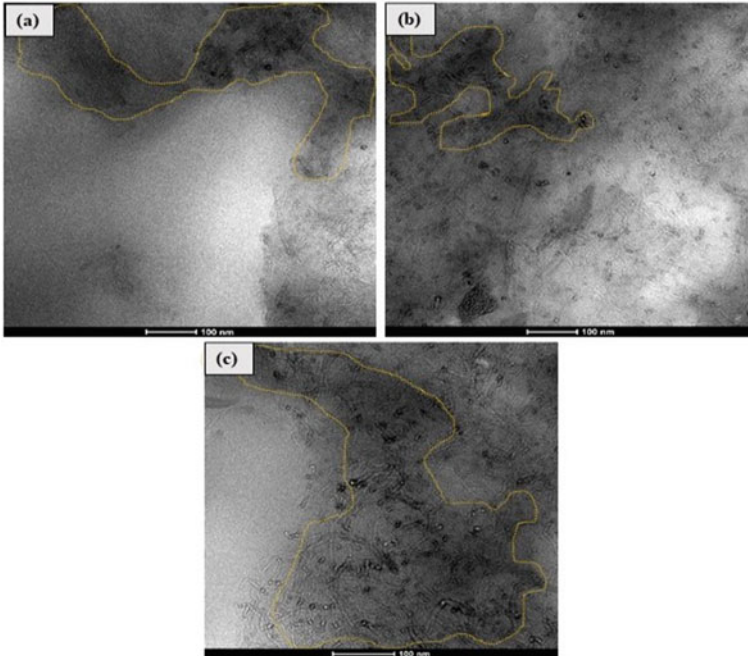


Fig. 2 Transmission electron micrographs of **a** NPM 6, **b** NPM 8 and **c** NPM 10

as PP starts melting at 165 °C and thereby enabling partial infiltration of MWCNTS into the PA-12 phase at around 178 °C.

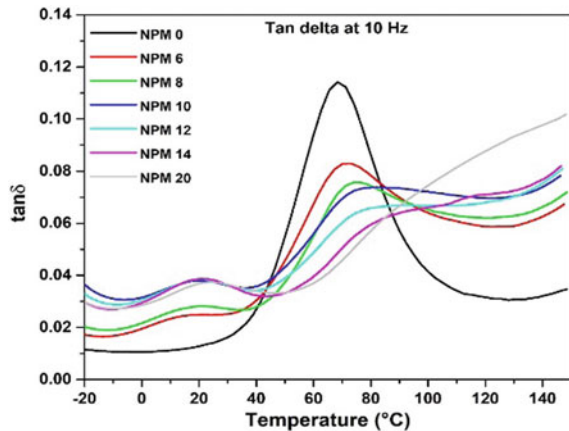
The micrographs revealed a decrease in the lighter contrast (PA-12 phase) from NPM 6 to NPM 10 which is well in agreement to the expected nanotube localization dynamics with increase of the MWCNT content. The lower melt viscosity of PA-12 eases the migration of nanotubes towards itself facilitated the partial transfer of MWCNTs to the PA-12 phase from the MWCNT-embedded-PP phase (PP-MWCNT masterbatch) by impingement across the PA-12/PP interface.

3.2 Solid-State Relaxation Properties

The temperature dependence of loss tangent ($\tan \delta$) curves for the PA-12/PP/MWNT nanocomposites is shown in Fig. 3. The two different peaks for the nanocomposites indicate immiscibility of PA-12 and PP phases. The peaks at ~20 °C correspond to T_g of PP phase while peaks at ~60 °C correspond to T_g of PA-12 phase. Additionally, peak shifting is observed for PA-12 phase, viz. the peak for NPM 0 (neat PA-12) is at 63 °C which shifts to higher temperatures with masterbatch incorporation which may be attributed to the segmental immobilization of PA-12 chains imposed by the nanotubes [16]. However, the T_g of PP phase for the nanocomposites shows a slight different shifting behaviour, i.e. NPM 20 has T_g of ~22 °C which shifts to lower temperatures after dilution of the PP-MWNT masterbatch with PA-12 which may be attributed to the effective increase in free volume as a result of increased segmental mobility in PP phase due to migration of MWCNT into PA-12 phase.

The broadening of loss tangent peak was observed for the nanocomposites which increased with an increase in nanotube loading indicating the retarded relaxation mechanism of the neat PA-12 matrix phase in the overall nanocomposite. The peak height $\tan \delta$ may be correlated with the interfacial interactions where the decrease

Fig. 3 Loss tangent curves for the polymer nanocomposites



in the peak height values may be due to the poor interfacial interactions between the domains of PA-12 and PP. A similar correlation of $\tan \delta$ peak heights to interfacial effects has been reported in literature in the case of [17].

3.3 Quasi-Static Mechanical Properties: Uniaxial Tensile Response

3.3.1 Low-Strain Tensile Response (<1%)

The uniaxial tensile responses of the nanocomposites are shown in Fig. 4a which showed linear deformation behaviour upto a strain of 1%. The stress–strain diagram showed absence of any yielding at macroscopic level under tensile load. The elastic moduli obtained from these plots have shown significant increase above 60 wt% of PP-MWCNT master batch loading in the nanocomposites, i.e. NPM 12. The tensile failure mechanics of these nanocomposites may theoretically be characterized by estimating the number of physical entanglements across the various phases per unit volume in the nanocomposites. Topologically, such entanglements are feasible only when the radius of gyration (R_g) exceeds the diameter of the nanotubes [18]. Typically, the diameter of multiwalled nanotubes remained in the range of 8–10 nm. The molecular weight (M_w) of PA-12 typically remain in the range of 3.5–10.5 ($\times 10^4$) g/mol.

Assuming the scaling law as $R_g \sim M_w^{2/3}$, the R_g may be estimated as ~15–16 nm. These estimated values theoretically facilitate the formation of physical entanglement networks in the investigated systems. The elastic properties of the polymer melt have been attributed to the dynamic entanglements between the chain segments of polymer-to-polymer and polymer-to-nanotube interaction. According to the classical theory of rubber elasticity [18], the molecular mass between the entanglements (physical) (M_e) can be calculated as

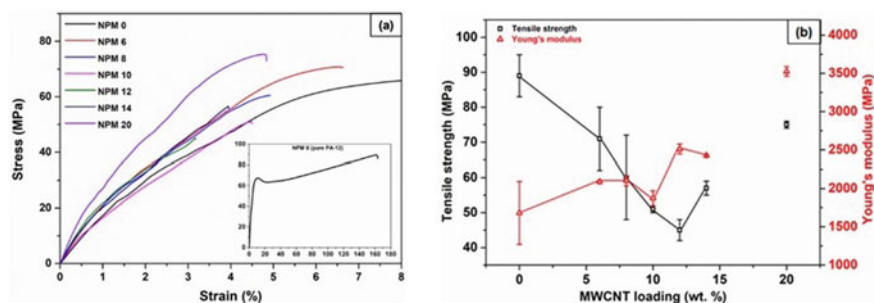


Fig. 4 a Stress–strain curve for nanocomposites and b tensile strength and Young's modulus as a function of MWCNT content

Table 2 Molecular mass between the entanglements and entanglement (physical) density

Specimen designation	$M_e^{\#}$ at 25 °C (mol ⁻¹ m ⁻¹)	$\nu_e^{\#}$ at 25 °C ($\times 10^{-23}$) mol/m ³
NPM 0	1.667	3.722
NPM 6	1.382	4.543
NPM 8	1.271	4.957
NPM 10	1.201	5.267
NPM 12	1.073	5.918
NPM 14	0.961	6.634
NPM 20	0.863	7.467

$^{\#}M_e$: molecular mass between the entanglements; ν_e : entanglement density

$$M_e = \frac{\rho RT}{G'} \quad (1)$$

and the entanglement density (ν_e) may be estimated by using the following equation,

$$\nu_e = \frac{\rho N_a}{M_e} \quad (2)$$

where ρ is the density of the polymer composites, R is universal gas constant, T is reference temperature, G' is the storage modulus at temperature T and N_a is Avogadro's number. The estimated entanglement density values are given in Table 2. A direct correspondence between the entanglement density (ν_e) and tensile failure response of the composites under tensile loading could be observed. The extent of ν_e increased with MWCNT (PP-MWCNT masterbatch) loading in the nanocomposites as evident from Table 2. The energy dissipation ability of the nanocomposites tends to have increased with increasing ν_e . The elastic moduli of the nanocomposites clearly show a resembling trend to that of the ν_e with increase in PP-MWCNT contents. Furthermore, the possibility of enhanced resistance to crack propagation in the nanocomposites attributed to increased ν_e needs experimental investigation and validation.

3.3.2 High-Strain Tensile Response (>2%)

The high-strain mechanical response of the nanocomposites may be seen in Fig. 4a the strain level of ~2%. It could be seen clearly that beyond a strain level of ~1% the nanocomposites failed by in a quasi-brittle manner and showed a nonlinear deformation behaviour characterized by absence of any signs of plastic deformation prior to failure as indicated from the failed surface micrographs (discussed in the subsequent section). The deformation of the nanocomposites thus remained largely limited to very small extent of strain maxima prior to failure as visually indicated by the

large-scale localization (failure zone) of strain in the tensile test specimen. A high elongation at break of $\sim 163\%$ is observed for NPM 0 (neat PA-12) as shown in inset of Fig. 4a. NPM 20, i.e. PP-MWCNT masterbatch has shown the highest tensile strength among the investigated nanocomposites. The nanocomposites, other than the compositions NPM 0 and NPM 20, have failed at a strain of $<7\%$. This may be attributed to the presence of more microagglomerates at higher loading levels of MWCNT (PP-MWCNT masterbatch) causing sufficient localization of the strain around the dense nanotube networks. Such strain localization intensifies the effect of modulus mismatch of the two-phase constituents of the composites, i.e. PA-12 and PP-MWCNT, leading to generation of cracks in the nanocomposites and eventually to failure.

The variation of Young's modulus and tensile strength with MWCNT loading is shown in Fig. 4b. The tensile strength of the nanocomposites decreased linearly from NPM 0 to NPM 12. However, on further increasing the MWCNT content, the tensile strength showed a linear increase upto NPM 20. Being an engineering plastic, NPM 0 (neat PA-12) has the highest tensile strength value of ~ 89 MPa which is about ~ 10 – 15% higher than that of NPM 20 (~ 75 MPa). However, NPM 12 showed the lowest tensile strength value of ~ 45 MPa among the investigated compositions. The trend of variation in tensile strength and modulus of the nanocomposites demonstrates a switch-over of mechanical properties in the composition range of NPM 8 to NPM 12 that corresponds to a composition-dependent phase inversion in the morphological attributes as already discussed in the section dealing with phase distribution micromorphology.

3.4 Tensile-Fractured Surface Morphology

The tensile-fractured surface morphology of neat PA-12 and the filled nanocomposites are shown in Fig. 5. The white dots represent the MWCNTs in the nanocomposites which had a relatively uniform dispersion in PP phase and insignificant agglomeration could be observed even at higher magnification (20 KX). The darker phase corresponds to polyamide 12 phase while the lighter phase with white dots (MWCNT) and mesh-like structures corresponds to phase of polypropylene with MWCNTs confined in the ternary nanocomposites. From the micrographs, clearly the white dots increased from NPM 0 to NPM 14 (Fig. 5a–f) while being the neat PP-MWCNT master batch, NPM 20 (Fig. 5g) has shown extensive distribution of MWCNT.

Such structures in the micrographs are consistent with composition. The MWCNT (white dots) are uniformly dispersed in the surface irrespective of the MWCNT loading which further established the fact that masterbatch dilution method is effective method for fabrication of such phase-selective conducting nanocomposite. Certain composition specific characteristics have also been observed in the micrographs such as domain dispersed co-continuity of polymer phases with interspersed MWCNT network in NPM 8 to NPM 14 (Fig. 5c, f). The failure surface topography further reveals the fact that above NPM 10 (Fig. 5d), i.e. $10\text{ wt}\%$ of effective MWCNT

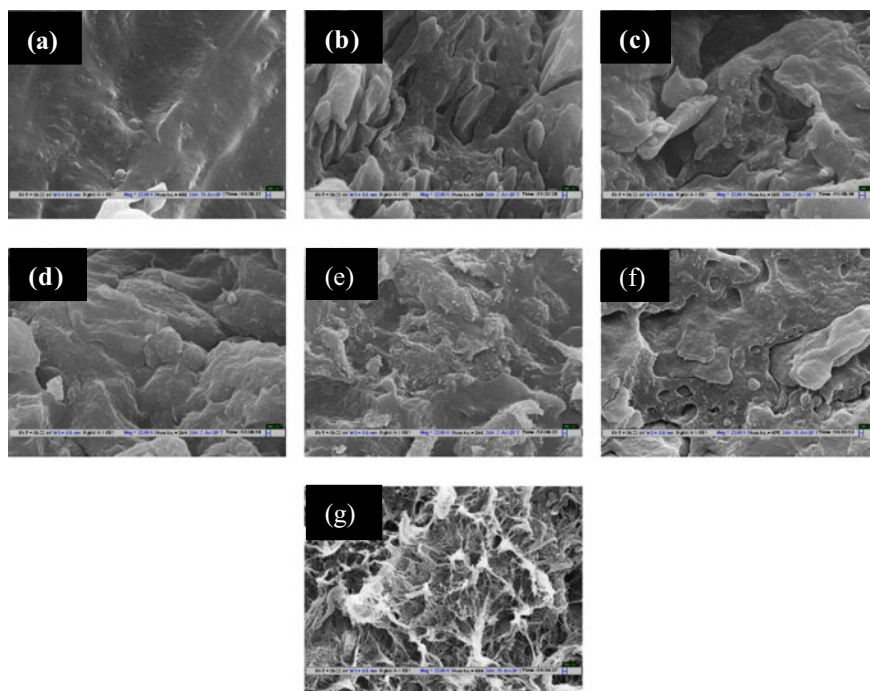


Fig. 5 Scanning electron microscopy of tensile failed surface of the polymer nanocomposites **a** NPM 0, **b** NPM 6, **c** NPM 8, **d** NPM 10, **e** NPM 12, **f** NPM 14 and **g** NPM 20

loading in the nanocomposites show pulled-out MWCNTs seen on the micrographs as white dots, to be responsible for offering additional resistance to applied stress prior to failure and thereby enhancing the elastic moduli in the composition regime of NPM 10 to NPM 14 (Fig. 5d, f). Further, these features suggest the possibility of MWCNT to be remaining largely confined in the PP phase even after they are melt-mixed with PA-12 to obtain the nanocomposites at a temperature little above the melting point of PP. This is consistent with increase in MWCNT loading according to the composition. As already mentioned, PA-12 and PP produce immiscible blends due to the differences in crystalline structure and polarity of both the components.

4 Conclusions

Ternary nanocomposites based on PA-12 and PP-MWCNT masterbatch have been fabricated melt blended by masterbatch dilution method. The fabricated nanocomposites showed phase-selective morphology as indicated by TEM and SEM studies. The morphology revealed the presence of conducting PP-MWCNT channels as selectively localized MWCNT in PP phase dispersed in a quasi-co-continuous-type

microstructure. The movement of MWCNTs to PA-12 matrix phase from PP phase has also been illustrated from TEM studies. Solid-state relaxation behaviour obtained from DMA revealed significant shifting and broadening of the $\tan \delta$ peaks with increase in MWCNT content. Such shifting in the relaxation peaks was attributed to hindered mobility of polymeric chains of PA-12 due to the incorporation of MWCNT, which also increased the T_g ($\sim 2\text{--}16$ °C) of the PA-12 phase in the nanocomposites. Estimations based on modified Kerner equation revealed that chain segments of PA-12 matrix are effectively immobilized by the inclusion of PP-MWCNT in the macroscale that is facilitated by the infiltration of MWCNT into the PA-12 phase as confirmed by TEM. The tensile failure response showed a direct correspondence with entanglement density (ν_e) calculated from the DMA results. The trend of tensile strength and modulus of the nanocomposites demonstrated a switch-over in the composition range of NPM 8 to NPM 12 that corresponds to a composition-dependent phase distribution micromorphology. The failure surface topography studied by SEM showed that pulled-out MWCNTs to be responsible for enhancement in the elastic moduli in the composition regime of nanocomposites with 50 wt% of PP-MWCNT (NPM 10) to 60 wt% of PP-MWCNT (NPM 14).

References

1. Jang KI, Chung HU, Xu S, Lee CH, Luan H, Jeong J, Cheng H, Kim GT, Han SY, Lee JW, Kim J, Cho M, Miao F, Yang Y, Jung HN, Flavin M, Liu H, Kong GW, Yu KJ, Rhee SI, Chung J, Kim B, Kwak JW, Yun MH, Kim JY, Song YM, Paik U, Zhang Y, Huang Y, Rogers JA (2015) Soft network composite materials with deterministic and bio-inspired designs. *Nat Commun* 6:6566
2. Kim J, Lee M, Shim HJ, Ghaffari R, Cho HR, Son D, Jung YH, Soh M, Choi C, Jung S, Chu K (2014) Stretchable silicon nanoribbon electronics for skin prosthesis. *Nat Commun* 5:5747
3. Lee H, Song C, Hong YS, Kim MS, Cho HR, Kang T, Shin K, Choi SH, Hyeon T, Kim DH (2017) Wearable/disposable sweat-based glucose monitoring device with multistage transdermal drug delivery module. *Sci Adv* 3:e1601314
4. Hong S, Lee H, Lee J, Kwon J, Han S, Suh YD, Cho H, Shin J, Yeo J, Ko SH (2015) Highly stretchable and transparent metal nanowire heater for wearable electronics applications. *Adv Mater* 27:4744–4751
5. Lee H, Choi TK, Lee YB, Cho HR, Ghaffari R, Wang L, Choi HJ, Chung TD, Lu N, Hyeon T, Choi SH (2016) A graphene-based electrochemical device with thermoresponsive microneedles for diabetes monitoring and therapy. *Nat Nanotechnol* 11:566–572
6. Choi MK, Yang J, Kang K, Kim DC, Choi C, Park C, Kim SJ, Chae SI, Kim TH, Kim JH, Hyeon T (2015) Wearable red–green–blue quantum dot light-emitting diode array using high-resolution intaglio transfer printing. *Nat Commun* 14:7149
7. Koo JH, Kim DC, Shim HJ, Kim TH, Kim DH (2018) Flexible and stretchable smart display: materials, fabrication, device design, and system integration. *Adv Funct Mater* 28:1801834
8. Cheng T, Zhang Y, Lai WY, Huang W (2015) Stretchable thin-film electrodes for flexible electronics with high deformability and stretchability. *Adv Mater* 27:3349–3376
9. Wang X, Li W, Zhang Z, Chen K, Gan W (2019) Selective localization of multi-walled carbon nanotubes in epoxy/polyetherimide system and properties of the conductive composites. *J Appl Polym Sci* 136:47911
10. Wiwattananukul R, Hachiya Y, Nobukawa S, Yamaguchi M (2017) Selective localization of carbon nanotubes in PC/PET blends. *Polym Compos* 38:1103–1111

11. Banerjee J, Dutta K (2019) Melt-mixed carbon nanotubes/polymer nanocomposites. *Polym Compos* 40:4473–4488
12. Liu XQ, Yang W, Xie BH, Yang MB (2012) Influence of multiwall carbon nanotubes on the morphology, melting, crystallization and mechanical properties of polyamide 6/acrylonitrile–butadiene–styrene blends. *Mater Des* 1:355–362
13. Rejisha CP, Soundararajan S, Sivapatham N, Palanivelu K (2014) Effect of MWCNT on thermal, mechanical, and morphological properties of polybutylene terephthalate/polycarbonate blends. *J Polym* 2014:1–7
14. Triantou MI, Stathi KI, Tarantili PA (2019) Thermal, mechanical, and dielectric properties of injection molded graphene nanocomposites based on ABS/PC and ABS/PP Blends. *Polym Compos* 40(S2):E1662–E1672
15. Zhang L, Wan C, Zhang Y (2009) Investigation on the multiwalled carbon nanotubes reinforced polyamide 6/polypropylene composites. *Polym Engg Sci* 49:1909–1917
16. Nair KM, Thomas S, Groeninckx G (2001) Thermal and dynamic mechanical analysis of polystyrene composites reinforced with short sisal fibres. *Compos Sci Technol* 61:2519–2529
17. Parameswaranpillai J, Joseph G, Chellappan RV, Zahakariah AK, Hameed N (2015) The effect of polypropylene-graft-maleic anhydride on the morphology and dynamic mechanical properties of polypropylene/polystyrene blends. *J Polym Res* 22:2
18. Rubinstein M, Colby RH (2003) *Polymer physics*. Oxford University Press, p 266

Effect of Cold Work on Microstructure and Corrosion Properties of 304L Stainless Steel



Asit Behera, Bikram Behera, D. K. Sahoo, Ashutosh Pattnaik, K. N. Barik, Priyabrata Mallick, Subrat Bhuyan, S. C. Mishra, and Ajit Behera

Abstract Type 304 stainless steels have profound application in engineering including springs, kitchen equipment, auto wheel covers, hose clamps, truck bodies, exhaust manifolds, storage tanks, piping and pressure vessels, etc. AISI 304 is rolled/deformed uniaxially to reduce the thickness to 20, 40, 60% of the initial thickness using rolling machine (notation CW00, CW20, CW40, CW60). The magnetic character of type 304 stainless steel was measured in terms of percentage martensite content using feritscope after cold rolling. It is observed that the cold work structure forms high dislocation density regions or tangles, which further develop onto tangled network; therefore, higher cold worked material has higher slip bands or planes. As the amount of percentage deformation increases, martensite formation increases, and hence, the magnetic nature increases. With increase in cold work, hardness also increases due to the formation of martensite in different systems of slip planes. Again, it is observed that corrosion test in H_2SO_4 and KSCN solution highly affects the slip planes.

Keywords 304L stainless steel · Deformation · Stacking fault energy · Cold working · Corrosion

A. Behera (✉)

School of Mechanical Engineering, Kalinga Institute of Industrial Technology (KIIT), Deemed to be University, Campus-8, Patia, Bhubaneswar, Odisha 751024, India
e-mail: asit.beherafme@kiit.ac.in

B. Behera · D. K. Sahoo · A. Pattnaik · S. Bhuyan · S. C. Mishra · A. Behera
Department of Metallurgical and Materials Engineering, National Institute of Technology Rourkela, Rourkela 769008, India

K. N. Barik
Department of Chemical Engineering, Indira Gandhi Institute of Technology, Sarang 759146, India

P. Mallick
Thermal Spray Division, Hindustan Aeronautics Limited (HAL), Sunabeda 763 002, India

© Springer Nature Singapore Pte Ltd. 2021

P. Pant et al. (eds.), *Advances in Mechanical Processing and Design*, Lecture Notes in Mechanical Engineering, https://doi.org/10.1007/978-981-15-7779-6_37

433

1 Introduction

Austenitic stainless steel (SS) demandingly used in automotive and aerospace industries to home appliances due to their superior corrosion resistance and mechanical properties. The 304 stainless steel is a T300 series austenitic stainless steel, also known as A2 stainless steel, or 18/8 stainless steel generally contains 17.5–20% chromium, 8–11% nickel and less than 0.08% carbon, 2% manganese, 1% silicon, 0.045% phosphorus and 0.03% sulfur. It is a nonmagnetic steel which cannot be solidified by heat treatment, yet should be cold attempted to get higher elastic qualities. The 18% least chromium substance gives consumption and oxidation obstruction. The composite's metallurgical attributes are set up principally by the nickel content (8% mm.), which additionally stretches out protection from consumption brought about by diminishing synthetic compounds. Carbon, a need of blended advantage, is held at a level (0.08% max.) that is helpful for most administration applications [1–3].

Non-titanium-settled evaluations for the most part have a superior surface finish than titanium balanced out evaluations. These evaluations are non-attractive in the toughened condition yet may turn out to be somewhat attractive because of phase change to martensite or ferrite after cold working and welding individually. A portion of these evaluations has higher auxiliary dependability than others. This is used for evaluation of 4318 austenitic stainless steel, which is effectively halfway changed to martensite during cold working tasks, bringing about an expansion of strength and hardness of the material. Then again, if changes are bothersome, evaluation of 4306 stainless steel, which has a somewhat higher nickel substance making changes all the more far-fetched, is ideal. Type 304, with its chromium–nickel content and low carbon, is the most versatile and widely used of the austenitic stainless steels. Type 304 is broadly used in various equipments as austenitic steel where low carbon content is used. Type 304 composites are largely changes of the 18% chromium, 8% nickel austenitic alloy [4, 5]. Applications for this gathering of compounds are fluctuated, and all have to some degree comparative attributes in protection from oxidation, erosion and durability.

This hardened steel can have assortment of physical necessities, making them utilized in trim, wheel covers, kitchen gear, springs, truck bodies, ventilation systems, tanks and weight vessels.

Corrosion properties with respect to cold working 304L stainless steel have not been studied extensively in the literature. In this paper, 304L stainless steel has been cold worked. To observe the variation in micrograph after cold work and the effect of these variation on the corrosion properties are the novelty of this paper.

2 Experimental Procedures

The as-received sample of type 304 stainless steel with initial thickness of 2.87 mm in the form of rectangular plate was cut into four pieces. The sample was then rolled/deformed uniaxially to reduce the thickness to 20, 40, 60% of the initial thickness using rolling machine (notation CW00, CW20, CW40, CW60). The magnetic character of type 304 stainless steel was measured in terms of percentage martensite content using feritscope after cold rolling. The sample of stainless steel was spot welded on one side of the specimen, and the wire was covered by an insulated sleeve. The samples were then mounted in a cold setting resin followed by polishing. The microstructure were observed using optical microscope (Lica DM microscopy) at different magnification. Before the electrochemical experiments, the surface of the sample was exposed to cathodic cleaning at -0.9 VSCE for 60 s to reduce the air-formed oxide film. Different solutions were prepared using the standard combination of H_2SO_4 and KSCN as activator. The solutions were deaerated using argon gas in a closed corrosion vessel for 45 min. The solutions were then used as the test solution. The sample was the working electrode, the platinum electrode as the counter electrode and saturated calomel electrode as the reference electrode. Then, the anodic polarization was carried out, and the potential was kept from -0.05 to 1.2 V. The potential scan rate used was 2 mV/s. After the completion of the test, the specimens were washes with distilled water and examined under optical microscope to determine the type and extend of corrosion. After etching by Beraha's reagent, micrograph analysis has been carried out using scanning electron microscope (JEOL 6480LV).

3 Results and Discussion

The microstructure of all the samples such as CW00, CW20, CW40, CW60 has been using optical microscope which are depicted in Fig. 1. When deformed, there is beginning of grain elongation with formation of uneven dislocations. When cold working rate increases, uniform cell size observed with heavy dislocation density at grain boundary. As there is local strain hardening due to interference of grains and occurrence of multiple slip system as observed from the surface morphology. The cold work structure forms high dislocation density regions, which further develops onto tangled network. The size of grain reduces very slowly and fixed value at the optimized condition of cold working. This indicates that as strain helps to proceed the dislocation across the grains and cease at the tangle in the cell walls. In polycrystalline metals, the crystallographic orientation of the grains differ with respect to the mechanical loading axis and thus of the active slip system vary from grain to grain. As the cold working increases, the stacking fault energy (SFE) also increases as given in Eq. (1) [6].

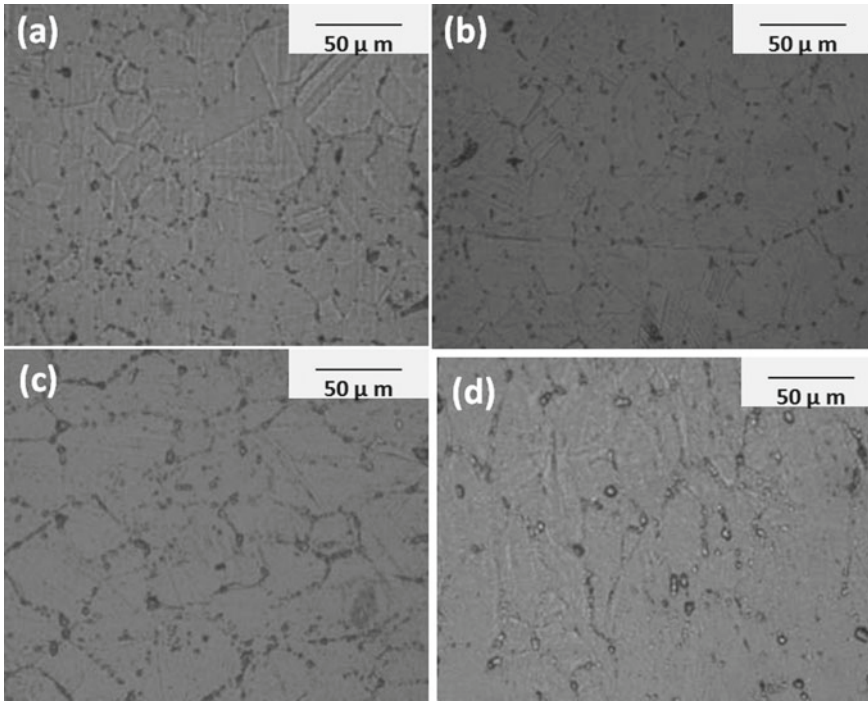


Fig. 1 Optical micrograph of **a** CW00, **b** CW20, **c** CW40, **d** CW60, respectively

$$\text{SFE} = -53 + 6.2 \text{ wt\%Ni} + 0.7 \text{ wt\% Cr} + 3.2 \text{ wt\% Mn} + 9.3 \text{ wt\% Mo} \quad (1)$$

But, it is less pronounced at lower temperature and increase strain rate deformation and in materials with low SFE (stacking fault energy) because cross slip is difficult. As we know that 304L stainless steel has low SFE of 20 mJ/m^2 , therefore the phenomenon is less pronounced. With increase in grain boundary, dislocation phase transformation and precipitation increases. Therefore, there is higher martensite formation at higher deformation. The fact that different slip systems can operate in adjacent regions of the same grain results in complex lattice rotations which results in the formation of deformation bands [7]. As more slips are found at grain boundary than grain center, hardness is more at grain boundary. As the grain diameter is reduced more of the effects of grain boundary will be felt at the grain centre. In the microstructure, there will be slip bands or planes. The first sign of permanent deformation in a metal is the appearance of slip bands or lines. Slip bands are observed upon slightest deformations as the degree of deformation is increased, the slip blocks in each separate crystallite turn to conform with the direction in which force acts and metal grains are elongated in that direction to form fibrous or banded structure.

Type 304L stainless steel is basically an austenitic stainless steel which is nonmagnetic in nature, but when the alloy is permanently deformed, some of the austenite

gets converted to martensite which has BCT structure and magnetic in nature, so the cold worked SS304 shows magnetic character [8]. As the amount of percentage deformation increases, martensite formation increases and hence the magnetic nature increases as shown in Fig. 2.

As the cold work increases, passive current density (current density at 0.2 V) also increases, that means corrosion resistance decreases, as illustrated in all the curves from the Fig. 3a–e). The passive film breaks at low current density for lower cold work and has high current density for higher cold work. This indicates that higher cold work materials are more prone to corrosion. The passive film form is strong and cannot be broken easily. The OCP of cold worked materials almost remains same; hence, OCP does not depend on cold work. The passive chromium usually protects

Fig. 2 Martensite content with respect to reduction of metal thickness during cold working

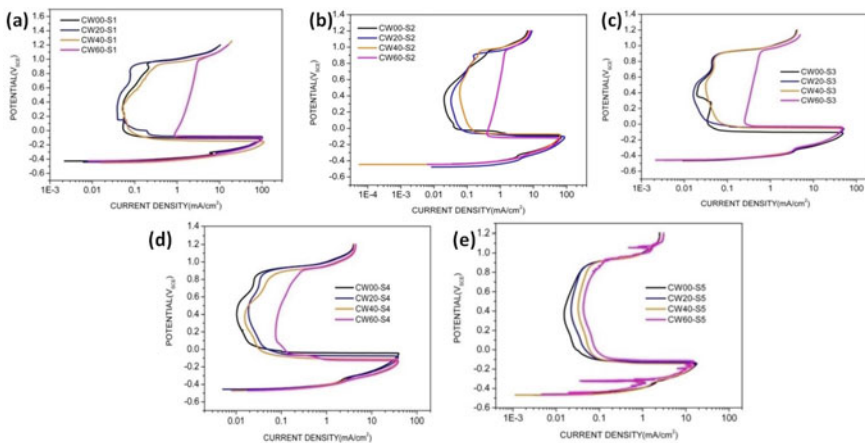
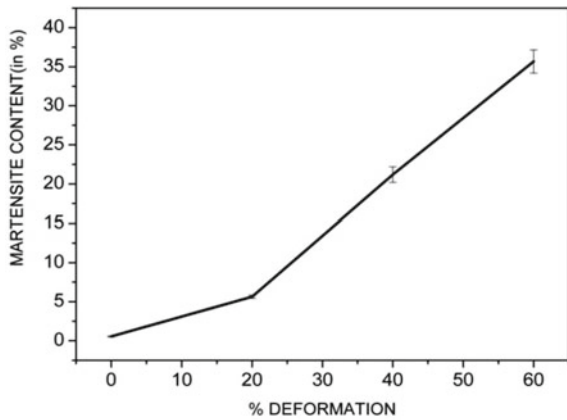


Fig. 3 Polarization curves in different solution: **a** in S1 (1M H₂SO₄, 0.01M KSCN), **b** in S2 (0.5M H₂SO₄, 0.01M KSCN), **c** in S3 (0.25M H₂SO₄, 0.01M KSCN), **d** in S4 (0.25M H₂SO₄, 0.005M KSCN), **e** in S5 (0.1M H₂SO₄, 0.001M KSCN)

it from corrosion. Generally, potential for transformation from passive is very low. However, at very high potential, current density varies exponentially with voltage, as it enters transpassive region [9].

The microstructure after polarization shows that there is patches formation near the grain boundaries because of the chromium depletion and also along the slip planes due to martensite transformation. We can see there is no intergranular corrosion or stress corrosion cracking. Corrosion test in H_2SO_4 and KSCN solution highly affects the slip plane. The cross-slip is clearly visible in the corroded sample in the form of wavy lines. For a particular sample in different solutions, we can see that critical current density increases as H^+ concentration increases. The upper portion of the curve also state that current density increases for more acidic solution. The passive current density does not depend on KSCN; therefore, for S3 and S4 solution, it is almost same in every samples. The passive current density increases with increase in H^+ concentration of the solution increases.

In CW00, we cannot see any martensite, but as the cold work increases, martensite also increases as shown in Fig. 4. The light portion was martensite. The sharp lines are slip lines/bands. These lines are thin in CW20 but becomes thicker at CW40. The lines even turn out to be wavy at CW60 due to cross-slip at higher cold work. Microstructure showing slip bands interactions, shear bands and martensite dislocations in moving slips interaction, and it grows in number.

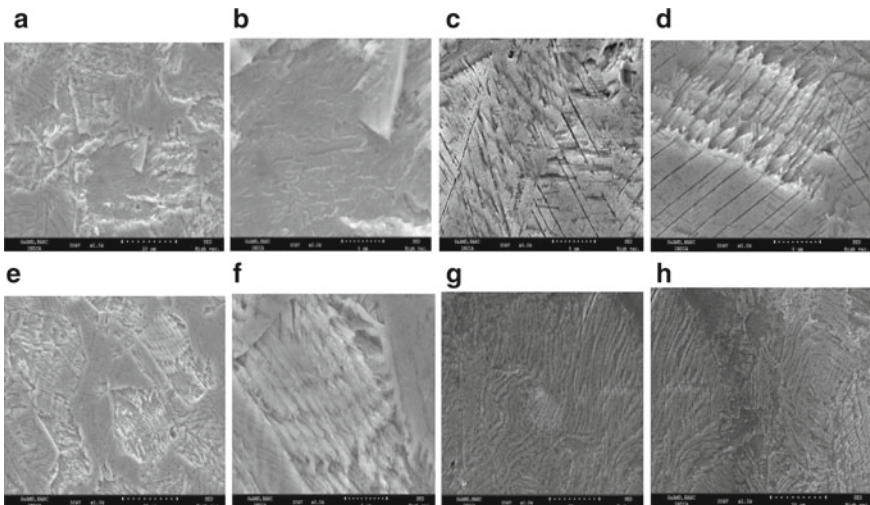


Fig. 4 Microstructure using Beraha's etchant. **a** CW00, **b** CW00, **c** CW20, **d** CW20, **e** CW40, **f** CW40, **g** CW60, **h** CW60

4 Conclusions

The cold work structure forms high dislocation density regions, which further develop onto tangled network; therefore, higher cold worked material has higher slip bands or planes. As the amount of percentage deformation increases martensite formation increases, the magnetic nature increases. When deformation increases, uniformity of cell size as well as heavy dislocation density at grain boundary takes place. As the cold work increases, passive current density (current density at 0.2 V) also increases that means corrosion resistance decreases. The passive film formed in higher cold work is weak and can be broken easily. The critical current density does not vary much for different cold worked specimens in S4 and S5 solution because they are less acidic and has less effect in corrosion.

References

1. Khan S, Kain V, Reddy AVR (2014) Corrosion in transpassive potential regime: effect of composition and microstructure of austenitic stainless steel. *Corrosion* 70:19–28
2. Narutani T (1989) Effect of deformation-induced martensite transformation on the plastic behavior of metastable austenitic stainless steel. *Mater Trans* 30:33
3. Varma SK, Kalyanam J, Murr LE, Srinivas V (1994) Effect of grain size on deformation-induced martensite formation in 304 and 316 stainless steels during room temperature tensile testing. *J Mater Sci Lett* 13:107
4. Fang XF, Dahl W (1991) Strain hardening and transformation mechanism of deformation-induced martensite transformation in metastable austenitic stainless steels. *Mater Sci Eng A* 141:189
5. Advani AH, Murr LE, Matlock DJ, Romero RJ (1993) Deformation-induced microstructure and martensite effects on transgranular carbide precipitation in type 304 stainless steels. *Acta Metall* 41:267
6. Staudhammer KP, Murr LE, Hecker SS (1983) Nucleation and evolution of strain-induced martensite embryos and substructure in stainless steel: a transmission electron microscopy study. *Acta Metall* 31:267
7. Choi Y, Jin W (1997) Strain-induced martensite formation and its effect on strain hardening behavior in the cold-drawn 304 austenitic stainless steels. *Scr Mater* 36:99
8. McDowell DL, Stahl DR, Stock SR, Antolovich SD (1988) Biaxial path dependence of deformation substructure of type 304 stainless steel. *Metall Trans A* 9:1277
9. Oh BW, Cho SJ, Kin YG, Kin YP, Kin WS, Hong SH (1995) Deformation microstructures and the shear strain rate of type 304 stainless steel in cylindrical deep D of warm working. *Mater Sci Eng A* 197:147

Comparative Study of Mechanical Properties of Natural Fibers



Mukesh and S. S. Godara

Abstract Here, various mechanical properties for composites were studied, and comparison between different mechanical properties namely theoretical density, actual density, tensile strength and flexural strength of two distinctive natural fibers is done. These natural fibers are made of jute and Luffa-glass fibers reinforced with epoxy hybrid composites. Twelve different types of laminates have been used for this purpose. The flexural properties of the jute glass and luffa-glass fibers reinforced epoxy hybrid composites are superior for stacking series of GJJG for jute glass 5% fly ash and jute glass 5% alumina and GLGL for luffa glass. The values of tensile properties are better for GJJG for jute glass 5% fly ash and jute glass 5% alumina and GLLG for luffa glass.

Keywords Natural fibers · Jute glass · Luffa-glass fibers · Hybrid composites · Mechanical properties

1 Introduction

Researchers are focusing on natural fiber composites compared to traditional composites due to various benefits of these natural fiber composites such as their excellent strength to weight ratio, biodegradable properties and recyclability. Due to cheaper, readily availability and excellent mechanical properties, they characterize good renewable and environmental replacement to the commonly used reinforcing fibers, i.e., glass fibers.

Ahmed and Vijayarangan [1] estimated the properties of flexural, tensile and ILSS of various jute fiber polyester composites. Sanjay and Yogesha [2] studied the flexural, tensile and ILSS properties of jute and glass fiber epoxy composite. de Silva et al. [3] calculated physical/mechanical properties of cement composites with durable sisal fiber. Niharika and Acharya [4] evaluated the mechanical properties of Luffa cylindrica fiber reinforced epoxy composites. Gowda et al. [5] estimated

Mukesh · S. S. Godara (✉)

Department of Mechanical Engineering, Rajasthan Technical University Kota, Rajasthan 324010, India

e-mail: ssgodara@rtu.ac.in

© Springer Nature Singapore Pte Ltd. 2021

P. Pant et al. (eds.), *Advances in Mechanical Processing and Design*, Lecture Notes in Mechanical Engineering, https://doi.org/10.1007/978-981-15-7779-6_38

441



Fig. 1 Natural luffa and jute fibers

the properties of flexural, tensile and ILSS of untreated jute fabric fiber polyester composites. Singh et al. [6] have studied mechanical behavior of hybrid composites. Soma and Acharya [7] studied the properties of flexural, tensile and ILSS for various natural fiber composites. Yoldas et al. [8] characterization of luffa cylindrical fibers has been studied. Niharika and Acharya [9] studied properties of Luffa cylindrical fiber epoxy hybrid composite. Kishore [10] estimated the properties of jute/glass sandwich composite. Abdul Khalil et al. [11] determined properties for the oil palm fiber composites. Gujjala et al. [12, 13] estimated the properties of flexural, tensile and ILSS of woven jute/glass hybrid reinforced polymer composite.

It is found that comparison between properties of various natural fiber composites has not been yet done. The objective is to carry out the comparative study of natural hybrid composites with and without including fly ash particles.

2 Raw Materials for Hybrid Composites

Raw materials used for the hybrid composites are luffa, jute and glass as fibers, polymer resin as matrix and also alumina (Micro) and fly ash (Micro) are used as a hardener. Natural luffa fiber and jute fiber mats are shown in Fig. 1.

3 Preparations of Composite Specimens

The hand-layup method was used for preparation of luffa-glass reinforced hybrid composite and jute glass reinforced hybrid composite. The samples of the composite were prepared using different sequence of the lamina. The dimension of the wooden

mold 150 mm length, 60 mm width and 5 mm thickness was used for composite preparation. The mold release sheet is used for easy and quick removal of the composite [4].

The experimental density (actual density) of laminates is calculated by Archimedes theory. The composite actual density is determined by weight fraction concept as shown in Eq. (1).

$$s_m = \frac{w_0}{(w_0 + (w_a - w_b))} \quad (1)$$

where s_m = Actual density, w_0 = Sample weight in air medium, w_a = Kerosene deeper wire weight, w_b = sample weight + wire deep in kerosene.

The theoretical density of the laminates is calculated using Agarwal and Broutman Eq. (2).

$$\rho_{ct} = \frac{1}{\frac{w_{f1}}{\rho_{f1}} + \frac{w_{f2}}{\rho_{f2}} + \frac{w_m}{\rho_m}} \quad (2)$$

where w_{f1} and w_{f2} are the weights of the fiber first and second for hybrid composite. ρ_{f1} and ρ_{f2} are the densities of the fiber first and second for hybrid composite. w_m and ρ_m are the weight and density of the matrix.

4 Tests Method

4.1 Tensile Test

The tension test for tensile strength is normally conducted on flat sample. For this purpose, the dog bone geometries of the specimens are mostly used. The faces of the specimen are straight with ends tabs. The most commonly ASTM D 3039-76 machine is used for tensile test. The span of the specimen is 150, mm and width of the specimen is 20 mm at both ends and 10 mm between ends. The tensile test is carried on the universal testing machine (INSTRON H10KS) according to ASTM D 3039-76 with the speed of the cross head is 10 mm/min. The tensile test is conducted for five samples, but the average data is used for analysis. The INSTRON H10KS machine is presented in Fig. 2a, b displays the specimen is loaded in test machine.

4.2 Flexural Strength

Flexural strength is estimate based on the three points banding using the UTM 201 machine as per ASTM D2344-84 standards. The specimen is put on the two end

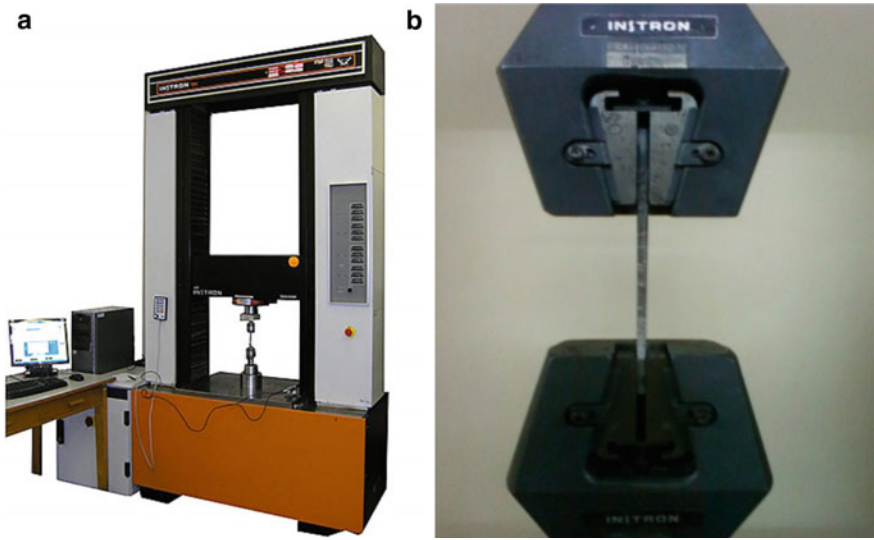


Fig. 2 a INSTRON H10KS tensile test machine. b Specimen loading condition

supports, and force is applied at the center of the specimen. The span of the specimen is 150 mm, and width of the specimen is 20 mm at both ends and 10 mm between ends. The universal testing machine (UTM) 201 is shown in Fig. 3 with the specimen in loading condition. During this test, crosshead speed was 2 mm/min, and load 10 KN was applied. The flexural stress is estimated by Eq. (3) in three-point bending test.

$$\sigma = \frac{3FL}{2bt^2} \tag{3}$$

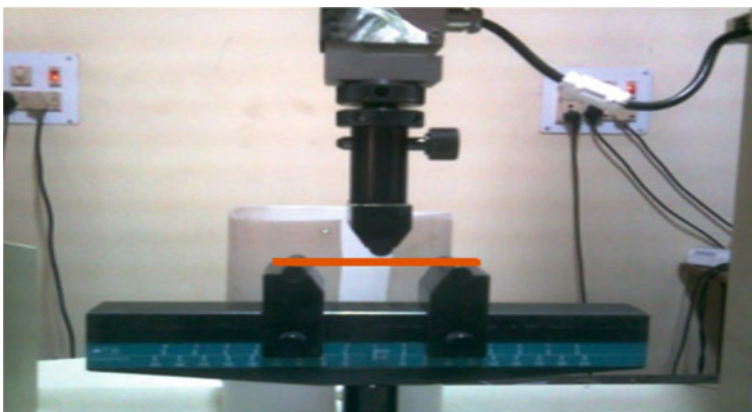


Fig. 3 Specimen test for flexural strength

where F = force, L = length of specimen, b = width and t = thickness.

5 Results

The composite properties are completely dependent on the properties of fiber. The composite strength varies because of loading of various fibers in composite. The densities of various hybrid composite laminates are shown in Table 1 and compared by graphs are shown in Figs. 4 and 5 for these composites. The variations of the

Table 1 Theoretical and measured densities of different laminates

Laminate	Symbol	Stacking sequence	Theoretical density	Measured density	Volume fraction of voids
Luffa	A_1	LLLL	1.01	1.009	1.2
Glass	A_2	GLGL	1.18	1.178	0.89
Epoxy	A_3	LGGL	1.187	1.177	0.878
	A_4	GLLG	1.188	1.179	0.78
Jute	C_1	JJJJ	1.247	1.222	2.005
Glass	C_2	GJGJ	1.297	1.273	1.850
Epoxy	C_3	JGGJ	1.297	1.271	2.005
5% alumina	C_4	GJJG	1.297	1.272	1.928
Jute	D_1	JJJJ	1.214	1.184	2.443
Glass	D_2	GJGJ	1.261	1.231	2.323
Epoxy	D_3	JGGJ	1.261	1.232	2.285
5% fly ash	D_4	GJJG	1.261	1.234	2.121

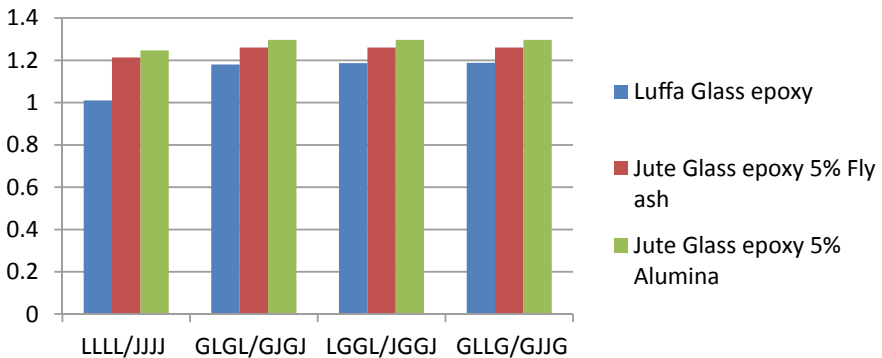


Fig. 4 Theoretical densities of different laminates

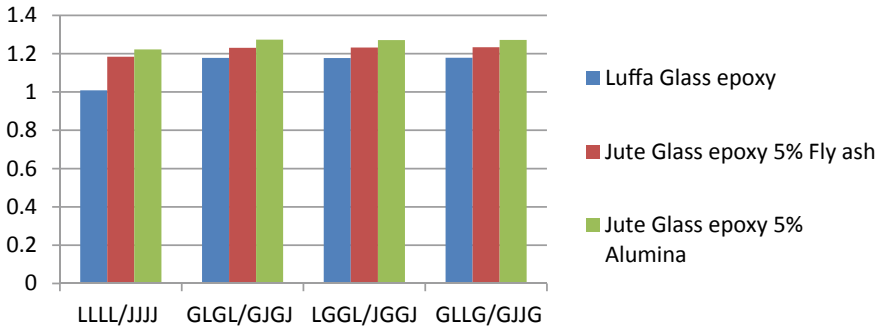


Fig. 5 Measured densities of the different stacking sequence of laminates

Table 2 Tensile and flexural properties of jute/glass and luffa/glass fiber polymer hybrid composite

Laminate	Symbol	Stacking sequence	Tensile strength (MPa)	Flexural strength (MPa)
Luffa	A ₁	LLLL	17.63	39.10
Glass	A ₂	GLGL	25.87	107.93
Epoxy	A ₃	LGGL	32.17	63.116
	A ₄	GLLG	35.34	108.36
Jute	C ₁	JJJJ	59.32	82.02
Glass	C ₂	GJGJ	95.75	175.47
Epoxy	C ₃	JGGJ	86.69	119.69
5% alumina	C ₄	GJJG	103.88	153.39
Jute	D ₁	JJJJ	57.32	79.02
Glass	D ₂	GJGJ	83.75	171.47
Epoxy	D ₃	JGGJ	79.69	109.69
5% fly ash	D ₄	GJJG	93.88	145.91

tensile and flexural properties of jute/luffa-glass hybrid composites are shown in Table 2 and compared by graphs are shown in Figs. 6 and 7.

6 Conclusions

The following conclusions are made based on the review study.

- The values of flexural properties are better for stacking sequence of GJGJ for jute glass 5% fly ash and jute glass 5% alumina and GLGL for luffa glass.
- The values of tensile properties are better for stacking sequence of GJJG for jute glass 5% fly ash and jute glass 5% alumina and GLLG for luffa glass.

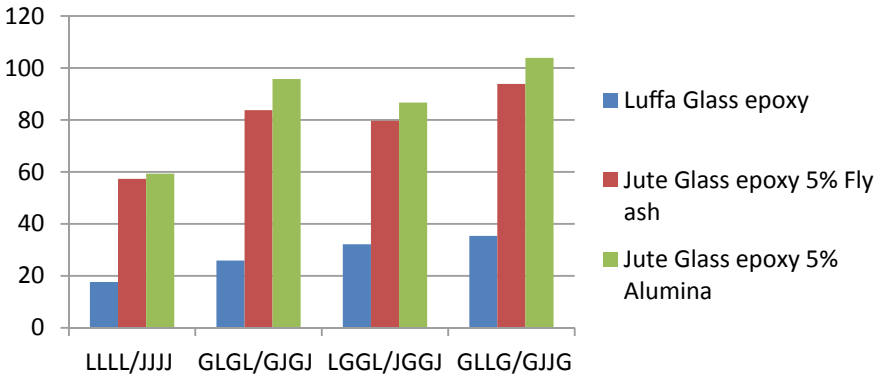


Fig. 6 Tensile properties of the Jute glass and Luffa-glass fiber epoxy hybrid composites

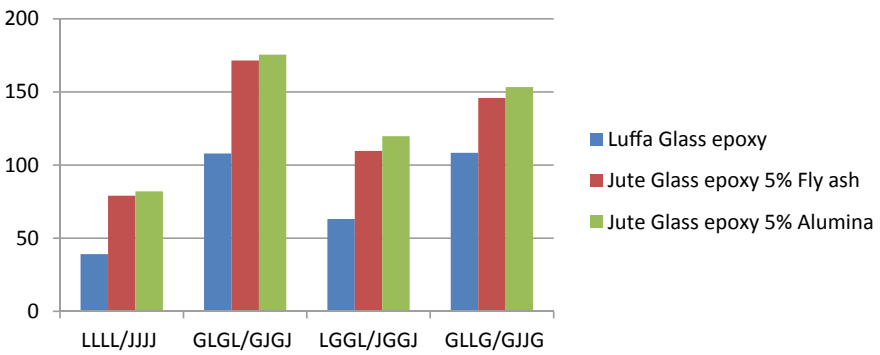


Fig. 7 Flexural strength of the jute glass and Luffa-glass fiber epoxy hybrid composite

- The tensile strength of the jute glass 5% fly ash/jute glass 5% alumina fiber epoxy hybrid composites is much higher than the Luffa-glass fiber reinforced epoxy hybrid composites.
- Flexural strength of the jute glass 5% fly ash/jute glass 5% alumina fiber reinforced epoxy hybrid composites is higher than the Luffa-glass fiber epoxy hybrid composites. But the flexural properties of the stacking sequence GLLG and GLGL of Luffa-glass fiber reinforced epoxy hybrid composite are near the stacking sequence JGGJ.
- The density of these composites laminates quit varies for various stacking sequence except neat jute and luffa fiber.

References

1. Ahmed KS, Vijayarangan S (2008) Tensile, Flexural and inter laminar shear properties of woven jute and jute glass fabric reinforced polyester composites. *Mater Process Technol* 207:330–335
2. Sanjay MR, Yogesha B (2016) Study on mechanical properties of jute/e-glass fiber reinforced epoxy composite. *J Min Mater Character Eng* 4:15–25
3. Silva F et al (2010) Physical and mechanical properties of durable sisal fiber cement composites. *Construct Build Mater* 24:777–785
4. Niharika M, Acharya SK (2013) Tensile, flexural and inter laminar shear properties of Luffa-cylindrica fiber reinforced epoxy composites. *Int J Macromol Sci* 3(2):6–10
5. Gowda M, et al (1999) Mechanical properties of untreated jute fabric-reinforced polyester composites. *Compos Part A* 30:277–284
6. Singh B et al (1995) Mechanical behavior of particulate hybrid composite laminates as potential building material. *Constr Build Mater* 9(1):39–44
7. Soma D, Acharya SK (2014) Study on mechanical properties of natural fiber reinforced woven jute-glass hybrid epoxy composites. *Adv Polym Sci Technol* 4(1):1–6
8. Yoldas S et al (2012) Characterization of luffa-cylindrica fibers and the effect of water aging on the mechanical properties of its composite with polyester. *J Appl Polym Sci* 123:2330–2337
9. Niharika M, Acharya SK (2015) Investigation of mechanical properties of Luffa-cylindrica fiber reinforced epoxy hybrid composite. *Int J Eng Sci Technol* 7(1):1–10
10. Kishore MR (1985) Jute-glass sandwich composite. *J Reinf Plast Compos* 4:186–194
11. Abdul Khalil HPS et al (2007) Agro-hybrid composite: The effects on mechanical and physical properties of oil palm fiber (EFB)/glass hybrid reinforced polyester composites. *J Reinf Plast Compos* 26:203–218
12. Gujjala R et al (2014) Mechanical properties of woven jute–glass hybrid-reinforced epoxy composite. *J Compos Mater* 48(28):3445–3455
13. Gujjala R et al (2014) A comparative analysis of woven jute/glass hybrid polymer composite with and without reinforcing of fly ash particles. *Polym Compos* 37:1–8

Parametric Appraisal of CNC Micro-drilling of Aerospace Material (PMMA) Using Taguchi-Based EDAS Method



Dilip Kumar Bagal, Sakti Kishore Panda, Abhishek Barua, Siddharth Jeet, Ajit Kumar Pattanaik, and Dulu Patnaik

Abstract Poly-methyl methacrylate (PMMA) has resilient corrosion resistance. At below zero temperature, their quality expands, in this way making them a valuable low-temperature polymer. PMMA has discovered its appropriate utility in aviation application. Mostly micro-drilling operation is used to engineer micro-holes in various materials according to their need. The target of this investigation was to streamline micro-drilling parameters, for example, rotational speed, feed given to tool and point angle on the circularity error, thrust force and machining time in CNC micro-drilling on aerospace material, i.e. PMMA. In this investigation, tests were completed according to Taguchi's method-based L_9 orthogonal array. The optimal parameters were determined with the help of a recent MCDM optimization method, i.e. evaluation based on distance from average solution method (EDAS).

Keywords Micro-drilling · PMMA · Taguchi's method · EDAS method

1 Introduction

Poly-methyl methacrylate (PMMA) is one of the vital evaluations of transparent thermoplastic having wide designing applications especially in aviation industries and vehicle industries. Micro-drilling is widely recognized and principal machining practice to produce micro-holes in many different categories. A few execution attributes which are usually utilized for assessing drilling operation, for example, thrust force, hole surface roughness, torque and tool wear, are strongly correlated

D. K. Bagal (✉) · S. K. Panda · A. K. Pattanaik
Department of Mechanical Engineering, Government College of Engineering, Kalahandi,
Bhawanipatna, Odisha, India
e-mail: dilipbagal90@gmail.com

A. Barua · S. Jeet
Department of Mechanical Engineering, Centre for Advanced Post Graduate Studies, BPUT,
Rourkela, Odisha, India

D. Patnaik
Department of Electrical Engineering, Government College of Engineering, Kalahandi,
Bhawanipatna, Odisha, India

with the machining parameters such as feed speed, cutting speed, drill and work-piece material, drill point angle, drill size and coolant conditions. Henceforth, drilling process served the medium for machining PMMA. The improvement of cutting pace and feed with a specific end goal to acquire great execution qualities is of much significance. It is likewise basic to think about efficiency (MRR), nature of the machined part (surface roughness) and necessity of dimensional steadiness (hole dimensional error) at the same time and streamline the machining parameters as needs be [1–8].

Amid the present examination, CNC-assisted drilling system with carbide drill bit of 1 mm diameter with three different point angles of 118°, 124°, 130° and 23 mm flute length is used in this investigation. The impact of all the drilling parameters, for example, rotational speed (N), feed (f) and point angle (degrees) has been explored on circularity error, thrust force and machining time for PMMA. In this investigation, tests were completed according to Taguchi's method-based L_9 orthogonal array. A comparative analysis has been carried out to find out optimal drilling parameters by using a recent MCDM optimization method, i.e. evaluation based on distance from average solution method (EDAS).

2 Experimental Detail and Methodology

During the experiment, a plate of poly-methyl methacrylate (PMMA) having thickness of 5 mm, length of 85 mm and width of 50 mm was drilled CNC drill machine (Make: HMT Ltd., Bangalore, India; FANUC controlled) in combination with drill bits of cemented carbide having diameter 1 mm, flute length of 23 mm and 3 different point angles of 118°, 124°, 130°. Table 1 shows the properties of PMMA and Fig. 1 shows the experimental set-up of the CNC-assisted drilling operation [1, 2]. Table 2 presents input factors of micro-drilling with three different levels.

Calculation of weights between conditions by pairwise comparison.

By means of geometric mean of AHP method, relative consequence of output responses was calculated. Saaty's nine-point preference scale was taken for calculation of pairwise comparison matrix as shown in Table 3. Output response weights were calculated by using following equations [9–12]

Table 1 Properties of PMMA

Compressive strength	83–124 MPa	Ultimate tensile strength	45–75 MPa
Poisson's ratio	0.34–0.4	Modulus of elasticity	5.0 GPa
Modulus of elasticity	3300 MPa	Refractive index	1.49
Modulus of rigidity	1700 MPa		



Fig. 1 Experimental set-up of CNC-assisted drill

Table 2 Pairwise comparison table between norms

	MRR	Kerf width	Tool wear rate
MRR	1	3	3
Kerf width	0.3	1	0.3
Tool wear rate	0.3	3	1

Table 3 L₉ orthogonal array design for experimental runs and results

Expt. No.	A	B	C	Local circularity error (%)	Thrust (N)	Machining time (s)
1	20	2000	118	0.012	5.64	25.51
2	20	2500	124	0.016	10.15	20.99
3	20	3000	130	0.022	8.35	16.89
4	25	2000	124	0.022	6.43	20.67
5	25	2500	130	0.002	4.13	19.15
6	25	3000	118	0.046	5.48	16.15
7	30	2000	130	0.006	2.38	16.82
8	30	2500	118	0.022	3.24	16.40
9	30	3000	124	0.052	8.24	9.30

$$GM_i = \left(\prod_{j=1}^n b_{ij} \right)^{1/n} \tag{1}$$

$$w_j = GM_i / \sum_{j=1}^n GM_i \tag{2}$$

3 EDAS Method

The steps for using the EDAS method are presented as follows:

Step 1: Most important criteria are selected which describe the alternative.

Step 2: Decision-making matrix is constructed as follows:

$$X = [x_{ij}]_{n \times m} = \begin{bmatrix} x_{11} & x_{12} & \dots & x_{1m} \\ x_{21} & x_{22} & \dots & x_{2m} \\ \dots & \dots & \dots & \dots \\ x_{n1} & x_{n2} & \dots & x_{nm} \end{bmatrix} \tag{3}$$

where X_{ij} represents performance value of i th alternative on j th criterion.

Step 3: Average solution is determined conferring to all criteria using Eqs. (4) and (5):

$$AV = [AV_j]_{1 \times m} \tag{4}$$

where

$$AV_j = \frac{\sum_{i=1}^n X_{ij}}{n} \tag{5}$$

Step 4: Positive distance from average (PDA) and negative distance from average (NDA) matrixes are constructed conferring to the kind of criteria shown as follows:

$$PDA = [PDA_{ij}]_{n \times m} \tag{6}$$

$$NDA = [NDA_{ij}]_{n \times m} \tag{7}$$

if j th norm is favourable,

$$PDA_{ij} = \frac{\max(0, (X_{ij} - AV_j))}{AV_j} \tag{8}$$

$$NDA_{ij} = \frac{\max(0, (AV_j - X_{ij}))}{AV_j} \tag{9}$$

and if j th norm is non-favourable,

$$PDA_{ij} = \frac{\max(0, (AV_j - X_{ij}))}{AV_j} \tag{10}$$

$$NDA_{ij} = \frac{\max(0, (X_{ij} - AV_j))}{AV_j} \tag{11}$$

where PDA_{ij} and NDA_{ij} represent positive and negative distance of i th alternative from average solution, respectively.

Step 5: Determine the weighted sum of PDA and NDA for every alternative is determined using Eqs. (12) and (13):

$$SP_i = \sum_{j=1}^m w_j PDA_{ij} \tag{12}$$

$$SN_i = \sum_{j=1}^m w_j NDA_{ij} \tag{13}$$

where w_j is the weight of j th criterion.

Step 6: SP and SN values for all alternative is normalized as follows:

$$NSP_i = \frac{SP_i}{\max_i(SP_i)} \tag{14}$$

$$NSN_i = 1 - \frac{SN_i}{\max_i(SN_i)} \tag{15}$$

Step 7: Appraisal score is determined for all alternative using Eq. (16) and ranked according to the decreasing values of appraisal score. The alternative with highest appraisal score is the best choice among the candidate alternatives:

$$AS_i = \frac{1}{2}(NSP_i + NSN_i) \tag{16}$$

where $0 \leq AS_i \leq 1$.

4 Results and Discussion

Specimens are machined according to L_9 orthogonal array of Taguchi’s experimental design shown in Table 3. The experimental results are then analysed using Minitab 18 software. The experimental results for the local circularity error, thrust and machining time are listed in Table 3.

Table 4 Weighted sum of PDA and NDA, normalized values of SP and SN, appraisal score and rank of all output responses

Expt. No.	SP	SN	NSP	NSN	AS	Rank
1	0.2744	0.1130	0.4732	0.8705	0.6719	4
2	0.1758	0.1350	0.3031	0.8454	0.5742	5
3	0.0164	0.0570	0.0283	0.9347	0.4815	6
4	0.0000	0.0556	0.0000	0.9363	0.4681	7
5	0.5799	0.0175	1.0000	0.9799	0.9900	1
6	0.0387	0.6424	0.0668	0.2640	0.1654	8
7	0.5443	0.0000	0.9386	0.6568	0.7977	2
8	0.0836	0.0061	0.5568	0.9931	0.7749	3
9	0.1304	0.8728	0.1555	0.0000	0.0777	9

The first step determines creating the normalized decision-making matrix and determines the average solution according to all criteria using Eqs. (4) and (5). The further step is to generate the positive distance from average (PDA) and the negative distance from average (NDA) matrixes conferring to type of criteria, i.e. benefit criteria in this case using Eqs. (10) and (11). Determination of the weighted sum of PDA and NDA for all alternatives was done in next step using Eqs. (12) and (13). After finding weighted sum of PDA and NDA, normalization is done using equation. Finally, the appraisal score (AS) was calculated for all alternative using Eq. (16) and ranking was done according to the decreasing values shown in Table 4.

From total relative significance values of alternatives, it was detected that investigational results obtained in experiment no. 5 is the best result according to the ranking.

Now, the appraisal score (AS) calculated for all alternative was used to plot mean effect for SN ratios. Based on this study, one can select a mixture of the levels that provide the smaller average response. In Fig. 2, the combination of A1 B2 C3 shows the smallest value of the main effect plot of factor A, B and C, respectively. Therefore, A1 B2 C1, i.e. feed of 20 mm/min, rotational speed of 2500 rpm and point angle of 130° are the optimum input parameter arrangement for micro-drilling operation on PMMA.

Table 5 represents the ANOVA results for the local circularity error, thrust and machining time using considered values from total relative importance of substitutes of Table 4. In Table 5, factor B, rotational speed with 64.43 % of contribution, is the most significant controlled parameters for the CNC micro-drilling followed by factor C, point angle with 25.26 % and factor A, feed with 5.66 % of contribution if the minimization of local circularity error, thrust and machining time are simultaneously considered. $S = 3.1229$, $R\text{-sq} = 95.35 \%$, $R\text{-sq(adj)} = 81.39 \%$.

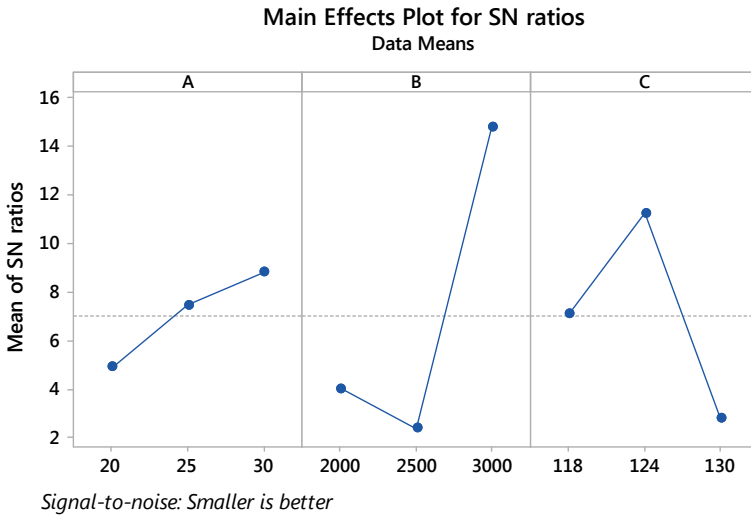


Fig. 2 Main effect plot for SN ratios

Table 5 ANOVA for AS

Source	DOF	Adj SS	Adj MS	F-test	P-test	% contribution
A	2	23.73	11.865	1.22	0.451	5.66
B	2	270.07	135.035	13.85	0.067	64.43
C	2	105.88	52.939	5.43	0.156	25.26
Residual error	2	19.50	9.752			4.65
Total	8	419.18				

5 Confirmation Experiment

The total relative importance of alternatives is valued using equation (17) [11].

$$\mu_{\text{predicted}} = a_{2m} + b_{1m} - 3\mu_{\text{mean}} \tag{17}$$

where a_{2m} and b_{1m} are the individual mean of total relative importance of alternatives with optimum level of each parameters and μ_{mean} is the overall mean of total relative importance of alternatives. The predicted mean ($\mu_{\text{predicted}}$) at optimal setting is found to be 1.000. Table 6 shows initial and optimal level performance.

Table 6 Initial and optimal level performance

Optimal setting	Predicted S/N ratio	Experimental S/N ratio
A1 B2 C3	1.0000	0.9906

6 Conclusion

The properties of input parameters, i.e. feed, rotational speed and point angle, experimentally studied throughout micro-drilling of PMMA using CNC drilling process. EDAS methods based on Taguchi's experimental design table were employed to improve the micro-drilling process parameters. Based on the outcomes of the present study, the following inferences are shown:

1. The optimal setting of input parameters for turning using EDAS method are shown in Table 7.
2. Based on the ANOVA result, it is found that rotational speed is the most significant controlled parameters for the CNC micro-drilling followed point angle and feed with if the minimization of local circularity error, thrust and machining time is simultaneously considered. Figure 3 shows the SEM image of micro-hole at feed 25 mm/min, speed 2500 rpm, point angle 130°, and Fig. 4 shows the SEM image of micro-hole at feed 20 mm/min, speed 2500 rpm and point angle 130°.
3. Confirmatory experiment was done at feed rate of 20 mm/min, spindle speed of 2500 rpm and point angle of 130° which mollifies the actual necessities of the determined ideal settings in micro-drilling operation of PMMA.

Table 7 Initial and optimal level performance

Algorithm	A (mm/min)	B (rpm)	C (°)
EDAS method	25	2500	130
Taguchi-EDAS method	20	2500	130

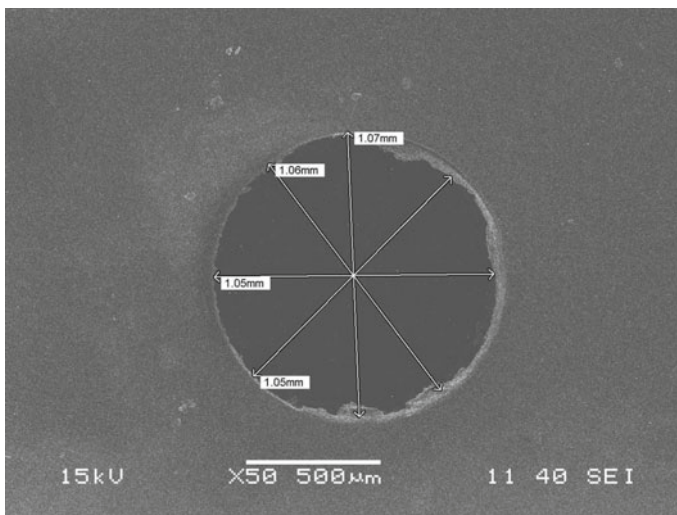


Fig. 3 SEM image of micro-hole at feed 25 mm/min, speed 2500 rpm and point angle 130°

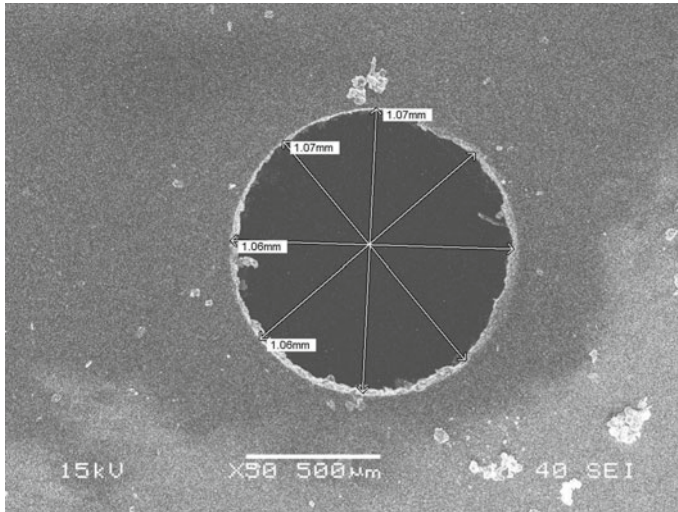


Fig. 4 SEM image of micro-hole at feed 20 mm/min, speed 2500 rpm and point angle 130°

Acknowledgements This research work is jointly supported by National Institute of Technology, Rourkela, India and Government College of Engineering, Kalahandi, Bhawanipatna, Odisha.

References

1. Bagal DK (2012) Experimental investigation and modelling micro drilling operation of aerospace material. Dissertation. National Institute of Technology, Rourkela
2. Jeet S, Barua A, Bagal DK, Pattanaik AK, Agrawal PK, Panda SN (2019) Multi-parametric optimization during drilling of aerospace alloy (UNS A97068) using hybrid RSM-GRA, GA and SA. *Int J Manag Technol Eng IX(II)*:2501–2509
3. Singh G, Jain V, Gupta D, Ghai A (2016) Optimization of process parameters for drilled hole quality characteristics during cortical bone drilling using Taguchi method. *J Mech Behav Biomed Mater* 62:355–365
4. Balaji M, Murthy BSN, Rao NM (2016) Optimization of cutting parameters in drilling of AISI 304 stainless steel using Taguchi and ANOVA. *Proc Technol* 25:1106–1113
5. Manikandan N, Kumaran S, Sathiyarayanan C (2016) Multiple performance optimization of electrochemical drilling of Inconel 625 using Taguchi based grey relational analysis. *Eng Sci Technol Int J* 20:662–667
6. Chaudhari AB, Chaudhary V, Gohil P, Patel K (2016) Investigation of delamination factor in high speed drilling on chopped GFRP using ANFIS. *Proc Technol* 23:272–279
7. Chakraborty S, Bhattacharyya B, Diyaley S (2019) Applications of optimization techniques for parametric analysis of non-traditional machining processes: a review. *Manag Sci Lett* 9(3):467–494
8. Prashanth P, Hiremath SS (2019) Multi-response optimization using grey relation analysis in mechanical micro drilling (MMD) of Titanium alloy—(CP–Ti) grade II. *Advances in manufacturing technology. Lecture notes in mechanical engineering*, pp 421–431

9. Naik B, Paul S, Barua A, Jeet S, Bagal DK (2019) Fabrication and strength analysis of hybrid jute-glass-silk fiber polymer composites based on hybrid Taguchi-WASPAS method. *Int J Manag Technol Eng IX(IV)*:3472–3479
10. Acharya KK, Murmu KK, Bagal DK, Pattanaik AK (2019) Optimization of the process parameters of dissimilar welded joints in FSSW welding process of aluminum alloy with copper alloy using Taguchi optimization technique. *Int J Appl Eng Res 14(13)*:54–60
11. Barua A, Jeet S, Bagal DK, Satapathy P, Agrawal PK (2019) Evaluation of Mechanical Behavior of Hybrid Natural Fiber Reinforced Nano SiC Particles Composite Using Hybrid Taguchi COCOSO Method. *Int J Innov Technol Explor Eng 8(10)*:3341–3345
12. Ghorabae MK, Zavadskas EK, Olfat L, Turskis Z (2015) Multi-criteria inventory classification using a new method of evaluation based on distance from average solution (EDAS). *Informatica 26(3)*:435–451

Multi-parametric Optimization of Wire-EDM of Inconel 718 Super Alloy Using Taguchi-Coupled WASPAS Method



Dilip Kumar Bagal, Santanu Kumar Mahapatra, Abhishek Barua, Siddharth Jeet, Ajit Kumar Pattanaik, and Dulu Patnaik

Abstract Wire electrical discharge machining is a multi-purpose method for fabrication of products with complex geometry which requires accuracy and precision during operation. Inconel 718 is a super alloy, due to its tremendous mechanical and chemical properties at preeminent temperatures which also make it challenging for WEDM operation on it. In this investigation, the influence of WEDM process constraints on kerf width, material removal rate, and tool wear rate of Inconel 718 super alloy was studied. Sixteen experimental runs were carried out based on Taguchi method and weighted aggregated sum product assessment method was used for finding an optimum parameter setting. From the ANOVA results, pulse ON time was found out as most momentous factor for controlling of tool wear rate, kerf width, and material removal rate.

Keywords WEDM · Inconel 718 · Taguchi method · WASPAS method

1 Introduction

Inconel 718, a nickel-based super alloy is extensively used in nuclear, aerospace, and chemical industries for its brilliant mechanical and chemical properties at raised temperatures. Due to poor thermal conductivity, high hardness, high toughness, and extremely high work hardening behaviour, machining difficulties of this alloy seems a challenge. Also, it comprises highly abrasive carbide particles which have a tendency to stick on the surface of tool which results in lower surface finish. Hence, machining

D. K. Bagal (✉) · S. K. Mahapatra · A. K. Pattanaik
Department of Mechanical Engineering, Government College of Engineering, Kalahandi,
Bhawanipatna, Odisha, India
e-mail: dilipbagal90@gmail.com

A. Barua · S. Jeet
Department of Mechanical Engineering, Centre for Advanced Post Graduate Studies, BPUT,
Rourkela, Odisha, India

D. Patnaik
Department of Electrical Engineering, Government College of Engineering, Kalahandi,
Bhawanipatna, Odisha, India

and machinability traits of Inconel alloy have become a prime research outline currently. Non-traditional machining techniques such as wire electrical discharge machining have the prospective which can be used for precise machining of Inconel 718. Though, it is significant for selection of best arrangement of WEDM constraints for the achievement of optimum machining enactment [1–9].

In this contemporary work, the impact of WEDM process constraints on tool wear rate, material removal rate, and kerf width of Inconel 718 super alloy was studied. Taguchi's experimental design was used for planning experiments and optimization of the machining parameters has been done using multi response optimization techniques, i.e., weighted aggregated sum product assessment (WASPAS) to find optimum results.

2 Experimental Methodology

Inconel 718 was chosen as workpiece material. Workpiece specimen of rectangular-shaped plate with dimension of 200 mm × 50 mm × 5 mm was used where 16 different cuts of 30 mm length were done according to the experimental design. Table 1 shows the composition of Inconel 718. The experimental studies were performed on Electronica Group Ecocut travelling WEDM machine [10]. A brass alloy wire was used in this Wire-EDM operation of 0.25 mm diameter. By utilizing this machine, workpiece can be cut in accord with fixed locus. Voltage, discharge current, pulse-on time and wire tension with different levels were taken as process parameters in this experimental investigation. Throughout the experiments, frequency setting was retained fix. The stereo-zoom microscope was used for measuring kerf width and tool wear rate was measured using scanning electron microscope. Figure 1 shows the specimen after machining. The input parameters for WEDM operation is shown in Table 2.

Table 1 Inconel 718 super alloy's chemical composition

Element	% Content	Element	% Content
Carbon, C	0.08	Titanium, Ti	0.65–1.15
Phosphorus, P	0.015	Aluminum, Al	0.20–0.80
Sulfur, S	0.015	Cobalt, Co	1.00
Silicon, Si	0.35	Manganese, Mn	0.35
Chromium, Cr	17–21	Boron, B	0.006
Nickel, Ni	50–55	Copper, Cu	0.30
Molybdenum, Mo	2.8–3.3	Tantalum, T	0.05
Columbium, Nb	4.75–5.50		

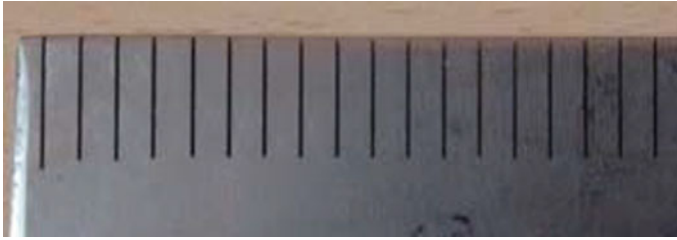


Fig. 1 Workpiece specimen after machining

Table 2 Input parameters

Factors	Symbol	Level 1	Level 2	Level 3	Level 4
Voltage (V)	<i>A</i>	40	50	60	70
Current (A)	<i>B</i>	6	8	10	12
Wire tension (N)	<i>D</i>	7	8	9	10
Pulse on time (<i>T</i> -on) (μs)	<i>C</i>	80	90	100	110

2.1 Calculation of Weights Between Norms by Pair-Wise Comparison

By means of geometric mean of AHP method, relative consequence of output responses was calculated. Saaty’s nine-point preference scale was taken for calculation of pair-wise comparison matrix as shown in Table 3. Output response weights were calculated by using following equations [11, 12]

$$GM_i = \left(\prod_{j=1}^n b_{ij} \right)^{1/n} \tag{1}$$

$$w_j = GM_i / \sum_{j=1}^n GM_i \tag{2}$$

Output response weights were obtained as 0.60 for MRR, 0.13 for kerf width, and 0.27 for tool wear rate after the consistency check.

Table 3 Pair-wise comparison table between norms

	MRR	Kerf width	Tool wear rate
MRR	1	3	3
Kerf width	0.3	1	0.3
Tool wear rate	0.3	3	1

2.2 *Weighted Aggregated Sum Product Assessment (WASPAS) Method*

The chief technique of WASPAS method for solving multi-criteria decision-making problems are [12, 13].

Step 1: Initial decision matrix is set.

Step 2: Decision matrix normalization using Eqs. (3) and (4) for maximization and minimization criteria, respectively:

$$\bar{x}_{ij} = x_{ij} / \max_i x_{ij} \quad (3)$$

$$\bar{x}_{ij} = \min_i x_{ij} / x_{ij} \quad (4)$$

where x_{ij} is the assessment value of i th alternate with respect to j th measure.

Step 3: Calculation of total comparative significance of i th alternate, based on weighted sum method (WSM) using Eq. (5):

$$Q_i^{(1)} = \sum_{j=1}^n \bar{x}_{ij} \cdot w_j \quad (5)$$

Step 4: Calculation of total comparative significance of i th alternate, based on weighted product method (WPM) using Eq. (6):

$$Q_i^{(2)} = \prod_{j=1}^n \bar{x}_{ij}^{w_j} \quad (6)$$

Step 5: Calculation of total comparative significance of alternatives is done using Eq. (7) and ranked from higher value to lower value [12]:

$$Q_i = \lambda \cdot Q_i^{(1)} + (1 - \lambda) \cdot Q_i^{(2)} \quad (7)$$

3 Results and Discussion

Specimens are machined according to L16 orthogonal array of Taguchi's experimental design shown in Table 4. Samples are cut into preferred size using the Wire-EDM process. The experimental results for the Kerf width, material removal rate (MRR), and tool wear rate (TWR) for Inconel 718 are shown in Table 4.

Since semantic terms, used to express the responses, have already been converted into crisp (real) values, normalization of the decision matrix by applying Eq. (4) for MRR, kerf width, and TWR was done with respected to their minimization. Consequently, total relative significance of alternatives based on WSM and WPM are designed by using Eqs. (5) and (6), respectively. Lastly, combined condition of optimality of WASPAS method is calculated by using Eq. (7). Table 5 shows the computational particulars of all alternatives of Inconel 718 using WASPAS method with λ value of 0.5.

From total relative significance values of alternatives, it was detected that investigational results obtained in experiment no. 7 is the best result according to the ranking. Now, the total relative importance of alternatives was taken for plotting mean effect for *SN* ratios with the help of Minitab 18 software. Based on this study, selection of mixture of the levels will be done in accordance to the smaller average response. In Fig. 2, the combination of A3 B3 C4 D1 displays the smallest value of the *SN* ratio plot for factors A, B, C, D, respectively, for machining of Inconel 718.

Table 4 L16 orthogonal array design for experimental runs and results

Expt. number	A	B	C	D	MRR (g/min)	Kerf width (mm)	TWR (g/min ³)
1	40	6	7	80	0.0061	0.2428	3.83
2	40	8	8	90	0.0080	0.2534	2.70
3	40	10	9	100	0.0120	0.2455	2.66
4	40	12	10	110	0.0189	0.2602	2.21
5	50	6	8	100	0.0125	0.2534	3.16
6	50	8	7	110	0.0195	0.2618	5.01
7	50	10	10	80	0.0032	0.2385	4.76
8	50	12	9	90	0.0093	0.2546	5.13
9	60	6	9	110	0.0210	0.2573	2.88
10	60	8	10	100	0.0158	0.2690	1.79
11	60	10	7	90	0.0073	0.2473	2.68
12	60	12	8	80	0.0040	0.2593	3.46
13	70	6	10	90	0.0111	0.2350	3.15
14	70	8	9	80	0.0080	0.2409	6.25
15	70	10	8	110	0.0154	0.2353	3.53
16	70	12	7	100	0.0145	0.2527	3.96

Table 5 Computational particulars of all alternatives

Expt. number	MRR	Kerf width	TWR	$Q_i^{(1)}$	$Q_i^{(2)}$	Q_i	Rank
1	0.5257	0.9678	0.4674	0.5674	0.5513	0.5594	3
2	0.4019	0.9275	0.6642	0.5410	0.5131	0.5271	5
3	0.2669	0.9571	0.6729	0.4663	0.4045	0.4354	7
4	0.1696	0.9032	0.8118	0.4384	0.3218	0.3801	12
5	0.2568	0.9274	0.5674	0.4278	0.3758	0.4018	11
6	0.1642	0.8975	0.3573	0.3117	0.2526	0.2821	16
7	1.0119	0.9855	0.3764	0.8369	0.7721	0.8045	1
8	0.3445	0.9230	0.3489	0.4209	0.3930	0.4070	10
9	0.1527	0.9135	0.6226	0.3784	0.2815	0.3300	15
10	0.2027	0.8736	1.0000	0.5052	0.3771	0.4411	6
11	0.4406	0.9503	0.6692	0.5686	0.5451	0.5568	4
12	0.8025	0.9062	0.5173	0.7390	0.7241	0.7316	2
13	0.2886	0.9998	0.5683	0.4566	0.4073	0.4319	8
14	0.4019	0.9756	0.2866	0.4453	0.4117	0.4285	9
15	0.2080	0.9987	0.5071	0.3915	0.3244	0.3580	13
16	0.2213	0.9301	0.4526	0.3759	0.3235	0.3497	14

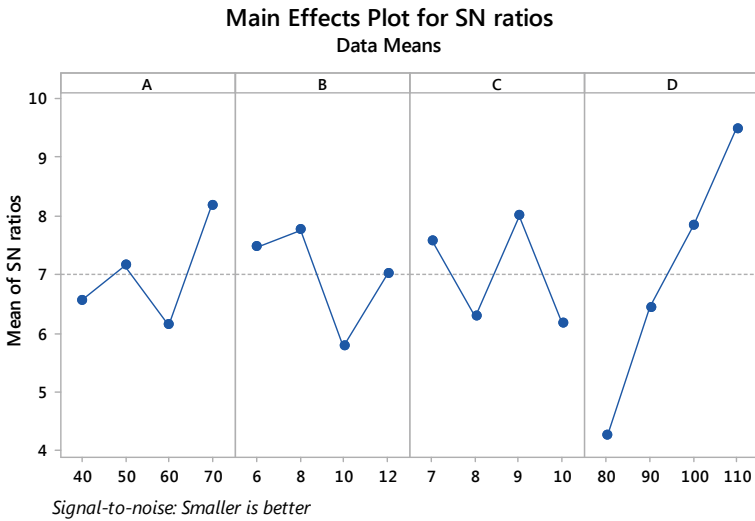


Fig. 2 SN ratio plot with factors and their levels for Inconel 718

Table 6 Response table for *SN* ratios for Inconel 718

Level	A	B	C	D
1	6.558	7.472	7.562	4.253
2	7.152	7.756	6.280	6.437
3	6.135	5.780	8.006	7.844
4	8.176	7.013	6.173	9.487
Delta	2.041	1.975	1.833	5.234
Rank	2	3	4	1

Table 7 ANOVA for *SN* ratios for Inconel 718

Source	DOF	Adj SS	Adj MS	F-test	P-test	% Contribution
A	3	9.395	3.1317	8.11	0.060	10.58
B	3	9.126	3.0419	7.88	0.062	10.27
C	3	10.118	3.3727	8.73	0.054	11.39
D	3	59.035	19.6784	50.95	0.005	66.46
Residual error	3	1.159	0.3863			1.30
Total	15	88.833				

Therefore, *A3 B3 C4 D1* is the optimal parameter combination for Wire-EDM of Inconel 718 alloy (Table 6).

3.1 Most Significant Factor

Table 7 shows the ANOVA for the MRR, kerf width, and TWR using the total relative importance of alternatives values of Table 5. Conferring to Table 7, factor *D*, pulse on time (*T*-on) with 66.46% of contribution, is the most substantial parameter for the machining followed by the factor *C*, wire tension with 11.39%, factor *A*, voltage with 10.58%, and factor *C*, current with 10.27% of contribution if the if the minimization of MRR, kerf width, and tool wear rate are simultaneously considered for Inconel 718.

$$S = 0.6215, R\text{-Sq} = 98.7\%, R\text{-Sq}(\text{adj}) = 93.48\%.$$

3.2 Confirmation Experiment

The total relative importance of alternatives is valued using Eq. (8) [14].

$$\mu_{\text{predicted}} = a_{2m} + b_{1m} - 3\mu_{\text{mean}} \quad (8)$$

Table 8 Initial- and optimal-level performance for Inconel 718

Optimal setting for WEDM	Predicted <i>S/N</i> ratio	Experimental <i>S/N</i> ratio
A2 B2 C4 D1	0.8067	0.8008

where a_{2m} and b_{1m} are the individual mean of total relative importance of alternatives with optimum level of each parameters and μ_{mean} is the overall mean of total relative importance of alternatives [9–11]. The predicted mean ($\mu_{\text{predicted}}$) at optimal setting is found to be 0.8067. Table 8 shows initial-level performance as well as optimal-level performance.

4 Conclusions

In this research, the machining investigation of Inconel 718 was done using Wire-EDM process to study the effect of four different process parameters (i.e., current, voltage, pulse time on, and wire tension) on three output responses (i.e., MRR, kerf width, and tool wear rate). The process parameters are optimized using Taguchi-based WASPAS method. Based on experiment studies carried out for picking optimum process parameters for Wire-EDM, some of the important conclusions are as follows:

1. The optimal levels of process parameters for Wire-EDM of Inconel 718 using Taguchi-based WASPAS method was found out to be current 60 V, voltage 10 A, wire tension 10 N, and pulse on time (T -on) 110 μs .
2. From the analysis of variance (ANOVA), pulse on time (T -on) is the important controlled parameter for machining trailed by wire tension, voltage, and current if the minimization of MRR, kerf width, and tool wear rate are simultaneously considered for Inconel 718.
3. The equation for forecasting multi-response performance index was confirmed by conducting confirmation experiment.

Thus, this study opens up further scope of optimization of the Wire-EDM characteristics with a larger number of parameters, along with their impacts on machining of composites for attaining better quality characteristics more rapidly.

Acknowledgements This research work is jointly supported by National Institute of Technology, Rourkela, India and Government College of Engineering Kalahandi, Bhawanipatna, Odisha, India.

References

1. Kumar A, Bagal DK, Maity KP (2014) Numerical modeling of wire electrical discharge machining of super alloy Inconel 718. *Procedia Eng* 97:1512–1523
2. Jadam T, Datta S, Mahapatra SS (2018) Electro-discharge machining of Inconel 718 using square cross sectioned copper tool electrode: studies on topography and metallurgical features of the EDMed work surface. *Mater Today Proc* 5:4847–4854
3. Rahul NA, Abhishek K, Datta S, Biswal BB, Mahapatra SS (2017) Machining performance optimisation during EDM of Inconel 718: a case experimental investigation. *Int J Prod Qual Manag* 21(4):460–489
4. Rahul, Datta S, Biswal BB, Mahapatra SS (2017) A novel satisfaction function and distance-based approach for machining performance optimization during electro-discharge machining on super alloy Inconel 718. *Arab J Sci Eng* 42(5):1999–2020
5. Rahul, Srivastava A, Mishra DK, Chatterjee S, Datta S, Biswal BB, Mahapatra SS (2018) Multi-response optimization during electro-discharge machining of super alloy Inconel 718: application of PCA-TOPSIS. *Mater Today Proc* 5:4269–4276
6. Rahul, Datta S, Biswal BB, Mahapatra SS (2019) Machinability analysis of Inconel 601, 625, 718 and 825 during electro-discharge machining: on evaluation of optimal parameters setting. *Measurement* 137:382–400
7. Kumar A, Abhishek K (2018) Influence of process parameters on MRR, kerf width and surface roughness during WEDM on Inconel 718: performance analysis of electrode tool material. *Int J Ind Syst Eng* 30(3):298–315
8. Rahul, Datta S, Masanta M, Biswal BB, Mahapatra SS (2018) Analysis on surface characteristics of electro-discharge machined Inconel 718. *Int J Mater Prod Technol* 56(1/2):135–168
9. Rahul, Datta S, Biswal B, Mahapatra SS (2018) Optimization of electro-discharge machining responses of super alloy Inconel 718: use of satisfaction function approach combined with Taguchi philosophy. *Mater Today Proc* 5:4376–4383
10. Bagal DK, Barua A, Jeet S, Satapathy P, Patnaik D (2019) MCDM optimization of parameters for wire-EDM machined stainless steel using hybrid RSM-TOPSIS, genetic algorithm and simulated annealing. *Int J Eng Adv Technol* 9(1):366–371
11. Barua A, Jeet S, Bagal DK, Satapathy P, Agrawal PK (2019) Evaluation of mechanical behavior of hybrid natural fiber reinforced nano SiC particles composite using hybrid Taguchi COCOSO method. *Int J Innov Technol Explor Eng* 8(10):3341–3345
12. Zavadskas EK, Turskis Z, Antucheviciene J, Zakarevicius A (2012) Optimization of weighted aggregated sum product assessment. *Electron Electr Eng* 122:3–6
13. Naik B, Paul S, Barua A, Jeet S, Bagal DK (2019) Fabrication and strength analysis of hybrid jute-glass-silk fiber polymer composites based on hybrid Taguchi-WASPAS method. *Int J Manag Technol Eng IX(IV):3472–3479*
14. Barua A, Jeet S, Cherkia H, Bagal DK, Sahoo BB (2019) Parametric optimization of FDM processed part for improving surface finish using MOORA technique and desirability function analysis. *Int J Appl Eng Res* 14(13):1–7

Effect of Graphene Oxide and Temperature on Dielectric Relaxation Behavior of Poly(Vinyl Alcohol)-Based Nanocomposite



Ganeswar Sahu, Bibhu Prasad Sahoo, and Jasaswini Tripathy

Abstract Development of multifunctional polymer nanocomposites with high dielectric properties is highly desirable for various dielectric applications. The present study explores the effect of graphene oxide (GO) loading and temperature on dielectric characteristics of poly(vinyl alcohol) (PVA) and GO-based conductive nanocomposites films fabricated using solution casting technique. The microstructure morphology of the films has been studied using scanning electron microscopy (SEM). The synthesis of GO has been confirmed using TEM. The variation of GO loading and temperature influenced the dielectric properties such as permittivity (ϵ'), real and imaginary impedance (Z' and Z''), AC conductivity (σ_{ac}) of PVA/GO nanocomposite films. These properties were studied in the frequency range of (1–10⁶ Hz) and temperature (25–150 °C). It has been observed that ϵ' and σ_{ac} increased while the impedance decreased with increase in GO loading and temperature. The significant decrease in the area under the semicircle in the Nyquist plot with increase in GO loading confirmed the charge storing ability of the developed nanocomposites.

Keywords Poly(vinyl alcohol) · Graphene oxide · Dielectric properties · Nyquist plot

1 Introduction

Recently, fabrication of composite materials with high dielectric constant is highly desirable due to their wide applications in dielectrics, micro-electro mechanical devices, energy storage devices [1–3]. One of the fascinating ways to realize these applications is by dispersing conducting fillers into polymeric matrix [4, 5].

Conducting fillers based polymer nanocomposites possess excellent dielectric properties [6–8]. They draw extensive interest due to their flexibility as well as easy processing. Even very low amount of conductive filler can contribute toward high dielectric properties [9, 10]. The conductive nanofillers used for fabrication

G. Sahu · B. P. Sahoo · J. Tripathy (✉)
School of Applied Sciences (Chemistry), Kalinga Institute of Industrial Technology (KIIT),
Deemed to be University, Campus-3, Patia, Bhubaneswar, Odisha 751024, India
e-mail: jasaswinitripathy@gmail.com

© Springer Nature Singapore Pte Ltd. 2021

P. Pant et al. (eds.), *Advances in Mechanical Processing and Design*, Lecture Notes
in Mechanical Engineering, https://doi.org/10.1007/978-981-15-7779-6_41

469

of polymer nanocomposites are metal nanoparticles [9, 11], carbon nanotube [12, 13], acetylene black [10], etc. These nanofillers enhance the dielectric permittivity of the polymer [14, 15]. Incorporation of fillers increases capacitance by inducing interfacial or space charge polarization between filler and polymer [16, 17]. Among the various reported nanofillers, graphene oxide (GO) is considered to be excellent filler for development of polymer nanocomposites due to its high dielectric constant [18, 19]. It possesses very good electrical and thermal conductivity with enhanced mechanical properties [20]. The graphene-based polymer nanocomposites exhibit superior mechanical properties as compared to the polymer nanocomposite films fabricated with other nanofillers [21, 22]. The interfacial bonding between GO and polymeric matrix allows it to be compatible with many polymers. Liang et al. [21] reported GO- and PVA-based composites with enhanced mechanical properties due to molecular level dispersion of GO. Deshmukh et al. [23] showed that fully exfoliated GO sheets in PSS/PVA blend nanocomposite exhibited enhanced dielectric properties.

PVA is a synthetic polymer with good dielectric strength [23]. PVA finds potential applications in coating materials, transparent electrode materials, optoelectronic devices, etc. [24, 25]. The abundant amount of hydroxyl groups present on PVA backbone prevents the agglomerations of nanofillers [26].

The present study shows the fabrication of PVA/GO conductive nanocomposites using solution casting technique with superior dielectric properties. An effort has been made to study the effect of GO loading as well as temperature variation on ϵ' , Z' , Z'' , σ_{ac} and Nyquist plot. The developed nanocomposite film may have a potential application in developing charge storing devices.

2 Experimental

2.1 Materials

The chemicals used in the present work were of analytical grade. PVA used here for the preparation of nanocomposites was procured from Sigma-Aldrich. H_2SO_4 , $NaNO_3$, $KMnO_4$ and H_2O_2 were supplied by S. D. Fine Chemicals, Mumbai, India.

2.2 Synthesis of Graphene Oxide (GO)

The nano-sized GO was successfully prepared using modified Hummers's method [27]. A 2 g of graphite powder was added to 1 g of $NaNO_3$ and 46 ml of ice-cooled concentrated H_2SO_4 followed by slow addition of $KMnO_4$. The resulted suspension was stirred for 2 h with slow addition of 92 ml of DI water at 98 °C. Excess $KMnO_4$ and

MnO₂ was removed by addition of 30% hydrogen peroxide. The obtained suspension was washed with HCl and DI water to attain pH 7.

2.3 Preparation of PVA/GO Film

A 2.5 gm of PVA was dissolved in 50 ml of DI water with stirring for 1 h at 80 °C. A solution of GO was prepared by sonicating a definite weight in 20 ml of DI water for 2 h. Thereafter, the dispersed GO was mixed with PVA solution and stirred for 4 h. The mixed solution was poured into the petri dish and dried to get the film of PVA/GO. Composite films with different GO content (1, 2, 3 wt%) were obtained by adding GO suspension to PVA solution. The samples were termed as PVA1, PVA2, and PVA3 for 1, 2, 3 wt% GO loading, respectively.

2.4 Characterization

2.4.1 Morphological Analysis

The microstructure analysis of the synthesized GO has been characterized through HRTEM using jem 2100, JEOL Limited, Japan. The surface morphology has been analyzed using FESEM using SUPRA 40, Carlo Zeiss, Germany.

2.4.2 Dielectric Relaxation Spectroscopy

The dielectric properties such as ϵ' , σ_{ac} , Z' , Z'' of PVA/GO conductive nanocomposites have been analyzed using phase-sensitive multimeter (PSM1735N4L) in a wide range of frequency (1–10⁶ Hz) and temperature (25–150 °C) in an external alternating electric field. Various formulae have been used for the calculation of different dielectric properties. The σ_{ac} was calculated using the equation

$$\sigma_{ac} = \omega \epsilon' \epsilon_0 \tan \delta \quad (1)$$

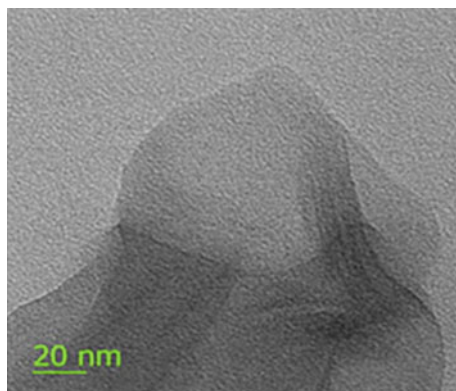
where ω is the angular frequency of the applied external electric field.

The ϵ' and the absolute permittivity (ϵ_o) are calculated by using the relation

$$\epsilon' = C_p / C_o \quad (2)$$

Here, the C_p and C_o are the capacitance of the dielectric material and vacuum, respectively.

Fig. 1 HRTEM image of graphene oxide



3 Results and Discussion

3.1 *High-Resolution Transmission Electron Microscopy (HRTEM).*

The HRTEM microphotographs of the nanosized graphene oxide synthesized from graphite is shown in Fig. 1. The formation of graphene oxide sheets is confirmed from the micrograph.

3.2 *Field Emission Scanning Microscopy (FESEM)*

The FESEM micrographs show the surface morphology of pristine PVA- and GO-filled PVA nanocomposites films in Fig. 2a, b, respectively. The surface of PVA/GO film is rough as compared to PVA confirming the uniform dispersion of GO in PVA matrix.

3.3 *Dielectric Permittivity*

The effect of GO loading and temperature on the dielectric permittivity (ϵ') of nanocomposites films is shown in Fig. 3. PVA/GO exhibits higher ϵ' as compared to virgin PVA which further enhanced with increase in GO loading irrespective of the frequency of the field as shown in Fig. 3a. The results show fivefold increase in ϵ' for PVA3 in comparison to unfilled PVA which is mostly due to the increase in the polarizable charge particles, free electrons and functional groups in the system with addition of GO [28, 29]. Further, at lower frequency region, the improvement is

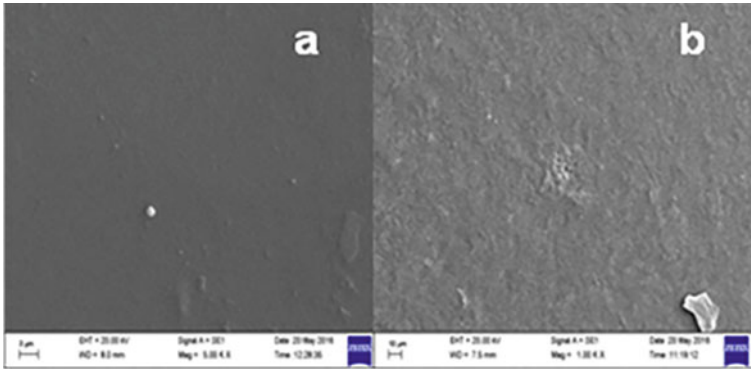


Fig. 2 FESEM image a PVA, b PVA/GO nanocomposite

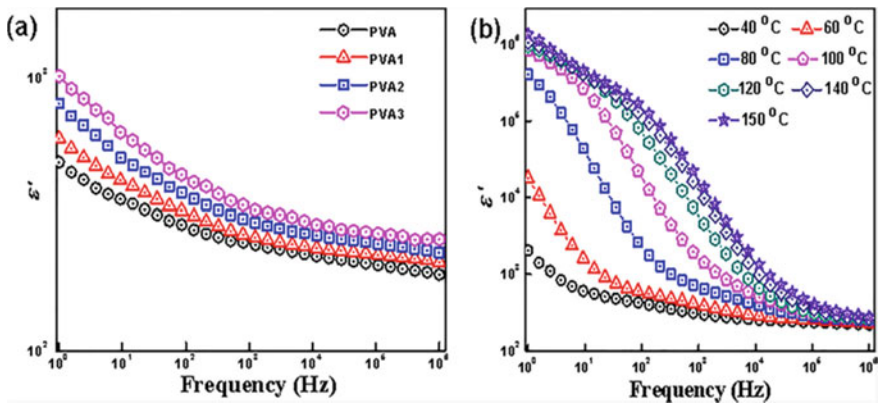


Fig. 3 Dielectric permittivity of PVA/GO nanocomposites as a function of a GO loading, b Temperature

more significant as the dipoles orient themselves in the direction of applied external electric field more easily. The effect of temperature on ϵ' is presented in Fig. 3b. The value of ϵ' is increased to eightfold at 40 °C in comparison to the room temperature. At 80 °C, the value of ϵ' is further improved which could be explained due to the increase in formation of more conductive channels in the bulk of the nanocomposites with increased temperature.

3.4 Electrical Conductivity (σ_{ac})

The effect of GO loading and temperature on the σ_{ac} of the PVA/GO conductive nanocomposites has been shown in Fig. 4a, b.

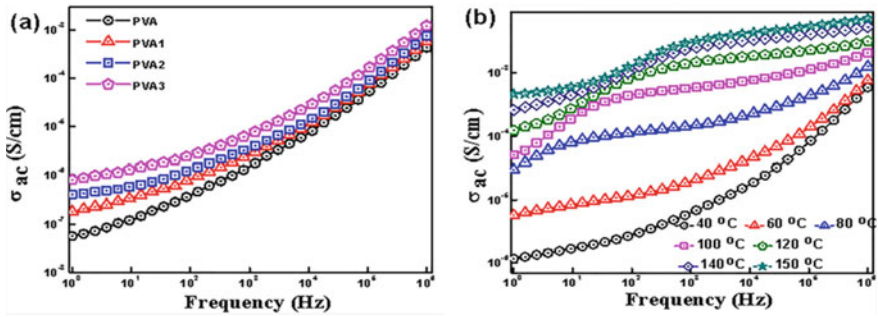


Fig. 4 AC conductivity of PVA/GO nanocomposites as a function of **a** GO loading **b** Temperature

The σ_{ac} is increased on incorporating GO into PVA matrix due to high conductivity and high surface area of GO nanofiller. The conductive phenomena in the heterogeneous conductive systems can be explained mainly by hopping and tunneling mode of conduction. Both the mechanisms become pronounced with the increase in incorporation of GO, and the conduction phenomenon is more facilitated due to the formation of crosslinked conductive networks in the insulating PVA matrix [30]. At higher temperature, increase in segmental mobility of the polymeric chain and redistribution of conductive GO phase due to breaking of the agglomerations facilitate the conduction phenomena resulting in enhancement in σ_{ac} of PVA3. In Fig. 4b, the exponential improvement in σ_{ac} is observed with increase in temperature [31]. However, the rate of improvement of σ_{ac} with increasing temperature becomes saturated at 140 °C, which may be due to the complete redistribution of the GO agglomerations at the bulk of the system.

3.5 Impedance Analysis

Impedance is the resistance offered to the movement of the charge carriers in the field direction, and this is a complex parameter containing the resistance part Z' (real part of impedance) and the reactance part Z'' (imaginary part of impedance), which are related to each other by the relation $Z^* = Z' + iZ''$.

The variation of Z' and Z'' with GO loading and temperature has been shown in Fig. 5.

The variation of Z' with frequency of applied field on varying GO loading for PVA/GO nanocomposites has been shown in Fig. 5a which represents a completely opposite trend as compared to σ_{ac} . Conductive GO facilitates the tunneling and hopping transport mechanism resulting in drastic reduction of Z' of the systems. The effect of temperature on Z' and Z'' for PVA3 nanocomposite is

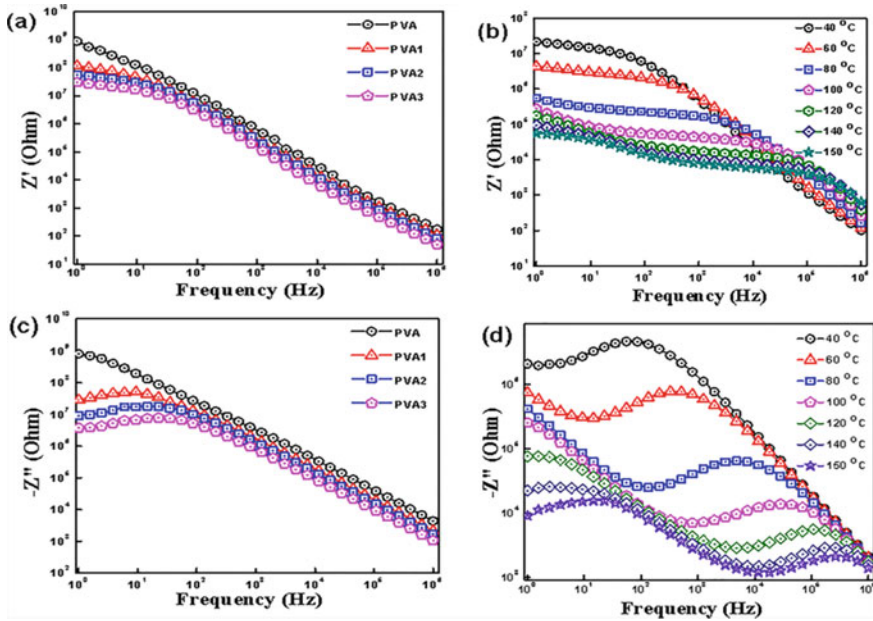


Fig. 5 a–d Impedance of PVA/GO nanocomposites as a function of GO loading and temperature

shown in Fig. 5b, c. The decreasing trend of Z' and Z'' with increasing temperature corresponds to the increase in conductive nature of the system. A characteristic peak is appeared which becomes more prominent with increasing temperature. With increase in temperature, shifting of peak position is observed (Fig. 5d) due to decrease of relaxation time which gives the idea of the dielectric loss factor at higher temperature [32].

3.6 Nyquist Plot

Nyquist plot is the plot between Z' and Z'' of a system which gives the idea about the capacitance and bulk resistance of a dielectric material. The Nyquist plot of neat PVA and PVA/GO nanocomposites showing characteristics semicircular plots is shown in Fig. 6a, b.

Interestingly, the area under the semicircular plots is getting decreased with increasing the GO loading. On extrapolating the semicircular plot toward X-axis, the bulk resistance can be calculated. The findings confirmed that the bulk resistance decreases with increase in GO loading. The diminished area under the semicircular plot is indicative of increase in capacitive nature of the system. It is mainly due to the increase in polarizable dipoles in the interface which is mainly due to the increase in GO loading level [33]. The effect of temperature on the Nyquist plot is shown in

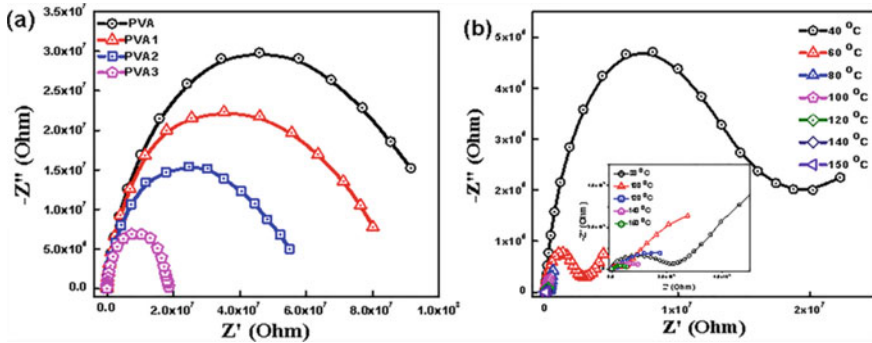


Fig. 6 Nyquist plot of PVA/GO nanocomposites as a function of **a** GO loading **b** temperature

Fig. 6b. At higher temperature, the Nyquist plot is semicircular followed by a spike and the area under the semicircle gives the idea about the increase in storage as well as the loss ability of the materials at higher temperature.

4 Conclusions

PVA/GO nanocomposite films were developed by solution casting method and characterized using FESEM and HRTEM. The dielectric properties of PVA/GO nanocomposites were studied with respect to GO loading at different frequencies at room temperature and high temperature (40–150 °C). The dielectric permittivity and AC conductivity increased with graphene oxide loading as well as temperature, whereas impedance (Z' and Z'') decreased. The developed nanocomposite films can be used for various dielectric applications.

References

1. Zhang QM, Li HF, Poh M, Xia F, Cheng ZY, Xu HS, Huang C (2002) An All-organic composite actuator material with a high dielectric constant. *Nature* 419:284–287
2. Hao X (2013) A review on the dielectric materials for high energy-storage application. *J Adv Dielect* 3:1330001–1330014
3. Kumar SK, Castro M, Saiter A, Delbreilh L, Feller JF, Thomas S, Grohens Y (2013) Development of poly(isobutylene-co-isoprene)/reduced graphene oxide nanocomposites for barrier, dielectric and sensing applications. *Mater Lett* 96:109–112
4. Xu HP, Dang ZM (2007) Electrical property and microstructure analysis of poly(vinylidene fluoride)-based composites with different conducting fillers. *Chem Phys Lett* 438:196–202
5. Zhang QM, Bharati V, Zhao X (1998) Giant electrostriction and relaxor ferroelectric behavior in electron-irradiated poly(vinylidene fluoride-trifluoroethylene) copolymer. *Science* 280:2101–2104

6. Kurahatti R, Surendranathan A, Kori S et al (2019) Scope of polymer/graphene nanocomposite in defense relevance: defense application of polymer/graphene. *J Def Sci* 60:551–563
7. Mandal A, Chakrabarty D (2014) Studies on the mechanical, thermal, morphological and barrier properties of nanocomposites based on poly(vinyl alcohol) and nanocellulose from sugarcane bagasse. *J Ind Eng Chem* 20:462–473
8. Denault J, Labrecque B (2014). Technology group on polymer nanocomposites—PNC-technology Canada. *Ind Mat Ins Nat Res Coun Canada* 751:159–178
9. Dang ZM, Lin YH, Nan CW (2003) Novel ferroelectric polymer composites with high dielectric constants. *Adv Mater* 15:1625–1629
10. Chen Q, Du PY, Jin L, Weng WJ, Han GR (2007) Percolative conductor/polymer composite films with significant dielectric properties. *Appl Phys Lett* 91:022912
11. Panda M, Srinivas PV, Thakur AK (2008) On the question of percolation threshold in polyvinylidene fluoride/nanocrystalline nickel composites. *Appl Phys Lett* 92:132905
12. Dang ZM, Wang L, Yin Y, Zhang Q, Lei QQ (2007) Giant dielectric permittivities in functionalized carbon-nanotube/electroactive-polymer nanocomposites. *Adv Mater* 19:852–857
13. Simoes R, Silva J, Vaia R, Sencadas V, Costa P, Gomes J, Lanceros-Mendez S (2009) Low percolation transitions in carbon nanotube networks dispersed in a polymer matrix: dielectric properties. *Nanotechnology* 20:035703
14. Lu JX, Wong CP (2008) Recent advances in high-*k* nanocomposite materials for embedded capacitor applications. *IEEE Trans Dielect Electr Insul* 15:1322–1328
15. Tanaka T (2005) Dielectric nanocomposites with insulating properties. *IEEE Trans Dielect Electr Insul* 12:914–928
16. Nan CW, Shen Y, Ma J (2010) Physical properties of composites near percolation. *Annu Rev Mater Res* 40:131–151
17. Barber P, Balasubramanian S et al (2009) Polymer composite and nanocomposite dielectric materials for pulse power energy storage. *Materials*. 2:1697–1733
18. Kumar SK, Suresh P, Srinath S, Pradip P (2015) A new single/few-layered graphene oxide with a high dielectric constant of 106: contribution of defects and functional groups. *RSC Adv* 5:14768–14779
19. Deshmukh K, Ahamed MB, Deshmukh RR et al (2016) Eco-friendly synthesis of graphene oxide reinforced hydroxypropyl methylcellulose/polyvinyl alcohol blend nanocomposites filled with zinc oxide nanoparticles for high-*k* capacitor applications. *Polym Plast Tech Eng* 55:1240–1253
20. Wang JG, Shen X, Wang B, Yao J, Park J (2009) Synthesis and characterisation of hydrophilic and organophilic graphene nanosheets. *Carbon* 47:1359–1364
21. Liang J, Huang Y, Zhang L et al (2009) Molecular-level dispersion of graphene into poly(vinyl alcohol) and effective reinforcement of their nanocomposites. *Adv Funct Mater* 19:2297–2302
22. Kim H, Macosko CW (2009) Processing-property relationships of polycarbonate/graphene composites. *Polymer* 50:3797–3809
23. Deshmukh K, Ahamed MB, Sadasivuni KK, Ponnamma D (2017) *Mater Chem Phys* 186:188–201
24. Rao JK, Raizada A, Ganguly D et al (2015) Investigation of structural and electrical properties of novel CuO–PVA nanocomposite films. *J Mater Sci* 50:7064
25. Aslam M, Kalyar MA et al (2018) Investigation of zinc oxide-loaded poly(vinyl alcohol) nanocomposite films in tailoring their structural, optical and mechanical properties. *J Electron Mater* 47:3912–3926
26. Haider MS, Muhammad Y, Wan MY, Ibtisam YA (2016) Influence of polymer matrix on nonlinear optical properties and optical limiting threshold of polymer-ZnO nanocomposites. *J Mater Sci Mater Elect* 27:9503–9513
27. Cote LJ, Kim F, Huang JX (2009) Langmyir-Blodgett assembly of graphite oxide single layers. *J Am Chem Soc* 131:1043–1049
28. Fritzsche J, Lorenz H, Kluppel M et al (2009) Advanced elastomer nano-composites based on CNT-hybrid filler systems. *Compos Sci Tech* 69:2135–2143

29. Li J, Kim JK (2007) Percolation threshold of conducting polymer composites containing 3D randomly distributed graphite nanoplatelets. *Compos Sci Tech* 67:2114–2120
30. Zhang W, Abbas A, Dehghani S, Blackburn RS (2007) Carbon based conductive polymer composites. *J Mater Sci* 42:3408
31. Patra A, Bisoyi DK (2011) Investigation of the electrical and mechanical properties of short sisal fiber-reinforced epoxy composite in correlation with structural parameters of the reinforced fiber. *J Mater Sci* 46:7206–7213
32. Mohanraj GT, Chaki TK, Chakraborty A, Khastgir D (2006) AC impedance analysis and EMI shielding effectiveness of conductive SBR composites. *Polym Eng Sci* 46:1342–1349
33. Sahoo BP, Naskar K, Tripathy DK (2012) Conductive carbon black-filled ethylene acrylic elastomer vulcanizates: physico-mechanical, thermal, and electrical properties. *J Mater Sci* 47:2421–2433

Effect of Sheet Temperature on Thickness Distribution of the Thermoformed Hemispherical Dome



Jeet P. Patil, Yogesh S. Gaikhe, Vilas Nandedkar, and Sushil Mishra

Abstract The thermoforming process is being used to process polymer sheets into numerous components for decades. A polymer sheet is first transformed into a rubbery state by the provision of heat and then deformed it into the required shape by the application of load (pressure, vacuum and contact thermoforming). Among all processing parameters, sheet temperature is the crucial one governing the material behaviour during the processing. However, many researchers have simplified the process by assuming no change in the thermal state of the process during the deformation. Since polymer behaviour is highly temperature-dependent, the assumption of isothermal deformation is not adequate. There is a need to investigate the effect of sheet temperature on process output. The presented study aims to study the effect of sheet temperature on the thickness distribution of the thermoformed product. Numerical investigations on contact thermoforming of transparent hemispherical domes of height 55 mm were simulated. Two processing conditions were simulated, one with constant material properties and other with temperature-dependent material properties. It was found that temperature dependency has a significant effect on the process output and must be incorporated for realistic results.

Keywords Thermoforming · PMMA · Thickness · Hyperelastic material

1 Introduction

The thermoforming process is being used to process polymer sheets into numerous components for decades. A polymer sheet is first transformed into a rubbery state by the provision of heat and then deformed it into the required shape by the application of load [1]. Depending upon the loading applied, the process is divided into the

J. P. Patil (✉) · V. Nandedkar
Department of Production Engineering, S. G. G. S. I. E. & T. Nanded, Nanded 431606, India
e-mail: Jeetupatilp7@gmail.com

Y. S. Gaikhe · S. Mishra
Department of Mechanical Engineering, Indian Institute of Technology Bombay, Powai, Mumbai 400076, India

main three types, viz. pressure thermoforming, vacuum thermoforming and contact thermoforming [2]. In case of pressure thermoforming, the rubbery sheet is deformed by applying air pressure on the top surface of the sheet, whereas a vacuum is created beneath of the sheet to deform it in the required shape by vacuum thermoforming process. The contact forming process is similar to the deep drawing process used for sheet metal operations where a punch forces the sheet against the die cavity to deform it into the shape of the die cavity. Depending upon the requirement of dimensional control over the product, each process is being used. For example, disposal products and packaging are some of the products which are mostly single used and don't require dimensional control, thus produced by pressure or vacuum forming process (thin gauge products). On the other hand, products such as automobile bonnets and aircraft canopy require high-dimensional control over the product so that they can serve the intended purpose (thick gauge products). This created an opportunity for the researchers to investigate the process to achieve dimensional control over the product. Various theories were proposed by the researcher to understand material behaviour during the deformation, along with the material model to replicate the material behaviour in numerical simulations [3–6].

Deformation pressure, punch stroke length, forming temperature, deformation rate are some of the parameters investigated by the researchers experimentally [7–10]. Several numerical investigations were also carried out by the researcher to investigate the process. Various processing parameters were investigated numerically to find out the most dominant processing parameters and their effect on process output [6, 11–14]. Some researchers have simplified the process by considering the no-heat transfer during the deformation of the sheet [6, 11, 15]. However, in industrial applications, in case of large components, isothermal deformation of the sheet is not possible. Usually, sheets are heated at some remote locations and deformed at the forming station. During sheet transfer, there is a chance of sheet temperature variation due to heat loss to the surrounding environment. Thus, the assumption of no change in the thermal state is not sufficient for realistic simulations. Moreover, it was found that sheet temperature and contact conditions are the most crucial parameters governing the process output. Morales et al. have investigated the effect of sheet temperature on the contact condition and proposed that contact conditions are temperature dependent [16]. Thus, there is a need to consider the thermal aspect of the process for reliable and realistic simulation of the process. The present study aims to investigate the thermal aspect of the process and find out the effect of sheet temperature on the thickness distribution of part. In the study of Eksi et al. [17], it was found that contact thermoformed products have uniform thickness distribution than pressure formed product. Therefore, for the present study, it is planned to investigate the production of the transparent hemispherical domes by contact thermoforming with help of numerical simulations. Two simulation cases were simulated, viz. isothermal processing with contact material properties and non-isothermal processing with temperature-dependent properties.

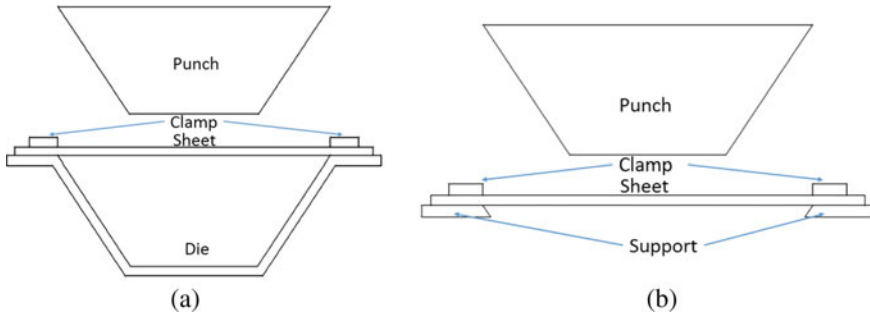


Fig. 1 Contact thermoforming: **a** closed contact thermoforming. **b** Open contact thermoforming

2 Contact Thermoforming

Contact forming is mostly used polymer processing method when there is a requirement of dimensional control of the product. Pre-heated polymer sheets get deformed against die cavity by a punch to acquired desired product shape. Depending on die being used, contact forming can be divided into two types, viz. open die forming [18] where the sheet makes contact only with punch surface. In close contact forming [5, 19], sheet not only makes contact with punch surface but also with die surface during the sheet deformation. Figure 1 shows the schematic of the contact thermoforming process. Clamped sheet gets deformed as punch progress inside the die cavity. Depending upon the contact conditions, the sheet gets stretched. For a high coefficient of friction, sheet gets stretched at the wall region more, whereas for low coefficient friction it may slip over the punch surface and results in uniform material distribution [4, 18]. As mentioned, the aim of the present study is to investigate the thermal aspect of the process. It is recommended to consider the maximum ways of heat transfer to the process, which is possible in the open thermoforming process. Thus, the open contact forming process is considered for investigation.

3 Numerical Studies

Figure 2 shows the numerical domain considered for investigation (for both processing approaches, isothermal and non-isothermal). To reduce the computational cost, only required components (punch, clamp, die and sheet) and one-fourth of the model was considered. Die has an inner diameter of 80 mm with a circular chamfer of 10 mm. Sheets having a thickness of 5 mm and a diameter of 160 mm were used to produce a hemispherical dome of height 51 mm. Two types of the element were used for discretization, 20-node brick element (C3D20R) to mesh the die, clamp and punch, whereas the sheet was discretized using a 20-node brick element having a hybrid formulation to account for the large deformation (C3D20RH).

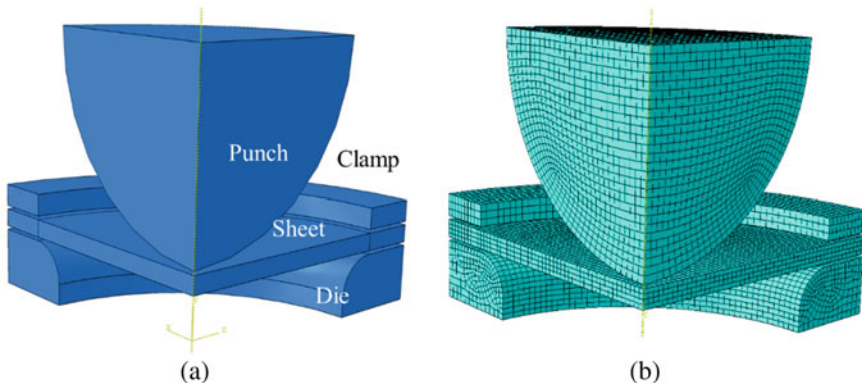


Fig. 2 Numerical domain; **a** Geometric model. **b** Discretized geometric model

3.1 Material Modelling

PMMA and SS304 are the material considered for the sheet and other components, respectively. It is assumed that processing is carried out at high deformation rate and reproducing the material behaviour hyperelastic Mooney–Rivlin material model is most suited. To incorporate temperature dependency to the numerical model, temperature-dependent material properties were used. All required properties were taken from the available literature and tabulated in Tables 1 and 2. For the

Table 1 Thermophysical properties [20, 21]

Properties	Temperature (°C)	28	50	100	150	200
Specific heat (J/kg K)	SS304	470.4	474.5	483.8	493	502.1
	PMMA	1099.1	1351	1945.9	2162.2	2306.3
Thermal conductivity (W/m K)	SS304	13.9	14.4	15.5	16.6	17.6
	PMMA	0.1604	0.186	0.2299	0.2104	0.2009
Density (kg/m ³)	SS304	7950.9	7941.6	7920.6	7899.5	7878.4
	PMMA	1238.2	1240	1230.6	1217.9	1191.6

Table 2 Temperature-dependent material properties [22]

Material	Temperature (°C)	120	130	140	150	160
PMAA (sheet)	C10 (Pa)	10,700	−1800	−12,500	−21,400	−28,500
	C01 (Pa)	542,600	528,600	506,600	476,600	438,600
	$D \times 10^{-7}$	3.61	3.77	4.05	4.05	4.39
(Die, clamp, punch)	E (GPa)	210				
	μ	0.3				

present study, the emphasis is only given to the sheet deformation; accordingly, only temperature-dependent structural properties of the sheet were provided.

3.2 Boundary Conditions and Interactions

Two types of boundary conditions were imposed, representing each processing approach. For isothermal processing, it was assumed that sheet deforms at an isothermal temperature of 160 °C. To simulate this, material properties at 160 °C for all components were provided to the numerical model. In the case of non-isothermal processing approach, the sheet initial temperature was 165 °C assigned (to compensate heat loss during transfer), and all other components were at a temperature of 28 °C. Die was fixed at the bottom, and the clamp has given a displacement of 1 mm to hold sheet periphery for both processing approaches. Punch was allowed to travel inside the die cavity by providing the displacement of 52 mm for both processing approaches.

In the case of isothermal processing, due to the assumption of constant thermal state during processing, only structural interaction is required, which is the coefficient of friction. For both cases, “0.4” coefficient of friction was imposed. As mentioned, the objective of the study is to investigate the effect of sheet temperature; for both approaches, the same coefficient of friction was used. So that the deformation caused due to the non-uniform sheet temperature can be studied without any influence of the variable contact condition. In the case of the non-isothermal processing approach, heat transfer is allowed during the processing. To simulate the heat transfer, a combined heat transfer coefficient (convection + radiation) of 5 W/m². K was imposed on the exposed surfaces. To simulate the heat transfer across the surface, thermal contact conductance of 227.55 W/m² K was imposed.

3.3 Numerical Procedure

Isothermal processing¹ simulation is two-step simulation; in the first step, the sheet was clamped to the die. In second step punch forces, the sheet inside the die cavity acquires hemispherical shape. As mentioned, the thermal state is constant; there will be no heat transfer during processing, whereas non-isothermal processing simulation comprises three steps, in the first step sheet is transferred from the heating station to the forming zone (30 s). In the second stage, the sheet was clamped to die (30 s). In the last step, punch deforms the sheet into the hemisphere (30 s). There is continuous heat transfer during sheet deformation, and to the punch and surrounding environment.

¹Proposed numerical model was validated in the paper, Patil Jeet et al. (2019) Contact analysis for contact thermoforming of PMMA sheet. Materials Performance and Characterization (accepted).

4 Results and Discussion

For the domes of height 51 mm, both cases were simulated. Figure 3 shows the von Mises stress distribution of the formed domes. It can be noted that the stress distribution pattern of both domes slightly different. In case of the non-isothermally processed dome, more stress is concentrated just below the neck, whereas in the isothermally processed dome, stress is more distributed at the neck region which is an indication of comparatively uniform stretching at the neck region than the non-isothermally processed sample. To investigate the formed dome, thickness analysis was carried out, and a comparison was made. For thickness comparison, sheet thickness was measured at 10 locations, as shown in Fig. 4a. Figure 4b shows the thickness comparison of the formed domes. It can be noted that the isothermally formed dome has more thickness than the non-isothermally formed dome. It can be observed that

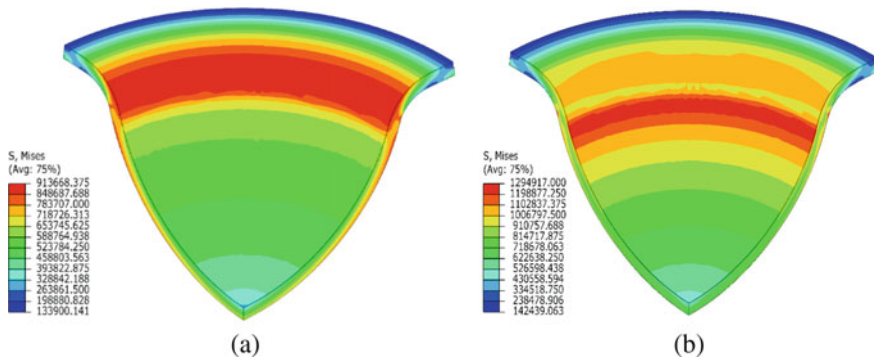


Fig. 3 Stress distribution of formed domes **a** Isothermally processed. **b** Non-isothermally processed

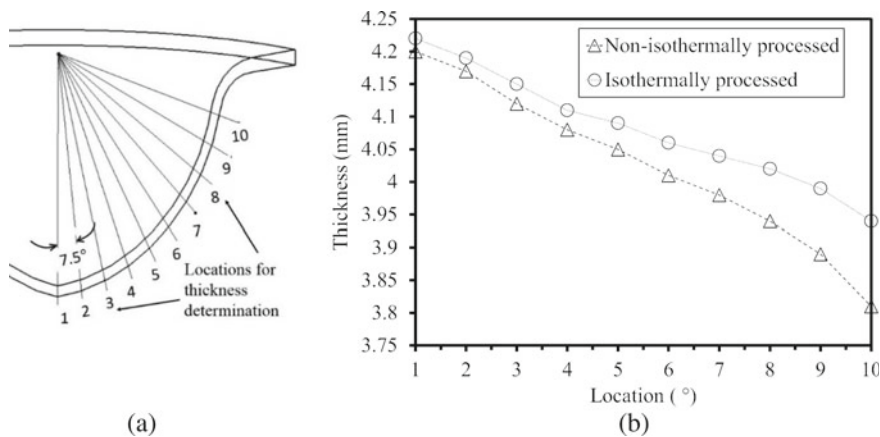


Fig. 4 **a** Locations for thickness measurement, **b** thickness comparison of the formed part

Table 3 Maximum principal stresses for isothermal and non-isothermal processed hemispherical domes

Location	Max. Principal stress (Pa): isothermal processed	Max. Principal stress (Pa): non-isothermal processed
1	667,389.8	717,544.4
2	676,779.3	735,565.4
3	700,089.3	770,941.6
4	723,742.4	812,122.7
5	744,457.3	855,687.1
6	778,162.1	960,435.4
7	792,385.6	1,030,372
8	805,332.8	1,126,891
9	821,935.4	1,303,502
10	860,517.3	1,289,514

the sheet thickness difference at each location for formed domes is increasing from location 1–10 which is due to the different stretching happening near the neck region, justifying more stress generation for the non-isothermally formed dome (Table 3).

5 Conclusion

The effect of sheet temperature on thickness distribution of the product was investigated using numerical simulations. Two hemispherical domes made from PMMA were produced numerically. Simulated cases represent the ideal and realistic processing approaches. To simulate the process more realistically, temperature dependency was incorporated in the proposed numerical model by providing temperature-dependent material properties and provision of heat transfer during the sheet processing. To investigate the thermal effect alone, constant contact conditions were provided, and comparison among the thermoformed dome was made. It was found that temperature dependency has a significant effect on the thickness distribution of the formed dome. Thus, it necessary to consider the thermal aspect of the process, along with the structural aspect and for reliable and realistic simulation, temperature dependency must be incorporated into the numerical models.

References

1. Throne JL (2008) Understanding thermoforming. Carl Hanser Verlag GmbH & Co KG. <https://doi.org/10.3139/9783446418554.fm>
2. Osswald TA (2010) Understanding polymer processing. Carl Hanser Verlag GmbH & Co KG. <https://doi.org/10.3139/9783446446038.fm>
3. Dooling PJ, Buckley CP, Rostami S, Zahlan N (2002) Hot-drawing of poly(methyl methacrylate) and simulation using a glass–rubber constitutive model. *Polymer* 43(8):2451–2465. [https://doi.org/10.1016/S0032-3861\(01\)00799-6](https://doi.org/10.1016/S0032-3861(01)00799-6)
4. O'Connor CPJ, Martin PJ, Sweeney J, Menary G, Caton-Rose P, Spencer PE (2013) Simulation of the plug-assisted thermoforming of polypropylene using a large strain thermally coupled constitutive model. *J Mater Process Technol* 213(9):1588–1600. <https://doi.org/10.1016/j.jmptotec.2013.02.001>
5. Guzman-Maldonado E, Hamila N, Naouar N, Moulin G, Boisse P (2016) Simulation of thermoplastic prepreg thermoforming based on a visco-hyperelastic model and a thermal homogenization. *Mater Des* 93:431–442. <https://doi.org/10.1016/j.matdes.2015.12.166>
6. Drozdov AD (1999) Modelling the nonlinear viscoelastic behavior of amorphous glassy polymers. *Math Comput Model* 30(5–6):49–72. [https://doi.org/10.1016/S0895-7177\(99\)00147-8](https://doi.org/10.1016/S0895-7177(99)00147-8)
7. DeLorenzi HG, Taylor CA (1993) The role of process parameters in blow molding and correlation of 3-D finite element analysis with experiment. *Int Polym Proc* 8(4):365–374. <https://doi.org/10.3139/217.930365>
8. Bhattacharyya D, Bowis M, Jayaraman K (2003) Thermoforming woodfibre–polypropylene composite sheets. *Compos Sci Technol* 63(3):353–365. [https://doi.org/10.1016/S0266-3538\(02\)00214-2](https://doi.org/10.1016/S0266-3538(02)00214-2)
9. Martin PJ, Duncan P (2007) The role of plug design in determining wall thickness distribution in thermoforming. *Polym Eng Sci* 47(6):804–813. <https://doi.org/10.1002/pen.20757>
10. McCool R, Martin PJ (2010) The role of process parameters in determining wall thickness distribution in plug-assisted thermoforming. *Polym Eng Sci* 50(10):1923–1934. <https://doi.org/10.1002/pen.21718>
11. Nied HF, Taylor CA, Delorenzi HG (1990) Three-dimensional finite element simulation of thermoforming. *Polym Eng Sci* 30(20):1314–1322. <https://doi.org/10.1002/pen.760302009>
12. Taylor CA, Delorenzi HG, Kazmer DO (1992) Experimental and numerical investigations of the vacuum-forming process. *Polym Eng Sci* 32(16):1163–1173. <https://doi.org/10.1002/pen.760321613>
13. Ghobadnam M, Mosaddegh P, Rezaei Rejani M, Amirabadi H, Ghaei A (2014) Numerical and experimental analysis of HIPS sheets in thermoforming process. *Int J Adv Manufact Technol* 76(5–8):1079–1089. <https://doi.org/10.1007/s00170-014-6329-y>
14. Dong Y, Lin RJT, Bhattacharyya D (2006) Finite element simulation on thermoforming acrylic sheets using dynamic explicit method. *Polym Polym Compos* 14(3):307–328
15. Makradi A, Belouettar S, Ahzi S, Puissant S (2007) Thermoforming process of amorphous polymeric sheets: modeling and finite element simulations. *J Appl Polym Sci* 106(3):1718–1724. <https://doi.org/10.1002/app.26869>
16. Morales RA, Candal MV, Santana OO, Gordillo A, Salazar R (2014) Effect of the thermoforming process variables on the sheet friction coefficient. *Mater Des* 53:1097–1103. <https://doi.org/10.1016/j.matdes.2013.08.009>
17. Eksi O, Karabeyoğlu SS (2017) The effect of process parameters on thickness distribution in thermoforming. *Adv Sci Technol Res J* 11(2):198–204. <https://doi.org/10.12913/22998624/71147>
18. Martin P, Choo HL, O'Connor CPJ (2012) Measurement & modelling of slip during plug-assisted thermoforming. *Key Eng Mater* 504–506:1105–1110. <https://doi.org/10.4028/www.scientific.net/KEM.504-506.1105>

19. Bernard CA, Correia JPM, Bahlouli N, Ahzi S (2013) Numerical simulation of plug-assisted thermoforming process: application to polystyrene. *Key Eng Mater* 554–557:1602–1610. <https://doi.org/10.4028/www.scientific.net/KEM.554-557.1602>
20. Gunel EM, Basaran C (2011) Damage characterization in non-isothermal stretching of acrylics. Part II: experimental validation. *Mech Mater* 43(12):992–1012. <https://doi.org/10.1016/j.mechmat.2011.09.003>
21. Narang VA (2005) Heat transfer analysis in steel structures. Worcester Polytechnic Institute
22. Dong Y, Lin RJT, Bhattacharyya D (2005) Determination of critical material parameters for numerical simulation of acrylic sheet forming. *J Mater Sci* 40(2):399–410. <https://doi.org/10.1007/s10853-005-6096-0>

A Review of Current Researches on Powder Mixed Electrical Discharge Machining (PMEDM) Technology



Pradipta Kumar Rout and Pankaj Charan Jena

Abstract Nowadays, electrical discharge machining (EDM) is becoming a more popular option for manufacturing hard material and complex geometry parts that are extremely difficult to cut by conventional machining processes. Continuous demand for the high-tech industry to use high and superalloys compelled the manufacturing industry to adhere EDM process. In present times, many researchers have been working in this area to find process suitability and optimum machining parameters. Powder mixed electric discharge machining (PMEDM) is a recent outcome in which different powders are mixed with the dielectric fluids to increase the material removal rate (MRR), surface roughness (SR), and property improvement of the machining surface. In this paper, an attempt has been made to review and discuss on PMEDM work of researchers. The paper discusses the EDM variables, optimum parameters, tool wear, surface texture, and mechanical properties of the machined surface. The outline of the discussion is stated in subsequent parts of the paper.

Keywords PMED · MRR · SR · Tool wear rate · White recast layer

1 Introduction

There has been substantial growth in modern manufacturing processes to machine exotic materials easily and accurately. Now, most of the manufacturing industry starts to prefer modern or unconventional machining processes rather than conventional machining processes. This is due to many reasons, such that, to achieve better efficiency, accuracy, and reliability. It has been the best choice since the last two decades to use high and superalloys as components for different high-tech industries to increase the durability of machines or mechanisms. Hence, substantial amounts

P. K. Rout (✉)

Kalinga Institute of Industrial Technology (KIIT), Deemed to be University, Campus-8, Patia, Bhubaneswar, Odisha 751024, India
e-mail: pradiptakumar.rout@kiit.ac.in

P. C. Jena

Veer Surendra Sai University of Technology, Burla, Odisha 768018, India
e-mail: pankajcharanjena@gmail.com

© Springer Nature Singapore Pte Ltd. 2021

P. Pant et al. (eds.), *Advances in Mechanical Processing and Design*, Lecture Notes in Mechanical Engineering, https://doi.org/10.1007/978-981-15-7779-6_43

of pressure mount on manufacturing industries to process them by the conventional method. New and novel materials are almost impossible to cut by any existing conventional processes. Besides, conventional machining is inefficient in machining hard materials like ceramics and composites. The demand for high-dimensional accuracy also sometimes creates hindrances during traditional machining. Again, during the machining process blank is affected severely by cutting forces, as a result, more stress is induced in the blank. To overcome such problems, new methods of machining such as modern or unconventional machining process have come in use. In current times, the process has been used by the manufacturing industry to manufacture automotive, aerospace, tool and die and forging machine tool parts.

The electric discharge machining is an electrothermal unconventional spark erosion machining process in which no chattering and vibrations are associated as those happen during conventional machining. The process is useful to cut difficult to cut materials for those having optimum hardness and toughness. The process with negligible distortion and stress concentration can easily machine high and superalloys. In the EDM device, electrical current is used to generate spark between electrode and workpiece. The electrode is in a fixed position maintaining a small distance from the workpiece and both submerged in a dielectric. A pulsating DC power supply is used to generate voltage pulses between electrode and blank. The gap between the workpiece and electrode is maintained by a servo-controlled unit mechanism, which is being incorporated with the EDM machine. When the current starts to flow through the electrode to workpiece, high heat is generated and spark is established. It heats the local area without affecting the other part of the workpiece (Fig. 1).

Recent advancement of EDM leads to the development of powder mixed EDM (PMEDM) where powders are mixed in the dielectric. There is a little modification in the traditional EDM system, and a submerged pump is installed with the system to inject powder mixed dielectric fluid on to the cutting zone. The objective to mix the powder with dielectric is to diminish the insulating strength of the dielectric and

Fig. 1 EDM machine



Fig. 2 PMEDM setup

to decrease the gap between work and electrode. Thus, the process becomes more stable, and good MRR value is obtained with relatively good surface finish (Fig. 2).

2 History

In 1970, the English scientist Priestly first found the erosive effects of electrical discharge on metals. Later, 1943 soviet scientists, Lazarenko developed a controlled method of metal machining. Now improved version electric discharge machine tools are used with various cutting modes such as EDM and PMEDM. EDM process has found ready application in machining titanium alloys, tungsten carbides, and any other hard steels. The process is useful to any electrically conductive materials where mechanical properties such as toughness, hardness, strength, and microstructures are not barriers to its application. Slender and fragile jobs can be machined easily as there is no contact of the cutting tool with the workpiece. Though EDM is a thermal erosion process, there is no heating in the bulk of the material because of dielectric uses. Accurate profile with minimum dimensional deviation can be easily achieved with a little attention of the operator.

In recent past, PMEDM has emerged as one of the suitable techniques to enhance the efficiency, surface quality, and mechanical properties of the recast layer. The added powder affects the performance of the process. Powder mixing techniques increase the spark gap distance and reduce the insulating strength between the tool electrode and workpiece. As a result, the process becomes more stable, hence the MRR increased significantly (Fig. 2).

3 Methodology

Recent advancement of EDM led to the development of powder mixed EDM (PMEDM) where powders are mixed in the dielectric. These powders are known to improve many output parameters. Because of these powders, the insulating strength of the dielectric decreases and the spark gap between tool electrode and workpiece increases, which leads to the process more stable, and ultimately results in improved MRR values and a relatively good surface finish [1–4]. Proper discharge parameters are the most criteria while machining workpieces as the study shows that machining efficiency and SR can be improved [5]. There are many methods to machine exotic alloy, namely conventional and non-conventional processes. Although conventional techniques have been employed to machine such alloys, the non-conventional techniques, especially electric discharge machining (EDM), is the best suited for machining hard alloys. In EDM, the material removal process is achieved by a series of continuous electric discharges between the workpiece and the electrode in the presence of a dielectric fluid [6]. So this unconventional technique is highly successful in its ability to machine and manufacture incredibly hard material and geometrically complex shapes with razor-sharp precision [7, 8]. While machining, there are numerous options for selecting the dielectric fluid but it has been found that the use of water as a dielectric instead of oil-based dielectrics significantly improves the material removal rate (MRR). Moreover, water-based dielectrics are more eco-friendly [9]. EDM is a well-researched technique. Research shows that the main reason behind the continuous EDM is the result of the formation of the pyrolytic carbon layer on the ceramic surface due to the cracked carbon dissipated from the carbonic dielectric [10]. While machining with EDM, the formation of the white recast layer (WRL) cannot be ignored. High pulse current and pulse on duration are found responsible for increasing the thickness of this WRL [11]. This increases with increasing the surface roughness (SR) but on the other hand increases the hardness of the surface of the workpiece. Tool wear rate [TWR] is one of the major disadvantages of this technique.

A study shows that when aluminum powders are mixed with IPOL oil to machine AISI D3, high MRR, low TWR, and low SR are achieved [12]. Gudur et al. studied that when aluminum and silicon powders were mixed with various dielectrics, MRR was found to increase and TWR was decreased compared to conventional EDM process [13]. Hastalloy steel is nickel molybdenum–chromium superalloy and has substantial corrosion resistance in several environments. Singh et.al tried to machine the metal by EDM and found maximum MRR of 0.063 gm/l at aluminum powder concentration of 6 gm/l in EDM oil. Further, the MRR decreased to 0.06 gm/min at a concentration of 12 gm/l. The experiment also reveals that fine grains of aluminum powder give less MRR results than the medium-sized grain powders. This is because of less suspended particles found in EDM oil than the medium-grain particles. Again suspended coarse grain size aluminum powder in a dielectric with little density bridges the gap between electrodes and leads to short-circuiting. As a result, MRR becomes less than MRR yields with pure EDM oil. It can be said to be an ideal EDM

process if the electrode erodes maximum materials from the workpiece than its self-erosion. In this verse, the paper states that minimum TWR is found with fine grain powder particles. However, TWR is more with pure EDM oil followed by coarse and medium grade particles. The surface roughness of $3.4 \mu\text{m}$ found at the machining surface of Hastalloy steel using fine grain aluminum powder, which is maximum as compared to medium and coarse grain powder SR results. EDM with pure EDM oil also produces more roughness value than the surface produced with fine-grained particles. Again, the concentration of powder has also a significant effect on SR. The value is inversely proportional to the amount of powder concentration in EDM oil. The powder concentration of 9 gm/l exhibits a good SR value of $2.85 \mu\text{m}$ and then the roughness increased [14].

Researchers have developed several ways for machining hard metals by the EDM process. The rotary tool EDM process is a recent development in which the electrode tool rotates at the desired speed. Patel et al. used a rotary tool in the PMEDM process to machine Inconel 718. Inconel 718 is a high-performance alloy and used for turbine components, cryogenic storage tanks, jet engine parts, rocket motors, nuclear fuel element spacer, and for hot extrusion tooling. They added aluminum oxide (Al_2O_3) powder with a concentration of $0.5\text{--}1.5 \text{ gm/l}$ into the dielectric fluid. The rotary tool shows better MRR results than the fixed electrode tool. It also reveals that peak current (I_p) takes prime responsibility to increase the MRR of Inconel 718 steel. MRR result shows low results at 9 A and higher at 28 A . MRR shows lower at pulse ON time $50 \mu\text{s}$ and minor increment at $150 \mu\text{s}$. Hence, pulse ON time has less significance in the rotary EDM process. Duty cycle has no significance on MRR. However, I_p has a significant role on TWR. TWR is lower at 9 A and higher at 28 A . TWR is also a function of T_{on} . Higher TWR shows at $50 \mu\text{s}$ and a minimum at $100 \mu\text{s}$. The most effective parameter also found for SR is I_p . Minimum SR is evidenced at 9 A and maximum at 28 A . Topography study of Inconel 718 EDMed surfaces by SEM analysis reveals that aluminum oxide (Al_2O_3) powder particles are deposited on the EDMed surface. [15]. When the performance of different powders like aluminum, silicon and silicon carbide were compared, aluminum powder gave the highest MRR. However, overall better machining performance was obtained from silicon powder [16]. Another study showed that when the aluminum powder was mixed with distilled water; a green dielectric to machine W300 die steel, a high MRR, good surface finish, and a minimum white layer thickness was reported [17].

A similar study showed that out of six parameters chosen, namely nozzle flushing, grain, the concentration of powder, pulse OFF time, pulse ON time and peak current, and nozzle flushing did not show any effect on MRR [18]. In another study, when SiC was mixed with a dielectric fluid to machine premium stainless mold steel, a reduction of machining time was reported [19]. Graphite is another such powder which is known to improve the MRR. When 4 g of graphite powder was mixed with kerosene, MRR was found to increase by 60% and TWR by 15% [20]. Another research in micro-EDM showed that when graphite powder was introduced in the dielectric, the machining time reduced by 5 times and when workpiece vibration was employed to the machining process the machining time was found to get reduced

by 3 times [21]. Tungsten powders have also shown improvements in MRR when mixed with pure kerosene [22].

Mohal et al. used Al 6061 reinforced with 10% silicon carbide particle as work-piece material. Multiwall carbon nanotube (MWCNT) mixed dielectric fluid and copper tool with –ve polarity is used for the EDM process. The experiment reveals that MRR increases with increasing CNT powder concentration. This is because of the high thermal conductivity of CNT particles. Thus, high electric current flows to the workpiece, as a result, more MRR is achieved. But the concentration of CNT equal or more than 8 gm/l increases derbies at the discharge gap makes the machining process unstable; as a result, MRR is reduced. It is found again from the experiment that the concentration of CNT powder plays a vital role in SR value apart from electrical parameters. The addition of CNT powder helps to establish more dissipation of discharge energy, which in turn minimizes the crater size. On the other hand, surface roughness increases by increasing CNT powder concentration to 0.4 gm/l in dielectric fluid. This is because at a very high concentration of CNT in dielectric loses its ability to distribute the powder particles uniformly. Again, machined surfaces are analyzed by SEM and found that larger craters are noticed at the machined surface as compared to CNT as additive [23].

Patel et al. compared machining characteristics of aluminum, silicon and silicon carbide powder and found aluminum powder has the highest MRR and silicon powder has better overall results among the three [24]. In another PMEDM process titanium, nanopowder is mixed with dielectric. The study revealed that the EDMed surface morphology of D_2 steel was improved. Low height ridges, shallower crater, and fewer voids were found at the machined surface. Furthermore, a very less amount of Ti nanopowder welded at the EDMed surface [25]. When mixing chromium powders with commercial grade EDM oil to machine H-11 die steel, the surface texture was improved with increasing powder concentration. A remarkable improvement in increasing micro-hardness was recorded by increasing I_p even at a constant C_p [26]. Similarly, when graphite was mixed with kerosene to machine Inconel 625, there was a reduction in surface tensile stress, which helped to enhance its fatigue strength [27]. Another advantage of the PMEDM process is during machining, and there is a scope of surface modification due to the transfer of suspended particles from dielectric to work surface. In this verse, Kumar et al. found that a significant amount of tungsten carbide powder transferred to the machined surface and welded on it, as a result surface defect diminished. Besides, hardness at EDMed surface enhanced due to the deposition of carbon. The negative polarity of the electrode, shorter T_{on} , longer T_{off} , and low discharge current are the considerable factors for metal transfer in which I_p is more significant [28]. Another research shows biomedical grade titanium alloy, when machined with nanoscaled aluminum powder, imparted high surface finish and enhanced surface morphology showing minimum voids, cracks, and craters [29].

EN-19 is known for its high tensile strength. This property of this alloy along with good ductility and shock resistance has it very popular in the automotive industry. Also, its extremely precise machining property has led its use in the oil and gas sector. However, one downside to this alloy is its low wear resistance and hence leads to a shorter service life [30]. It is reported that optimized process parameters by Taguchi

method for maximum MRR to cut EN 19 are 24 A, pulse OFF time of 2300 μs , pulse ON time of 400 μs , and a voltage of 40 V. But the process parameters for EN 41 are 40 V, 24 A, pulse ON time of 400 μs , and pulse OFF time of 2100 μs [31]. Kolli et al. used the Taguchi method to optimize the graphite powder concentration and machining surface characteristics of Ti-6Al-4V. Their detailed investigation revealed that an improvement in MRR and reduction in TWR, SR, and WLT is noticed by using mixing graphite powder with dielectric. MRR increased in increasing C_p from 4 to 6 g/l and again decreased beyond 6 g/l [32]. Taguchi's L_{27} orthogonal array was employed to machine H-11 die steel taking copper as an electrode material and SiC as powder material. The experiment revealed that maximum surface roughness, cracks, pores, and holes were found by machining without powder; whereas, substantial improvement in surface topology was seen while adding powder with dielectric. Higher MRR with improved micro-hardness at EDMed surface and lower surface roughness and cracks were found at higher C_p [33]. Kansal et al. investigated that when Si powder was mixed with dielectric higher MRR and surface finish were reported. Further, it was observed that I_p and C_p are the most significant parameters which affect MRR and SR [34].

4 Conclusion

From the above evidential study, it can be concluded that EDM and its novel method PMEDM are suitably found more efficient to cut hard alloys, where a conventional process fails to do so. Good MRR value and complex geometry with tight accuracy can be obtained by PMEDM. But still researchers are troubled to explore the optimum parameters as the process is concerned to many complex activities. Therefore, more research is required to explore all angles of the process.

5 Future Scope

In this discussion, it is clear that many researchers are showing their interest and have been working in improving MRR, surface finish, strength, and recast layer integrity. They also worked to reduce tool wear rate and white layer thickness. They do not have any adequate control over spark density and its interface area. If we would control the spark density and its interface area, then we could use a standard electrode for cutting different dimensions of different alloys. Further, electrode manipulation is restricted in the process. Hence, a great scope lies in this process for further research. Still, many things are to explore for optimizing the process parameters. Moreover, EDM is a gray area for researchers, and the process holds a bright future for the manufacturing industry [35].

References

1. Kansal HK, Singh S, Kumar P (2007) Technology and research developments in powder mixed electric discharge machining (PMEDM). *J Mater Process Technol* 184:32–41
2. Rozenek M, Kozak J, Dabrowski L (2003) Electrical discharge machining in dielectric-powder media. *Proc Inst Mech Eng Part B J Eng Manufact* 217:1597–1602
3. Rana D, Pal AK, Tiwari P (2015) Study of powder mixed dielectric in EDM—a review. *Intl J Eng Sci Adv Res* 1(2):69–74
4. Singh S, Bhardwaj A (2011) Review to EDM by using water and powder-mixed dielectric fluid. *J Min Mater Character Eng* 10(2):199–230
5. Zhao WS, Meng QG, Wang ZL (2002) The application of research on powder mixed EDM in rough machining. *J Mater Process Technol* 129:30–33
6. Abbas NM, Yusoff N, Mahmod@Wahab R (2012) Electrical discharge machining (EDM): practices in Malaysian industries and possible change towards green manufacturing. In: *International symposium on robotics and intelligent sensors 2012 (IRIS 2012)*
7. Ho KH, Newman ST (2003) State of the art electrical discharge machining (EDM). *Advanced Manufacturing Systems and Technology Centre, Wolfson School of Mechanical and Manufacturing Engineering, Loughborough University, Loughborough, Leicestershire LE11 3TU, UK*
8. Singh NK, Pandey PM, Singh KK, Sharma MK (2016) Steps towards green manufacturing through EDM process: a review. *Cogent Eng* 3:1272662
9. Singh H, Chatha SS, Singh H (2013) Role of dielectric and tool material on EDM performance: a review. *Int J Eng Res Dev* 7:67–72
10. Abdussabur MY, Ali M, Maleque A, Khan AA (2013) Investigation of material removal characteristics in EDM of nonconductive ZrO₂ ceramic. *Proc Eng* 56:696–701
11. Tai TY, Lu SJ (2009) Improving the fatigue life of electro-discharge-machined SDK11 tool steel via the suppression of surface cracks. *Int J Fatigue* 31:433–438
12. Jamadar MM, Kavade MV (2014) Effect of aluminium powder mixed EDM on machining characteristics of die steel (AISI D3). *Int J Mech Prod Eng* 2:2320–2092
13. Gudur S, Potdar VV, Gudur S (2007) A review on effect of aluminum & silicon powder mixed EDM on response variables of various materials. *Int J Innov Res Sci Eng Technol* 12:17937–17945
14. Singh P, Kumar A, Beri N, Kumar V (2010) Some experimental investigation on aluminum powder mixed EDM on machining performance of hastelloy steel. *Int J Adv Eng Technol* 1:28–45
15. Patel S, Thesiya D, Rajurkar A (2018) Aluminium powder mixed rotary electric discharge machining (PMEDM) on Inconel 718. *Aust J Mech Eng* 16:21–30
16. Shinde R, Patil N, Raut D, Pawade R, Brahmankar P (2017) Experimental investigations into powder-mixed electrical discharge machining (PMEDM) of HCHCR D2 die steel. In: *ICCASP/ICMMD-2016. Advances in intelligent systems research, vol 137, pp 298–303*
17. Syed KH, Palaniyandi K (2012) Performance of electrical discharge machining using aluminium powder suspended distilled water. *Turkish J Eng Env Sci* 36:195–207
18. Kansal HK, Singh S, Kumar P (2007) Effect of silicon powder mixed EDM on machining rate of AISI D2 die steel. *J Manufact Process* 9:13–22
19. Razak MA, Abdul-Rani AM, Nanimina AM (2015) Improving EDM efficiency with silicon carbide powder-mixed dielectric fluid. *Int J Mater Mech Manufact* 3(1):40–43
20. Jeswani ML Effect of the addition of graphite powder to kerosene used as the dielectric fluid in electrical discharge machining, vol 70. Elsevier Sequoia SA, Lausanne, pp 133–139
21. Prihandana GS, Sriani T, Mahardika M (2012) Improvement of machining time in micro-EDM with workpiece vibration and graphite powder mixed in dielectric fluid. *Indian J Eng Mater Sci* 19:375–378
22. Singh B, Kumar J, Kumar S (2015) Influences of process parameters on MRR improvement in simple and powder-mixed EDM of AA6061/10%SiC composite. *Mater Manufact Process* 30:303–312

23. Sachinmohal HK (2017) Study on the multiwalled carbon nano tube mixed EDM of Al-SiC_p metal matrix composite. *Mater Today Proc* 4:3987–3993
24. Sagar P, Thesiya D, Rajurkar A (2018) Aluminium powder mixed rotary electric discharge machining (PMEDM) on Inconel 718. *Aust J Mech Eng* 16(1):21–30
25. Marashi H, Sarhan AAD, Hamdi M (2015) Employing Tinano-powder dielectric to enhance surface characteristics in electrical discharge machining of AISI D2 steel. *Appl Surf Sci* 357:892–907
26. Tripathy S, Tripathy DK (2017) An approach for increasing the micro-hardness in electrical discharge machining by adding conductive powder to the dielectric. *Mater Today Proc* 4:1215–1224
27. Gangadharudutalla T, Gangopadhyay S, Biswas CK (2017) Influence of graphite powder mixed EDM on the surface integrity characteristics of Inconel 625. *Part Sci Technol Int J* 35:219–226
28. Kumar S (2012) Batra U (2012) Surface modification of die steel materials by EDM method using tungsten powder-mixed dielectric. *J Manufact Process* 14:35–40
29. Abdul-Rani AM, Nanimina AM, Ginta TL, Razak MA (2017) Machined surface quality in nano aluminum mixed electrical discharge machining. *Proc Manufact* 7:510–517
30. Diwakar NV, Bhagyanathan C, Rathnaraj JD (2014) Analysis of mechanical properties of En19 steel and En41b steel used in diesel engine camshaft. *Int J Curr Eng Technol*, 162–167
31. Shashikant V, Roy AK, Kumar K (2014) Effect and optimization of machine process parameters on MRR for EN19 & EN41 materials using Taguchi. *Proc Technol* 14:204–210
32. Muraharikolli AK (2015) Effect of dielectric fluid with surfactant and graphite powder on electrical discharge machining of titanium alloy using Taguchi method. *Eng Sci Technol Int J* 18:524–535
33. Tripathy S, Tripathy DK (2017) Surface characterization and multi-response optimization of EDM process parameters using powder mixed dielectric. *Mater Today Proc* 4:2058–2067
34. Kansal HK, Singh S, Kumar P (2005) Parametric optimization of powder mixed electrical discharge machining by response surface methodology. *J Mater Process Technol* 169, 427–436 (2005)
35. Srivastava V, Pandey PM (2013) Study of ultrasonic assisted cryogenically cooled EDM process using sintered (Cu–TiC) tooltip. *J Manufact Process* 15:158–166

Understanding the Deformation Micro-mechanism in Ti–6Al–4V Alloy U-Notched Specimen



Hitarth Maharaja, Satyaprakash Mishra, Pawan Patel, Sushil K. Mishra, and Jyoti S. Jha

Abstract High strength-to-low weight ratio, corrosion resistance, and excellent mechanical properties make the Ti–6Al–4V alloy a favorable material for aerospace application. In this study, digital image correlation (DIC) techniques together with the electron back scatter diffraction (EBSD) were employed to understand the deformation micro-mechanism. A uniaxial tensile test was carried out on the notched flat specimen, which failed at 3200 N. A further interrupted tensile test was performed, for the load applied up to 2000, 2500, and 3000 N. The microstructure analysis using EBSD was performed just beneath the notch region to understand the deformation micro-mechanism. Plastic deformation evident was significant at the lower load itself. Moreover, a significant variation in the local texture has been observed at the notch tip, where the plastic deformation is very high.

Keywords Ti–6Al–4V · EBSD · Tensile test · DIC · FEA

1 Introduction

Titanium alloy Ti–6Al–4V is used in aerospace applications due to high strength-to-weight ratio, excellent mechanical properties, and superior corrosion resistance [1]. The mechanical properties such as fatigue life of the component are significantly affected by the stress concentration features [2]. This stress concentration feature acts as a stress raiser leading to localized plastic deformation [3]. Various methods have been suggested to calculate the stress concentration [4–7]. In this paper, the stress concentration has been calculated employing digital image correlation after the tensile test of single U-notched specimen. Further microstructure analyses employing EBSD have been carried out at the notch tip. The influence of increasing load on the crystallographic orientation has been studied.

H. Maharaja · S. Mishra · P. Patel · S. K. Mishra · J. S. Jha (✉)
Indian Institute of Technology Bombay, Powai, Mumbai, Maharashtra 400076, India
e-mail: Jyoti.jha@iitb.ac.in

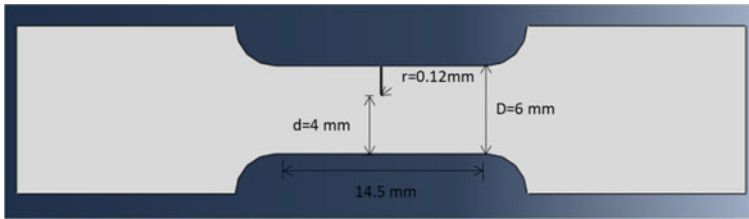


Fig. 1 Flat-notched-tensile specimen geometry

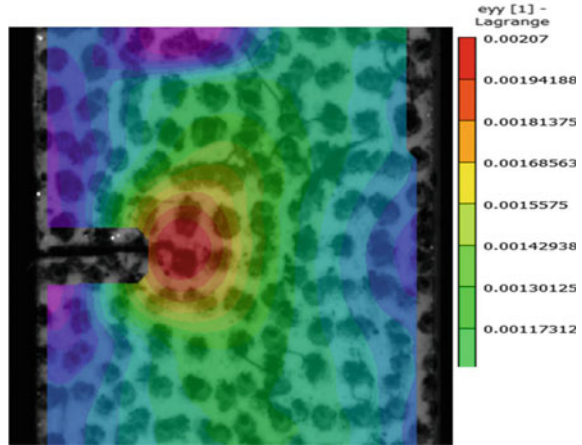
2 Experimental

A commercially available Ti–6Al–4V alloy with chemical composition of 0.13Fe, 4.035 V, 6.37Al, 0.03C, 0.2O, 0.013 N, and Ti (wt%) was used for this study. Flat tensile specimens with dimensions of 14.5 mm gauge length, 6 mm width, and 1 mm thickness (as shown in Fig. 1) were prepared for the uniaxial tensile tests. A single U-notch of dimensions 2 mm length and radius 0.12 mm was produced with electro discharge machining (EDM) at the center of the specimen. Tensile tests were performed in a servo motor-controlled 10 kN INSTRON 5566A system. The tensile specimen was painted with white spray and further stamped with black spot to measure the strain employing digital image correlation (DIC). The tensile test was performed with DIC interface using BASLER ACE AC2440 75 μm area scan camera and TOKINA lense AT-X PRO. The strain contour map was produced using VIC 2D software. Microstructure analysis using electron back scatter diffraction (EBSD) was carried out near the notch location. A series of emery papers of increasing grid size from 500 to 2500 was used for polishing and the final polishing was done using DKIC-MMMF Laboratory IIT, Bombay, made MetSil 40 colloidal silica of 0.04 μm . The EBSD analyses were carried out in ZEISS, Gemini 300 field emission scanning electron microscopy (FESEM) equipped with OXFORD fast CCD detector. A minimum step size of 0.5 μm was taken for the EBSD analysis.

3 Results and Discussion

The tensile test was carried on three dog-bone-shaped specimens till failure and in all the condition, the specimen failure was observed at load of 3200 N. The crack initiation was observed at the notch tip in all the test specimens. To find the notched tensile strength, stress concentration factor (K_t) was calculated using the DIC technique. The DIC strain contour in Fig. 2 shows that the maximum strain developed at the notch tip is 0.00207 and the average strain is 0.000915. A ratio of maximum strain to average strain within the elastic range suggests the $K_t = 2.26$ for the U-notch.

Fig. 2 Strain contour for stress concentration calculation within the elastic limit



For the maximum load of 3200 N, the nominal stress (load/effective area) is 800 MPa, whereas the notched tensile strength ($K_t \times$ nominal stress) is 1810 MPa. Thus, such enormous stress at the notch tip suggests the notch tip might have undergone the plastic deformation. To study the influence local plastic deformation on the microstructure near the notch, further tensile tests were carried out on fresh specimens at 2000, 2500, 3000, and 3200 N. The maximum stresses at the notch tip for various magnitude of load are provided in Table 1. EBSD analysis was carried out before and after each test in succession near the notch, where maximum strain was observed.

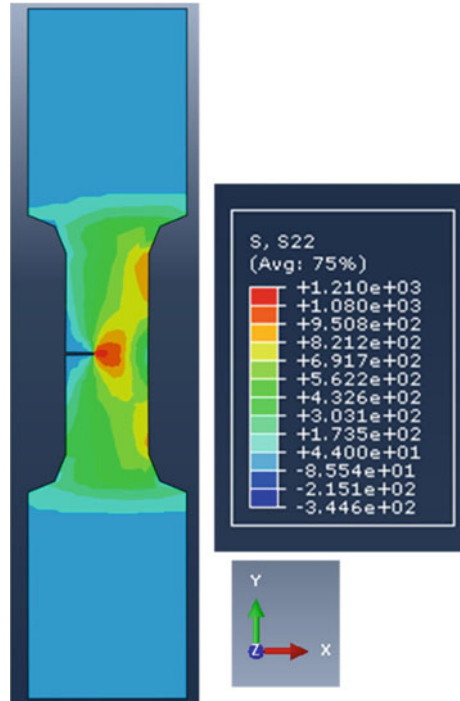
The finite element model (FEA) in a commercial ABAQUS® was performed on the tensile specimen to validate the maximum stress at the notch tip. The flow stress data from uniaxial tensile tests were directly used to define plastic behavior. Quad linear plane stress element CPS4 was used. A constant load of 2000 N was applied in the axial direction and the lower end was fixed. The maximum stress in the Y-direction at the notch tip was 1210 MPa (Fig. 3), which is close to the calculated stress using DIC.

The maximum strain at the notch tip DIC strain analyses for load 2000 N, 3000 N, and 3200 N is 1.3%, 1.5%, and 1.7%, respectively. Thus, both FEA and experimental results suggest the localized plastic deformation at the notch tip. To understand

Table 1 Maximum and nominal stresses for various loads

Load (N)	Effective stress (MPa)	Max. stress (MPa)
2000	500	1131
2500	625	1414
3000	750	1697
3200	800	1810

Fig. 3 Stress profile for applied load of 2000 N



the influence of localized plasticity on the crystallographic orientation, EBSD analysis was performed near the notch region and discussed in the following paragraph (Fig. 4).

Figure 5 shows the inverse pole figure, local misorientation, and pole figure of

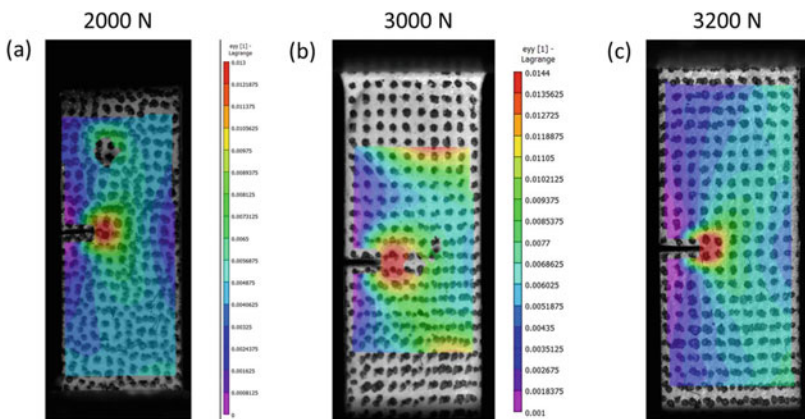


Fig. 4 Strain contour at **a** 2000 N, **b** 3000 N and **c** 3200 N

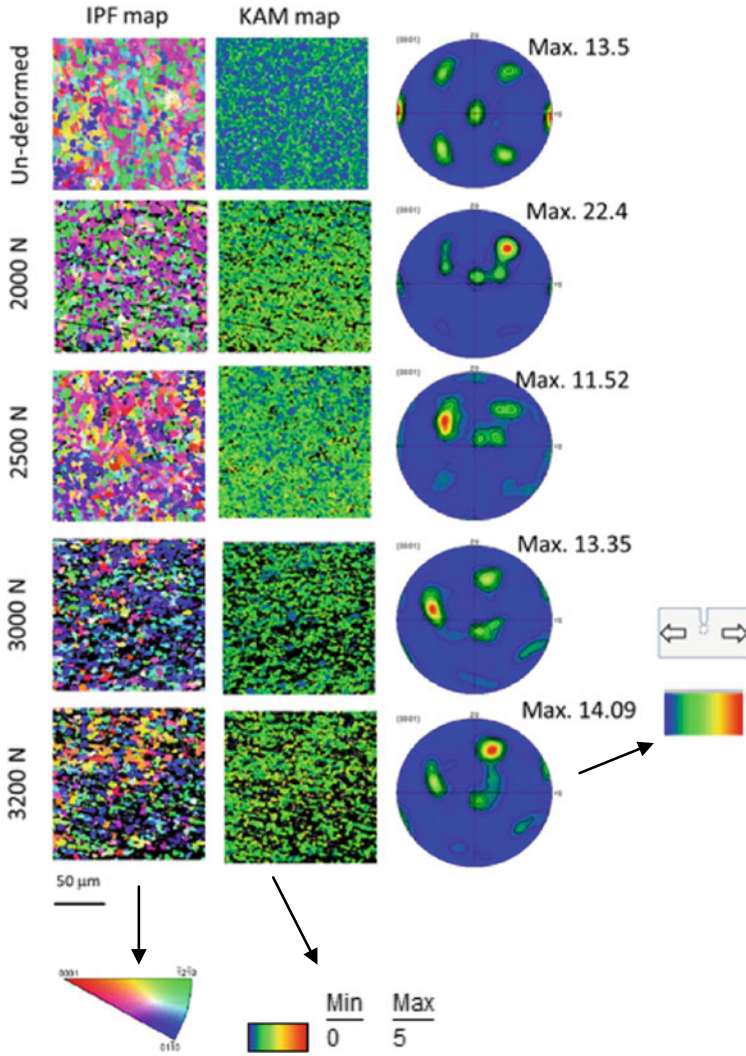


Fig. 5 IPF map, KAM map, and pole figures for various load amplitudes

the undeformed specimen before the test, and at the various magnitudes of loads. The undeformed specimen exhibits the recrystallized microstructure of grain average misorientation (GAM) 0.8. The pole figure shows the distribution of various crystallographic orientations. On application of 2000 N load, significant plastic deformation can be evident from the local misorientation map, with a high GAM (1.3). IPF map and pole figure map for this condition also suggest a localized crystallographic texture of very high intensity. This may be due to the stress concentration feature resulting in higher stress. However, on further loading of the same specimen to 2500 N, local

texture intensity weakens but the GAM was nearly the same (1.27). The shear band that was evident in the case of 2000 N was absent for 2500 N. On further deformation to 3000 N, though a higher deformation appears from the IPF and local misorientation map, the GAM value surprisingly decreases. GAM indicates the extent of deformation and its higher value suggests the high dislocation density. On the other hand, the lower GAM demonstrates the recovery type process due to formation of low angle boundaries inside the grain. A further analysis employing transmission electron microscope (TEM) can provide more insight into the mechanism. It can also be observed that the texture intensity increased to 13.35 on applying the load to 3000 N. The pole figure plot for 3200 N shows that the intensity further increased to 14.09. The shear band which was observed first time at 2000 N reappeared at 3200 N.

Thus, the applied load as low as 2000 N is enough to introduce plastic deformation at the notch tip of $K_t = 2.26$ resulting a high local texture. This is due to the significant crystallographic rotation with respect to the loading direction. On further loading the specimen (after terminating the first test at 2000 N) to 2500 N, a substantial drop in texture intensity is possibly due to high plastic deformation. At higher loads (>2500 N), texture intensity increases slightly due to higher plastic deformation. Thus, the maximum texture intensity at 2000 N may be due to significant plastic deformation. But to understand the further anomalous behavior, a further study may be needed.

4 Conclusion

1. Notched tensile specimen with single U-notch demonstrates a significant plastic deformation at a much lower load than the failure.
2. High texture intensity was observed at applied load of magnitude 2000 N suggesting a high crystallographic rotation may possible at lower load.
3. At higher load, the decrease in the order of texture intensity is again due to crystallographic rotation at enormous plastic deformation.

References

1. Boyer RR (1996) An overview on the use of titanium in the aerospace industry. *Mater Sci Eng A* 213:103–114
2. Lanning D (1999) Influence of stress state on high cycle fatigue of notched Ti-6Al-4V specimens. *Int J Fatigue* 21:87–95
3. Meyers MA, Subhash G, Kad BK, Prasad L (1994) Evolution of microstructure and shear-band formation in α -hcp titanium. *Mech Mater* 17:175–193
4. Noda N (1995) Stress concentration factors for round and flat test specimens with notches. *Int J Fatigue* 17:163–178
5. Pilkey WD (2008) Peterson's stress concentration

6. Hodhigere Y, Jha JS, Tewari A, Mishra S (2018) Finite element analysis-based approach for stress concentration factor calculation. Lecture notes mechanical engineering, pp 1–6
7. Young WC, Budynas RG (2002) Roark's formulas for stress and strain

Influence of Annealing Time on Local Texture Evolution in Forged Ti–6Al–4V Alloy



Satyaprakash Mishra, Hitarth Maharaja, Sushil K. Mishra, Jitesh Vasavada, and Jyoti S. Jha

Abstract The $\alpha + \beta$ titanium alloy Ti–6Al–4V is extensively used in the aero-engine components such as turbine blades and discs where the service temperature is less (<300 °C). These parts are mainly fabricated by the thermomechanical processing under the isothermal condition. A microstructure inhomogeneities (or local texture) can be observed after the secondary processing such as closed die forging. The origin of the inhomogeneities is believed to be the microstructure development stage only, and it persists even after the secondary processing. Such inhomogeneities in the forged component such as the turbine blade may cause crack initiation under the fatigue loading. Therefore, the primary processing is paid more attention to develop a homogenous microstructure. With the advent of advanced material characterization techniques such as electron backscatter diffraction (EBSD), the microstructure inhomogeneities have been recently characterized. In this study, two specimens were sectioned out from the different locations of the forged part, exhibiting different levels of inhomogeneities. These specimens were heat-treated for varying periods, and the influence of annealing time on the local texture evolution has been characterized using EBSD.

Keywords Ti–6Al–4V · EBSD · Local texture

1 Introduction

Ti–6Al–4V alloys have been extensively used in aerospace, energy and military application due to high strength-to-weight ratio and high corrosion resistance [1, 2]. The properties and performance under different processes of titanium alloy were highly depended on its microstructure. In case of titanium alloy, morphological and crystallographic microstructures have an equal influence on the properties and performance of the material [3]. Normally, these alloys are produced through forging at high temperature to achieve specific requirement. However, macrozone was observed

S. Mishra · H. Maharaja · S. K. Mishra · J. Vasavada (✉) · J. S. Jha
Department of Mechanical Engineering, Indian Institute of Technology Bombay, Powai, Mumbai 400076, Maharashtra, India
e-mail: jiteshvsvd@gmail.com

during thermomechanical deformation. Microzone contained grain with near parallel crystallographic direction different from their neighbourhood region [3, 4]. This microzone would act as nucleation site for the crack and also helped the crack to propagate. This microzone reduces the fatigue life significantly [5, 6]. Therefore, it is necessary to understand the formation of the microzone and possible way to dissolve these microzones after thermomechanical deformation.

In this study, the effect of heat treatment on microzone of deformed samples was studied. Crystallographic analysis was performed on deformed and heat-treated samples to understand the formation and dissolution of the microzone. The next sections describe the experimental procedure followed by result, discussion and conclusion.

2 Experimental

Commercially available Ti–6Al–4V was procured in the form of a rod. For compression test, samples were prepared of size 10 mm diameter and 15 mm height using wire EDM. Compression tests were carried out for six samples, three samples at 40% and three samples at 60%, deformation, at strain rate 0.1 s^{-1} and temperature $850 \text{ }^\circ\text{C}$. Two samples from each deformation (40 and 60%) were annealed at $950 \text{ }^\circ\text{C}$ for 1 and 5 h in muffled furnace followed by air-cooled. All the deformed and heat-treated samples were cut in loading direction using wire EDM and hot mounted for further metallographic analysis. These mounted samples were mechanical polished using 300, 600, 1200, 1500 and 2500 emery paper followed by colloidal silica of $0.03 \text{ }\mu\text{m}$ particle size for 45 min using automatic Tegramin-25 system Struers Inc. Microstructure characterization was done on Zeiss GEMINI 300 SEM equipped with Oxford detector. The scan was taken at 20 kV accelerating voltage with step size of $0.35 \text{ }\mu\text{m}$. HKL software is used to post-process the EBSD data. Orientation distribution function (ODF), inverse pole figure (IPF), misorientation distribution, grain size and kernel average misorientation (KAM) were measured from HKL software.

3 Result and Discussion

The microstructure of the as-received material is shown in Fig. 1. Compression tests were performed on as-received samples at $850 \text{ }^\circ\text{C}$ for 40% and 60% deformation with strain rate 0.1 s^{-1} . IPF maps of 40% and 60% deformed samples were shown in Fig. 2a, d, respectively. It was observed from the IPF micrograph that larger and dominant microzone was observed in 60% deformed sample (Fig. 2d) compared to 40% deformed sample (Fig. 2a). These microzones will behave as nucleation site for the crack during further mechanical processing such as fatigue. It was also observed that from IPF micrograph of both deformed sample that grain in the microzone

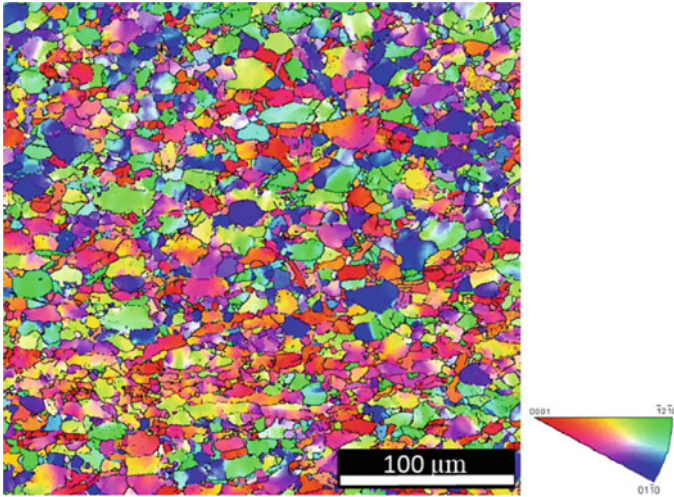


Fig. 1 IPF map of as-received Ti-6Al-4V alloy

contain near-parallel crystallographic direction. In this case, near-parallel crystallographic direction in microzone was $\langle 10 \bar{1} 0 \rangle$ which was almost parallel to loading direction as shown in Fig. 2a, d.

Further, 40 and 60% samples were heat-treated at 950 °C for 1 and 5 h. IPF map of heat-treated samples for 1 h and 5 h of 40% and 60% deformed samples is shown in Fig. 2b, c, e, f, respectively. It was clearly seen that microzone was dissolved in both, 40 and 60% deformed samples. Due to heat treatment of the deformed samples, recovery and recrystallization happened which remove the microzone from the deformed samples.

Distributions of KAM of deformed and heat-treated samples were plotted in Fig. 3. It is clearly observed that distribution of KAM of 60% sample has more spread and higher mean KAM than 40% deformed sample. This is because of higher dislocation density in 60% sample due to higher deformation than 40% sample. After heat treatment of 1, distribution of KAM of 60% sample coincided with 40% sample and skewed towards lower KAM angle. Distribution of KAM of 60% sample after 5 h of heat treatment is more skewed towards lower angle than 40% sample. 60% deformed samples have higher dislocation density. Therefore, it was more prone towards the recrystallization due to higher number of nuclei site compared to 40% deformed sample.

Mean grain size is plotted for deformed and heat-treated samples as shown in Fig. 4. Grain size of 60% deformed sample was less than 40% deformed samples which was due to higher deformation as well as formation of microzone where grain size is significantly less than other area in the sample. After 1 h of heat treatment, grain size of 60% samples increases significantly while 40% sample shown nearly same grain size as deformed samples. Grain size of 40 and 60% samples increased

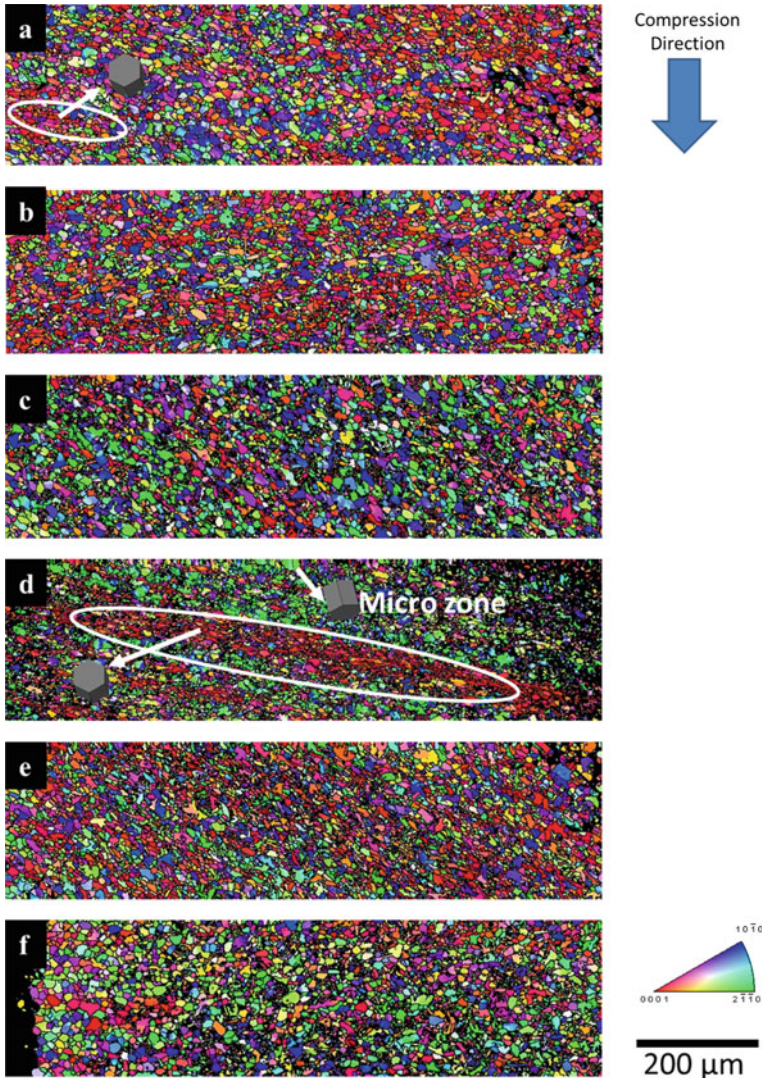


Fig. 2 IPF map of **a** 40% deformed, **b, c** 40% deformed followed by 1 and 5 h heat treatment, **d** 60% deformed, **e, f** 60% deformed followed by 1 and 5 h heat treatment

after 5 h of heat treatment at 950 °C. Grain size of 40% deformed sample was almost equal to 60% deformed sample after both samples were heat-treated for 5 h as shown in Fig. 4.

Misorientation angle distributions for 40% and 60% deformed and heat-treated samples were plotted in Fig. 5a, b, respectively. It is clear that deformed sample has peak at lower angle due to microzone formation. Microzone has grain with near-parallel orientation. Therefore, the misorientation angle between the grains in

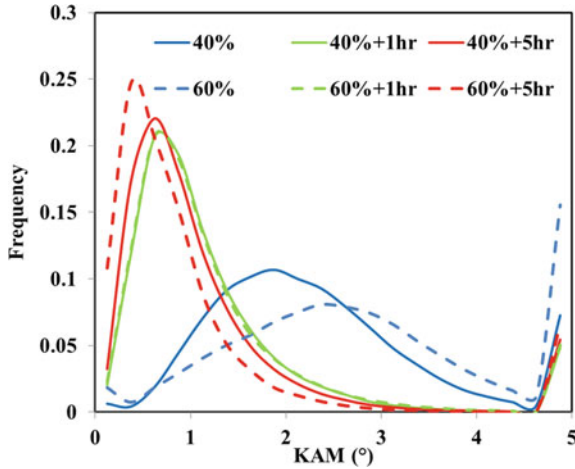


Fig. 3 Distribution of KAM for 40 and 60% deformed and annealed samples

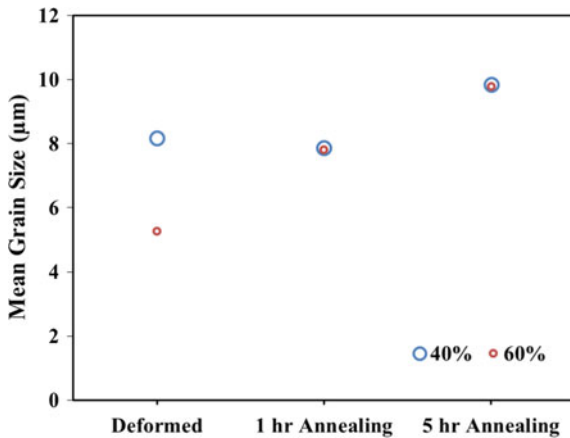


Fig. 4 Variation of mean grain size with different processing condition

microzone was nearly 3–10°. 60% deformed sample has larger microzone compared to 40% which can be seen from peak difference of misorientation distribution at lower angle. After annealing 1 and 5 h, lower angle peak is dissolved into three different peaks at ~10°, ~60° and ~90°. It is well known that five alpha variants are observed in titanium alloy fulfilling burgers relationship which are 10.5°, 60°, 60.83°, 63.26° and 90° [7]. Two distinct peaks of 60 and 63.26 are clearly observed in both the samples after heat treatments as shown in Fig. 5.

In general, dissolution of microzone formed due to compression at high temperature was studied using EBSD technique. The change in mechanical properties

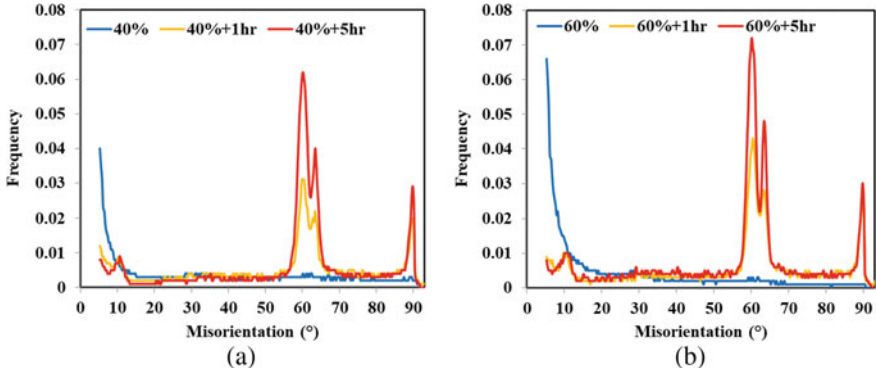


Fig. 5 Misorientation distribution of **a** 40% and **b** 60% deformed samples

(fatigue) after dissolution of microzone can be studied. The formation of the microzone can be studied using multimodal characterization.

4 Summary and Conclusion

From this study, following conclusions were drawn:

1. Small microzone is observed in 40% deformation sample. However, at higher strain (60%), large and dominant microzone was observed. After heat treatment of 1 h and 5 h, macrozone dissolved is completely due to recovery and recrystallization.
2. It was observed that basal direction in the grain of microzone is perpendicular to loading direction.
3. Grain size of 60% deformed sample was smaller than 40% sample due to higher deformation. After 5 h heat treatment, mean grain size of 40 and 60% deformed samples is saturated and almost equal.
4. Due to higher dislocation density, distribution of KAM of 60% is more spread than 40% deformed sample. After the heat treatment of 1 and 5 h, distribution of KAM in both the samples skewed towards lower angle which indicates fully recovery.

Acknowledgements The authors gratefully acknowledge the electron microscopy facility of Microstructural Mechanics and Microforming (MMM) laboratory and Four-Dimensional X-ray Microscopy (FDXM) facility at IIT Bombay for characterization. The authors also acknowledge CoEST IIT Bombay for providing experimental facilities for thermomechanical treatment.

References

1. Warwick JLW, Jones NG, Bantounas I, Preuss M, Dye D (2013) In situ observation of texture and microstructure evolution during rolling and globularization of Ti-6Al-4V. *Acta Mater* 61:1603–1615. <https://doi.org/10.1016/j.actamat.2012.11.037>
2. Germain L, Gey N, Humbert M, Vo P, Jahazi M, Bocher P (2008) Texture heterogeneities induced by subtransus processing of near α titanium alloys. *Acta Mater* 56:4298–4308. <https://doi.org/10.1016/j.actamat.2008.04.065>
3. Sheng J, Wang Z, Zheng L, Masset PJ, Wu D, Bai W, Zhang L, Liu L (2019) Characterization of microstructure and texture evolution in Ti664 Titanium alloy after multidirectional forging and annealing treatments. *Jom*. <https://doi.org/10.1007/s11837-019-03772-6>
4. Davies PS, Wynne BP, Thomas MJ, Rainforth WM (2018) Quantifying crystallographic texture variation in a titanium billet. *IOP Conf Ser Mater Sci Eng* 375. 10.1088/1757-899X/375/1/012019
5. Glavicic MG, Bartha BB, Jha SK, Szczepanski CJ (2009) The origins of microtexture in duplex Ti alloys. *Mater Sci Eng A* 513–514:325–328. <https://doi.org/10.1016/j.msea.2009.02.003>
6. Humbert M, Germain L, Gey N, Bocher P, Jahazi M (2006) Study of the variant selection in sharp textured regions of bimodal IMI 834 billet. *Mater Sci Eng A* 430:157–164. <https://doi.org/10.1016/j.msea.2006.05.047>
7. Harcuba P, Bartha K, Čapek J, Stráský J, Janeček M, Janovská M (2015) Alpha variant selection determined from grain misorientations in Ti-6Al-7Nb alloy with a duplex microstructure. *Acta Phys. Pol A* 128:570–574. <https://doi.org/10.12693/APhysPolA.128.570>

SUS304 Material Coating with Nickel Through Electroplating



D. Nurhadiyanto, Mujiyono, W. Abbas, Sutopo, and S. Haruyama

Abstract Material coating may improve the material surface by repairing the appearance of a material and hardening or softening the surface. Stainless steel is hard to be coated because it is not a conductor in nature. Thus, there is a need to put an effort and creativity to coat stainless steel. SUS304 stainless steel has a relatively hard surface which functions as a seal, so it needs to be coated with softer materials in order to fill the flange surface roughness. This study aims to coat SUS304 with nickel using the electroplating method. Electroplating is a procedure that is initiated with the activation and nickel strike plating processes. The results of this study show that nickel can fully coat the SUS304. The nickel coat attaches well to the material, and there is no nickel crack on the material surface.

Keywords Stainless steel · Coating · Nickel · Electroplating

1 Introduction

Material coating is usually done with the purpose of increasing resistance to corrosion, protecting the base metal against corrosion, or obtaining certain properties of materials. Coating may be done by melting, spraying, vacuum deposition, cladding, and electroplating. A coating method depends on the purpose of coating as well as the materials being coated.

A study focusing on the uses of corrugated metal gaskets reveals that in a high level of flange surface roughness, there is a leak in the metal gasket since the gasket material does not fill and completely cover the roughness of the surface Haruyama et al. [1]. Thus, the outermost surface should be coated with softer material. Three softer layers are used in the forming process Haruyama et al. [2] and Karohika et al.

D. Nurhadiyanto (✉) · Mujiyono · W. Abbas · Sutopo
Mechanical Engineering Education, Universitas Negeri Yogyakarta, Colombo street No 1
Karangmalang, 55281 Yogyakarta, Indonesia
e-mail: didiknur@uny.ac.id

S. Haruyama
Graduate School of Innovation and Technology Management, Yamaguchi University, Yamaguchi,
Japan

[3]. The weakness of this modification is that the softer material does not blend well with the base material, and they even tend to come apart after the cold forming process.

Nurhadiyanto et al. [4] conducted a study that employed the finite element method (FEM) to coat a SUS304 gasket with copper. The study aimed to determine the contact width and contact stress of the gasket after being coated with copper. It was found that the contact width increased and contact stress decreased after the gasket was coated.

Since copper-coated SUS304 gasket has been investigated, a further study needs to be conducted on corrugated stainless steel gasket coating with nickel in order to provide support for the previous study. However, there is a problem in determining the method of coating SUS304 with nickel.

Agboola et al. [5] reviewed the properties and parameters of nickel coating. The energy needed in the electroplating process and material costs is of important considerations in conducting the study. The most important coating criteria are the quality and uniformity of the deposited metal. Nickel coating is widely used for decoration and engineering purposes. The appearance and properties of deposited nickel material may vary in accordance with the control of coating operation parameter.

Wahab et al. [6] conducted a study on nickel-coated cemented carbide. This nickel coating improves the quality of the gasket surface, for example, in obtaining certain thickness and uniformity. The thickness of the coating is directly proportional to the period of coating and inversely proportional to the width between the anode and the cathode (electrode), whereas consistency tends to increase in the large electrode gaps. Empirical models of both coating thickness and uniformity are developed with various coating thicknesses and periods, and then optimized solutions are determined using these models.

This study focuses on coating SUS304 material with nickel. The coating is done using the electroplating method. The purposes of this study are coating SUS304 with nickel, examining the bond strength between SUS304 and the nickel layer, and investigating whether there is a crack on the nickel layer.

2 Material and Method

The base material used in this study is SUS304, which is characterized by the nominal stress of 398.8 MPa, tangent modulus of 1900.53 MPa, and elastic modulus of 210 GPa. The coating material is nickel having a nominal stress of 210 MPa, tangent modulus of 200 MPa, and elastic modulus of 170 GPa [7] and [8]. Nickel is softer than SUS304 in nature.

The SUS304 material is in the form of a perforated disk with ridges in its top and bottom. Based on the shape, this material is called a corrugated metal gasket. The corrugated surface on the disk is formed using the cold forming method with a certain pressure [1]. The disk thickness is 1.5 mm with 7.5 mm inner diameter and 20 mm outer diameter.

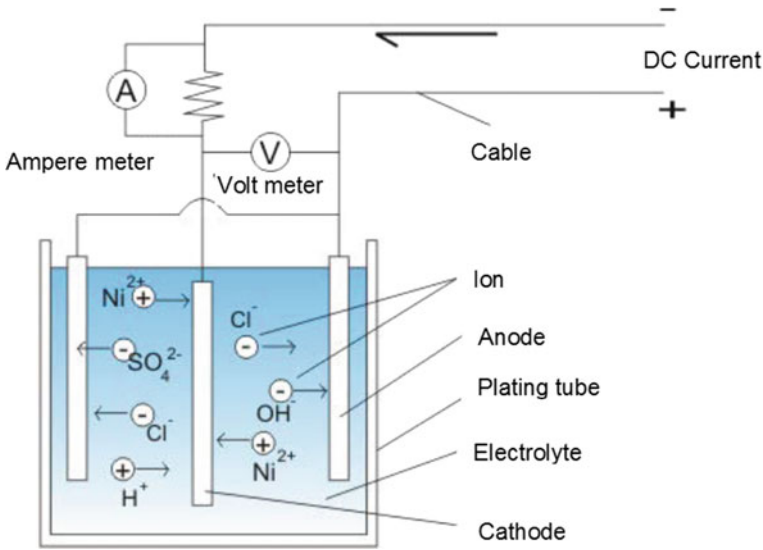


Fig. 1 The process of electroplating

Electroplating is a process of coating a metal with other metals using electrical current. In this study, the main purpose of electroplating is to make SUS304 surface softer without affecting its original stiffness. The coating material is resistant to corrosion and destructive chemicals. The process of electroplating is presented in Fig. 1 [9].

Nickel coating is an electrochemical deposition process. The SUS304 material was put in an electrolyte as a cathode. The nickel bar functioned as an anode that would stay in the SUS304 material. The electroplating on SUS304 is not an easy process since SUS304 is not a conductor. Nickel cannot be easily attached in the SUS304 material before the activation and nickel strike processes are in place. Those procedures were carried out to make the surface/pores of the stainless steel open. The flowchart of the electroplating process for coating stainless steel with nickel is presented in Fig. 2.

Hot degreasing cleans fat attached on the SUS304 material. The fat cleansing is done by rubbing the surface of the gasket with the alkaline solution for 2–3 min before rinsing with water for 1–2 min.

The pickling process was to remove rust on SUS304 by immersing the gasket in 20% hydrochloric acid (HCl) solution for 15 min. When the process was done, the gasket was rinsed with water to remove dirt. Then, the stainless steel was again immersed in the 30% H₂SO₄ solution for about one minute until gas came out of the gasket. This procedure was carried out in order to activate the stainless steel ions, so the gasket can be coated with nickel.

The next step, nickel strike plating, is carried out only if the object being coated is stainless steel. The solution for nickel strike plating was composed of nickel chloride

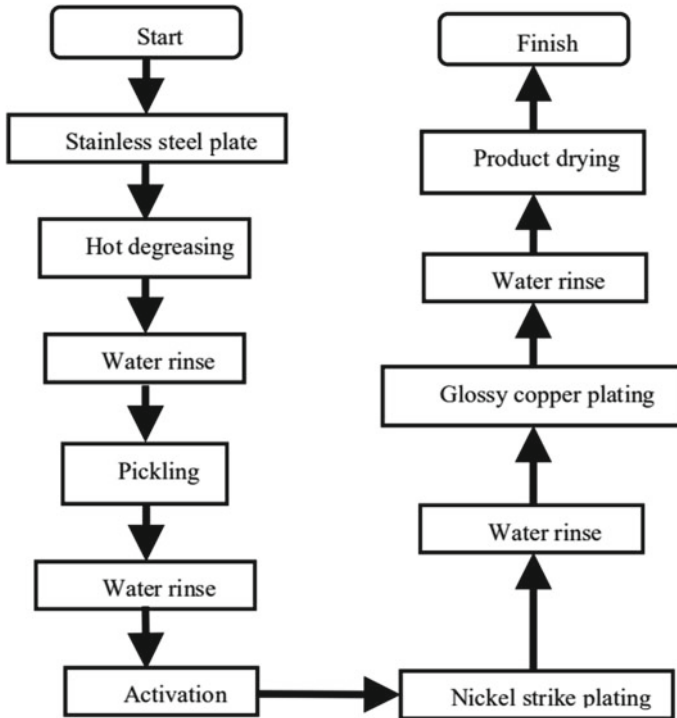


Fig. 2 Flowchart of the electroplating process

($\text{NiCl}_2 \cdot 6\text{H}_2\text{O}$) 240–300 gr/L and pure hydrochloric acid 86 gr/L. This procedure was done by immersing the gasket into the solution for 2 min anodic and 3 min cathodic. The last step of this procedure was rinsing the object with water.

After going through the nickel strike plating process, SUS304 was ready to be coated with nickel under the process of shiny nickel plating. The solution used in this process was nickel sulfate ($\text{NiSO}_4 \cdot 6\text{H}_2\text{O}$) 250–325 gr/L, nickel chloride ($\text{NiCl}_2 \cdot 6\text{H}_2\text{O}$) 45–65 gr/L, boric acid (H_3BO_3) 25–40 gr/L, and 4 cc/L brightener. Current and voltage values were used 1 A and 4 V, respectively. The duration of the coating process depends on the desired and required thickness. After completing each step of the procedure, the gasket was rinsed with water. The thickness of the nickel layer on the stainless steel gasket varied from 20 to 30 μm . Figure 3 presents the gasket before and after being coated.

The microstructure test was a procedure to examine whether the nickel attached well to the SUS304 material. Before the gasket was tested, it was cut in accordance with the required specimen. Sandpaper was used to make the surface of the specimen softer, into the 1500 level. After the test specimens were formed using resin, microstructure testing was done by examining the specimens under a microscope with 400 times magnification. The microspecimen structure is shown in Fig. 4, and the equipment used in microstructure testing is shown in Fig. 5.

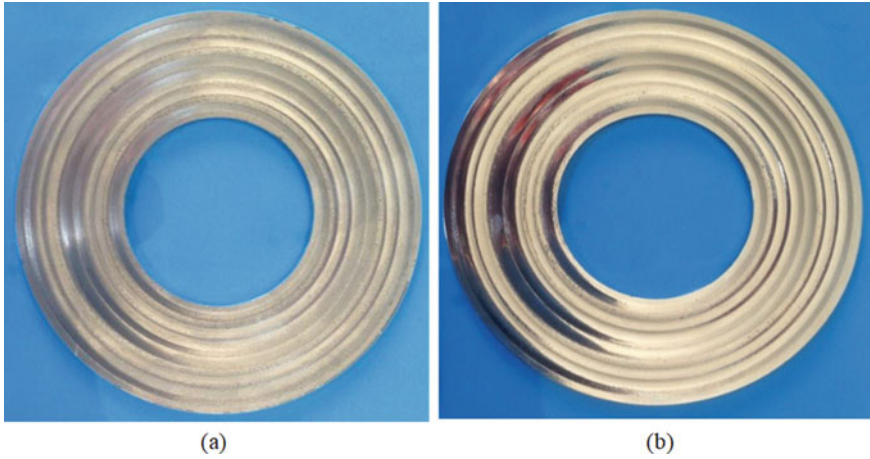


Fig. 3 Flowchart of the electroplating process **a** gasket before being coated with nickel, **b** gasket after being coated with nickel



Fig. 4 Specimens in the microstructure test

3 Results and Discussion

The bond strength of nickel coated to SUS304 is examined using the microstructure test from the visual state only. The bond of the nickel layer is presented in Fig. 6.

Figure 6 shows the results of nickel coating on SUS304 material. From two images of the gasket, it can be seen that there is a nickel layer on the edge of the stainless steel surface. In addition, from the upper and lower sides, there is a line dividing two layers. This means that there is no diffusion of nickel coating on SUS304. Moreover, the nickel layer attaches well on the SUS304 surface since there is no crack on it.

The SUS304 material's outer diameter (D) is 74.6 mm, its inner diameter is 35.1 mm, (d), and it has 1.6 mm thickness (t). Nickel coating covers a total of



Fig. 5 Specimens in the microstructure test

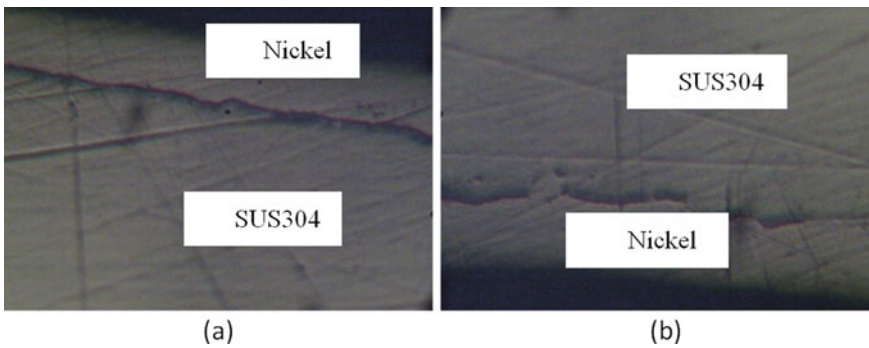


Fig. 6 Nickel bond on SUS304 **a** the top surface of tge gasket, **b** the bottom surface of the gasket

7354.1828 mm² of the stainless steel surface. The specific gravity of nickel is 0.008908 gr/mm³. The bond strength (ρ) is formulated in Eq. (1), while the thickness of the layer is shown in Eq. (2).

$$\rho = \frac{\text{Layer weight}}{\text{Layer volume}} \tag{1}$$

Table 1 Weight gained after 40 min of coating

No	Initial weight (gram)	Shiny nickel weight (g)		
		20 min	10 min	10 min
1	39.38	39.44	39.54	39.75
2	39.68	39.71	39.86	39.91
3	39.34	39.55	39.63	39.87
4	39.63	39.69	39.79	39.97
5	39.39	39.90	40.04	40.06
Average	39.484	39.658	39.772	39.912

$$\text{layer thickness} = \frac{\text{Layer weight}}{\rho \cdot \text{Layer area}} \quad (2)$$

Table 1 shows the data of SUS304 weight and the amount of nickel coating its surface. Those data present the initial weight and weight gained after 20, 30, and 40 min of coating which employs 1 A of current for each procedure.

Table 1 shows that the average weight gained in 40 min is 0.428 g. It indicates that as time increases, the material gains more weight. Thus, it is easy to predict the weight of nickel after certain periods of coating. The coating thickness is calculated using the Eq. (2).

Based on the above data, it is predicted that it takes 120 min to obtain the specified thickness of 20 μm , and 184.6 min to obtain 30 μm .

In accordance with the discussion above, SUS304 coating with nickel may be carried out using the electroplating procedure, but since SUS304 is not a conductor in nature, activation and nickel strike plating processes need to be done beforehand. The above-mentioned processes activate the ions and open up the stainless steel's pores. Nickel is not diffused into the material since it is well attached on the surface of the material. The bond of both materials is massive and even, so there is no crack on the surface being coated. The activation process should be done until gas comes out of the SUS304 gasket. If no gas comes out of the material during the process, the nickel may not be attached well on SUS304.

4 Conclusions

Based on the results of coating and microstructure testing in this study, the following conclusions can be drawn.

1. The electroplating procedure is done to coat the SUS304 material with nickel. In order to make the nickel fully coat the stainless steel surface, activation and nickel strike processes to open up the SUS304 ions should be conducted. Then, shiny nickel coating may be done as required.

2. There is no diffusion of nickel on SUS304 surface because the coating attaches only on the base material.
3. There is a quite strong bond between the SUS304 material and nickel, and there is no crack on the material surface.

Acknowledgements This project was supported by Ministry of Research, Technology, and Higher Education of the Republic of Indonesia by the scheme of “Penelitian Terapan Unggulan Perguruan Tinggi” year 2019.

References

1. Haruyama S, Nurhadiyanto D, Choiron MA, Kaminishi K (2013) Influence of surface roughness on leakage of new metal gasket. *Int J Press Vessels Pip* 111–112:146–154
2. Haruyama S, Karohika IMG, Sato A, Nurhadiyanto D, Kaminishi K (2016) Development of 25A-size three-layer metal gasket by using FEM simulation. *Int J Mech Aerosp Indust Mechatron Manuf Eng* 10:527–533
3. Karohika IGM, Haruyama S, Kaminishi K, Oktavianty O, Nurhadiyanto D (2017) Analysis of contact width and contact stress of three-layer corrugated metal gasket. *Int J Mech Aerosp Ind Mechatron Manuf Eng* 11:870–879
4. Nurhadiyanto D, Mujiyono, Sutopo, Ristadi FA (2018) Simulation analysis of 25A-size corrugated metal gasket coated copper to increase its performance. *IOP Conf Ser Mater Sci Eng* 307:1–6
5. Agboola OS, Sadiku ER, Biotidara OF (2012) The properties and the effect of operating parameters on nickel plating (review). *Int J Phys Sci* 7(3):349–360
6. Wahab HA, Noordin MY, Izman S, Kurniawan D (2013) Quantitative analysis of electroplated nickel coating on hard metal. *Sci World J*
7. *Materials Data Book* (2003) Edition Cambridge University Engineering Department
8. Cambridge Engineering Selector software (CES 4.1) (2003) Granta design Limited. Rustat
9. Belkin PN, Yerokin A, Kusmanov SA (2016) Plasma electrolytic saturation of steel with nitrogen and carbon. *Surf Coat Technol* 307:1134–1218

Three-dimensional FE Model for Stress Analysis of Adhesively Bonded Single Lap Joints with Hard Steel Adherend



Ranjan K. Behera, S. K. Parida, and R. R. Das

Abstract The three-dimensional (3-D) variation of stresses of the single lap joint (SLJ) made from hard steel and epoxy (AV119) under tensile loading is studied using 3-D FE (finite element) analysis. The peel (tension) stress, direct shear (in-plane shear) stress and transverse shear (out-of-plane shear) stress are the responsible for opening (mode-I), sliding (mode-II) and tearing (mode-III) mode of failures, respectively, are computed in the overlap region of the joint. Thin adhesive layer used to join the upper (lap) adherend and the lower (strap) adherend is modelled by surface to surface contact elements. The nonlinear material properties of adhesive and adherend (stress and strain graph obtained from the experiments) are input to the finite element programme. The results show that the variations of peel stress and shear stresses in the overlap region are very complicated in nature and hence a 3-D FE analysis is recommended to have a clear visualisation of these stress variations. The peel stress among all the failure-inducing stresses at the overlap ends are dominant and important for adhesive bonded joint as adhesives are weaker than the stronger adherends. The results of the 3-D FE analysis of the SLJ are in good agreement with the experimental results. This research work is may be considered as detail study of the stress distributions in the vulnerable region of the joint under tensile loading.

Keywords Single lap joint · Structural adhesive bonding · Hard steel · FE analysis · Adhesion failure · VCCT

R. K. Behera (✉)

School of Mechanical Engineering, Kalinga Institute of Industrial Technology, Deemed To Be University, Bhubaneswar, Odisha 751024, India

e-mail: ranjancet@gmail.com

S. K. Parida

Department of Manufacturing Engineering, National Institute of Foundry and Forge Technology (NIFFT), Hatia, Ranchi 834003, India

e-mail: sambitparida@gmail.com

R. K. Behera · R. R. Das

Department of Mining Machinery Engineering, Indian Institute of Technology (ISM), Dhanbad, Jharkhand 826004, India

1 Introduction

Adhesive bonding offers numerous benefits over bolting, riveting and welding methods. Some of these advantages are reduced weight penalty, reduction of stress concentrations and easy manufacturability, etc. Some of the theories against lap joint developed by so many researchers, such as Wang and Yau [1], Adams and Peppiat [2], daSilva and Adams [3], Carpenter [4], Tong [5], Tsai and Morton [6], Fernlund [7], Penado [8], Hart-Smith [9], Parida and Pradhan [10] and Liljedahl et al. [11], etc. has shown that the stresses such as peel stresses shear and cross-shear stresses are very important and responsible for failure propagation in adhesive bonded joints. This may be region out because of the complicated variation of the peel and shear stresses and they are highly dependent on adhesive and adherend properties, geometrical configurations, types of loading conditions, etc. These theories are two dimensional in nature.

The experimental way of finding the joint is expensive, time consuming, needs a lot of sophistications and sometime not possible. Significant aspects, such as material nonlinearity, large deformation and complicated geometry may be considered into account by FE analysis. Adams and Peppiat [2] and Hart-Smith [9] are among those who first carried out FE analysis to compute two-dimensional stress distributions in adhesively bonded joints. Behera et al. [12, 13] have studied 3-D failure analysis in the SLJ specimen with various circular and rectangular defects.

The effect of ductility of adherends and adhesive on the joint strength with pre-embedded artificial damage has been reported by Karachalios et al. [14]. They have shown that when the size and shape of the adhesion failure are small (as compared to the dimensions of the overlap region) and located centrally in the overlap region does not influence the strength much or at all. The effect of ductile adherends yielding on the joint strength have been highlighted in the reference [15, 16]. Extreme yielding of adherend at the overlap region can initiate early joint failure because large plastic deformation seen at these regions [17].

Objective of this research; (i) to simulate the 3-D distribution of the peel and shear stresses responsible for failure of the joint by inputting the actual stress–strain behaviour of the adherend (high strength) and the thin adhesive (AV119) from the experiments, (ii) to have an idea about of the extent of the severity of that the stresses put on the failure and (iii) identify the stress critical region in the joint so that the joint designer can have the methods to reduce these stresses.

2 3-D Finite Element Modelling of the SLJ

The overall geometrical configuration of SLJ is shown in Fig. 1a and boundary conditions and loading of the SLJ is shown in Fig. 1b. High strength steel is used as the adherend and AV119 (structural epoxy) is used as the adhesive. The material properties of adhesive and adherend of the SLJ are given details in Table 1. The

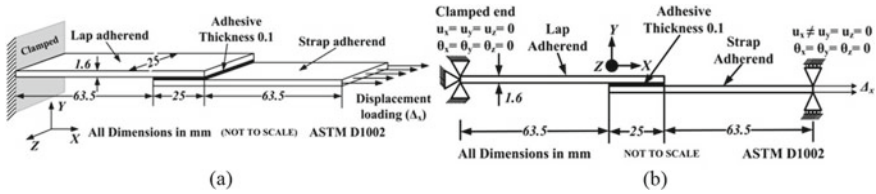


Fig. 1 Configuration of SLJ as per ASTM D1002 **a** 3-D SLJ and **b** 2-D SLJ with boundary conditions and loading

Table 1 Material properties of adherends (hard steel) and adhesive (AV119) of SLJ ([14] and [20])

Elastic modulus (E)	Adherend (hard steel)		Adhesive (AV119)	
	200.00	GPa	3.03	GPa
Yield tensile stress, (σ_t) _y	1800.00	MPa	71.00	MPa
Yield shear stress, (σ_s) _y	–		50.00	MPa
Poisson’s ratio (ν)	0.29		0.34	

stress–strain behaviour of the adhesive (AV119) in tension (Fig. 2a) and in shear (Fig. 2b) are given for reference. The stress–strain behaviour of the adherend (hard steel) is presented in Fig. 2c.

The FE programme Abaqus Standard was used to perform the numerical analysis of the SLJ. Three-dimensional eight noded elements (C3D8R) have been used to model the strap (lower) adherend and lap (upper) adherends. Thin adhesive used to join lower and upper adherend is modelled by surface to surface contact elements. The critical energy release rate from the literature and virtual crack closure technique (VCCT) method was used to input to the FE programme as fracture criterion in the contact properties, to simulate the thin adhesive layer. In boundary conditions, fully constrained (clamped) at left end of upper adherend and quasi-static displacement

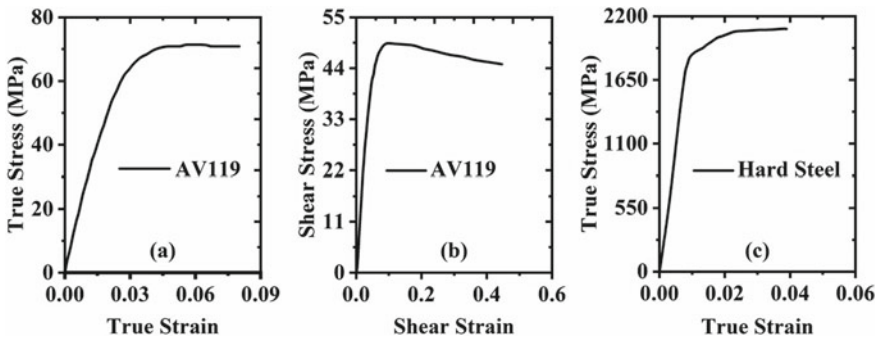


Fig. 2 For AV119 adhesive **a** true stress–strain curve, **b** shear stress–strain curve and for hard steel adherend, **c** true stress–strain curve [14]

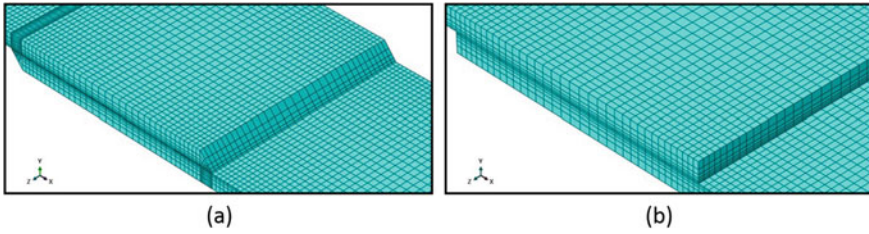


Fig. 3 Zoomed view of 3-D FE meshing pattern of SLJ at the overlap end **a** with fillet (45°) and **b** without fillet

loading (up to 1 mm) at right end of lower adherend in SLJ is applied as shown in Fig. 1b. The mesh densities of the FEs have been enhanced at the overlap end to record the sudden changes of stresses in this region. The mesh convergence studies have been carried out according to the advices given by Tay et al. [18] and Raju et al. [19]. The zoomed view of the FE mesh around the overlap region as presented in Fig. 3a, b for the SLJ having with and without fillet at overlap end, respectively.

3 Validate the Experiment Results with FEA

To validate the results of the numerical computations, 3-D models of the SLJ (as per ASTM D1002) with and without fillet as presented in Fig. 3a, b have been created as per the modelling procedure discussed in the previous section. The geometrical dimensions and boundary conditions of the SLJ are applied as given in Fig. 1b. The material properties of both adhesives (AV119) and adherends (hard steel) are input to the FE analysis from the stress vs. strain curve (as shown in Fig. 2 [14]) by extracting the point-to-point data using reverse engineering technique. The loads vs. displacements have been computed from the 3-D FE analysis and are plotted in Fig. 4

Fig. 4 Load versus displacement curve of the SLJ made with hard steel adherends (with and without fillet)

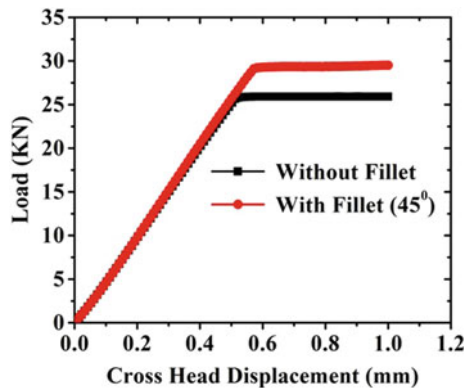


Table 2 Failure load from the experiment and failure load computed from 3-D FE analysis of the SLJ

	Experiment [20] with fillet (45°)	Present (FEA)		
		With fillet (45°)	% Error	Without fillet
Failure load of the SLJ (KN)	30.76 kN	29.71 kN	3.413	26.08 kN

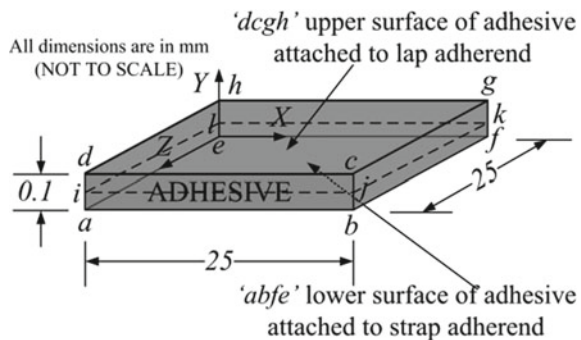
for the SLJ with fillets and without fillets. The experimental peak load obtained by Karachalios et al. [20] and present FEA model are in close agreement and are given in Table 2.

4 Results and Discussion

The stress concentration in the interfaces of the adherends and adhesive of the SLJ is prevalent mainly because of the mismatch of the engineering properties and sudden change of geometry of the structural joint near the overlap region. Hence, the peel stress (σ_{yy}), direct shear stress (τ_{yx}) and transverse shear stress (τ_{yz}) are responsible for opening (i.e. mode-I, tension), direct sliding (i.e. mode-II, in-plane shear) and cross-sliding or tearing (mode-III, out-of-plane shear) mode of adhesion failure, respectively, of the SLJ (in the overlap region) need to be carefully evaluated.

Figure 5 represents the exaggerated 3-D views of adhesive layer in the SLJ in the overlap region. The lower bonded area ('abfe') and upper bonded area ('dcgh') are attached to lower (strap) and upper (lap) adherend, respectively. The layer 'ijkl' represents the mid-plane of the adhesive layer. Distribution of peel, direct shear and transverse shear stresses in the mid-plane of the adhesive layer and the interfacial overlap region between adhesive and adherends are given below.

Fig. 5 Dimensional view of adhesive layer at bonded area of SLJ near the overlap region



4.1 Distribution of Peel Stress (σ_{yy}) in the Overlap Region

Figure 6a represents the 3-D distribution of the peel stress in the plane ‘ijkl’. It is observed that the graph is symmetrical about the planes parallel to Z and X-planes in the middle of the overlap region. The peel stress in the central region of the overlap is substantially less compared to those at overlap ends and remains almost constant between approx. 5 and 20 mm in the overlap region. The peel stress even becomes compressive in nature in this region. Hence, the peel stress can cause closure the microcrack in this region. The peel stress variations along the width direction (‘jk’ and ‘il’) can be visualised from Fig. 6a. Greater values of the peel stress are seen in the central part than at extreme ends. Magnitudes and nature of the peel stress are found to be same at both the overlap ends. That’s why the cohesion failure in mode-I may initiate not from the ends rather from middle location region of along the width ‘jk’ and ‘il’. Similar observations are also reported in literatures [21, 22].

Figure 6b represents 3-D peel stresses distribution in the plane ‘abfe’. The magnitudes of the peel stress variation along the line ‘ae’ is higher than the peel stress in the corresponding location along the line ‘il’ in the mid-plane (i.e. in the plane ‘ijkl’) of the adhesive layer. Again, the peel stresses of lower adherend at edge ‘ae’ and ‘bf’ have different magnitude unlike in the middle of the adhesive layer. So, the adhesion failure may initiate at the edge (‘ae’) in interface having higher peel stress. The distribution of the peel stress (Fig. 6c) in the bond line interface of the adhesive and the upper adherend is the reverse order of the peel stress distribution in the bond line interface of the lower adherend (Fig. 6b). Similarly, the peel stresses of upper adherend at edge ‘dh’ and ‘cg’ have a different magnitude unlike in the middle of the adhesive layer. So, the adhesion failure may initiate at the edge (‘cg’) in interface having higher peel stress.

Compare all the peel stresses as above; we conclude that the peel stress is greater at two ends of the overlap region rather than the middle of the overlap region. The magnitude of the peel stress variation along the width ‘ae’ (which is attached to strap adherend with adhesive layer) and ‘cg’ (which is attached to lap adherend with

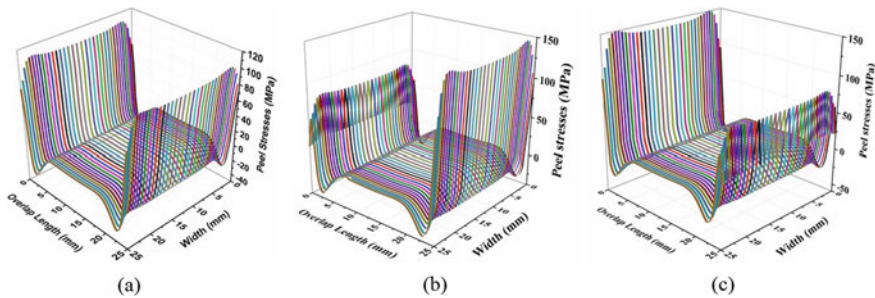


Fig. 6. 3-D peel stresses distribution at **a** the mid-plane of the adhesive layer, **b** interface between adhesive and strap (lower) adherend, **c** interface between adhesive and lap (upper) adherend in the overlap region

adhesive layer) is greater as compared to other bond line interface. So, the adhesion failure may initiate at width region rather than overlap region.

4.2 Distribution of Direct Shear Stresses (τ_{yx}) in the Overlap Region

Figure 7a represents 3-D direct shear stresses variation along the overlap lengths. The magnitude of shear stress does not vary much along width 'il' and 'jk'. It indicates that maximum direct shear stresses are developed at middle of the width than the two ends of adhesive. So, the mode-II type cohesion failure may occur from the middle of the (along the line 'il' or 'jk') adhesive rather than the ends of the adhesive. However, the shear stress magnitude in this plane is smaller than that of the magnitude of the peel stress.

Figure 7b shows 3-D direct shear stresses distribution of lower adherend along overlap length which attached to lower surface 'abfe' of adhesive. We found the direct shear stress maximum at free edge 'ae' which are tensile in nature rather than edge 'fb' which are compressive in nature of lower adherend. The magnitude of direct shear stresses of lower adherend at edge 'ae' is greater than the magnitude of direct shear stresses of adhesive at middle edge ('il'). So, the adhesion failure may occur in between lower adherend and adhesive rather than the cohesion failure in adhesive. However, the magnitude of the direct shear stress in this plane is smaller than that of the magnitude of the peel stress. Figure 7c 3-D direct shear stress variation in the bond line interface of the adhesive and the upper adherend is the reverse order of the direct shear stresses distribution in the bond line interface of the lower adherend and adhesive. Similarly, the direct shear stresses of upper adherend at edge 'dh' and 'cg' have different magnitude unlike in the mid-plane of the adhesive layer. So, the adhesion failure may initiate at the edge ('cg') in interface having higher direct shear stress.

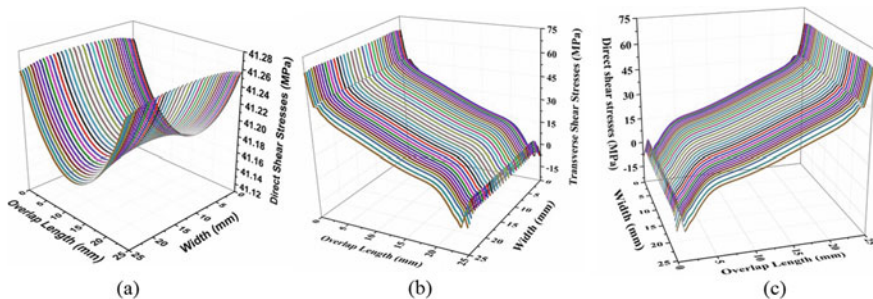


Fig. 7. 3-D direct shear stresses variation at **a** the mid-plane of the adhesive layer, **b** the interface between adhesive and strap (lower) adherend, **c** the interface between adhesive and lap (upper) adherend in the overlap region

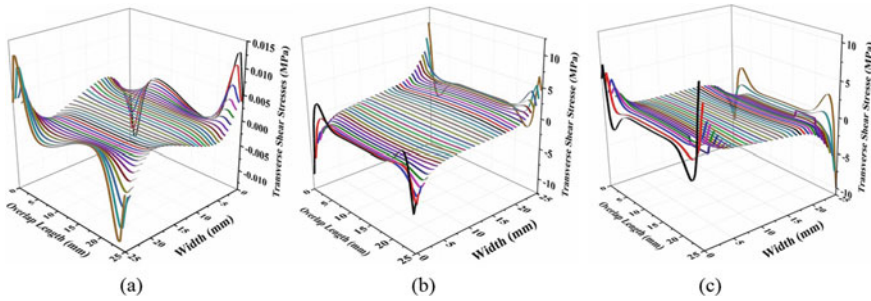


Fig. 8. 3-D transverse shear stresses distribution at **a** the mid-plane of the adhesive layer, **b** the interface between adhesive and strap (lower) adherend, **c** the interface between adhesive and lap (upper) adherend in the overlap region

Compare all the direct shear stresses as above; we conclude that the direct shear stress is greater at two ends of the overlap region rather than the mid-plane of the overlap region. The value of the direct shear stress variation along the width ‘*ae*’ (which is attached to strap adherend with adhesive layer) and ‘*cg*’ (which is attached to lap adherend with adhesive layer) is greater as compared to other bond line interface. So, the adhesion failure may initiate at width region rather than overlap region. But its magnitude is less than the peel stress at that region.

4.3 Distribution of Transverse Shear Stresses (τ_{yz}) in the Overlap Region

Figure 8a–c shows 3-D transverse shear stresses distribution of middle of the adhesive layer (‘*ijkl*’), interface of the adhesive and lower adherend (‘*abfe*’) and interface of the adhesive and upper adherend (‘*dcgh*’) along overlap length. The magnitude of transverse shear stress is very small as compared to peel and direct shear stress in the corresponding locations. So, these stresses can be neglected. Hence, the failure due to mode-III can be neglected.

5 Conclusions

Following 3D nonlinear FE analyses have been carried out for SLJ:

- Mode-I failure: The peel stress is greater at two ends of the overlap region rather than the mid-plane of the overlap region. The magnitude of the peel stress variation along the width ‘*ae*’ (which is attached to strap adherend with adhesive layer) and ‘*cg*’ (which is attached to lap adherend with adhesive layer) is greater as compared

to other bond line interface. So, the adhesion failure may initiate at width region rather than overlap region.

- Mode-II failure: The direct shear stress is greater at two ends of the overlap region rather than the middle of the overlap region. The value of the direct shear stress variation along the width 'ae' (which is attached to strap adherend with adhesive layer) and 'cg' (which is attached to lap adherend with adhesive layer) is greater as compared to other bond line interface. So, the adhesion failure may initiate at width region rather than overlap region. But its magnitude less than the peel stress at that region.
- Mode-III failure: The transverse shear stresses (out-of-plane shear stresses) are very small in magnitude as compared to peel and direct shear stresses. Hence, the failure due to mode-III can be neglected.
- Out of three modes of failure, mode-I is the dominating mode of failure in case of adhesive bonded SLJ.

References

1. Wang SS, Yau JF (1982) Interface cracks in adhesively bounded lap-shear joints. *Int J Fract* 19:295–309
2. Adams RD, Peppiatt NA (1974) Stress analysis of adhesive-bonded lap joints. *J Strain Anal Eng Des* 9:185–196
3. da Silva FML, Adams DR (2007) Techniques to reduce the peel stresses in adhesive joints with composites. *Int J Adhes Adhes*
4. Carpenter WC (1991) A comparison of numerous lap joint theories for adhesively bonded joints. *J Adhes* 35:55–73
5. Tong L (1998) Strength of adhesively bonded single-lap and lap-shear joints. *Int J Solids Struct* 35:2601–2616
6. Tsai MY, Morton J (1994) Three-dimensional deformations in a single-lap joint. *J Strain Anal Eng Des* 29:137–145
7. Fernlund G (2007) Stress analysis of bonded lap joints using fracture mechanics and energy balance. *Int J Adhes Adhes*
8. Penado FE (2000) Analysis of singular regions in bonded joints. *Int J Fract* 105:1–25
9. Hart-Smith LJ (1987) Design of adhesively bonded joints. *Join Fibre Reinforced Plast*. 271–311
10. Parida SK, Pradhan AK (2014) 3D finite element analysis of stress distributions and strain energy release rates for adhesive bonded flat composite lap shear joints having pre-existing delaminations. *J Mech Sci Technol* 28:481–488
11. Liljedahl CDM, Crocombe AD, Wahab MA, Ashcroft IA (2006) Damage modelling of adhesively bonded joints. *Int J Fract*
12. Behera RK, Parida SK, Das RR (2019) Effect of the aspect ratio of the pre-existing rectangular adhesion failure on the structural integrity of the adhesively bonded single lap joint. *J Adhes Sci Technol* 33:2093–2111
13. Behera RK, Parida S, Das R (2019) Three-dimensional adhesion failure analysis of the single lap joint having pre-embedded circular defects. *J Strain Anal Eng Des* 54:293–309
14. Karachalios EF, Adams RD, Da Silva LFM (2013) Strength of single lap joints with artificial defects. *Int J Adhes Adhes* 45:69–76
15. Kafkalidis MS, Thouless MD (2002) The effects of geometry and material properties on the fracture of single lap-shear joints. *Int J Solids Struct* 39:4367–4383

16. Volkersen O (1938) Die Nietkraftverteilung in zugbeanspruchten \mbox{Nietverbindungen} mit konstanten Laschenquerschnitten. *Luftfahrtforschung* 15:41–47
17. Haghpanah B, Chiu S, Vaziri A (2014) Adhesively bonded lap joints with extreme interface geometry. *Int J Adhes Adhes* 48:130–138
18. Tay TE, Shen F, Lee KH, Scaglione A, Di Sciuva M (199) Mesh design in finite element analysis of post-buckled delamination in composite laminates. In: *Composite structures*
19. Raju IS, Crews JH, Aminpour MA (1988) Convergence of strain energy release rate components for Edge-Delaminated composite laminates. *Eng Fract Mech*
20. Karachalios EF, Adams RD, da Silva LFM (2013) Single lap joints loaded in tension with high strength steel adherends. *Int J Adhes Adhes* 43:81–95
21. Adams RD, Comyn JC, Wake CW (1997) *Structural adhesive joints in engineering*, 2nd edn
22. Adams RD, Davies R (1996) Strength of joints involving composites. *J Adhes* 59:171–182

Numerical Simulation of Sand Casting Process: A Case Study on Globe Valve



Yash Mittal, Nikhil Parasar, Jambeswar Sahu, Umakant Mishra,
and Chinmaya P. Mohanty

Abstract Globe valves are primarily manufactured by a casting process are extensively used for controlling the fluid flow in pipelines in various mechanical devices, viz. boilers, condensers, overhead tanks, etc. However, the component faces a lot rejection due to various casting defects occurring during the manufacturing process majorly because of the improper gating system design. In view of this, the present work proposes a numerical simulation on globe valves prepared by the sand casting process by varying the number of gates in gating system design. The effectiveness of both the designs is evaluated in terms of flow front, air entrapment and porosity percentages obtained from both the designs. From the simulation results, it is observed that an increasing number of gates in gating system design can result in better flow front, lesser air entrapment, promotion of directional solidification and lesser porosity percentage in casted product. The proposed model can be useful for producing sound casted product and defect-free casting thereby reducing the manufacturing costs.

Keywords Sand casting · Numerical simulation · Shrinkage · Porosity · Solidification

1 Introduction

Casting is a conventional manufacturing process for manufacturing complex metal objects. The process involves pouring molten metal at high temperature into the mold cavity and ejection of the desired component after permissible solidification time. However, involving the complexity of the process, viz. high pouring temperature, optimum velocity of the molten metal into the mold cavity, it is extremely difficult

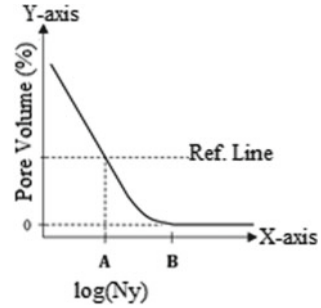
Y. Mittal · N. Parasar · J. Sahu · C. P. Mohanty (✉)
School of Mechanical Engineering, Vellore Institute of Technology University University,
Gorbachev Rd, Vellore 632014, India
e-mail: chinmaymohantymech@gmail.com

U. Mishra
School of Advanced Sciences, Vellore Institute of Technology University University, Gorbachev
Rd, Vellore 632014, India

to accomplish the process experimentally. However, regardless of these difficulties to achieve defect-free and sound casted components, various studies reported by researchers are discussed in the following lines. Survey conducted by Ravi concluded that overall usage of casting simulation software is 5% in India, whereas it is 90% and 75% in Germany and America, respectively. He also concluded that only 30% of engineers use simulation software for casting. He has also attempted to summarize the concept of simulation of casting in his paper [1]. Hétu et al. discussed two approaches, viz. 2D shell element model and 3D finite element analysis which were used for simulation of laminar or turbulent flow of the molten metal and analysis of low pressure casting, respectively [2]. Pequet et al. applied Darcy equation and micro segregation of gases for pipe shrinkage prediction. Finite volume grid superimposed onto the finite element was used for heat flow computation [3]. Bhatt and Barot concluded that design optimization of the feeder system reduces the casting defect of cast iron in foundries which were generated during mold filling and solidification. Using AutoCAST software, design of gate and riser was simulated which helped in decreasing casting defect in gear box of automobile [4]. Choudhari et al. used modeling and simulation method to minimize defect in casting. They analyzed that by placing feeder in a region where solidification is last but did not shift the hot spot completely to the feeder, so they introduced exothermic sleeve to the feeder which resulted in complete shift of hot spot to the feeder system [5]. Sutaria worked on enhancing casting feeder with the help of computation of feeder path using vector element method [6]. C. M. Choudhari et al. worked on all the design parameters of casting using AutoCAST software so that the whole porosity is shifted to feeder. An attempt was made to enhance the quality of the casting. Later, radiography test was done to ensure that no shrinkage porosity is present [7]. Nimbulkar and Dalu studied existing design of feeder and gating system. They simulated and redesigned the feeder and gating system. They used AutoCAST X1 simulation software and compared the experimental and theoretical results. They were able to reduce 30% casting defects [8]. Dabade and Bhedasgaonkar used Taguchi method to optimize process parameter like moisture content, green strength permeability number and mold hardness. Using Taguchi method, they managed to reduce defect from 10 to 3.59%. To improve the quality of casting, they used CAD simulation software [9]. Lebon et al. their paper is based on finite volume continuum model using a moving reference frame. They concluded that direct chill and melt conditioned results in smaller solidification time and larger temperature gradient. This resulted in getting finer and uniform grain structure [10]. Hobde and Shinde worked on contact wheel manufacturing company situated in Aurangabad, Maharashtra and aimed to improve casting yield and reducing volume metric shrinkage using advance simulation software [11]. Seo et al. worked on proposing two types of gating and feeding system: bottom L type junction and top L type junction. They also used simulation software to reduce the casting defect [12]. Sama et al. worked on improving the gating system using 3D sand printing. They have used novel simulation model for sprue and to enhance the metal flow into the cavity [13].

Literatures on casting process indicate numerous experimental, and numerical studies have been reported till now to produce a casted product which will be free

Fig. 1 Relationship between Niyama value and shrinkage



from defects and voids. However, no study reported till now to evaluate the casting defects by varying the number of gates in a globe valve. Therefore, the present study presents a numerical simulation of globe valve by varying the number of gates using Click2Cast software. The proposed model can be effectively used to predict the defect and failures occurring in sand casting process. Foundry engineers will be able to produce defect free and sound casting which can save a lot of time and overhead costs.

2 Numerical Simulation

Numerous softwares like AutoCAST-X, MAGMA, ProCAST, Solid-CAST and Mold-flow Software are available for simulation. In this work, Click2Cast software is used which uses Niyama criterion for evaluating design. Niyama, a Japanese researcher, developed this criterion. The criterion is being given by the Eq. 1 (Fig. 1).

$$\text{Niyama criterion} = \frac{\text{Temperature Gradient}}{\sqrt{\text{Cooling Rate}}} \tag{1}$$

3 Governing Equation

The casting simulation process works on four governing equations viz. (1) Equation of continuity (2) Momentum conservation (3) Energy conservation equation and (4) Volume of fluid-function equation. The equations have been discussed in the following segments.

4 Continuity Equation

It states that the mass of a system is always conserved.

$$A_1 V_1 = A_2 V_2 \quad (2)$$

where A_1 and A_2 are area of cross sections and V_1 and V_2 are velocities.

5 Momentum Conservation

When collision between two objects takes place, then momentum before and after collision remains same.

$$\sum \dot{m}_{in} = \sum \dot{m}_{out} \quad (3)$$

where \dot{m}_{in} is rate of mass inflow and \dot{m}_{out} is rate of mass outflow for incompressible fluid flow.

6 Energy Conservation Equation

$$\sum E_{in} = \sum E_{out} \quad (4)$$

where E_{in} is inlet energy and E_{out} is outlet energy.

7 Volume of Fluid-Function Equation

$$\frac{\partial F}{\partial t} + u \frac{\partial F}{\partial x} + v \frac{\partial F}{\partial y} + w \frac{\partial F}{\partial z} = 0 \quad (5)$$

n

where u , v and w being velocity vectors and x , y and z being directions, F is shear force experienced by the fluid flow and t is layer thickness

$$F = \frac{O_v}{A_v} \quad (6)$$

where O_v = Fluid volume in single grid and A_v = Volume of grid.

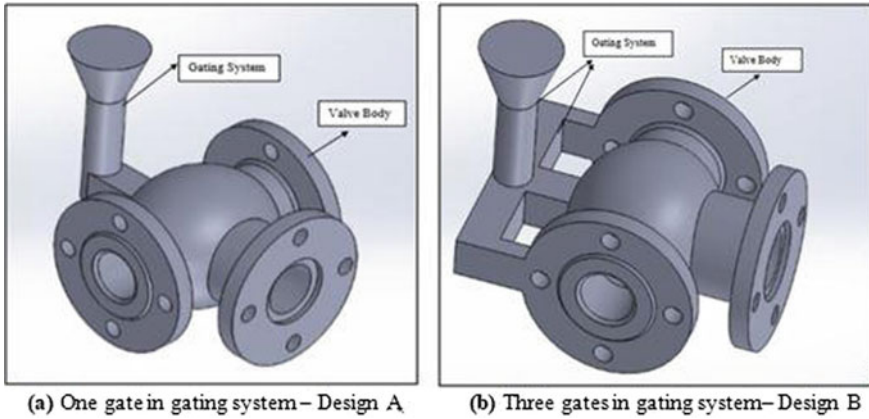


Fig. 2 Gating system with two different designs

8 Model Development

To simulate the casting process, two globe valve models are developed using SolidWorks software and the models imported into the Click2Cast software for simulation purpose. Iterative method is used to find the best design. Two designs of different gates A (one gate in gating system) and B (three gates in getting system) are developed have been shown in Fig. 2. The procedural steps for development of both the models and importation into the Click2Cast environment have been discussed in the following lines.

1. SolidWorks 2016 is used to develop two globe valve designs A and B were made have been shown in Fig. 2a and b, respectively. Design A shows gating system with one gate, while design B shows the gating system with three gates.
2. Globe valve geometry is imported in Click2Cast software by a suitable path.
3. Meshing is done up to 1 μm element size.
4. Boundary condition is defined for the gates before simulation.
5. Parameters are initiated and defined to start the simulation.
6. Simulations of results are obtained after convergence of solutions.

9 Results and Discussion

The models are simulated in Click2Cast software to evaluate the effectiveness of both the designs, viz. gating system with one gate and gating system with three gates. Following parameters are taken into consideration for analyzing the best design out of the two gating and feeder system designs amongst A and B:

1. Flow front analysis
2. Air entrapment

3. Porosity percentage

Flow Front Analysis

Figure 3 shows the flow front analysis of globe valve in both the designs. Flow front analysis helps to analyze how the molten metal will be filled in the mold cavity. It also aids in deciding the appropriate positions in gates to minimize air entrapment. In Fig. 3a, flow front analysis shows that the flow of molten metal is not directional, as a result, there is probability that by the time one flow front meets the other flow, and it might have already solidified which can lead to casting defects. In Fig. 3b, it is observed that directional solidification is achieved easily due to multi-directional flow of molten metal from the multigates present, thus, there are less chances of defects in casting.

Air Entrapment

Figure 4 shows the air entrapment in the globe valve in both the designs. Air entrapment is observed when there is a discontinuity in the casted component. It can be due to various reasons like air bubble in the molten metal, residual humidity on mold cavity surface converts to vapor when it comes in contact with hot molten metal, etc. From Fig. 4a, it can be concluded that due to air entrapment in one side of the flange of the globe valve, the molten metal could not fill the mold cavity completely, and as a result, casting defect can be seen. In Fig. 4b, there is negligible air entrapment.

Porosity Percentage

Figure 5 shows porosity percentage analysis in both the designs. According to Fig. 5a, it is observed that more than 10% porosity defect is existing in design A, whereas Fig. 5b shows only 5% porosity defect. Owing to high air entrapment, higher porosity percentage is existing in design A. However, in design B owing to less air entrapment, less porosity is observed.

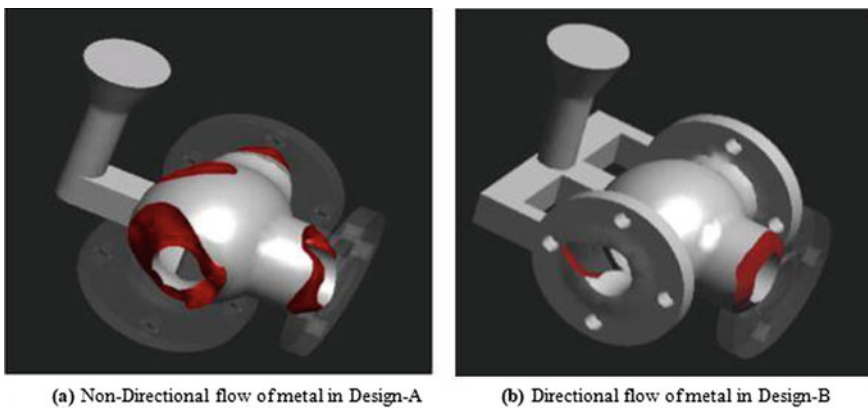


Fig. 3 Flow front analysis of design A and B

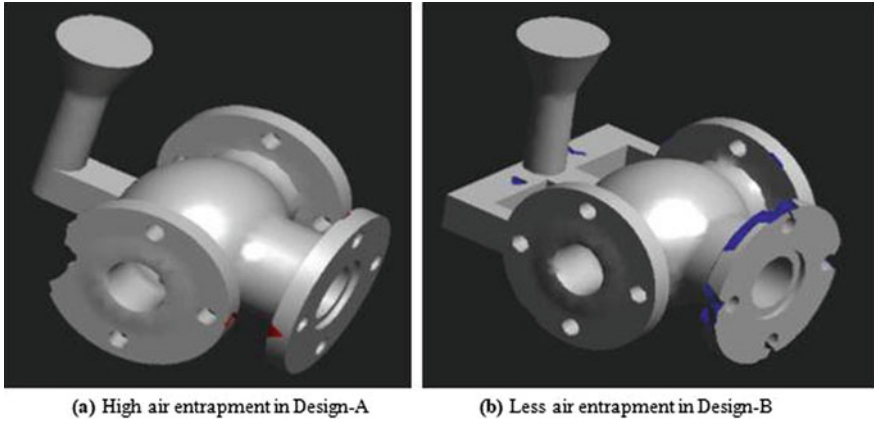


Fig. 4 Air entrapment analysis of design A and B

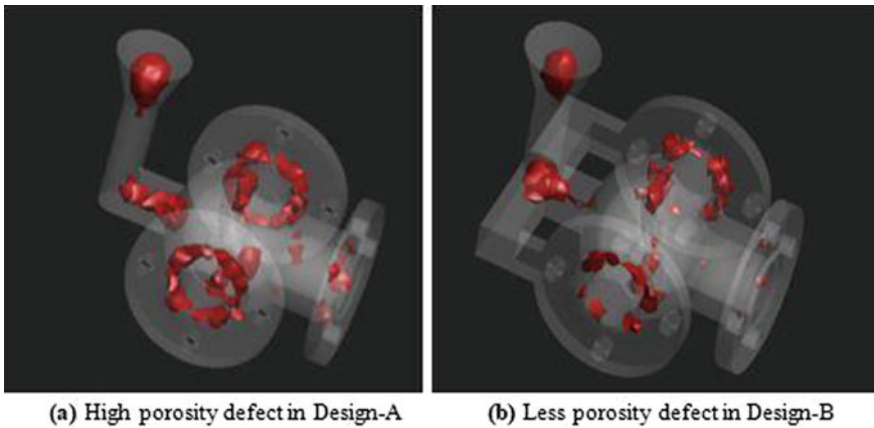


Fig. 5 Porosity percentage analysis of design A and B

10 Experimental Validation

To validate the numerical simulation of the globe valve, an experiment is conducted to quantify the porosity percentage, and for this, X-ray diffraction of globe valve is conducted. The following equation is used to calculate the experimental values of porosity percentage

$$\text{Porosity percentage} = \text{number of pores} \times \left(\frac{\text{Pore volume}}{\text{Casting volume}} \right) \times 100 \quad (7)$$

where number of pores and pore volume is obtained from X-ray diffraction.

Table 1 Comparison of numerical results with experimental results

Design	Number of gate	Numerically obtained porosity in %	Experimentally obtained porosity in %	Error % in porosity
A	1	10	9.4	6
B	3	5	4.6	4

Table 1 shows the comparison of results obtained from numerical simulation and experiment work. From the table, it can be clearly seen numerical and experimental results are close to each other predicting an error percentage of less than ten percentage, which confirms the validation of numerical simulation.

11 Conclusions

A numerical simulation of glove valve is conducted in this work. The result obtained from the study is validated by conducting a confirmative test. From the simulation results, it can be concluded that gating system design with multiple gates can produce a casting with least defects happening due to flow front, air entrapment and porosity which can lead to result in least number of rejections. The approach can be considered as an aid in assisting to analyze the quality of final cast globe valve prior to the actual casting of the component resulting in much lesser defects and bringing the overall cost down by a large margin. The approach can be used as a substitute to the experimental method resulting in saving time and manufacturing cost of the globe valve.

References

1. Ravi B (2008) Casting simulation and optimisation: benefits, bottlenecks and best practices. *Indian Foundry J* 54(1):47
2. Héту JF, Gao DM, Kabanemi KK, Bergeron S, Nguyen KT, Loong CA (1998) Numerical modeling of casting processes. *Adv Perform Mater* 5(1–2):65–82
3. Bhatt H, Barot R, Bhatt K, Beravala H, Shah J (2014) Design optimization of feeding system and solidification simulation for cast iron. *Procedia Technol* 14:357–364
4. Choudhari CM, Narkhede BE, Mahajan SK (2014) Methoding and simulation of LM 6 sand casting for defect minimization with its experimental validation. *Procedia Eng* 97:1145–1154
5. Sutaria M (2010) Casting simulation case study: shaft pin (cast iron-green sand casting). *Indian Foundry J* 56(12):5
6. Choudhari CM, Narkhede BE, Mahajan SK (2016) Casting design and simulation of cover plate using AutoCAST-X software for defect minimization with experimental validation. *Procedia Mater Sci* 6:786–797
7. Nimbalkar SL, Dalu RS (2016) Design optimization of gating and feeding system through simulation technique for sand casting of wear plate. *Perspect Sci* 8:39–42
8. Dabade UA, Bhedasgaonkar RC (2013) Casting defect analysis using design of experiments (DoE) and computer aided casting simulation technique. *Procedia CIRP* 7:616–621

9. Lebon GB, Li HT, Patel JB, Assadi H, Fan Z (2020) Numerical modelling of melt-conditioned direct-chill casting. *Appl Math Model* 77:1310–1330
10. Hodbe GA, Shinde BR (2018) Design and simulation of LM 25 sand casting for defect minimization. *Mater Today Proc* 5(2):4489–4497
11. Seo HY, Seo PK, Kang CG (2019) A study on the S/W application for a riser design process for fabricating axisymmetric large offshore structures by using a sand casting process. *Int J Naval Archit Ocean Eng* 11(1):462–473
12. Sama SR, Badamo T, Lynch P, Manogharan G (2019) Novel sprue designs in metal casting via 3D sand-printing. *Additive Manuf* 25:563–578

Effect of Polarity on MRR and TWR in Electric Discharge Machining



Jambeswar Sahu, Sonam Shrivastava, Chinmaya Mohanty, Swagatika Mishra, and Tapan Kumar Mahanta

Abstract Electrical energy is used to machine metals in electric discharge machining (EDM) process. EDM is a thermoelectric process, in which machining occurs without cutting force. Hence, electrical energy is converted to thermal energy to remove material. Usually, straight polarity is used in EDM, i.e., workpiece is connected to positive terminal (anode) and tool is connected to negative terminal (cathode). But, reverse can be possibly have rarely studied. An in-house designed table-top EDM was built to perform the experiments in straight and reverse polarity. Copper material was used as tool and workpiece to avoid the effect of different material. The voltage and polarity have significant effect on removal of material from workpiece.

Keywords Straight polarity · Reverse polarity · EDM · MRR · TWR · Copper

1 Introduction

The industry demands for complicated and precise components having some special features. The challenges are taken by the new development taking place in manufacturing field. The non-traditional methods of machining have several advantages over traditional machining process. Non-traditional machining processes are not

J. Sahu (✉) · C. Mohanty
School of Mechanical Engineering, Vellore Institute of Technology University, Gorbachev Rd,
Vellore 632014, India
e-mail: jambeswar@gmail.com

S. Shrivastava
School of Electrical Engineering, Vellore Institute of Technology University, Gorbachev Rd,
Vellore 632014, India

S. Mishra
Department of Mechanical Engineering, Veer Surendra Sai University of Technology, Burla
768018, India

J. Sahu · T. K. Mahanta
Department of Mechanical Engineering, BEC, Bapatla 522101, India

limited by the material properties like brittleness, toughness, hardness to produce different features on workpiece [1–3]. Non-traditional machining process like electrical discharge machining (EDM) can be used to machine both soft and hard materials to form any complicated features. In EDM, the workpiece and tool are part of the machining circuit and connected to two terminals such as anode and cathode.

The polarity was investigated along with current, pulse duration, tool material, etc.[4]. The polarity effect was observed in silver steel. The cathode erosion was found 2/3 times more than anode erosion in EDM of copper workpiece and copper tool [5]. This also increased with pulse duration. Similar work was investigated by Xia et al., in which 40% energy distribution was observed at anode and 25% at cathode [6, 7]. The straight polarity MRR was observed to be 4–11 times than reverse polarity [8]. In the current work, workpiece material, tool material, current, voltage (two voltages are used separately), and other EDM parameters are kept constant. The investigation was carried out to analyze the effect of polarity on tool wear and material removal rate.

2 Experimental

A table-top EDM was fabricated to investigate the polarity effect on material removal rate and tool wear rate. The detailed specification of machine, power supply, properties of workpiece–tool material and the dielectric are described in this section.

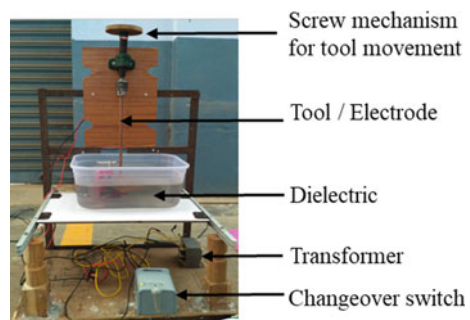
2.1 Machine tool

The in-house designed table-top electrical discharge machine (EDM) was fabricated as shown in Fig. 1. The circuit used for fabrication is shown in Fig. 2.

Circuit description.

The supply voltage is step down from 230 V to 24–48 V using a step-down transformer having primary to secondary turns ratio of $N1:N2$ Fig. 2. Further, the

Fig. 1. In-house designed table top electrical discharge machine



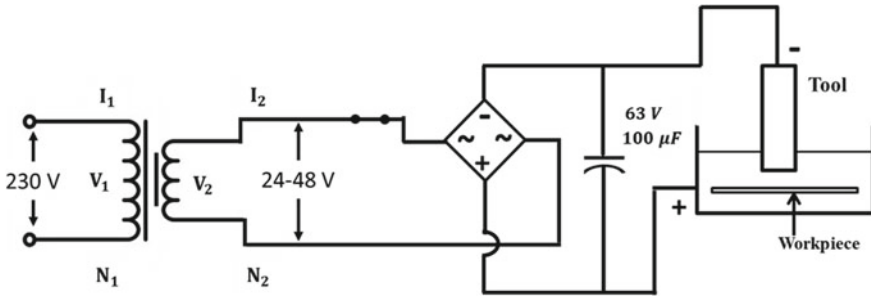


Fig. 2. Circuit diagram used for EDM spark generation

full-wave bridge rectifier circuit is employed to convert the AC input signal into a DC signal. This DC voltage charges a 100μF capacitor. The capacitor is connected to the tool and workpiece arrangement in straight polarity.

Power supply

A step-down transformer was used to reduce the supply voltage and current for suitable working of EDM process. The step-down transformer of the conversion capacity of stepping down current input of 230 V ac supply to a variable 50–100 V steady output. The transformer used in the setup is used to obtain multiple voltage outputs with ranges of 12-0-12 and 24-0-24 voltages at the output for the steady 230 V input.

Bridge rectifier

Bridge rectifier is used to convert the stepped down AC current from the transformer into DC power output for utilization of the DC output for the spark generation shown in Fig. 3.

Changeover switch

Changeover switch Fig. 4 was used switch between the multiple output voltages. The subsequent switch actuation helps in the choosing of the voltage output over which the spark generation occurs and material removal happens.

Fig. 3. Bridge rectifier



Fig. 4. Changeover switch



2.2 Dielectric

The dielectric medium used here is distilled water for die sinking EDM. The tool and workpiece are inside the distilled water can transport the ions between for conducting the sparks by breaking down at the appropriate applied voltage. The dielectric also flushes out the erode material from machined area and reduces temperature of the workpiece.

2.3 Materials

Copper tool electrode and workpiece were used to investigate the effect of polarity. Similar material was used to eliminate the effect of material. Copper was used as EDM tool material by several researcher, due to its good conductivity as shown in Fig. 5.

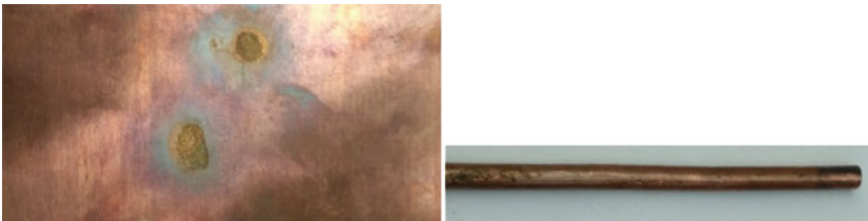


Fig. 5. Copper workpiece (left) and electrode (right)

Fig. 6. Workpiece holder (left) and tool holder (right)



2.4 Holding device

C-clamp was used to hold workpiece, and drill chuck was used to hold the electrode shown in Fig. 6. The tool and workpiece spark gap was maintained by screw mechanism as shown in Fig. 1.

2.5 Experimental Procedure

The table-top EDM machine was build according to the circuit as shown in Fig. 2. The tool was connected to chuck and workpiece was hold by C-clamp. Supply was given to the transformer, and open-circuit voltage was measured as 74 and 44 V by changing the voltage in changeover switch. The current was maintained at 5A for all experiments. The spark was produced in dielectric medium between cathode tool and anode workpiece. Machining was carried out for 5 min. The weight of tool and workpiece was measured before machining, and after machining for calculation of material removal rate (MRR) and tool wear rate (TWR). The process was repeated by changing the polarity.

3 Results and Discussion

The MRR and TWR were calculated from the weight difference of before and after measured weight. The MRR and TWR were estimated using Eq. (1). The MRR and TWR are represented in Table 1. Two different voltage was used to observe the effect of polarity.

$$\text{MRR or TWR} = (1000 \times \Delta W) / (\rho \times t) \quad (1)$$

where ΔW is weight difference, ρ is density of copper and t is machining time.

Table 1 MRR and TWR values at different voltage and polarity

Voltage	Electrode/workpiece	Polarity	MRR (cm ³ /min)	Tool wear (cm ³ /min)
74	Copper	Straight	0.00446	0.00206
74	Copper	Reverse	0.00076	0.00156
44	Copper	Straight	0.00067	0.00116
44	Copper	Reverse	0.00116	0.00069

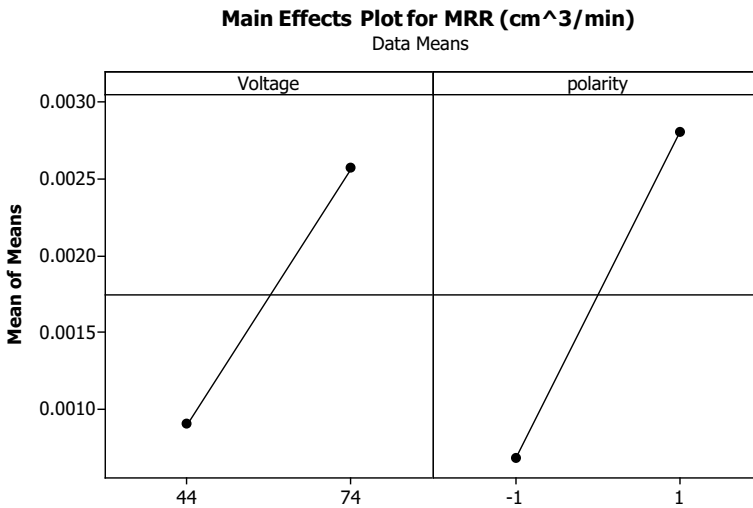


Fig. 7. Main effect plot for MRR

The power supply as shown in EDM circuit Fig. 2, creates an intense electric field inside the dielectric medium between the tool and the workpiece. The imperceptible particles present in the dielectric medium are intrigued by the electric field and aggregated at the center point of the field. This creates a highly conducting bridge between the tool and the metal workpiece. The increase in the capacitor voltage increases the field voltage, which results in temperature rise of the bridge and some pieces ionized to form a path for spark between the two. At this point, both the temperature and the pressure in the channel increase resulting in a spark. At spark contact, the material is heated up and vaporized from both the metal tool and the metal workpiece. This heat generation causes the metal eradication in workpiece, which further results in the cavity formation of same shape as of the tool.

The mean (mean of means¹) MRR and mean TWR are plotted with respect to voltage and polarity in Figs. 7 and 8, respectively. MRR was increasing in higher voltage, due to increase of velocity of electron from tool to workpiece. MRR value was very less in reverse polarity Fig. 7 due to striking of electron from workpiece to

¹In case of multiple response, the Minitab software calculates the mean value and in case of multiple input dataset (Experiments), the mean value is calculated and presented in graph.

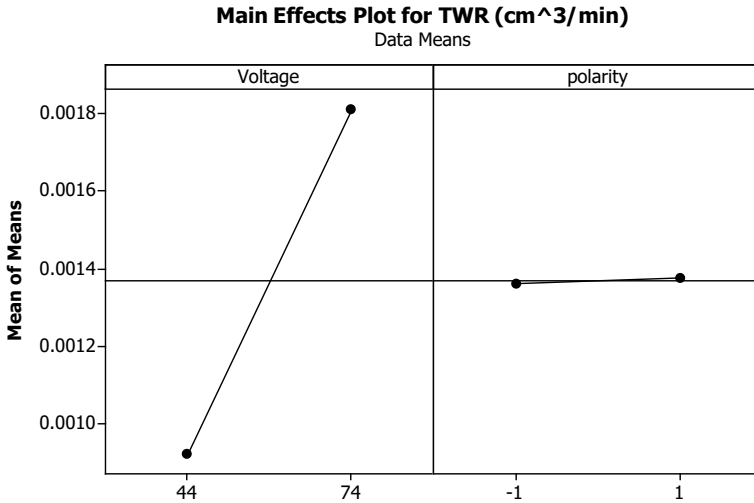


Fig. 8. Main effect plot for TWR

tool. TWR was also increasing with increasing voltage in the terminals. The polarity has less effect on TWR Fig. 8.

The mutual effect of voltage and polarity for MRR and TWR is explained in Figs. 9 and 10, respectively. Figure 9 shows that the MRR is maximum a higher voltage and straight polarity. This occurs due to more heat generation at workpiece by the striking of higher velocity electron at higher voltage. The polarity has less effect on TWR, but Fig. 10 shows that the tool wear is more at higher voltage as the heat generation is more. The heat generation depends on the voltage and current ($Heat = VI t$, where V is applied voltage, I is the current and the t is the time). This results in higher metal removal from tool as well as the workpiece.

Fig. 9 Surface plot of MRR (cm³/min) versus voltage, polarity

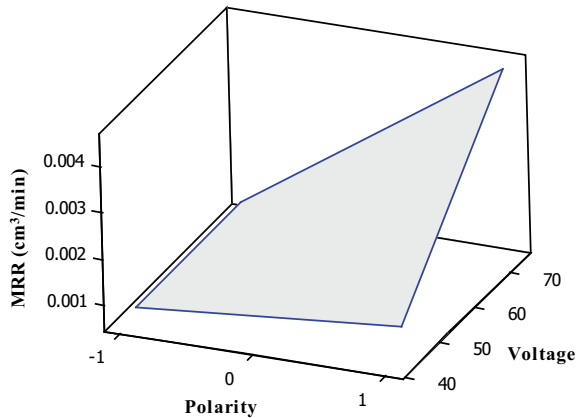
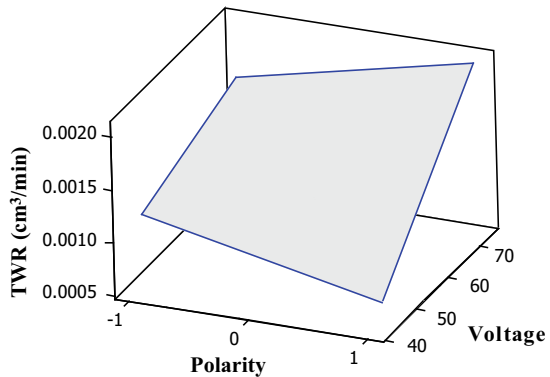


Fig. 10 Surface plot of tool wear (cm^3/min) versus voltage, polarity



4 Conclusions

The effect of polarity was investigated without changing the EDM parameters and materials. The material removal rate (MRR) was found to be higher in straight polarity due to more heat distribution at anode (workpiece). The MRR was also increases in higher voltage. The setup can be applied for wide range of material and controlling parameter.

Acknowledgements I would like to acknowledge the work done by Krishna, Venkatesh, Dinesh and Anil on table-top EDM setup fabrication.

References

1. Benedict GF (1987) *Nontraditional manufacturing processes*. CRC Press, New York
2. Ramakrishnan R, Karunamoorthy L (2006) Multi response optimization of wire EDM operations using robust design of experiments. *Int J Adv Manuf Technol* 2(29):05–112
3. Sanchez JA, Rodil JL, Herrero A, Lacalle LNL, Lamikiz A (2007) On the influence of cutting speed limitation on the accuracy of wire-EDM corner-cutting. *J Mater Process Technol* 3(182):574–579
4. Ho KH, Newman ST (2003) State of the art electrical discharge machining. *Int J Mach Tools Manuf* 13(43):1287–1300
5. Patel MR, Barrufet MA, Eubank PT (1989) Theoretical model of the electrical discharge machining process—II, the anode erosion model. *J Appl Phys* 66(9):4104–4111
6. Xia H, Hashimoto H, Kunieda M, Nishiwaki N (1996) Measurement of energy distribution in continuous EDM process. *J JSPE* 62(8):1141–1145
7. Xia H, Kunieda M, Nishiwaki N (1996) Removal amount difference between anode and cathode in EDM process. *Int J Electr Mach* 1(1):45–52
8. Lee SH, Li XP (2001) Study of the effect of machining parameters on the machining characteristics in electrical discharge machining of tungsten carbide. *J Mater Process Technol* 3(115):344–358

Design of a Torque Controller with Application to a Single Degree of Freedom Haptic Device



Saurav Kumar Dutta, Jithin Krishnan Balathil, Paluchani Anirudh Reddy, and Annem Narayana Reddy

Abstract The main aim of the work is to design a torque controller which is a critical element in a haptic device. Since, the torque is related to the current in a DC motor, the paper comes up with a current control circuit by which current can be controlled across a branch in the circuit. From experiments, an empirical current–torque relationship is obtained for the DC motor using a constant current power source. The DC motor is then integrated with the current control circuit so as to generate a theoretical relation between the voltage of the current control circuit and the torque of the DC motor. This theoretical voltage–torque relationship is also validated experimentally. The working of the entire set-up with reference to a single degree of freedom haptic device is also explained. The proposed work would draw the attention of more researchers for the development of affordable haptic devices.

Keywords Current control circuit · DC motor · Torque estimation

1 Introduction

Haptics, that is, the sense of touch, is very useful for training programs in the fields of biomedical and defense applications. In these types of applications, a virtual environment is created with similar work conditions, and the budding doctors and defense personnel do their work on the virtual environment with feel of the actual work conditions. Haptics have been used for the training of astronauts for space missions, as can be found in the work of Loftin and Kenney [1]. Cormier et al. [2] also emphasized the need and advantages of developing a haptic simulator for dental education. Virtual training has been found to be very effective in cases where reproducing the real work conditions would be very expensive or hazardous [1–3].

There is an another type of haptic device which works in a remote environment. This haptic device comprises a master robot, a virtual interface and a slave robot. This

Saurav Kumar Dutta (✉) · Jithin Krishnan Balathil · Paluchani Anirudh Reddy · Annem Narayana Reddy
Department of Mechanical Engineering, Indian Institute of Technology Guwahati, Guwahati, Assam 781039, India
e-mail: d.saurav@iitg.ac.in

type of haptic device is used for teleoperations. The surgeon operates the master robot by looking at the patient's body at the virtual interface, and the slave robot performs the operation on the patient at some remote environment by mimicking the master robot's actions. The research related to teleoperations can be found in the work of Li et al. [4], Mihelj and Podobnik [5].

As stated earlier, haptics have several potential applications in the fields of biomedical devices, telescopic surgery and defense applications. To realize the complicated tasks in telescopic surgery and other engineering applications, there is a need to draw the attention of more researchers into this field. This can be realized by the availability of affordable haptic devices. Some research related to the development of affordable haptic devices can be found in the work of Sandoval et al. [6], Sinclair et al. [7]. The motivation behind the present work is to build such a cost-effective haptic device using locally available resources.

A haptic device has three important parts: first, the torque control of the motor; second, the virtual interface and third, the force feedback mechanism. Since, torque control is the most critical part in realizing the haptic device, this paper focuses only on the design of the torque control of the motor using an in-house built current control circuit. Researchers have used different kinds of motors in haptics like capstan drives [8] and DC motor [9]. However, in this work, a DC motor is used due to its easy availability.

The paper has six sections. Section 2 introduces the model of the single degree of freedom haptic device, Sect. 3 is about the design of the torque controller, Sect. 4 discusses the method employed for measuring the torque of the motor, Sect. 5 documents the experimental results, and Sect. 6 concludes the paper.

2 Model of the Haptic Device

The proposed model of the haptic device is shown in Fig. 1. A pinion is coupled to the shaft of the DC motor. The pinion is in mesh with the rack. The proposed model can be used for the development of a cost-effective injection simulator. The handle in Fig. 1 is representing the plunger of a syringe. The clinician pushes the plunger forward by looking at the virtual interface. The moment the bevel of the needle touches the patient's body at the virtual interface, the DC motor applies an opposing torque and tries to push the rack backward. Thus, the clinician experiences a backward force at the handle tip. This backward force is similar to the one exerted by living tissues on the thumb of a clinician when he administers a fluid into the body through syringe. The torque to be exerted by the motor depends on the deformation of the strain gauge attached to the rack. The strain gauge shows an initial reading or zero reading when the rack is not in contact with the pinion. But as the rack is moved forward by the handle of the haptic device and the rack starts moving in mesh with the pinion, the rack undergoes deformation which is picked up by the strain gauge and the motor starts applying an opposing torque on to the rack. As one continues to apply force on to the handle, the opposing torque acted upon by the motor on the rack

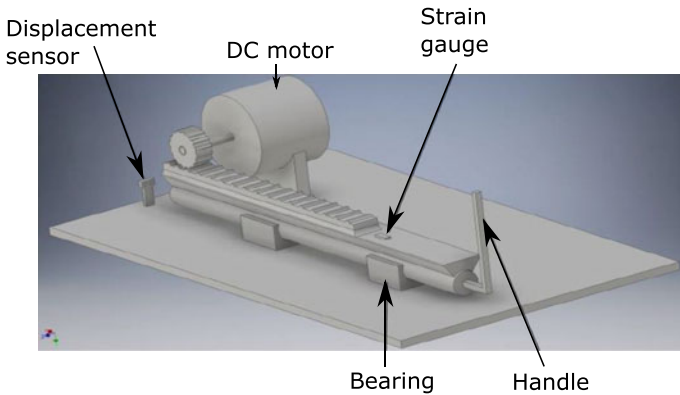


Fig. 1 The CAD model of the haptic device

increases, the rack deforms further, and the mechanical strain of the rack increases. The virtual interface of the haptic device displays a pointer or a needle which moves in one direction corresponding to the end position information of the rack given by the displacement sensor.

The three parts of a haptic device, that is, the torque control, the virtual interface and the force feedback, should work synchronously or in real time. This can be done by using Arduino which takes the strain signals from the rack in real time and accordingly directs the flow of current to the motor for the opposing torque.

3 Design of the Torque Controller

In a DC motor, the armature current is related to the torque. Hence, the torque of the motor can be controlled if the current going into the motor can be controlled. To control the current at a constant value, an in-house current control circuit is built. The schematic diagram of the current control circuit is shown in Fig. 2.

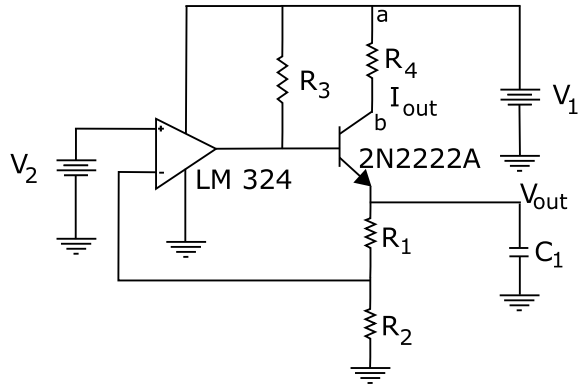
In the current control circuit, the current can be regulated and kept constant in the branch *ab* by regulating V_2 . The V_2 can be a power source or voltage supplied by an Arduino. The DC motor is placed in the branch *ab*. R_4 is the electrical resistance of DC motor. By using Kirchoff’s voltage law, the current flowing through the branch *ab* can be obtained as-

$$I_{out} = \frac{V_{out}}{(R_1 + R_2)} \tag{1}$$

where

$$V_{out} = V_2 \frac{(R_1 + R_2)}{R_2} \tag{2}$$

Fig. 2 A schematic diagram of the current control circuit



In Eq. (1), I_{out} is the current flowing through the branch ab , as shown in Fig. 2. I_{out} can be regulated by regulating V_2 , and I_{out} would remain constant even if the mechanical load of the motor changes. By utilizing the current–torque relationship of the DC motor and the Eqs. (1) and (2), a relationship can be obtained between the voltage V_2 , that is, the voltage required to power the amplifier of the current control circuit, and torque of the DC motor.

4 Methodology for Determining the Torque of the Motor

The basic principle of the DC motor is that as it is attached to a power source, it starts rotating. When the motion of the shaft of the DC motor gets opposed, the current flowing through the DC motor increases, as the DC motor requires more torque so as to maintain the inertia of the motor. Every power source has a limit on the maximum current that it can supply. When the power source supplies the maximum available current, the torque becomes constant. At such a stage, the current flowing through the motor can no longer increase even if the mechanical load of the motor increases, and hence, the torque becomes constant.

From experiments, it is found that a current greater than 100 mA burns the circuitry inside the motor, and hence, the motor gets damaged. Hence, while carrying out experiments, it is ensured that the current flowing through the motor does not exceed 100 mA. The experimental set-up for determining the current–torque relationship of the DC motor is shown in Fig. 3. The length and diameter of the shaft of the DC motor are 23 mm and 6 mm, respectively. There is an internal hole for coupling in the shaft. The diameter of the internal hole is 6 mm. A rod is fixed into that hole, as shown in Fig. 3. At one end of the rod, a high tension thread is attached with a loop at the bottom end of the thread. Dead weights with a hanger are put into the loop of the thread.

Since, DC motor is purchased from local sources, no current–torque relationship is available beforehand. Hence, experiment is carried out to see the variation of torque

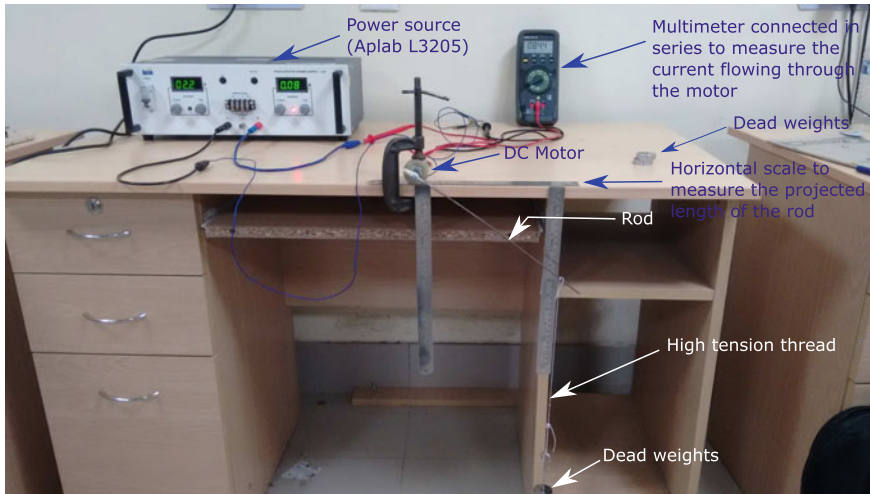


Fig. 3 Experimental set-up for determining the current–torque relationship of the DC motor using the constant current power source

with current by using a constant current power source. The experimental set-up for carrying out this experiment is shown in Fig. 3. In this experiment, the maximum current that the power source can supply is set manually in the beginning, and then, the torque is found out corresponding to that current. Every time before the start of the experiment, the position of the rod is set in vertical position and it is aligned with the vertical scale, as shown in Fig. 3. When the load is put in the hanger at the loop of the high tension thread attached to the rod, the torque of the DC motor increases as it needs to overcome the moment exerted by the dead weights. The increase in torque demands an increase in current. But the current cannot increase beyond the maximum limit set in the beginning of the experiment. When the DC motor gets the maximum available current, the torque becomes constant, no matter whatever be the mechanical load. At such a stage, the DC motor stops rotating. It can be said that at this stage, the torque exerted by the motor is equal to the torque exerted by the dead weights. The values of dead weights and the projected horizontal distance of the rod are known. The torque is calculated, and also, the maximum current going into the motor is known. Thus, the torque corresponding to a particular value of current is obtained. This process is repeated by setting different values of maximum current in the power source. Then, these experimental data points are used to obtain an empirical current–torque relationship of the DC motor.

After getting an empirical current–torque relationship of the DC motor, the DC motor is integrated with the current control circuit. The experimental set-up for determining the relation of torque of the DC motor with the voltage, V_2 , of the current control circuit is shown in Fig. 4. The same procedure is adopted as before to get the torque. V_2 in the current control circuit, as shown in Fig. 2, is adjusted to

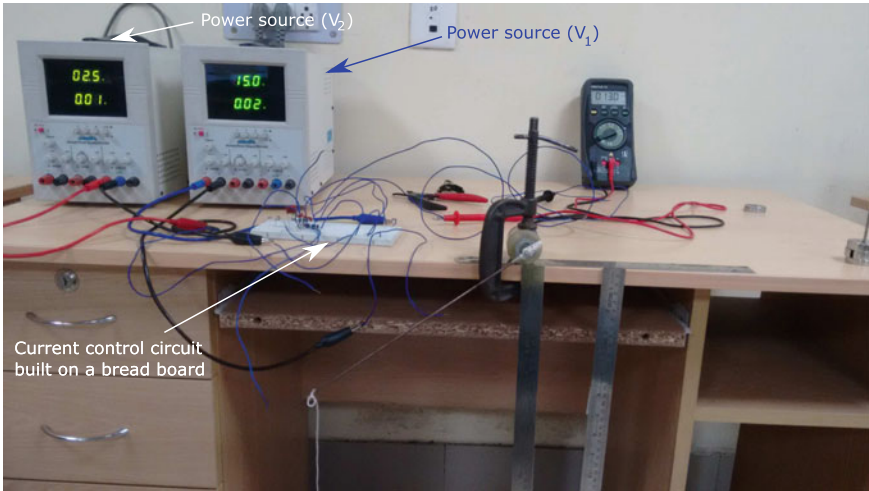


Fig. 4 Experimental set-up for determining a relation between the torque of the DC motor and V_2 of the current control circuit

fix the current in the branch ab of the current control circuit. Hence, experimental data points are obtained between V_2 and torque of the DC motor.

5 Results and Discussion

Table 1 gives the relation of torque of the DC motor with current, supplied from a constant current power source.

Table 1 Relation between torque of the DC motor and current using a constant current power source

Current readings in power source (A)	Current readings in multimeter (mA)	Weights (g)	Projected length of rod on horizontal scale (cm)	Torque (kg cm)
0.04	49	100	19	1.9
0.06	69	150	17.4	2.61
0.08	89	200	16.8	3.36
0.1	114	250	19.4	4.85

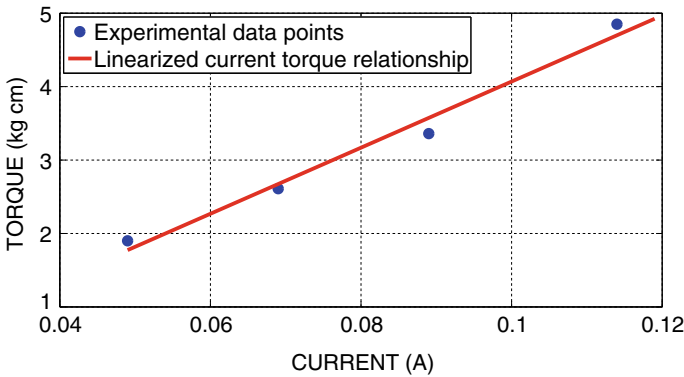


Fig. 5 Variation of torque of the DC motor with current

The relation between the torque and the current given in Table 1 is plotted in Fig. 5 where dots represent the experimental data points and the solid line represents the linear least square fit. The empirical linearized current–torque equation for the DC motor is given as-

$$T = 45.0027I - 0.4315 \tag{3}$$

where T is the torque in kg cm and I is the current in A.

The results of the second experiment are given in Table 2. The second experiment involves determining the torque of the DC motor for different values of voltage V_2 of the current control circuit. As shown in Fig. 2, the values of R_1, R_2, R_3, C_1, V_1 and V_2 are chosen in a way that the current flowing through branch ab does not become greater than 100 mA. For this, a simulation software, called Pspice is used. Based on the simulation results, the values chosen are $R_1 = 200 \Omega, R_2 = 50 \Omega, R_3 = 500 \Omega, C_1 = 100 \text{ nF}, V_1 = 15 \text{ V}$ and the value of V_2 can be regulated from 0.5 V to 5 V. The resistance of the motor, R_4 , is found to be 17Ω . An increase of V_2 beyond 5 V will make the current flowing through the branch ab greater than 100 mA which would damage the motor. Hence, V_2 is regulated from 0.5 V to 2.5 V.

Table 2 Relation between the torque of the DC motor and V_2 of the current control circuit

Voltage readings in power source V_2 (V)	Current flowing through motor I_{out} (mA)	Weights (g)	Projected length of rod on horizontal scale (cm)	Torque (kg cm)
0.5	12	10	2.1	0.021
1	23	50	8.2	0.410
1.5	32	50	21.6	1.08
2	43	100	14.2	1.42
2.5	52	150	13	1.95

Table 3 Comparison between the theoretical and experimental results between torque of the DC motor and V_2 of the current control circuit

V_2 (V)	Theoretical torque (kg cm)	Experimental torque (kg cm)	Absolute percentage deviation
0.5	0.0185	0.021	13.51
1	0.4685	0.410	12.49
1.5	0.9185	1.08	17.58
2	1.3685	1.42	3.76
2.5	1.8185	1.95	7.23

On substituting Eqs. (1) and (2) in Eq. (3), the following equation is obtained

$$T = 0.9V_2 - 0.4315 \quad (4)$$

Equation (4) can be considered as the theoretical voltage–torque relationship between the voltage of the current control circuit and the torque of the DC motor. Table 3 gives a comparison between the theoretical results, obtained using Eq. (4) and the experimental results, recorded in Table 2.

Table 3 indicates that the absolute percentage deviation for all the experimental data points is less than 20% with respect to the theoretical data points. This percentage can be further reduced by the use of precision resistors. However, the use of precision resistors may increase the overall cost of the haptic device.

Experimental results show that Eq. (4) holds experimentally and can be used for controlling torque of the DC motor by regulating the voltage of the current control circuit with a reasonable accuracy.

6 Conclusion

This paper presented the model of a single degree of freedom haptic device. Such a model can be used for the development of a cost-effective injection simulator. A torque controller was designed, as a part of the work for the realization of the single degree of freedom haptic device. An in-house current control circuit was built and was integrated with the current–torque characteristics of the DC motor to obtain a relation between the torque of the DC motor and the voltage required to power the amplifier of the current control circuit. The theoretical values of this voltage–torque relationship are validated with the experimental results. The future work would be to develop the strain-based feedback circuit and to integrate both the torque controller and the feedback mechanism in an Arduino which would ensure that the device works in real time.

Acknowledgements The authors thank Dr. A. Ravindranath of Electronics and Electrical Engineering Department, IIT Guwahati, for supporting us during various stages of the experiment. The

authors also greatly acknowledge the initial support provided by Sreenivasulu Moddu and Vinay Kakara, summer interns at IIT Guwahati in the year 2017.

References

1. Loftin RB, Kenney P (1995) Training the hubble space telescope flight team. *IEEE Comput Graph Appl* 15(5):31–37
2. Cormier, J, Pasco D, Syllebranque C, Querrec R (2011) VirTeaSy a haptic simulator for dental education. In: *The 6th international conference on virtual learning ICVL*, pp 61–68
3. Adams RJ, Klowden D, Hannaford B (2001) Virtual training for a manual assembly task. *Haptics-e* 2(2):1–7
4. Li H, Kawashima K, Tadano K, Ganguly S, Nakano S (2011) Achieving haptic perception in forceps manipulator using pneumatic artificial muscle. *IEEE/ASME Trans Mechatron* 18(1):74–85
5. Mihelj M, Podobnik J (2012) *Haptics for virtual reality and teleoperation*, vol 67. Springer Science & Business Media
6. Sandoval J, Laribi MA, Zegloul S (2019) A low-cost 6-DoF master device for robotic teleoperation. In: *IFTToMM international symposium on robotics and mechatronics*, Springer, pp 473–480
7. Sinclair M, Ofek E, Gonzalez-Franco M, Holz C (2019) CapstanCrunch: a haptic VR controller with user supplied force feedback. In: *Proceedings of the 32nd annual ACM symposium on user interface software and technology*, pp 815–829
8. Chakravarthy S, Balakuntala MV, Rao AM, Thakur RK, Ananthasuresh G (2018) Development of an integrated haptic system for simulating upper gastro intestinal endoscopy. *Mechatronics* 56:115–131
9. Giland JJ, Diaz I (2019) Haptic performance using voltage-mode motor control. *IEEE Trans Indus Electron* 67(1):698–705

Surface Gas Nitriding of Titanium (Ti–6Al–4V) Alloy



Shanta Chakrabarty, Smita R. Panda, Sonal, Jyoti S. Jha, and Sushil K. Mishra

Abstract The effects of gas nitriding were studied for Ti–6Al–4V alloy at different time and temperatures. Gas nitriding was performed from 600 to 1200 °C for the duration of 4–8 h using Dilatometer. The surface roughness was also compared to get insight into the tribology behaviour. Specimen color appearance after nitriding was different from the base metal, and the changes of color demonstrated the variation, with time and temperature. After nitriding, the basic metallic silver color was converted into blue, golden and gray. At lower temperatures, blue and golden colors were common, and as temperature increased, the color changed to grayish. Initially, at lower temperatures (i.e., 600 and 700 °C), titanium alloy's silver metallic color turned into blue/golden, and the intensity of this color was increased with the increase in temperature and time of nitriding. Moreover, above β -transus temperature at 1000, 1100 and 1200 °C, the material appeared to be gray. The hardness after nitriding was increased with increase in nitriding layer thickness. The maximum hardness value HV_{0.5} was reported to be 1735. Surface micrographs were taken by scanning electron microscopy (SEM), and these micrographs revealed that the formation of nitrides was started from the grain boundaries.

Keywords Gas nitriding · Ti–6Al–4V · Surface morphology · Hardness · Surface roughness · Surface texture

1 Introduction

The fourth most profuse material in the earth's crust is titanium, and its alloy named Ti–6Al–4V is widely used in aerospace industries for various purposes such as aircraft

S. Chakrabarty (✉) · S. R. Panda
School of Mechanical Engineering, Kalinga Institute of Industrial Technology (Deemed to be University), Bhubaneswar, Odisha 751024, India
e-mail: shanta.chakrabartyfme@kiit.ac.in

Sonal · J. S. Jha · S. K. Mishra
Department of Mechanical Engineering, Indian Institute of Technology Bombay, Powai, Mumbai, Maharashtra 400076, India

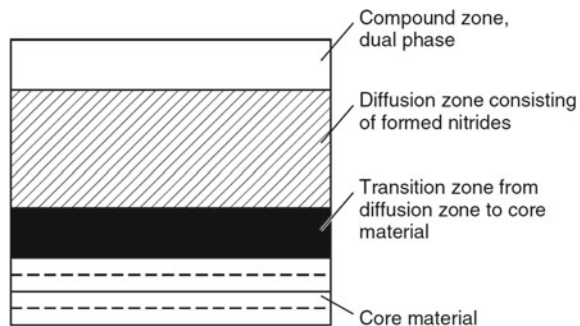
turbine engine components due to its high strength-to-weight ratio, corrosion resistance and excellent fatigue behavior. However, titanium and its alloy show poor tribological behavior (i.e., high friction coefficient and low hardness) which limits their use in mechanical applications [1].

Nitriding was introduced in 1900s, and this process does not result any phase change or dimensional variation. However, nitrogen diffusion commences slight increase due to volumetric changes [2]. A typical gas nitride case structure is shown in Fig. 1. In order to improve tribological properties of titanium and its alloy, researchers have performed different thermo-chemical treatments such as plasma and gas nitriding [3, 4] which improves the hardness and wear resistance. However, gas nitriding can easily improve the surface by producing a hard layer of titanium nitride. Consequently, it is believed to be the most promising method [5–7]. Nitriding of Ti–6Al–4V develops a titanium nitride layer on the surface that is mainly attracting the researchers due to some of its interesting properties such as the high melting point of titanium nitride (2949 °C), and it has single phase for a wider range of composition [8].

Titanium alloys are categorized into four categories: alpha, near alpha, alpha–beta and beta titanium alloys [9].

As we know that the diffusion of a particular gas into solid mainly depends on the gas pressure, temperature and time duration. Therefore, the present study is concerned with the consequences of gas nitriding of the $\alpha + \beta$ titanium alloy at different temperatures with varied time period by analyzing the microstructure and phase transformation. Gas nitriding has been carried out at different temperatures of 600, 700, 1000, 1100 and 1200 °C for different time periods of 2, 4, 6 and 8 h. In gas nitriding process, the nitrogen is supplied to the furnace at relatively high temperature (more than 1000 °C) to generate compound layer of titanium nitride at the material surface [10]. Some researchers have also claimed that the gas nitriding improves the fatigue strength of titanium by improving resistance to the crack initiation and growth [6]. It is expected that hardness, mechanical properties and wear resistance of Ti–6Al–4V alloy will improve with time and temperature due to formation of compound layer on the surface. Initially, Ti–6Al–4V has equiaxed microstructure,

Fig. 1 Typical gas nitrided case structure



and the Vicker's hardness value is $HV_{0.5}$ of the 410. Scanning electron microscopy images were obtained to see the surface morphology after nitriding.

2 Experimental Details

2.1 Sample Preparation

Ti-6Al-4V plate of width 2 mm was used, and samples of $100 \times 4 \text{ mm}^2$ dimension were cut with the help of wire electric discharge machining. Polishing was performed by Struers Tegramin-25 automatic polishing equipment. Initially, 220 grit SiC paper was used at 300 rpm for 5 min. In the subsequent steps, samples were polished with 2500 grit SiC paper for 10 min at 300 rpm and finally with MD Chemical OPS (20 nm colloidal silica solution) for 10 min with MD-Chem plate at 300 rpm. At the end, the samples were ultrasonically cleaned in an acetone bath for 2 min.

3 Gas Nitriding

Gas nitriding experiments were performed with the help of dilatometer DIL 805 A/D at Gleeble laboratory as per experimental specifications and time schedule mentioned in Table 1. After putting the sample in holder and securing with thermocouple, the air was pumped out of the chamber and a vacuum of 1.5×10^{-3} mbar was generated. Nitrogen gas was pumped inside. Sample was heated at a rate of $5 \text{ }^\circ\text{C/s}$. After reaching the target temperature, the sample was kept for the required time in nitrogen atmosphere, and again, the sample was cooled down at a rate of $5 \text{ }^\circ\text{C/s}$ by nitrogen gas.

Table 1 Gas nitriding experimental specifications and schedule

Sample	Temperature ($^\circ\text{C}$)	Time (h)
T_1, T_2, T_3	600	2, 4, 6
T_4, T_5, T_6	700	2, 4, 6
T_7, T_8	1000	4, 8
T_9, T_{10}	1100	4, 8
T_{11}, T_{12}	1200	4, 8

3.1 *Hardness Testing, SEM Analysis and Roughness Measurement*

Hardness was calculated by HMV-2 SHIMADZV microhardness tester. During the testing, the dwell time and indentation load were kept as 4.903 N and 10 s. \query{Please check the usage of the term 'indentated' .}The surface area was divided into eight equal parts, and each section was indentated with the indenter. The average of these eight hardness values was taken as final hardness. Hardness value was determined by using the following equation (Eq. 1).

$$HV = 1854.4(F/d^2) \quad (1)$$

where

HV = Hardness value,

F = Applied load, and

d = Mean diagonal of the indentation.

SEM images were taken by Gemini SEM 300 at 2000X magnification by keeping the voltage value at 10 and 15 kV. Roughness was calculated by Zeta Instruments. Microscope magnification was kept to be 5kX. Roughness value was calculated on a profile (line).

4 Results and Discussion

4.1 *Surface Appearance*

According to Sha et al., the most evident difference in the physical properties of the alloy due to nitriding was its appearance [12]. Sample appearance is shown in Fig. 2a–h. The metallic mark on the samples is a result of thermocouple attachment. Sample gave blue/golden/gray appearance after nitriding. Initially, the Ti–6Al–4V alloy was metallic silver.

After nitriding at 600 °C for 4 h (shown in Fig. 2a), exterior was mostly blue with some of the golden-colored area. Furthermore, blue-colored area was reduced when time of nitriding was increased to 6 h at 600 °C (shown in Fig. 2b) which was also convicted by Shibata et. al [13]. Therefore, it can be concluded that initial appearance of blue color was temporary and it slowly vanished when nitrogen started to diffuse in the sample. Figure 2c, d shows the image of the sample nitrided at 700 °C. The color of the material shown in 6c is pale golden and 6d is grayish. Moreover, Fig. 2e–h indicates gas nitrided Ti–6Al–4V at 1000 °C and 1200 °C. It is gray in appearance.

Initially, at lower temperature, the material started to give a blue and golden appearance and intensity of this color was increased with time and temperature. Furthermore, at higher temperatures, the samples appeared to be gray and the intensity of this color increased with time and temperature. The golden or gray appearance

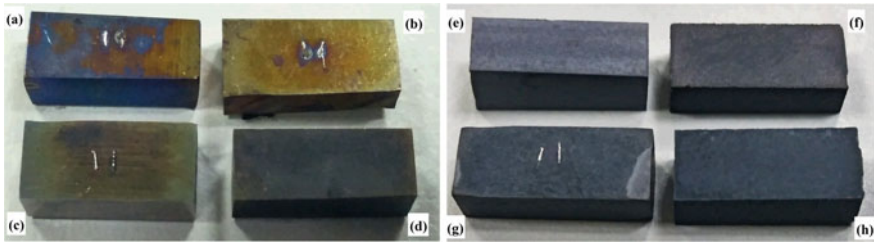


Fig. 2 Ti-6Al-4V appearance after gas nitriding. **a** Appearance of Ti-6Al-4V after gas nitriding at 600 °C for 4 h. **b** Appearance of Ti-6Al-4V after gas nitriding at 600 °C for 6 h. **c** Appearance of Ti-6Al-4V after gas nitriding at 700 °C for 4 h. **d** Appearance of Ti-6Al-4V after gas nitriding at 700 °C for 6 h. **e** Appearance of Ti-6Al-4V after gas nitriding at 1000 °C for 4 h. **f** Appearance of Ti-6Al-4V after gas nitriding at 1000 °C for 8 h. **g** Appearance of Ti-6Al-4V after gas nitriding at 1200 °C for 4 h. **h** Appearance of Ti-6Al-4V after gas nitriding at 1200 °C for 8 h

can be attributed to the titanium phases containing nitrogen content and the random color of the sample can be explained by the amount of the nitrogen diffusion.

Above observations draw our attention toward the possibility of oxidization which gave blue exterior. When the temperatures of nitriding were set above the β -transus temperatures, then the entire area showed gray exterior and intensity of this color was increased with the time and temperature.

This discussion of sample appearance complies with the finding of the previous researchers [12, 13, 15, 16].

4.2 Scanning Electron Micrographs

Figure 3a, b illustrates micrographs of the differently nitrided titanium alloys. At

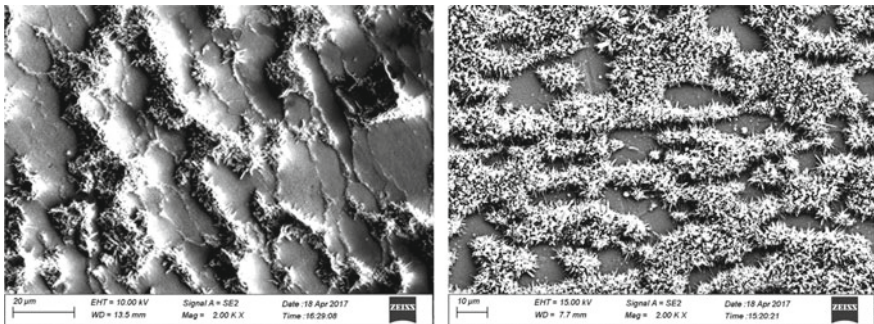


Fig. 3 SEM micrograph after nitriding. **a** Sample surface after nitrided at 700 °C for 4 h. **b** Sample surface after nitrided at 700 °C for 6 h

600 °C, there was no change in the surface morphology. But as the chamber temperature increases to 700 °C, some nitride formation is started at the grain boundaries. This can be observed in Fig. 3a which is the micrograph taken after nitriding at 700 °C for 4 h, and a formation is visible at grain boundaries, and as the time is increased to 6 h, this nitride formation increases drastically as shown in Fig. 3b. Hereafter, it can be suggested that the formation of titanium nitrides has started to form at the grain boundaries, so diffusion of nitrogen first starts at grain boundaries. These findings can be attributed to the fact that the diffusion of nitrogen is three times higher in beta phase of Ti–6Al–4V than alpha phase [14].

4.3 Surface Morphology and Roughness

The surface roughness of Ti–6Al–4V was measured after gas nitriding at various temperatures and time. The average Ra value is 67.75 at nitriding temperature of 1000 °C and time 4 h which is the highest roughness acquired. As the temperature and time increase, the surface roughness decreases as shown in Fig. 4, where roughness value is decreasing both with nitriding duration and temperature.

Improvement in the hardness value was also quantified after nitriding. Initial hardness of the material was 410 HV_{0.5}. The maximum noted hardness value was 1735 HV_{0.5} which was reported for the sample nitride at 1200 °C temperature and 8 h of nitriding time. \query{Please check the clarity of the sentence 'After nitriding at 600 and 700 °C was almost same to the base material...'} After nitriding at 600

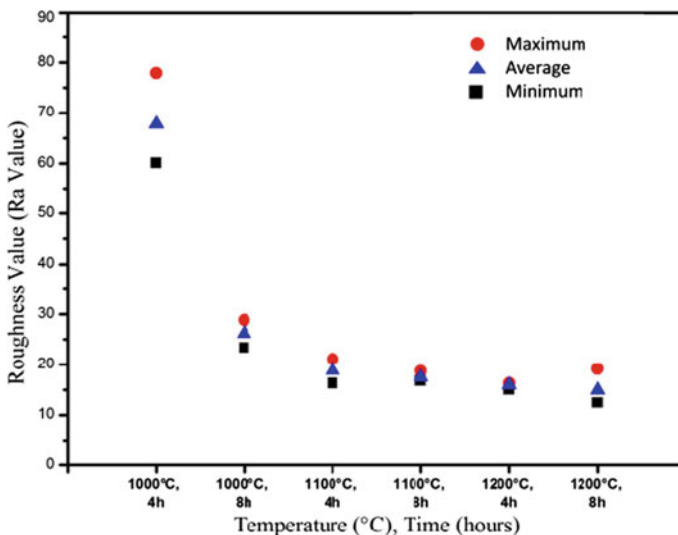


Fig. 4 Surface roughness values (Ra Value) of Ti–6Al–4V measured after gas nitriding at various temperatures and time

and 700 °C was almost same to the base material. It was increased once Ti–6Al–V was nitrided at a temperature of more than 1000 °C. The hardness value $HV_{0.5}$ at 1000 °C for 4 h of nitriding time was accounted to be 1050 $HV_{0.5}$.

The increase in hardness by nitriding could be explained by the fact that hardness of the material increases with titanium nitride layer formed on the surface [17], and this layer thickness increases with the temperature and duration of gas nitriding, which in turn increases the hardness..

5 Conclusions

The thermo-chemical treatment of Ti–6Al–4V alloy by gas nitriding improved its properties. Therefore, the following conclusions could be drawn from the above discussion:

1. When nitrogen diffusion started in the material, the color of the specimen changed from metallic silver to golden. This intensity of golden color increases with increase in temperature and duration of nitriding. Finally, at higher temperatures, the samples turned to a gray appearance that also intensified with time and temperature.
2. The hardness was improved up to maximum value of 1735 $HV_{0.5}$, and it depends on the nitriding parameters.
3. The roughness (Ra value) reduced with the increase in nitriding time and temperature. It was the lowest in case of the nitriding at 1200 °C for 8 h.
4. Nitrogen diffusion into Ti–6Al–4V was started from the grain boundaries.

Acknowledgements The authors gratefully acknowledge the full support provided for this work by National Centre for Aerospace Innovation and Research (NCAIR) at Indian Institute of Technology Bombay (IIT Bombay), a Department of Science and Technology—Government of India, The Boeing Company and IIT Bombay Collaboration.

References

1. Guleryuz H, Cimenoglu H (2005) Surf Coat Technol 192:164
2. Pye D (2003) Practical nitriding and ferritic nitrocarburizing. ASM international
3. Sha W, Ali H, Wu X (2008) Gas nitriding of titanium alloy Ti metal 205. Surf Coat Technol 202(6):5832–5837
4. Zhecheva A, Malinov S, Sha W (2006) Titanium alloys after gas nitriding. Surf Coat Technol 201(6):2467–2474
5. Boyer R, Welsh G, Collings EW (1994) Materials properties handbook—titanium alloys. Materials Park, OH, ASM International, p 78
6. Bell T et al (1986) Surface engineering of titanium with nitrogen. Surf Eng 2(2):133–143
7. Wu SK, Lin HC, Lee CY (1999) Gas nitriding of an equiatomic TiNi shape memory alloy: II. Hardness, wear and shape memory ability. Surf Coat Technol 113(1):13–16

8. Abautret F, Eveno P (1990) Diffusion of nitrogen implanted in titanium nitride (TiN_{1-x}). *Rev De Phys Appl* 25(11):1113–1119
9. Boyer RR (1996) An overview on the use of titanium in the aerospace industry. *Mater Sci Eng* 213(1–2):103–114
10. Yoshida M, Ichiki R, Utsumi N (2013) Surface hardening of titanium using gas nitriding. *Int J Precis Eng Manuf* 14(6):971–976
11. Tokaji K, Ogawa T, Shibata H (1994) The effect of gas nitriding on fatigue behaviour in pure titanium. *Int J Fatig* 16(5):331–336
12. Sha W, Haji AMFAP, Wu X (2008) Gas nitriding of titanium alloy Timetal 205. *Surf Coat Technol* 202(24):5832–5837
13. Shibata H et al (1994) The effect of gas nitriding on fatigue behaviour in titanium alloys. *Int J Fatig* 16(6):370–376
14. Wasilewski RJ, Kehl GL (1954) Diffusion of nitrogen and oxygen in titanium. *J Inst Metals* 83
15. Yilbas BS, Plasma nitriding of Ti–6Al–4V alloy to improve some tribological properties [*Surf. Coat. Technol.* 80, et al (1996) 287–292].” . *Surf Coat Technol* 106(1998):81
16. Shashkov DP (2001) Effect of nitriding on mechanical properties and wear resistance of titanium alloys. *Met Sci Heat Treat* 43(5):233–237
17. Zhecheva A, Malinov S, Sha W (2003) Surface gas nitriding of Ti-6Al-4V and Ti-6Al-2Sn-4Zr-2Mo-0.08 Si alloys. *Z Für Metallkund* 94(1):19–24

Mechanical Systems Design

Navigation Method for Pioneer P3-DX Ground Wheeled Robot in V-REP Platform Using Type-2 Fuzzy Neural Network (T2FNN) Architecture



Anish Pandey, Arnab Guha, Ambesh Kumar, Nilotpala Bej, and Dayal R. Parhi

Abstract This article presents the navigational architecture for a Pioneer P3-DX Ground Wheeled Robot (PGWR) by applying the minimum rule-based type-2 fuzzy neural network (T2FNN) architecture to control the motion, direction and orientation of PGWR between obstacles and help the PGWR to reach the goal. The real-time obstacle distance information received from the ring of ultrasonic sensors of PGWR is feed to the T2FNN as inputs, and necessary wheel velocity control commands for obstacle avoidance are obtained as outputs form rule-based system architecture of T2FNN. The experimental results in the Virtual Robot Experimentation Platform (V-REP) software show that the T2FNN method has successfully guided the PGWR under unknown scenarios. Also, the comparison analysis has been done with the previous benchmark neural network (NN) approach and found smoother trajectory during obstacle avoidance because the T2FNN provided an additional degree of freedom over NN to handle uncertainty situations.

Keywords Pioneer P3-DX Ground Wheeled Robot · Type-2 fuzzy neural network · Ultrasonic sensor · Virtual Robot Experimentation Platform · Neural network

1 Introduction

Soft computing-based wheeled robot navigation and obstacle avoidance have been attracted much attention in the past two decades. In the past few years, several soft computing methods, like fuzzy logic, neural network, adaptive neuro-fuzzy inference system (ANFIS), type-1 fuzzy neural network (T1FNN), different nature-inspired algorithm, etc., have been used for wheeled robot navigation, obstacle avoidance and

A. Pandey (✉) · A. Guha · A. Kumar · N. Bej
School of Mechanical Engineering, Kalinga Institute of Industrial Technology Deemed To Be University, Patia, Bhubaneswar 751024, India
e-mail: anish06353@gmail.com

D. R. Parhi
Department of Mechanical Engineering, National Institute of Technology Rourkela, Sundergarh 769008, India

© Springer Nature Singapore Pte Ltd. 2021
P. Pant et al. (eds.), *Advances in Mechanical Processing and Design*, Lecture Notes in Mechanical Engineering, https://doi.org/10.1007/978-981-15-7779-6_52

wall-following purposes. However, most of the authors have focused on type-1 fuzzy logic and T1FNN-based wheeled robot navigation and obstacle avoidance in different known and unknown scenarios. Pandey et al. [1] have presented the multiple ANFIS architecture to control the motion of a differential drive two-wheeled robot between static and dynamic obstacles in the environments. The ant colony optimization (ACO) and gravitational search algorithm (GSA) bio-inspired algorithms tuned Mamdani type-2 fuzzy logic [2] has been used for trajectory tracking of an autonomous two-wheeled robot. Cascade neuro-type-1 fuzzy architecture-based motion planning of two-wheeled robot between the static and dynamic obstacle conditions has been presented in the article [3]. In the article [4], the authors have controlled the navigation of wheeled robot in an uncertain environment with cluttered obstacles using dual ANFIS controllers one for left motor velocity control and another for right motor velocity control. Improved ant colony algorithm (ACO) and artificial potential field (APF) methods-based grid map path planning for a wheeled robot have been presented in the article [5]. In [6], the authors have implemented the Voronoi diagram (VD) and computation geometry technique (CGT) to control the motion and direction of a wheeled robot between moving obstacles. Vision-based interval type-2 fuzzy logic (IT2FIS) technique has been proposed in [7] to solve the global path planning problem of a wheeled robot in unstructured, static and dynamic environments. Al-Mutib et al. [8] have presented the trajectory tracking strategy for a wheeled robot without measuring velocity using nonlinear Elman neural network. Type-1 fuzzy neural network-based multisensor-actuator controlled obstacle avoidance method for two-wheeled robot has been designed in the article [9]. Artificial neural tuned type-1 fuzzy logic controlled Kinect camera vision-based movement strategy for wheeled robot has been proposed in the article [10].

Most of the authors have used the T1FNN [3, 9, 10] for wheeled robot motion and direction control between different scenarios. Therefore, the authors have designed and implemented T2FNN architecture to navigate the PGWR between obstacles and also help the PGWR to reach the goal. Rest of the manuscript has organized in the following manners: Sect. 2 presents the brief description of type-2 fuzzy neural network (T2FNN) architecture for velocity control. V-REP-based three-dimensional (3D) experimental results and comparison with previous benchmark neural network (NN) approach [11] have been done in Sect. 3. Also, the conclusion and future work are summarized in Sect. 4.

2 Type-2 Fuzzy Neural Network (T2FNN) Architecture for Velocity Control

This section presents a brief description of T2FNN, which controls the left and right motor velocities of the PGWR. Figure 1 illustrates the basic architecture of the designed T2FNN, which is the summation of different layers. The T2FNN has five major layers: input layer (Layer 1), membership function layer (Layer 2),

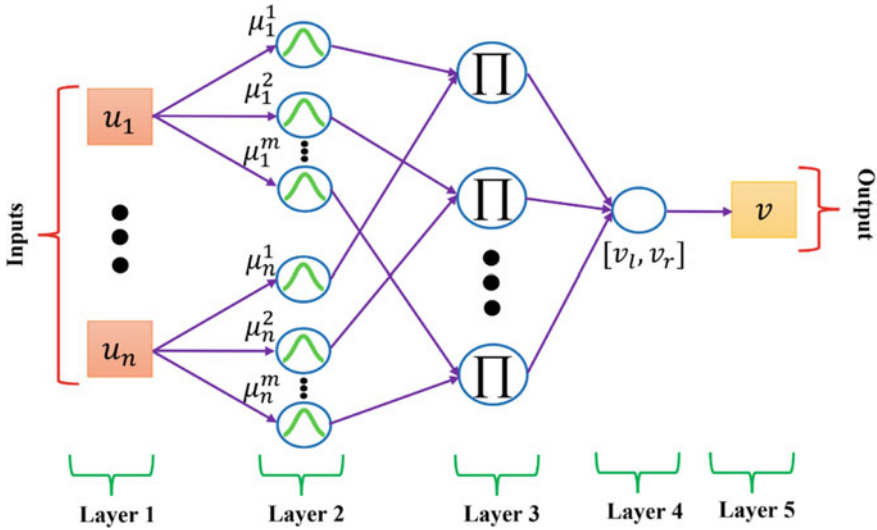


Fig. 1 Basic architecture of the T2FNN

firing layer (Layer 3), consequent layer (Layer 4) and output layer (Layer 5). These layers perform the different actions for the architecture, and each layer is connected through the appropriate weights. The proposed T2FNN receives the input information (obstacle distance) from the sensory system of the PGWR and then provides the left and right motor velocities to achieve collision-free smooth path. Three inputs namely front sensor obstacle distance (FSOD), left sensor obstacle distance (LSOD) and right sensor obstacle distance (RSOD) have been taken for T2FNN architecture. Similarly, two outputs: left motor velocity (LMV) and right motor velocity (RMV) have been selected for T2FNN architecture. The two Gaussian-type membership function, i.e. “Close (Upper and Lower)” and “Far (Upper and Lower)”, have been chosen for inputs (FSOD, LSOD and RSOD) ranging from 10 to 150 cm. Figure 3 shows the Gaussian type-2 fuzzy membership functions of all inputs (FSOD, LSOD and RSOD). The outputs select constant-type (Takagi Sugeno) fuzzy type-2 singleton membership function. The rules of the T2FNN can be expressed in the following forms:

$$\text{Rule}^i : \text{IF } u_1 \text{ is } M_1^i, u_2 \text{ is } M_2^i, \dots \text{ AND } u_n \text{ is } M_n^i \text{ THEN } v \text{ is } f_0^i + \sum_{j=1}^n f_j^i u_j \quad (1)$$

where $i = 1, 2, 3 \dots m$ (m rules), $j = 1 \dots n$ (input variables), u_1, u_2, \dots, u_n are input variables; and v indicates the output variable. The $M_1^i, M_2^i, \dots, M_n^i$ are the interval of T2FNN sets of the antecedent parameters, and $f_0^i + \sum_{j=1}^n f_j^i u_j$ represents

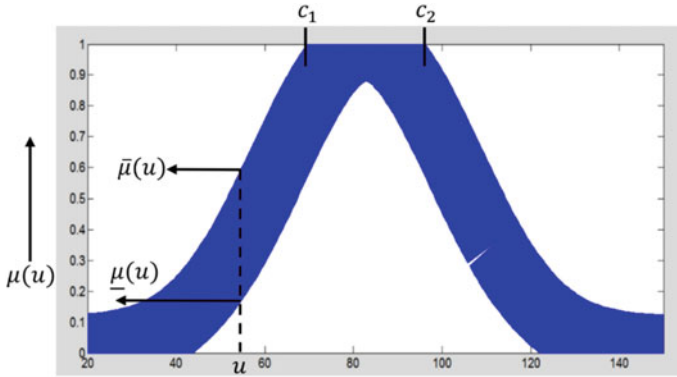


Fig. 2 Model of the Gaussian membership function of type-2 fuzzy set

the Takagi Sugeno linear function. The brief mathematical expressions of all five layers are given below: -

Layer 1: This layer sends the inputs $U = [u_1, u_2, \dots, u_n]$ into the next layer in the following forms:

$$U_j = u_j \tag{2}$$

Layer 2: This layer is also known as fuzzification layer. This layer converts the input variables into linguistic form. The model of the Gaussian membership function of type-2 fuzzy set is illustrated in Fig. 2. In this layer, the T2FNN set M_j^i uses Gaussian membership function in the following forms:

$$\mu_j^i(u_j; c, \sigma) = \exp \left\{ -\frac{1}{2} \left(\frac{u_j - c_j^i}{\sigma_j^i} \right)^2 \right\} \tag{3}$$

where $j = 1 \dots n$ (three input variables), the c_j^i and σ_j^i are tuning/adjusting parameters of the membership function, known as centre and width, respectively. The width (σ_j^i) has been fixed and c_j^i is variable that is $c_j^i \in [c_{j1}^i, c_{j2}^i]$, where c_{j1}^i and c_{j2}^i are the centres of upper and lower membership functions of $\mu_j^i(u_j)$ (Fig. 3).

Layer 3: By applying the product inference function, the firing strength δ^i has been calculated by the following function:

$$\delta^i = [\underline{\delta}^i, \bar{\delta}^i] = \left\{ \prod_{j=1}^n \underline{\mu}_j^i(x_j), \prod_{j=1}^n \bar{\mu}_j^i(x_j) \right\} \tag{4}$$

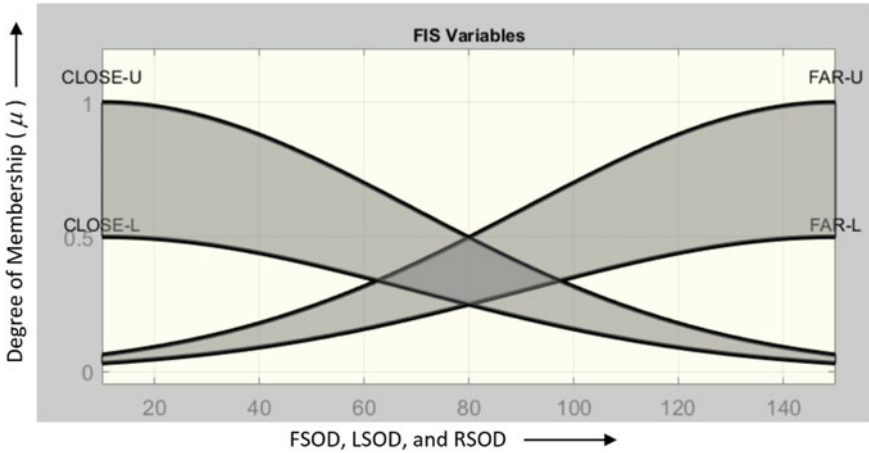


Fig. 3 Gaussian type-2 fuzzy membership functions for the inputs (FSOD, LSOD and RSOD)

where δ^i and $\bar{\delta}^i$ are the firing strengths of lower and upper bounds, respectively. The $\mu_j^i(u_j)$ uses $\underline{\mu}_j^i(u_j)$ and $\bar{\mu}_j^i(u_j)$ as lower and upper membership Gaussian functions, respectively, of T2FNN.

Layer 4: This layer is also called as output processing layer. After firing strength calculation, the type-reduced set is composed through the following equation:

$$V(x) = [v_l, v_r] = \int_{a_1} \dots \int_{a_m} \int_{\delta^1 \in [\underline{\delta}^1, \bar{\delta}^1]} \dots \int_{\delta^m \in [\underline{\delta}^m, \bar{\delta}^m]} \frac{1}{\left(\frac{\sum_{i=1}^m \delta^i \cdot f^i}{\sum_{i=1}^m \delta^i} \right)} \tag{5}$$

where the terms l and r denote the maximum and minimum bound values of v , respectively. If the values of δ^i and f^i are considered for v_l then these are specified by δ_l^i and f_l^i , respectively. Similarly, if the values of δ^i and f^i are considered for v_r then these are specified by δ_r^i and f_r^i , respectively. The defuzzification values of maximum (v_l) and minimum (v_r) have been calculated by the weighted average method in the following forms:

$$v_l = \frac{\sum_{i=1}^m \delta_l^i \cdot f_l^i}{\sum_{i=1}^m \delta_l^i} \tag{6}$$

$$v_r = \frac{\sum_{i=1}^m \delta_r^i \cdot f_r^i}{\sum_{i=1}^m \delta_r^i} \tag{7}$$

Layer 5: The final defuzzification (or average of v_l and v_r) of the crisp value of output v of T2FC as follows:

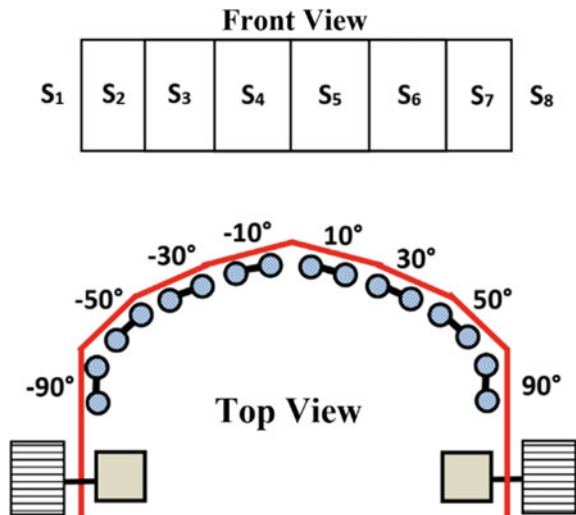
$$v = \frac{v_l + v_r}{2} \tag{8}$$

3 V-REP-Based Three-Dimensional (3D) Experimental Results and Comparison with Previous Benchmark Neural Network (NN) Approach [11]

In this section, the experimental results have been performed in the Virtual Robot Experimentation Platform (V-REP) software. The Pioneer P3-DX Ground Wheeled Robot (PGWR) developed by Adept Technology is a two-wheeled differential-drive robot and it is used in this study. The PGWR contains eight ultrasonic sensors, which have distributed between 90° and 90° from left corner S_1 to right corner S_8 as shown in Fig. 4. The PGWR is made by 1.6 mm thick aluminium sheet, the width of the PGWR is 39 cm, the length is 44 cm, height is 23 cm and its top speed is 1.2 m/s. The width and diameter of the wheel of PGWR are 4.7 cm and 19.5 cm, respectively. The least value of sensors S_1 to S_3 is chosen as LSOD, the least value of sensors S_4 to S_5 is used as FSOD and the least value of sensors S_6 to S_8 is taken as RSOD. The values of FSOD, LSOD and RSOD are feed into the T2FNN architecture as inputs. According to the sensor data interpretation from S_1 to S_8 and by using user-defined “Eight IF–Then” rules, the T2FNN architecture provides the LMV and RMV control commands to the PGWR in V-REP platform during navigation through MATLAB program synchronize with remote API functions.

Figure 5 shows the $300 \times 300 \text{ cm}^2$ three-dimensional (3D) training platform and navigation result of PGWR between red colour rectangular and blue colour

Fig. 4 Sensor arrangement of Pioneer P3-DX Ground Wheeled Robot (PGWR) from S_1 to S_8



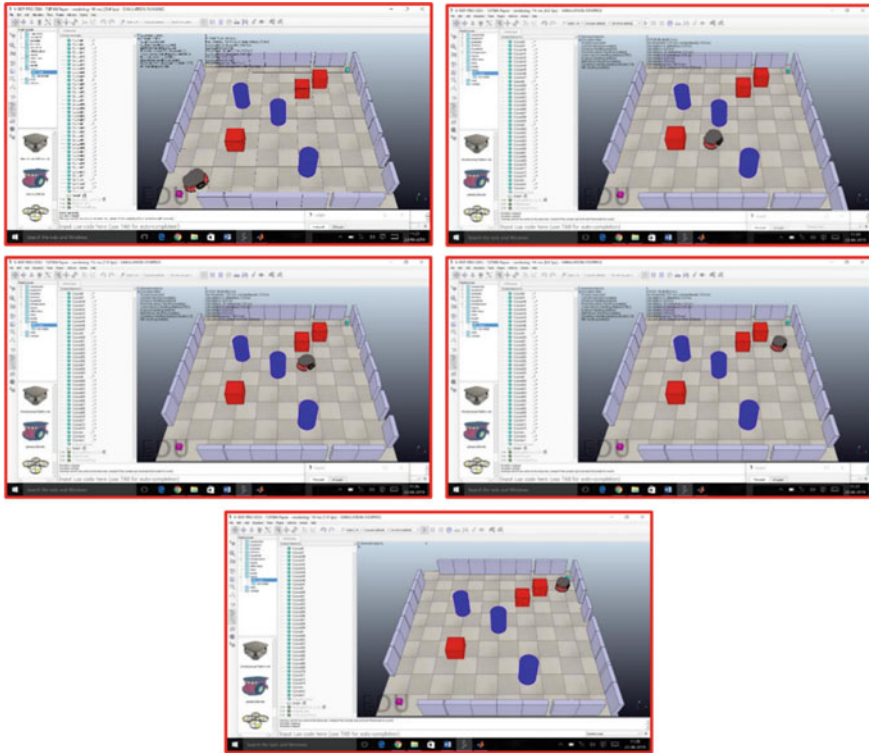
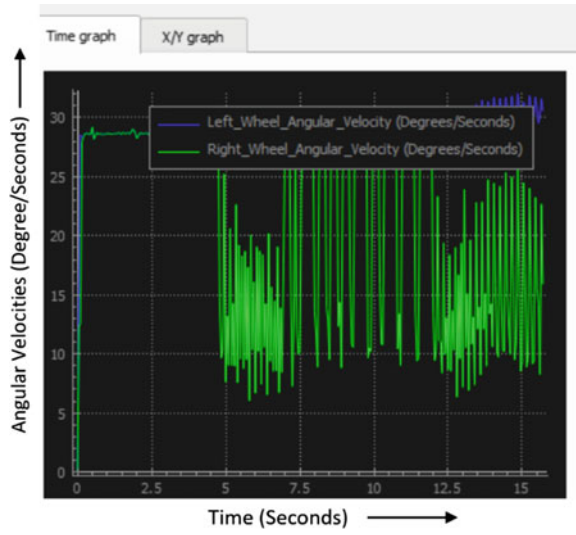


Fig. 5. 3D navigation result of PGWR between red colour rectangular and blue colour cylinder boxes: start position (10, 10 cm) and goal position (250, 250 cm)

cylinder boxes (obstacles). In experiments, except start and goal point, the position of obstacles and environment are unknown for PGWR. The red colour rectangular and blue colour cylinder boxes are the obstacles, which are randomly placed in the 3D platform. Three conditions are specified in the experiments: (a) When the sensors S_1 to S_3 find obstacles nearby then the PGWR turns right side that means the T2FNN gives the high-velocity command to the left motor and low-velocity command to the right motor. (b) Similarly, when the sensors S_6 to S_8 find obstacles nearby then the PGWR turns left side that means the T2FNN gives the high-velocity command to the right motor and low-velocity command to the left motor. (c) When the sensors S_1 to S_8 do not find any obstacles then the PGWR directly moves forward to reach the goal. Figure 6 presents the real-time recorded left and right angular velocities (in degree/seconds) of wheels of PGWR of navigation result of Fig. 5. In Fig. 6, the blue colour and green colour lines indicate the left and right wheel angular velocities, respectively. The value of left wheel velocity is more compared to the right wheel angular velocity because PGWR turns more time right side to reach the goal and avoid the obstacles.

Fig. 6 Real-time recorded left and right angular velocities of wheels of PGWR in Fig. 5



In article [11], the authors have designed the sensor-actuator controlled multilayer perceptron neural network for static and dynamic obstacle avoidance of a wheeled robot. Figures 7 and 8 illustrate the 2D trajectory comparison of PGWR between red colour rectangular and blue colour cylinder obstacles in the platform by applying previous developed NN approach [11] and proposed T2FNN, respectively. We have taken the similar start position (20, 20 cm) and goal position (280, 280 cm) with the same obstacle positions for comparative study. Table 1 shows the numerical comparison data of trajectory path length in centimeter covered by the PGWR in the same 2D platform by taking previous developed NN approach [11] and proposed

Fig. 7. 2D navigation result of PGWR using NN approach [11]

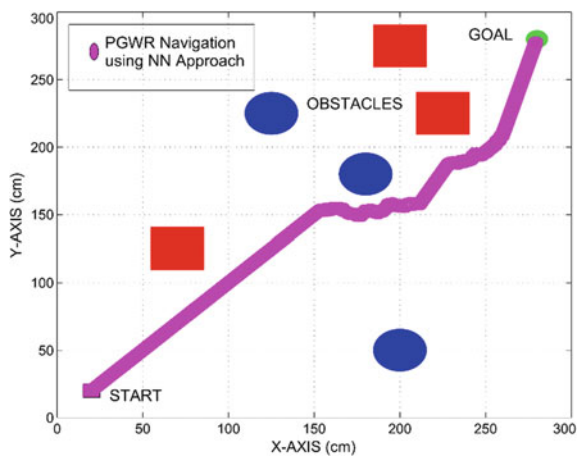


Fig. 8. 2D navigation result of PGWR using proposed T2FNN (X and Y axes illustrate the 2D distance in centimeter)

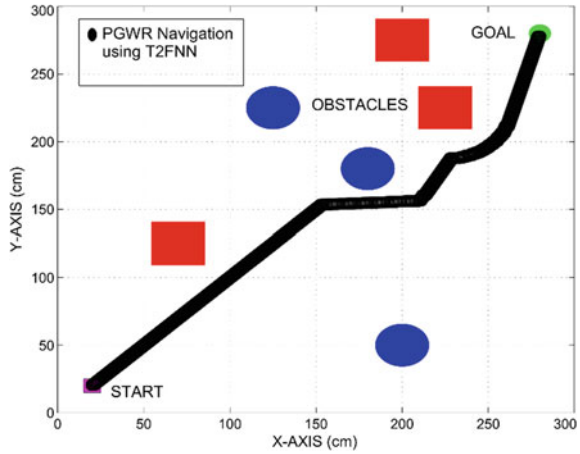


Table 1 Path length comparison between T2FNN and previous developed NN approach [11] in the same 2D platform

Applied approaches	Figures number	Start position	Goal position	Trajectory path length (cm)	Final trajectory path length error (cm)
NN approach [11]	Figure 7	(20, 20 cm)	(280, 280 cm)	148	4.67
T2FNN	Figure 8	(20, 20 cm)	(280, 280 cm)	139	3.15

T2FNN. After seeing Figs. 7 and 8, we can conclude that the proposed T2FNN takes shorter distance with smoother path to reach the goal from start positions.

4 Conclusions

This article discusses the navigational and control strategies for a PGWR under unknown scenarios between obstacles using T2FNN. The left and right motor velocities of the PGWR have been controlled separately by interpreting the sensor data through T2FNN. As we can see in the experimental results, the T2FNN controlled PGWR has successfully avoided the obstacles in different scenarios and also helps the PGWR to reach the goal. The comparison analysis of the smoother trajectory during obstacle avoidance and the less moved trajectory distance with lesser path length error show that the T2FNN controlled robot performed better compared to the previous NN approach [11]. In future work, the authors will take multiple PGWR instead of single PGWR for testing this developed T2FNN under unknown and dynamic scenarios.

References

1. Pandey A, Kashyap AK, Parhi DR, Patle BK (2019) Autonomous mobile robot navigation between static and dynamic obstacles using multiple ANFIS architecture. *Wo J Eng* 16:275–286
2. Castillo O (2019) Bio-inspired optimization of type-2 fuzzy controllers in autonomous mobile robot navigation. In: Kondratenko Y, Chikrii A, Gubarev V, Kacprzyk J (eds) *Advanced control techniques in complex engineering systems: theory and applications*, vol 203. Springer, Cham
3. Pandey A, Burse K (2016) Cascade neuro-fuzzy architecture based mobile robot navigation and obstacle avoidance in static and dynamic environments. *Int J Adv Rob and Auto* 1:1–9
4. Subbash P, Chong KT (2019) Adaptive network fuzzy inference system based navigation controller for mobile robot. *Fro Info Tech Elec Eng* 20:141–151
5. Chen G, Liu J (2019) Mobile robot path planning using ant colony algorithm and improved potential field method. *Com Inte Neur* 2019:1–10
6. Ayawli BBK, Mei X, Shen M, Appiah AY, Kyeremeh F (2019) Mobile robot path planning in dynamic environment using voronoi diagram and computation geometry technique. *IEEE Acc* 7:86026–86040
7. Dirik M, Castillo O, Kocamaz AF (2019) Visual-servoing based global path planning using interval type-2 fuzzy logic control. *Axioms* 8:1–16
8. Al-Mutib K, Abdessemed F, Hedjar R, Alsulaiman M, Bencherif M, Faisal M, Mekhtiche M (2015) Mobile robot nonlinear feedback control based on Elman neural network observer. *Adv Mech Eng* 7:1–14
9. Shi W, Wang K, Yang SX (2009) A fuzzy-neural network approach to multisensor integration for obstacle avoidance of a mobile robot. *Int Automation Soft Com* 15:289–301
10. Bajrami X, Dërmaku A, Demaku N (2015) Artificial neural fuzzy logic algorithm for robot path finding. *IFAC-Pap OnLine* 48:123–127
11. Singh NH, Thongam K (2019) Neural network-based approaches for mobile robot navigation in static and moving obstacles environments. *Int Ser Rob* 12:55–67

Design and Analysis of Weld Bead Cutting Tool Using FEA Technique with Experimental Verification of Cutting Force



Santosh Kumar

Abstract During the production of tube and pipe, a weld bead is developed on inner and outer side of the tube diameter. By electric resistance welding (ERW), the weld bead is very rough and sharp and not favoured for finished tube. Weld bead could be reason for personal injury, loss time accident and product rejection. In this paper, a new kind of cutting tool is developed in which disc spring is introduced and being analyzed numerically using FEA technique. It is found that the force needed to cut the weld bead thickness should be less than the numerical calculated force value.

Keywords ERW tube · Weld bead · Cutting tool · Disc spring · FEA

1 Introduction

In most of the welding, methods used in the tube and pipe production yield an upset or weld bead, on both the outer and inner diameter of the tube. The formation of bead is valid for any working parameter of electric resistance welding (ERW). It is irrespective of high frequency (HF) or direct current (DC), and it is also independent of the current transfer methods, such as shoes, contact wheels or induction coils. Weld bead upset zone is characterized as a rough, sharp and not favoured in the most of finished goods. Therefore, in order to make the product marketable, the removal of weld bead is necessary. Non-removal of weld bead may cause consequences such as personnel injury, lost-time accidents and product rejection. Removal of weld beads in the outside of the tube is easier compared to that of weld beads of ID. Improper handling of the outer weld beads causes the undesired beads which can be reworked to troubleshoot the problem. But the weld bead scarfed from the tube follows a spherical path and continues to follow the path until it is cut or till the structural integral limit is met. The processing of the tube scarf by cutting the bead requires a special tool which will be usually made up of carbide. Tooling life, weld fit up and the weld bead are affected by strip edge condition. Work coils and impeder location affect the heat

S. Kumar (✉)

School of Mechanical and Building Sciences, Vellore Institute of Technology Chennai Campus, Vandalur-Kelambakkam Road, Chennai 600127, India
e-mail: santumrj@gmail.com

© Springer Nature Singapore Pte Ltd. 2021

P. Pant et al. (eds.), *Advances in Mechanical Processing and Design*, Lecture Notes in Mechanical Engineering, https://doi.org/10.1007/978-981-15-7779-6_53

581

coupling to the skelp edge and thereby affect weld bead scarfing. The cutting of the weld bead to a prescribed size for proper and safe handling of the tube manufacturing can be solved by developing a robust and reliable tool. The damage for the ductile plating was predicted by using the design equation when the plating was under the mass impact impulsive loading and dynamic pressure. The design equation used for different shape of plates obtained large deflection due to the impulsive loading, large mass-low velocity impact and the dynamic pressures. Different design equations were obtained for impact loading, dynamic pressure and the impulsive loading of various shape of plates, respectively [1]. Comparison between the analytical calculation and the testing for impact force has been done when one end was connected with the rigid anchor and the other end with the weight. The result obtained from the predicted force equation was less accurate than the test weights and the fall factors were increased at least by 30% in few cases [2]. Simulation of trusses was done with considering the change in variables which shows the performance of the model on the basis of stress, strain, etc. [3]. The factors influencing the spring force have been studied in this paper which shows that the grid-to-rod gap was dependent on the spring force, spring force relaxation and cladding creep down. The spring force was decreased while increasing the larger spring deflection. Therefore, the lower rod loading speed was recommended [4]. Based on the finite element theory, an improved spring method was developed with consideration of the bolt hole clearance and friction effects. As results, the developed spring method was showing the time efficiency for the predicted load distribution [5]. To study about the coned disc spring, the relationships for static load deflection and their stiffness properties were ignored. Friction has been noticed while considering the face-to-face contact and by ignoring the edge-to-surface contact. The load deflection characteristics were analyzed and compared with the load deflection characteristic obtained considering the coefficient of friction between interfacial and edge. As results, an expression for continuously nonlinear stiffness was derived analytically which matched with the measurement [6].

2 Problem Statement

Maximum 6 mm thickness weld bead is to be cut for a long length tube of around 10 m in which the load is going to act on it is 3 ton. 240 mm length of the weld bead is assumed to be cut at a speed of 40,000 mm/m. Three numbers of cuts/s are expected to get cut for which 1 kW power is required to run the machine.

3 Material

Mild steel is being used as setup material. EN 19 (euronorm) is used for cam shaft, HC. High carbon high chromium (HCr) is used for cutter blade design and 50crV4

Table 1 Material properties [7, 8]

Material name	Description
Mild steel (0.14–0.20% C, 98.81–99.26% Fe, 0.60–0.90% Mn, <0.04% P, <0.05% S)	Tensile strength—370 MPa Ultimate strength—440 MPa Modulus of elasticity—205 GPa Elongation—15%
EN 19 (0.80–1.10% Cr, 0.75–1.00% Mn, 0.38–0.43% C, 0.15–0.30% Si, 0.15–0.25% Mo, 0.04% S, 0.03% P)	Tensile strength—555 MPa Ultimate strength—925 MPa Modulus of elasticity—210 GPa Elongation—13%
Hc. Hcr (1.40–1.60% C, 0.60% Mn, 0.60% Si, 1.00% Co, 0.03% P, 11–13% Cr, 0.70–1.20% Mo, 1.10% V, 0.30% Ni, 0.25% Cu, 0.03% S)	Tensile strength—862 MPa Ultimate strength—1030 MPa Modulus of elasticity—210 GPa Elongation—20%
50crV4 (0.47–0.55% C, 0.70–1.10% Mn, 0.15–0.40% Si, 0.03% S, 0.03% P, 0.90–1.20% Cr, 0.10–0.20% V)	Tensile strength—1160 MPa Ultimate strength—1200 MPa Modulus of elasticity—206 GPa Elongation—14.5%

(DIN EN 10277 spring steel grade—40 to 45 HRC) is used for spring. Table 1 represents the properties of the material used for the manufacturing of the tool.

4 Design Calculation for Disc Spring

Figure 1 shows the schematic diagram of the disc spring. The springs were placed with series stacking.

Table 2 explains about the dimensional requirements of the spring to be designed for achieving the load for cutting the weld bead.

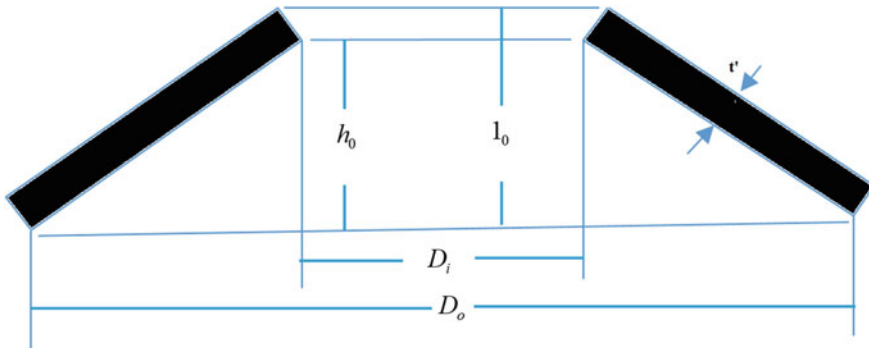


Fig. 1 Schematic diagram of the disc spring shaft

Table 2 Dimensions of the disc spring

<i>Dimensions</i>	
Outer diameter (D_e)	70 mm
Inner diameter (D_i)	28 mm
Spring thickness (t)	3 mm
Reduced thickness (t')	2.5 mm
Spring height (l_0)	4 mm
<i>Data</i>	
	$h_0 = 1$ mm
$h_0/t = 0.333$	$h'_0 = 1$ mm
$h'_0/t' = 0.333$	$D_e/D_i = 2.5$ mm

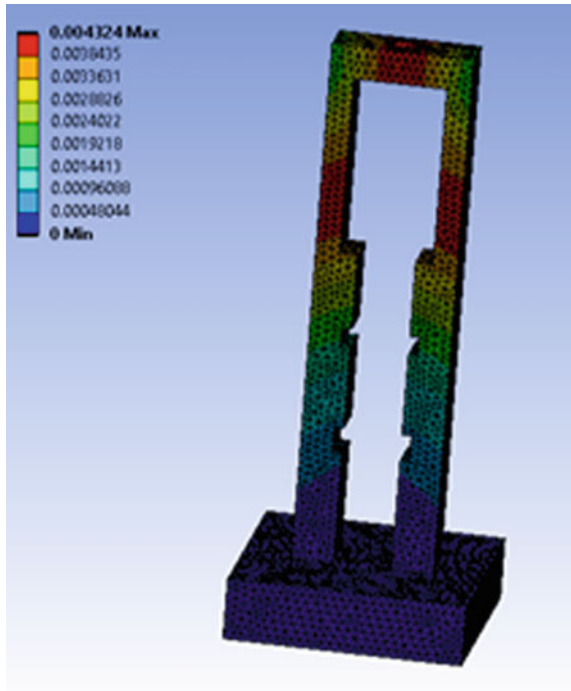
Table 3 Calculated value for load and stress

Load points of one spring				Calculated stresses			
Load point	Height l (mm)	Travel s (mm)	Load F (N)	s_I	s_{II}	s_{III}	s_{OM}
				MPa			
0	4.000						
1	0.488	3.512	27,892	-3144	4857	1136	-2444
2	0.363	3.637	29,572	-3183	5103	1137	-2531

Table 3 gives the numerical value for load and stress obtained from spring dimensions. The stress is calculated from the relationship between force and thickness [9].

5 FE Analysis

To check whether the structure is stable under 3 ton loading condition, a FEA analysis is required before manufacturing. The structural analysis is done by using ANSYS in which material is considered as linear elastic under quasi-static analysis. Force loading control method is used. A 3D force component is applied in Z-direction on top of the plate and displacement of bottom plate is given as zero in all direction. The element type is autoselected by ANSYS programme in which the number of elements is 28,509.

Fig. 2 Total deformation

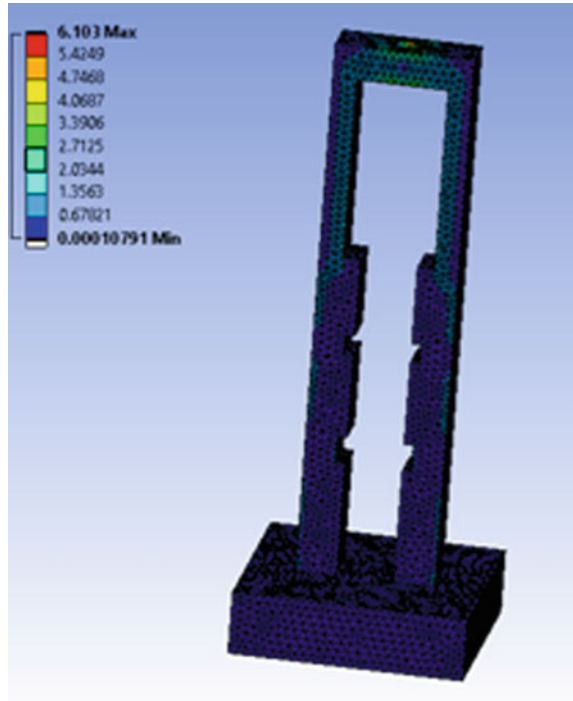
6 Results

The total deformation and the stress obtained on the structural frame due to the load were 0.4 mm and 6 MPa, respectively, which were safe as per the material strength aspects and loading conditions. Figures 2 and 3 show the total deformation and stress obtained due the applied load.

7 Experiment

Figure 4 shows the complete setup for the testing. The test setup is run at a speed of 40,000 mm/min for cutting three numbers of strips of 240 mm length. 1.5 kW motor has been used for the testing. The cutter part of the setup is manufactured in such a way that the strip will be moving directly to the bin during the cutting operation which can help the operator to handle the strips without touching it. Total height and width of the machine were 1100 mm and 350 mm, respectively.

Figures 5 and 6 show the design of cam shaft used for the machine to achieve two cuts in one stroke. As per the design of spring and cam profile, spring can be compressed with 10 mm distance to obtain 3 ton of load for cutting the weld bead. The top face cam and bottom face cam were mirror to each other. The top face cam

Fig. 3 Stress

was attached with the shaft and a punch was press fitted with it, whereas the bottom face cam was fixed with the base structure of machine. The hexagonal part of the shaft was connected with the motor and the rotation was helped to compress the spring for achieving the cutting load.

Figures 7 and 8 show the cutter assembly and individual cutter design. The cutter was used to cut the weld bead. It was attached with a plate of the cutter assembly in which two springs were fitted to allow the cutter for up and down movement during cutting operation. Figure 9 shows the tool is in semi-assembled condition which consists of two side plates, shaft with hexagonal profile at the top, top and bottom face cam. Figure 10 describes the hexagonal shaft with top face cam attached on it, attachment of bottom face cam with bottom base plate and top plate welded with a cylindrical body.

The cutter in assembled condition with the spring and main block of the assembly was shown in Fig. 11 which placed below the upper half of the complete tool during the operation for achieving the cutting requirement. In Fig. 12, the upper and lower half of the cutting tool shown individually.

Fig. 4 Experimental test setup

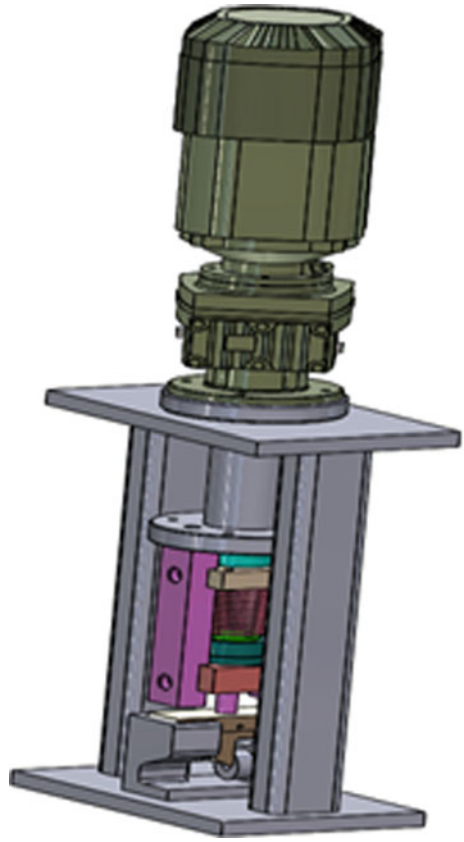
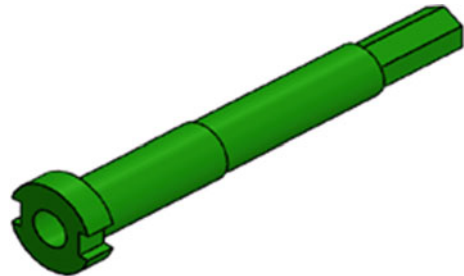


Fig. 5 Hexagonal shaft



8 Results

In experiment, complete three numbers of strips of 240 mm length were cut and collected in the bin. During the experiment, it was observed that the load coming on the cutter was not always being 3 ton. It was varying from 2 to 2.6 ton as the strip coming out after welding operation was in hot condition. Figures 13 and 14 show

Fig. 6 Face cam

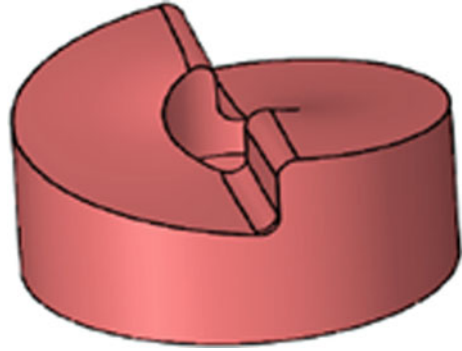


Fig. 7 Cutter assembly

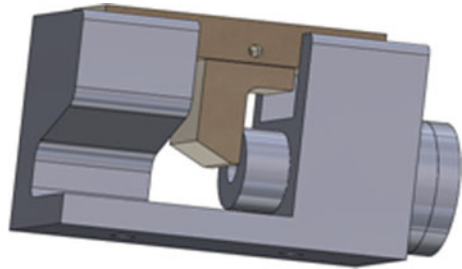
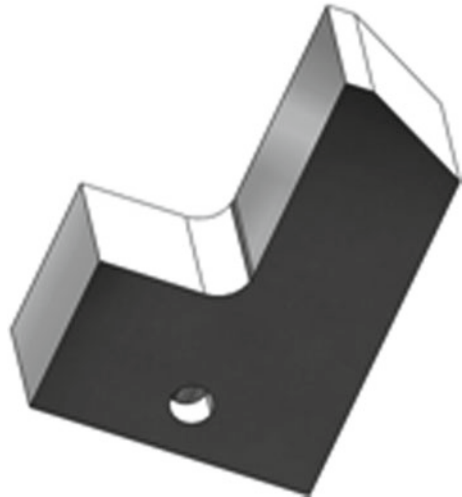


Fig. 8 Design of cutter



the weld bead before and after stage of the cutting operation. The cut length of the weld bead was observed uniform with length of 240 mm.

Fig. 9 Semi-assembled tool



Fig. 10 Top and bottom face cam, top plate



9 Conclusions

During the comparative study, it was concluded that the validation of experiment with the theory was met. The cut length of the weld bead and the number of cuts were observed in the experiment was found to be 240 mm and 3, respectively, and in the calculation, it was 240 mm and 2.7. It means the fabricated cutting tool was able to cut the weld bead efficiently. But it can vary with varying the operating parameters like speed of motor, length of the weld bead to be cut, speed at which the tube will

Fig. 11 Cutter assembly

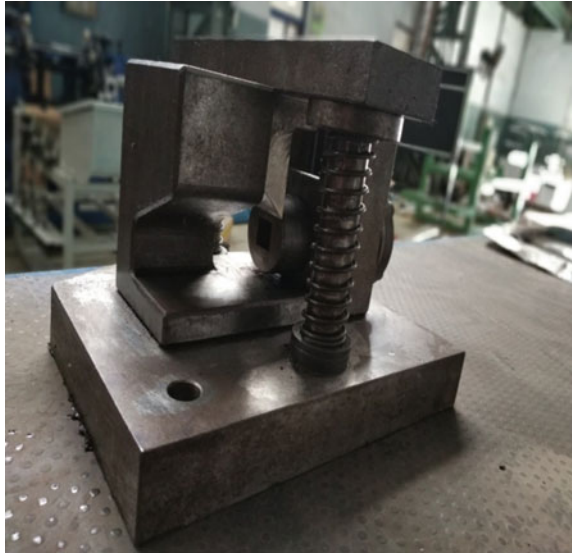


Fig. 12 Upper and lower half



move. It can be used in the manufacturing industry in order to make less hazardous workplace for the operator to handle the rough and hot weld beads.

Fig. 13 Weld bead before cutting



Fig. 14 Weld bead after cutting



Acknowledgements I would like to thanks VIT Chennai campus for providing research facility and also like to thanks my colleague who supported me directly or indirectly during research.

References

1. Jones N (2013) Damage of plates due to impact, dynamic pressure and explosive loads. *Lat Am J Solids Struct* 10:767–780
2. Weber C (2002) Analysis of impact force equations. In: *International technical rescue symposium*, pp 1–7
3. Zheng Z, Bai Y (2017) Effects of impact loads on mechanical performance for truss structure. *World J Eng Technol* 05:135–140
4. Kim K-T (2010) The effect of fuel rod loading speed on spacer grid spring force. *Nucl Eng Des* 240:2884–2889
5. Xiang J, Zhao S, Li D, Wu Y (2017) An improved spring method for calculating the load distribution in multi-bolt composite joints. *Compos Part B* 117:1–8
6. Masticola NP, Singh R (2017) Nonlinear load deflection and stiffness characteristics of coned springs in four primary configuration. *Mech Mach Theory* 116:513–528

7. www.azom.com
8. www.aerospacealloy.com
9. <https://schnorr.com/wp-content/uploads/2018/05/Schnorr-Engineering-Design-Handbook.pdf>.
Accessed 15 Sept 2019

Design, Fabrication of Human-Powered Vehicle



Pratik Kale and Pankaj Ardak

Abstract In this paper, design, fabrication and analysis of a human-powered vehicle are discussed. The current scenario of HPVs can be changed with the used of highly engineered techniques [1]. This research work has been carried out to provide people new vehicle which is energy efficient, eco-friendly and economical thereby contributing to nature and surrounding. The proper planning and design attributes play very crucial role in it. The major attributes are frame design, steering system, 339 transmission and braking. Fabrication of HPV may not require high precision and does not involve critical methods, subsequently reducing the cost of production of vehicle. Testing is the most important parameter of HPVs.

Keywords Human-powered vehicles (HPVs) · Transmission

1 Introduction

Human-powered vehicles are supposed to be the most appropriate option over the vehicles using non-renewable energy sources. If built properly with the use of proper engineering and considering human ergonomics, these vehicles become more efficient than conventional HPVs [2]. The human-powered vehicles were designed and developed for the daily life travelling and for short distances. The long-distance efficiency of HPV is not high and not even decent (1). In urban areas, these vehicles are not used mostly because of their slow speed and discomfort (2). Speed is one of the biggest reason or parameters which have contributed towards the growth of fuel-consuming vehicles. The fuel consumed by the vehicles causes very large amount of pollution, and that amount of pollution can be reduced with the help of human-powered vehicles (3).

P. Kale

Department of Mechanical Engineering, P. R. Pote College of Engineering and Management, Amravati, India

P. Ardak (✉)

Assistant Prof. Department of Mechanical Engineering, P. R. Pote College of Engineering and Management, Amravati, India

e-mail: pankajardak@gmail.com

© Springer Nature Singapore Pte Ltd. 2021

P. Pant et al. (eds.), *Advances in Mechanical Processing and Design*, Lecture Notes in Mechanical Engineering, https://doi.org/10.1007/978-981-15-7779-6_54

593

Table 1 Comparison between Tadpole and Delta

Parameter	Tadpole (finalized)	Delta
Speed	Better speed can be achieved	Moderate speed
Aerodynamic	Better aerodynamic tear drop can be easily achieved	Less aerodynamic design
Brakes	Good braking stability	Moderate braking stability
Steering	Low turning radius can be achieved with better safety	Better turning radius but not too safe
Stability	Excellent stability when cornering	Moderate stability
Drive system	Simple drive system	Complex drive system
Ergonomics	Ergonomics is noble for Tadpole design	

2 Methodology

Design, fabrication and analysis of a HPV consist following attributes.

2.1 Design Selection

For the human-powered vehicle, only two competitive designs are used a recumbent with two wheels and a recumbent with three wheels, and in order to make a selection between two, a comparison of two was conducted [3]. It has been decided to use three wheels, and the reason was stability, so for three-wheel recumbent, two of the most variant alternative were ‘Tadpole’ and ‘Delta’ (Table 1).

2.2 Frame

While considering primary materials for frame design materials physical properties, its weight was the main constraint. Aluminium 6061 T6 and AISI 4130 were the first priorities of team while selecting material because of their better properties compared to materials like mild steel [4]. Though Aluminium 6061 T6 is lightweight and has less percentage of elongation, it faces huge problems about weldability. Aluminium has the least weldability among the all materials shortlisted [5]. Also there were huge problems about its welding. MIG welding can be easily done on this material providing better strength (Table 2).

Table 2 Material properties

Properties	AISI 4130
Elastic modulus	410 MPa
Density	7.80 g/cm ³
Strength-to-weight ratio	86
Tensile strength	630 MPa
Yield strength	435 MPa
Thermal expansion	11.8
Cost	Moderate

2.2.1 Frame Design

Main motive behind of designing a frame or chassis is to provide better comfort and safety to the rider and must provide proper mounting to other components of vehicle. To make vehicle more comfortable, several parameters were considered like knee angle, back rest angle, etc. Those were studied from the old reports and research papers; also a prototype was created which gave us few values. The most important finding from this research was the back rest angle which should be considered as 130°. As per ASME HPVC Asia Pacific 2018 Rulebook, RPS should be the most important part of vehicle, so teams' focus was also on designing the proper RPS for better safety to rider. Survey should be done for checking comfort. As specified in the ASME HPVC Rulebook 2018, a load of 2670 was applied at an angle of 12 from the vertical. The FEA in ANSYS was done by considering the assumption that the member away from the RPS was made fixed and the member near to the RPS was made flexible. For side loading load of 1330 N is applied horizontally to the side of roll bar at the height of shoulder of stoker (Fig. 1).

The ANSYS results for the side loading and top loading conditions show the factor for safety to be more than 2.5; also the deformations in the frames were also less than the extreme limits given in the rulebook.

2.3 Steering System

As an alternative, there are choices to use simple four bar mechanism with connecting rod and steering arm or Go-cart type. The reason rack and pinion were not selected because after research, we concluded that rack and pinion would be an oversized and weight too much; from this, it was decided to use type linkage which inculcates connecting rod two steering arm; this type of steering is easy to design and set handling. As HPV has Tadpole trike type of configuration, i.e. it has two wheels in front. So front steered tadpole was selected [6]. For designing steering system, Ackerman's principle should be chosen.

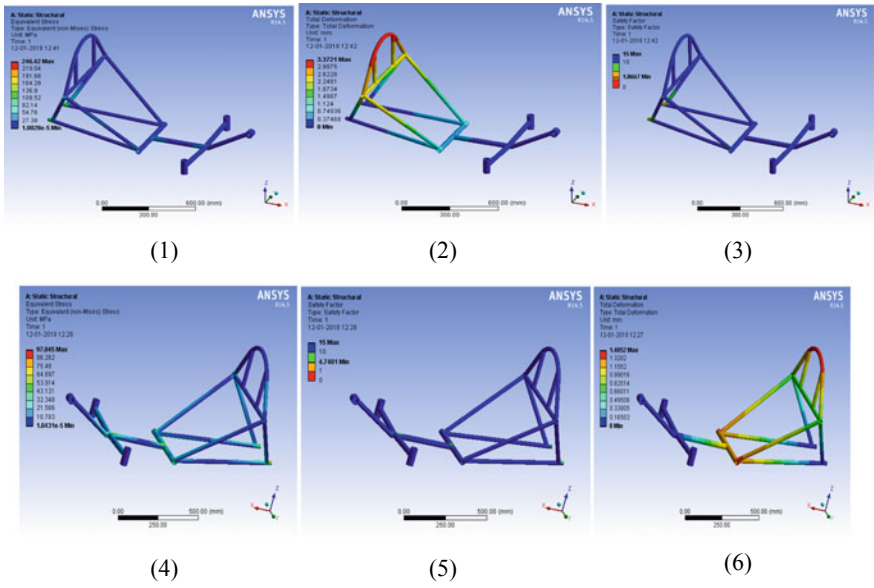


Fig. 1 Results of top loading analysis

For the analysis of proper steering system, we calculated following parameter, which gave us the proper information like how much the steering will move at the ends, how much the movement of hand will give how much deflection at the steering (Table 3).

Results should be verified by using perfect steer condition

$$\cot(\text{Inner Angle}) - \cot(\text{Outer Angle}) = \frac{\text{Wheel Track}}{\text{Wheel Base}} \tag{1}$$

$$\cot(24) - \cot 15.25 = \frac{877.2}{1260} \tag{2}$$

LHS = RHS.

Table 3 Steering system parameters and values after calculations

Sr. No.	Parameter	Calculated values
1	Inner angle	24°
2	Outer angle	15.25°
3	Ackerman angle	17.19°
4	Ackerman percentage	70%
5	Turning radius	4.2 m
6	Steering ratio	1:1
7	Connecting rod length	700 mm

Table 4 Braking system calculations

Sr. No.	Parameter	Calculated values
1	Braking force	105 N
2	Force on calliper	11,875.22 N mm
3	Clamping force	4750.088 N mm
4	Deceleration	9.04 m/s ²
5	Stopping distance	2.04 m
6	Stopping time	0.99 s

This shows that the steering satisfies the perfect steering condition.

Also the turning radius of vehicle should not be more than 8 m, and this proposed vehicle has a turning radius of 4.3 m which is far less than the requirement.

2.4 Braking System

The alternative option of vehicle was disc brake and rim brake. The best option for our HPVC is mechanical disc brake. At the initial assessment, it is being decided to provide a disc brake at front as well as at rear but as the time passed, it was confirmed to provide the brake at the rear. Secondly, there would be two option either to use hydraulic disc brake or cable-actuated disc brake. Between two, cable-actuated disc brake was selected. This is done because the installation and adjustment were researched to be more tiresome and they require negligible maintenance. After further research, the team decided to use a compatible rotor of 160 mm (Table 4).

The parameters give brief about the performance of the braking system. Braking time and stopping time for this system are well below the restrictions given by the ASME HPVC Rulebook. This makes this braking system sustainable and safer to ride.

2.5 Drive Train (Transmission)

As per the requirement, the drive mechanism being powered by a human operator the drive train will have configuration advance to as compared to bicycle. Length of the chain is the major issue in recumbent cycles. Idler should be used at every bent into the frame. Use of idler increases losses in transmission, so there is need of arrangement which will decrease number of idler and collectively increase the efficiency of the system. Rear wheel drive system has been used. Instead of using single chain, we have used two chains (one from pedal to compound assembly and other from compound assembly to rear wheel). Compound assembly is simply shaft carrying two different freewheels. Due to this assembly, we're able to achieve more speed.

Table 5 Gear train calculation

No of teeth (Rear sprocket)	Gear ratio	N (RPM)	Speed (kmph)
14	3:14	209.51	26.1
16	2:75	183.32	22.82
18	2:44	162.95	20.28
21	2:09	139.67	17.38
24	1:83	122.21	15.21
28	1:57	104.75	13.03

Six-speed gear box containing teeth from 14 to 28 is used on the rear wheel to provide variable gear ratio due to this speed of 25–45 kmph can be achieved.

By considering rate of pedalling minimum (Table 5).

3 Conclusion

In engineering, there is a constant need for improvements as there is a never-ending list of flaws. These flaws, with the correct processes, can and should be predicted and dealt with before catastrophic failure. Mitigating the cause of failure of the suspension found to be instability of vehicle coupled with unexpected steering problems and could have been accomplished with more testing. The RPS testing should be done with to verify the analytical values. Dynamic modelling software would have been useful, but only as a preliminary step before physical testing. Performance testing needs to be more through. Theoretically, steering will work with the calculated values. There are assumptions involved in the calculations, and in reality, there are errors during manufacturing. It is recommended that instead of doing steering analysis, to perform steering testing, similarly, for braking, more tests should be performed instead of calculations only.

References

1. Abhilash J, Sri MRSR (2014) Design, analysis and fabrication of a human powered vehicle. *Int J Eng Sci Res.* ISSN: 2277-9655
2. Abdullah MA, Rahman MHA, Azis1 MZ, Shamsudin SA, Ramli FR, Sudin MN (2017) "Ergonomic study on human-powered vehicles" at MATEC Conference
3. Gupta US, Chandak S, Dixit D (2015) Design of Efficycle—human powered hybrid tricycle. *Int J Eng Trends Technol (IJETT)* 19(3)
4. "Human Powered Vehicle: Mjölñir" by Portland State University Mechanical Engineering Department 1930 S.W. 4th Ave Portland, OR 97201 (503)725-4290
5. Khurmi RS, Gupta JK (2010) A textbook of machine design. Eurasia Publishing House (Pvt.) Ltd.
6. "Human Powered Vehicle Challenge 2018 Rulebook" by ASME

Detection of Breathing Crack Using Vibration Signal Analysis



Smaranika Nayak, Jatin Sadarang, Manisha Maurya, and Isham Panigrahi

Abstract In this paper, an attempt has been made to predict breathing crack location and severity from the vibration signal measured by a frequency analyzer. The crack beam is subjected to impact excitation to get natural frequencies. Then, harmonic excitation technique is used on crack beam by attaching it to an electrodynamic exciter. The beam is excited within 0–2000 Hz frequency band. The FFT results of crack beam clearly show the presence of super-harmonics and sub-harmonics in vibration signatures as compared to beam without crack. The concentration of sidebands is more around the natural frequency which is most affected by the location of the crack. These results will be helpful in detecting crack severity and location in beam-like structures in real-life situations.

Keywords Breathing crack · FFT · Vibration · Beam · Crack detection

1 Introduction

A crack in a beam opens and closes alternatively when subjected to cyclic loading. This effect is called crack breathing. The crack which shows breathing behavior is known as breathing crack [1]. The crack in closed condition, the beam can be considered as a continuous beam without crack. On the other hand when the crack is fully open, it can be modeled as open [2] crack beam. Chondros et al. [3] have formulated a new theory to find out the vibration parameters of a pinned-pinned beam with breathing crack. They have concluded that open crack model and breathing crack model give different results. Cui et al. [4] also studied that for every cycle of vibration, the crack is partially open for half of the cycle. Wang and Gang [5] this half cycle there are gradual increase in contact and gradual loss of contact between crack surfaces, which introduces nonlinearity into the system. This nonlinearity leads to excitation of number of higher harmonics in the vibration signal and change in natural frequency as compared to an open crack beam. The nonlinear effects in the

S. Nayak (✉) · J. Sadarang · M. Maurya · I. Panigrahi
School of Mechanical Engineering, Kalinga Institute of Industrial Technology Deemed To Be
University, Bhubaneswar, Odisha 751024, India
e-mail: smaranika.nayakfme@kiit.ac.in

measured vibration signal of a crack beam can be used to predict the severity and location of crack (Prime et al. [6]). Douka and Hadjileontiadis [7] have used variation in instantaneous frequency model to predict the crack size of a beam with breathing crack. Andreaus et al. [8] have used nonlinear dynamics to predict crack in a cantilever beam. Peng et al. [9] have used nonlinear output FRF to detect cracks. They have found out a large change in super-harmonic amplitude with increase in crack size. Srinivasarao et al. [10] have used wavelet analysis to identify breathing cracks in cantilever beam. In the present research, an attempt has been made to predict the breathing crack and severity from vibration signal measured by frequency analyzer. Harmonic excitation technique was used on the crack beam, then vibration signature analysis software was used to conduct FFT analysis of the recorded vibration signal, and finally results were plotted in frequency domain.

2 Experimental Setup and Testing Procedure

The experimental setup consists of aluminum cantilever beam, vibration analyzer, accelerometer, electrodynamic exciter and a laptop with fast Fourier transform software loaded on it. The breathing crack is simulated using three pieces of aluminum beams of cross section (19 mm × 3.5 mm) joint firmly with each other by use of adhesive bonding. The length of the aluminum beam specimen is taken as 400 mm. The crack surfaces are made to be in close contact like real-life fatigue crack. First, the crack beam and beam without crack are subjected to impact excitation to get frequency response. Vibration analyzer is used to find out FFT of the vibration signal, and five natural frequencies are found out within 0–2000 Hz frequency band. In harmonic excitation technique, crack beam was attached to electrodynamic exciter, the vibration is given to the beam with the help of amplifier cum signal generator within 0–2000 Hz frequency band and then the frequency response is measured with the help of a four-channel vibration analyzer. The vibration is sensed with an accelerometer mounted at free end and recorded in a computer. Vibration signature analysis software is used to conduct FFT analysis of the recorded vibration signal, and the result is plotted in frequency domain [11].

Figure 1 shows some three-piece aluminum specimens bonded with superglue and firmly wounded by thread to simulate breathing crack. Figure 2 shows the line diagram of experimental setup having the following elements: (1) beam specimen, (2) accelerometer, (3) amplifier cum Signal generator, (4) electrodynamic exciter, (5) vibration analyzer, (6) computer with FFT software.

3 Results and Discussion

In case of harmonic analysis, the beam is fixed on the electrodynamic exciter table and the 38 g accelerometer is mounted in the free end. This leads to some mass effect



Fig. 1 Photograph of different aluminum crack beam specimens

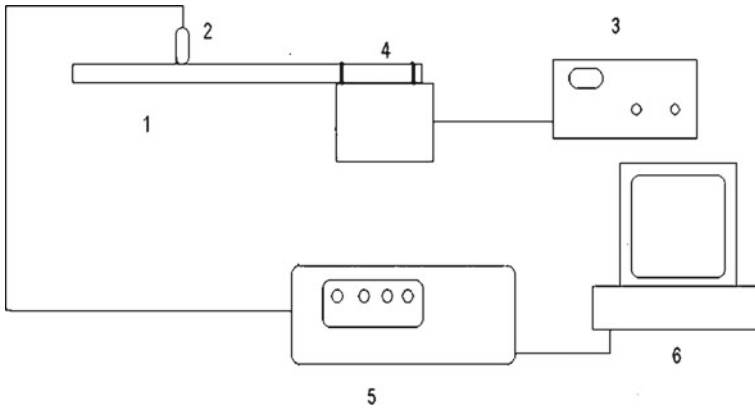


Fig. 2 Diagram of experimental setup for cracked aluminum beam

on the natural frequency results. In this paper, Fig. 3 shows the frequency domain plot of aluminum beam without crack in it. The plot has no super-harmonics or sub-harmonics present in it. But in Fig. 4 for the same beam with crack at the middle, we can see lot of super- and sub-harmonics present in the FFT signal because of crack breathing. We can also see in Fig. 5 the sideband concentration is more near second natural frequency as second mode is most affected by crack present at the middle of the cantilever beam. At the same time, frequency of these modes substantially

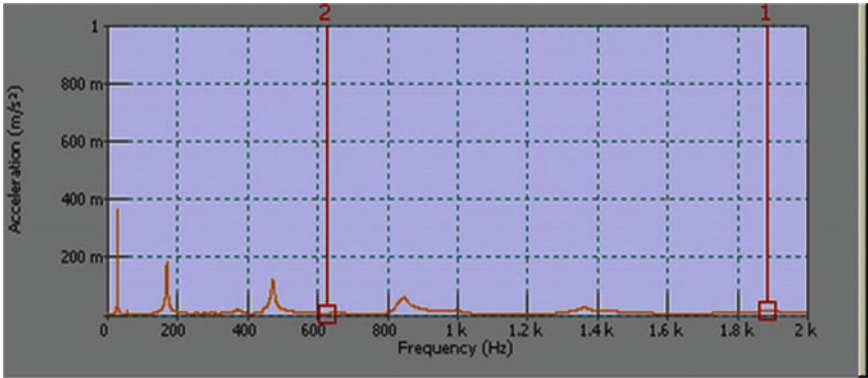


Fig. 3 FFT plot of beam without crack subjected to impact excitation

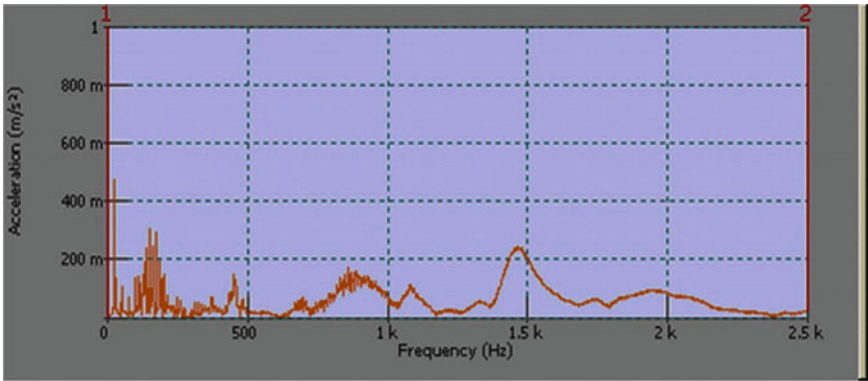


Fig. 4 FFT plot of beam with crack at middle subjected to impact excitation

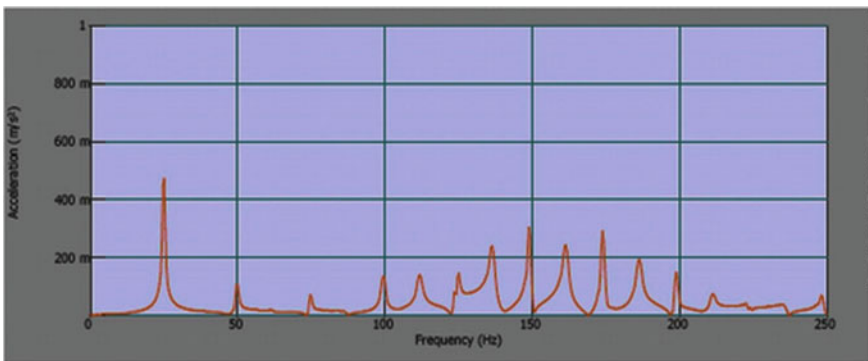


Fig. 5 Sidebands produced by breathing crack at the middle

gets affected. If these two observations are correlated with each other, then we can predict the crack location accurately with FFT signal study. Table 1 shows the natural frequencies for different crack locations [12].

It can be seen the first natural frequency increases as the crack location moves toward free end; also, it is measured that the second and third natural frequencies got affected because of change in crack location in cantilever beam [13]. In Fig. 6, FFT plot harmonic signal taken at first natural frequency, clearly no higher harmonic is seen in the FFT plot but if we see Fig. 7 number of harmonics can be seen; this is a clear indication of the presence of breathing crack.

Similar observation is made when harmonic excitation is given at second natural frequency as shown in Figs. 8 and 9. Finally to verify the crack breathing observations, the beam is excited at frequency away from natural frequency of the beam and it is seen that the super-harmonics are seen very prominently with higher amplitude in case of crack beam as compared to beam without crack. The results for 3 Hz frequency excitation are shown in Figs. 10 and 11.

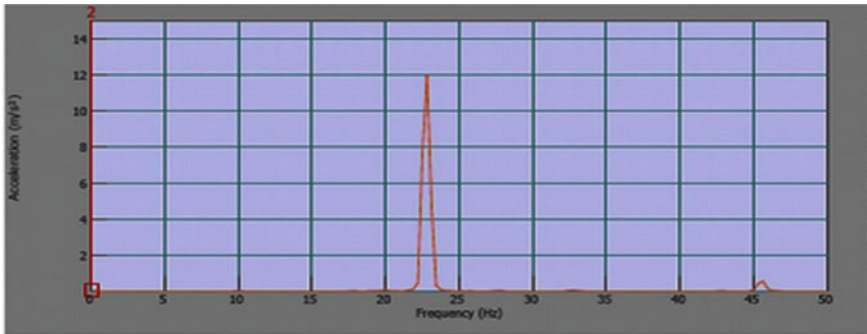


Fig. 6 FFT plot of beam without crack subjected to harmonic excitation at first natural frequency

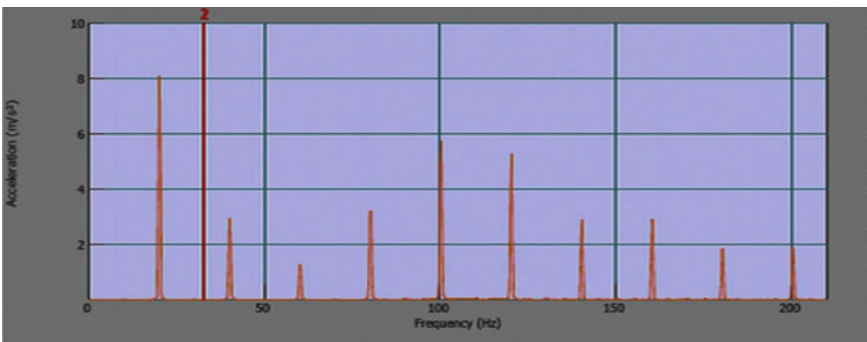


Fig. 7 FFT plot of beam with crack at middle in harmonic excitation at first natural frequency

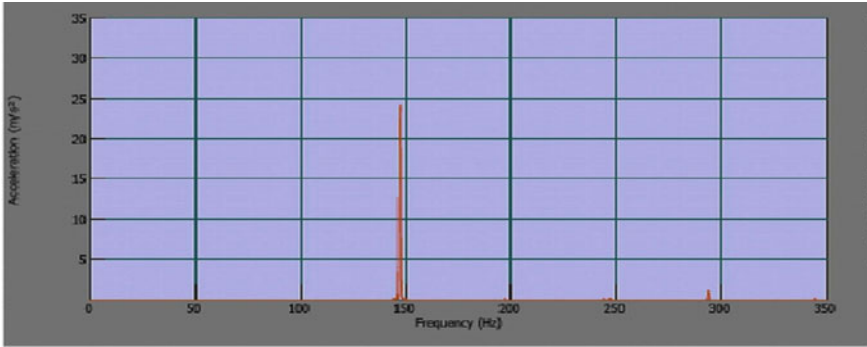


Fig. 8 FFT plot of beam without crack subjected to harmonic excitation at second natural frequency

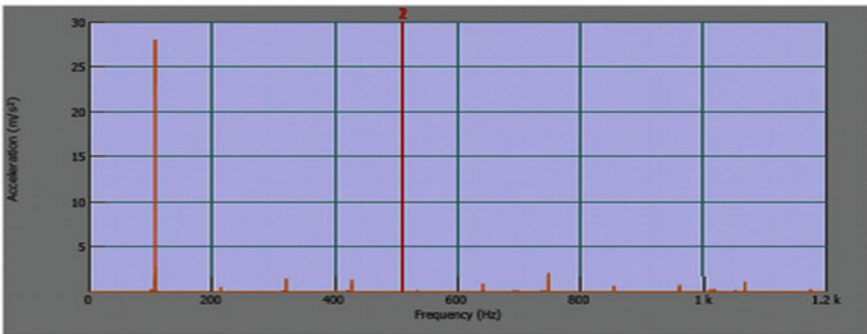


Fig. 9 FFT plot of beam with crack at middle in harmonic excitation at second natural frequency

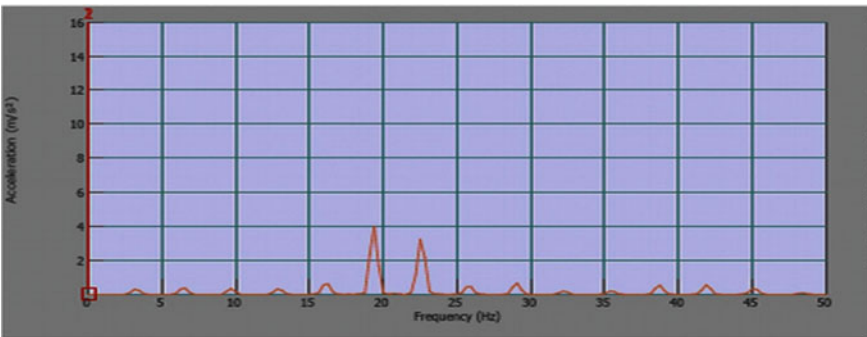


Fig. 10 FFT plot of beam without crack subjected to harmonic excitation at 3 Hz frequency

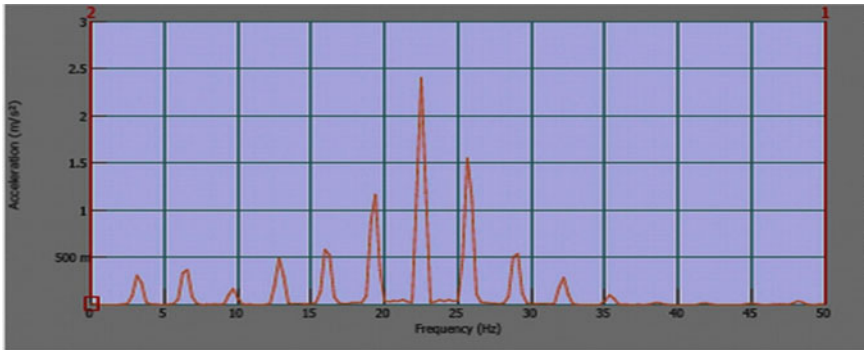


Fig. 11 FFT plot of beam with crack at middle subjected to harmonic excitation at 3 Hz frequency

Table 1 First three natural frequencies for different positions of crack

Natural frequency (in Hz)	Crack positions from the fixed end in mm				
	No crack	0	100	200	300
First	31.25	15.31	21.25	24	27.50
Second	175	162	170	148	157.50
Third	488	430	410	470	398

4 Conclusions

Breathing crack in a beam can be predicted experimentally with the help of FFT results. In case of the presence of breathing crack, the FFT results show super-harmonics and sub-harmonics. The concentration of sidebands is more around the natural frequency peak which is most affected by crack location in it. This can be used to predict the crack location point in beam-like structure in real-life applications. The FFT result of harmonic excitation can also be used to predict the presence of crack in beam. A crack beam FFT result shows more numbers of prominent super-harmonics peaks as comparative to result of beam with no crack. The extents to which a particular mode shape and its corresponding natural frequency affect depend on the location of crack. If crack is located at point of maximum deflection for that particular mode, then the corresponding frequency is affected the most as comparatively when the crack is located at node point. These observations if used logically can be of great help in detecting breathing cracks in beam-like structures.

References

1. Dash AK, Parhi DR (2014) Analysis of an intelligent hybrid system for fault diagnosis in cracked structure. Arab J Sci Eng 39(2):1337–1357

2. Thatoi DN, Das HC, Parhi DR (2012) Review of techniques for fault diagnosis in damaged structure and engineering system. *Adv Mech Eng* 4:327569
3. Chondros TG, Dimarogonas AD, Yao J (2001) Vibration of a beam with a breathing crack. *J Sound Vib* 239(1):57–67
4. Cui W, Wang JJ (2012) Coupling analysis of vibration and fatigue crack propagation for a breathing cracked beam. *Appl Mech Mater* 164:338–343
5. Wang G (2012) Nonlinear vibration response of a beam with a breathing crack. In *ASME conference on smart materials, adaptive structures and intelligent systems*, pp 411–418
6. Prime MB, Shevitz DW (1996) Linear and nonlinear methods for detecting cracks in beams. In: *Proceedings of the 14th international modal analysis conference*, pp 1437–1443
7. Douka E, Hadjileontiadis LJ (2005) Time–frequency analysis of the free vibration response of a beam with a breathing crack. *NDT E Int* 38(1):3–10
8. Andreus U, Casini P, Vestroni F (2007) Non-linear dynamics of a cracked cantilever beam under harmonic excitation. *Int J Non-Lin Mech* 42(3):566–575
9. Peng ZK, Lang ZQ, Billings SA (2007) Crack detection using nonlinear output frequency response functions. *J Sound Vib* 301(3–5):777–788
10. Srinivasarao D, Rao KM, Raju GV (2010) Crack identification on a beam by vibration measurement and wavelet analysis. *Int J Eng Sci Technol* 2(5):907–912
11. Parhi DR, Kumar DA (2009) Analysis of methodologies applied for diagnosis of fault in vibrating structures. *Int J Veh Noise Vib* 5(4):271–286
12. Rossit CA, Bambill DV, Ratazzi AR, Maiz S (2016) Vibrations of L-shaped beam structures with a crack: analytical approach and experimental validation. *Exp Tech* 40(3):1033–1043
13. Behzad M, Meghdari A, Ebrahimi A (2005) A continuous model for forced vibration analysis of a cracked beam. In: *ASME international mechanical engineering congress and exposition*, 1849–1855

Wear Behavior of Orange Peel Reinforced Epoxy Composite



P. Naik, S. Pradhan, S. K. Acharya, and P. Sahoo

Abstract The present paper describes the wear behavior of biowaste (orange peel particulate) reinforced epoxy composites with different filler (0, 10, 20, and 30 wt%) loading. The wear analysis was performed according to ASTM G-99 standard by pin-on-disk apparatus at room temperature by varying the filler loading, applied load, and sliding velocities. The optimum wear resistance was obtained for 20 wt% filler loading. Subsequently, the morphology of selected specimen is analyzed by scanning electron microscope (SEM) to examine the wear analysis such as micro-plowing, fiber matrix debonding, fiber pullout, and micro-cracking.

Keywords Orange peel particles · Particulate composite · Pin-on-disk machine · Wear

1 Introduction

These days researchers gave their attention to develop non-conventional materials which are biodegradable, recyclable, eco-friendly, and sustainable due to growing environmental awareness. The composites due to their superior properties such as excellent stiffness, low density, and good thermal and mechanical properties over tradition metals have emerged as a prime material in different sectors such as automotive industry, furniture industries, building construction material, packaging industries. The polymers used as matrix material in composite industries show different friction and wear properties. However, unmodified polymers are seldom used for

P. Naik · P. Sahoo

Department of Mechanical Engineering, Jadavpur University, Kolkata 700032, India

S. Pradhan (✉)

School of Mechanical Engineering, Kalinga Institute of Industrial Technology University, Bhubaneswar, Odisha 751024, India

e-mail: Smitirupa@gmail.com

S. K. Acharya

Department of Mechanical Engineering, National Institute of Technology, Rourkela, Rourkela 769008, India

the wear resistance because of its poor combination of tribological and mechanical properties.

Bio-fibers are used as promising reinforcing material in composite industry as they have high strength and due to their other properties according to their utilizations. Bio-fiber reinforced composite materials are preferred over traditional synthetic fiber composite material in different sectors due to their inherent properties such as low cost, low density, eco-friendly, recyclable and less abrasive and good mechanical properties. Several researchers across the globe have tried and proved that the bio fiber such as banana, bamboo, jute, coir, oil palm, sisal can be used successfully as a reinforcement material in composite industries [1–6].

The supremacy of bio-fiber composite material in tribological applications has been explored by several authors and well-documented in several journal papers [7–10]. Hashmi et al. [8] studied the tribo potential of cotton–polyester composites and reported that the wear properties of composite material increases with addition of reinforcement material. Tong et al. [11] studied the abrasive wear behavior of bamboo fiber composite material and observed that the wear resistance enhances with increase of fiber wt%. Dwivedy and Chand [12] also studied the tribo potential of wood flour (WF) reinforced composite material and found that WF loading reduces the wear resistance but enhances the load carrying capacity. However, to the best of authors' knowledge, there is no information available on the tribo-application of fruit waste reinforced composites. Hence, the present work aims to explore the possibility of using orange peel particulate (OPP) as reinforcement in polymer matrix and to study its wear behavior.

2 Experimental Details

2.1 Materials

The present experimental work was performed by epoxy resin Araldite LY556 and hardener HY 951. The orange is a hybrid between pomelo and mandarin. Orange trees are grown in tropical and subtropical regions, and these were most cultivated fruit tree across the globe as per 1987. Orange is the main fruit in India after banana and mango. Consumption of orange is also very high in all over India. The OP material generally comprises cellulose, proteins, essential oils, and carbohydrates. The orange peels were the outer part of orange collected from local market, and they are washed number of times with distilled water to remove the unwanted particles that attach to the materials. After that, the materials were dried by sun ray for 48 h to eradicate the water content from the materials. To get OPP, the material was grinded with the help of ball milling machine as shown in Fig. 1. With the help of sieve analysis, 212 + microns size particulate has been taken for the experiment. The proximate analysis of orange peel particulate is presented in Table 1 to analyze the composition of OPP.



Fig. 1 Different stages of the formation of OPP

Table 1 Composition of OPP by proximate analysis

Sample	OPP
Fixed carbon	17.21
Moisture	8.8
Ash	0.89
Volatile	73.1

2.2 Fabrication of Composite

To fabricate different composition of composite material, required amount of epoxy and hardener in the ratio of 10:1 was mixed thoroughly at normal atmospheric conditions. Different wt% of filler material (OPP) added to the mixture and stirred with a glass rod for 10 min to get homogenous mixture. Then the mixture is poured into specially designed steel molds to get 35 mm length and 10 mm diameter cylindrical sample (Fig. 2).

Fig. 2 Fabricated cylindrical samples



Table 2 Percentage of void in the OPP composite

Filler wt (%)	Experimental density (gm/cm ³)	Theoretical density (gm/cm ³)	Void wt (%)
Epoxy	1.1	1.189	0.74
10	1.116	1.223	0.088
20	1.145	1.261	0.091
30	1.0138	1.299	0.124

2.3 Density and Void Fraction

The density (theoretical and actual) of developed composite materials can be calculated by using Agrawal and Broutman and Archimedes' principle as shown in Eqs. (1) and (2), respectively.

$$\rho_{ct} = \frac{1}{\left(\frac{W_p}{\rho_p}\right) + \left(\frac{W_m}{\rho_m}\right)}, \quad (1)$$

$$S_{ct} = \frac{W_o}{W_o + (W_a - W_b)}, \quad (2)$$

where W and ρ stand for the weight fraction and density of composite specimen, respectively. The suffixes p , m and ct , ca signify the filler material, the matrix, theoretical density, and actual density of specimen, respectively. S is the specific gravity of the composite, W_o , W_a , and W_b correspond to the mass of the sample, mass of the kerosene and bottle, and sum of the total mass (bottle + Kerosene + sample), respectively. The volume fraction of voids (V_v) is calculated by Eq. (3). The void fraction of different specimens is shown in Table 2.

$$V_v = \frac{\rho_{ct} - \rho_{ca}}{\rho_{ct}}, \quad (3)$$

2.4 Abrasive Wear Test

In this experimental work, ASTM G-99 standard was used to investigate the tribo potential of fabricated composite materials through pin-on-disk apparatus is presented in Fig. 3. The device was supplied by Magnum Engineers, Bangalore. The 120-mm-diameter rotating disk (EN 31 Steel disk) is fixed with a abrasive paper of 400-grade using adhesive tape. The specimen (Pin) fixed with sample holder is placed at 100 mm track diameter for the whole experiment. The abrasive paper or track diameter was changed after completion each experiment.



Fig. 3 Pin-on-disk setup for test

Load is applied in various ranges such as 5, 10, 15, and 20 N. Three sliding velocities are selected for the test, i.e., 1.0472, 1.5708, and 2.0944 m/s. To remove the unwanted material from the tested samples, the samples were cleaned with acetone. Electronic weighing device (accuracy 0.001 mg) was used to record the weightloss for each experiment. Wear rate was calculated by measuring the weight loss of the sample after each test. The abrasive wear (W) and specific wear rate (K_0) which relates to the weight loss of material can be calculated by using the following formula:

$$W = \frac{\Delta w}{L} \quad (6)$$

$$K_0 = \frac{\Delta w}{\rho \times L \times F}, \quad (7)$$

where L is the sliding distance (m), Δw is the weightloss (gm), ρ is the density in (gm/m^3) and F is the applied load (N).

3 Results and Discussions

The various specific wear rates of fabricated composite materials with sliding distance at different sliding velocities are presented in Fig. 4. It has been observed from the figure that irrespective of the sliding velocities the specific wear rate value reduces gradually with increase of sliding distance. Similar behavior is also observed for different filler (0–30 wt%) materials. At the initial stage of experiment, the specific wear is maximum (abrasive paper is new) and decreases gradually and remains steady due to smoothness of abrasive paper. This is because of the filling up of spaces between the abrasive particles by the wear debris that in turn decreases the removal of material as the sliding distance increases.

The abrasive wear of developed composites for neat epoxy as well as reinforced composites at the sliding velocities 1.05 and 1.5 m/s under different applied load (5,

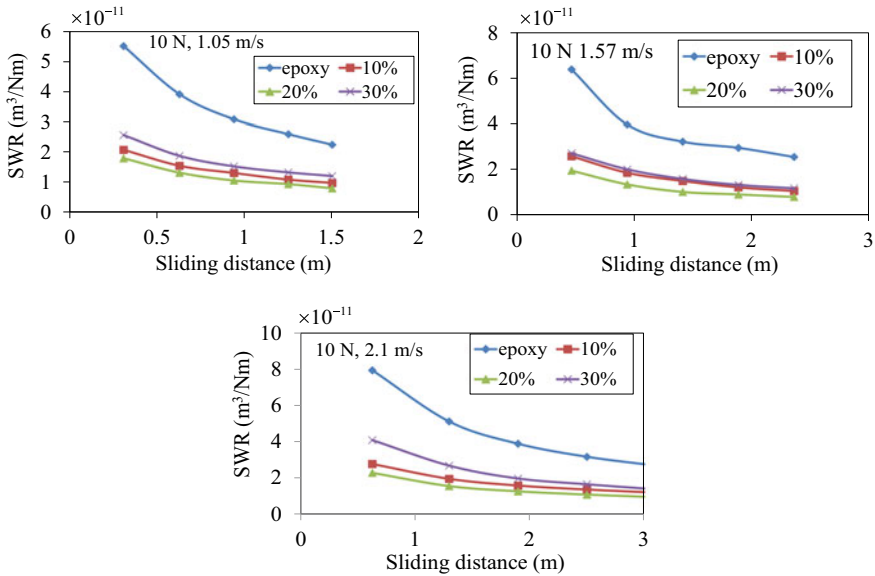


Fig. 4 Specific wear rate variation at different sliding velocity

10, 15, and 20 N) is represented in Fig. 5. The mass loss of the fabricated materials increases with increasing the applied load. For all composite material, it has been observed that, the weightloss is comparatively low at the lower applied load (5 N). At low load, the less penetration is observed between the rubbing surfaces. So that very less amount of abrasive particles is in action with the rubbing surface. From the figure, it is also observed that more material is removed from the tested material at higher applied load. This might have happened due to more number of abrasive particle penetrations into the surface at higher load which creates more grooves resulting higher rate of material removal. It is also noticed that the weightloss is more in case of pure epoxy gradually reduces with incorporation of OPP filler material. This trend

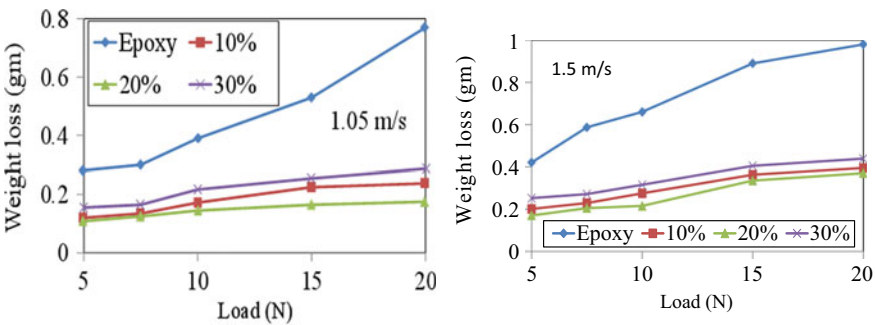


Fig. 5 Weight loss at different sliding velocities

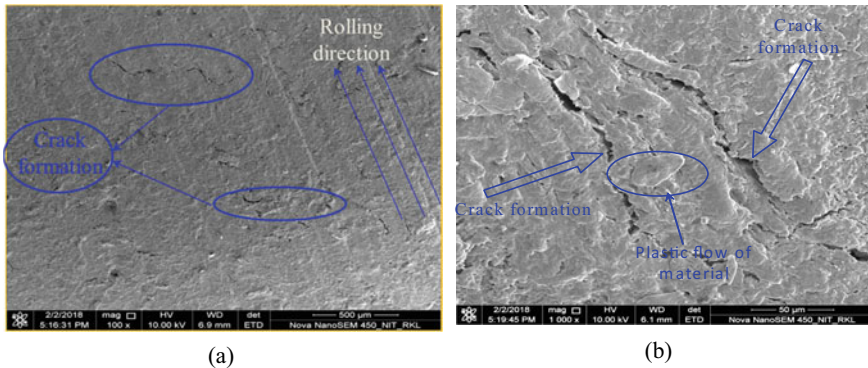


Fig. 6 SEM micrograph of worn surface of 20 wt% of OPP composite under 20 N load: **a** lower magnification and **b** higher magnification

was observed up to 20 wt% filler material. The experimental results reveal that the tribo behavior of unmodified epoxy material enhances considerably by adding OPP filler material. However, the addition of more filler (30 wt%) material into pure epoxy reduces the wear resistance of material. This might be due to the agglomeration of particulates that reduce interfacial interaction between matrix and filler material.

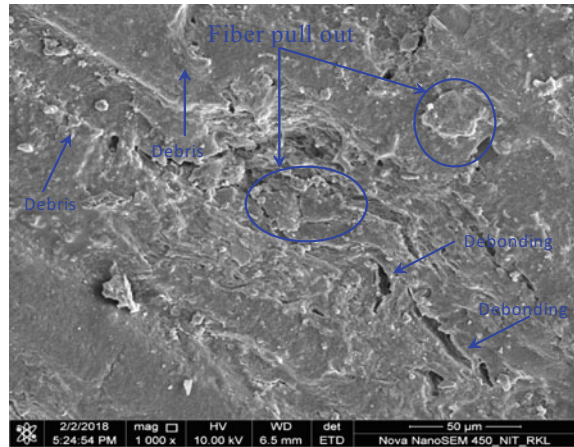
3.1 SEM Observation

The SEM observations of worn surface of tested samples are presented in Fig. 6. It has been observed (20 wt% filler material at 20 kN load) that the surfaces of tested specimens are not smooth. Cracking in the material surface is clearly noticeable; however, there is no indication of detachment of material from the matrix material that in turn enhances the wear resistance of fabricated specimens. The surface morphology of 30 wt% filler material at 20 kN load is represented in Fig. 7. The figure shows the development of craters in the worn surface of specimen. That is due to the removal of filler materials from the matrix, which confirms the low wear resistance in higher filler loading.

4 Conclusions

The material loss and specific wear rate as well as morphological analysis of worn surfaces of the OPP reinforced epoxy composites have been studied, and some experimental results are summarized as follows:

Fig. 7 SEM micrograph of worn surface of 30 wt% of OPP composite under 20 N load



- The tribological properties of the developed composites enhanced significantly due to the addition of filler (OPP) material into polymer matrix. The optimum value was observed in case of 20 wt% of filler loading. The excess addition of filler material into polymer matrix decreases the wear resistance due to poor interfacial adhesion between matrix and filler material as observed from the SEM analysis.
- The abrasive wear of the fabricated composite material is more approachable towards applied load in comparison to sliding velocities as observed from the experimental observation.
- The sliding distance has greater impact on specific wear and its value reduces with increase of sliding distance.

References

1. D'Souza KP, D'Souza L (2017) Processing and characterisation of banana fiber reinforced polymer nano composite. *Nanosci Nanotechnol* 7(2):34–37
2. Kakhandaki DGS, Suresha A, B, (2014) Wear behaviour of coir reinforced treated and untreated hybrid composites. *Int J Innov Res Dev* 3(5):632–639
3. Dwivedi UK, Chand N (2009) Influence of MA-g-PP on abrasive wear behaviour of chopped sisal fibre reinforced polypropylene composites. *J Mater Process Technol* 209(12–13):5371–5375
4. Tong J, Ren L, Li J, Chen B (1995) Abrasive wear behaviour of bamboo. *Tribol Int* 28(5):323–327
5. Chand N, Dwivedi UK (2006) Effect of coupling agent on abrasive wear behaviour of chopped jute fibre-reinforced polypropylene composites. *Wear* 261(10):1057–1063
6. Yousif BF, El-Tayeb NSM (2009) Mechanical and wear properties of oil palm and glass fibres reinforced polyester composites. *Int J Prec Technol* 1(2):213–222
7. Sanjay MR, Arpitha GR, Yogesha B (2015) Study on mechanical properties of natural-glass fibre reinforced polymer hybrid composites: a review. *Mater Today Proc* 2(4–5):2959–2967
8. Hashmi SAR, Dwivedi UK, Chand N (2007) Graphite modified cotton fibre reinforced polyester composites under sliding wear conditions. *Wear* 262(11–12):1426–1432

9. Mohan N, Natarajan S, KumareshBabu SP (2012) The role of synthetic and natural fillers on three-body abrasive wear behaviour of glass fabric–epoxy hybrid composites. *J Appl Polym Sci* 124(1):484–494
10. Sumithra H, Sidda Reddy B (2018) A review on tribological behaviour of natural reinforced composites. *J Reinf Plast Compos* 37(5):349–353
11. Tong J, Ma Y, Chen D, Sun J, Ren L (2005) Effects of vascular fiber content on abrasive wear of bamboo. *Wear* 259(1–6):78–83
12. Dwivedi UK, Chand N (2008) Influence of wood flour loading on tribological behavior of epoxy composites. *Polym Compos* 29(11):1189–1192

Industrial Engineering

Design and Implementation of a Safety Poka-Yoke for Workers Safety: A Case Study



Nitin S. Solke and Anirban Sur

Abstract This paper presents the case study on design and implementation of a Poka-Yoke setup for protecting vision of the workers working on the final assembly line of an axle manufacturing assembly, where workers worked with unprotected exposure to welding arc rays emanating from the welding booth. The setup prior to modification used stripped fiber curtains to protect the workers working on stations adjacent to the welding booth from the welding arc rays. This method while inexpensive was also ineffective, as each time an axle would pass through it, the curtain strips would split wide open, allowing escape of the welding arc rays to pass through unchecked, posing a serious hazard to the vision of the workers working on the stations near the welding booth. Introducing a retractable door to shield the workers from the welding arc rays was proposed as a Poka-Yoke for this in the industry. However, the existing layout of the assembly line meant that, more often than not, there would always be one axle carrying pallet partially inside and partially outside the welding booth, at its exit. Thus, the retractable door would not be able to close under said conditions and installation of the door would require removal of the mentioned pallet, reducing production capacity of the line. Keeping these issues in mind, Poka-Yoke has been implemented wherein a retractable door is designed that closes when the welding action is carried out without affecting the productivity of the line either. The electro-pneumatic logic for the operation of the Poka-Yoke setup has been done on Festo's Fluid SIM software.

Keywords “Safety” “modification” · “Poka-Yoke” · “Logical circuit” · “Productivity”

1 Introduction

A number of industries have been implementing lean production strategies extensively [1, 2]. Since the beginning of the spread of the “Toyota Production System”

N. S. Solke (✉) · A. Sur
Symbiosis International (Deemed University), Symbiosis Institute of Technology, Pune 412115,
India
e-mail: nitinsolke@gmail.com

© Springer Nature Singapore Pte Ltd. 2021
P. Pant et al. (eds.), *Advances in Mechanical Processing and Design*, Lecture Notes
in Mechanical Engineering, https://doi.org/10.1007/978-981-15-7779-6_58

619

[3], Poka-Yoke systems have been a topic of interest in the manufacturing industry, mainly due to their apparent simplicity of function and their intuitive design features [4]. Poka-Yoke systems have been used in a variety of contexts, such as construction, health care and information technology also encompassing areas not necessarily associated with lean production systems [5–7].

A Poka-Yoke device is defined as a device that addresses abnormalities in a system which might be detrimental either to product quality or to employees' health and safety, by either preventing or detecting them [8].

A Poka-Yoke would fit into any one of the following categories based on its method of operation [9]:

1. Physical; if it blocks the flow of mass, energy or information, and does not depend on users interpreting said features.
2. Functional; if it may be turned ON or turned OFF due to an event, without depending on users' interpretation.
3. Symbolic; if they require interpretation, yet are physically present at the moment they are necessary.

Based on their purpose, Poka-Yokes can be broadly classified into three categories [8], namely prevention Poka-Yoke, detection Poka-Yoke and safety Poka-Yoke. While a lot of literature exists for the first two Poka-Yoke, very less literature is available on safety Poka-Yoke, devices and their deployment in various contexts.

2 Problem Observed in Industry

In axle manufacturing, final assembly set up the portion of the conveyor of the Salisbury.

Assembly line is inside the welding booth, at the welder's operating station. It has a pneumatic jack fitted beneath it. The pneumatic jack is operated by a pneumatic supply at a pressure of 6 bar. The workpiece is stopped at the welder's station by automatic spring actuated stoppers that exist solely for that purpose. Once stopped, the welder presses a two hand pressing button to actuate the jack and lift the workpiece off the conveyor. This action also completes the welding setup's earth connection thereby permitting the welder to weld the needed parts together. It has been observed that (Fig. 1) the welding booth has a stripped curtain at its exit to prevent the welding arc rays from going beyond the booth, while allowing an axle on its pallet to be stationed partially inside and partially outside the booth. While this may be cost effective and allow for a higher production rate, it poses a serious health hazard to the operators/workers working on subsequent stations following the welding booth, in the form of a high risk of permanent vision loss due to retinal scarring caused by unprotected overexposure to the high intensity welding arc rays [10].

Welding arc rays are dangerous for human beings. In a similar manner, a case study by Michael Naidoff and Sliney [11] reported that an 18-year-old, arc-welding student, who complained of pain, had swollen eyelids, and poor vision in the right



Fig. 1 Unchecked welding arc light passing through striped curtain

eye. When examined for vision, the visual perception in the right eye was 3/200 with eccentric fixation and was 20/20 in the left eye. The left eye and left facial area were normal. In his right eye, periorbital edema (2+) and erythema (2+) that extended to the frontal and maxillary areas were seen. Moderate blepharoptosis existed covering at least half the pupil of the right eye and the bulbar conjunctiva showed 2+ injection. It was later found out that a protective curtain had been drawn across the entrance of the welding booth, and the subject was staring at the welding arc with his right eye from outside the booth, about 200 cm away from the arc, through a gap between the side wall and curtain edge, proving a strong link exists between unprotected exposure to the welding arc radiation and severe eye damage.

In the case of this paper's subject, the workers working on the stations following the welding booth on the assembly line are exposed to the welding arc for much larger time periods, significantly upping the risk of serious eye damage if not permanent vision loss.

3 The Safety Poka-Yoke

While it was imperative for the welding booth curtain to be replaced by a retractable door, eventuality that the door might not close because of a workpiece being right underneath it coupled with the chances of the welder starting the welding operation while the door was not fully closed was very real possibilities.

As such, a complete system needed to be designed which would mitigate all aforementioned issues while also fulfilling the primary condition and purpose of preventing the welding arc rays from escaping the booth (Fig. 2).

Methodology followed for solving the problem involves scientific approach, and it is depicted in the flowchart as under:

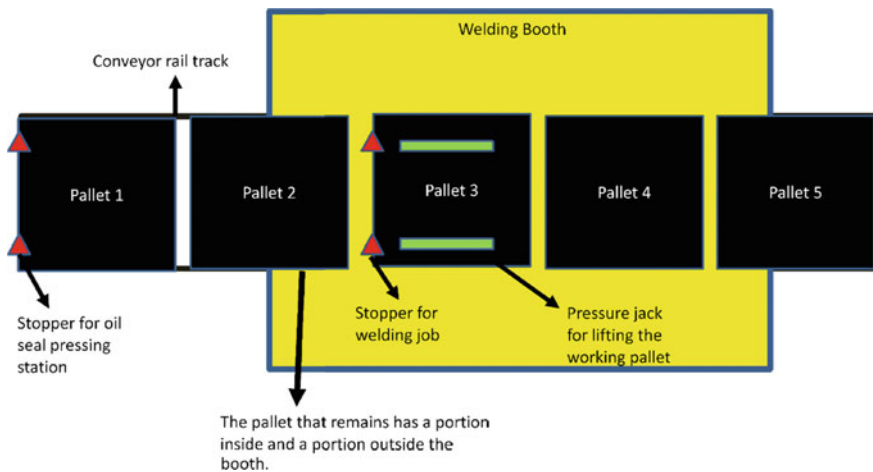
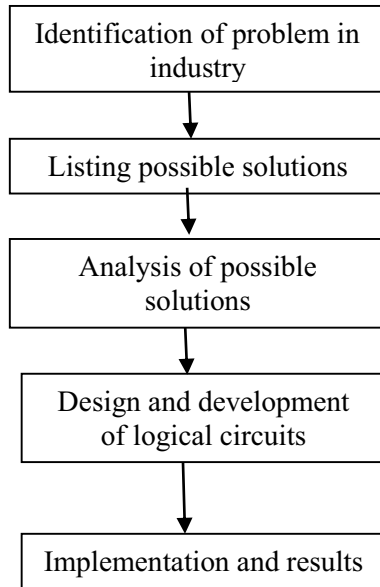


Fig. 2 Schematic explaining issue faced with Pallet 2

3.1 Listing Possible Solutions

Three logical and feasible solutions to the aforementioned problems surfaced upon brainstorming. They were shifting the welding booth back or forth by 500 mm, which is half the length of the pallet; vacating pallet 2s spot permanently by asking welder to start welding only when pallet 2s position is vacant and door after door has been closed; and design and installation of a system that would automatically sense pallet 1 and pallet 2s position and relay that information to a PLC or microprocessor which would permit the retractable door to close and the welding to commence only if pallet 2s position was vacant.

3.2 Merits and Demerits of Each System

Shifting the Welding Booth 500 mm Back or Forth

The proposed system, while offering the simplest solution, would disturb the entire assembly line. Given that the space available for the stations in front of or behind the booth is just enough to carry out the station's operations, any shift would seriously cramp the worker for room to carry out his operation. As a result, this idea was discarded.

Vacating Pallet 2s Spot Permanently

This proposition would give a freedom of choice to the welder, as he may choose to weld even which may be misused on purpose or otherwise and negate the whole purpose of this action by preventing the door from closing properly. Any such event could damage the door or the axle assembly or both.

Using an Automatic Sensor Relay System

This method, theoretically, provided the ideal solution, whereby the retractable door and the pneumatic jack would be coupled with the inputs from two proximity sensors, A and B, as seen in Fig. 3.

The system would be thus configured so as to not permit welding by preventing the jack from extending and preventing the door from closing by coupling their inputs to the binary output from the proximity sensors, in which should sensor B return a value of zero.

3.3 Selection of Actuating Piston and Actuating Power Supply

The piston required for actuating the retraction and extension of the door was chosen to be a solenoid actuated double-acting pneumatic piston. The nature was chosen to be pneumatic because of a preexisting connection of compressed pneumatic supply

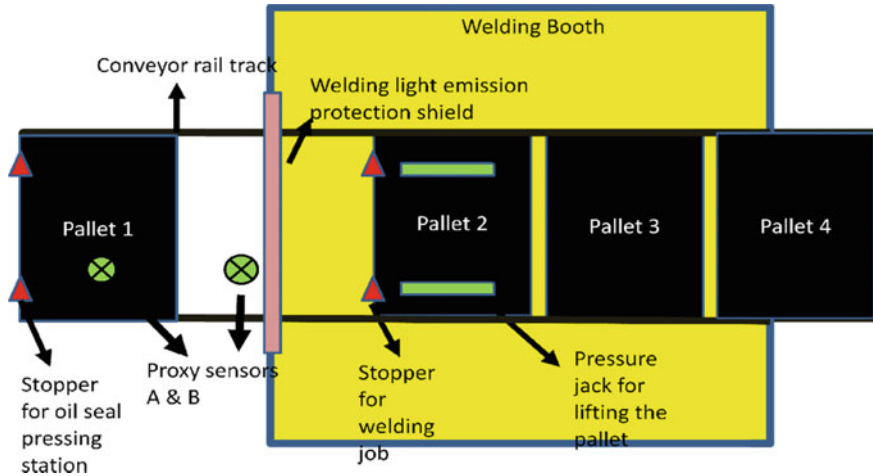


Fig. 3 Automatic sensor relay system

of 6 bar being present in the jack on the welding booth against others like hydraulic, which would incur the company an additional cost to setup.

3.4 Piston Parameters Selection

The length of retraction and extension stroke of the cylinder were considered by measurement of the maximum height of the diffcase carrier assembled on the line to be 500 mm. The material of the door was chosen to be mild steel due to its ready availability in the market, its cheap machinability and due to the material being opaque. The thickness of the retractable portion, considered to be 3 mm, and the ideal density of MS being 7850 kg/m^3 resulted in the weight of door amounting to 35 kg, which upon allowing for irregularities in manufacturing of the door was taken to be 40 kg. Calculating the downward force by multiplying the weight with the acceleration due to gravity, "g" and considering the resistance to motion offered against a sliding contact at the door frames as per the ideal coefficient of friction of MS, the net force required to actuate the cylinder was found to be around 650 N.

Festo, a German company supplying pneumatic and electrical automation technology, provides a catalog of options on its Web site when supplied with the required engineering specifications. This feature was used to find a list of cylinders that would be a fit against the calculated specifications. Of the list of cylinders thus obtained, the most economical one was selected for use.

3.5 Electro-pneumatic Circuit Design

An electro-pneumatic circuit was designed coupling the binary output of the proximity sensors to the solenoids actuating the pneumatic pistons. The working electronic logic of the circuit is as shown in Table 1.

Proximity sensors at logic 1 indicate the presence of a pallet above them, while logic 0 shows the absence of a pallet at the position of the respective sensor. Logic one at the pneumatic jack and door indicates that the double cylinders may perform their extension stroke. Logic 0 at the jack and the door indicates that the door may not close even if the welder presses the two hand button to operate it (Fig. 4).

An electro-pneumatic circuit fitting the logic mentioned in Table 1 was created using FESTO's.

“FluidSIM” software. This electro-pneumatic diagram is shown in Fig. 5.

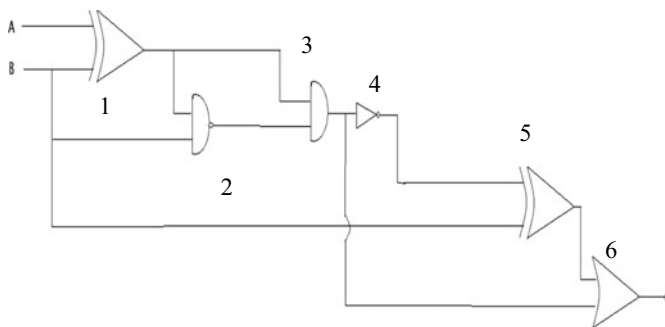
The extension strokes and retraction strokes of the pneumatic cylinders were simulated in FluidSIM (Figs. 6, 7 and 8).

Implementation and Result

This design was manufactured and installed by an external vendor on the welding booth. The assembly line needed restarting from zero station; however, it was observed that the system functioned smoothly, albeit with a slight increase in lead time for the process. This may however be overlooked in light of the fact that the main purpose of this safety poka-yoke was to ensure the well-being of the workers and of their visual faculties. The logic circuits developed and implemented showed

Table 1 Logic table

Proximity sensor A logic	Proximity sensor B logic	Pneumatic Jack and door logic
1	1	0
1	0	1
0	1	0
0	0	1



LEGEND

- 1. EOR Gate 1
- 2. AND Gate
- 3. NAND Gate
- 4. NOT Gate
- 5. EOR Gate 2
- 6. OR Gate

Fig. 4 Developed logic circuit

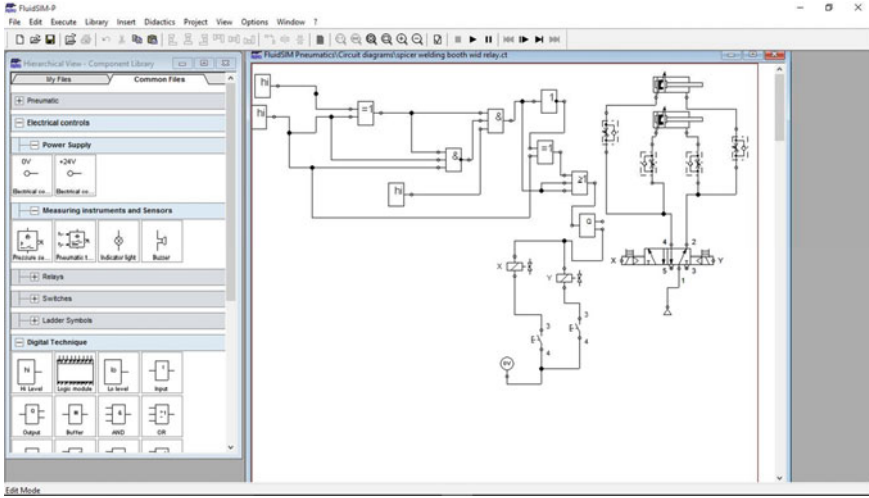


Fig. 5 Created electro-pneumatic diagram using FluidSIM

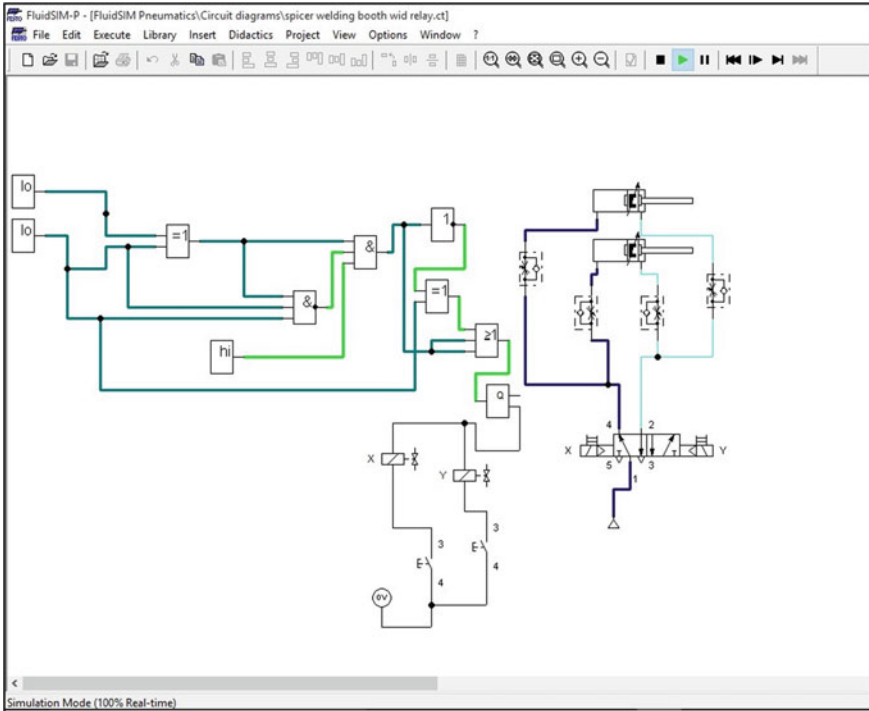


Fig. 6 Extension stroke under 0 0 input condition

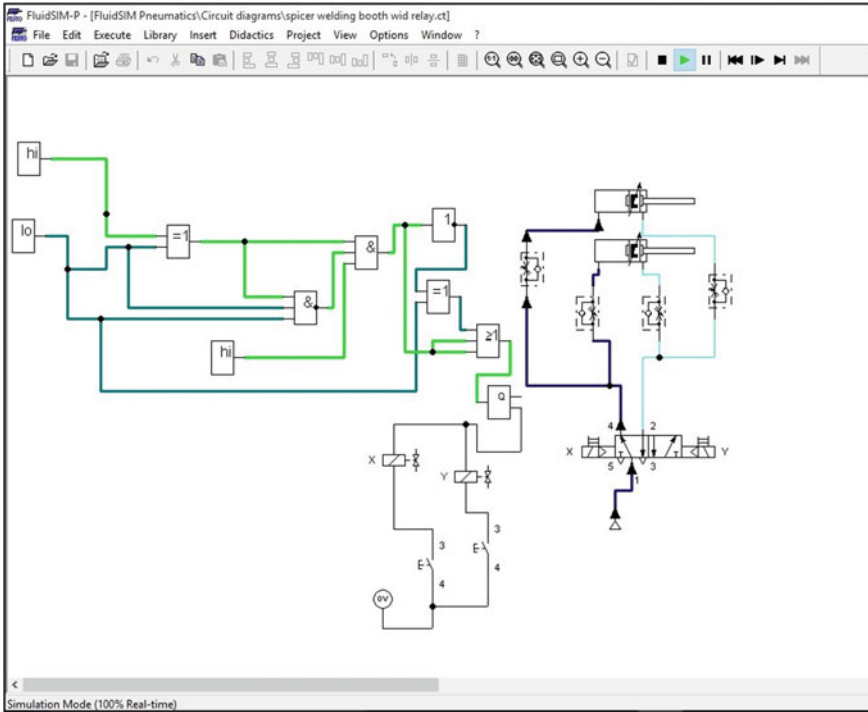


Fig. 7 Extension stroke under I 0 input condition

positive and implementable results. It ensured the safety of workers as rays were effectively hindered by the modified workspace. The setup successfully ensured that the welding arc rays do not get past the welding booth without any significant loss in productivity (Fig. 9).

4 Conclusion

A retractable door at the inlet and outlet ends of a welding booth in manufacturing industries is a much more effective solution than the commonly used stripped curtains. This may be coupled with logic circuits to also function as a Poka-Yoke system. While this type of system may increase the lead time of the welding process by a small extent, it may not be considered a very pressing concern given the nature and severity of the health and safety hazard such a system addresses.

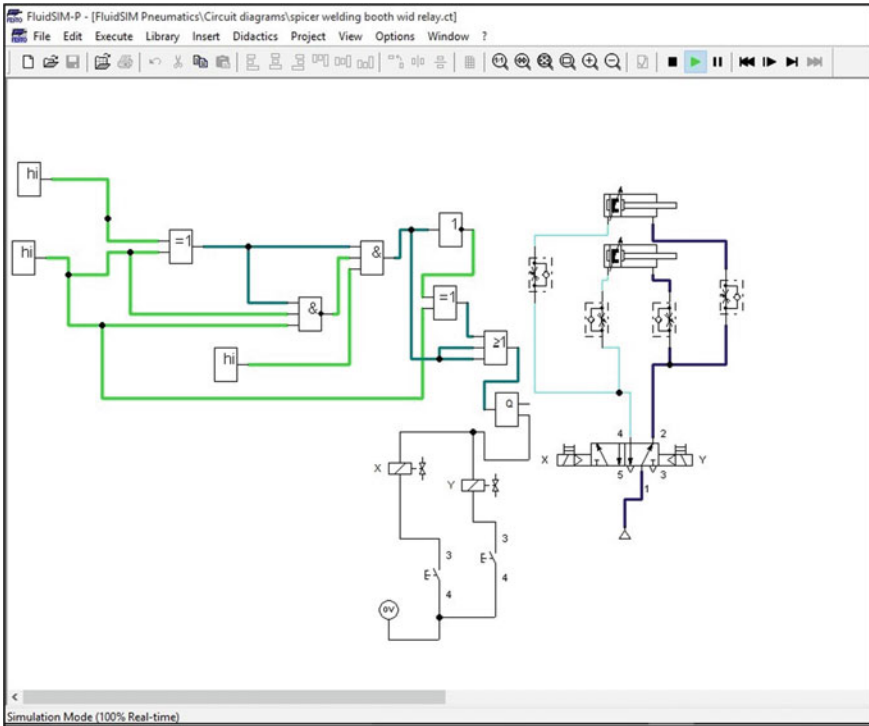


Fig. 8 Extension stroke prevention 1 1 input condition

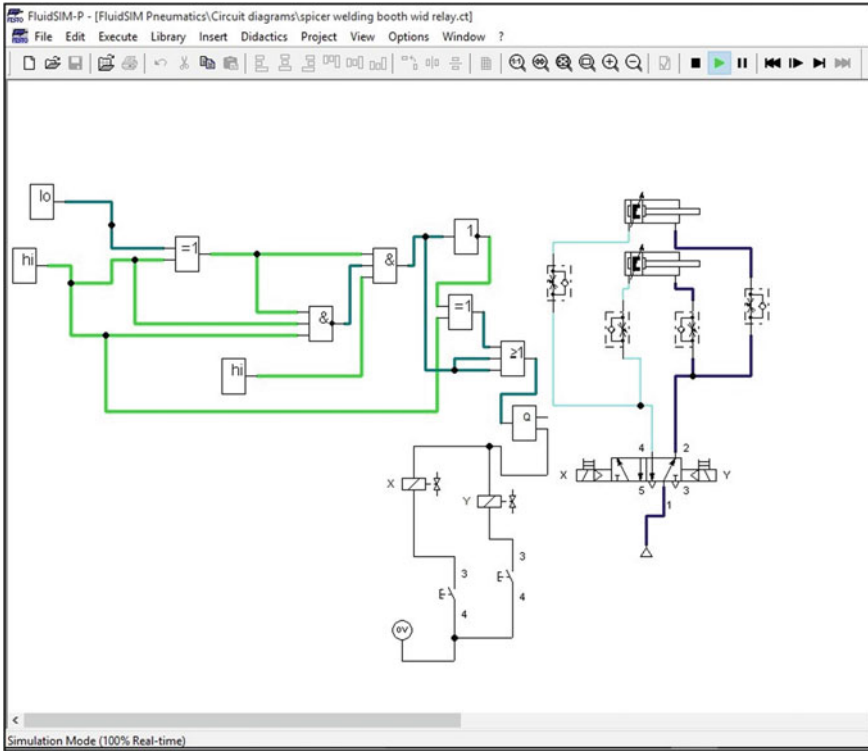


Fig. 9 Extension stroke prevention 0 1 input condition

References

1. Liker J (2004) *The Toyota way: 14 management principles from the world's greatest manufacturer*. McGraw-Hill
2. Smalley A (2004) *Creating level pull*. Lean Enterprise Institute
3. Shingo S (1988) *Zero quality control: source inspection and the Poka yoke system*. Productivity Press
4. Stewart M, Grout R (2001) The human side of mistake-proofing. *Prod Oper Manag* 10(4):440–459
5. Grout J (2007) Mistake-proofing the design of health care processes. Agency for Health Care Research and Quality
6. Formoso CT, Santos AD, Powell J (2002) An exploratory study on the applicability of process transparency in construction sites. *J Constr Res* 3(1):35–54
7. Shimbun N K. (1988) *Poka-yoke: improving product quality by preventing defects*. Productivity Press
8. Saurin TA, Ribeiro JLD, Vidor G (2012) A framework for assessing poka-yoke devices. *J Manuf Syst* 31(3):358–366
9. Hollnagel E (2003) *Barrier analysis and accident prevention*. Ashgate
10. Amrik S, Pabley A, Keeney H (1988) Welding processes and ocular hazards and protection. *Am J Ophthalmol* 92(1):77–84
11. David H, Sliney Michael A, Naidoff (1974) Retinal injury from a welding arc. *Am J Ophthalmol* 77(5):663–668

Identifying the Features Influencing Sustainable Products: A Study on Green Cosmetics



Akankshya Patnaik, Sushanta Tripathy, and Aishwarya Dash

Abstract Today's world is becoming more sensible about health and hygiene. Everyone wants to give their family the preeminent care. But nowadays, many products are sneaky and may use harsh or even toxic chemicals to make their product cheaper. To identify and eliminate those harmful products and techniques government, NGOs and welfare organization are exercising extra conscious effort. This sensible effort by various agencies had led business spry a new range of product called green/sustainable product. Thus, the purpose of the study is to delve into various factors driving a customer toward green cosmetic products. Statistical analysis using factor analysis and regression analysis has been done in order to step into a factual outcome. This paper also highlights the impact of green labeling and pricing on purchase intension of customers. Intension behind the paper is to promote sustainable cosmetics within our society.

Keywords Sustainable product · Consumer perception · Green label · Price · Purchase decision · Green cosmetic product

1 Introduction

Environmental concerns like global warming, diminution of natural resources and fluctuating weather are highly burning problems nowadays. This may affect the way ones conduct, especially while making a purchase decision. In order to satisfy the unending desire of today's man, nature had paid its cost. Many such instances

A. Patnaik

Department of Management, National Institute of Science & Technology, Berhampur, Odisha 760001, India

S. Tripathy (✉)

School of Mechanical Engineering, Kalinga Institute of Industrial Technology Deemed To Be University, Bhubaneswar, Odisha 751024, India

e-mail: sushant.tripathy@gmail.com

A. Dash

Industrial and System Engineering Department, Indian Institute of Technology Kharagpur, Kharagpur, West Bengal 721302, India

© Springer Nature Singapore Pte Ltd. 2021

P. Pant et al. (eds.), *Advances in Mechanical Processing and Design*, Lecture Notes in Mechanical Engineering, https://doi.org/10.1007/978-981-15-7779-6_59

631

like the World Health Organization (WHO) Report air effluence is the cause of 5, 27,700 deaths in India every year, and 21% of communicable diseases in India are related to pollute water leading to a horrified picture. Moreover, National Geographic (May, 2008) Indian is ranked at the bottoms of the list of 14 nationalities which are conscious about environmental protection and safety. In order to patch the huge climatic intricacy or environmental convolution today, government has set many norms and policies. Not only this, many changes have been noticed in the lifestyle of common man. To overcome this burning issue and giving a hand to reality, business came with a unique solution of satisfying the common mass without depicting the environment. This exceptional and exciting way of differencing its products and services is widely known as green marketing, eco-marketing, sustainable marketing, eco-friendly marketing, etc.

The word green/sustainable marketing is marketing of a specialized kind of ozone-free depleting chemicals and in toxic product which include a range of activities (goods such as fuel efficient cars or no or least chemical used/processed food or cosmetics, goods are regularly developed from recycled materials or from renewable and sustainable sources with sustainable notions like save oil or conserve natural habitat).

Hence, the goods those are yielded through green technology and that caused the lowest effect to environmental safety are called green products. The promotion of sustainable products and sustainable technologies is essential for conservation of natural resources and sustainable long-term eco-friendly environment. This study basically intends to promote eco-friendly cosmetics which assure a healthy lifestyle and leads to a protective environment too.

2 Literature Review and Hypothesis Formation

Literature has been collected from various well-established theories and robust studies. The first emblem of curiosity in green marketing was noticed in 1970s but it was in dark smog till 1980s. In early 1990s, green marketing gathered diligence from wider range of public [6]. Green marketing transpires from societal marketing [8]. "Green marketing" denotes to holistic marketing concept which includes the planning, organizing, executing, producing, marketing, consuming resources and implementing products or services occur in a way that is less harmful to the environment with growing awareness about the implications of global warming, recyclable solid waste, negative impact of toxic pollutants, etc. It refers to the process of selling products or services based on their environmental and health benefits. Both marketers and consumers are becoming sensitive toward green products and services.

Chase and smith [4] also shown that 70% of the consumer purchase decisions were influenced by environmental security message from advertising and product labeling. Consumers require clear information about picking one product over other which ultimately benefits the environment. Most consumer products that provide eco-friendly evidence emphasize symbols or logos that is the effort to display of ecological data.

Unfortunately, it is seen many consumers could not interpret the implications of these labels, and research also indicates that consumers also face trouble in understanding the meaning the labels speaks [12]. So, many consumers become tangled in taking a decision about green product. Eco-labels such as “biodegradable”, “sustainable”, “environmental friendly” and “recyclable” are usually unfamiliar to many consumers.

H1: Labeling of the green cosmetics products affects the green purchase intension of customer.

Price is one of the non-product aspects of brand still it is measured as one of the most prominent features in the green marketing mix. Many consumers are ready to pay premium if they perceive that the product has extra value. This value can be in the form of a superior taste, extra hygiene, ingenious design, value-added performance, eye-catching appearance or an enhanced function [11].

A communal apprehension is shared by environmentalists regarding the concern for high cost of eco-products [3, 59]. Price has always been considered as a vital gauge of sustainable products which affects green purchasing behaviors of the consumers positively [1, 7]. It is observed many environmental conscious consumer feel reluctant to buy eco-product due its premium price [9]. The study also discovered that most of the respondents are willing to pay high price, but the level of acceptability differs extensively [2]. In general, only top two percent will pay more than 20% for many green cosmetics; whereas, majority of buyers are looking for equivalence pricing related to more sustainable products [10].

H2: Price of green cosmetics products affects the green purchase intension of customer.

3 Objectives

The objectives of this study are as follows:

1. To study the level of customer’s awareness and attitude regarding sustainable products.
2. To know the factors influencing eco-buying behavior.

4 Methodology

Primary data was used for the analysis of data. Firstly, stratified sampling technique was used to identify the sample who have a mere knowledge about green cosmetics. Then 105 responses have been collected through simple random sampling technique. First-hand data incurred through interview and observation conducted on people who use green cosmetic products. Then data was collected through a predesigned questionnaire. Data analysis was done by taking the help of MS excel and SPSS

software. Factor analysis and regression analysis techniques were used in order to reach into a genuine outcome.

5 Results and Discussion

Study is basically structured in two broad bases primarily, and it covers demographic profile of customers; secondly, it includes factors effecting green purchase behavior. As the initial part of survey was basically on demographics, it intends behind a purchase behavior. Present survey shows those respondents are mostly female which are about 76% in comparison with 24% male. Further the study tries to locate the influential age group. It is noticed that respondents in 18–35 age group are most passionate about green cosmetic product. It is observed from the responses that higher educated mass like graduates and postgraduate are more concerned about green cosmetics.

As per the customers, they make green purchase decision considering various factors which differs from respondents to respondents. So researcher made a survey on it and found the following. Under each head, researchers have considered two variables so total there are 24 questionnaires under 12 heads as the data collected from primary source is too large. So researcher used factor analysis to reduce the factors. Researcher has taken 24 variables for the survey from E1 to ST2 (Table 1).

Table 2 shows the significance of each of the 24 factors component. Only the first eight have eigen values over 1.00 and together these explain over 68.9% of the total variability in the data. Here one should note that the first factor accounts for 27.437, second factor accounts for 9.270, third factor accounts for 7.296, fourth factor accounts for 6.107, fifth factor accounts for 5.191, sixth factor accounts for 4.929, seventh factor accounts for 4.469, and eighth factor accounts for 4.247% of the variance before rotation while 14.681%, 10.242%, 8.881%, 8.251%, 8.079%, 7.760%, 5.724% and 5.328% of variance explained by all five factors, respectively, after rotation. All the remaining factors are not significant as shown in Table 2.

The above loadings (extracted standards of each item under five variables) of the 24 variables on the eight factors are extracted. The higher the absolute of the loadings, the more the factor contributes to the variable. Since eight variables are extracted, the 24 items are divided into eight variables according to the most important items with similar responses in component 1 and simultaneously in component 2, 3, 4, 5, 6, 7 and 8.

From the factor analysis, we could find that opinion of friends and family, labeling and packaging, social influence, environmental concern, price, availability and product features are the most influential factors which impacts the green purchase intension of the customers.

Table 1 Variable wise statements considered for the analysis

Variables	Statement
E1	I will buy brands which are less damaging to the environment
E2	I should go with my own bags to the super market
PF1	I prefer to buy products based on product features and uses regardless of environmental outcomes
PF2	If I get better green attributes I may compromise with the price
P1	I prefer to buy low priced product regardless of society
P2	I will only purchase sustainable products if I get it in low price or better offer
A1	I will only purchase sustainable product if they are readily available in my door step
A2	I may go for extensive search of a sustainable product if it's really rational
G1	I never miss the credit to convince my family to opt for eco-friendly products
G2	I purchase green products if its advertisement is simple and affective
L1	I should only purchase products by seeing environment friendly labeling
L2	Environment friendly packaging is the most important thing I see in my product
SO1	I may buy the product if my friends or relatives suggested it for its better effect
SO2	I may compromise price and features for the betterment of society
SI1	Buying eco-product improves my status and dignity
SI2	Buying eco-friendly products make me proud
GPI1	I buy eco-friendly product to show my friends and relatives
GPI2	I prefer to buy green product if it is available in low prices
AW1	I feel green marketing is responsible for environmental betterment
AW2	I find most consumers know about eco-product
O1	My family's and friend's opinion matter a lot before buying green cosmetic products
O2	I collect feedback from my family, friends and relatives before buying cosmetic products
ST1	Although it is more expensive I buy green product to show my elegant choice as compared to others
ST2	Use of green cosmetic products influence our status

5.1 Result of Hypothesis

To examine the effect of labeling of green cosmetics (H1) and price of green cosmetics (H2) on green purchase intension of customer regression analysis was conducted.

1. Regression Analysis Results for H1—The Effect of Labeling on Green Purchase Intension

Table 2 Total variance method

Component	Initial eigenvalues			Extraction sums of squared loadings			Rotation sums of squared loadings		
	Total	% of variance	Cumulative %	Total	% of variance	Cumulative %	Total	% of variance	Cumulative %
1	6.585	27.437	27.437	6.585	27.437	27.437	3.523	14.681	14.681
2	2.225	9.270	36.707	2.225	9.270	36.707	2.458	10.242	24.923
3	1.751	7.296	44.003	1.751	7.296	44.003	2.131	8.881	33.804
4	1.466	6.107	50.110	1.466	6.107	50.110	1.980	8.251	42.055
5	1.246	5.191	55.301	1.246	5.191	55.301	1.939	8.079	50.134
6	1.183	4.929	60.230	1.183	4.929	60.230	1.862	7.760	57.893
7	1.073	4.469	64.699	1.073	4.469	64.699	1.374	5.724	63.618
8	1.019	4.247	68.946	1.019	4.247	68.946	1.279	5.328	68.946
9	0.924	3.849	72.795						
10	0.827	3.447	76.242						
11	0.767	3.197	79.439						
12	0.661	2.756	82.195						
13	0.637	2.656	84.850						
14	0.584	2.433	87.283						
15	0.556	2.317	89.600						
16	0.456	1.902	91.501						
17	0.398	1.660	93.161						
18	0.347	1.447	94.608						
19	0.307	1.278	95.887						
20	0.261	1.088	96.975						

(continued)

Table 3 Model summary

Model	R	R square	Adjusted R square	Std. error of the estimate
1	0.311 ^a	0.097	0.079	0.8006

^aPredictors: (constant), labeling, pricing

^bDependent variable: green purchase intension

Table 4 Standardized estimates for relationship between green purchase intension and various factors (labeling and pricing)

	Dependent variable	Independent variable	Standardized estimates	S.E.	Sig (<i>P</i> -value)	Result (Hypothesis supported/not supported)
Case 1	Purchase decision	Labeling	0.296	0.074	0.003**	Supported
Case 2	Purchase decision	Pricing	0.178	0.070	0.048*	Supported

*Significant at $p < 0.05$, **significant at $p < 0.01$, ***insignificant at $P > 0.05$

Regression analysis was conducted between labeling and packaging of green cosmetics and green purchase behavior, where labeling and packaging are the independent variable and green purchase intension is the dependent variable. The results reported in the Tables 3 and 4 indicate that the effect of labeling and packaging on buying behavior of the customer, as hypothesized, is statistically significant as ($p < 0.05$). The result, therefore, supports H1. Thus, it indicates that accurate labeling and packaging can successfully gain the trust of consumers and which further leads to increase the purchase of eco-cosmetic items.

2. Regression Analysis Results for H2—The Effect of Pricing on Green Purchase Intension

In order to examine the relationship between pricing of green cosmetics and green purchase intension, a regression analysis was conducted, taking green purchase intension as the dependent variable and pricing of green cosmetic as the independent variable. The results shown in the Tables 3 and 4 indicate that there is a statistically significant relationship between pricing of green cosmetics and green purchase intension as ($p < 0.05$). Hence, hypothesis H2 is also supported. Our finding on pricing of green cosmetics owing to green purchase intension of the customer is consistent.

6 Conclusion

The hypothesized relationship between labeling of green cosmetics and green purchase intension is found to be positively significant. This confirms that Indian

consumers are very much conscious about labeling of green products. The present study explores that the consumers look for the sincerity of the companies. It matters a lot how they provide the true information about the material and use of products. If those green companies who fail to convince the consumers regarding their honest and sincere intention with respect to transparency and eco-consciousness, the adverse effect would be on their businesses. Our second hypothesis (H2) is also in the assumed direction, that is, pricing of green cosmetics has a statistically positive influence on consumer purchase behavior. It is noticed that price significantly plays a very important role in influencing the customer toward green cosmetic purchase. It is also seen that if green cosmetics being marketed in a marginal price, it can multiply its purchases. At the same time, we can assure that there are a range of target customers who are absolutely comfortable with its premium pricing with a 100% quality assurance.

6.1 Limitation of the Study and Scope for Future Research

As every study has its own boundary, present study is also not free from it. Primarily, the present study analyzed only 105 respondents from two states, Hyderabad and Odisha of South India, and results may vary if North India or any other country is considered. However, for more robustness and validity of results, future research in this direction should go for a larger sample size. Also, forthcoming research in this trend can be industry-specific to have unbiased results as consumers from different industries have different perceptions and expectations toward green cosmetics. So sample selected for the study has an important role. If new set of sample is considered with respect to their economic status, culture, lifestyle and purchase behavior, then one may not guarantee the same outcome. Third, the current study attempted to observe consumer green purchase behavior only on two grounds that are with respect to labeling and pricing of the product. Fifth, the product is specified (green cosmetic product), and the picture may vary if other fast moving consumer goods (FMCG) or slow moving consumer goods (SMCG) products are considered. Future research may be considered including product features, availability, green promotion, green purchase intension, status, opinion of family and friends.

References

1. Boztepe A (2012) Green marketing and its impact on consumer buying behavior. *Eur J Econ Polit Stud* 5(1):5–21
2. Aryal KP, Chaudhary P, Pandit S, Sharma G (2009) Consumer's willingness to pay for organic products: a case from Kathmandu Valley. *J Agric Environ* 10:12–22
3. Blend JR, van Ravenswaay EO (1999) Measuring consumer demand for eco labeled apples. *Am J Agr Econ* 81(5):1072–1077

4. Chase D, Smith TK (1992) Consumer Keen on green but marketers don't deliver. *Advert Age* 63:82–84
5. D'Souza C, Taghian M, Lamb P, Peretiako R (2006) Green decisions: demographics and consumer understanding of environmental labels DOI: <https://doi.org/10.1111/j.1470-6431.2006.00567.x>
6. Hess E, Timen P (2008) Environmental friendliness—a marketing strategy, master thesis within business administration. Internationella Handelshogskolan Hogskolan Jonkoping.
7. Kaufmann HR, Panni MFAK, Orphaned Y (2012) Factors affecting consumers green purchasing behavior: an integrated conceptual framework. *Amfiteatru Econ J* 14:50–69
8. Kotler P (1999) *Marketing management: The Millennium*. Prentice Hall of India, New Delhi
9. Ken P (2001) *Mark Rev* 2(2):129–146
10. Sachdev S (2011) Eco-friendly products and consumer perception. *Int J Multidisc Res* 1(5):279–287
11. Sharma Y (2011) Changing consumer behaviour with respect to green marketing—a case study of consumer durables and retailing. *Int J Multidisc Res* 1(4):152–162
12. Thogersen J (2000) Psychological determinants of paying attention to eco-labels in purchase decisions: model development and multinational validation. *J Consum Policy* 23(3):285–315

A Framework of Lean–Six Sigma: An Evolutionary Approach



**Biswajit Mohapatra, Aneesh Kuruvilla, Aishwarya Dash,
and Sushanta Tripathy**

Abstract The concerned paper analyses the evolution of lean and six sigma independently. Then, it analyses the tools required in each of them and the associated common tools. Eventually, a model or framework is developed to ascertain the permeable aspects of lean and six sigma leading to a new lean–six sigma model. 23 scholarly articles were reviewed from year 2000 to 2019 to predict the model. The website primarily used is Google scholar. It is a new model that gives clarity to the lean–six sigma in bringing excellence into the industrial world with a breathe of freshness in it.

Keywords Lean · Six sigma · Lean–six sigma · Model · Framework

1 Introduction

Lean is a production methodology that focuses on the internal need of a business entity. It is an operational philosophy which maximizes the value-added activities with the aim to bring about excellence in all the aspects of a business viz. cost, quality, profitability, way of doing things (Kata), utilization of resources whose aim is to bring harmony in the work life and with a vision to enhance the quality of life by adopting the best practices in work life. The improvement of the standard of living is then a by-product of this modern philosophy.

This philosophy operates with tools and methodologies just as any other work philosophy to bring about the best in processes, performance, quality, and ultimately customer satisfaction with minimum of effort and resources.

B. Mohapatra · A. Kuruvilla · S. Tripathy (✉)
School of Mechanical Engineering, KIIT Deemed To Be University, Bhubaneswar, Odisha
751024, India
e-mail: sushant.tripathy@gmail.com

A. Dash
Industrial and System Engineering, IIT Kharagpur, Kharagpur, West Bengal, India

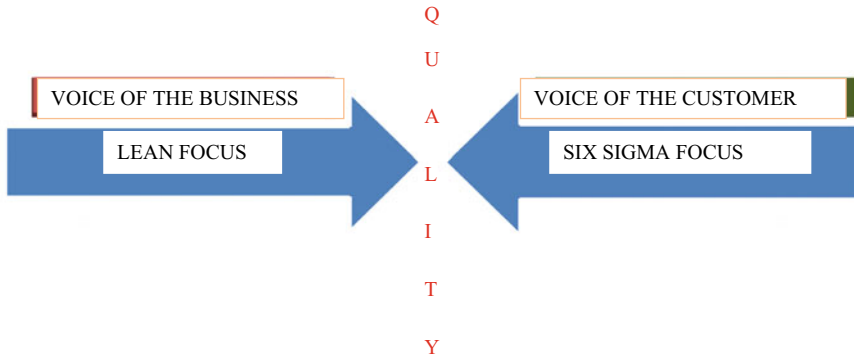


Fig. 1 Convergence of lean and six sigma into one goal

A tool is an item or implement used for a specific purpose. Tools are the basis for executing operations to the best under the prevalent conditions. The philosophy acts as a driving force to direct the course of actions with the aid of tools.

A method may consist of one or several tools as per the need or purpose to be fulfilled.

Six sigma finds its way to the firm as a quality improvement method which uses statistical tools to measure quality and precision of a product or service. It provides businesses with a comprehensive tool set to improve the capability of business processes and quality of products and services.

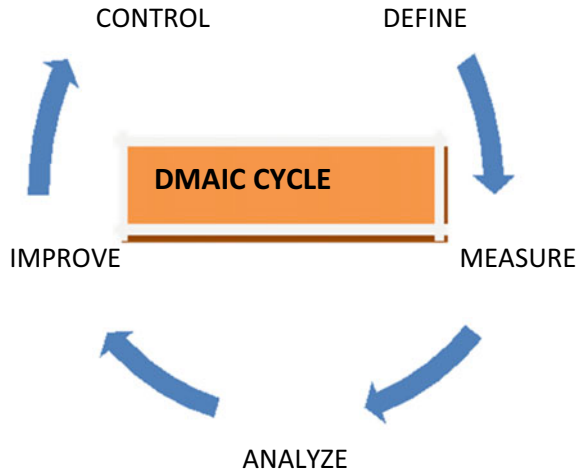
The lean and Six Sigma combination represents the new six sigma generation. This new methodology is the offspring of two very essential components of business process improvement that complement and reinforce one another. Lean on its own cannot bring a process under statistical control to achieve quality targets, whilst six sigma alone cannot significantly improve process speed or reduce waste that can improve operational cost and capital Fig. 1.

Lean–six sigma is a methodology driven by the need to change, to continuously improve and eliminate complexities, and to meet the goals of the business and shareholders through a single crucial element-Voice of the Employee or simply organizational effectiveness.

The structure in which the toolsets are organized is based on the DMAIC framework, i.e., the phases that a lean–six sigma undergoes Fig. 2.

DMAIC unifies the language that was originally created by the application of individual toolsets originating from various methods such as statistical process control, total quality management, theory of constraint, six sigma, and lean. The DMAIC framework enables the lean–six sigma practitioner to develop a roadmap on how to resolve business issues that affect quality and productivity.

Fig. 2 DMAIC cycle



2 Literature Survey

We have considered twenty-three scholarly articles to find out the evolution of lean and six sigma independently. Further, the tools were identified which characterize lean and six sigma along with the common tools under execution. These tables form the basis of creating a model/framework depicting the permeability of lean and six sigma as both strive to achieve perfection. The literature review is divided into three categories: (1) Focus, (2) Outcomes, and (3) Limitations/Future Research.

2.1 Focus

From the literature, we found out the history of lean and six sigma. We also reviewed to find out the tools individually characterising both and then proceeded to find the common tools under use.

2.2 Outcomes/Conclusions

The lean was discovered when a project was launched by MIT to determine the crisis in the automobile sector throughout the world. The International Motor Vehicle Program (IMVP) clearly stated that Toyota, Japan, is able to sustain growth and maintain its quality through a different production technique, called lean. Since then, lean has evolved in the world (Table 1).

Table 1 Evolution of lean [1, 2, 5, 8–18]

Sl. No.	Phase/period	Lean
1	Discovery (1970–1990)	MIT’s International Motor Vehicle Program results published
2	Dissemination (1991–1996)	Countries began to learn lean-think lean (TQM, JIT, KANBAN, KAIZEN)
3	Implementation (1997–2000)	Lean thinking entered into the field of implementation worldwide
4	Enterprise (2001–2005)	Lean gains acceptance as an integrated operational better result-oriented philosophy Value stream methods expand use beyond manufacturing and entered into service sectors
5	Performance (2006–2010)	Lean was measured quantitatively to assess performance HR and cultural aspects were highlighted
6	Sustainability (2010-till date)	Collaborating lean with sustainability to achieve the common goal of excellence in economic, environmental, and social aspects

On similar grounds, in 1986, Motorola Inc., USA, discovered a technique for lower levels of defects (3.4 defects per million opportunities (DPMO)). To achieve this, a deployment process and two data-driven methodologies (DMAIC and DFSS) were used. DMAIC is *Define, Measure, Analyze, Improve, Control* [21, 22]. DFSS is *Design for Six Sigma* [23]. Table 2 depicts its evolution.

Further, tools were identified for each with some common tools forming the base for the model (Table 3).

Table 2 Evolution of six sigma [1–5]

Sl. No.	Phase/period	Six sigma
1	Discovery (1986)	Motorola, USA
2	Dissemination (1986–1993)	Within Motorola to check inconsistencies in semiconductors
3	Spread (1993–2003)	To other competitors as a tool to reduce defects
4	Implementation (2001–2005)	Got implemented worldwide
5	Performance (2005–2013)	Measurement advances resulted in peak results
6	Sustainability (2013-till date)	about excellence in in economic, environmental and social aspects

Table 3 Lean, six sigma, and common tools [6–20]

Sl. No.	Six sigma tools	Lean tools	Lean–six sigma tools (Common)
1	Hypothesis testing	Kanban	Brain storming
2	Control charts	Visual workplace	Process mapping
3	Regression	SMED	Standardization
4	Design of experiments	Single piece flow	Poke-yoke
5	Measurement analysis	Layout planning	5 Whys(?)
6	Taguchi function	Value stream mapping	Seven quality tools and the new seven quality tools

2.3 Future Research/Limitations

It is possible that many new tools can be formed in the future to accelerate the objectives of achieving excellence in lean–six sigma.

All the tools are designed for a different purpose, so all have different compatibility and their domain of operation varies. So, it becomes difficult to compare and find a relation of their diffusibility with each other.

3 Lean–Six Sigma Model

See Fig. 3.

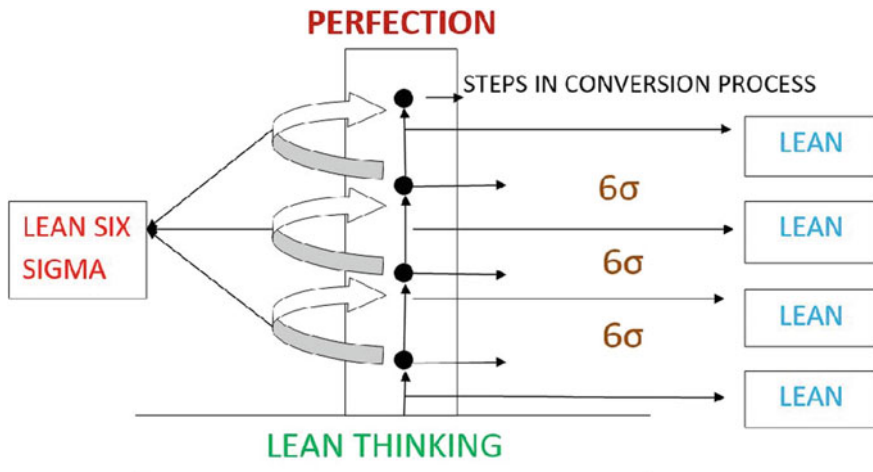


Fig. 3. Lean six sigma framework

4 Discussion and Analysis

Lean–six sigma Fig. 3 is the combination of lean production system and six sigma methodology. Lean concentrates on the way of doing things which include the managerial areas like marketing, finance, and HR as well as the operations like planning (Hoshin kanri), production levelling (Heijunka), and automation with the human mind (Jidoka). Six sigma improves the processes while in operations. Both together accelerate the goal of perfection in industrial world. Perfection essentially means less cost in making a component with high quality or quality in service with same price thus earning higher profits.

The “dots” in the model represent processes (such as machining) which can be set accordingly to complete the job with no error. For that, statistical methodology six sigma is used as a standard. The “arrows” connecting the dots (straight) represent activities such as workforce/machines employed in movement and storage of semi-finished piece of work which at the final stage gives the product, if single or by assembly of components is the product is a larger one. Lean is used in these activities to lessen effort and increase productivity and quality. The “U-shaped arrows” represent the connectivity from process to the next through workforce and technology. Together, the lean–six sigma model is elucidated.

5 Conclusions and Future Scope

We have presented a framework in this research based on the evolutionary trends and tools used which may act as a paper of interest for those who want to see the lean–six sigma at a glance. The evolutionary trends of both have been focused to delineate a smooth miscible model to depict a harmonious picture of these two magnanimous methodologies under industrial operations. The model can be used as a base for researchers for further research in their endeavor to create a more coherence between lean and six sigma in the future research.

References

1. Albliwi S, Antony J, Halim Lim SA, Wiele TV (2014) Critical failure factors of Lean Six Sigma: a systematic literature review. *Int J Qual Reliab Manage* 31(9):1012–1030
2. Andersson R, Eriksson H, Torstensson H (2006) Similarities and differences between TQM, six sigma and lean. *TQM Mag* 18(3):282–296
3. Antony J (2011) Six sigma vs lean. *Int J Prod Perform Manage* 60(2):185–190
4. Arnheiter ED, Maleyeff J (2005) The integration of lean management and six sigma. *TQM Mag* 17(1):5–18
5. Assarlind M, Gremyr I, Bäckman K (2013) Multi-faceted views on a lean six sigma application. *Int J Qual Reliab Manag* 30(4):387–402

6. Basu R (2004) Six-Sigma to operational excellence: role of tools and techniques. *Int J Six Sigma Compet Adv* 1(1):44
7. Corbett LM (2011) Lean six sigma: the contribution to business excellence. *Int J Lean Six Sigma* 2(2):118–131
8. Drohomerski E, Gouvea da Costa SE, Lima De EP, Rosa Garbuio PA (2014) Lean, six sigma and lean six sigma: an analysis based on operations strategy. *Int J Prod Res* 52(3):804–824
9. Hilton RJ, Sohal A (2012) A conceptual model for the successful deployment of lean six sigma. *Int J Qual Reliab Manag* 29(1):54–70
10. Pepper MPJ, Spedding TA (2010) The evolution of lean Six Sigma
11. Jeyaraman K, Kee Teo L (2010) A conceptual framework for critical success factors of lean Six Sigma. *Int J Lean Six Sigma* 1(3):191–215
12. Kumar M, Antony J, Madu CN, Montgomery DC, Park SH (2008) Common myths of Six Sigma demystified. *Int J Qual Reliab Manage* 25(8):878–895
13. Lande M, Shrivastava RL, Seth D (2016) Critical success factors for Lean Six Sigma in SMEs (small and medium enterprises). *TQM J* 28(4):613–635
14. Manville G, Greatbanks R, Krishnasamy R, Parker DW (2012) Critical success factors for Lean Six Sigma programmes: a view from middle management. *Int J Qual Reliab Manage* 29(1):7–20
15. Näslund D (2008) Lean, six sigma and lean sigma: fads or real process improvement methods? *Bus Process Manage J* 14(3):269–287
16. Näslund D (2013) Lean and six sigma—critical success factors revisited. *Int J Qual Serv Sci* 5(1):86–100
17. Raisinghani MS, Ette H, Pierce R, Cannon G, Daripaly P (2005) Six Sigma: concepts, tools, and applications. *Indus Manage Data Syst* 105(4):491–505
18. Ricondo I, Viles E (2005) Six Sigma and its link to TQM, BPR, lean and the learning organisation. *Int J Six Sigma Compet Adv* 1(3):323
19. Salah S, Rahim A, Carretero JA (2010) The integration of Six Sigma and lean management. *Int J Lean Six Sigma* 1(3):249–274
20. Snee RD (2010) Lean Six Sigma—getting better all the time. *Int J Lean Six Sigma* 1(1):9–29
21. Su C, Chiang T, Chang C (2006) Improving service quality by capitalising on an integrated Lean Six Sigma methodology. *Int J Six Sigma Compet Adv* 2(1):1
22. Tenera A, Pinto LC (2014) A Lean Six Sigma (LSS) project management improvement model. *Proc Soc Behav Sci* 119:912–920
23. Thomas A, Barton R, Chuke-Okafor C (2008) Applying lean six sigma in a small engineering company—a model for change. *J Manuf Technol Manage* 20(1):113–129

Study of Customer Relationship Management in Automobile Industry



Lalit Kumar Pothal, Sushanta Tripathy, Kaustuv Kumar,
and Aishwarya Dash

Abstract Customer relationship management is a concept which is widely used for managing an organization's interaction with its customers and its sales prospectus. Customer relationship management is gaining a lot of importance in the present business world, especially in the field of automobile industry. Here, we evaluate how customer relationship management helps in improving the business of the automobile industry especially focusing in the areas of product quality, brand building, customer loyalty and after-sales service. The methodology adopted here is to gather information and data through online research and a ground survey of the automobile dealers in and around and analysing those data using statistical analysis thereby reaching a suitable conclusion.

Keywords CRM · Automobile industry · Statistical analysis

1 Introduction

Customer relationship management is a concept based on methodologies and procedures followed by a company to manage customer-related information throughout the customer's interaction with the company. It centralizes all the information about a customer within an organization such that all the employees of the organization starting from support and marketing have all the required information about the customer [1].

Customer relationship management helps to improve an organization with individual people thereby giving more importance to individuals. In today's world, surviving in any business field is very tough because the competition is very high. Now to last in any business field, an organization needs a strategy for the future

L. K. Pothal · S. Tripathy (✉) · K. Kumar
School of Mechanical Engineering, Kalinga Institute of Industrial Technology (KIIT), Deemed to be University, Bhubaneswar, Odisha 751024, India
e-mail: sushant.tripathy@gmail.com

A. Dash
Industrial and System Engineering, Indian Institute of Technology, Kharagpur, Kharagpur, West Bengal, India

related to sales target, profitability target and business objectives [2–5]. But getting up to date and having information to achieve the goal is very tricky as there is a need for streamlining all sorts of data from various departments. Using customer relationship management helps an organization to streamline related data in relation to a particular topic [6–8]. Customer relationship management is gaining attention and is of paramount importance in the current business world. It is because earlier companies were much more product-centric [3, 4, 9]. Nowadays, companies are becoming much more customer-centric as customers have huge resources of information about a product through the advancement of technologies. Customer relationship management is very vital for every organization for profit making through long-term relationships with customers [1, 10, 11]. Automobile industries face unique challenges in the modern economy with strong competition between new car and used car market. Customer relationship management is the most effective methodology to maintain and create relationship with customer which is very important for the business to thrive successfully. Developing such relationships builds the business to greater heights of success. Nowadays, automobile companies are becoming much more customer-centric rather than the orthodox product-centric [8, 12–14]. As result, great amount of resource is invested in building and maintaining customer relationship. For automobile industry, customers are the most important factor in determining the success of an organization and to maintain this success automobile companies are using customer relationship management to improve their business. Just like Henry Ford said “*it is not the employer who pays the wages, employer only handles the money, it is the customer who pays the wages*”.

Automobile industry is one such industry where the customers do not return to the market for many number of years. Previously companies were much more product-centric. In earlier times, automobile companies considered after-sales service section as negligible source of income. Nowadays, customers have voluminous and insightful information available through Internet, review system and social media. With change in the demand needs and the market trends, automobile companies are becoming much more customer-centric [6, 15]. Nowadays, automobile companies are considering after-sales service section as a volumetric source of income because companies are looking to retain loyal customers, and research has shown that loyal customers help in brand building and bringing new customers to the firm [16]. To achieve all the above goals, customer relationship management is the best solution as customer relationship management is a critical priority to every company who seek to be in profit through long-term relationships with customers. So, that is why customer relationship management is the best approach in maintaining strong relationships with customers [17–19].

The Objective of this paper is as follows.

1. To study the customer relationship management with respect to the customer satisfaction, customer loyalty, brand building and after-sales service of automobile industry.
2. To evaluate the customer’s perception regarding quality of services, pricing, skill level, time of servicing and satisfaction level of customer.

2 Literature Review

Various journals were referred to find out the different key factors in the field of customer relationship management in automobile industry and summarized in Table 1.

After thorough online research and literature review, we found out that majority of the research work in relation to customer relationship management in automobile industry has been done in the field of customer retention. Very less amount of work has been done in relation to CRM in the field customer loyalty, customer satisfaction, brand building and after-sales service section of the automobile industry. So, the aim of our project is to do a research work on how customer relationship management influences and impacts the customer loyalty, customer satisfaction, brand building, after-sales service of the automobile industry and the steps to improve CRM.

3 Methodology

Online study was performed to understand the concept of customer relationship management in automobile industry. Local survey of the automobile dealers and interaction with the managers of various automobile dealers was done on the basis of certain questionnaire. Some of the questions that were asked are as follows

What is your opinion about customer relationship management?

Why is there a need for customer relationship management in automobile industry?

Previously, it had been that companies were much more product-centric. Nowadays, companies are becoming much more customer centric. Why?

How has customer relationship management been helpful in customer satisfaction, customer loyalty, customer retention, brand building, service quality?

Examples of some customer relationship management software used by the firm.

What is the future of customer relationship management in automobile industry?

What are the drawbacks of customer relationship management?

What are the factors affecting customer relationship management in automobile industry? Responses were recorded.

Besides, interaction with various customers was carried out in various automobile dealership shops using questionnaire method. Some of the questions that were asked are

How much satisfied are you with the services provided by the company?

Are the employees helpful in nature?

How has been the behaviour of the employees?

Table 1 Brief summary of literature review

Authors	Objective of the study	Methodology	Results
Reichheld and Sasser (1990)	This study was aimed to find out how customer relationship management impacts on customer retention	Conceptual study	The results obtained showed that a 5% retention of the customers can lead to a change in the profitability of 25–75% in revenues. The results also showed that customers embraced with feel of loyalty tend to buy more number of products from the firm and bring in new customers
Wills (2009)	The study aimed at finding how customer relationship management impacts the revenue of an automobile industry	Conceptual study	The result obtained showed that it costs an organization much less to retain a customer rather than acquiring a new customer
Sathish Balamurugan, Sharma and Karthikeyan (2013)	The aim of this study was to determine how customer relationship management impacts the automobile service industries and how dealers ensure customer satisfaction through after-sales service	The study was done on the basis of data provided by the car dealers in Coimbatore	The results obtained from the above study indicate that the customer expectation from the after-sales service is rising. With the introduction of high-technology cars, customer satisfaction from the dealers is surging in terms of service facilitation. In 14 other words to achieve success in the current business scenario, the first thing required is to create a bond with the customer rather than selling the products

(continued)

Table 1 (continued)

Authors	Objective of the study	Methodology	Results
Dibesssh (2016)	The study performed was to understand the impact of customer relationship management in relation to customer retention in automobile industry	The study was performed by using a set of questionnaire as parameters of study and using those to receive data	The study indicated that the customers who were part of the study were highly satisfied with the dealer. It also indicated that customer satisfaction is a prerequisite for customer loyalty and customer retention
Elena (2015)	The study tries to understand how social media helps in the development of customer relationship management	Conceptual study	The study shows that the organizations use social media as a customer relationship management tool, and they have a better understanding and bonding with the customers
Mathur and Samma (2010)	To study the role of customer relationship management related to customer retention	Conceptual study	The findings from the above show that the customer's loyalty and preference for an organization can change at any time. In such cases, the customer relationship management of the organization will encourage the customer to visit their organization from time to time
AMR research report 1999 from Wartner	The study was aimed to find the importance of after-sales sector in automobile industry	Conceptual study	The study showed that the industries are getting about 45% of its profit from the after-sales market
Danish Ahmed and Sanatullah (2010)	The study aimed to find how availability of spare parts, mechanic have a positive impact on customer buying impact	Conceptual study	The study showed that automobile industry's future depends upon the service quality provided by them

How much are you aware of the organization’s various schemes and discount?

How far have the employees been able to detect the problem?

Questionnaire survey technique was used to obtain information from the customers. Percentages and bar graphs are used for interpreting the data.

Interpretation of the response obtained from the managers and the customers was done and final results were obtained in the field of customer satisfaction, customer loyalty, brand building and the after-sales service section of the automobile industry in relation to customer relationship management.

4 Results and Discussion

4.1 Customer Relationship Management Related to Customer Satisfaction and Customer Loyalty in Automobile Industry

Availability of service: It is an important factor for customer satisfaction which depends upon two variables, i.e. availability of the service and receiving the service.

Prompt service: It is an important factor which depends upon the promptness of the service. Replacement: It is an important factor which depends upon the promptness in replacing the products or parts.

User-friendly: It is one of the most important factors which depends upon the behaviour of the customer service people. The more user-friendly the customer care section is, better is the customer satisfaction.

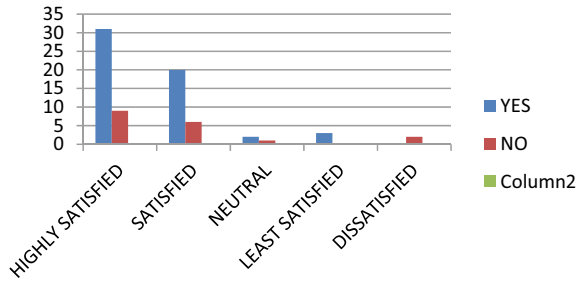
Other factors: Other important factors include online booking service and pick up and drop facility after servicing and a proactive approach to the customers to maintain long-term relationship with them. Satisfaction and loyalty: Table 2 shows the relation between satisfaction of the respondents and they recommended the vehicle and service to their friends or relatives.

Satisfaction and loyalty: Table 2 shows the relation between satisfaction of the respondents and they recommended the vehicle and service to their friends or relatives (Fig. 1).

Table 2 Customer satisfaction and loyalty

Parameters	Recommended to others		Total
	Yes	No	
Highly satisfied	31	9	40
Satisfied	20	6	26
Neutral	2	1	3
Least satisfied	3	0	3
Dissatisfied	0	2	2

Fig. 1 Satisfaction and loyalty



4.2 Customer Relationship Management Related to Brand Building in Automobile Industry

To build a brand image for any automotive manufacturing company, the company should give a clear picture of the uniqueness of its business [4]. Customer relationship management is a great tool as it helps in gathering knowledge to know its audiences and their preferences which in turn assists marketing and sales expert to achieve to devise a strategy to reach out to its customers. In today’s world, the competitiveness in the automotive industry is so high that brand building requires a personalized touch. Customer relationship management software helps in having a deeper understanding of the customers and their preferences in order to reach out to them in a much more personalized manner. One of the core aspects of brand building is to have a consistent relationship with the customer. Everything said or advertised about the company should reach out to the customers through all channels. Customer relationship management will help to attain that consistency by tracking all the communications between the brand and the customer.

4.3 Customer Relationship Management Related to the After-Sales Service Section of the Automobile Industry

See Table 3.

Table 3 Company’s rating for the after-sales services provided

Expectation level	No. of respondents	Percentage (%)
Excellent	28	60.86
Good	14	30.4
Average	3	6.5
Poor	1	2.2

Table 4 Quality of service provision

Expectation level	Never		Often		Rare	
	No. of respondents	%	No. of respondents	%	No. of respondents	%
Percentage of negative speaking by personnel	38	82.6	3	6.5	5	10.86
Average service experience of the people	(<4 years) 25	54.37	(4–8 years) 15	32.6	(>8 years) 6	13.04
Capacity to identify the problem	10	21.7	30	65.2	6	13.04

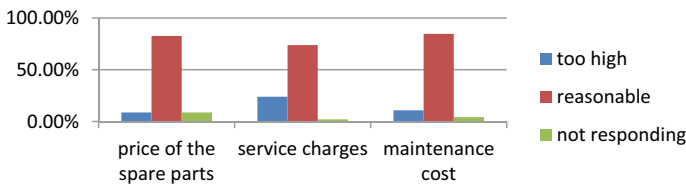


Fig. 2 Price vis-a-vis expectation level

4.4 Expectation Levels on the Quality of Service Provided by the Company

See Table 4.

4.5 Expectation Levels of the Customers Regarding Prices

See Fig. 2 and Table 5.

4.6 Opinion About the Manager

See Fig. 3 and Table 6.

Table 5 Expectation level and price

Expectation level	Too high		Reasonable		Not responding	
	No. of respondents	%	No. of respondents	%	No. of respondents	%
Price of the spare parts	4	8.7	38	82.6	4	8.7
Service charges	11	23.9	34	73.9	1	2.1
Maintenance cost	5	10.86	39	84.72	2	4.3

OPINION ABOUT THE MANAGER

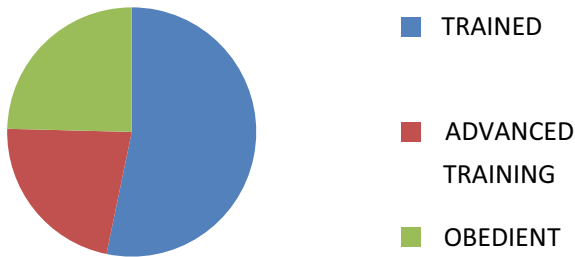


Fig. 3 Opinion about managers

Table 6 Service manager training levels

Background information about the service manager	No. of respondents	Percentage (%)
Trained	22	47
Advance training	9	19.56
Obedient	10	21.7

4.7 Inconvenience by the Time Taken for Servicing

See Table 7.

Table 7 Service inconvenience by respondents

Inconvenience caused	No. of respondents	Percentage
Yes	33	72
No	13	28

Fig. 4 Satisfaction level

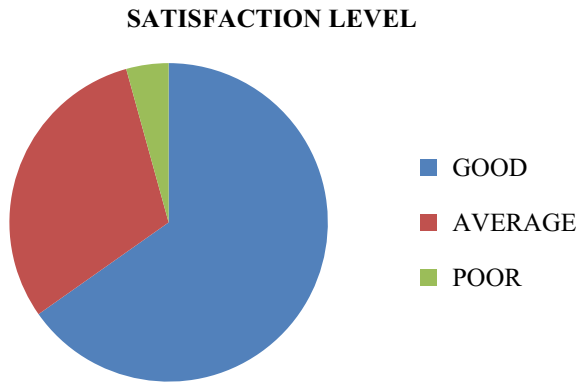


Table 8 Level of satisfaction

Satisfaction level	No. of respondents	%
Good	30	65.2
Average	14	30.4
Poor	2	4.3

4.8 Satisfaction Level of the Customer

See Fig. 4 and Table 8.

5 Findings and Suggestions

From the above study, it can be seen that 65.86% customers have rated the services provided by the company as excellent and 30.4% as good. It is advisable to the firm to conduct a research to find where they are facing problem and why they have failed to achieve 100%. The capacity of finding the problem is around 66%. The firm under study should take more initiative so that its employees can have a greater ability of understanding the problem. 84% of the customers are satisfied with the prices of the products. It is advisable to the firm maintain this track record and take new initiatives to improve it. 47% of the customers find the service manager trained and 20% find it highly trained. It is expedient on the part of the firm to conduct training sessions to improve these percentages. 72% of the customers have gone through a lot of inconvenience by the time taken for servicing the vehicle which results in a poor brand image. It is recommended to the firm not to provide any inconvenience to its customer.

The foremost thing that a CRM should be used is for collecting, storing and keeping track records of the personal details of the customer. In other words, CRM should not only be used to store the sales history of the customer but also be used

for storing personal information thereby having an insightful understanding of the customer as an individual. In automobile industry, majority of the business comes from 20 to 30% of the customers. Therefore, it is vital to properly tune up the CRM to keep track of the customers which in return will help allocating the resources such that those fraction of the customers will always get the best customer service. It is extremely important to improve the existing relationship with the customers. CRM should be tuned up in such a way that it uses the personal information and the details of the customer in the CRM database and thereby to send out regular and timely progressive updates about the business and the organization. It will make them feel more valued, involved and part of the business family which in turn will make them prefer the organization preferentially for business. One of the most important business segments wherein CRM should be used is customer complaint. CRM should be tuned up in such a way that it quickly responds to queries and the complaints of the customer. In today's world, a CRM should be integrated with the social media platform. It allows the users to insert without hassle new contact's mail address and detect virtually every social media profile related to the mail.

6 Conclusion

So from the above research, we can see how customer relationship management is becoming a pivotal part of the automobile industry and how implementation of customer relationship management has drastically improved the automobile industry especially in the field of customer loyalty, customer satisfaction, customer retention, brand building and service quality thereby taking the competitiveness of the automobile industry to a higher notch.

The study was cross-sectional in nature and the primary data were collected through longitudinal study as is considered best for customer loyalty development studies. The effort has not taken into consideration the past behaviours of customers. The statistical data could have been more accurate and precise with a larger sample size.

References

1. Chen J, Popovich K (2003) Understanding customer relationship management (CRM): people, process, technology. *Bus Process Manag* 9(5)
2. Day GS (1969) A two dimensional concept of brand loyalty. *J Advert Res* 9:29–35. Reichheld FF, Sasser WE (1990) Zero defections: quality comes to services. *Harv Bus Rev* 68(5):105–111
3. Ghavami AO (2006) The impact of CRM on customer retention. Master thesis, Lulea University of Technology
4. Hawkes P (1994) Building brand loyalty and commitment. *J Bus Manag* 1:337–347
5. Ismail HB et al (2007) Technology dimension of CRM: the orientation level and its impact on the business performance of SMEs in Malaysia. *Int J Electron Cust Relat Manag* 1(1)

6. Kumar V, Reinartz W (2006) *Customer relationship management: a data based approach*. New York, Wiley
7. Mellens M, Dekimpe MG, Steenkamp JBEM (1996) A review of brand loyalty measures in marketing. *Tijdschr Econ Manage* 41(4):507–533
8. Milovic B (2012) Application of CRM strategy in different business areas. *Econ Organ* 9(3):341–354
9. Mithas S et al (2005) Why do customer relationship management applications affect customer satisfaction? *J Mark* 69(4)
10. Mukherjee K, Singh K (2009) CRM: a strategic approach. *Icfaian J Manag Res* VIII(2):68–82
11. Paltimer RW, Dant RP, Grewal D, Evans KR (2006) Factors influencing the effectiveness of relationship marketing: a meta-analysis. *J Mark* 70(4):136–153
12. Payne A, Frow P (2005) A strategic framework for customer relationship management. *J Mark* 69(4):167–176
13. Peelen E, Van Montfort K, Beltman R, Klerkx A (2009) An empirical study into the foundations of CRM success. *J Strateg Mark* 17(6):453–471
14. Parvatiyar A, Sheth JN (2001) CRM: emerging practices, process and discipline. *J Econ Soc* 4(1):43–54
15. Rigby DK, Ledingham D (2004) CRM done right. *Harv Bus Rev* 82(11):118–129
16. Sirinivasan R, Moorman C (2005) Strategic firm commitments and rewards for customer relationship management in online retailing. *J Mark* 69(4)
17. Coltmana T, Devinney TM, Midgley DF (2011) Customer relationship management and firm performance. *J Inf Technol* 26(3):205–219
18. Xu M, Walton J (2005) Gaining customer knowledge through analytical CRM. *Ind Manag Data Syst* 105(7):955–971
19. Zineldin M (2006) The royalty of loyalty: CRM, quality and retention. *J Consum Mark* 23(7):430–437

Supplier Relationship Management Is a Key to Supply Chain Management



**Purab Mohapatra, Sushanta Tripathy, Aishwarya Dash,
and Anshumaan Biswal**

Abstract Given today's market conditions and economy, be it a product-based company or service-based organization, being efficient is not enough. In order to prosper in one's market, a healthy and co-operative supply chain is a must. There is a common misunderstanding regarding supply chain management and logistics. Logistics emphasizes only on cost minimization, whereas supply chain management (SCM) along with cost minimization includes the aspect of soft factors. This research has been carried out to narrow down the factors responsible for maintaining long-term relationships with both players up and down the supply chain. This soft skilled aspect of SCM is known as supplier relationship management (SRM). The concluding result of our research was the list of factors that were best suited for a variety of industries in current scenario of the Indian market for benefiting SRM.

Keywords Supply chain management (SCM) · Supplier relationship management (SRM) · Logistics

1 Introduction

Supply chain itself means aggregating all the actors involved in fulfilling the request of the customer. It involves not only manufacturers and distributors, but also actors like carriers, warehouses, distributors and even customers. The supply chain also includes the tasks to receive and complete the customer's application. Supply chain management for logistics is often misunderstood. Logistics is a very significant

P. Mohapatra
Xavier Institute of Management, Bhubaneswar, Odisha, India

S. Tripathy (✉) · A. Biswal
Kalinga Institute of Industrial Technology (KIIT) Deemed to be University, Bhubaneswar,
Odisha, India
e-mail: sushant.tripathy@gmail.com

A. Dash
Industrial and System Engineering, Indian Institute of Technology, Kharagpur, Kharagpur, West
Bengal, India

element of the manufacturing process and the fulfilment of client requests, but it assumes that all the interactions between the process performers are healthy and never takes into account the soft factor element when dealing with individuals in the chain. Whereas supply chain management has a specified section for the consideration of the soft factors in the supply chain, i.e., supplier relationship management (SRM). The role of SRM is to streamline and make more effective the processes between the supplier and enterprise in the chain. There is a very close integration between SRM and internal supply chain management (ISCM) as integrating supplier constraints is very crucial. The challenges faced by firms in this aspect are the integration of information between the various actors of the supply chain. Among the three objects that flow in the supply chain, i.e., information, product and fund; it is information which is very essential for the smooth running of the supply chain. The strategy that our project is based upon is trial and error. At first, our team reviewed large amount of literature and decided on certain factors for many objectives under SRM. The factors chosen then were completely theoretical and needed practical testing via a questionnaire survey. Upon survey, the factors which were not rated to that extent of others and had negative standard deviation were eliminated from the questionnaire. For the initial survey, 200 companies took the survey which spanned for 5–6 months. The data gained from the survey was completely anonymous and in no way biased. Even companies were asked to take the survey not with a narrow vision but with a holistic vision for both supplier and consumer. Suggestions regarding supplier relationship were also taken from the survey participants. The objective of our survey was to find the best components for the following subject like objective to maintain long-term SRM, challenges to face, supplier competency, continuous improvement orientation, facts based on finance, management vision and mission.

2 Literature Review

Author(s)	Findings
Lei et al. [15]	In order to shorten the distance between enterprises and between enterprise and individual, ability to integrate information via rapid development of information technology and computer network are essential
Watson [28] and Cox [3]	Long-term commitment and mutual trust between supply chain players are fragmented by imbalance in dependency
Lee et al. [14]	Considering outsourcing and due dates of customer orders the best schedule is drawn using alternative operation sequences and machines
Mills et al. [17]	Better balance and synergy between perspectives for business top management's involvement need to make sure the co-ordination of these activities

(continued)

(continued)

Author(s)	Findings
Kwon and Suh [13]	Successful supply chain performance is ensured by the presence of mutual trust
Chen et al. [2]	Supply uncertainties and imprecise data can be dealt with fuzzy set theory adequately
Stevenson and Spring [24]	Empirical research via cross-sectional questionnaire at firm level fails to improve inter-organizational supply chain flexibility's components
Sandberg [21]	An active role of top management when it comes to new dynamic capabilities should be considered
Kähkönen [10]	Supply chain relationships focus on dyadic relationships which are already present in buyer supplier relationship
Tang and Musa [25]	Mitigation, location and existence of risk exhibits a research challenge in supply chain management
Handley and Benton [8]	Both positive and negative effects of the influence of power on collaboration within the supply chain were identified
Shi and Yu [22]	In order to realize the full financial advantages of effective SCM integration with IT, outsource ability, SC alignment and SC relationship management are essential
Tripathy and Aich [26]	The key to SCM achievement of competitive SCM practices in India is held by IT
Xiong [30]	Ways to avoid credit problems is an important direction in supply chain study
Donato et al. [5]	The way interaction among actors affects partner selection allowing them to identify and deal with the positive and negative aspects of the relationship
Wang et al. [27]	Prompt response to feedback trouble from maker is very essential because of competition in the markets
Kunttu and Kohtamaki [12]	Joint learning mediates the link between resources and relational transaction efficiency in supplier–customer relationships
Liu et al. [16]	Private control and collective control are two distinct control practices, and pure private or collective control is almost non-existent, even though one type of control may prevail in a particular buyer supplier relationship
Dubey and Gunasekaran [6]	Top Management commitment positively mediates the effects of external institutional pressures on supplier relationship management
Nimeh et al. [18]	Production companies should focus on building long-term relationships with key customers to avoid future problems and respond to their complaints and requirements in a timely manner
Kam and Lai [11]	Mutual trust can be attained through asymmetrical trust in dyadic exchange relationships

Literature review of the above-stated authors and their findings helped us define the components of the various subjects that influence SRM hugely.

3 Methodology

3.1 Survey Data Analysis

See Tables 1, 2, 3 and 4.

Table 1 Respondents from different companies

Sector of the company	No. of companies	No. of respondents
Automobile	2	2
Cement	1	1
Chemicals and fertilizers	1	1
Food processing	4	4
Healthcare	2	2
Machinery and equipment	3	3
Mining and construction	2	2
Rubber and plastics	4	4
Steel	6	7
Textiles	3	3
Petroleum and refineries	4	6
Composites	1	1
Seeds and biotechnology	1	1
IT solutions	1	1
Transportation	1	1
Non-government organization	1	1
Total	37	40

Table 2 Workforce size of companies

Workforce size	Frequency	% of responses
Less than 50	13	32.5
50–500	13	32.5
500–1000	2	5
More than 1000	12	30
Total	40	100

Table 3 Experience of respondents

Experience	Frequency	% of responses
Less than 5 years	5	12.5
5–10 years	8	20
10–15 years	5	12.5
15–20 years	6	15
More than 20 years	16	40
Total	40	100

Table 4 Annual turnover of respondents

Annual turnover	Frequency	% of responses
Less than 1 crore	13	32.5
1–10 crore(s)	6	15
10–20 crores	3	7.5
More than 20 crores	18	45
Total	40	100

4 Statistical Analysis

4.1 Principal Component Analysis

Figures 1 and 2 show us the means of the various components of the subjects that govern SRM. The information gathered from Figs. 1 and 2 helped us decide upon the dependent and independent factors for regression analysis (as per the values obtained).

4.2 Regression Analysis

After going through previous stages, we went for regression analysis in which one factor was taken as dependent factor, decision of taking the dependent factor was based on group discussion, and the independent factors were taken having mean value close to subject's mean.

Objective to maintain long-term SRM

Long-Term Commitment = 1.07 + 0.40 Mutual Trust + 0.1 Open Communication + 0.500 Role and Responsibility, R^2 (adj.) = 68.51%.

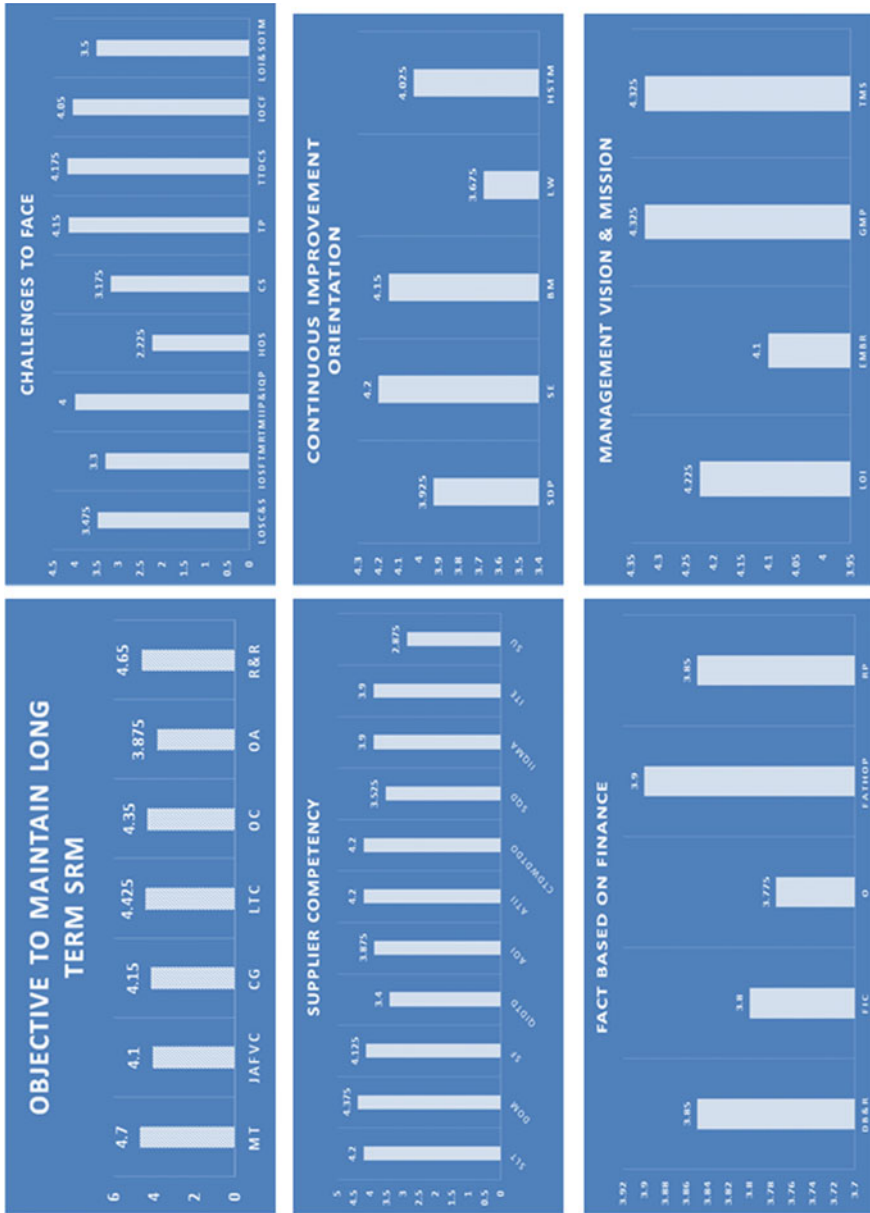


Fig. 1 Graph of mean values of components for each subject

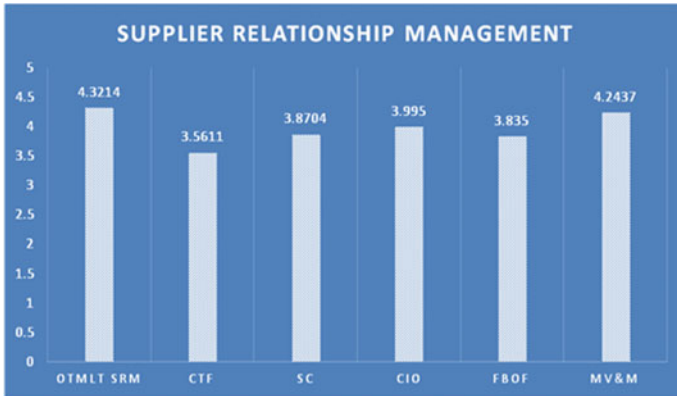


Fig. 2 Graph of mean of the subjects influencing SRM

Objective to maintain day to day operation

Capability to deal with day to day operation = 0.814 + 0.152 Supply Lead Time + 0.204 Delivery of Material + 0.441 Ability to integrate Information, R^2 (adj.) = 70.76%.

Objective to maintain supplier evaluation

Supplier Evaluation = 1.390 + 0.533 Supplier Development Programmes + 0.1788 Higher Speed to Market, R^2 (adj.) = 68.37%.

Objective to financially hold on price

Financial Ability to hold on price = 2.419 + 0.318 Dedicated Budget and Resource + 0.176 Formal Informal Contracts + 0.2862 Outsourcing, R^2 (adj.) = 68.27%.

Objective to maintain good management practice

Good Management Practice = 1.633 + 0.165 Level of Involvement + 0.461 Top Management Support, R^2 (adj.) = 67.03%.

The above-depicted analysis also tells us how close our survey is to market acceptability. As per our target we expected a R^2 value close to 70% and we also obtained the same in our final results.

5 Results and Discussion

In this section, we will discuss about the subjects that we have undertaken for a successful SRM. For objective to maintain long-term SRM, according to Wonglor-saichon [29] satisfaction of relationship between different actors, commitment to the

relationship and trust had a positive effect the long-term orientation of the relationship between seller and retailer. Redondo and Fierro [20] conducted an examination which showed through results that co-operation, trust, communication, satisfaction and commitment can explain a long-term orientation in SRM. For challenges to face, communication and information sharing, training of workers, similarities in technology and industry influence the effectiveness of supplier-buyer relationship [23]. Supplier competency as a whole refers to the ability of a supplier to deal with supply and demand efficiently by incorporating the principles of industrial management such as lead time and various models for minimizing cost and increasing output. Being responsive to supply chain is a competitive strategy in networked economy [7]. Continuous improvement orientation is the amalgam of a measurement system, strategic system and a communication tool [19]. Jha et al. [9] established a close link between continuous improvement and quality in their survey. Caffyn [1] defined continuous improvement as the ability of an organization to gain strategic advantage by extending involvement in innovation. The above-stated readings compelled us to consider continuous improvement orientation as a vital subject for SRM. For facts based on finance, Cronie [4] described financial supply chain requirement as effective internal process, effective collaboration with partners, the right structures and effective financing techniques. Managers are the pivotal point in the supply chain as they are the ones who are responsible for implementing their prowess to the smooth maintenance of supplier relations.

6 Conclusion

Upon doing our research on SRM, we were able to draw certain conclusions regarding the shortcomings and successful practices in the current market scenario. It is evident that we have focused and analysed all the subjects that influence SRM. The different factors as per our research are lack of supplier competency, ignorance of soft factors and top management involvement in planning and implementing quality programs, harassment of suppliers, cultural difference, timely payment, inclusion of customer feedback, lack of involvement and sponsorship of top management. Through this research, we illustrate that factors like mutual trust, open communication, role and responsibility, supply lead time, delivery of material, ability to integrate information, supplier development programmes, higher speed to market, dedicated budget and resource, formal-informal contracts, outsourcing, level of involvement and top management support are the drivers of the dependent factors such as long-term commitment, capability to deal with day-to-day operation, supplier evaluation, financial ability to hold on price and objective to maintain good management practice. The dependent factors stated above are the pre-cursors to successful SRM. The result also indicates that objective to maintain long-term SRM and management vision, and mission are the deciding factors for the betterment and outcome of SRM.

References

1. Caffyn S (1999) Development of a continuous improvement self-assessment tool. *Int J Oper Prod Manag* 19(11):1138–1153
2. Chen et al (2005) A fuzzy approach for supplier evaluation and selection in supply chain management. <https://doi.org/10.1016/j.ijpe.2005.03.009>
3. Cox A (2001) The art of the possible: relationship management in power regimes and supply chains. <https://doi.org/10.1108/13598540410560739>
4. Cronie G (2008) ING guide to financial supply chain optimisation. In: *ING wholesale banking*, pp 54–65
5. Donato M, Ahsan K, Shee H (2015) Resource dependency and collaboration in construction supply chain: literature review and development of a conceptual framework. *Int J Procure Manage* 8(3):344
6. Dubey R, Gunasekaran A, Childe SJ, Papadopoulos T, Helo P (2019) Supplier relationship management for circular economy: influence of external pressures and top management commitment. *Manage Decis* 57(4):767–790
7. Gunasekaran A et al (2008) Responsive supply chain: a competitive strategy in a networked economy. *Omega* 36(4):549–564
8. Handley SM, Benton WC (2009) Unlocking the business outsourcing process model. *J Oper Manag* 27(5):344–361
9. Jha K et al (1996) A supply chain network design model for biomass co-firing in coal-fired power plants. *Transp Res Part E Logist Transp Rev* 61:115–134
10. Kähkönen AK (2011) Conducting a case study in supply management. *Oper Supply Chain Manage* 4(1):31–41
11. Kam, Lai (2018) Buyer-supplier exchange relationship: how do exchange partners behave across the relationship life-cycle? <https://doi.org/10.1016/j.tre.2017.12.007>
12. Kunttu, Kohtamaki (2017) The relationship between supplier resources and governance efficiency – the impact of learning
13. Kwon IW, Suh T (2004) Factors affecting the level of trust and commitment in supply chain relationships
14. Lee HL (2002) Aligning supply chain strategies with product uncertainties. *Calif Manage Rev* 44(3):105–119
15. Lei D et al (2001) Supply chain contracts under demand and cost disruptions with asymmetric information. *Int J Prod Econ* 139(1):116–126
16. Liu et al (2017) A diagnostic model of private control and collective control in buyer-supplier relationships. <https://doi.org/10.1016/j.indmarman.2016.11.003>
17. Mills et al (2004) A strategic review of “supply networks”. <http://dx.doi.org/10.1108/01443570410558058>
18. Nimeh et al (2018) Lean supply chain management practices and performance: empirical evidence from manufacturing companies
19. Niven (2002) The application of balanced scorecard in the performance evaluation of higher education 18(2):190–205. <https://doi.org/10.1108/09544780610647892>
20. Redondo Y, Fierro JJ (2011) Post-satisfaction factors affecting the long-term orientation of supply relationships. *J Bus Ind Mark* 26(6):395–406
21. Sandberg (2007) Logistics collaboration in supply chains: practice vs. theory. *Int J Logist Manage* 18(2):274–293. <https://doi.org/10.1108/09574090710816977>
22. Shi M, Yu W (2013) Supply chain management and financial performance: literature review and future directions. *Int J Oper Prod Manage* 33(10):1283–1317
23. Smith, Greenwood (1998) Integrating supply chain and network analyses: the study of net chains
24. Stevenson M, Spring M (2007) Flexibility from a supply chain perspective: definition and review. *Int J Oper Prod Manage* 27(7):685–713
25. Tang O, Musa SN (2011) Identifying risk issues and research advancements in supply chain risk management. *Int J Prod Econ* 133(1):25–34

26. Tripathy S, Aich S (2014) An interpretive structural model of green supply chain management in Indian computer and its peripheral industries. *Int J Procure Manag* 7(3):239–256
27. Wang Y, Wallace SW, Shen B, Choi T-M (2015) Service supply chain management: a review of operational models. *Eur J Oper Res* 247(3):685–698
28. Watson G (2001) Sub regimes of power and integrated supply chain management. *J Supply Chain Manag* 37(1)
29. Wonglorsaichon (2004) The effect of customer loyalty program and service quality on customer loyalty: hypermarket in Bangkok
30. Xiong Y (2014) The effects of a trust mechanism on a dynamic supply chain network. *Expert Syst Appl* 41(6):3060–3068. <https://doi.org/10.1111/j.1745-93X.2001.tb00098.x>

Identification of Factors Influencing Mental Workload in Manual Sorting



N. Sai Rama Krishna Harish , Madineni Vamshi , K. Bhanu Prakash , Putta Ezra , Francis J. Emmatty , and Vinay V. Panicker 

Abstract Repetitive manual sorting tasks cause mental fatigue leading to the poor performance of workers. Due to the excessive mental workload, the worker takes more time to complete the task and may commit errors. Depending upon the importance of the task at hand, errors might have serious repercussions on the organization as well as on the environment. The present work studies the effect of mental workload on the subjects (workers) performing sorting task on a linear worktable consisting of three workstations and having 120 items of varying size, colour and shape, within a laboratory setup. Different levels of workload were induced on subjects by designing experiments of varying difficulty. The number of items to be sorted, the number of items left as residue and the shape and size of the items differ according to the subject. For the range included in the experiment, there is no significant effect on the height of the sorting table. The mental workload is assumed to be related to the time taken by the worker to complete the task and on the number of errors that the worker has committed.

Keywords Manual sorting · Mental workload · Visual task · Sort ratio

1 Introduction

Manual sorting is a widely used technique in micro, small and medium enterprises in India. Some of the real-world applications of manual sorting include the food industry, waste processing, e-commerce industry, etc. Manual sorting involves both physical and cognitive work. When the worker is exposed to continuous repetitive work, they experience mental fatigue. Excessive workload results in errors, leading to decreased efficiency of performing the task and is a loss to society. Hence, the estimation of mental workload helps not only in increasing the efficacy of worker but also in avoiding the fatigue-related health issues. According to Young et al. [1], the

N. Sai Rama Krishna Harish · M. Vamshi · K. Bhanu Prakash · P. Ezra · F. J. Emmatty · V. V. Panicker (✉)
Department of Mechanical Engineering, Industrial Engineering Laboratory, National Institute of Technology Calicut, Kozhikode, Kerala 673601, India
e-mail: vinay@nitc.ac.in

importance of the estimation of mental workload has increased, as modern technology is demanding more cognitive aspect. Thus, the present work focuses on the estimation of mental workload during the sorting task in a laboratory condition. Sort ratio is defined as the ratio of the number of items to be sorted to the number of items in the pallet. In the above-stated scenarios, the following variables are considered: (1) height of the worktable, (2) number of items to be sorted, (3) number of items in the pallet, (4) sort ratio, (5) position of the workstation where the subject is performing sorting task and (6) subject (or worker).

The rest of the paper is structured as follows: Sect. 2 presents a brief review of relevant literature. Section 3 describes the problem and the experimental methodology is provided in Sect. 4. Section 5 details the result analysis and findings. The paper concludes in Sect. 6.

2 Review of Literature

According to Bollen and Prussia [2], the workers involved in manual sorting experience a lot of mental fatigue. Similarly, Joli-Coeur [3] presents the risk factors associated with the development of the most prevalent occupational hazard, musculoskeletal disorders (MSDs), leading towards discomfort and/or injury for the worker. Most of the studies carried out to investigate the prevalence of MSDs in the workplace recommend ergonomic intervention at the workplace. Dalager et al. [4] reported the reduction in the consumption of analgesics by doctors before the surgery when the height of the operation table was changed. This proves that the table height is a crucial factor in worker well-being.

In addition, due to the advent of modern technology which demands more cognitive skills, the importance of mental workload has increased [1]. Longo et al. [5] studied the statistical significance of original and modified webpages, in terms of mental workload required by typical tasks and perceived usability. In a study carried out by Wastlund et al. [6], the focus is on optimizing the page layout for onscreen viewing for reducing mental workload.

de Waard [7] conducted an elaborate study on the measurement of mental workload among drivers using electrooculography and electroencephalogram techniques. Verwey and Veltman [8] tested the merits of nine workload assessment techniques with relatively short periods of workload in a car-driving task. Piechulla et al. [9] addressed the problem of increasing mental workload of drivers' through a man-machine interface that redirects the incoming calls to the telephone mailbox, when the workload exceeds a threshold value. Lin and Cai [10] proposed a novel methodology using electrocardiogram signal to construct a measure of mental workload with a continuous real number representation. Casner [11] conducted a test to measure the effectiveness of advanced technological cockpit systems in reducing the pilots' mental workload and error.

Lyu et al. [12] presented a study to estimate the traffic safety and correlates the drivers' behaviour and performance under the cognitive workload. In this work, the

authors have used static traffic signs and driving simulator for a driving task and to expose the subjects to a complex environment. Silva [13] ergonomically estimated the mental workload of workers involved in the tasks, and the sorting activities in a material recycling cooperative in Brazil using observational techniques and NASA-TLX method.

Therefore, the importance to assess the mental workload of sorting task is understood. In this direction, the present work considers the factors such as the height of the worktable, number of items in the pallet and number of items to be sorted for the estimation of mental workload in a laboratory setup.

3 Problem Description

As stated in the above sections, estimation of mental workload in manual sorting is very crucial as it may lead to direct and indirect consequences on the work as well as on the worker. With an objective to measure the mental workload, the present work investigates the relationship between the work environment factors such as height of the work table, number of items in the pallet, the number of items to be sorted, the subject (worker), the position of the work station and sorting ratio and on the mental fatigue experienced by the worker in the sorting task.

4 Experimental Methodology and Design

The sorting task is carried out in a linear sorting table consisting of three workstations. At each workstation, the worker has a pallet with the items to be sorted. The size of the pallet is $50 \times 50 \times 0.3$ cm. The items used for sorting are 10 balls each of diameter 6 cm with varying colours of red, violet, pink, green, yellow and orange; 10 balls each of diameter 3.5 cm with varying colours of red, pink and yellow; 10 coins each of diameter 2.5 cm with varying colours of red, blue and green.

The experiment is carried out under the following scenarios. Scenario 1: In this scenario, only the items to be sorted by the individual subjects are present in the pallet, i.e., the pallet is empty after sorting is done. Scenario 2: With residue—in this scenario, residue along with the items to be sorted by the individual subjects are present in the pallet, i.e., the pallet is not empty after sorting is done (indicating a complex scenario compared to scenario 1) (Fig. 1).

In these stated scenarios, the variables are varied at different levels as shown in the following Table 1

From the experiments, the following data is collected: (1) Total time to complete the task, (2) number of misplace errors, (3) number of forgotten errors and (4) number of dropping errors. The samples of data collected are given in Table 2a, b.

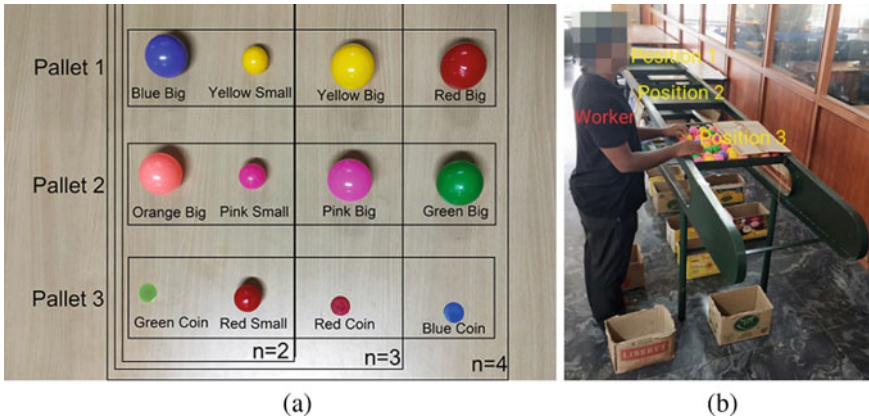


Fig. 1 **a** Different sorting items in each pallet and experimental design, **b** experimental setup

Table 1 Various treatment levels of the parameter in the experimental design

Sl. No.	Parameter	Description
1	Height of the working table (<i>H</i>)	$H = 94 \text{ cm}, H = 102 \text{ cm}, H = 110 \text{ cm}$
2	Subject	Worker 1, Worker 2, Worker 3, Worker 4
3	Position of the subject	Position 1, Position 2, Position 3
4	Varieties of items to be sorted (<i>n</i>)	$n = 2 \quad n = 3 \quad n = 4$
5	Number of items in the pallet at position 1	Without residue: (i) for $n = 2$ is 60 (ii) for $n = 3$ is 90 (iii) for $n = 4$ is 120 With residue: for $n = 2, 3, 4$ is 120
6	Number of items in the pallet at position 2	Without residue: (i) for $n = 2$ is 40 (ii) for $n = 3$ is 60 (iii) for $n = 4$ is 80 With residue: (i) for $n = 2$ is 100 (ii) for $n = 3$ is 90 (iii) for $n = 4$ is 80
7	Number of items in the pallet at position 3	Without residue: (i) for $n = 2$ is 20 (ii) for $n = 3$ is 30 (iii) for $n = 4$ is 40 With residue: (i) for $n = 2$ is 80 (ii) for $n = 3$ is 60 (iii) for $n = 4$ is 40

Table 2 Samples of collected data may require different sections

(a)

Two varieties of items at a time with residue $H = 110$ cm

Subject	Position	Wrong box error	Dropping error	Forgotten error	Total time (s)
1	1	0	0	0	31
2	2	0	0	0	29
3	3	0	0	0	31
4	1	0	1	0	31
1	2	0	0	0	35
2	3	0	1	0	34
3	1	0	0	0	29
4	2	0	0	0	28
1	3	0	1	0	31
2	1	0	0	0	30
3	2	1	0	1	31
4	3	0	0	0	35

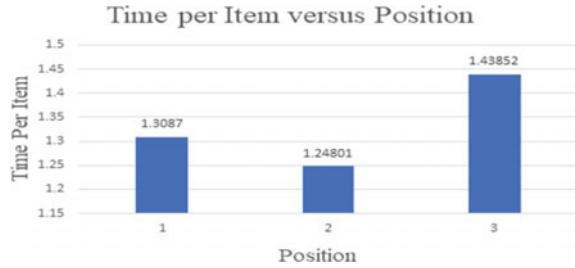
(b)

Two varieties of items at a time without residue $H = 110$ cm

Subject	Position	Wrong box error	Dropping error	Forgotten error	Total time (s)
1	1	0	0	2	21
2	2	0	2	0	18
3	3	0	0	0	20
4	1	0	1	0	23
1	2	0	0	0	24
2	3	0	0	0	19
3	1	0	0	0	19
4	2	0	2	0	21
1	3	0	0	0	23
2	1	0	0	0	19
3	2	0	1	0	26
4	3	0	1	0	25

Similarly, data is collected for all other heights with three trials each for both the scenarios containing a total of 540×8 experimental data sets. Further analysis using the collected data is done with statistical software and SPSS software.

Fig. 2 Time taken by the worker per item at different positions of the worktable



5 Results, Analysis and Findings

Figure 2 shows the relationship between time taken by the worker per item at different positions of the worktable. The time taken per item is found to be more at position 3. The various graphical plots between mean time per item to sort and sort ratio are given in Fig. 3a–e.

From the analysis, it is found that the variation of the subject with respect to sort ratio shows statistical significance with $p = 0.05$. It is found that sorting time decreases with an increase in table height (not shown in the figure) and is statistically significant with $p = 0.05$. As sorting work is light work, this effect of variation due to height may be because of the learning effect of the subjects. The work surface should be below the elbow height for light and heavy work, and above the elbow height for precision work [14]. The variation of the height of the table with respect to sort ratio also shows statistical significance with $p = 0.05$ but contradicts the principle of ergonomics, and the reason may be because of learning being done by the individual subject. In this section, your results and their interpretation should be given. It can be two separate sections if appropriate.

Except in the graphical plot 3a, the remaining plots provides the following pattern in mean time taken per item, i.e., time at position 3 > at position 1 > at position 2. This may be because of the reason that in position 3, the shape and size of items to be sorted are more complex compared to the other two positions, whereas among position 1 and position 2, the time taken for position 1 is the highest because irrespective of the scenario the number of items in the pallet at position 1 are always greater than the number of items in the pallet at position 2 which leads for the subject to take high time. Regarding the errors, the statistical analysis shows significance only for dropping errors and insignificance for misplacing and forgotten errors.

6 Conclusions

Repetitive sorting tasks can lead to mental fatigue among sorting workers. The mental fatigue can result in errors leading to poor defects and damages. In this regard, an experiment on manual sorting has been carried out with a linear sorting table,

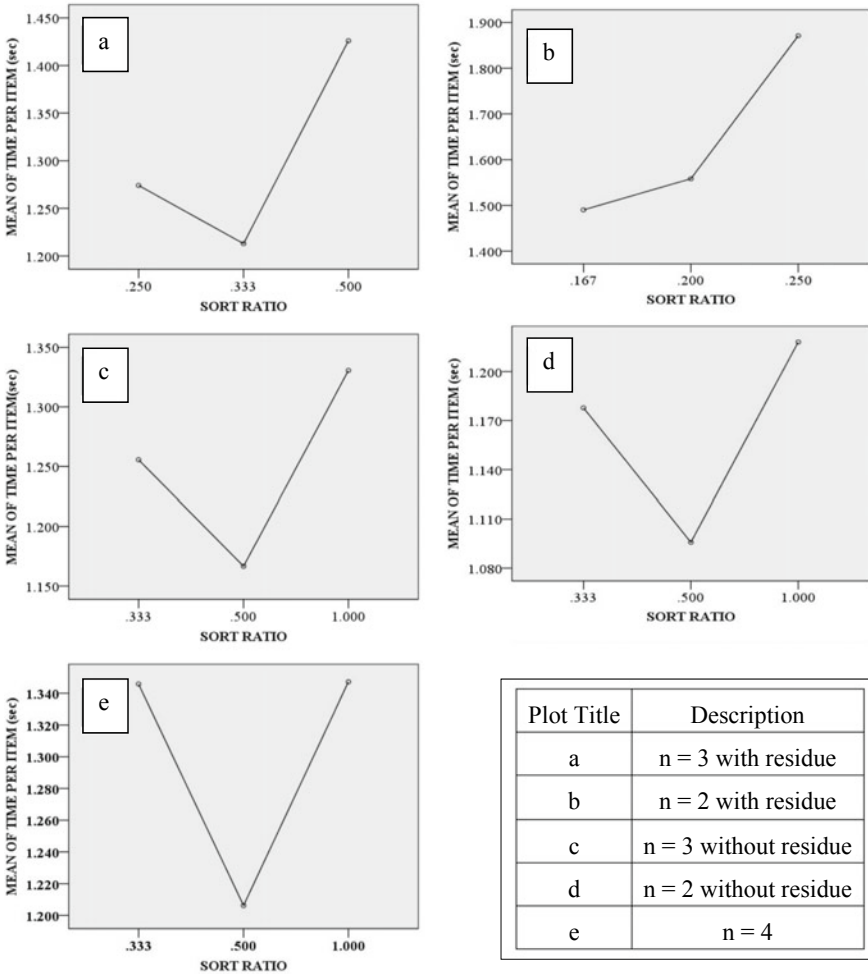


Fig. 3 Graphical plots between mean time per item to sort and sort ratio

composed of three workstations and to be sorted items of different sizes and colours. Based on the experiment, it is identified that the sorting time varies with respect to the subject, number of items to be sorted, number of items left as residue and the shape and size of the items. There is no significant effect on the height of the sorting table for the range considered in the experiment. More research work needs to be carried out to assess mental workload accurately. A causal relationship between the significant factors and sorting time and the weight distribution of different factors influencing mental workload may be established in future works.

Acknowledgements We would like to thank the Director and Dean (Research & Consultancy) of National Institute of Technology Calicut, Kerala, India for providing the financial support to carry out

the project under the scheme of UG Innovative Research projects. We would like to thank Technical Education Quality Improvement Programme (TEQIP) Phase III for giving financial assistance to present the work in the International Conference on Advances in Mechanical Processing's and Design-2019.

References

1. Young MS, Brookhuis KA, Wickens CD, Hancock PA (2014) State of science: mental workload in ergonomics. *Ergonomics* 58(1):1–17
2. Bollen AF, Prussia SE (2014) Sorting for defects. Postharvest handling, 3rd edn. Elsevier, San Diego, pp 341–362
3. Joli-Coeur C (2010) Ottawa valley waste recovery. Industrial Accident and Prevention Association, Ontario
4. Dalager T, Sogaard K, Boyle E, Jensen PT, Mogensen O (2019) Surgery is physically demanding and associated with multisite musculoskeletal pain: a cross-sectional study. *J Surg Res* 240:3039
5. Longo L, Rusconi F, Noce L, Barrett S (2012) The importance of human mental workload in web design. In: Proceedings of the 8th international conference on web information systems and technologies, vol 1, Webist, pp 403–409
6. Wastlund E, Norlander T, Archer T (2008) The effect of page layout on mental workload: A dual-task experiment. *Comput Hum Behav* 24(3):1229–1245
7. de Waard D (1996) The measurement of drivers' mental workload. Ph.D. thesis. Traffic Research Centre, University of Groningen, Haren
8. Verwey W, Veltman H (1996) Detecting short periods of elevated workload. A comparison of nine workload assessment techniques. *J Exp Psychol Appl* 2:270–285
9. Piechulla W, Mayser C, Gehrke H, König W (2003) Reducing drivers' mental workload by means of an adaptive man–machine interface. *Transp Res Part F Traff Psychol Behav* 6(4):233–248
10. Lin Y, Cai H (2009) A method for building a real-time cluster-based continuous mental workload scale. *Theor Issues Ergon Sci* 10(6):531–543
11. Casner, S. M. (2009). Perceived versus measured effects of advanced cockpit systems on pilot workload and error: are pilots' beliefs misaligned with reality? *Appl Ergon* 40(3):448–456
12. Lyu N., Xie L, Wu C, Fu Q, Deng C (2017) Driver's cognitive workload and driving performance under traffic sign information exposure in complex environments: a case study of the highways in China. *Int J Environ Res Publ Health* 14(2), p 203
13. Silva HR (2020) Analysis of the mental workload applied to the sorting activity of recyclable materials. In: Ahram T, Taiar R, Colson S, Choplin A (eds) Human interaction and emerging technologies. IHMET 2019. Advances in intelligent systems and computing, vol 1018. Springer, Cham
14. Sanders MS, McCormick EJ (1993) Human factors in system design. Human factors in engineering and design, 7th edn. McGraw-Hill